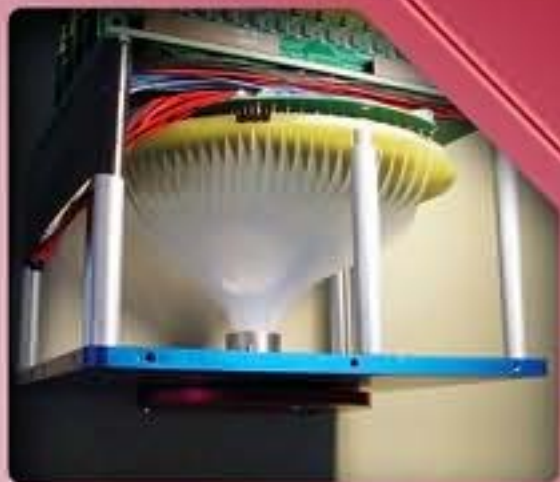


Sadao Adachi

Properties of Semiconductor Alloys

Group-IV, III-V and II-VI
Semiconductors



 WILEY

Wiley Series
in Materials for
Electronic
& Optoelectronic
Applications

Properties of Semiconductor Alloys: Group-IV, III–V and II–VI Semiconductors

Wiley Series in Materials for Electronic & Optoelectronic Applications

Series Editors

Peter Capper, SELEX Sensors and Airborne Systems Infrared Ltd, Southampton, UK
Safa Kasap, University of Saskatchewan, Canada
Arthur Willoughby, University of Southampton, Southampton, UK

Published titles

Bulk Crystal Growth of Electronic, Optical and Optoelectronic Materials, Edited by P. Capper
Properties of Group-IV, III-V and II-VI Semiconductors, S. Adachi
Charge Transport in Disordered Solids with Applications in Electronics, Edited by S. Baranovski
Optical Properties of Condensed Matter and Applications, Edited by J. Singh
Thin Film Solar Cells: Fabrication, Characterization and Applications, Edited by J. Poortmans and V. Arkhipov
Dielectric Films for Advanced Microelectronics, Edited by M. R. Baklanov, M. Green and K. Maex
Liquid Phase Epitaxy of Electronic, Optical and Optoelectronic Materials, Edited by P. Capper and M. Mauk
Molecular Electronics: From Principles to Practice, M. Petty
Luminescent Materials and Applications, Edited by A. Kitai
CVD Diamond for Electronic Devices and Sensors, Edited by R. S. Sussman

Forthcoming Titles

Zinc Oxide Materials for Electronic and Optoelectronic Device Applications, Edited by C. Litton, D. C. Reynolds and T. C. Collins
Mercury Cadmium Telluride: Growth, Properties and Applications, Edited by P. Capper and J. Garland
Photovoltaic Materials: From Crystalline Silicon to Third-Generation Approaches, Edited by G. J. Conibeer
Silicon Photonics: Fundamentals and Devices, J. Deen and P. K. Basu
Inorganic Glasses for Photonics: Fundamentals, Engineering and Applications, A. Jha, R. M. Almeida, M. Clara Goncalves and P. G. Kazansky

Properties of Semiconductor Alloys: Group-IV, III–V and II–VI Semiconductors

SADAO ADACHI

Gunma University, Gunma, Japan



A John Wiley and Sons, Ltd, Publication

This edition first published 2009
© 2009 John Wiley & Sons Ltd

Registered office

John Wiley & Sons Ltd, The Atrium, Southern Gate, Chichester, West Sussex, PO19 8SQ, United Kingdom

For details of our global editorial offices, for customer services and for information about how to apply for permission to reuse the copyright material in this book please see our website at www.wiley.com.

The right of the authors to be identified as the authors of this work has been asserted in accordance with the Copyright, Designs and Patents Act 1988.

All rights reserved. No part of this publication may be reproduced, stored in a retrieval system or transmitted, in any form or by any means, electronic, mechanical, photocopying, recording or otherwise, except as permitted by the UK Copyright, Designs and Patents Act 1988, without the prior permission of the publisher.

Wiley also publishes its books in a variety of electronic formats. Some content that appears in print may not be available in electronic books.

Designations used by companies to distinguish their products are often claimed as trademarks. All brand names and product names used in this book are trade names, service marks, trademarks or registered trademarks of their respective owners. The publisher is not associated with any product or vendor mentioned in this book. This publication is designed to provide accurate and authoritative information in regard to the subject matter covered. It is sold on the understanding that the publisher is not engaged in rendering professional services. If professional advice or other expert assistance is required, the services of a competent professional should be sought.

The publisher and the author make no representations or warranties with respect to the accuracy or completeness of the contents of this work and specifically disclaim all warranties, including without limitation any implied warranties of fitness for a particular purpose. This work is sold with the understanding that the publisher is not engaged in rendering professional services. The advice and strategies contained herein may not be suitable for every situation. In view of ongoing research, equipment modifications, changes in governmental regulations and the constant flow of information relating to the use of experimental reagents, equipment and devices, the reader is urged to review and evaluate the information provided in the package insert or instructions for each chemical, piece of equipment, reagent or device for, among other things, any changes in the instructions or indication of usage and for added warnings and precautions. The fact that an organization or Website is referred to in this work as a citation and/or a potential source of further information does not mean that the author or the publisher endorses the information the organization or Website may provide or recommendations it may make. Further, readers should be aware that Internet Websites listed in this work may have changed or disappeared between when this work was written and when it is read. No warranty may be created or extended by any promotional statements for this work. Neither the publisher nor the author shall be liable for any damages arising herefrom.

Library of Congress Cataloging-in-Publication Data

Adachi, Sadao, 1950–

Properties of semiconductor alloys : group-IV, III–V and II–VI
semiconductors / Sadao Adachi.

p. cm.

Includes bibliographical references and index.

ISBN 978-0-470-74369-0

1. Semiconductors–Materials. 2. Semiconductors–Analysis.

3. Silicon alloys. I. Title.

TK7871.85.A32 2009

621.3815'2–dc22

2008046980

A catalogue record for this book is available from the British Library.

ISBN 978-0-470-74369-0 (HB)

Typeset in 10/12pt Times by Thomson Digital, Noida, India.

Printed and bound in Great Britain by CPI Antony Rowe, Ltd, Chippenham, Wiltshire

Front cover image of a photodiode array reproduced by kind permission of Dr. Jian-young Wu. Courtesy of Wutech Instruments and RedShirtImaging.

Contents

Series Preface	xvii
Preface	xix
Abbreviations and Acronyms	xxi
Introductory Remarks	1
A.1 An Alloy and a Compound	1
A.2 Grimm–Sommerfeld Rule	2
A.3 An Interpolation Scheme	4
References	7
1 Structural Properties	9
1.1 Ionicity	9
1.2 Elemental Isotopic Abundance and Molecular Weight	9
1.3 Crystal Structure	11
1.3.1 Random Alloy	11
1.3.2 Spontaneous Ordering	11
(a) Group-IV Semiconductor Alloy	11
(b) III–V Semiconductor Alloy	14
(c) II–VI Semiconductor Alloy	15
1.4 Lattice Constant and Related Parameters	15
1.4.1 CuAu Alloy: Ordered and Disordered States	15
1.4.2 Non-alloyed Semiconductor	16
1.4.3 Semiconductor Alloy	19
(a) Group-IV Semiconductor	19
(b) III–V Semiconductor	22
(c) II–VI Semiconductor	29
1.5 Coherent Epitaxy and Strain Problem	32
1.5.1 Bilayer Model	32
1.5.2 Elastic Strain and Lattice Deformation	33
1.5.3 Critical Thickness	37
1.6 Structural Phase Transition	39
1.7 Cleavage Plane	41
1.7.1 Cleavage	41
1.7.2 Surface Energy	41
References	42

2 Thermal Properties	45
2.1 Melting Point and Related Parameters	45
2.1.1 Phase Diagram	45
(a) Group-IV Semiconductor Alloy	45
(b) III-V Semiconductor Alloy	45
(c) II-VI Semiconductor Alloy	48
2.1.2 Melting Point	51
2.2 Specific Heat	51
2.2.1 Group-IV Semiconductor Alloy	51
2.2.2 III-V Semiconductor Alloy	54
2.2.3 II-VI Semiconductor Alloy	56
2.3 Debye Temperature	56
2.3.1 General Considerations	56
2.3.2 Group-IV Semiconductor Alloy	57
2.3.3 III-V Semiconductor Alloy	58
2.3.4 II-VI Semiconductor Alloy	58
2.4 Thermal Expansion Coefficient	59
2.4.1 Group-IV Semiconductor Alloy	59
2.4.2 III-V Semiconductor Alloy	61
2.4.3 II-VI Semiconductor Alloy	63
2.5 Thermal Conductivity and Diffusivity	63
2.5.1 Thermal Conductivity	63
(a) General Considerations	63
(b) Group-IV Semiconductor Alloy	66
(c) III-V Semiconductor Alloy	68
(d) II-VI Semiconductor Alloy	74
2.5.2 Thermal Diffusivity	75
(a) General Considerations	75
(b) Alloy Value	75
References	76
3 Elastic Properties	81
3.1 Elastic Constant	81
3.1.1 General Considerations	81
3.1.2 Room-temperature Value	81
(a) Group-IV Semiconductor Alloy	81
(b) III-V Semiconductor Alloy	81
(c) II-VI Semiconductor Alloy	84
3.1.3 External Perturbation Effect	86
(a) Temperature Effect	86
(b) Pressure Effect	88
3.2 Third-order Elastic Constant	89
3.3 Young's Modulus, Poisson's Ratio and Similar Properties	89
3.3.1 Group-IV Semiconductor Alloy	89
3.3.2 III-V Semiconductor Alloy	89
3.3.3 II-VI Semiconductor Alloy	90

3.4	Microhardness	92
3.4.1	Group-IV Semiconductor Alloy	92
3.4.2	III–V Semiconductor Alloy	92
3.4.3	II–VI Semiconductor Alloy	93
3.5	Sound Velocity	96
	References	97
4	Lattice Dynamic Properties	99
4.1	Phonon Dispersion Relationships	99
4.2	Phonon Frequency	99
4.2.1	General Considerations	99
4.2.2	Room-temperature Value	100
	(a) Group-IV Semiconductor Alloy	100
	(b) III–V Semiconductor Alloy	104
	(c) II–VI Semiconductor Alloy	109
4.2.3	External Perturbation Effect	112
	(a) Group-IV Semiconductor Alloy	112
	(b) III–V Semiconductor Alloy	113
	(c) II–VI Semiconductor Alloy	115
4.3	Mode Grüneisen Parameter	119
4.3.1	Phonon Deformation Potential	121
	References	123
5	Collective Effects and Some Response Characteristics	125
5.1	Piezoelectric Constant	125
5.1.1	General Considerations	125
5.1.2	Alloy Value	125
5.2	Fröhlich Coupling Constant	129
5.2.1	General Considerations	129
5.2.2	Alloy Value	129
	References	131
6	Energy-band Structure: Energy-band Gaps	133
6.1	Introductory Remarks	133
6.1.1	Quasi-cubic Band Model	133
6.1.2	Bowing Parameter	136
6.1.3	Ordered Alloy	136
6.2	Group-IV Semiconductor Alloy	139
6.2.1	Binary Alloy	139
	(a) CSi	139
	(b) CGe	140
	(c) SiGe	141
	(d) GeSn	144
6.2.2	Ternary Alloy	145
	(a) CSiGe	145
	(b) SiGeSn	147
6.2.3	Summary	147

6.3	III–V Semiconductor Ternary Alloy	149
6.3.1	(III, III)–N Alloy	149
	(a) <i>c</i> -AlGaN	149
	(b) <i>w</i> -AlGaN	150
	(c) <i>c</i> -AlInN	152
	(d) <i>w</i> -AlInN	152
	(e) <i>c</i> -GaInN	152
	(f) <i>w</i> -GaInN	152
6.3.2	(III, III)–P Alloy	153
	(a) AlGaP	153
	(b) AlInP	153
	(c) GaInP	155
6.3.3	(III, III)–As Alloy	157
	(a) AlGaAs	157
	(b) AlInAs	160
	(c) GaInAs	161
6.3.4	(III, III)–Sb Alloy	163
	(a) AlGaSb	163
	(b) AlInSb	165
	(c) GaInSb	166
6.3.5	Dilute-nitride III–(V, V) Alloy	166
	(a) General Considerations	166
	(b) GaNP	170
	(c) GaNAs	171
	(d) GaNSb	172
	(e) InNP	173
	(f) InNAs	173
	(g) InNSb	174
6.3.6	Al–(V, V) Alloy	174
6.3.7	Ga–(V, V) Alloy	175
	(a) GaPAs	175
	(b) GaPSb	176
	(c) GaAsSb	178
6.3.8	In–(V, V) Alloy	179
	(a) InPAs	179
	(b) InPSb	179
	(c) InAsSb	181
6.3.9	Summary	183
6.4	III–V Semiconductor Quaternary Alloy	184
6.4.1	Dilute-nitride Quaternary Alloy	184
	(a) AlGaInAs	184
	(b) GaInNP	185
	(c) GaInNAs	185
	(d) GaNPAs	185
6.4.2	(III, III)–(V, V) Alloy	186
	(a) AlGaPAs	186
	(b) AlGaAsSb	187

	(c) AlInAsSb	188
	(d) GaInPAs	189
	(e) GaInAsSb	191
6.4.3	(III, III, III)–V Alloy	193
	(a) AlGaInP	193
	(b) AlGaInAs	194
6.4.4	III–(V, V, V) Alloy	195
6.4.5	Summary	196
6.5	II–VI Semiconductor Alloy	197
6.5.1	(II, II)–O Ternary Alloy	197
	(a) BeZnO	197
	(b) MgZnO	197
	(c) ZnCdO	198
6.5.2	(II, II)–S Ternary Alloy	198
	(a) MgZnS	198
	(b) ZnCdS	200
	(c) ZnHgS	200
	(d) CdHgS	200
6.5.3	(II, II)–Se Ternary Alloy	201
	(a) BeZnSe	201
	(b) BeCdSe	202
	(c) MgZnSe	202
	(d) MgCdSe	202
	(e) ZnCdSe	203
	(f) CdHgSe	203
6.5.4	(II, II)–Te Ternary Alloy	204
	(a) BeZnTe	204
	(b) MgZnTe	205
	(c) MgCdTe	206
	(d) ZnCdTe	206
	(e) ZnHgTe	207
	(f) CdHgTe	208
6.5.5	Zn–(VI, VI) Ternary Alloy	208
	(a) ZnOS	208
	(b) ZnOSe	209
	(c) ZnSSe	209
	(d) ZnSTe	210
	(e) ZnSeTe	210
6.5.6	Cd–(VI, VI) Ternary Alloy	210
	(a) CdSSe	210
	(b) CdSTe	211
	(c) CdSeTe	211
6.5.7	(II, II)–(VI, VI) Quaternary Alloy	212
	(a) MgZnSSe	212
	(b) MgZnSeTe	213
6.5.8	(II, II, II)–VI Quaternary Alloy	213
	(a) BeMgZnSe	213

	(b) BeZnCdSe	213
	(c) MgZnCdSe	214
	6.5.9 Summary	214
	References	216
7	Energy-band Structure: Effective Masses	229
7.1	Introductory Remarks	229
	7.1.1 Electron Effective Mass	229
	7.1.2 Hole Effective Mass	230
	7.1.3 Interpolation Scheme	232
7.2	Group-IV Semiconductor Alloy	234
	7.2.1 CSi Binary Alloy	234
	7.2.2 SiGe Binary Alloy	237
7.3	III–V Semiconductor Ternary Alloy	238
	7.3.1 (III, III)–N Alloy	238
	7.3.2 (III, III)–P Alloy	238
	7.3.3 (III, III)–As Alloy	239
	(a) AlGaAs	239
	(b) AlInAs	241
	(c) GaInAs	241
	7.3.4 (III, III)–Sb Alloy	242
	7.3.5 Dilute-nitride III–(V, V) Alloy	243
	(a) Ga–(N, V) Alloy	243
	(b) In–(N, V) Alloy	244
	7.3.6 Al–(V, V) Alloy	245
	7.3.7 Ga–(V, V) Alloy	245
	(a) GaPAs	245
	(b) GaAsSb	246
	7.3.8 In–(V, V) Alloy	246
	(a) InPAs	246
	(b) InAsSb	247
7.4	III–V Semiconductor Quaternary Alloy	248
	7.4.1 Dilute-nitride Quaternary Alloy	248
	7.4.2 (III, III)–(V, V) Alloy	248
	(a) GaInPAs	248
	(b) GaInAsSb	249
	7.4.3 (III, III, III)–V Alloy	250
	(a) AlGaInP	250
	(b) AlGaInAs	250
	7.4.4 III–(V, V, V) Alloy	250
7.5	II–VI Semiconductor Alloy	251
	7.5.1 (II, II)–VI Ternary Alloy	251
	7.5.2 II–(VI, VI) Ternary Alloy	253
	7.5.3 (II, II)–(VI, VI) Quaternary Alloy	253
7.6	Concluding Remarks	254
	7.6.1 Composition Dependence	254
	7.6.2 External Perturbation Effect	254
	References	256

8 Deformation Potentials	259
8.1 Intravalley Deformation Potential: Γ Point	259
8.1.1 Group-IV Semiconductor Alloy	259
8.1.2 III–V Semiconductor Ternary Alloy	261
(a) AlGaN	261
(b) GaInN	262
(c) AlInP	262
(d) GaInP	263
(e) AlGaAs	263
(f) AlInAs	264
(g) GaInAs	265
(h) GaNAs	265
(i) GaPAs	266
8.1.3 III–V Semiconductor Quaternary Alloy	266
8.1.4 II–VI Semiconductor Alloy	266
8.2 Intravalley Deformation Potential: High-symmetry Points	267
8.2.1 Group-IV Semiconductor Alloy	267
8.2.2 III–V Semiconductor Alloy	269
8.2.3 II–VI Semiconductor Alloy	270
8.3 Intervalley Deformation Potential	270
8.3.1 Group-IV Semiconductor Alloy	270
8.3.2 III–V Semiconductor Alloy	271
8.3.3 II–VI Semiconductor Alloy	272
References	272
9 Heterojunction Band Offsets and Schottky Barrier Height	275
9.1 Heterojunction Band Offsets	275
9.1.1 General Considerations	275
9.1.2 Group-IV Semiconductor Heterostructure System	275
(a) CSi/Si	275
(b) SiGe/Si	276
(c) CSiGe/Si	276
(d) CSi/SiGe	277
9.1.3 III–V Semiconductor Heterostructure System: Lattice-matched Ternary-alloy System	277
(a) GaInP/GaAs	277
(b) GaInP/AlInP	277
(c) GaInP/AlGaAs	278
(d) AlGaAs/GaAs	278
(e) AlInAs/InP	279
(f) GaInAs/InP	279
(g) GaInAs/AlInAs	280
(h) InAsSb/GaSb	280
9.1.4 III–V Semiconductor Heterostructure System: Lattice-matched Quaternary Alloy	280
(a) GaInPAs/InP	280

	(b) AlGaAsSb/GaSb	281
	(c) AlGaAsSb/InP	281
	(d) AlGaAsSb/InAs	281
	(e) GaInAsSb/GaSb	281
	(f) GaInAsSb/InP	281
	(g) GaInAsSb/InAs	281
	(h) AlGaAsSb/GaInAsSb	282
	(i) AlInAsSb/GaInAsSb	282
	(j) AlGaInP/AlInP	282
	(k) AlGaInP/GaInP	282
	(l) AlGaInAs/GaInAs	283
9.1.5	III–V Semiconductor Heterostructure System: Lattice-mismatched Alloy System	283
	(a) w -AlGaN/ w -GaN	283
	(b) w -AlInN/ w -InN	284
	(c) w -GaInN/ w -GaN	284
	(d) GaInAs/GaAs	284
	(e) Dilute-nitride-based Heterostructure System	286
9.1.6	II–VI Semiconductor Heterostructure System	287
	(a) (II, II)–O-based Heterostructure System	287
	(b) (II, II)–S-based Heterostructure System	287
	(c) (II, II)–Se-based Heterostructure System	287
	(d) (II, II)–Te-based Heterostructure System	288
	(e) Zn–(VI, VI)-based Heterostructure System	289
	(f) (II, II)–VI-based and II–(VI, VI)-based Heterostructure Systems	289
	(g) (II, II)–(VI, VI)-based Heterostructure System	289
	(h) (II, II, II)–VI-based Heterostructure System	289
9.2	Schottky Barrier Height	289
9.2.1	General Considerations	289
9.2.2	Group-IV Semiconductor Alloy	290
	(a) SiGe Binary Alloy	290
	(b) CSiGe Ternary Alloy	291
9.2.3	III–V Semiconductor Ternary Alloy	291
	(a) (III, III)–N Alloy	291
	(b) (III, III)–P Alloy	292
	(c) (III, III)–As Alloy	292
	(d) (III, III)–Sb Alloy	294
	(e) Ga–(V, V) Alloy	295
9.2.4	III–V Semiconductor Quaternary Alloy	296
	(a) (III, III)–(V, V) Alloy	296
	(b) (III, III, III)–V Alloy	297
9.2.5	II–VI Semiconductor Alloy	299
	(a) (II, II)–Te Ternary Alloy	299
	(b) Zn–(VI, VI) Ternary Alloy	300
	References	300

10 Optical Properties	307
10.1 Introductory Remarks	307
10.1.1 Optical Dispersion Relations	307
10.1.2 Static and High-frequency Dielectric Constants	308
10.2 Group-IV Semiconductor Alloy	308
10.2.1 Binary Alloy	308
(a) CSi	308
(b) CGe	309
(c) SiGe	309
(d) GeSn	310
10.2.2 Ternary Alloy	311
10.3 III–V Semiconductor Ternary Alloy	311
10.3.1 (III, III)–N Alloy	311
(a) <i>c</i> -(III, III)–N Alloy	311
(b) <i>w</i> -AlGaN	312
(c) <i>w</i> -AlInN	313
(d) <i>w</i> -GaInN	313
10.3.2 (III, III)–P Alloy	314
(a) AlGaP	314
(b) AlInP	314
(c) GaInP	315
10.3.3 (III, III)–As Alloy	316
(a) AlGaAs	316
(b) AlInAs	316
(c) GaInAs	318
10.3.4 (III, III)–Sb Alloy	319
(a) AlGaSb	319
(b) GaInSb	319
10.3.5 Dilute-nitride III–(V, V) Alloy	320
(a) GaNP	320
(b) GaNAs	321
(c) GaNSb	321
(d) InNP	322
(e) InNAs	322
10.3.6 Al–(V, V) Alloy	322
10.3.7 Ga–(V, V) Alloy	323
(a) GaPAs	323
(b) GaPSb	324
(c) GaAsSb	324
10.3.8 In–(V, V) Alloy	324
(a) InPAs	324
(b) InPSb	325
(c) InAsSb	325
10.4 III–V Semiconductor Quaternary Alloy	326
10.4.1 Dilute-nitride Quaternary Alloy	326
(a) GaInNP	326
(b) GaInNAs	326

10.4.2	(III, III)–(V, V) Alloy	326
	(a) AlGaPAs	326
	(b) AlGaAsSb	327
	(c) GaInPAs	327
	(d) GaInAsSb	328
10.4.3	(III, III, III)–V Alloy	330
	(a) AlGaInP	330
	(b) AlGaInAs	331
10.4.4	III–(V, V, V) Alloy	332
10.5	II–VI Semiconductor Alloy	332
10.5.1	(II, II)–O Ternary Alloy	332
	(a) BeZnO	332
	(b) MgZnO	332
	(c) ZnCdO	333
10.5.2	(II, II)–S Ternary Alloy	333
	(a) MgZnS	333
	(b) ZnCdS	334
10.5.3	(II, II)–Se Ternary Alloy	335
	(a) BeZnSe	335
	(b) BeCdSe	335
	(c) MgZnSe	335
	(d) MgCdSe	337
	(e) ZnCdSe	337
	(f) CdHgSe	338
10.5.4	(II, II)–Te Ternary Alloy	339
	(a) BeZnTe	339
	(b) MgZnTe	339
	(c) MgCdTe	340
	(d) ZnCdTe	340
	(e) ZnHgTe	342
	(f) CdHgTe	342
10.5.5	Zn–(VI, VI) Ternary Alloy	343
	(a) ZnOS	343
	(b) ZnSSe	343
	(c) ZnSTe	343
	(d) ZnSeTe	344
10.5.6	Cd–(VI, VI) Ternary Alloy	344
	(a) CdSSe	344
	(b) CdSTe	345
	(c) CdSeTe	346
10.5.7	(II, II)–(VI, VI) Quaternary Alloy	346
	(a) MgZnSSe	346
	(b) MgZnSeTe	346
10.5.8	(II, II, II)–VI Quaternary Alloy	346
	(a) BeMgZnSe	346
	(b) BeZnCdSe	346
	(c) MgZnCdSe	346
	References	347

11 Elasto-optic, Electro-optic and Nonlinear Optical Properties	357
11.1 Elasto-optic Effect	357
11.1.1 Group-IV Semiconductor Alloy	357
11.1.2 III–V Semiconductor Alloy	357
11.1.3 II–VI Semiconductor Alloy	357
11.2 Linear Electro-optic Constant	358
11.2.1 Group-IV Semiconductor Alloy	358
11.2.2 III–V Semiconductor Alloy	358
11.2.3 II–VI Semiconductor Alloy	358
11.3 Quadratic Electro-optic Constant	360
11.3.1 Group-IV Semiconductor Alloy	360
11.3.2 III–V Semiconductor Alloy	360
11.3.3 II–VI Semiconductor Alloy	360
11.4 Franz–Keldysh Effect	360
11.4.1 Group-IV Semiconductor Alloy	360
11.4.2 III–V Semiconductor Alloy	360
11.4.3 II–VI Semiconductor Alloy	360
11.5 Nonlinear Optical Constant	361
11.5.1 Group-IV Semiconductor Alloy	361
11.5.2 III–V Semiconductor Alloy	361
11.5.3 II–VI Semiconductor Alloy	362
References	362
12 Carrier Transport Properties	365
12.1 Introductory Remarks	365
12.2 Low-field Mobility	367
12.2.1 Group-IV Semiconductor Alloy	367
(a) CSi Binary Alloy	367
(b) SiGe Binary Alloy	367
12.2.2 III–V Semiconductor Ternary Alloy	368
(a) (III, III)–N Alloy	368
(b) (III, III)–P Alloy	369
(c) (III, III)–As Alloy	369
(d) (III, III)–Sb Alloy	369
(e) Dilute-nitride III–(V, V) Alloy	371
(f) Ga–(V, V) Alloy	371
(g) In–(V, V) Alloy	371
12.2.3 III–V Semiconductor Quaternary Alloy	371
(a) Dilute-nitride Alloy	371
(b) (III, III)–(V, V) Alloy	372
(c) (III, III, III)–V Alloy	373
12.2.4 II–VI Semiconductor Alloy	374
(a) (II, II)–O Ternary Alloy	374
(b) (II, II)–Se Ternary Alloy	374
(c) (II, II)–Te Ternary Alloy	375
(d) Zn–(V, V) Ternary Alloy	376

12.3	High-field Transport	376
12.3.1	Group-IV Semiconductor Alloy	376
12.3.2	III-V Semiconductor Ternary Alloy	376
	(a) (III, III)-N Alloy	376
	(b) (III, III)-P Alloy	376
	(c) (III, III)-As Alloy	377
	(d) Dilute-nitride III-(V, V) Alloy	378
12.3.3	III-V Semiconductor Quaternary Alloy	378
12.3.4	II-VI Semiconductor Alloy	379
12.4	Minority-carrier Transport	379
12.4.1	Group-IV Semiconductor Alloy	379
	(a) SiGe Binary Alloy	379
	(b) CSiGe Ternary Alloy	380
12.4.2	III-V Semiconductor Ternary Alloy	380
	(a) (III, III)-N Alloy	380
	(b) (III, III)-As Alloy	380
	(c) Ga-(V, V) Alloy	381
12.4.3	III-V Semiconductor Quaternary Alloy	381
	(a) (III, III)-(V, V) Alloy	381
	(b) (III, III, III)-V Alloy	382
12.4.4	II-VI Semiconductor Alloy	382
12.5	Impact Ionization Coefficient	382
12.5.1	Group-IV Semiconductor Alloy	382
12.5.2	III-V Semiconductor Ternary Alloy	382
	(a) (III, III)-N Alloy	382
	(b) (III, III)-P Alloy	383
	(c) (III, III)-As Alloy	383
	(d) (III, III)-Sb Alloy	384
	(e) Dilute-nitride III-(V, V) Alloy	384
	(f) Ga-(V, V) Alloy	385
	(g) In-(V, V) Alloy	385
12.5.3	III-V Semiconductor Quaternary Alloy	385
	(a) (III, III)-(V, V) Alloy	385
	(b) (III, III, III)-V Alloy	385
12.5.4	II-VI Semiconductor Alloy	386
	References	386

Preface

Semiconductor alloys provide a natural means of tuning the magnitude of the band-gap energy and other material properties so as to optimize and widen the application of semiconductor devices. Current research and development in semiconductor alloys is focused on areas of improved materials growth, development of unique materials characterization and suitable process technologies, fabrication of novel devices using artificially controlled materials structures and better understanding of degradation mechanisms in electronic and optoelectronic devices for improved device reliability.

Even though the basic semiconductor alloy concepts are understood at this time, the determination of some device parameters has been hampered by a lack of definite knowledge of many material parameters. The main purpose of this book is to provide a comprehensive treatment of the materials aspects of group-IV, III–V and II–VI semiconductor alloys used in various electronic and optoelectronic devices. The topics treated in this book include the structural, thermal, mechanical, lattice vibronic, electronic, optical and carrier transport properties of such semiconductor alloys. The book covers not only commonly known alloys (SiGe, AlGaAs, GaInPAs, ZnCdTe, etc.) but also new alloys, such as dilute-carbon alloys (CSiGe, CSiSn, etc.), III–N alloys, dilute-nitride alloys (GaNAs, GaInNAs, etc.) and Mg- or Be-based II–VI semiconductor alloys.

The reader may also find the companion book '*Properties of Group-IV, III–V and II–VI Semiconductors*' published in this series useful since it emphasizes the endpoint semiconductor principles and properties.

The extensive bibliography is included for those who wish to find additional information if required. It is hoped that the book will attract the attention of not only semiconductor device engineers, but also solid-state physicists and materials scientists, and particularly postgraduate students, R&D staff and teaching and research professionals.

Sadao Adachi,
Gunma University, Japan

Series Preface

WILEY SERIES IN MATERIALS FOR ELECTRONIC AND OPTOELECTRONIC APPLICATIONS

This book series is devoted to the rapidly developing class of materials used for electronic and optoelectronic applications. It is designed to provide much-needed information on the fundamental scientific principles of these materials, together with how these are employed in technological applications. The books are aimed at (postgraduate) students, researchers and technologists, engaged in research, development and the study of materials in electronics and photonics, and industrial scientists developing new materials, devices and circuits for the electronic, optoelectronic and communications industries.

The development of new electronic and optoelectronic materials depends not only on materials engineering at a practical level, but also on a clear understanding of the properties of materials, and the fundamental science behind these properties. It is the properties of a material that eventually determine its usefulness in an application. The series therefore also includes such titles as electrical conduction in solids, optical properties, thermal properties, and so on, all with applications and examples of materials in electronics and optoelectronics. The characterization of materials is also covered within the series in as much as it is impossible to develop new materials without the proper characterization of their structure and properties. Structure-property relationships have always been fundamentally and intrinsically important to materials science and engineering.

Materials science is well known for being one of the most interdisciplinary sciences. It is the interdisciplinary aspect of materials science that has led to many exciting discoveries, new materials and new applications. It is not unusual to find scientists with a chemical engineering background working on materials projects with applications in electronics. In selecting titles for the series, we have tried to maintain the interdisciplinary aspect of the field, and hence its excitement to researchers in this field.

Peter Capper
Safa Kasap
Arthur Willoughby

Abbreviations and Acronyms

BAC	band anticrossing
bct	body-centered tetragonal
BZ	Brillouin zone
<i>c</i> -	cubic-
CB	conduction band
CL	cathodoluminescence
Cl-VPE	chloride-transport vapor-phase epitaxy
CP	critical point
CR	cyclotron resonance
<i>C</i> - <i>V</i>	capacitance-voltage
CVD	chemical vapor deposition
DLTS	deep-level transient spectroscopy
DOS	density of states
DP	deformation potential
ER	electroreflectance
EXAFS	extended X-ray absorption fine-structure spectroscopy
fcc	face-centered cubic
FET	field effect transistor
FTIR	Fourier transform infrared
HBT	heterojunction bipolar transistor
HH	heavy-hole
HREELS	high-resolution electron-energy-loss spectroscopy
HRXRD	high-resolution X-ray diffraction
HT-VPE	hydride-transport vapor-phase epitaxy
IR	infrared
<i>I</i> - <i>V</i>	current-voltage
LA	longitudinal acoustic
LH	light-hole
LO	longitudinal optical
LPE	liquid-phase epitaxy
MBE	molecular beam epitaxy
MDF	model dielectric function
MOCVD	metalorganic chemical vapor deposition

MOMBE	metalorganic molecular beam epitaxy
MQW	multiple quantum well
MREI	modified random-element-isodisplacement
PDP	phonon deformation potential
PIXE	particle-induced X-ray emission
PL	photoluminescence
PLD	pulsed-laser deposition
PLE	photoluminescence excitation
PR	photoreflectance
PzR	piezoreflectance
QW	quantum well
RBS	Rutherford backscattering spectrometry
rf	radio-frequency
RHEED	reflection high-energy electron diffraction
SE	spectroscopic ellipsometry
SL	superlattice
SO	spin-orbit
TA	transverse acoustic
TEM	transmission electron microscopy
THM	traveling heater method
TO	transverse optical
TP	triple-period
TR	thermoreflectance
UHV	ultrahigh vacuum
UV	ultraviolet
VB	valence band
VCA	virtual crystal approximation
VPE	vapor-phase epitaxy
w-	wurtzite
WDXS	wavelength-dispersive X-ray spectroscopy
XPS	X-ray photoelectron spectroscopy
XRD	X-ray diffraction
1D	one-dimensional
2D	two-dimensional
3D	three-dimensional

Introductory Remarks

A.1 AN ALLOY AND A COMPOUND

An alloy is a combination, either in solution or compound, of two or more elements. An alloy with two components is called a binary alloy; one with three is a ternary alloy; one with four is a quaternary alloy; one with five is a pentanary alloy. The resulting alloy substance generally has properties significantly different from those of its components. The proportions of the ingredients are available.

A chemical compound is a substance consisting of two or more chemical elements that are chemically combined in fixed proportions. The ratio of each element is usually expressed by chemical formula. For example, water is a compound consisting of two hydrogen atoms bonded to an oxygen atom (H_2O). The atoms within a compound can be held together by a variety of interactions, ranging from covalent bonds to electrostatic forces in ionic bonds. A continuum of bond polarities exists between the purely covalent and ionic bonds. For example, H_2O is held together by polar covalent bonds. NaCl is an example of an ionic compound.

Simply, an alloy is formed from a physical mixture of two or more substances, while a compound is formed from a chemical reaction. An alloy crystal is sometimes called a mixed crystal or a solid solution. For example, GaAs is a compound consisting of Ga atoms bonded to As atoms. It is not an alloy. $\text{Al}_x\text{Ga}_{1-x}\text{As}$ is an alloy compound consisting of AlAs and GaAs with a mole ratio of $x:(1-x)$. The bonds in GaAs and AlAs are not adequately described by any of these extreme types, but have characteristics intermediate to those usually associated with the covalent and ionic terms. The bonds in diamond, $\text{C}-\text{C}$, can be described by the covalent bond term only. It is an elemental semiconductor, not a compound semiconductor. Similarly, Si and Ge are elemental semiconductors. Like $\text{Al}_x\text{Ga}_{1-x}\text{As}$, $\text{Si}_x\text{Ge}_{1-x}$ ($0 \leq x \leq 1.0$) is an alloy semiconductor. The bonds $\text{Si}-\text{Ge}$, $\text{Si}-\text{Si}$ and $\text{Ge}-\text{Ge}$ in $\text{Si}_x\text{Ge}_{1-x}$ are, therefore, described by the covalent term only. It should be noted, however, that silicon carbide (SiC) is a compound, not an alloy. This is because that the chemical bonds in SiC cannot be described only by the covalent term, but have characteristics intermediate to those associated with the covalent and ionic terms, like GaAs and AlAs .

There is an ordered alloy phase in $\text{Si}_x\text{Ge}_{1-x}$ binary alloy [1]. This phase exhibits long-range order rather than random arrangement of atoms as expected previously. The ordered phase, as expected, occurs mostly in bulk $\text{Si}_x\text{Ge}_{1-x}$ layers at $x \sim 0.5$ and can be explained by the rhombohedral structure. Note that SiC is thought to be an ordered alloy. It crystallizes in a large number of polytypes. The various types of SiC differ one from another only by the order in which successive planes of Si (or C) atoms are stacked along the c axis; one polytype is the cubic, zinc-blende structure (3C) while the remainder, including two of the more frequently occurring forms, 6H (hexagonal) and 15R (rhombohedral), possess uniaxial symmetry [2]. There is no diamond structure in the SiC polytypes. An ordered alloy phase has been found not only in $\text{Si}_x\text{Ge}_{1-x}$, but also in many III-V and II-VI semiconductor alloys [3].

A.2 GRIMM–SOMMERFELD RULE

The periodic law is most commonly expressed in chemistry in the form of a periodic table or chart. An important part of this table is shown in Table A.1. The so-called short-form periodic table, based on the Mendeleev table, with subsequent emendations and additions, is still in widespread use. The elements in this table are arranged in seven horizontal rows, called the periods, in order of increasing atomic weights, and in 18 vertical columns, called the groups. The first period, containing two elements, H and He, and the next two periods, each containing eight elements, are called the short periods. The remaining periods, called the long periods, contain 18 elements, as in periods 4 and 5, or 32 elements, as in period 6. The long period 7 includes the actinide series, which has been filled in by the synthesis of radioactive nuclei through element 103, lawrencium (Lr). Heavier transuranium elements, atomic numbers 104 to 112, have also been synthesized.

Table A.1 Periodic table

	Ia (1)																VIIIa (18)
1	1 H	IIa (2)		IIIa (13)	IVa (14)	Va (15)	VIa (16)	VIIa (17)	2 He								
2	3 Li	4 Be		5 B	6 C	7 N	8 O	9 F	10 Ne								
3	11 Na	12 Mg		IIb (12)	13 Al	14 Si	15 P	16 S	17 Cl	18 Ar							
4	19 K	20 Ca	30 Zn	31 Ga	32 Ge	33 As	34 Se	35 Br	36 Kr							
5	37 Rb	38 Sr	48 Cd	49 In	50 Sn	51 Sb	52 Te	53 I	54 Xe							
6	55 Cs	56 Ba	80 Hg	81 Tl	82 Pb	83 Bi	84 Po	85 At	86 Rn							
7	87 Fr	118 Uuo							

The elemental semiconductors in column IVa of the periodic table are diamond, Si and Ge, and they are of some importance in various device applications. Note that gray tin (α -Sn) is a semiconductor (semimetal) and Pb is a metal. SiC is the only compound semiconductor formed by column IVa elements. The III–V and II–VI semiconductors possess a crystal structure similar to either one of the cubic mineral, sphalerite or to hexagonal wurtzite. There are 15 III–V, 18 II–VI and four I–VII compound semiconductors. The four I–VII compound semiconductors are: CuCl, CuBr, CuI and AgI.

A substantial development in the search for semiconducting materials with new combinations of physical and chemical properties was reached when Goryunova using the ideas of Huggins [4] and Grimm and Sommerfeld [5], developed a method of prediction of the composition of chemical compounds with the tetrahedral and octahedral (NaCl-type) coordination of atoms in their crystal lattice [6]. His method is based on consideration of the number of valence electrons in the elements, which is assumed to be equal to the number of the group in

the periodic table to which they belong (so-called full or normal valency) and can be expressed in the form of the equation system [7]

$$\begin{aligned}
 \sum_{i=1}^A B_i x_i &= 4 \\
 \sum_{i=1}^n B_i x_i &= \sum_{i=n+1}^A (8-B_i) x_i \\
 \sum_{i=1}^A x_i &= 1
 \end{aligned}
 \tag{A.1}$$

for calculating the content of the representatives of different groups of the periodic table in a compound containing A components, n of which are considered as cations, where B_i is the number of the group in the periodic table to which the i th component of the compounds belongs, and x_i is its concentration in the compound. The first expression in Equation (A.1) represents the condition that the average number of valence electrons per atom is equal to four (tetrahedral rule). The second equation states that in the compound, the number of valence electrons, which 'cations' give to 'anions' is equal to the number of electrons the anion needs to form the octet (i.e. the normal valency condition). The quotation marks here are used to remind us that in the solids with dominating covalent bonds, which factually form the class of semiconductor, the ion concept is quite conditional. Based on these criteria, it is possible to obtain all probable types of tetrahedral substances, taking into consideration only the location of their components in one or another group of the periodic table. Table A.2 briefly summarizes these results.

Table A.2 Summary of valence binary compounds and ternary analogs of binary valence compounds which satisfy tetrahedral rule ($Z=4$). ch=chalcopyrite; zb=zinc-blende; t=tetragonal; or=orthorhombic; w=wurtzite; h=hexagonal ($P6_3mc$ (C_{6v})); rh=rhombohedral

Cation	Compound	Typical compound (Crystal structure)
I	I-III-VI ₂	CuGaSe ₂ (ch)
	I-IV ₂ -V ₃	CuGe ₂ P ₃ (zb)
	I ₂ -IV-VI ₃	Cu ₂ GeSe ₃ (t)
	I ₃ -V-VI ₄	Cu ₃ PS ₄ (or)
	I-VII	γ-CuCl (w)
II	II ₄ -III-VII ₃	
	II-IV-V ₂	ZnSiP ₂ (ch)
	II ₃ -IV-VII ₂	
	II ₂ -V-VII	
II-VI	CdTe (zb)	
III	III ₂ -IV-VI	Al ₂ CO (w)
	III ₃ -IV ₂ -VII	
	III-V	GaAs (zb)
IV	IV-IV	SiC (zb, w, h, rh)

Table A.3 All the possible types of valence binary compound

Cation	Cation to anion content ratio x/y , (Z), Typical compound					
	II	III	IV	V	VI	VII
I	6:1 (1.14)	5:1 (1.33)	4:1 (1.60)	3:1 (2.00) K ₃ Sb	2:1 (2.67) Ag ₂ S	1:1 (4.00) γ -CuCl
II	—	5:2 (2.29)	2:1 (2.67) Mg ₂ Si	3:2 (3.20) Cd ₃ As ₂	1:1 (4.00) CdTe	1:2 (5.33) HgI ₂
III	—	—	4:3 (3.43) GaAs	1:1 (4.00)	2:3 (4.80) Ga ₂ Se ₃	1:3 (6.00)
IV	—	—	1:1 (4.00) SiC	3:4 (4.57)	1:2 (5.33) SnS ₂	1:4 (6.40)
V	—	—	—	—	2:5 (5.71)	1:5 (6.67)
VI	—	—	—	—	—	1:6 (6.86)

In analyzing the normal valency compounds, not only tetrahedral phases but all compounds of this category can be grouped, first of all, in accordance with the average valence electron content per atom of a compound, Z . We list in Table A.3 all possible types of the binary valence compounds [7]. If A and B are the cation valencies in a binary compound, the atomic ratio of components in a valence compound A_xB_y is given by

$$\frac{x}{y} = \frac{8-B}{A} \quad (\text{A.2})$$

and the valence electron concentration per atom in the corresponding binary compound is

$$Z = \frac{8A}{8-(B-A)} = \frac{8A}{8+(A-B)} \quad (\text{A.3})$$

as following from Equation (A.1).

In Table A.3, there are 22 types of binary valence compounds. Goryunova [6] concluded from the available experimental data that the phases possessing semiconducting properties are those with Z between two and six; the phases smaller than two are either metal alloys or the compounds with typical metallic crystal structure and properties. Goryunova also showed that there are 148 types of ternary compounds which are the electron analogs of the binary valence compounds [7]. Among them, there are 10 types of ternary compounds which satisfy the tetrahedral rule $Z=4$, as listed in Table A.2.

A.3 AN INTERPOLATION SCHEME

The electronic energy-band parameters of semiconductor alloys and their dependence on alloy composition are very important, and so they have received much attention in the past. Investigation

of many device parameters have, however, been hampered by a lack of definite knowledge of various material parameters. This necessitates the use of some sort of interpolation scheme.

If the linear interpolation scheme is used, the ternary material parameter T for an alloy of the form $A_xB_{1-x}C$ can be derived from binary parameters (B) by

$$T(x) = xB_{AC} + (1-x)B_{BC} \equiv a + bx \quad (\text{A.4})$$

where $a \equiv B_{BC}$ and $b \equiv B_{AC} - B_{BC}$. Some material parameters, however, deviate significantly from the linear relationship shown in Equation (A.4), and exhibit an approximately quadratic dependence on x . The ternary material parameter in such a case can be very efficiently approximated by the relationship

$$T(x) = xB_{AC} + (1-x)B_{BC} + x(1-x)C_{AB} \equiv a + bx + cx^2 \quad (\text{A.5})$$

where $a \equiv B_{BC}$, $b \equiv B_{AC} - B_{BC} + C_{AB}$ and $c \equiv -C_{AB}$. The parameter c is called a bowing parameter.

The quaternary material $A_xB_{1-x}C_yD_{1-y}$ is thought to be constructed from four binaries: AC, AD, BC and BD. If the linear interpolation scheme is used, the quaternary material parameter Q can be derived from the binary parameters by

$$Q(x,y) = xyB_{AC} + x(1-y)B_{AD} + (1-x)yB_{BC} + (1-x)(1-y)B_{BD} \quad (\text{A.6})$$

If one of the four binary parameters (e.g. B_{AD}) is lacking, Q can be estimated from

$$Q(x,y) = xB_{AC} + (y-x)B_{BC} + (1-y)B_{BD} \quad (\text{A.7})$$

The quaternary material $A_xB_yC_{1-x-y}D$ is thought to be constructed from three binaries: AD, BD and CD. The corresponding linear interpolation is given by

$$Q(x,y) = xB_{AD} + yB_{BD} + (1-x-y)B_{CD} \quad (\text{A.8})$$

If relationships for the ternary parameters are available, the quaternary material parameter Q can be expressed either as ($A_xB_{1-x}C_yD_{1-y}$)

$$Q(x,y) = \frac{x(1-x)[yT_{ABC}(x) + (1-y)T_{ABD}(x)] + y(1-y)[xT_{ACD}(y) + (1-x)T_{BCD}(y)]}{x(1-x) + y(1-y)} \quad (\text{A.9})$$

or ($A_xB_yC_{1-x-y}D$)

$$Q(x,y) = \frac{xyT_{ABD}(u) + y(1-x-y)T_{BCD}(v) + x(1-x-y)T_{ACD}(w)}{xy + y(1-x-y) + x(1-x-y)} \quad (\text{A.10})$$

with

$$\begin{aligned} u &= (1-x-y)/2 \\ v &= (2-x-2y)/2 \\ w &= (2-2x-y)/2 \end{aligned} \quad (\text{A.11})$$

If a quaternary bowing term $D_{ABCD} = -d$ is considered in Equation (A.9) or Equation (A.10), we can obtain

$$Q(x,y) = \{x(1-x)[yT_{ABC}(x) + (1-y)T_{ABD}(x) + y(1-y)D_{ABCD}] + y(1-y) \times [xT_{ACD}(y) + (1-x)T_{BCD}(y) + x(1-x)D_{ABCD}] \times [x(1-x) + y(1-y)]^{-1} \quad (\text{A.12})$$

for the $A_xB_{1-x}C_yD_{1-y}$ quaternary or

$$Q(x,y) = \frac{xyT_{ABD}(u) + y(1-x-y)T_{BCD}(v) + x(1-x-y)T_{ACD}(w) + xy(1-x-y)D_{ABCD}}{xy + y(1-x-y) + x(1-x-y)} \quad (\text{A.13})$$

for the $A_xB_yC_{1-x-y}D$ quaternary.

The weighted form of Equation (A.12) can be written as

$$Q(x,y) = y(1-x)B_{BC} + xyB_{AC} + (1-y)xB_{AD} + (1-x)(1-y)B_{CD} + x(1-x)(1-y)C_{AB(D)} + x(1-x)yC_{AB(C)} + (1-x)y(1-y)C_{(B)CD} + xy(1-y)C_{(A)CD} + x(1-x)y(1-y)D_{ABCD} \quad (\text{A.14})$$

where $C_{AB(D)}$ is the ternary bowing parameter for an alloy $A_xB_{1-x}D$ and so on. Expression (A.14) can be conveniently compacted into an inner product whose 3×3 matrix includes only the alloy parameters and closely resembles the map of the quaternary alloy in its compositional space [8]

$$Q(x,y) = [y \ y(1-y) \ 1-y] \begin{bmatrix} B_{BC} & C_{AB(C)} & B_{AC} \\ C_{(B)CD} & D_{ABCD} & C_{(A)CD} \\ B_{BD} & C_{AB(D)} & B_{AD} \end{bmatrix} \begin{bmatrix} 1-x \\ x(1-x) \\ x \end{bmatrix} \quad (\text{A.15})$$

If the bowing parameters C and D in Equation (A.15) are zero, Vegard law is recovered in its bilinear formulation. Equation (A.15) is valid for quaternaries of types $A_xB_{1-x}C_yD_{1-y}$ and $A_xB_yC_{1-x-y}D$ ($AB_xC_yD_{1-x-y}$). For the latter, one binary can be assigned twice in the same row or column of the alloy matrix with a zero bowing factor (i.e. $B_{AC} = B_{AD}$ and $C_{(A)CD} = 0$). The composition for such an alloy is given by $(B_{AD})_x[(B_{BD})_y(B_{CD})_{1-y}]_{1-x}$ (e.g., $Al_x(Ga_yIn_{1-y})_{1-x}P$).

The essentially same expressions can be obtained for group-IV semiconductor alloys. The binary material parameter B in the form of A_xB_{1-x} can be written using the elemental material parameters (A) as

$$B(x) = xA_A + (1-x)A_B \equiv a + bx \quad (\text{A.16})$$

The bowing effect modifies Equation (A.16) in the form

$$B(x) = xA_A + (1-x)A_B + x(1-x)C_{AB} \equiv a + bx + cx^2 \quad (\text{A.17})$$

Similarly, the ternary material parameter T in $A_xB_yC_{1-x-y}$ can be expressed as

$$T(x,y) = xA_A + yA_B + (1-x-y)A_C \quad (\text{A.18})$$

and

$$T(x,y) = \frac{xyB_{AB}(u) + y(1-x-y)B_{BC}(v) + x(1-x-y)B_{AC}(w)}{xy + y(1-x-y) + x(1-x-y)} \quad (\text{A.19})$$

or

$$T(x,y) = \frac{xyB_{AB}(u) + y(1-x-y)B_{BC}(v) + x(1-x-y)B_{AC}(w) + xy(1-x-y)C_{ABC}}{xy + y(1-x-y) + x(1-x-y)} \quad (\text{A.20})$$

with u , v and w given in Equation (A.11). In Equation (A.20), C_{ABC} is a ternary bowing parameter.

REFERENCES

- [1] W. Jäger, in *Properties of Strained and Relaxed Silicon Germanium*, EMIS Databooks Series No. 12 (edited by E. Kasper), INSPEC, London, 1995, p. 53.
- [2] S. Adachi, *Properties of Group-IV, III-V and II-VI Semiconductors*. John Wiley & Sons, Ltd, Chichester, 2005.
- [3] A. Mascarenhas, *Spontaneous Ordering in Semiconductor Alloys*. Kluwer Academic, New York, 2002.
- [4] M. L. Huggins, *Phys. Rev.* **27**, 286 (1926).
- [5] H. Grimm and A. Sommerfeld, *Z. Phys.* **36**, 36 (1926).
- [6] N. A. Goryunova, *The Chemistry of Diamond-Like Semiconductors*. MIT Press, Cambridge, 1965.
- [7] L. I. Berger, *Semiconductor Materials*. CRC, Boca Raton, 1997.
- [8] G. P. Donati, R. Kaspi, and K. J. Malloy, *J. Appl. Phys.* **94**, 5814 (2003).

1 Structural Properties

1.1 IONICITY

Details of ionicity f_i are given in Adachi [1]. Any given definition of ionicity is likely to be imperfect. We present in Table 1.1 f_i values for a number of group-IV, III–V and II–VI semiconductors, including Be-based semiconductors and CdO. We have Phillips ionicity of $f_i = 0$ for all group-IV elemental semiconductors (diamond, Si, Ge and α -Sn) and $f_i > 0.9$ for some alkali halides (NaCl, KCl, etc.).

Figure 1.1(a) plots f_i versus x for C_xSi_{1-x} . Note that $f_i = 0.177$ for silicon carbide (SiC). This means that the bond character of SiC resembles that of III–V or II–VI semiconductors rather than of Si or diamond, so that its crystal structure must be zinc-blende, hexagonal or rhombohedral. Similarly, an ordered alloy of Si_xGe_{1-x} may have a nonzero f_i value near the ordered-phase composition $x \sim 0.5$. In fully disordered alloys (C_xSi_{1-x} , Si_xGe_{1-x} , etc.), we should have $f_i = 0$ over the whole alloy range $0 \leq x \leq 1.0$.

The plots of f_i versus x or y for $Al_xGa_{1-x}As$, $Ga_xIn_{1-x}P_yAs_{1-y}/InP$ and $Mg_xZn_{1-x}S_ySe_{1-y}/GaAs$ are shown in Figure 1.1(b). These values are obtained from the linear interpolation of Equations (A.4) and (A.6) between the endpoint data in Table 1.1. The resulting f_i versus x (y) plots can be expressed in the usual power form as

$$f_i(x) = 0.310 - 0.036x \quad (1.1a)$$

for $Al_xGa_{1-x}As$,

$$f_i(y) = 0.335 + 0.065y + 0.021y^2 \quad (1.1b)$$

for $Ga_xIn_{1-x}P_yAs_{1-y}/InP$ and

$$f_i(x) = 0.630 + 0.154x + 0.003x^2 \quad (1.1c)$$

for $Mg_xZn_{1-x}S_ySe_{1-y}/GaAs$. The values of f_i for fully disordered alloys should be safely estimated from the linear interpolation scheme.

1.2 ELEMENTAL ISOTOPIC ABUNDANCE AND MOLECULAR WEIGHT

In Tables 1.2 and 1.3 of Adachi [1], the elements which form at least one tetrahedrally coordinated $A^N B^{8-N}$ semiconductor, together with their natural isotopic abundance in percent and atomic weight are listed. Let us add an element of beryllium: natural abundance of ${}^9\text{Be} = 100\%$; atomic weight = 9.012182(3).

Table 1.1 Phillips’s ionicity f_i for a number of group-IV, III–V and II–VI semiconductors

IV	f_i	III–V	f_i	II–VI	f_i
Diamond	0	BN	0.221	BeO	0.602
Si	0	BP	0.032	BeS	0.286
Ge	0	BAs	0.044	BeSe	0.261
Sn	0	AlN	0.449	BeTe	0.169
SiC	0.177	AlP	0.307	MgO	0.841
		AlAs	0.274	MgS	0.786
		AlSb	0.250	MgSe	0.790
		GaN	0.500	MgTe	0.554
		GaP	0.327	ZnO	0.616
		GaAs	0.310	ZnS	0.623
		GaSb	0.261	ZnSe	0.630
		InN	0.578	ZnTe	0.609
		InP	0.421	CdO	0.785
		InAs	0.357	CdS	0.685
		InSb	0.321	CdSe	0.699
				CdTe	0.717
				HgS	0.790
				HgSe	0.680
				HgTe	0.650

The molecular weight M for an $A^N B^{8-N}$ compound semiconductor ($N \neq 4$) can be simply given by the sum of the atomic weights of atoms A and B. For an elemental semiconductor ($N = 4$), it is given by the atomic weight of the element atom $A = B$. The molecular weight M of any alloy semiconductors can be obtained from the linear interpolation scheme.

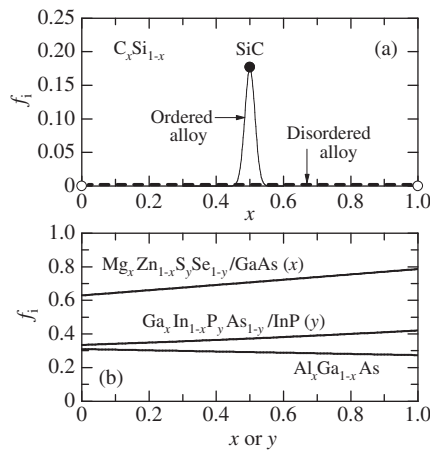


Figure 1.1 Phillips ionicity f_i versus x or y for (a) C_xSi_{1-x} and (b) $Al_xGa_{1-x}As$, $Ga_xIn_{1-x}P_yAs_{1-y}/InP$ and $Mg_xZn_{1-x}S_ySe_{1-y}/GaAs$. The open and solid circles in (a) show the endpoint and SiC ($x = 0.5$) values, respectively. The solid lines in (b) are calculated from Equation (1.1)

1.3 CRYSTAL STRUCTURE

1.3.1 Random Alloy

Table 1.2 summarizes the crystal classes for easily obtained or normally grown: (a) group-IV elemental semiconductors, (b) III–V and (c) II–VI binary semiconductors. In Table 1.2(a), the crystal classes for an easily grown compound semiconductor SiC are also included.

Table 1.2 Summary of crystal structure for: (a) group-IV, (b) III–V and (c) II–VI semiconductors. d = diamond; zb = zinc-blende; w = wurtzite (C_{6v}); h = hexagonal (C_{6v} or D_{6h}); rh = rhombohedral; t = tetragonal; rs = rocksalt; or = orthorhombic. Note that β -Sn (t) is a metal

(a)				
IV	C	Si	Ge	Sn
C	d	zb, w, h, rh		
Si	zb, w, h, rh	d		
Ge			d	
Sn				d, t
(b)				
III/V	N	P	As	Sb
B	zb, h	zb	zb	
Al	w	zb	zb	zb
Ga	w	zb	zb	zb
In	w	zb	zb	zb
(c)				
II/VI	O	S	Se	Te
Be	w	zb	zb	zb
Mg	rs	rs	zb	w
Zn	w	zb, w	zb	zb
Cd	rs	w	w	zb
Hg	rh, or	zb, rh	zb	zb

1.3.2 Spontaneous Ordering

(a) Group-IV semiconductor alloy

The phenomenon of spontaneous ordering in semiconductor alloys is observed to occur spontaneously during epitaxial growth of certain semiconductor alloys and results in a modification of their structural, electronic and optical properties [2]. Substantial effort has been focused on learning how to control this phenomenon so that it may be used for tailoring desirable material properties. We summarize in Table 1.3 the spontaneous ordering phases observed in some group-IV, III–V and II–VI semiconductor alloys.

Table 1.3 Types of spontaneous ordering phases observed in some group-IV, III-V and II-VI semiconductor alloys

System	Ordering type	Material	Epitaxial growth
IV	RS1 (CuPt)	SiGe	MBE ^d
	RS2 (CuPt)	SiGe	MBE ^d
	RS3 (CuPt)	SiGe	MBE ^d
III-V	CuPt-B	AlInP	MBE, ^b MOCVD ^c
		GaInP	Cl-VPE, ^d HT-VPE, ^e MBE, ^f MOCVD ^g
		AlInAs	MEB, ^h MOCVD ⁱ
		GaInAs	Cl-VPE, ^j MOCVD ^k
		GaInSb	MOCVD ^l
		GaPAs	MOCVD ^m
		GaPSb	MOCVD ⁿ
		GaAsSb	MBE ^o
		InPAs	MOCVD ^p
		InPSb	MOCVD ^q
		InAsSb	MOCVD, ^r MBE ^s
		GaInPAs	Cl-VPE, ^j MOCVD ^t
		AlGaInP	MOCVD ^c
	CuPt-A	AlInP	MBE ^b
		AlInAs	MBE ^u
	CuAu-I	AlGaAs	MOCVD ^v
		GaInAs	MBE ^w
GaAsSb		MBE, ^x MOCVD ^y	
TP-A	AlInAs	MBE ^z	
	GaInAs	MBE ^{aa}	
II-VI	CuPt-B	ZnCdTe	MOCVD ^{ab}
		CdHgTe	LPE ^{ac}
		ZnSeTe	MOCVD ^{ad}
	CuAu-I	ZnCdTe	MBE ^{ae}
		ZnSeTe	MBE ^{af}
	Cu ₃ Au	ZnCdTe	MBE ^{ag}

^aSee, W. Jäger, in *Properties of Strained and Relaxed Silicon Germanium*, EMIS Datareviews Series No. 12 (edited by E. Kasper), INSPEC, London, 1995, p. 53

^bA. Gomyo *et al.*, *Jpn. J. Appl. Phys.* **34**, L469 (1995)

^cT. Suzuki *et al.*, *Jpn. J. Appl. Phys.* **27**, 2098 (1988)

^dO. Ueta *et al.*, *J. Appl. Phys.* **68**, 4268 (1990)

^eK. Nishi and T. Suzuki (unpublished)

^fA. Gomyo *et al.*, *Mater. Res. Symp. Proc.* **417**, 91 (1996)

^gA. Gomyo *et al.*, *Phys. Rev. Lett.* **60**, 2645 (1988)

^hT. Suzuki *et al.*, *Appl. Phys. Lett.* **73**, 2588 (1998)

ⁱA. G. Norman *et al.*, *Inst. Phys. Conf. Ser.* **87**, 77 (1987)

^jM. A. Shahid *et al.*, *Phys. Rev. Lett.* **58**, 2567 (1987)

^kT.-Y. Seong *et al.*, *J. Appl. Phys.* **75**, 7852 (1994)

^lJ. Shin *et al.*, *J. Electron. Mater.* **24**, 1563 (1995)

^mG. S. Chen *et al.*, *Appl. Phys. Lett.* **57**, 2475 (1990)

ⁿG. B. Stringfellow, *J. Cryst. Growth* **98**, 108 (1989)

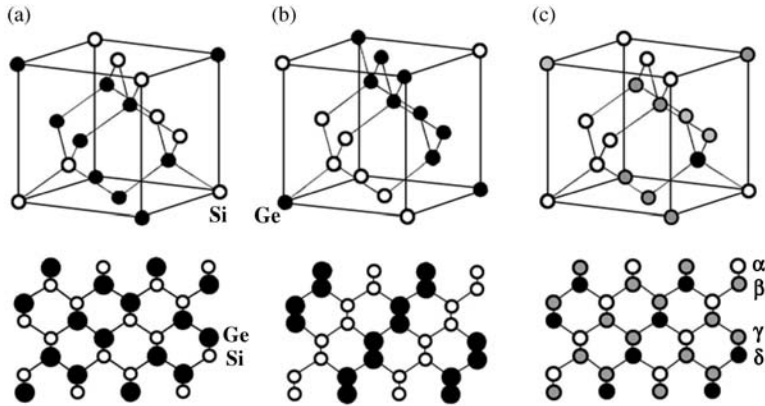


Figure 1.2 Si–Ge ordered structures of types (a) RS1, (b) RS2 and (c) RS3. In (c), the four projected compositions α , β , γ and δ correspond to specific Si- and Ge-rich sites

Normally, $\text{Si}_x\text{Ge}_{1-x}$ crystallizes in the diamond structure which contains of two fcc sublattices shifted by one quarter of the body diagonal. Observations of long-range ordering of group-IV semiconductor alloy have been made on $\text{Si}_x\text{Ge}_{1-x}$ layers grown on Si(100) by MEB [3] and subsequently at interfaces of SLs [2]. Different order structures were suggested in bulk $\text{Si}_x\text{Ge}_{1-x}$ on the basis of experimental results and are depicted in Figure 1.2. They are RS1, RS2 and RS3 with the rhombohedral structures (CuPt ordering, $R3m$). The stoichiometry for RS1 and RS2 is $\text{Si}_{0.5}\text{Ge}_{0.5}$, while RS3 allows compositional differences on specific lattice sites. As seen in Figure 1.2, RS1 (RS2) has the widely (closely) spaced $\{111\}$ planes occupied by the same atom type, while RS3 allows compositional differences between projected sites or columns with compositions α , β , γ and δ corresponding to specific Si- and Ge-rich sites.

^oY.-E. Ihm *et al.*, *Appl. Phys. Lett.* **51**, 2013 (1987)

^pD. H. Jaw *et al.*, *Appl. Phys. Lett.* **59**, 114 (1991)

^qSee, H. R. Jen *et al.*, *Appl. Phys. Lett.* **54**, 1890 (1989)

^rH. R. Jen *et al.*, *Appl. Phys. Lett.* **54**, 1154 (1989)

^sT.-Y. Seong *et al.*, *Appl. Phys. Lett.* **64**, 3593 (1994)

^tW. E. Plano *et al.*, *Appl. Phys. Lett.* **53**, 2537 (1988)

^uT. Suzuki *et al.*, *Appl. Phys. Lett.* **73**, 2588 (1998)

^vT. S. Kuan *et al.*, *Phys. Rev. Lett.* **54**, 201 (1985)

^wO. Ueda, *et al.*, *J. Cryst. Growth* **115**, 375 (1991)

^xO. Ueta *et al.*, *Proc. 7th Int. Conf. InP and Related Materials Sapporo, Japan*, p. 253 (1995)

^yH. R. Jen *et al.*, *Appl. Phys. Lett.* **48**, 1603 (1986)

^zA. Gomyo *et al.*, *Phys. Rev. Lett.* **72**, 673 (1994)

^{aa}D. Shindo *et al.*, *J. Electron Microscopy* **45**, 99 (1996)

^{ab}N. Amir *et al.*, *J. Phys. D: Appl. Phys.* **33**, L9 (2000)

^{ac}K. T. Chang and E. Goo, *J. Vac. Sci. Technol. B* **10**, 1549 (1992)

^{ad}K. Wolf *et al.*, *Solid State Commun.* **94**, 103 (1995)

^{ae}H. S. Lee *et al.*, *Appl. Phys. Lett.* **83**, 896 (2003)

^{af}H. Luo *et al.*, *J. Vac. Sci. Technol. B* **12**, 1140 (1994)

^{ag}H. S. Lee *et al.*, *Solid State Commun.* **137**, 70 (2006)

The long-range order parameter in RS1 and RS2 can be defined by

$$S = \frac{r_{\text{Si}} - x}{1 - x} \quad (1.2)$$

where r_{Si} is the fraction of Si sites occupied correctly and x is the fraction of Si atoms in $\text{Si}_x\text{Ge}_{1-x}$. $S = 1$ means perfect and complete order, while $S = 0$ means random alloy. The degree of long-range order can be quantitatively deduced from the electron diffraction intensity of superstructure reflections. However, because of the presence of crystalline defects, of superposition of various domains and of the multiple scattering, the actual intensity substantially deviates from the kinematic value so that quantitative determination from selected-area electron diffraction intensity is usually obscured [2].

Observations of the long-range ordering have been made on bulk SiGe or SL samples prepared by MBE at medium temperature and for various compositions. However, no observations of ordered phases are reported for bulk SiGe grown from the melt [4].

(b) III-V semiconductor alloy

In 1985, Kuan *et al.* [5] first observed an ordered phase (CuAu-I type) in III-V semiconductor alloy which was an AlGaAs epilayer grown on GaAs(100) at 600–800 °C by MOCVD. Since the finding of CuPt-type ordering in SiGe alloy [3], this type of ordering (CuPt-B) has also been reported for many III-V alloys, such as AlInP, GaInP, AlInAs and GaInAs ([6], see also Table 1.3). New types of ordering, CuPt-A and TP-A, are also found in AlInP [7] and AlInAs alloys [8]. Other types of ordering, CuAu-I, famatinite and chalcopyrite, are reported in the early history of the spontaneous ordering in III-V alloys; however, mechanism of these phases seems to be quite different from those of CuPt-B, CuPt-A and TP-A [6].

The unit cells of (a) CuPt-B, (b) CuAu-I and (c) chalcopyrite structures are shown in Figure 1.3. The metallurgical CuPt alloy has a random fcc structure at high temperatures, but quenching at low temperatures produces a rhombohedral phase with $1/2\{111\}$ chemical ordering. The CuPt-B structure is among the most widely discussed and accessed forms of spontaneous ordering in III-V ternaries, and occurs in both common anion and common cation alloys (Table 1.3). It is a monolayer SL of III_A (V_A)-rich planes and III_B (V_B)-rich planes ordered in the $[\bar{1}11]$ or $[1\bar{1}1]$ directions, as depicted in Figure 1.4. The CuPt-A and

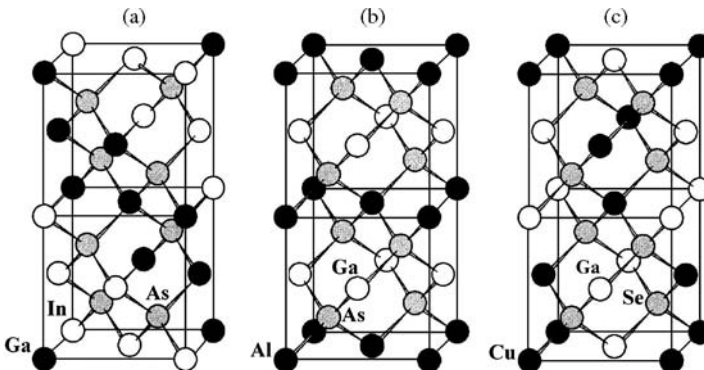


Figure 1.3 Unit cells of (a) CuPt-B (GaInAs), (b) CuAu-I (AlGaAs) and (c) chalcopyrite structures (CuGaSe₂)

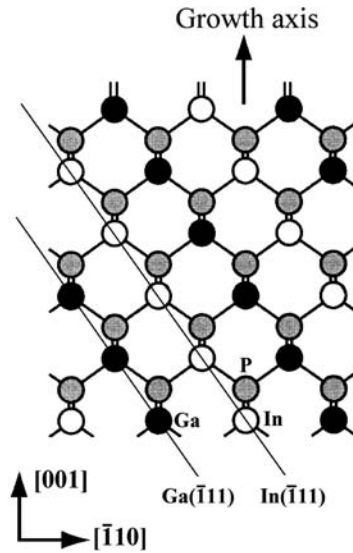


Figure 1.4 $[110]$ projection of CuPt-B ordering (GaInP)

TP-A phases occur in the $[\bar{1}\bar{1}\bar{1}]$ and $[11\bar{1}]$ directions, in which CuPt-B ordering is never observed. The metallic CuAu alloy shows two prominent ordered phases: (i) CuAu-I trigonal phase with alternating (002) planes of pure Cu and Au compositions and (ii) orthorhombic CuAu-II phase. The CuAu-I ordering occurs spontaneously within fcc sublattices of some III–V pseudobinary alloys, such as AlGaAs, GaInAs and GaAsSb (Table 1.3).

An earlier thermodynamic calculation based on a first-principles theory predicted that an ordered phase with a large lattice-constant mismatch is more stable than the corresponding random phase [9]. Some experimental data, on the other hand, showed that the kinetics of crystal growth plays an important role in the formation of an ordered structure as discussed in Mascarenhas [2].

(c) II–VI semiconductor alloy

Only a few studies have been carried out on spontaneous ordering of II–VI semiconductor alloys. These studies reported ordering of CuPt and CuAu-I types (Table 1.3). Recently, a new ordering phase, Cu_3Au , has been observed in $\text{Zn}_{0.9}\text{Cd}_{0.1}\text{Te}$ epilayers grown on GaAs(100) substrates [10]. We can see a tendency in Table 1.3 to observe the CuPt (CuAu-I) phase if samples were grown by MOCVD (MBE).

1.4 LATTICE CONSTANT AND RELATED PARAMETERS

1.4.1 CuAu Alloy: Ordered and Disordered States

Cu–Au alloy is among the best studied of all metallic alloys. The most interesting feature of this alloy is that CuAu ($x = 0.5$), CuAu_3 ($x = 0.25$) and Cu_3Au ($x = 0.75$) can be obtained in either ordered or disordered form. The ordered CuAu alloy crystallizes in the Ll_0 tetragonal structure

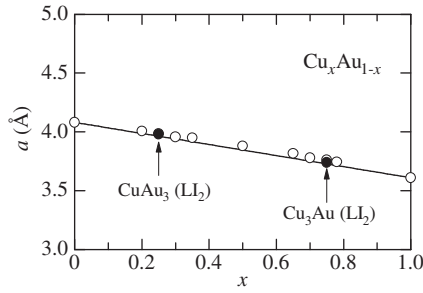


Figure 1.5 Lattice constant a versus x for $\text{Cu}_x\text{Au}_{1-x}$. The solid and open circles represent the ordered ($x = 0.25, 0.75$) and disordered alloy values, respectively. The solid line shows the linear interpolation result between the endpoint elemental data

(space group = $P4/mmm$), while the ordered CuAu_3 and Cu_3Au alloys crystallize in the LI_2 cubic structure ($Pm\bar{3}m$).

In Figure 1.5 the lattice constant a has been plotted as a function of x for $\text{Cu}_x\text{Au}_{1-x}$. The solid and open circles represent the ordered and disordered alloy data, respectively. The solid line shows the linear interpolation result between the Au ($x = 0$) and Cu ($x = 1.0$) values. It can be seen from Figure 1.5 that the Cu–Au ordering has no strong effect on the lattice parameter. Similarly, no clear spontaneous ordering effect has been observed on the lattice parameters of semiconductor alloys.

1.4.2 Non-alloyed Semiconductor

The lattice parameters for a number of the most easily grown group-IV, III–V and II–VI semiconductors are listed in Table 1.4. Tables 1.5, 1.6 and 1.7 also list the molecular weight (M), lattice constants (a and b) and crystal density (g) for a number of group-VI, III–V and II–VI semiconductors crystallizing in the diamond, zinc-blende and wurtzite structures, respectively. These values can be used to obtain alloy values using the interpolation scheme.

Table 1.4 Most easily grown crystal structure and lattice constants at 300 K for a number of easily or normally grown group-IV, III–V and II–VI semiconductors. d = diamond; zb = zinc-blende; h = hexagonal; w = wurtzite; rs = rocksalt; or = orthorhombic; rh = rhombohedral

System	Material	Crystal structure	a (Å)	c (Å)
IV	Diamond	d	3.5670	
	Si	d	5.4310	
	Ge	d	5.6579	
	Sn	d	6.4892	
	3C-SiC	zb	4.3596	
	6H-SiC	h	3.0806	15.1173

Table 1.4 (Continued)

System	Material	Crystal structure	a (Å)	c (Å)	
III-V	BN	zb	3.6155		
	BN	h	2.5040	6.6612	
	BP	zb	4.5383		
	BAs	zb	4.777		
	AlN	h (w)	3.112	4.982	
	AlP	zb	5.4635		
	AlAs	zb	5.66139		
	AlSb	zb	6.1355		
	GaN	h (w)	3.1896	5.1855	
	GaP	zb	5.4508		
	GaAs	zb	5.65330		
	GaSb	zb	6.09593		
	InN	h (w)	3.548	5.760	
	InP	zb	5.8690		
	InAs	zb	6.0583		
InSb	zb	6.47937			
II-VI	BeO	h (w)	2.6979	4.380	
	BeS	zb	4.865		
	BeSe	zb	5.137		
	BeTe	zb	5.617		
	MgO	rs	4.203		
	MgS	rs	5.203		
	MgSe	zb	5.91		
	MgTe	h (w)	4.548	7.390	
	ZnO	h (w)	3.2495	5.2069	
	ZnS	h (w)	3.8226	6.2605	
	ZnS	zb	5.4102		
	ZnSe	zb	5.6692		
	ZnTe	zb	6.1037		
	CdO	rs	4.686		
	CdS	h (w)	4.1367	6.7161	
	CdSe	h (w)	4.2999	7.0109	
	CdTe	zb	6.481		
	HgO		or	3.577 (<i>a</i>)	
				8.681 (<i>b</i>)	
				2.427 (<i>c</i>)	
				0.745 (<i>u</i>)	
				4.14 (<i>a</i>)	
				9.49 (<i>b</i>)	
2.292 (<i>c</i>)					
HgS	rh		0.720 (<i>u</i>)		
			0.480 (<i>v</i>)		
			6.084		
			6.4603		
HgSe	zb	6.084			
HgTe	zb	6.4603			

Table 1.5 Molecular weight M , lattice constant a and crystal density g for a number of cubic, diamond-type semiconductors at 300 K

System	Material	M (amu)	a (Å)	g (g/cm ³)
IV	Diamond	12.0107	3.5670	3.5156
	Si	28.0855	5.4310	2.3291
	Ge	72.61	5.6579	5.3256
	Sn	118.710	6.4892	5.7710

Table 1.6 Molecular weight M , lattice constant a and crystal density g for a number of cubic, zinc-blende-type semiconductors at 300 K

System	Material	M (amu)	a (Å)	g (g/cm ³)
IV	3C-SiC	40.0962	4.3596	3.2142
III-V	BN	24.818	3.6155	3.4880
	BP	41.785	4.5383	2.9693
	BAs	85.733	4.777	5.224
	AlN	40.98828	4.38	3.24
	AlP	57.955299	5.4635	2.3604
	AlAs	101.903098	5.66139	3.73016
	AlSb	148.742	6.1355	4.2775
	GaN	83.730	4.52	6.02
	GaP	100.696	5.4508	4.1299
	GaAs	144.645	5.65330	5.31749
	GaSb	191.483	6.09593	5.61461
	InN	128.825	4.986	6.903
	InP	145.792	5.8690	4.7902
	InAs	189.740	6.0583	5.6678
InSb	236.578	6.47937	5.77677	
II-VI	BeO	25.0116	3.80	3.03
	BeS	41.078	4.865	2.370
	BeSe	87.97	5.137	4.310
	BeTe	136.61	5.617	5.120
	MgO	40.3044	4.21	3.59
	MgS	56.371	5.62	2.11
	MgSe	103.27	5.91	3.32
	MgTe	151.91	6.42	3.81
	ZnO	81.39	4.47	6.05
	ZnS	97.46	5.4102	4.0879
	ZnSe	144.35	5.6692	5.2621
	ZnTe	192.99	6.1037	5.6372
	CdO	128.410	5.148 ^a	6.252 ^a
	CdS	144.477	5.825	4.855
	CdSe	191.37	6.077	5.664
	CdTe	240.01	6.481	5.856
	HgS	232.66	5.8514	7.7135
	HgSe	279.55	6.084	8.245
HgTe	328.19	6.4603	8.0849	

^aTheoretical

Table 1.7 Molecular weight M , lattice constants a and c and crystal density g for a number of hexagonal, wurtzite-type semiconductors at 300 K

System	Material	M (amu)	Lattice constant (Å)		g (g/cm ³)
			a	c	
IV	2H-SiC	40.0962	3.0763	5.0480	3.2187
III-V	AlN	40.98828	3.112	4.982	3.258
	GaN	83.730	3.1896	5.1855	6.0865
	InN	128.825	3.548	5.760	6.813
II-VI	BeO	25.0116	2.6979	4.380	3.009
	BeS ^a	41.078	3.440	5.618	2.370
	BeSe ^a	87.97	3.632	5.932	4.311
	BeTe ^a	136.61	3.972	6.486	5.120
	MgO	40.3044	3.199	5.086	2.970
	MgS	56.371	3.972	6.443	2.127
	MgSe	103.27	4.145	6.723	3.429
	MgTe	151.91	4.548	7.390	3.811
	ZnO	81.39	3.2495	5.2069	5.6768
	ZnS	97.46	3.8226	6.2605	4.0855
	ZnSe	144.35	3.996	6.626	5.232
	ZnTe	192.99	4.27	6.99	5.81
	CdO ^a	128.410	3.678	5.825	6.249
	CdS	144.477	4.1367	6.7161	4.8208
	CdSe	191.37	4.2999	7.0109	5.6615
	CdTe	240.01	4.57	7.47	5.90
	HgS ^a	232.66	4.1376	6.7566	7.7134
	HgSe ^a	279.55	4.302	7.025	8.246
	HgTe ^a	328.19	4.5681	7.4597	8.0850

^aEstimated or theoretical

1.4.3 Semiconductor Alloy

(a) Group-IV semiconductor

Table 1.8 gives the lattice-matching condition between some group-IV ternary alloys and Si substrate. The incorporation of carbon into Si or SiGe gives rise to additional flexibility for group-IV-based heterostructure design [11]. Due to huge lattice mismatch between diamond

Table 1.8 Lattice-matching conditions of some group-IV ternaries at 300 K

Material	Substrate	Expression	Remark
C _x Si _y Ge _{1-x-y}	Si	$x = 0.109 - 0.109y$	$0 \leq y \leq 1.0, x/(1-x-y) = 0.122$
C _x Si _y Sn _{1-x-y}	Si	$x = 0.362 - 0.362y$	$0 \leq y \leq 1.0, x/(1-x-y) = 0.567$
C _x Ge _y Sn _{1-x-y}	Si	$x = 0.362 - 0.284y$	$0 \leq y \leq 0.89$

and Si, a small amount of substantially incorporated C induces a substantial tensile strain in pseudomorphic C_xSi_{1-x} layers on Si. This effect can be exploited for $C_xSi_yGe_{1-x-y}/Si$, $C_xSi_ySn_{1-x-y}/Si$ and $C_xGe_ySn_{1-x-y}/Si$ heterostructures by properly choosing pseudomorphic compositions x and y . It should be noted, however, that the solubility of C into Si is only about 6×10^{-6} at% ($\sim 3 \times 10^{-17} \text{ cm}^{-3}$) at the melting point of Si. Carbon incorporated into substitutional lattice sites up to a few atomic percent has been achieved only using growth techniques far from thermodynamic equilibrium [12].

Figure 1.6 shows the plot of the lattice constant a versus x for bulk C_xSi_{1-x} . The open circles represent the experimental data for diamond and Si, while the solid circle shows the data for

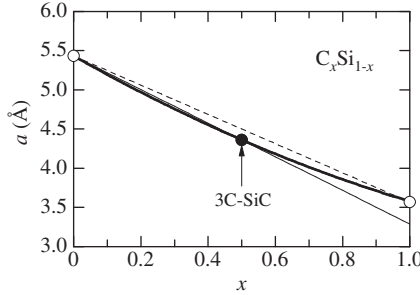


Figure 1.6 Lattice constant a versus x for bulk C_xSi_{1-x} at 300 K. The open and solid circles represent the experimental data. The light solid and dashed lines represent the results of Vegard law between Si ($x=0$) and 3C-SiC ($x=0.5$) and between Si ($x=0$) and diamond ($x=1.0$), respectively. The heavy solid line shows the theoretical values obtained from a Monte Carlo simulation by Kelires [13]

3C-SiC ($x=0.5$). The light solid line is obtained from Vegard law between Si and 3C-SiC ($x=0.5$), while the dashed line is obtained between Si and diamond ($x=1.0$). The 3C-SiC value is smaller than the linearly interpolated value. The heavy solid line in Figure 1.6 represents the theoretical a values for C_xSi_{1-x} obtained from a Monte Carlo calculation [13]. These values can be expressed as (in Å)

$$a(x) = 5.4310 - 2.4239x + 0.5705x^2 \quad (1.3)$$

The negative deviation $a(x)$ seen in Figure 1.6 has been confirmed experimentally from pseudomorphic C_xSi_{1-x} epilayers ($x < 0.012$) grown on Si(100) by solid-source MBE [14].

Si and Ge, both crystallize in the diamond structure, form a continuous series of Si_xGe_{1-x} alloys with x ranging from 0 to 1.0. The most precise and comprehensive determination of the lattice constant a and crystal density g across the whole alloy range was undertaken by Dismukes *et al.* [15]. The values they obtained for a and g are plotted versus x for Si_xGe_{1-x} in Figure 1.7. These data reveal a small deviation from Vegard law, i.e. from the linearity between the endpoint values. The lattice parameter a shows a downward bowing, while the density parameter g gives an upward bowing. From Figure 1.7, we obtain parabolic relation for a and g as a function of x (a in Å, g in g/cm^3)

$$a(x) = 5.6575 - 0.2530x + 0.0266x^2 \quad (1.4a)$$

$$g(x) = 5.3256 - 2.5083x - 0.4853x^2 \quad (1.4b)$$

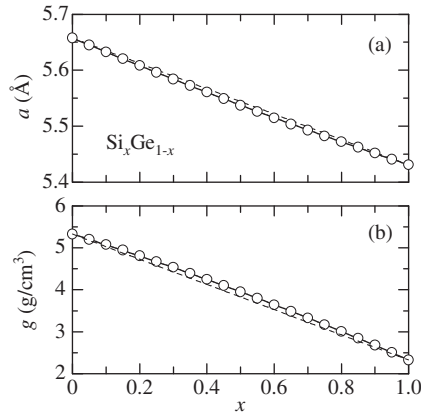


Figure 1.7 (a) Lattice constant a and (b) crystal density g for $\text{Si}_x\text{Ge}_{1-x}$ at 300 K. The experimental data are taken from Dismukes *et al.* [15]. The solid and dashed lines represent the parabolic and linear fit results, respectively

As shown in Figure 1.8, the diamond-type lattice, e.g. Si has only one type of first-neighbor distance

$$d(\text{Si}-\text{Si}) = \frac{\sqrt{3}}{4} a \text{ (four bonds)} \quad (1.5)$$

EXAFS has been popularly used to determine bond lengths for different types of neighbor atom pairs and the corresponding fractional occupancy of each type of neighbor. Recent EXAFS and XRD studies performed on strained $\text{Si}_x\text{Ge}_{1-x}/\text{Si}$ layers indicated that the Si-Si, Si-Ge and Ge-Ge nearest-neighbor distances are 2.35 ± 0.02 , 2.42 ± 0.02 and 2.38 ± 0.02 Å, respectively, close to the sum of their constituent-element covalent radii and independent of x , while the lattice constant varies monotonically with x [16,17]. More recently, Yonenaga *et al.* [18] investigated the local atomistic structure in bulk Czochralski-grown $\text{Si}_x\text{Ge}_{1-x}$ using EXAFS. As shown in Figure 1.9, the bond lengths Si-Si, Si-Ge and Ge-Ge in the bulk $\text{Si}_x\text{Ge}_{1-x}$ remain distinctly different lengths and vary in linear fashion of x over the entire composition range $0 \leq x \leq 1.0$, in agreement with expectation derived from *ab-initio* electronic structure calculation. These results suggest that $\text{Si}_x\text{Ge}_{1-x}$ is a typical disorder material and that the bond lengths and bond angles are disordered with x in $\text{Si}_x\text{Ge}_{1-x}$.

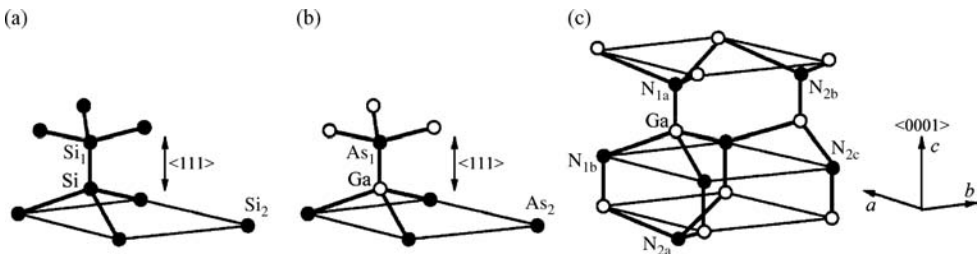


Figure 1.8 Bond distances in (a) diamond (Si), (b) zinc-blende (GaAs) and (c) wurtzite structures (GaN)

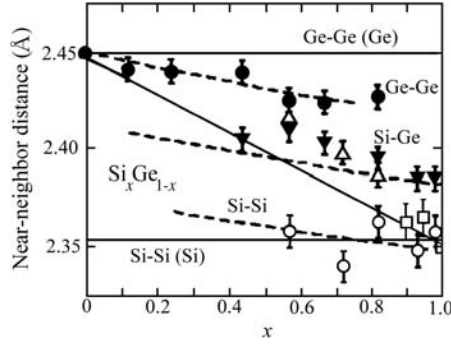


Figure 1.9 Near-neighbor distance in $\text{Si}_x\text{Ge}_{1-x}$ at 300 K. The experimental data are taken from Yonenaga *et al.* [18]. The horizontal lines show the bond lengths in bulk Si and Ge. The middle thin line is obtained from Vegard law

(b) III–V semiconductor

The expressions for a versus alloy composition can be obtained from Vegard law. The crystal density can also be calculated from $g = Md_M/N_A$, where M is the molecular weight, $N_A = 6.022 \times 10^{23} \text{ mol}^{-1}$ is the Avogadro constant and d_M is the molecular density [1].

The III–V quaternaries can be epitaxially grown on some III–V binaries (GaAs, InP, etc.). Introducing the binary lattice parameters in Table 1.6 into Equation (A.6) or Equation (A.8), we can obtain the lattice-matching conditions for $A_x\text{B}_{1-x}\text{C}_y\text{D}_{1-y}$ and $A_x\text{B}_y\text{C}_{1-x-y}\text{D}$ quaternaries on various III–V binary substrates. These results are summarized in Tables 1.9–1.11. The lattice-matching conditions in Tables 1.9–1.11 can be approximated by more simple expressions. Some results are presented in Table 1.12.

The lattice parameter a at 300 K as a function of x for $\text{Al}_x\text{Ga}_{1-x}\text{As}$ is shown in Figure 1.10. The experimental data are taken from Takahashi [19]. From a least-squares fit, we obtain

$$a(x) = 5.6533 + 0.0083x - 0.0003x^2 \quad (1.6)$$

The solid line in Figure 1.10 shows the calculated result of Equation (1.6). This equation promises that the lattice parameter for $\text{Al}_x\text{Ga}_{1-x}\text{As}$ can be given by Vegard law with good

Table 1.9 Lattice-matching conditions for some cubic, zinc-blende-type III–V quaternaries of type $A_x\text{B}_{1-x}\text{C}_y\text{D}_{1-y}$ at 300 K

$$x = \frac{A_0 + B_0y}{C_0 + D_0y}$$

Quaternary	Substrate	A_0	B_0	C_0	D_0	Remark
$\text{Al}_x\text{In}_{1-x}\text{P}_y\text{As}_{1-y}$	GaAs	0.4050	-0.1893	0.3969	0.0086	$0.04 \leq y \leq 1.0$
	InP	0.1893	-0.1893	0.3969	0.0086	$0 \leq y \leq 1.0$
$\text{Ga}_x\text{In}_{1-x}\text{P}_y\text{As}_{1-y}$	GaAs	0.4050	-0.1893	0.4050	0.0132	$0 \leq y \leq 1.0$
	InP	0.1893	-0.1893	0.4050	0.0132	$0 \leq y \leq 1.0$

Table 1.10 Lattice-matching conditions for some cubic, zinc-blende-type III–V quaternaries of type $A_xB_{1-x}C_yD_{1-y}$ at 300 K

$$y = \frac{A_0 + B_0x}{C_0 + D_0x}$$

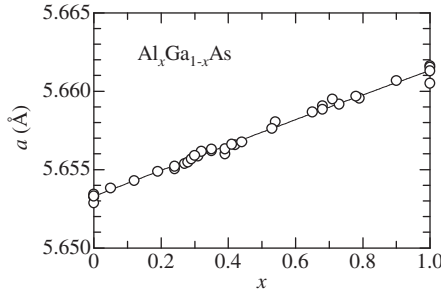
Quaternary	Substrate	A_0	B_0	C_0	D_0	Remark
$Al_xGa_{1-x}P_yAs_{1-y}$	GaAs	0	0.0081	0.2025	-0.0046	$0 \leq x \leq 1.0$
$Al_xGa_{1-x}P_ySb_{1-y}$	GaAs	0.4426	0.0396	0.6451	0.0269	$0 \leq x \leq 1.0$
	GaSb	0	0.0396	0.6451	0.0269	$0 \leq x \leq 1.0$
	InP	0.2269	0.0396	0.6451	0.0269	$0 \leq x \leq 1.0$
	InAs	0.0376	0.0396	0.6451	0.0269	$0 \leq x \leq 1.0$
$Al_xGa_{1-x}As_ySb_{1-y}$	GaSb	0	0.0396	0.4426	0.0315	$0 \leq x \leq 1.0$
	InP	0.2269	0.0396	0.4426	0.0315	$0 \leq x \leq 1.0$
	InAs	0.0376	0.0396	0.4426	0.0315	$0 \leq x \leq 1.0$
$Al_xIn_{1-x}P_ySb_{1-y}$	GaAs	0.8261	-0.3439	0.6104	0.0616	$0.53 \leq x \leq 1.0$
	GaSb	0.3834	-0.3439	0.6104	0.0616	$0 \leq x \leq 1.0$
	InP	0.6104	-0.3439	0.6104	0.0616	$0 \leq x \leq 1.0$
	InAs	0.4211	-0.3439	0.6104	0.0616	$0 \leq x \leq 1.0$
$Al_xIn_{1-x}As_ySb_{1-y}$	GaSb	0.3834	-0.3439	0.4211	0.0530	$0 \leq x \leq 1.0$
	InP	0.6104	-0.3439	0.4211	0.0530	$0.48 \leq x \leq 1.0$
	InAs	0.4211	-0.3439	0.4211	0.0530	$0 \leq x \leq 1.0$
$Ga_xIn_{1-x}P_ySb_{1-y}$	GaAs	0.8261	-0.3834	0.6104	0.0348	$0.52 \leq x \leq 1.0$
	GaSb	0.3834	-0.3834	0.6104	0.0348	$0 \leq x \leq 1.0$
	InP	0.6104	-0.3834	0.6104	0.0348	$0 \leq x \leq 1.0$
	InAs	0.4211	-0.3834	0.6104	0.0348	$0 \leq x \leq 1.0$
$Ga_xIn_{1-x}As_ySb_{1-y}$	GaSb	0.3834	-0.3834	0.4211	0.0216	$0 \leq x \leq 1.0$
	InP	0.6104	-0.3834	0.4211	0.0216	$0.47 \leq x \leq 1.0$
	InAs	0.4211	-0.3834	0.4211	0.0216	$0 \leq x \leq 1.0$

Table 1.11 Lattice-matching conditions for some cubic, zinc-blende-type III–V quaternaries of the type $A_xB_yC_{1-x-y}D$ or $AB_xC_yD_{1-x-y}$ at 300 K

Quaternary	Substrate	Expression	Remark
$Al_xGa_yIn_{1-x-y}P$	GaAs	$y = 0.5158 - 0.9696x$	$0 \leq x \leq 0.53$
$Al_xGa_yIn_{1-x-y}As$	InP	$y = 0.4674 - 0.9800x$	$0 \leq x \leq 0.48$
$AlP_xAs_ySb_{1-x-y}$	GaAs	$x = 0.7176 - 0.7055y$	$0 \leq y \leq 1.0$
	InP	$x = 0.3966 - 0.7055y$	$0 \leq y \leq 0.56$
	InAs	$x = 0.1149 - 0.7055y$	$0 \leq y \leq 0.16$
$GaP_xAs_ySb_{1-x-y}$	GaAs	$x = 0.6861 - 0.6861y$	$0 \leq y \leq 1.0$
	InP	$x = 0.3518 - 0.6861y$	$0 \leq y \leq 0.51$
	InAs	$x = 0.0583 - 0.6861y$	$0 \leq y \leq 0.08$
$InP_xAs_ySb_{1-x-y}$	GaSb	$x = 0.6282 - 0.6899y$	$0 \leq y \leq 0.91$
	InAs	$x = 0.6899 - 0.6899y$	$0 \leq y \leq 1.0$

Table 1.12 Approximated lattice-matching expression for some important cubic, zinc-blende-type III–V quaternaries at 300 K

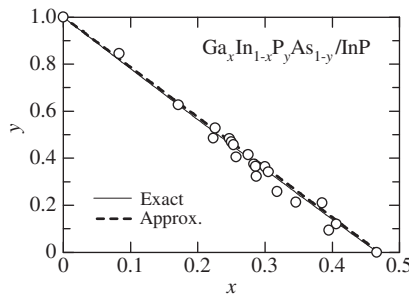
Quaternary	Substrate	Expression	Remark
$\text{Al}_x\text{Ga}_{1-x}\text{As}_y\text{Sb}_{1-y}$	GaSb	$y = 0.084x$	$0 \leq x \leq 1.0$
	InAs	$y = 0.085 + 0.078x$	$0 \leq x \leq 1.0$
$\text{Ga}_x\text{In}_{1-x}\text{P}_y\text{As}_{1-y}$	InP	$x = 0.47 - 0.47y$	$0 \leq y \leq 1.0$
	GaSb	$y = 0.91 - 0.91x$	$0 \leq x \leq 1.0$
$\text{Al}_x\text{Ga}_y\text{In}_{1-x-y}\text{P}$	InAs	$y = 1.00 - 0.91x$	$0 \leq x \leq 1.0$
	GaAs	$y = 0.52 - 0.97x$	$0 \leq x \leq 0.53$
$\text{Al}_x\text{Ga}_y\text{In}_{1-x-y}\text{As}$	InP	$y = 0.47 - 0.98x$	$0 \leq x \leq 0.48$

**Figure 1.10** Lattice parameter a as a function of x for $\text{Al}_x\text{Ga}_{1-x}\text{As}$ at 300 K. The experimental data are taken from Takahashi [19]. The solid line represents the quadratic least-squares fit

approximation. The difference in a between $\text{Al}_x\text{Ga}_{1-x}\text{As}$ and GaAs can also be written as

$$\frac{a(\text{Al}_x\text{Ga}_{1-x}\text{As}) - a(\text{GaAs})}{a(\text{GaAs})} = 0.0015x = 0.15x\% \quad (1.7)$$

Figure 1.11 shows the experimental x – y plots for $\text{Ga}_x\text{In}_{1-x}\text{P}_y\text{As}_{1-y}/\text{InP}$ [20]. The solid line shows the exactly calculated x – y relation in Table 1.9

**Figure 1.11** Plots of x versus y for $\text{Ga}_x\text{In}_{1-x}\text{P}_y\text{As}_{1-y}$ nearly lattice-matched to InP at 300 K. The experimental data are taken from Nahory *et al.* [20]. The solid and dashed lines show the lattice-matching relationships obtained from Vegard law in Equations (1.8) and (1.9), respectively

$$x = \frac{0.1893 - 0.1893y}{0.4050 + 0.0132y} \quad (1.8)$$

The dashed line also shows the calculated result using an expression in Table 1.12

$$x = 0.47 - 0.47y \quad (1.9)$$

Both expressions can explain the experimental x - y relation very well and simultaneously indicate the validity of Vegard law for $\text{Ga}_x\text{In}_{1-x}\text{P}_y\text{As}_{1-y}/\text{InP}$. It has, however, been reported that strained $\text{Al}_x\text{Ga}_{1-x}\text{Sb}/\text{GaSb}$ does not obey Vegard law [21].

The crystal density g versus y for $\text{Ga}_x\text{In}_{1-x}\text{P}_y\text{As}_{1-y}/\text{InP}$ is shown in Figure 1.12. The solid line represents the X-ray crystal density calculated from Equation (1.16) of Adachi [1], while the dashed line is obtained from the linear interpolation between the endpoint densities ($y=0, 1.0$). Their difference is within 2%.

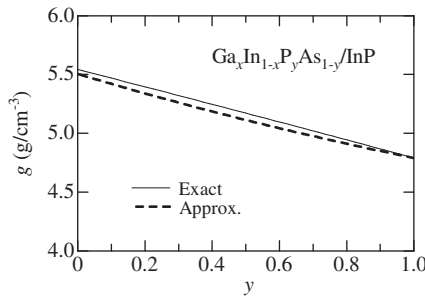


Figure 1.12 X-ray crystal density g versus y for $\text{Ga}_x\text{In}_{1-x}\text{P}_y\text{As}_{1-y}/\text{InP}$ at 300 K. The solid line represents the exact X-ray crystal density calculated from Equation (1.16) of Adachi [1], while the dashed line is obtained from the linear interpolation between the endpoint binary data

The experimental lattice parameter c as a function of x for $w\text{-Ga}_x\text{In}_{1-x}\text{N}$ is plotted in Figure 1.13. The experimental data are taken from Bearch *et al.* [22] (solid circles) and Romano *et al.* [23] (open circles). The $\text{Ga}_x\text{In}_{1-x}\text{N}$ layers ($0 \leq x \leq 0.14$) used by Bearch *et al.* [22] were grown on (0001) sapphire by MOCVD and were believed to be fully relaxed. On the other hand, the $\text{Ga}_x\text{In}_{1-x}\text{N}$ layers in Romano *et al.* [23] were pseudomorphically grown on 5 μm thick GaN on (0001) sapphire by MOCVD ($x=0-0.114$). The solid line in Figure 1.13 obeys Vegard law using $c = 5.1855 \text{ \AA}$ for GaN and $c = 5.760 \text{ \AA}$ for InN (Table 1.7).

Figure 1.14 shows the lattice parameter c versus x for strained $\text{Al}_x\text{Ga}_{0.9-x}\text{In}_{0.1}\text{N}$ alloy grown by MOCVD [24]. The dashed line represents the linear interpolation result using the endpoint values taken from Table 1.7. The lattice parameter c is found to decrease almost linearly with increasing x . The prediction of Vegard law gives no good agreement with the experimental data.

It can be concluded from Figure 1.13 that the fully relaxed $\text{Ga}_x\text{In}_{1-x}\text{N}$ films follow Vegard law well; however, no good agreement can be achieved in the case of the pseudomorphic alloy layers. As we will see later (Section 1.5.2), Vegard law may be applicable if any strain effects are artificially removed from such pseudomorphically strained layers.

HRXRD has been widely used and demonstrated that almost all III-V semiconductor alloys obey Vegard law well. It has also been reported that Vegard law remains valid in dilute nitrides, such as $\text{GaN}_x\text{As}_{1-x}$ and $\text{Ga}_x\text{In}_{1-x}\text{N}_y\text{As}_{1-y}$, as long as all N atoms in the dilute nitrides locate at the arsenic sites [25]. The N-N pairs are thought to be the predominant N-related defects that cause deviation from Vegard law [26]. Germini *et al.* [21], however, observed a deviation

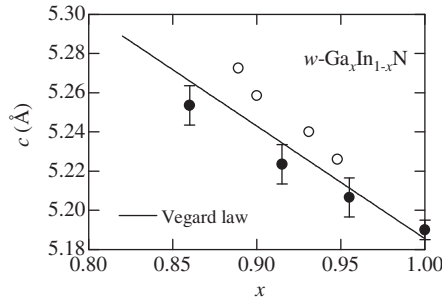


Figure 1.13 Lattice parameter c as a function of x for $w\text{-Ga}_x\text{In}_{1-x}\text{N}$ at 300 K. The experimental data are taken from Bearch *et al.* [22] (fully relaxed layers, solid circles) and Romano *et al.* [23] (pseudomorphic layers, open circles). The solid line represents the simply estimate of the c versus x relationship obtained from Vegard law

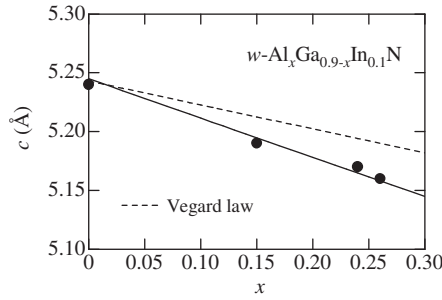


Figure 1.14 Lattice parameter c versus x for strained $w\text{-Al}_x\text{Ga}_{0.9-x}\text{In}_{0.1}\text{N}$ at 300 K. The experimental data are taken from Aumer *et al.* [24]. The dashed and solid lines represent the results of applying Vegard law before and after correcting for the biaxial strain effect

from Vegard law in MBE-grown $\text{Al}_x\text{Ga}_{1-x}\text{Sb}/\text{GaSb}$ layers by HRXRD, RBS and RHEED. These results are plotted in Figure 1.15. The experimental unstrained lattice parameters can be described by

$$a(x) = 6.09593 + 0.04360x - 4.229 \times 10^{-3} x^2 \quad (1.10)$$

The deviation from linearity is found to be larger than the prediction of a perfect random alloy in the frame of the Fournet model [27].

There is a significant structural difference between the bond distance in the zinc-blende and wurtzite structures of $\text{A}_x\text{B}_{1-x}\text{C}$ alloy. The first-neighbor distance in the zinc-blende structure is given from Figure 1.8 by

$$d(\text{Ga-As}) = \frac{\sqrt{3}}{4} a \text{ (four bonds)} \quad (1.11)$$

Yet, the wurtzite structure has two types of the first-neighbor anion-cation bond distances (Figure 1.8)

$$d(\text{Ga-N}_1) = ua \text{ (one bond)} \quad (1.12a)$$

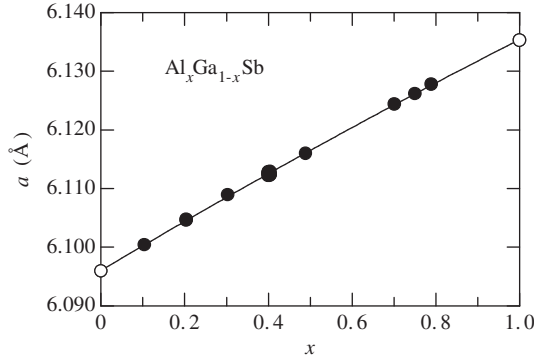


Figure 1.15 Room-temperature lattice constant a as a function of x for $\text{Al}_x\text{Ga}_{1-x}\text{Sb}$ grown on GaSb. The experimental data are taken from Germini *et al.* [21]. The solid line represents the quadratic best-fit result obtained using Equation (1.10)

$$d(\text{Ga}-\text{N}_2) = \sqrt{\frac{1}{3} + \left(\frac{1}{2}-u\right)^2 \left(\frac{c}{a_w}\right)^2} a_w \text{ (three bonds)} \quad (1.12b)$$

where u represents the cell-internal structural parameter and a_w and c show the lengths of the lattice vectors of the wurtzite structure. In the case of an ideal tetragonal ratio $c/a_w = (8/3)^{1/2} = 1.6330$ and an ideal cell internal parameter $u = 3/8$, it follows from Equation (1.12) that $d(\text{Ga}-\text{N}_1) = d(\text{Ga}-\text{N}_2)$.

In the zinc-blende lattice, we have only one type of second neighbor cation–anion bond distance

$$d(\text{Ga}-\text{As}) = \frac{\sqrt{11}}{4} a \text{ (12 bonds)} \quad (1.13)$$

On the other hand, the wurtzite lattice has three types of second neighbor cation–anion distances concerning the cation A (Ga) to anions C_{2a} , C_{2b} and C_{2c}

$$d(\text{Ga}-\text{N}_{2a}) = (1-u) \frac{c}{a_w} a_w \text{ (one bond)} \quad (1.14a)$$

$$d(\text{Ga}-\text{N}_{2b}) = \sqrt{1 + \left(\frac{uc}{a_w}\right)^2} a_w \text{ (six bonds)} \quad (1.14b)$$

$$d(\text{Ga}-\text{N}_{2c}) = \sqrt{\frac{4}{3} + \left(\frac{1}{2}-u\right)^2 \left(\frac{c}{a_w}\right)^2} a_w \text{ (three bonds)} \quad (1.14c)$$

For ideal wurtzite parameters of $c/a_w = (8/3)^{1/2} = 1.6330$ and $u = 3/8$, the following expression can be obtained from Equation (1.14)

$$d(\text{Ga}-\text{N}_{2a}) = 1.0206a_w, \quad d(\text{Ga}-\text{N}_{2b}) = d(\text{Ga}-\text{N}_{2c}) = 1.1726a_w \quad (1.15)$$

The spacing between the near-neighbor In–In or P–P atoms in InP is equal to $(1/\sqrt{2})a$. It would be anticipated that for an alloy the interatomic bond length of each constituent remains constant with alloy composition. Unfortunately, however, standard XRD techniques give information only on the lattice structure that is averaged over an area larger than the scale of

lattice constant. The interatomic structure in such semiconductor alloys was, therefore, not well understood until 1982. Mikkelsen and Boyce [28] reported in 1982 the interatomic structure of $\text{Ga}_x\text{In}_{1-x}\text{As}$ using an EXAFS. They found that the Ga–As and In–As near-neighbor distances change by only 0.04 Å as the In composition varies from 1 to 99 at% despite the fact that this alloy accurately follows Vegard law with a change in average near-neighbor spacing of 0.17 Å. We reproduce in Figure 1.16 the results of Mikkelsen and Boyce [28]. They also observed that the cation sublattice approaches a virtual crystal (i.e. an average fcc lattice) with a broadened single distribution of second-neighbor distances, whereas the anion sublattice exhibits a bimodal anion–anion second-neighbor distribution.

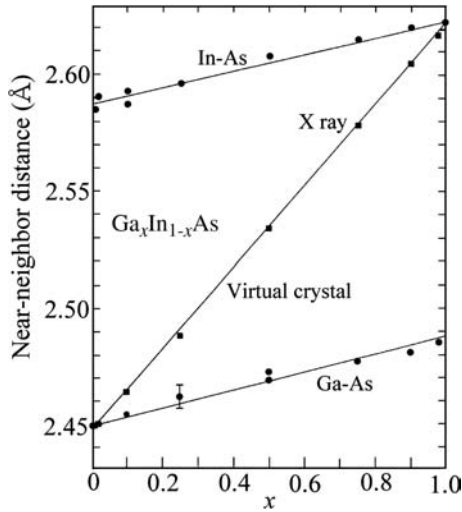


Figure 1.16 Near-neighbor distance in $\text{Ga}_x\text{In}_{1-x}\text{As}$ at 300 K. The middle thin line represents the bond length curve estimated from Vegard law. [Reprinted with permission from J. C. Mikkelsen, Jr. and J. B. Boyce, *Phys. Rev. Lett.* **49**, 1412 (1982). Copyright (1982) by the American Physical Society]

The essentially same EXAFS results, but on $\text{Ga}_x\text{In}_{1-x}\text{P}_y\text{As}_{1-y}/\text{InP}$, were reported by Oyanagi *et al.* [29]. They reported that the cation–anion distances in $\text{Ga}_x\text{In}_{1-x}\text{P}_y\text{As}_{1-y}/\text{InP}$ deviate from the average interatomic distance, but are rather close to the bond lengths in pure parent crystals. The cation–anion distances obtained from this study are plotted in Figure 1.17.

The near-neighbor distances in $w\text{-Ga}_x\text{In}_{1-x}\text{N}$ versus x are shown in Figure 1.18. The experimental data are taken from Jeffe *et al.* [30]. The theoretical lines are taken from Mattila and Zunger [31] in which the valence force field simulation with large supercells (512–1280 atoms) was used. It has been shown [31] that while the first-neighbor cation–anion bonds for different cations (Ga– N_1 and In– N_1) retain distinct values in the wurtzite and zinc-blende alloys, the second-neighbor cation–anion bonds Ga– N_2 and In– N_2 merge into a single bond length. However, the second-neighbor cation–anion bonds for the same cation exhibit a crucial difference between the wurtzite and zinc-blende structures. This is thought to be an intrinsic property of the binary constituents and persists in the alloy. The small splitting of the first-neighbor cation–anion bonds in the wurtzite structure is also preserved in the alloy, but obscured by bond length broadening [31].

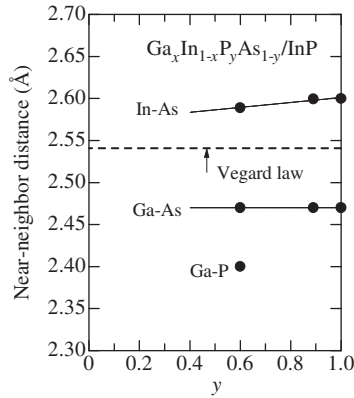


Figure 1.17 Near-neighbor distance in $Ga_xIn_{1-x}P_yAs_{1-y}/InP$ at 300 K. The experimental data are taken from Oyanagi *et al.* [29]. The dashed line represents the bond length curve obtained from Vegard law

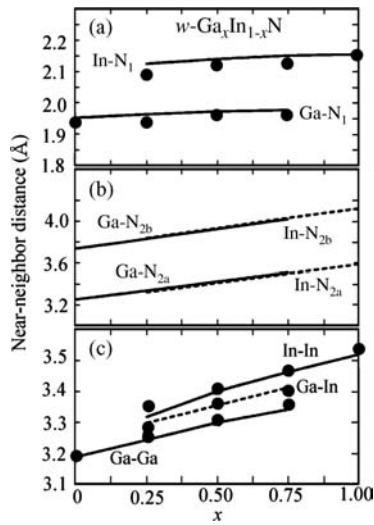


Figure 1.18 Near-neighbor distances versus x for $w-Ga_xIn_{1-x}N$. The experimental data were measured at 300 K by Jeffe *et al.* [30]. The theoretically calculated lines are taken from Mattila and Zunger [31] who used the valence force field simulation with large supercells (512–1280 atoms)

(c) II–VI semiconductor

Several II–VI semiconductor quaternaries can be epitaxially grown on III–V binary substrates. The corresponding lattice-matching relationships are shown in Tables 1.13 and 1.14. These relationships can be approximated using more simple expressions, as listed in Table 1.15.

Figure 1.19 shows the lattice constant a as a function of x for $Zn_xCd_{1-x}Te$. The experimental data were obtained at 300 K using an XRD combined with a WDXS [32]. The combination with WDXS led to an absolute composition error Δx of less than 0.01. These data suggest that Vegard

Table 1.13 Lattice-matching conditions for some cubic, zinc-blende-type II–VI quaternaries of the type $A_xB_{1-x}C_yD_{1-y}$ at 300 K

$$y = \frac{A_0 + B_0x}{C_0 + D_0x}$$

Quaternary	Substrate	A_0	B_0	C_0	D_0	Remark
$Mg_xZn_{1-x}S_ySe_{1-y}$	GaAs	0.016	0.241	0.259	0.031	$0 \leq x \leq 1.0$
$Mg_xZn_{1-x}Se_yTe_{1-y}$	InP	0.235	0.314	0.435	0.075	$0 \leq x \leq 0.84$

Table 1.14 Lattice-matching conditions for some cubic, zinc-blende-type II–VI quaternaries of the type $A_xB_yC_{1-x-y}D$ at 300 K

Quaternary	Substrate	Expression	Remark
$Be_xMg_yZn_{1-x-y}Se$	GaAs	$x = 0.030 + 0.453y$	$0 \leq y \leq 0.67$
$Mg_xZn_yCd_{1-x-y}Se$	InP	$y = 0.510 - 0.409x$	$0 \leq x \leq 0.83$

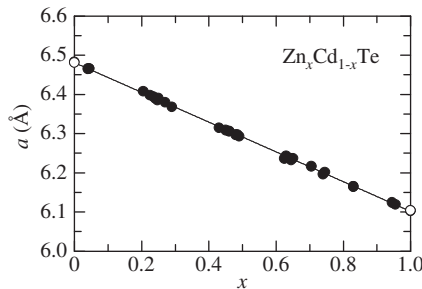
Table 1.15 Approximated lattice-matching expression for some important cubic, zinc-blende-type II–VI quaternaries at 300 K

Quaternary	Substrate	Expression	Remark
$Mg_xZn_{1-x}S_ySe_{1-y}$	GaAs	$y = 0.08 + 0.82x$	$0 \leq x \leq 1.0$
$Mg_xZn_{1-x}Se_yTe_{1-y}$	InP	$y = 0.55 + 0.54x$	$0 \leq x \leq 0.84$
$Be_xMg_yZn_{1-x-y}Se$	GaAs	$x = 0.03 + 0.45y$	$0 \leq y \leq 0.67$
$Mg_xZn_yCd_{1-x-y}Se$	InP	$y = 0.51 - 0.41x$	$0 \leq x \leq 0.83$

law is exactly valid within the limits of error $\Delta a/a \leq 4 \times 10^{-4}$ and follows the equation (in Å)

$$a(x) = 6.4822 - 0.3792x \quad (1.16)$$

CdS_xTe_{1-x} shows a zinc-blende–wurtzite crystalline phase change at any alloy composition. Early studies failed to grow alloys for the full range of compositions, concluding that a large

**Figure 1.19** Lattice constant a as a function of x for $Zn_xCd_{1-x}Te$ at 300 K. The experimental data are taken from Schenk *et al.* [32]. The solid line represents the linear best fit of Equation (1.16)

miscibility gap exists in the CdS–CdTe pseudobinary system [33]. In 1973 Ohata *et al.* [34] studied the bulk alloy system for the full range of compositions and reported a change in the crystalline phase at $x \sim 0.2$.

Figure 1.20 plots the lattice constants a and c versus x for bulk $\text{CdS}_x\text{Te}_{1-x}$ crystals as measured by Wood *et al.* [35] using XRD. The composition x of each pellet was determined independently using PIXE. In Figure 1.20, the phase change occurs at $x \sim 0.2$, in agreement with Ohata *et al.* [34]. The solid triangles represent the effective cubic lattice parameters $a_{\text{eff}} = (\sqrt{3}a^2c)^{1/3}$ defined in Adachi [1]. It can be concluded from Figure 1.20 that the lattice parameters both in the zinc-blende and wurtzite phases obey Vegard law well. It is also understood that if we consider a_{eff} , instead of a or c , in the wurtzite phase ($0.2 < x \leq 1.0$), $\text{CdS}_x\text{Te}_{1-x}$ gives the linear relationship between a and x over the whole alloy range ($0 \leq x \leq 1.0$).

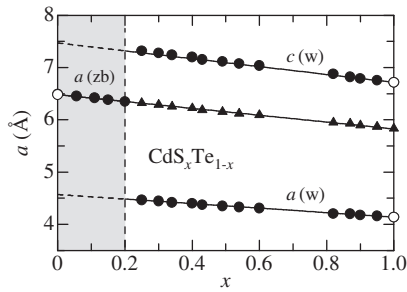


Figure 1.20 Lattice constants a and c versus x for bulk $\text{CdS}_x\text{Te}_{1-x}$ in the zinc-blende (zb) and wurtzite (w) structures at 300 K. The experimental data are taken from Wood *et al.* [35]. The solid triangles represent the effective cubic parameters $a_{\text{eff}} = (\sqrt{3}a^2c)^{1/3}$

Motta *et al.* [36] carried out EXAFS measurements on $\text{Zn}_x\text{Cd}_{1-x}\text{Te}$. These results are shown in Figure 1.21 by the open circles. The solid circles correspond to the XRD data by Schenk *et al.* [32]. We can see that the EXAFS bond lengths in Figure 1.21 change much less than the nearest-neighbor distances determined from the XRD. As in the case of the III–V alloys (Figures 1.16 and 1.17), the XRD lattice parameters in II–VI alloys do not reflect the actual bond lengths of the nearest neighbors. The EXAFS data of Motta *et al.* [36] agreed with a random distribution of atoms in the mixed cation sublattice.

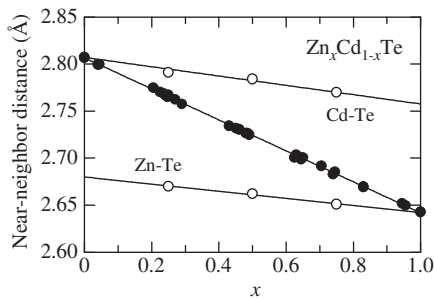


Figure 1.21 Near-neighbor distance in $\text{Zn}_x\text{Cd}_{1-x}\text{Te}$ at 300 K. The experimental data (open circles) are taken from Motta *et al.* [36]. The solid circles represent the bond lengths obtained from the XRD data by Schenk *et al.* [32]

1.5 COHERENT EPITAXY AND STRAIN PROBLEM

1.5.1 Bilayer Model

Recent semiconductor devices usually have multilayer structures. The distribution of strains in multilayer structures is the subject of perennial, great interest since internal strains normally arise in thin epitaxial films during the preparation by heteroepitaxial growth. Internal strains or stresses are a consequence of the mismatch of lattice constants and/or the difference in the thermal expansion coefficients of the individual layers. The strain and stress are related through the fourth-rank elastic stiffness $[C]$ or compliance tensor $[S]$ [1].

Let us consider the case of bonding a thin plate of zinc-blende crystal of size $N_e a_e \times N_e a_e \times t_e$ onto a substrate of a different size $N_s a_s \times N_s a_s \times t_s$, where N_i is the number of lattice atoms along the edge of the crystal plate, a_i is the lattice constant and t_i is the thickness of the plate; see Figure 1.22(a) [37]. To achieve a coherent interface, N_e is set to equal N_s . Let us assume that a_e is less than a_s and thus $l_e = N_e a_e$ is less than $l_s = N_s a_s$. The bonding operation is carried out in the following manner: equal and opposite forces F are applied to the plates to stretch plate ‘e’ and compress plate ‘s’ uniformly in the lateral direction to the same final dimension $l_f \times l_f$. The two plates are then bonded together with a perfect alignment of the atomic planes; see Figure 1.22(b). At the moment when the two plates are bonded together, the composite experiences an applied bending moment given by $F(t_s + t_e)/2$, which is counterbalanced by the moment resulting from the internal elastic stress. Finally, the applied forces are relieved, and the moments from the elastic stresses bend the composite in the direction shown in

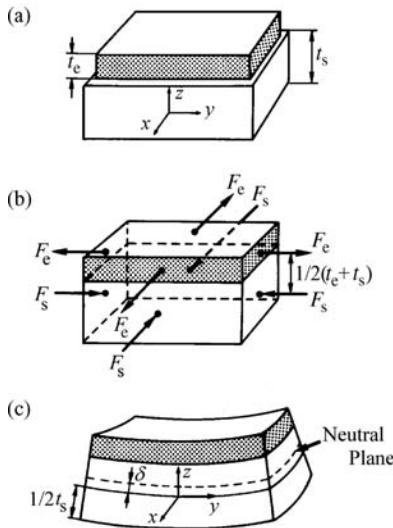


Figure 1.22 Formation of a two-layer composite: (a) two single-crystalline plates with the lattice constants a_e and a_s ($a_e < a_s$) and thicknesses t_e and t_s , respectively; (b) layer ‘e’ is stretched and layer ‘s’ is compressed to match the macroscopic dimension, and the two layers are then bonded together to form a composite; (c) the composite bends toward the side with the shorter lattice constant after removal of the external stresses F_e and F_s

Figure 1.22(c). The bending of the composite relaxes some of the stress, and the radius of curvature is determined by the final state of the internal stress.

Based on this bilayer model, Noyan and Segmüller [37] obtained the coherency condition in terms of the curvature radius R

$$\frac{a_e - a_s}{a_s} = \frac{2}{R} \left[\frac{t_s}{4} \left(1 + \frac{a_e t_e}{a_s t_s} \right) + \frac{1}{E_e t_s t_e (1 + t_e/t_s)} \frac{a_e}{a_s} \left(1 + \frac{a_s E_e t_e}{a_e E_s t_s} \right) \left(\frac{E_s t_s^3}{12} + \frac{E_e t_s^2 t_e}{4} \right) \right] \quad (1.17)$$

where

$$E_i = \frac{Y_i}{1 - P_i} \quad (1.18)$$

with Y = Young's modulus and P = Poisson's ratio. The term δ shown in Figure 1.22(c) represents the shift of the neutral axis of the composite from $t_s/2$. This quantity is given by

$$\delta = \frac{t_e E_e}{2 E_s} \frac{1 + t_e/t_s}{1 + (E_e t_e/E_s t_s)} \quad (1.19)$$

Solving the elastic force and momentum balance equations, Noyan and Segmüller [37] gave the elastic stress component X_{xx} parallel to the film as

$$X_{xx}^e = - \frac{E_e}{1 + (a_s E_e t_e/a_e E_s t_s)} \frac{a_s}{a_e} \left[\frac{a_e - a_s}{a_s} - \left(1 + \frac{a_e t_e}{a_s t_s} \right) \frac{t_s}{2R} \right] \quad (1.20)$$

The relationship between the film and substrate stresses is given by

$$X_{xx}^s = - \frac{t_e}{t_s} X_{xx}^e \quad (1.21)$$

The dependence of X_{xx} on z is now given by

$$X_{xx}^e(z) = X_{xx}^e + E_e \left(\frac{z - t_e/2}{R} \right) \quad \text{for } 0 \leq z \leq t_e \quad (1.22a)$$

$$X_{xx}^s(z) = -X_{xx}^e \frac{t_e}{t_s} + E_s \left(\frac{z + t_e/2}{R} \right) \quad \text{for } 0 \geq z \geq -t_s \quad (1.22b)$$

In the case where $a_e < a_s$, these expressions give $X_{xx}^s < 0$, $X_{xx}^e > 0$, and $R < 0$.

1.5.2 Elastic Strain and Lattice Deformation

Since X_{zz} is equal to zero in the bilayer model discussed above, the lattices are free to expand or contract in the z direction, that is, perpendicular to the interface. As seen in Figure 1.23, this causes the cubic lattice structure to be tetragonally distorted. Since both X_{xx}^i and X_{yy}^i have opposite signs for $i = s$ compared to $i = e$, the two cubic lattices are tetragonally distorted in the opposite sense, one with the lattice constant perpendicular to the interface lengthened and

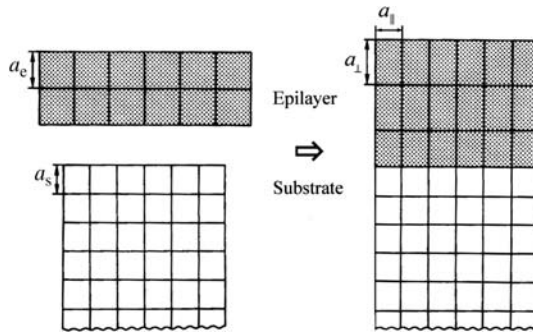


Figure 1.23 Cross section of an ‘epilayer–substrate’ system, where a_e and a_s are the unstrained lattice parameters of the epilayer and substrate, respectively

the other shortened. Therefore, the measured vertical mismatch is enhanced by the tetragonal distortion.

Lattice deformation between the epilayer and substrate can be determined by conventional XRD. For example $Ga_xIn_{1-x}P_yAs_{1-y}$ epilayers on InP(100) are shown in Figure 1.24 [38], where the $Ga_xIn_{1-x}P_yAs_{1-y}/InP$ samples were grown by LPE with the Ga atomic fractions in liquid solution between 0.4 and 1.0 at%. The experimental lattice deformation $\Delta a/a$ perpendicular to the layer surface for layers with a Ga fraction lower than ~ 0.0065 has a positive value (i.e. compressive strain in the growth direction), while it has negative values (tensile strain) for layers with a fraction larger than 0.0065.

In practical cases where the thickness of the epilayer is very small compared to that of the substrate, the lattice mismatch can be taken up totally by the tensile or compressive strain inside the epilayer, giving a coherent interface. A discontinuity in the lattice constant parallel to the interface can exist only in the presence of misfit dislocations. Nagai [39] studied the

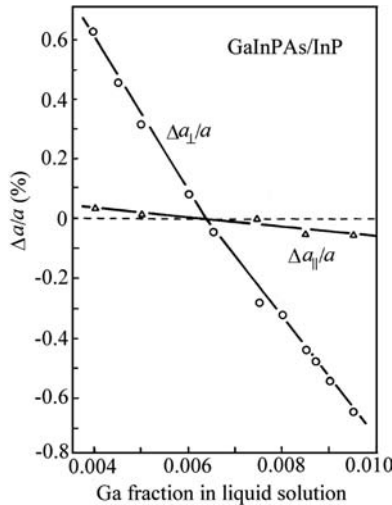


Figure 1.24 Lattice mismatch in a GaInPAs/InP heterostructure as a function of the Ga atom fraction in LPE-growth liquid solution. [Reprinted with permission from K. Oe and K. Sugiyama, *Appl. Phys. Lett.* **33**, 449 (1978). Copyright (1978) by the American Institute of Physics]

effects of lattice misfit on the lattice deformation for $\text{Ga}_x\text{In}_{1-x}\text{As}$ on GaAs by HT-VPE. The thickness of the substrates was in the range 2–5 mm and the epilayer was in the range 5–10 μm . His results are shown in Figure 1.25, where a_{\parallel} is the unstrained lattice parameter of the substrate (GaAs) and a_{\perp} is the strained lattice parameter of the epilayer due to tetragonal distortion.

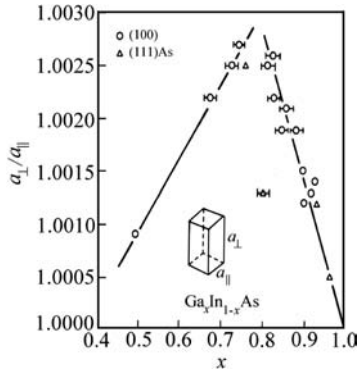


Figure 1.25 Lattice-constant ratio a_{\perp}/a_{\parallel} for HT-VPE-grown $\text{Ga}_x\text{In}_{1-x}\text{As}$ on (1 0 0) and (1 1 1)As planes of GaAs. [Reprinted with permission from H. Nagai, *J. Appl. Phys.* **45**, 3789 (1974). Copyright (1974) by the American Institute of Physics]

The lattice constant of InAs (6.0583 Å) is larger than that of GaAs (5.65330 Å). Thus, the $\text{Ga}_x\text{In}_{1-x}\text{As}$ lattice on GaAs is expected to be tetragonally distorted with the lattice constant perpendicular to the interface being lengthened. The measured lattice constants perpendicular to the film are indeed larger than that along the surface. In the region $x > 0.8$ the degree of deformation increased with decreasing x , but in the region $x < 0.8$ it decreased with decreasing x . With the aid of defect revealing etching, it was concluded that in the region $x > 0.8$ the lattice mismatch is relieved only by tetragonal distortion and for $x < 0.8$ it is relieved by both misfit dislocation and tetragonal distortion.

Figure 1.26 plots the lattice constant a versus x for strained $\text{C}_x\text{Si}_{1-x}$ alloy grown on Si(100) by solid-source MBE. The experimental data are taken from Berti *et al.* [14]. The dash-dotted

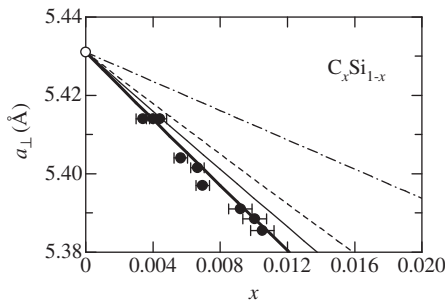


Figure 1.26 Lattice constant a versus x for strained $\text{C}_x\text{Si}_{1-x}$ grown on Si(1 0 0) by solid-source MBE. The experimental data are taken from Berti *et al.* [14]. The dash-dotted line represents the linearly interpolated values between diamond and Si. The light solid and dashed lines are calculated from Equation (1.23) by introducing a_0 values estimated from Vegard law between Si and 3C-SiC ($x = 0.5$) and between Si and C ($x = 1.0$), respectively. The heavy solid line is calculated by introducing the Monte Carlo-simulated lattice constants reported by Kelires [13] as a_0

line shows the linear interpolation result between diamond ($a = 3.5670 \text{ \AA}$) and Si ($a = 5.4310 \text{ \AA}$). We can see that the linear interpolation scheme predicts quite different lattice parameters from the experimental data.

The strain in the epilayer and hence the lattice constant in growth direction a_{\perp} can be calculated from the elastic theory [37]

$$a_{\perp} = (a_0 - a_{\parallel}) \left(1 + \frac{2P}{1-P} \right) + a_{\parallel} \quad (1.23)$$

where a_0 is the lattice constant of the relaxed material, a_{\parallel} is the in-plane lattice constant assumed to be the same as the substrate parameter and P is Poisson's ratio. In the case of cubic materials, Equation (1.23) can be rewritten as

$$a_{\perp} = (a_0 - a_{\parallel}) \left(1 + \frac{2C_{12}}{C_{11}} \right) + a_{\parallel} \quad (1.24)$$

where C_{ij} is the elastic stiffness constant.

The light solid and dashed lines in Figure 1.26 represent the calculated results of Equation (1.23) by introducing a_0 values estimated from Vegard law between Si and 3C-SiC ($x = 0.5$) and between Si and diamond ($x = 1.0$), respectively (Figure 1.6). The heavy solid line is also obtained from Equation (1.23) by introducing Monte Carlo-simulated lattice constants [13] as a_0 . The P values in Equation (1.23) are obtained from the linear interpolation between diamond and Si [1]. The results in Figure 1.26 suggest that the lattice constant a in C_xSi_{1-x} significantly deviates from Vegard law. The relationship between a and x can be finally given by Equation (1.3).

Figure 1.27 shows the lattice parameters perpendicular and parallel to the epilayer surface of MOMBE-grown GaN_xAs_{1-x} on GaAs(100) [40]. The experimental data clearly suggest that the GaN_xAs_{1-x} layers are coherently grown on the GaAs(100) substrates. The dashed line is simply estimated from the linear interpolation between c -GaN and GaAs. The solid lines are calculated from Equation (1.23) with $a_{\parallel} = 5.6517 \text{ \AA}$. The relaxed parameter a_0 and Poisson's ratios used in the calculation are taken from Vegard law between c -GaN and GaAs [1]. We can see in Figure 1.27 excellent agreement between the calculated and experimental lattice parameters.

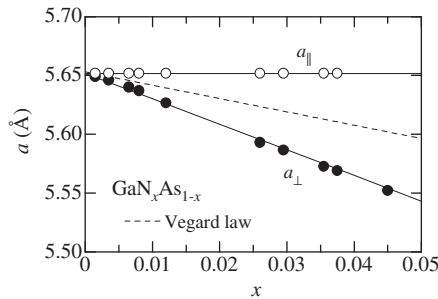


Figure 1.27 Lattice parameters perpendicular (a_{\perp}) and parallel (a_{\parallel}) to the epilayer surface of MOMBE-grown dilute-nitride GaN_xAs_{1-x} on GaAs(100). The experimental data are taken from Uesugi *et al.* [40]. The dashed line is simply estimated from Vegard law between c -GaN and GaAs. The solid lines are calculated from Equation (1.23) with $a_{\parallel} = 5.6517 \text{ \AA}$ (const.). The relaxed parameters a_0 and Poisson's ratios P are taken from Vegard law between c -GaN and GaAs

The essentially same analysis as in Figure 1.27 is performed on strained $\text{Al}_x\text{Ga}_{0.9-x}\text{In}_{0.1}\text{N}$ grown by MOCVD [24]. The solid line in Figure 1.14 represents the result of this analysis. Note that Poisson's ratio is a crystallographic plane- and direction-dependent quantity. The expressions of Poisson's ratio P and corresponding numeric values for some hexagonal semiconductors are summarized in Tables 3.19 and 3.20 of Adachi [1]. The quaternary P values used in Equation (1.23) are estimated from Vegard law. The in-plane lattice constant a_{\parallel} is assumed to be 5.240 Å. In Figure 1.14, there is good agreement between the calculated and experimental values even in the wurtzite crystal structure. However, in the case of relaxed $\text{Al}_x\text{In}_{1-x}\text{N}$ alloy Vegard law leads to an overestimation of the In mole fraction, which cannot be explained by either strain state or impurity levels. The In atomic fraction can be overestimated by as much as 6–37% in the range of $0.18 < x < 0.93$ [41].

Figures 1.28(a) and 1.28(b) show the experimental lattice parameters a and c for $\text{Mg}_x\text{Zn}_{1-x}\text{O}$ layers on sapphire (0001) [42] and on 6H-SiC (0001) [43]. The solid lines show the linear interpolation results of c and a between MgO and ZnO. The effective cubic lattice parameters $a_{\text{eff}} = (\sqrt{3}a^2c)^{1/3}$ for MgO and ZnO are, respectively, 4.484 and 4.567 Å, while those for sapphire and 6H-SiC are 6.335 Å and 4.359 Å, respectively. Coherently grown $\text{Mg}_x\text{Zn}_{1-x}\text{O}$ films on the sapphire and 6H-SiC substrates will be tensile- and compressive-strained, respectively. The ZnO ($x=0$) layers, however, exhibited virtually relaxed lattice constants of 3.246 and 5.205 Å along the a and c axes, respectively. As seen in Figure 1.28, the c - (a -) axis length decreased (increased) with increasing x for $\text{Mg}_x\text{Zn}_{1-x}\text{O}$ both on the sapphire and 6H-SiC substrates. The resulting ratio c/a decreased with increasing x , indicating that the $\text{Mg}_x\text{Zn}_{1-x}\text{O}$ films are considerably distorted from the ideal wurtzite although they are in the relaxed states.

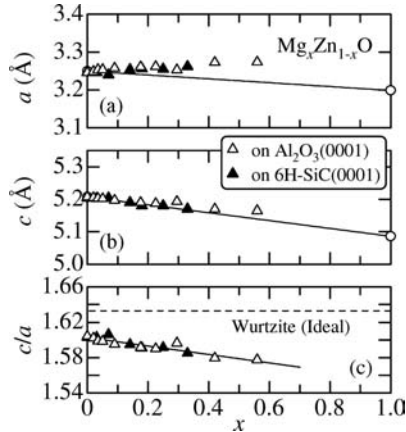


Figure 1.28 (a) a -axis and (b) c -axis lattice parameters at 300 K for $\text{Mg}_x\text{Zn}_{1-x}\text{O}$ grown on Al_2O_3 (0001) substrate by Ohtomo *et al.* [42] and on 6H-SiC (0001) substrate by Ashrafi and Segawa [43]. The solid lines in (a) and (b) show the linearly interpolated values of a and c between MgO and ZnO. The corresponding c/a ratios are plotted in (c)

1.5.3 Critical Thickness

Pseudomorphic epitaxy, in which a high-quality thin film is epitaxially grown on a lattice-mismatched substrate, has found its application in many areas [44]. SLs and QWs are high-quality multilayered structures grown from lattice matched and mismatched materials.

The large lattice mismatch is totally accommodated by uniform elastic strains in the layers if the layer thicknesses are kept below certain critical values. The idea for thin films emerged from a critical layer thickness h_c below which a dislocation-free, coherently strained interface would be stable and above which a misfit dislocation structure and semi-coherent interface would be stable. Knowledge of the so-called critical thickness is essential for realizing the advantages of lattice-mismatched heterostructure systems.

The critical thickness h_c of an epilayer, which was first considered by Frank and van der Merwe [45], is a parameter introduced to explain the experimental observation of coherent, pseudomorphic or strained-layer epitaxy. The breakdown of coherency can be determined in several ways. XRD and PL are commonly employed methods of determining the loss of coherency by demonstrating a change in average lattice constant (XRD) or a shift in PL peak energy and a reduction in PL intensity, following the release of strain. TEM is the direct manifestation of the breakdown of coherency.

We show in Figure 1.29 the critical thickness h_c versus x for (a) $\text{Si}_x\text{Ge}_{1-x}$ layer on Si, (b) $\text{Ga}_x\text{In}_{1-x}\text{As}$ layer on InP and (c) $\text{GaN}_x\text{As}_{1-x}$ layer on GaAs, respectively. Note that $x = 0.47$ in Figure 1.29(b) is the lattice-matching composition to InP.

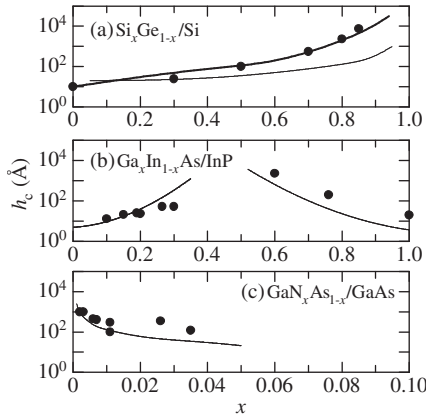


Figure 1.29 Critical thickness h_c versus x for (a) $\text{Si}_x\text{Ge}_{1-x}$ layer on Si, (b) $\text{Ga}_x\text{In}_{1-x}\text{As}$ layer on InP and (c) $\text{GaN}_x\text{As}_{1-x}$ layer on GaAs. The solid lines represent the theoretical model of Matthews and Blakeslee [46]. The heavy solid line in (a) is obtained from an energy-balanced misfit dislocation generation model by People and Bean [47]

Although several theories have been proposed to predict h_c [44], most semiconductor device designers rely upon the model of Matthews and Blakeslee [46]. The solid lines in Figure 1.29 show the results based on this model. The experimental h_c data usually exceed the Matthews–Blakeslee’s prediction. It is also understood that for $\text{Si}_x\text{Ge}_{1-x}$ there is little dependence of h_c on x . The heavy solid line in Figure 1.29(a) represents the theoretical curve obtained from an energy-balanced misfit dislocation generation model by People and Bean [47]. This model is in excellent agreement with the experimental data.

The critical thicknesses h_c for $\text{Al}_x\text{Ga}_{1-x}\text{N}$ and $\text{Ga}_x\text{In}_{1-x}\text{N}$ on relaxed GaN layers were measured by Akasaki and Amano [48]. The experimental h_c values were in the range 300 to 700 nm for $\text{Al}_x\text{Ga}_{1-x}\text{N}/\text{GaN}$ ($0.05 \leq x \leq 0.2$) and ~ 40 nm for $\text{Ga}_x\text{In}_{1-x}\text{N}/\text{GaN}$ ($0.8 \leq x \leq 0.95$).

The h_c values for $\text{Si}_x\text{Ge}_{1-x}/\text{Si}$ and some III–V and II–VI semiconductors grown on various lattice-mismatched substrates are summarized in Figure 1.30. The solid lines are obtained by least-squares fitting with (h_c in Å, $\Delta a/a$ in at%)

$$h_c = \left(\frac{A}{\Delta a/a} \right)^n \quad (1.25)$$

with $A = 7.5$ and $n = 3.5$ for $\text{Si}_x\text{Ge}_{1-x}/\text{Si}$, $A = 16$ and $n = 2.4$ for III–V semiconductors and $A = 52$ and $n = 1.5$ for II–VI semiconductors. It should be noted that the II–VI semiconductors have weak bond strength. The dislocation energy in such semiconductors is much smaller than those in $\text{Si}_x\text{Ge}_{1-x}/\text{Si}$ and III–V semiconductors. Therefore, dislocations can be more easily generated in the II–VI semiconductors.

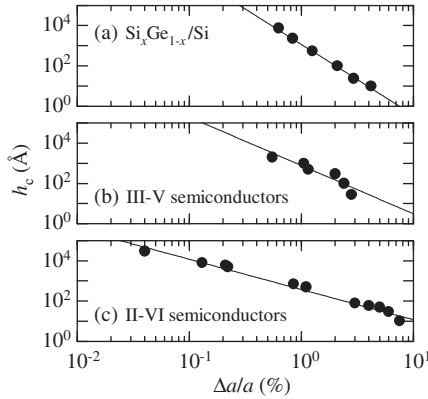


Figure 1.30 Critical thickness h_c for (a) $\text{Si}_x\text{Ge}_{1-x}$, (b) III–V and (c) II–VI semiconductors grown on various lattice-mismatched substrates. The solid lines represent the least-squares fit using Equation (1.25)

1.6 STRUCTURAL PHASE TRANSITION

At high pressure the group-IV elemental semiconductors show metallic transitions in a sequence from cubic (diamond) \rightarrow tetragonal (β -Sn) \rightarrow simple hexagonal \rightarrow hexagonal close packed. Similarly, the III–V and II–VI binary semiconductors exhibit a variety of the crystal structures at high pressures. In Tables 1.8 and 1.9 of Adachi [1], transition pressure to the first phase (P_T) and transition sequences can be found for some group-IV, III–V and II–VI semiconductors. The additional data are: $P_T = 56$ GPa (zinc-blende \rightarrow hexagonal (NiAs)) for BeSe; $P_T = 35$ GPa (zincblende \rightarrow hexagonal (NiAs)) for BeTe; and $P_T = 90.6$ GPa (rocksalt \rightarrow CsCl) for CdO.

There are a very few studies on the structural phase transition in semiconductor alloys. Some of these studies are summarized in Table 1.16. Webb *et al.* [49] observed the phase transition in $\text{Zn}_x\text{Cd}_{1-x}\text{Te}$ from the zinc-blende to rocksalt structures. However, the recent studies on ZnTe and CdTe suggest the presence of cinnabar phase between the zinc-blende and rocksalt structures [50]. Vnuk *et al.* [51] studied the effect of pressure on semiconductor

Table 1.16 Phase-transition sequence observed for some III–V and II–VI ternaries at high pressures. zb = zinc-blende; or = orthorhombic; w = wurtzite; rs = rocksalt (NaCl); cin = cinnabar

System	Material	Sequence	Ref.
III–V	$\text{Ga}_x\text{In}_{1-x}\text{P}$	semiconductor \rightarrow metal (optical absorption)	<i>a</i>
	$\text{Al}_x\text{Ga}_{1-x}\text{As}$	zb \rightarrow or (<i>Pmm2</i>)/or (<i>Cmcm</i>) (GaAs like)	<i>b</i>
	$\text{Ga}_x\text{In}_{1-x}\text{Sb}$	zb \rightarrow β -Sn	<i>c</i>
II–VI	$\text{Mg}_x\text{Zn}_{1-x}\text{O}$	w \rightarrow rs	<i>d</i>
	$\text{Zn}_x\text{Cd}_{1-x}\text{S}$	zb \rightarrow rs	<i>e</i>
	$\text{Zn}_x\text{Cd}_{1-x}\text{Se}$	zb \rightarrow rs ($x=0.9$)	<i>f</i>
		semiconductor \rightarrow metal ($0 \leq x \leq 0.32$)	<i>g</i>
	$\text{Zn}_x\text{Cd}_{1-x}\text{Te}$	zb \rightarrow rs	<i>h</i>
	$\text{ZnS}_x\text{Se}_{1-x}$	semiconductor \rightarrow metal (resistance)	<i>i</i>
	$\text{ZnSe}_x\text{Te}_{1-x}$	zb \rightarrow cin \rightarrow rs ($0 \leq x \leq 0.55$)	<i>j</i>
		zb \rightarrow rs ($0.55 < x \leq 1$)	<i>j</i>

- ^aA. R. Goñi *et al.*, *Phys. Rev. B* **39**, 3178 (1989)
- ^bW. Paszkowicz *et al.*, *Acta Phys. Pol. A*, **91**, 993 (1997)
- ^cC. Y. Liu *et al.*, *J. Phys. Chem. Solids* **39**, 113 (1978)
- ^dJ. A. Sans and A. Segura, *High Pressure Res.* **24**, 119 (2004)
- ^eA. Béliveau and C. Carlone, *Phys. Rev. B* **44**, 3650 (1991)
- ^fC.-M. Lin *et al.*, *Phys. Rev. B* **58**, 16 (1998)
- ^gY. C. Lin *et al.*, *J. Appl. Phys.* **101**, 073507 (2007)
- ^hA. W. Webb *et al.*, *J. Appl. Phys.* **61**, 2492 (1987)
- ⁱS. R. Tiong *et al.*, *Jpn. J. Appl. Phys.* **28**, 291 (1989)
- ^jJ. Pellicer-Porres *et al.*, *Phys. Rev. B* **71**, 035210 (2005)

(α -Sn)-to-metal (β -Sn) transition temperature in dilute $\text{Ge}_x\text{Sn}_{1-x}$ ($x \leq 1$ at%). They obtained a slope of -48.4 ± 6 K/kbar, in good agreement with thermodynamic prediction.

Figure 1.31 plots the transition pressure to the first phase P_T versus x for $\text{Ga}_x\text{In}_{1-x}\text{Sb}$. The experimental data are taken from Liu *et al.* [52]. A slight bowing can be found in the P_T versus

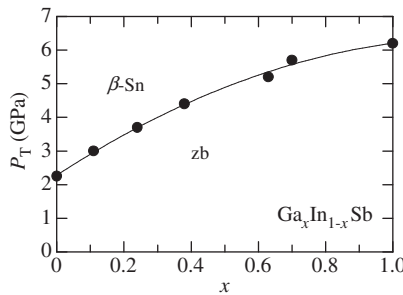


Figure 1.31 Transition pressure to the first phase P_T versus x for $\text{Ga}_x\text{In}_{1-x}\text{Sb}$. The experimental data are taken from Liu *et al.* [52]. The solid line shows the quadratic-fit result using Equation (1.26). zb = zinc-blende

x plots. The solid line shows the best-fit result of the quadratic expression (in GPa)

$$P_T(x) = 2.3 + 6.5x - 2.6x^2 \tag{1.26}$$

The transition pressures to the first phase P_T against alloy composition x for some II–VI semiconductors are shown in Figure 1.32. The experimental data are taken for $Zn_xCd_{1-x}S$ from Béliveau and Carlone [53], for ZnS_xSe_{1-x} from Tiong *et al.* [54] and for $ZnSe_xTe_{1-x}$ from Pellicer-Porres *et al.* [55]. In Figure 1.32(c), the transition pressure to the second phase is also plotted with the open circles. The linear interpolation is concluded to be an efficient tool to estimate the phase transition pressure in semiconductor alloys.

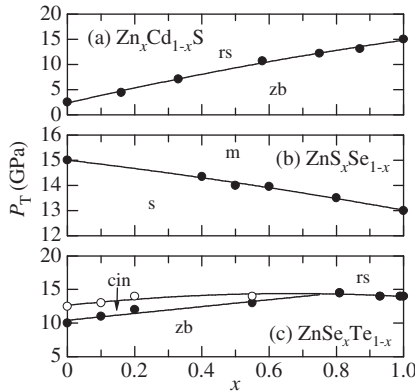


Figure 1.32 Transition pressures to the first phase P_T against x for (a) $Zn_xCd_{1-x}S$, (b) ZnS_xSe_{1-x} and (c) $ZnSe_xTe_{1-x}$. The transition pressure to the second phase is plotted in (c) by the open circles. The experimental data are taken for (a) $Zn_xCd_{1-x}S$ from Béliveau and Carlone [53], for (b) ZnS_xSe_{1-x} from Tiong *et al.* [54] and for (c) $ZnSe_xTe_{1-x}$ from Pellicer-Porres *et al.* [55]. cin = cinnabar; m = metal; rs = rocksalt (NaCl); s = semiconductor; zb = zinc-blende

1.7 CLEAVAGE PLANE

1.7.1 Cleavage

The cleavage properties of a crystal are strongly related to the atomic arrangement and corresponding electron density map. The most readily cleaved crystallographic planes can then be determined only by the crystalline structure. They are (111) plane for alloys of diamond type, (1 1 0) plane for zinc-blende type, (11 $\bar{2}$ 0) and (10 $\bar{1}$ 0) planes for wurtzite type and (100) plane for rocksalt type [1].

1.7.2 Surface Energy

The cleavage energy is assumed equal to twice the surface energy of that plane. There is a dearth of experimental measurements on surface energy. The surface energies for several group-VI elemental, III–V and II–VI binary semiconductors are listed in Tables 1.11–1.13 of Adachi [1]. No surface energy data are available for semiconductor alloys.

REFERENCES

- [1] S. Adachi, *Properties of Group-IV, III-V and II-VI Semiconductors*, John Wiley & Sons Ltd, Chichester, 2005.
- [2] A. Mascarenhas, *Spontaneous Ordering in Semiconductor Alloys*, Kluwer Academic, New York, 2002.
- [3] A. Ourmazd and J. C. Bean, *Phys. Rev. Lett.* **55**, 765 (1985).
- [4] J. Schilz and V. N. Romanenko, *J. Mater. Sci.: Mater. Electron.* **6**, 265 (1995).
- [5] T. S. Kuan, T. F. Kuech, W. I. Wang, and E. L. Wilkie, *Phys. Rev. Lett.* **54**, 201 (1985).
- [6] T. Suzuki, in A. Mascarenhas, *Spontaneous Ordering in Semiconductor Alloys*, Kluwer Academic, New York, 2002, p. 1.
- [7] A. Gomyo, M. Sumino, I. Hino, and T. Suzuki, *Jpn. J. Appl. Phys.* **34**, L469 (1995).
- [8] A. Gomyo, K. Makita, I. Hino, and T. Suzuki, *Phys. Rev. Lett.* **72**, 673 (1994).
- [9] A. A. Mbaye, L. G. Ferreira, and A. Zunger, *Phys. Rev. Lett.* **58**, 49 (1987).
- [10] H. S. Lee, S. Yi, T. W. Kim, Y. J. Park, J. Y. Lee, M. S. Kwon, and H. L. Park, *Solid State Commun.* **137**, 70 (2006).
- [11] R. A. Soref, *Proc. IEEE* **81**, 1687 (1993).
- [12] E. T. Croke, A. T. Hunter, C. C. Ahn, T. Laursen, D. Chandrasekhar, A. E. Bair, D. J. Smith, and J. W. Mayer, *J. Cryst. Growth* **175-176**, 486 (1997).
- [13] P. C. Kelires, *Phys. Rev. B* **55**, 8784 (1997).
- [14] M. Berti, D. D. Salvador, A. V. Drigo, F. Romanato, J. Stangl, S. Zerlauth, F. Schäffler, and G. Bauer, *Appl. Phys. Lett.* **72**, 1602 (1998).
- [15] J. P. Dismukes, L. Ekstrom, and R. J. Paff, *J. Phys. Chem.* **68**, 3021 (1964).
- [16] M. Matsuura, J. M. Tonnerre, and G. S. Cargill III, *Phys. Rev. B* **44**, 3842 (1991).
- [17] H. Kajiyama, S. Muramatsu, T. Shimada, and Y. Nishino, *Phys. Rev. B* **45**, 14005 (1992).
- [18] I. Yonenaga, M. Sakurai, M. H. F. Sluiter, Y. Kawazoe, and S. Muto, *J. Mater. Sci.: Mater. Electron.* **16**, 429 (2005).
- [19] N. S. Takahashi, in *Properties of Aluminium Gallium Arsenide*, EMIS Datareviews Series No. 7 (edited by S. Adachi), INSPEC, London, 1993, p. 3.
- [20] R. E. Nahory, M. A. Pollack, W. D. Johnston, Jr., and R. L. Barns, *Appl. Phys. Lett.* **33**, 659 (1978).
- [21] F. Germini, C. Bocchi, C. Ferrari, S. Franchi, A. Baraldi, R. Magnanini, D. D. Salvador, M. Berti, and A. V. Drigo, *J. Phys. D: Appl. Phys.* **32**, A12 (1999).
- [22] J. D. Bearch, H. Al-Thani, S. McCray, R. T. Collins, and J. A. Turner, *J. Appl. Phys.* **91**, 5190 (2002).
- [23] L. T. Romano, B. S. Krusor, M. D. McCluskey, and D. P. Bour, *Appl. Phys. Lett.* **73**, 1757 (1998).
- [24] M. E. Aumer, S. F. LeBoeuf, F. G. McIntosh, and S. M. Bedair, *Appl. Phys. Lett.* **75**, 3315 (1999).
- [25] G. Bisognin, D. D. Salvador, C. Mattevi, M. Berti, A. V. Drigo, G. Ciatto, L. Grenouillet, P. Duvaut, G. Gilet, and H. Mariette, *J. Appl. Phys.* **95**, 48 (2004).
- [26] S. Z. Wang, S. F. Yoon, W. J. Fan, W. K. Loke, T. K. Ng, and S. Z. Wang, *J. Appl. Phys.* **96**, 2010 (2004).
- [27] G. Fournet, *J. Phys. Radium* **14**, 374 (1953).
- [28] J. C. Mikkelsen, Jr., and J. B. Boyce, *Phys. Rev. Lett.* **49**, 1412 (1982); *Phys. Rev. B* **28**, 7130 (1983)
- [29] H. Oyanagi, Y. Takeda, T. Matsushita, T. Ishiguro, and A. Sasaki, in *Gallium Arsenide and Related Compounds*, IOP, Bristol, 1986, p. 295.
- [30] N. J. Jeffe, A. V. Blant, T. S. Cheng, C. T. Foxon, C. Bailey, P. G. Harrison, J. F. W. Mosselmans, and A. J. Dent, *Mater. Res. Soc. Symp. Proc.* **512**, 519 (1998).
- [31] T. Mattila and A. Zunger, *J. Appl. Phys.* **85**, 160 (1999).
- [32] M. Schenk, I. Hähnert, L. T. H. Duong, and H.-H. Niebsch, *Cryst. Res. Technol.* **31**, 665 (1996).
- [33] E. Cruceanu and D. Niculesciu, *Compt. Rend. Acad. Sci.* **261**, 935 (1965).
- [34] K. Ohata, J. Saraale, and T. Tanaka, *Jpn. J. Appl. Phys.* **12**, 1198 (1973).
- [35] D. A. Wood, K. D. Rogers, D. W. Lane, G. J. Conibeer, and D. Parton, *J. Mater. Sci. Lett.* **17**, 1511 (1998).

- [36] N. Motta, A. Balzarotti, P. Letardi, A. Kisiel, M. T. Czyzyk, M. Zimnal-Starnawska, and M. Podgorny, *Solid State Commun.* **53**, 509 (1985).
- [37] I. C. Noyan and A. Segmüller, *J. Appl. Phys.* **60**, 2980 (1986).
- [38] K. Oe and K. Sugiyama, *Appl. Phys. Lett.* **33**, 449 (1978).
- [39] H. Nagai, *J. Appl. Phys.* **45**, 3789 (1974).
- [40] K. Uesugi, N. Morooka, and I. Suemune, *Appl. Phys. Lett.* **74**, 1254 (1999).
- [41] T. Seppänen, L. Hulman, J. Birch, M. Beckers, and U. Kreissig, *J. Appl. Phys.* **101**, 043519 (2007).
- [42] A. Ohtomo, M. Kawasaki, T. Koida, K. Masubuchi, H. Koinuma, Y. Sakurai, Y. Yoshida, T. Yasuda, and Y. Segawa, *Appl. Phys. Lett.* **72**, 2466 (1998).
- [43] A. B. M. A. Ashrafi and Y. Segawa, *J. Vac. Sci. Technol. B* **23**, 2030 (2005).
- [44] S. Jain, M. Willander, and R. Van Overstraeten, *Compound Semiconductors Straiend Layers and Devices*. Kluwer Academic. Boston, 2000.
- [45] F. C. Frank and J. H. van der Merwe, *Proc. Roy. Soc. A* **201**, 261 (1950).
- [46] J. W. Matthews and A. E. Blakeslee, *J. Cryst. Growth* **27**, 118 (1974).
- [47] R. People and J. C. Bean, *Appl. Phys. Lett.* **49**, 229 (1986).
- [48] I. Akasaki and H. Amano, in *Semiconductors and Semimetals*, Vol. **50** (edited by J. I. Pankove and T. D. Moustakas), Academic, New York, 1998, p. 459.
- [49] A. W. Webb, S. B. Qadri, E. R. Carpenter, Jr., E. F. Skelton, and J. Kennedy, *J. Appl. Phys.* **61**, 2492 (1987).
- [50] S. Adachi, *Handbook on Physical Properties of Semiconductors: Volume 3 II–VI Semiconductors*. Kluwer Academic, Boston, 2004.
- [51] F. Vnuk, A. D. Monte, and R. W. Smith, *J. Appl. Phys.* **55**, 4171 (1984).
- [52] C. Y. Liu, I. L. Spain, and E. F. Skelton, *J. Phys. Chem. Solids* **39**, 113 (1978).
- [53] A. Béliveau and C. Carlone, *Phys. Rev. B* **44**, 3650 (1991).
- [54] S. R. Tiong, M. Hiramatsu, Y. Matsushima, and E. Ito, *Jpn. J. Appl. Phys.* **28**, 291 (1989).
- [55] J. Pellicer-Porres, D. Martínez-García, Ch. Ferrer-Roca, A. Segura, and V. Muñoz-Sanjosé, *Phys. Rev. B* **71**, 035210 (2005).

2 Thermal Properties

2.1 MELTING POINT AND RELATED PARAMETERS

2.1.1 Phase Diagram

(a) Group-IV semiconductor alloy

Figure 2.1 shows the phase diagram for the Si–Ge system at temperatures near the melting point. The experimental data are taken from various sources. The solid lines show the quadratic fit results (in °C)

$$\text{Solidus surface : } T_s(x) = 937 + 244x + 231x^2 \quad (2.1a)$$

$$\text{Liquidus surface : } T_l(x) = 937 + 916x - 442x^2 \quad (2.1b)$$

The phase diagram in Figure 2.1 suggests that Si and Ge are completely miscible as liquid and as solid. Stable phases formed by Si and Ge are the liquid and a cubic diamond-type substitutional solid solution. No phase changes or decompositions were detected roentgenographically after annealing homogeneous $\text{Si}_x\text{Ge}_{1-x}$ solid solutions for several months at temperatures in the range 177–925 °C [1]. At high pressures above ~15 GPa, the bct structure of a Si–Ge solid solution is estimated to be more stable than the diamond structure [2]. The Si–Ge system is a typical representative of a system with strong segregation, i.e. a solid solution in which the solid and liquid phases are separated by a large regime of coexistence.

(b) III–V semiconductor alloy

A series of papers demonstrated the feasibility of calculating phase diagrams in III–V ternary systems based upon the regular or quasichemical equilibrium model for the solid and liquid phases [3–5]. Because of the small lattice difference between GaAs and AlAs, their solid solutions are the closest in the III–V semiconductor systems to being ideal and the alloys are among the easiest to prepare by LPE. A perspective diagram depicting the solidus surface, liquidus surface and binary boundaries of the Al–Ga–As ternary system is shown in Figure 2.2(a). Figure 2.2(b) also shows the pseudobinary phase diagram of AlAs–GaAs system.

We can see in Figure 2.2 that AlAs and GaAs are completely miscible as liquid and as solid. Stable phases formed by these binary compounds are the liquid and a cubic zinc-blende substitutional solid solution of Al and Ga atoms in the cation site. The solid lines in Figure 2.2(b) represent the solidus and liquidus surfaces (in °C) [6]

$$\text{Solidus surface : } T_s(x) = 1238 - 54x + 560x^2 \quad (2.2a)$$

$$\text{Liquidus surface : } T_l(x) = 1238 + 1082x - 580x^2 \quad (2.2b)$$

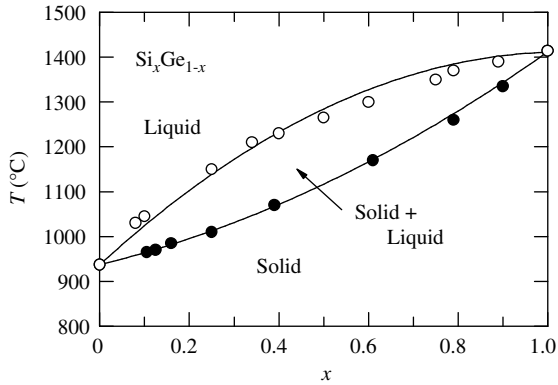


Figure 2.1 Normal-pressure phase diagram of a Si–Ge system. The solid lines represent the quadratic fits using Equation (2.1)

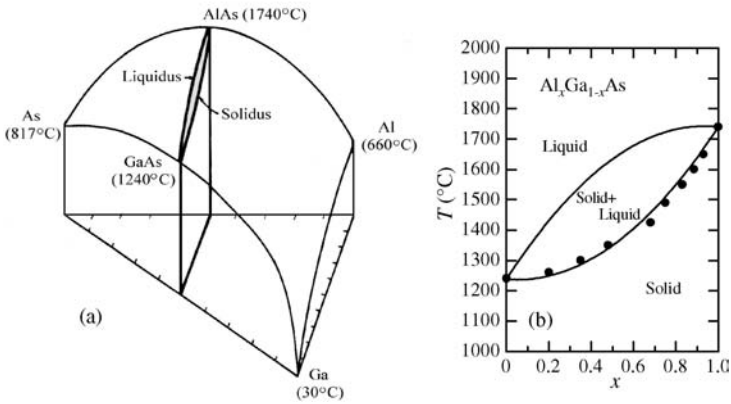


Figure 2.2 (a) Perspective diagram depicting the solidus surface, liquidus surface and binary boundaries in the Al–Ga–As ternary system. (b) Solidus and liquidus curves for the AlAs–GaAs pseudobinary system. The solid lines in (b) represent the solidus and liquidus surfaces calculated from Equation (2.2)

Figure 2.3 shows the solidus and liquidus curves for (a) GaP–InP, (b) GaAs–InAs and (c) GaSb–InSb systems. These systems provided a homogeneous series of alloys differing only in the anion substitution. The pseudobinary GaSb–InSb system can be approximated by the quadratic expressions (in °C)

$$\text{Solidus surface : } T_s(x) = 524 - 72x + 261x^2 \tag{2.3a}$$

$$\text{Liquidus surface : } T_l(x) = 524 + 280x - 90x^2 \tag{2.3b}$$

This is not the case for the GaP–InP and GaAs–InAs systems, as seen in Figures 2.3(a) and 2.3(b).

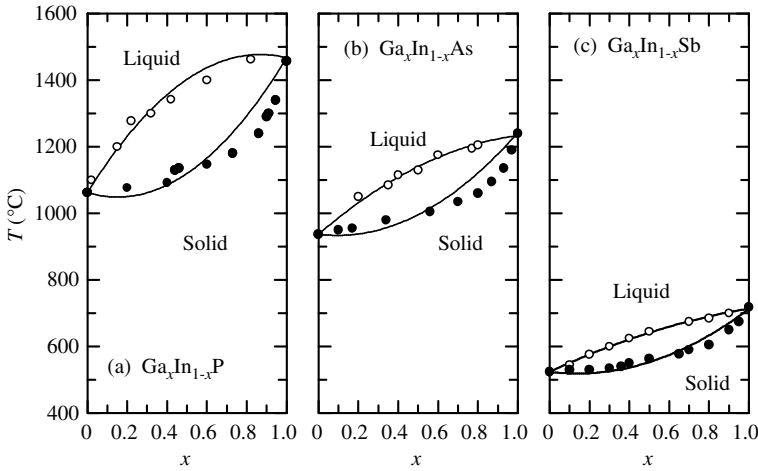


Figure 2.3 Solidus and liquidus curves for (a) GaP–InP, (b) GaAs–InAs and (c) GaSb–InSb pseudobinary systems. The solid lines in (c) represent the solidus and liquidus surfaces calculated from Equation (2.3)

$\text{Ga}_x\text{In}_{1-x}\text{N}$ is a random alloy having the wurtzite structure. Due to the large difference ($\sim 11\%$) in the lattice constants between GaN and InN, the solid solution has a tendency to undergo phase separation. It is possible to grow thin epitaxial $\text{Ga}_x\text{In}_{1-x}\text{N}$ layers with the cubic structure. The phase stability of $\text{Ga}_x\text{In}_{1-x}\text{N}$ has been the subject of several experimental [7,8] and theoretical studies [9–15].

We reproduce in Figure 2.4 the pseudobinary diagram of zinc-blende and wurtzite $\text{Ga}_x\text{In}_{1-x}\text{N}$ obtained theoretically by Gan *et al.* [15]. A direct comparison of the predicted phase diagram to an experimental phase diagram cannot be made since the latter has never been determined. However, an experimental study on $\text{Ga}_{0.91}\text{In}_{0.09}\text{N}$ [8] suggested that this alloy does

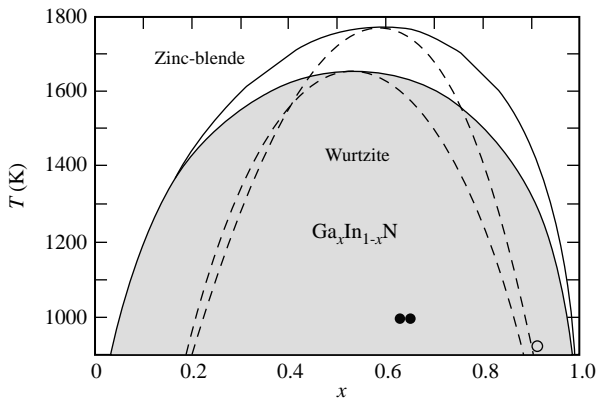


Figure 2.4 Pseudobinary phase diagram of zinc-blende and wurtzite $\text{Ga}_x\text{In}_{1-x}\text{N}$. The solid and open circles represent the experimental data for which phase separation was and was not observed, respectively; data taken from Doppalapudi *et al.* [8]. [Reprinted with kind permission from C. K. Gan, Y. P. Feng, and D. J. Srolovitz, *Phys. Rev. B* **73**, 235214 (2006). Copyright (2006) by the American Physical Society]

not phase separate at the growth temperature of 923 K. The corresponding data point $(x, T) = (0.09, 923 \text{ K})$ is shown by the open circle in Figure 2.4. It lies in the region between the binodal and spinodal, suggesting that the solid solution is metastable with respect to phase segregation. Additional experimental points in Figure 2.4 show that phase separation occurs in both $\text{Ga}_{0.63}\text{In}_{0.37}\text{N}$ and $\text{Ga}_{0.65}\text{In}_{0.35}\text{N}$ grown at 998 K (solid circles) [8], in agreement with the predicted phase diagram (i.e. the data fall in the spinodal region). Gan *et al.* [15] suggested that the wurtzite structure is thermodynamically more stable than the zinc-blende structure at all temperatures and alloy compositions. They also demonstrated that the lattice vibrations can drastically alter the thermodynamic properties and phase diagram of $\text{Ga}_x\text{In}_{1-x}\text{N}$.

(c) *II–VI semiconductor alloy*

Figure 2.5 shows the phase diagram of the MgO–ZnO system at 4.4 GPa (solid lines) and at ambient pressure (dashed lines). The ambient and high-pressure diagrams are taken from Raghavan *et al.* [16] and Solozhenko *et al.* [17], respectively. At ambient pressure [16], the MgO–ZnO system is of eutectic type and is characterized by the extensive solubility of ZnO in MgO and the restricted solubility of MgO in ZnO. The two-phase region in the MgO–ZnO system extends from 3.5 to 70.5 mol% ZnO at 1000 °C and becomes narrower at higher temperatures. Solozhenko *et al.* [17] observed a phase transition of $w\text{-Mg}_x\text{Zn}_{1-x}\text{O}$ solid solution into rocksalt by stepwise heating at various temperatures. The quenching of the

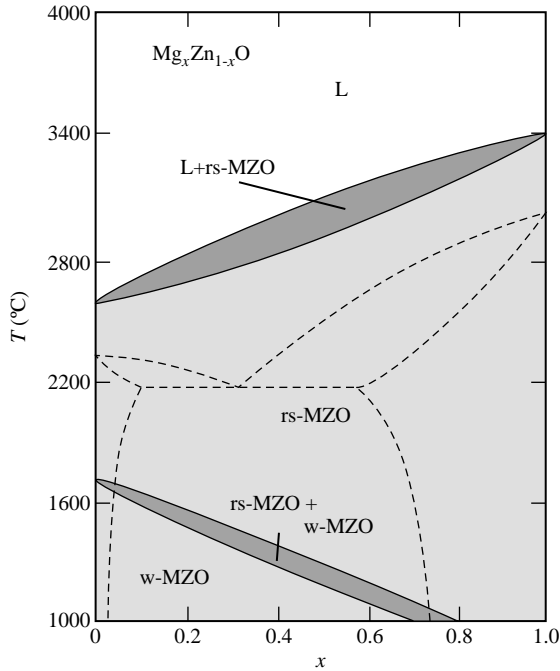


Figure 2.5 Phase diagram of MgO–ZnO pseudobinary system at ambient pressure taken from Raghavan *et al.* [16] (dashed lines) and at 4.4 GPa (solid lines). MZO = MgZnO ; L = liquid; rs = rocksalt; w = wurtzite. [Reprinted with permission from V. L. Solozhenko *et al.*, *Solid State Commun.* **138**, 534–537 (2006), Copyright (2006) Elsevier]

reaction mixtures resulted in the formation of stable $Mg_xZn_{1-x}O$ solid solutions with the rocksalt structure. The phase diagram at 4.4 GPa in Figure 2.5 was proposed based on these facts [17].

Figure 2.6 shows the ZnTe–CdTe solidus and liquidus curves. The experimental data are taken from Steininger *et al.* [18]. XRD measurements indicated that $Zn_xCd_{1-x}Te$ forms a complete series of solid solutions with lattice parameters varying almost linearly with x . The solidus and liquidus curves in Figure 2.6 represent monotonic and sublinear variations with x from the melting point of CdTe to that of ZnTe. This type of x versus T variation suggests small and nearly comparable positive deviations from ideality in the solid and liquid phases and is similar to those observed in other II–VI systems, such as ZnSe–ZnTe [19], CdSe–CdTe [20] and HgSe–HgTe (Figure 2.9).

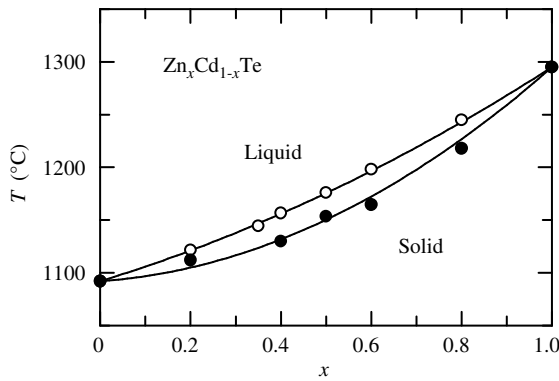


Figure 2.6 Solidus and liquidus curves for ZnTe–CdTe pseudobinary system. The experimental data are taken from Steininger *et al.* [18]. The solid lines represent the solidus and liquidus surfaces calculated from Equation (2.4)

The solid lines in Figure 2.6 represent the quadratic expressions (in °C)

$$\text{Solidus surface : } T_s(x) = 1092 + 30x + 173x^2 \tag{2.4a}$$

$$\text{Liquidus surface : } T_l(x) = 1092 + 131x + 72x^2 \tag{2.4b}$$

Of particular interest in Figure 2.6 is the slow increase in liquid temperatures and the relatively narrow gap between solidus and liquidus curves (less than 0.16 mole fraction). These are very favorable for the growth of alloys from the melts in standard quartz ampoules up to relatively high values of Zn content [21].

The CdS–CdTe system has different crystal structures, that is, the zinc-blende and wurtzite structures, when prepared high temperatures. Early studies on this alloy system failed to produce mixed crystals for the full range of compositions, concluding that a large miscibility gap exists in the CdS–CdTe system. More recently, Ohata *et al.* [22] studied the system for the full range of compositions and observed a change of phase from the zinc-blende to wurtzite at $x \sim 0.2$. Wood *et al.* [23] confirmed using PIXE and XRD that bulk CdS_xTe_{1-x} alloy has the zinc-blende structure for $x \leq 0.2$ and the wurtzite structure for $x \geq 0.25$. Figure 2.7 shows the phase diagram of the CdS–CdTe system obtained by these authors [22,23].

Figure 2.8 illustrates the phase diagram for the CdSe–CdTe system [21]. This system and the ZnTe–CdTe system in Figure 2.6 show typical ‘lens-shape’ phase diagrams with sublinear

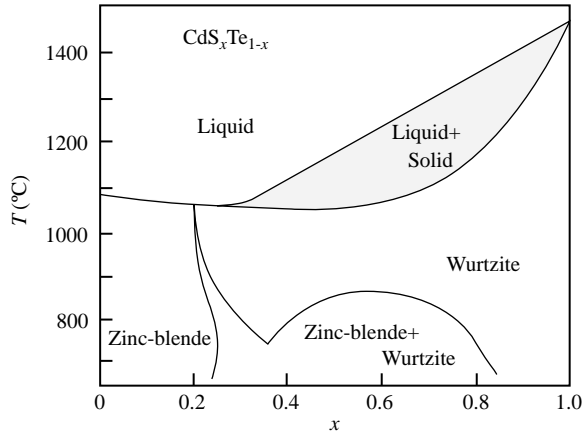


Figure 2.7 Phase diagram of CdS–CdTe pseudobinary system. The experimental curves are taken from Ohata *et al.* [22] and Wood *et al.* [23]

variations in temperature with composition and relatively narrow solidus–liquidus gaps. The CdSe–CdTe system represents almost the same type of solidus–liquidus diagram with a degenerate eutectic near 20 mol% CdSe. The narrow zincblende–wurtzite two-phase region inside the solidus field shows increasing stability of the wurtzite phase with increasing temperature.

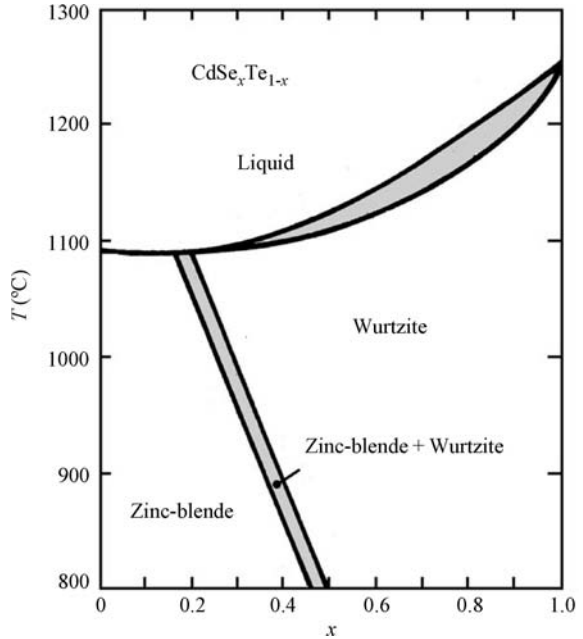


Figure 2.8 Phase diagram of CdSe–CdTe pseudobinary system. [Reprinted with permission from *J. Cryst. Growth*, Phase diagrams and crystal growth of pseudobinary alloy semiconductors by J. Steininger and A. J. Strauss, **13–14**, 657. Copyright (1972), Elsevier]

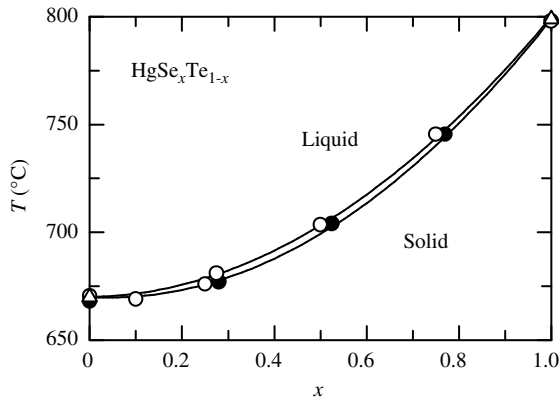


Figure 2.9 Phase diagram of HgSe–HgTe pseudobinary system. The experimental data are taken from Harman [24]. The solid lines represent the solidus and liquidus surfaces calculated from Equation (2.5)

Harman and Strauss [24] determined the phase diagram for the HgSe–HgTe system. The liquidus data in Figure 2.9 were measured by differential thermal analysis of cooling curves, while the solidus points were obtained by determining the composition of the alloys that were the first to freeze from melts of known composition [24]. The solidus and liquidus curves show a very small separation (about 3 mol% between 25 and 75 mol% HgSe). The solid lines in Figure 2.9 represent the quadratic expressions (in °C)

$$\text{Solidus surface : } T_s(x) = 670 - 12x + 141x^2 \quad (2.5a)$$

$$\text{Liquidus surface : } T_l(x) = 670 + 3x + 127x^2 \quad (2.5b)$$

2.1.2 Melting Point

The melting point T_m is one of the most essential thermophysical parameters. Some thermophysical parameters, including T_m , for a number of group-IV, III–V and II–VI semiconductors are summarized in Table 2.1.

Figure 2.10 shows the melting point T_m versus x for C_xSi_{1-x} . The open circles show the experimental data for diamond and Si, while the solid circle represents the 3C–SiC ($x=0.5$) data. The solid line represents Vegard law. It predicts generally acceptable alloy values. We have, however, already shown in Section 2.1.1 that a quadratic function or a higher-order polynomial can be fitted to the solidus curves of many alloys. Therefore, attention should be paid to the estimation of T_m using the linear interpolation scheme.

2.2 SPECIFIC HEAT

2.2.1 Group-IV Semiconductor Alloy

Specific heat is a strongly temperature-dependent quantity [25]. There has been no experimental data on the specific heat of group-IV semiconductor alloys. Kagaya *et al.* [26]

Table 2.1 Melting point T_m , specific heat C_p , Debye temperature θ_D , thermal expansion coefficient α_{th} and thermal conductivity K for some group-IV, III-V and II-VI semiconductors at 300 K. d = diamond; zb = zinc-blende; w = wurtzite; h = hexagonal ($P6_3/mmc$ (D_{6h})); rs = rocksalt; rh = rhombohedral

System	Material	T_m (K)	C_p (J/g K)	θ_D (K)	α_{th} ($10^{-6} K^{-1}$)	K (W/cm K)
IV	Diamond (d)	4100 ^a	0.5148	1870	1.05	22
	Si (d)	1687	0.713	643	2.616	1.56
	Ge (d)	1210.4	0.3295 ^b	348 ^b	5.75	0.6
	Sn (d)		0.278 ^c	238 ^c	5.25 ^d	
	3C-SiC (zb)	2810	0.677 ^e	1122	2.77	3.4 ^f
	2H-SiC (w)	2810				
III-V	BN (zb)	> 3246	0.643	1613	1.15	~13 ^g
	BN (h)	> 3246	0.805	323	-2.75 ($\perp c$) 38.0 ($\parallel c$)	3.9 ^h
	BP (zb)	> 3300	0.75	1025 ⁱ	2.94	3.5
	BAs (zb)	2300	0.408	800		
	AlN (zb)	3487				
	AlN (w)	3487	0.728	988	3.042 ($\perp c$) 2.227 ($\parallel c$)	3.19 ^h
	AlP (zb)	2823	0.727	687		0.9
	AlAs (zb)	2013	0.424	450	4.28	0.91
	AlSb (zb)	1338	0.326 ^b	370 ^b	4.2 ^j	0.57
	GaN (zb)	2791				
	GaN (w)	2791	0.42	821	5.0 ($\perp c$) 4.5 ($\parallel c$)	1.95 ^h
	GaP (zb)	1730	0.313	493 ^k	4.89	0.77
	GaAs (zb)	1513	0.327	370	6.03	0.45
	GaSb (zb)	991	0.344 ^b	240 ^b	6.35	0.36
	InN (zb)	2146				
	InN (w)	2146	2.274	674	3.830 ($\perp c$) 2.751 ($\parallel c$)	0.45 ^{h,l}
	InP (zb)	1335	0.322	420 ^b	4.56	0.68
	InAs (zb)	1210	0.352	280 ^b	5.50 ^m	0.3
	InSb (zb)	797	0.350 ^b	161 ^b	5.04	0.165–0.185
II-VI	BeO (w)	2851	1.029	1280	7.2 ($\perp c$) ⁿ 6.0 ($\parallel c$) ⁿ	3.7 ^h
	BeS (zb)		0.83	900		
	BeTe (zb)				7.66	
	MgO (rs)	3250	0.928	745	10.5	0.52
	MgS (rs)	2783 ^o				
	MgSe (zb)	~1560				
	MgTe (w)	> 1300				
	ZnO (zb)	1975				
	ZnO (w)	1975	0.497	416	4.31 ($\perp c$) 2.49 ($\parallel c$)	0.54 ^h
	ZnS (zb)	2196	0.486	440	6.71	0.27

Table 2.1 (Continued)

System	Material	T_m (K)	C_p (J/g K)	θ_D (K)	α_{th} ($10^{-6} K^{-1}$)	K (W/cm K)
	ZnS (w)	2196		351	6.54 ($\perp c$) 4.59 ($\parallel c$)	0.17 ^{h,p}
	ZnSe (zb)	1793	0.360	340	7.8	0.19
	ZnTe (zb)	1568	0.258	260	8.33	0.18
	CdO (rs)	1700	0.340	255	14	0.007
	CdS (zb)	1748				
	CdS (w)	1748	0.3280	310	4.30 ($\perp c$) 2.77 ($\parallel c$)	0.20 ^{h,q}
	CdSe (zb)	1531				
	CdSe (w)	1531	0.281	135	4.13 ($\perp c$) 2.76 ($\parallel c$)	$\sim 0.09^h$
	CdTe (zb)	1365	0.211	185	4.70	0.075
	HgS (zb)	1723			4.3 ^r	
	HgSe (zb)	1072	0.355	242	1.41	0.001–0.035
	HgTe (zb)	943	0.162	143	4.70	0.0238

^aAt 12.5 GPa

^bAt 273 K

^cAt 100 K

^dAt 220 K

^e C_v value

^fAt 290 K

^gEstimated

^hThis semiconductor has two tensor components, K_{\perp} and K_{\parallel} ; however, the difference between K_{\perp} and K_{\parallel} appears to be less than the experimental uncertainty at room temperature

ⁱAt 320 K

^jAt 280 K

^kAt 150 K

^lCeramics

^mObtained from an analysis of GaInPAs quaternary data

ⁿAt 373 K

^oTheoretical

^pNote that the *w*-ZnS crystal used in the experiment may be faulted; therefore, the value for this crystal is much smaller than that for *c*-ZnS

^qAt 283 K

^r $T = 484 - 621$ K

investigated theoretically the specific heat of Si_xGe_{1-x} from 0 to 500 K. The difference in specific heat between at constant pressure and constant volume $C_p - C_v$ was found to be negligible at low temperatures, but increased by less than 3–3.5% at 500 K. The calculated C_p values fell between the endpoint values of Si and Ge.

Figure 2.11 shows the specific heat C_p versus x for C_xSi_{1-x} at 300 K. The experimental data for diamond, Si and 3C-SiC ($x = 0.5$) are shown by the open and solid circles. The dashed line represents the linear interpolation result between the experimental diamond and Si values written as (in J/g K)

$$C_p(x) = 0.713 - 0.198x \tag{2.6}$$

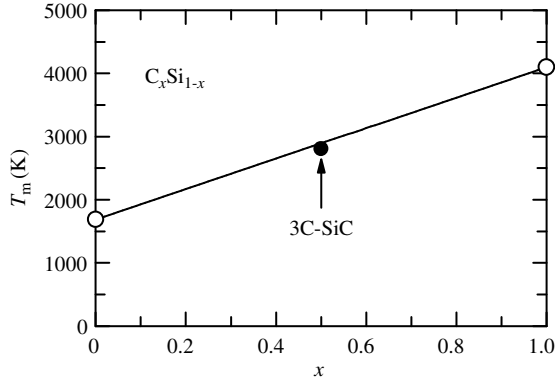


Figure 2.10 Melting point T_m versus x for C_xSi_{1-x} . The open and solid circles show the experimental data. The solid line represents the result of Vegard law between diamond and Si

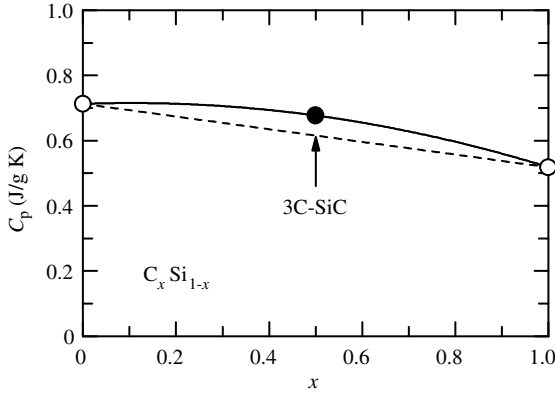


Figure 2.11 Specific heat C_p versus x for C_xSi_{1-x} at 300 K. The open and solid circles show the experimental data. The dashed line shows the linear interpolation result given by Equation (2.6), while the solid line is calculated from Equation (2.7)

The linear interpolation is concluded to estimate generally acceptable alloy C_p values. The solid line in Figure 2.11 shows the result of quadratic fit (in J/g K)

$$C_p(x) = 0.713 + 0.051x - 0.245x^2 \tag{2.7}$$

2.2.2 III-V Semiconductor Alloy

Sirota *et al.* [27] determined the C_p and C_v values of InP_xAs_{1-x} from 5 to 160 K and their C_p data obtained at 160 K are shown graphically in Figure 2.12. The solid line shows the linear interpolation result between InP and InAs (in J/g K)

$$C_p(x) = 0.220 + 0.027x \tag{2.8}$$

The linear interpolation scheme is found to yield generally acceptable alloy values.

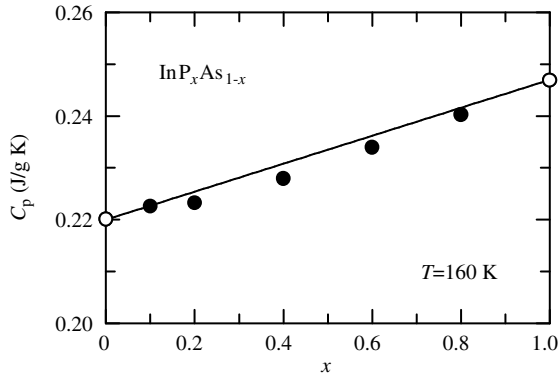


Figure 2.12 Specific heat C_p versus x for $\text{InP}_x\text{As}_{1-x}$ at 160 K. The experimental data are taken from Sirota *et al.* [27]. The solid line shows the linear interpolation result between the endpoint binary data

Sirota *et al.* [28] measured the C_p and C_v values of $(\text{GaAs})_x(\text{InP})_{1-x}$ quaternary from 5 to 300 K. Figure 2.13 shows the C_p data measured at 300 K. The solid line represents the result of linear interpolation given by (in J/g K)

$$C_p(x) = 0.309 + 0.014x \quad (2.9)$$

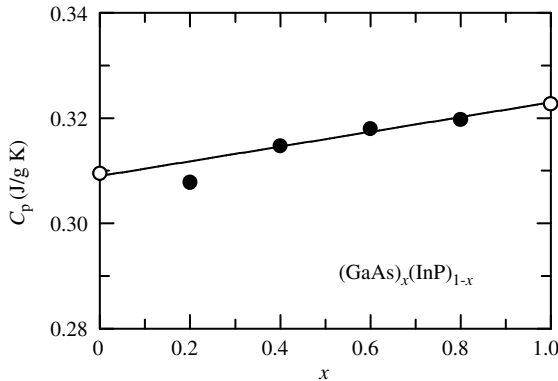


Figure 2.13 Specific heat C_p versus GaAs composition x for $(\text{GaAs})_x(\text{InP})_{1-x}$ at 300 K. The experimental data are taken from Sirota *et al.* [28]. The solid line shows the linear interpolation result between the endpoint binary data

It should be noted that the GaAs and InP values of 0.323 and 0.309 J/g K reported by Sirota *et al.* [28] are slightly smaller than those listed in Table 2.1. It can be seen in Figure 2.13, however, that the linear interpolation scheme is a useful tool for estimating alloy C_p values. Using the linear interpolation scheme, we obtain C_p versus x ($0 \leq x \leq 1.0$) and T ($300 \leq T \leq 1500$ K) for $\text{Al}_x\text{Ga}_{1-x}\text{As}$ as (C_p in J/g K) [29]

$$C_p(x, T) = (0.343 + 0.133x) + (4.7 + 1.5x) \times 10^{-5}T - (3.2 + 3.3x) \times 10^3T^{-2} \quad (2.10)$$

2.2.3 II–VI Semiconductor Alloy

The specific heat of $\text{Cd}_x\text{Hg}_{1-x}\text{Te}$ was measured from 5 to 300 K by Sirota *et al.* [30] and from room temperature up to 523 K by Gambino *et al.* [31]. The data of Gambino *et al.* revealed a remarkable anomaly in the form of an abrupt increase below a ‘step temperature’ which depended on x , as shown in Figure 2.14(a). The step temperature reached a maximum at about mid-range composition. It clearly signified an equilibrium solid-state phase change, which they suggested, could be a miscibility gap. As plotted in Figure 2.14(b), this phase change reaches 358 K at $x = 0.253$ and might reach 240 K at $x = 0.2$. Maleki and Holland [32] subjected Gambino’s data to a polynomial fit and summarized their results in tabular form. Sirota *et al.* [30] mentioned ‘an anomaly’ which caused their data to scatter from 15 to 80 K, but did not observe the phase boundary reported by Gambino *et al.*, possibly because their temperatures were too low [32].

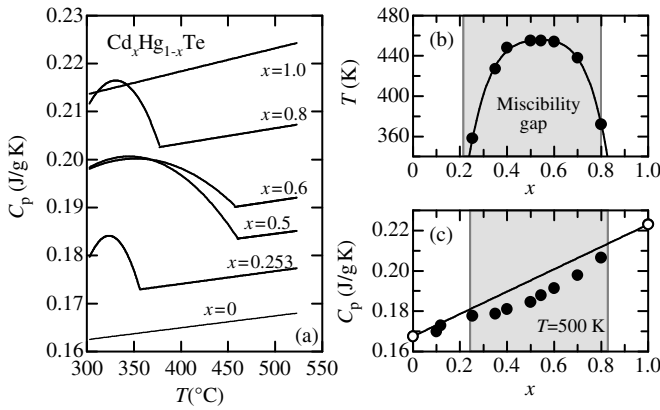


Figure 2.14 (a) Specific heat C_p versus temperature T for $\text{Cd}_x\text{Hg}_{1-x}\text{Te}$ with $x = 0 - 1.0$. (b) Miscibility gap versus x for $\text{Cd}_x\text{Hg}_{1-x}\text{Te}$. (c) Specific heat C_p versus x for $\text{Cd}_x\text{Hg}_{1-x}\text{Te}$ at 500 K. The experimental data in (a)–(c) were obtained from Gambino *et al.* [31]. The solid line in (c) shows the linear interpolation result between the endpoint binary data

The C_p versus x data for $\text{Cd}_x\text{Hg}_{1-x}\text{Te}$ measured at 500 K by Gambino *et al.* [31] are shown in Figure 2.14(c). The solid line represents the linear interpolation between CdTe and HgTe. It is understood that C_p can be successfully estimated from the linear interpolation scheme; however, a shallow dip in the experimental C_p – x plots is observed in the region centered at $x \sim 0.5$. Gambino *et al.* [31] considered that the dip in C_p at $x \sim 0.5$ is due to the presence of two phases and to the thermal effect associated with the change in equilibrium ($\text{solid} \leftrightarrow \text{solid}_{(1)} + \text{solid}_{(2)}$) during C_p measurement, i.e. sample heating.

2.3 DEBYE TEMPERATURE

2.3.1 General Considerations

Principally, the X-ray Debye temperature θ_D for pure metal can be given by [33]

$$\mu\theta_D^2 = \frac{9f\hbar^2}{Ck_B^2a} \quad (2.11)$$

where μ is the displacement of an atom from its lattice site, f is an average nearest-neighbor force constant, C is a numeric constant which depends on the lattice structure, k_B is Boltzmann's constant and a is the atomic mass unit. For a random alloy, the Debye temperature can be simply written as [33]

$$\mu\theta_D^2 = \sum_i x_i \mu_i \theta_{Di}^2 + \frac{1}{2} \sum_{i \neq j} A_{ij} x_i x_j (\mu_i \theta_{Di}^2 + \mu_j \theta_{Dj}^2) \tag{2.12}$$

where A_{ij} is the factor accounting for the effect of an alloy disorder on the nearest-neighbor force constant.

Although Equation (2.12) is for X-ray Debye temperature, it can also be applied to specific-heat Debye temperatures since the two differ by a factor depending on Poisson's ratio, which does not vary significantly from metal to metal and also from semiconductor to semiconductor [25]. If μ_i is not dependent on material and A_{ij} is negligibly small, Equation (2.12) can then be simply written as

$$\theta_D^2(x) = \sum_i x_i \theta_{Di}^2 \tag{2.13}$$

The simplest Vegard law can be expressed as

$$\theta_D(x) = \sum_i x_i \theta_{Di} \tag{2.14}$$

2.3.2 Group-IV Semiconductor Alloy

Figure 2.15 shows the Debye temperature θ_D versus x for C_xSi_{1-x} at 300 K. The open and solid circles represent the experimental data for diamond, Si and 3C-SiC ($x = 0.5$). The light solid line is calculated from Equation (2.13), while the dashed line is obtained from Equation (2.14).

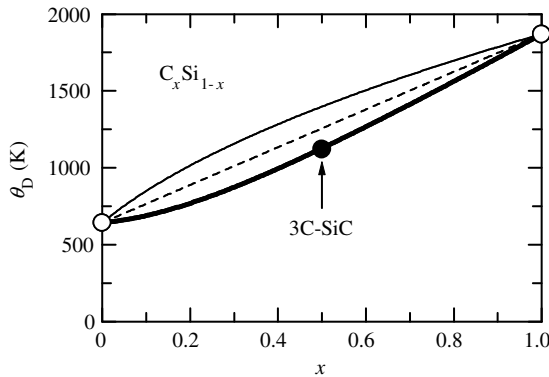


Figure 2.15 Debye temperature θ_D versus x for C_xSi_{1-x} at 300 K. The heavy solid, light solid and dashed lines are calculated from Equations (2.12), (2.13) and (2.14), respectively

The heavy solid line can also be obtained from Equation (2.12) with $\mu = \mu_i (= \mu_j) = 1$ and $A_{ij} = 1.4$ (all these quantities are assumed to be non-dimensional). The high Debye temperature reflects low atomic mass and therefore short interatomic bond length in $A^N B^{8-N}$ semiconductors [25].

2.3.3 III–V Semiconductor Alloy

The specific-heat Debye temperature θ_D for (a) $\text{InP}_x\text{As}_{1-x}$ at 160 K and (b) $(\text{GaAs})_x(\text{InP})_{1-x}$ at 300 K is shown in Figure 2.16. The experimental data are taken from Sirota *et al.* [27,28]. The solid lines show the calculated results obtained using Equation (2.14). It was found that the θ_D versus x data can be satisfactorily explained by this expression. The Debye temperatures for these alloys are also found to vary with temperature in the same way as for the endpoint binaries, passing through a deep minimum in the region 10–20 K [27,28].

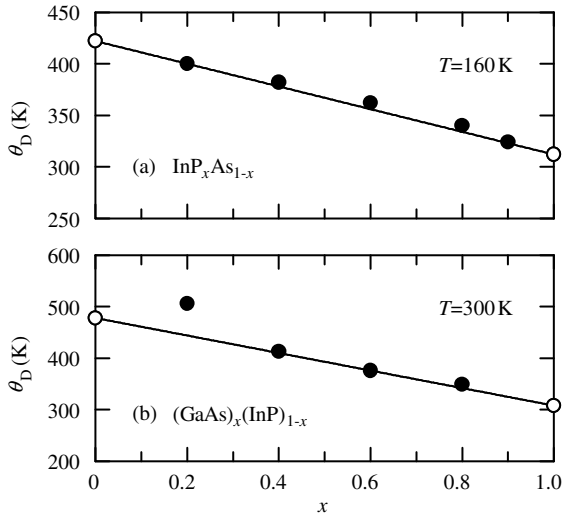


Figure 2.16 Debye temperature θ_D versus x for (a) $\text{InP}_x\text{As}_{1-x}$ at 160 K and (b) $(\text{GaAs})_x(\text{InP})_{1-x}$ at 300 K. The experimental data for $\text{InP}_x\text{As}_{1-x}$ are taken from Sirota *et al.* [27] and for $(\text{GaAs})_x(\text{InP})_{1-x}$ from Sirota *et al.* [28]. The solid lines show the results calculated using Equation (2.14)

2.3.4 II–VI Semiconductor Alloy

Nikiforov and Sredin [34] determined the specific-heat Debye temperature θ_D for $\text{Cd}_x\text{Hg}_{1-x}\text{Te}$ using a calorimeter. These results are shown in Figure 2.17. The solid line represents the linear interpolation result between the endpoint data in Table 2.1. As in the case of the III–V semiconductor alloys, the Debye temperature of $\text{Cd}_x\text{Hg}_{1-x}\text{Te}$ is a smooth and monotonic function of x ; however, we can see an abrupt change at $x = 0.2$. This may be due to an experimental error or may be the effect of any difference in crystalline quality. Since the Debye temperature is a model parameter that cannot be measured directly, it may contain considerable uncertainty, including numeric error.

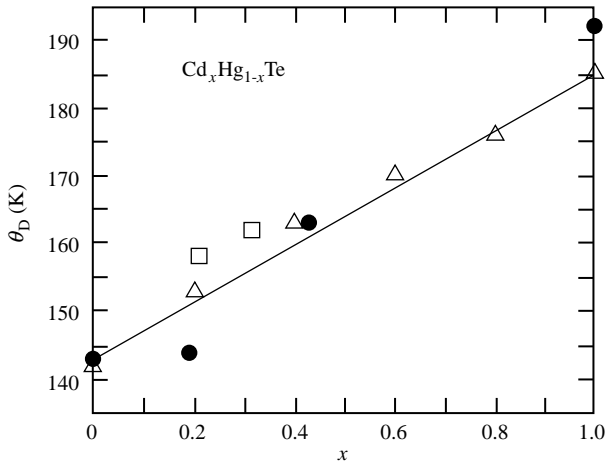


Figure 2.17 Debye temperature θ_D versus x for $\text{Cd}_x\text{Hg}_{1-x}\text{Te}$ at 300 K. The experimental data are taken from Nikiforov and Sredin [34]. The solid line shows the linear interpolation result using Equation (2.14) between the endpoint binary data

2.4 THERMAL EXPANSION COEFFICIENT

2.4.1 Group-IV Semiconductor Alloy

During cooling down in epitaxial growth, a difference in thermal expansion can produce the driving force that moves the defects in the semiconductor heterostructure. Knowledge of the thermal expansion coefficient is, thus, essential not only from a physical point of view, but also for semiconductor device engineering.

Figure 2.18 shows the linear thermal expansion coefficient α_{th} for $\text{C}_x\text{Si}_{1-x}$ at 300 K. The experimental data are shown by the open and solid circles. The dashed line represents the

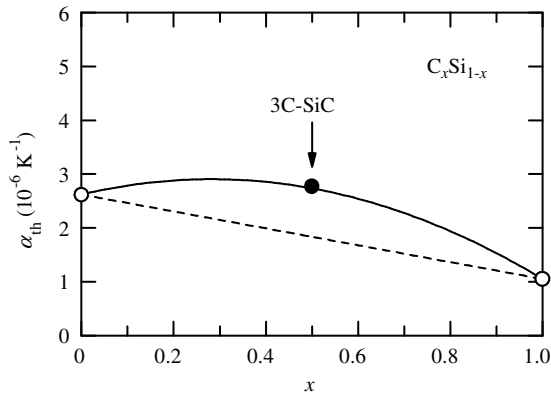


Figure 2.18 Linear thermal expansion coefficient α_{th} versus x for $\text{C}_x\text{Si}_{1-x}$ at 300 K. The dashed line represents the linearly interpolated result of Equation (2.15). The solid line shows the quadratic fit of Equation (2.16)

linear interpolation between diamond and Si (in 10^{-6} K^{-1})

$$\alpha_{\text{th}}(x) = 2.62 - 1.57x \quad (2.15)$$

3C-SiC can be regarded as an alloy of C and Si ($x = 0.5$); however, the linearly interpolated $x = 0.5$ value in Figure 2.18 does not show good agreement with the experimental 3C-SiC data. It should be noted that C and Si crystallize in the diamond structure, but 3C-SiC crystallizes in the zinc-blende structure. The solid line in Figure 2.18 represents the quadratic fit (in 10^{-6} K^{-1})

$$\alpha_{\text{th}}(x) = 2.62 + 2.03x - 3.60x^2 \quad (2.16)$$

The α_{th} value for $\text{Si}_x\text{Ge}_{1-x}$ was measured by Zhdanova *et al.* [35] and their results obtained at temperatures between 473 and 773 K are reproduced in Figure 2.19. The expansion decreased monotonically from Ge to Si. A gradual increase in α_{th} was also found with increasing temperature from ~ 300 K up to ~ 1100 K. In Figure 2.19, there is a sudden change in the slope at $x \sim 0.15$, which coincides with the transition of electronic properties from Ge-like to Si-like (Figure 6.8).

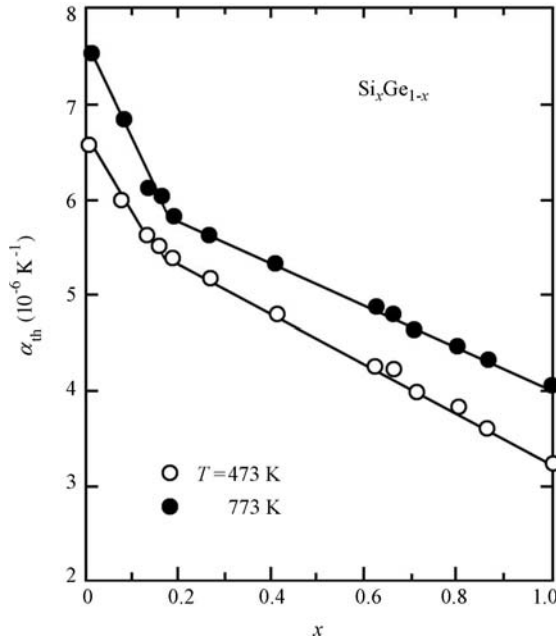


Figure 2.19 Linear thermal expansion coefficient α_{th} versus x for $\text{Si}_x\text{Ge}_{1-x}$ at 473 and 773 K. [Reprinted from *Izv. Akad. Nauk. SSSR Neorg. Mater.* **3**, 1263 (1967)]

The linear expansion coefficient α_{th} is proportional to the specific heat C_v (Grüneisen rule) [25]

$$\alpha_{\text{th}} = \frac{1}{a} \left(\frac{\partial a}{\partial T} \right)_p = \frac{\gamma C_v C_0}{3V} \quad (2.17)$$

where γ is the averaged Grüneisen parameter, C_v is the specific heat at constant volume, C_o is the isothermal compressibility and V is the volume of the crystal. Theoretical work on α_{th} , γ and C_v was carried out by Kagaya *et al.* [26]. A simplified model was used where the lattice vibrations of Si and Ge atoms in the Si–Ge solid solution were assumed to be those of pure Si and Ge except that the lattice constant of the alloy was used. As in pure Si and Ge, the negative thermal expansion was predicted at low temperatures in Si_xGe_{1-x} .

2.4.2 III–V Semiconductor Alloy

Figure 2.20 shows the x dependence of α_{th} for $Al_xGa_{1-x}As$ at 300 K. The experimental data are taken from Takahashi [36] and Bak-Misiuk [37]. The result of linear interpolation between AlAs and GaAs is shown by the solid line. The difference in α_{th} between the GaAs substrate and the $Al_xGa_{1-x}As$ epilayer can be approximated in Figure 2.20 by (in K^{-1})

$$\Delta\alpha_{th}(x) = 1.75x \times 10^{-6} \tag{2.18}$$

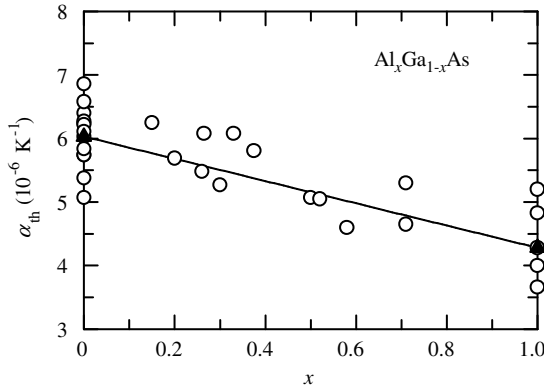


Figure 2.20 Linear thermal expansion coefficient α_{th} versus x for $Al_xGa_{1-x}As$ at 300 K. The experimental data are taken from Takahashi [36] and Bak-Misiuk *et al.* [37] (open circles). The linear interpolation result between the AlAs and GaAs values is shown by the solid line

The linear thermal expansion coefficients α_{th} plotted against x for $Ga_xIn_{1-x}P$ and GaP_xAs_{1-x} at 300 K are shown in Figures 2.21(a) and 2.21(b), respectively. The experimental data are taken for $Ga_xIn_{1-x}P$ from Kudman and Paff [38] and Leszczynski *et al.* [39] and for GaP_xAs_{1-x} from Straumanis *et al.* [40]. It is apparent from Figure 2.21(a) that the thermal expansion of $Ga_xIn_{1-x}P$ by Kudman and Paff [38] can be expressed as a linear function of x (solid circles). However, the endpoint values extrapolated from these data seem to be considerably larger than the generally accepted values (Table 2.1). Leszczynski *et al.* [39] measured the α_{th} value of relaxed $Ga_{0.5}In_{0.5}P$ layers grown on GaAs by LPE and reported it as $\sim 4.6 \times 10^{-6} K^{-1}$. This value (open circle) agrees well with the linear interpolation scheme (solid line).

The data in Figure 2.21(b) can be approximated by the linear interpolation scheme (solid line). The experimental data can be read more exactly from the dashed curve written as (in $10^{-6} K^{-1}$)

$$\alpha_{th}(x) = 6.03 - 3.14x + 2.00x^2 \tag{2.19}$$

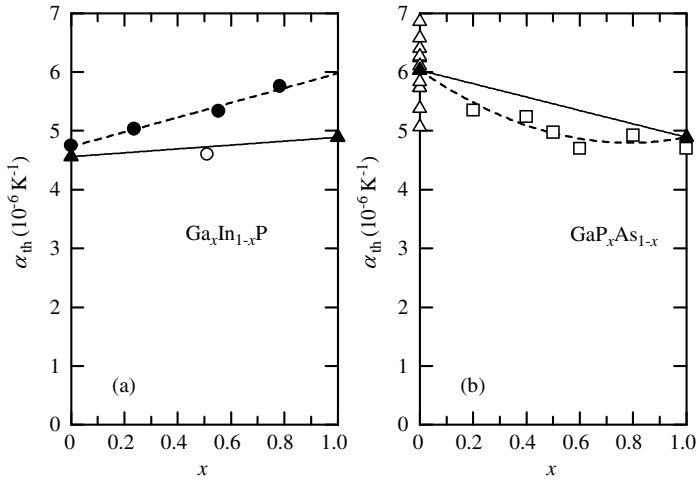


Figure 2.21 Linear thermal expansion coefficients α_{th} as a function of x for (a) $Ga_xIn_{1-x}P$ and (b) GaP_xAs_{1-x} at 300 K. The experimental data in (a) are taken from Kudman and Paff [38] (solid circles) and Leszczynski *et al.* [39] (open circle) and in (b) from Straumanis *et al.* [40] (open squares). The solid lines in (a) and (b) show the linear interpolation results between the endpoint binary data. The dashed line in (b) represents the result calculated using Equation (2.19)

The x dependence of α_{th} for $Ga_xIn_{1-x}P_yAs_{1-y}$ has been investigated by many authors (see Adachi [41]). The experimental α_{th} versus y for $Ga_xIn_{1-x}P_yAs_{1-y}/InP$ at 300 K is plotted in Figure 2.22 [41]. The α_{th} values are found to almost linearly decrease with increasing y . The endpoint binary data are available for GaP, GaAs and InP, but not for InAs (Table 2.1). The solid line in Figure 2.22 represents the linear interpolation expression (in $10^{-6} K^{-1}$)

$$\alpha_{th}(x) = 4.89xy + 6.03x(1-y) + 4.56(1-x)y + 5.50(1-x)(1-y) \tag{2.20}$$

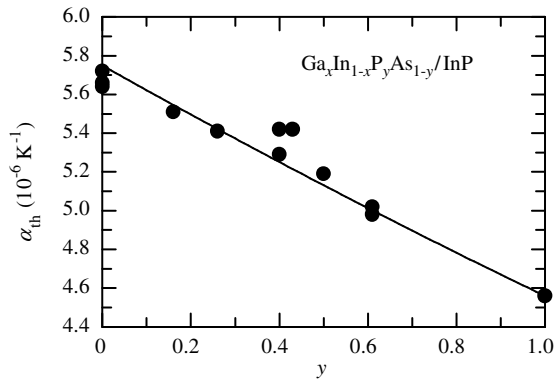


Figure 2.22 Linear thermal expansion coefficients α_{th} versus y for $Ga_xIn_{1-x}P_yAs_{1-y}/InP$ at 300 K. The experimental data are taken from Adachi [41]. The solid line represents the linear interpolation result of Equation (2.20)

In obtaining Equation (2.20), we assumed the InAs value to be $\alpha_{th} = 5.50 \times 10^{-6} \text{ K}^{-1}$. The linear interpolation expression in Figure 2.22 explains the experimental data satisfactorily. The α_{th} value for $\text{Al}_x\text{Ga}_{1-x}\text{P}$ has also been reported by Bessolov *et al.* [42].

2.4.3 II–VI Semiconductor Alloy

The α_{th} variations in $\text{Zn}_x\text{Hg}_{1-x}\text{Te}$ and $\text{Cd}_x\text{Hg}_{1-x}\text{Te}$ have been measured from 4 to 290 K [43]. The bulk crystals were grown by the THM. The negative thermal expansions at temperatures below $\sim 65 \text{ K}$ were clearly observed in ZnTe, CdTe and HgTe binaries and also in their alloys. The solid circles and triangles in Figure 2.23 show the experimental data measured at 280 K [43]. They are largely scattered. This is especially true for $\text{Zn}_x\text{Hg}_{1-x}\text{Te}$.

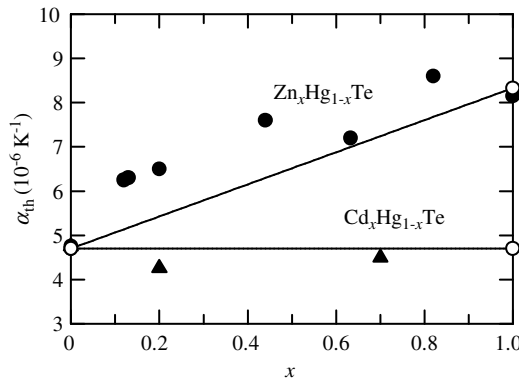


Figure 2.23 Linear thermal expansion coefficients α_{th} as a function of x for $\text{Zn}_x\text{Hg}_{1-x}\text{Te}$ and $\text{Cd}_x\text{Hg}_{1-x}\text{Te}$ at 280 K. The experimental data are taken from Bagot *et al.* [43]. The solid lines represent the linear interpolation results between the endpoint binary data

The thermal expansion behaviors were also studied for $\text{ZnS}_{0.03}\text{Se}_{0.97}$ from 300 to 550 K [44] and for $\text{Mg}_x\text{Zn}_{1-x}\text{Se}$ ($0.1 \leq x \leq 0.5$) from 10 to 300 K [45]. The negative thermal expansion in conjunction with abnormal temperature dependence of the E_0 edge was observed at $T \leq 75 \text{ K}$ for $\text{Mg}_x\text{Zn}_{1-x}\text{Se}$ [45].

2.5 THERMAL CONDUCTIVITY AND DIFFUSIVITY

2.5.1 Thermal Conductivity

(a) General considerations

An exact calculation of the lattice thermal conductivity K is possible in principle, but lack of knowledge of various material parameters and the difficulty of obtaining an exact solution of phonon–phonon interactions are formidable barriers. In the case of semiconductor alloys, an additional contribution, which is the result of a random distribution of constituent atoms in sublattice sites, should be taken into consideration. A phenomenological model of the lattice thermal conductivity for semiconductor alloys was first proposed by Abeles [46]. His model starts from three kinds of relaxation times: $\tau_N^{-1} = B_1\omega^2$ (three-phonon normal process), $\tau_U^{-1} = B_2\omega^2$ (three-phonon Umklapp process) and $\tau_D^{-1} = A\Gamma\omega^2$ (strain and mass point defects),

where ω is the phonon frequency, B_1 , B_2 and A are constants independent of ω and Γ is the disorder parameter depending on the masses and radii of the constituent atoms.

The lattice thermal resistivity $W = K^{-1}$ obtained by Abeles [46] is given by

$$\frac{W(x)}{W_p(x)} = \left(1 + \frac{5}{9}\alpha\right) \left\{ \frac{\tan^{-1}U}{U} + \frac{[1 - (\tan^{-1}U/U)]^2}{[(1 + \alpha)/5\alpha]U^4 - (1/3)U^2 - (\tan^{-1}U/U) + 1} \right\}^{-1} \quad (2.21)$$

with

$$U(x)^2 = U_0(x)^2 \left(1 + \frac{5}{9}\alpha\right)^{-1} \quad (2.22)$$

where

$$U_0(x)^2 = A_1 \Gamma(x) W_p(x)^{-1} \quad (2.23)$$

In Equations (2.21)–(2.23), $W_p(x)$ is the lattice thermal resistivity of the crystal in which the disorder lattice is replaced by an ordered virtual crystal, α is a normal/Umklaup ratio ($\alpha = B_1/B_2$) and A_1 is nearly constant within a group of $A^N B^{8-N}$ semiconductors. $\Gamma(x)$ can be written as

$$\Gamma(x) = x(1-x) \left\{ \left[\frac{\Delta M}{M(x)} \right]^2 + \varepsilon \left[\frac{\Delta \delta}{\delta(x)^2} \right] \right\} \quad (2.24)$$

where $\Delta M = M_A - M_B$, $\Delta \delta = \delta_A - \delta_B$, $M(x) = xM_A + (1-x)M_B$ and $\delta(x) = x\delta_A + (1-x)\delta_B$ (M_i and δ_i ($i = A, B$) are the masses and radii of the constituent atoms). ε is regarded as a phenomenological, adjustable parameter. The first and second terms in the curly brackets in Equation (2.24) correspond to the contributions from the mass-defect and strain scatterings, respectively.

Abeles's model was used by Adachi [47,48] and Nakwaski [49] for several III–V alloys. Adachi [47] showed that for an $A_x B_{1-x} C$ alloy

$$W(x) = xW_{AC} + (1-x)W_{BC} + x(1-x)C_{AB} \quad (2.25)$$

is essentially the same as Equation (2.21), where W_{AC} and W_{BC} are the binary thermal resistivities and C_{AB} is a contribution arising from the lattice disorder (Γ) due to the random distribution of A and B atoms in the cation sublattice sites. Equation (2.25) is known as the Nordheim rule [50,51] and can be readily converted to the lattice thermal conductivity K

$$K(x) = \frac{1}{W(x)} = \frac{1}{xW_{AC} + (1-x)W_{BC} + x(1-x)C_{AB}} \quad (2.26)$$

In an $A_x B_{1-x} C_y D_{1-y}$ quaternary alloy, not only should the A–B disorder due to the random distribution of the A and B atoms in the cation sublattice and the C–D disorder due to the random distribution of the C and D atoms in the anionic sublattice be taken into consideration, but also the fact that both the cation and anion sublattices are disordered as well. Neglecting the

cation–anion interaction effect, we obtain

$$K(x,y) = \frac{1}{W(x,y)} = \frac{1}{xyW_{AC} + x(1-y)W_{AD} + (1-x)yW_{BC} + (1-x)(1-y)W_{BD} + x(1-x)C_{AB} + y(1-y)C_{CD}} \tag{2.27}$$

In doped semiconductors, the thermal conductivity can be given by the sum of the lattice and electronic contributions. In a metal, the electronic thermal conductivity K and electrical conductivity σ at temperature T are related by the Wiedemann–Franz law

$$K = LT\sigma \tag{2.28}$$

or, equivalently

$$\rho = LTW \tag{2.29}$$

where L is the Lorenz number and ρ is the electrical resistivity.

The thermal resistivity W as a function of x for $\text{Cu}_x\text{Au}_{1-x}$ is shown in Figure 2.24. Cu–Au alloy is among the best studied of all metallic alloy systems. The solid and open circles represent the experimental data for the ordered (CuAu and Cu_3Au) and disordered phases,

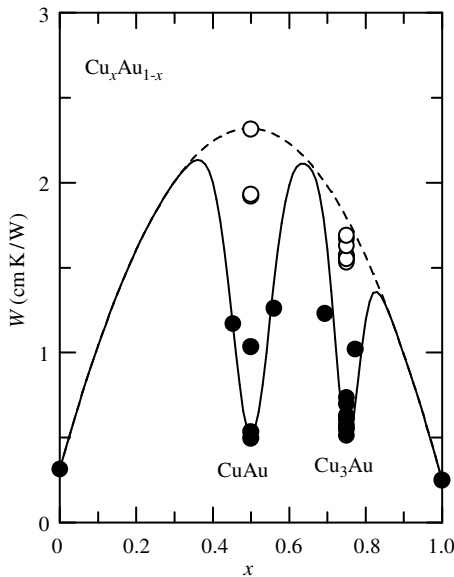


Figure 2.24 Thermal resistivity W as a function of x for $\text{Cu}_x\text{Au}_{1-x}$ at 300 K. The solid circles represent the experimental data obtained from ordered alloys (CuAu and Cu_3Au), while the open circles represent the data taken from disordered alloys. The solid and dashed lines are calculated from Equation (2.25) with $C_{\text{CuAu}} = 8.15 \text{ cm K/W}$ and with and without properly taking into account the alloy ordering effect at $x = 0.5$ and 0.75 (CuAu and Cu_3Au), respectively

respectively. These data were obtained from various sources (e.g. Jacobsson and Sundqvist [52]). The solid and dashed lines are calculated from Equation (A.5) (Equation (2.25)) with $C_{\text{CuAu}} = 8.15 \text{ cm K/W}$ and with and without properly taking into account the ordering effect at $x = 0.5$ and 0.75 (CuAu and Cu_3Au), respectively. It is evident from Figure 2.24 that the ordered alloy data are much smaller than those estimated from Equation (2.25) (dashed line). The ordering in metallic alloy is, thus, found to greatly decrease W , irrespective of the ordered structure (CuAu = $L1_0$ (tetragonal) or Cu_3Au = $L1_2$ (cubic)). Similarly, the electrical resistivity ρ of the ordered phase is much lower than that of the disordered phases (Figure 12.1).

The ordering effect in semiconductor alloys was observed to occur spontaneously during epitaxial growth [53]. Kuan *et al.* [54] first observed an ordered phase (CuAu-I type) in an MOCVD-grown AlGaAs epilayer. Since the first finding of CuPt-type ordering in SiGe alloy [55], this type of ordering and others have also been reported in many III–V and II–VI semiconductor alloys (Section 1.3.2). However, no clear ordering effect on the carrier transport properties in semiconductor alloys has been observed. In the following, therefore, we pay no attention to the spontaneous ordering effect, except for $\text{C}_x\text{Si}_{1-x}$ with $x = 0.5$ (3C-SiC).

Since the lifetimes of the dominant phonons in semiconductor alloys are $\sim 100 \text{ ps}$, the frequency dependence of K would not be observable in experiments unless $f > 1 \text{ GHz}$. However, the frequency-dependent K of $\text{Si}_{0.4}\text{Ge}_{0.6}$, $\text{Ga}_{0.51}\text{In}_{0.49}\text{P}$ and $\text{Ga}_{0.47}\text{In}_{0.53}\text{As}$ was clearly observed over a wide range of modulation frequencies $0.1 < f < 10 \text{ MHz}$ and temperatures $88 < T < 300 \text{ K}$ from time-dependent TR measurements [56]. The reduction in K at high frequencies was consistent with a model calculation assuming that phonons with mean free paths larger than the thermal penetration depth do not contribute to K as measured in the experiment.

(b) Group-IV semiconductor alloy

There has been no experimental or theoretical work on the thermal conductivity of $\text{C}_x\text{Si}_{1-x}$. This is because of the low solubility of C in Si ($\sim 6 \times 10^{-6}$) [57]. In Figure 2.25 only the experimental K and W data for 3C-SiC ($x = 0.5$) together with those for diamond and Si have been plotted [48]. Note that diamond and Si crystallize in the diamond structure, while 3C-SiC crystallizes in the zinc-blende structure. It is, therefore, considered that 3C-SiC is an ordered form of $\text{C}_x\text{Si}_{1-x}$ ($x = 0.5$), or more succinctly, it is a compound, not an alloy.

The solid lines in Figure 2.25 are calculated from Equations (2.25) and (2.26) without taking into account the contribution of alloy disorder (i.e. $C_{\text{CSi}} = 0 \text{ cm K/W}$), while the dashed lines are obtained by assuming $C_{\text{CSi}} = 15 \text{ cm K/W}$ and properly taking into account the ordering effect at $x = 0.5$. The diamond and Si values used in the calculation are taken from Table 2.2. In Figure 2.25, the thermal conductivity and resistivity of 3C-SiC can be satisfactorily interpreted by the linear interpolation scheme ($C_{\text{AB}} = 0 \text{ cm K/W}$). It is also expected from Figure 2.25(b) that the alloying leads to a large increase in W due to increased disorder scattering (dashed line). Similarly, not only a large increase in W in doped Si [58,59], but also a decrease in W in isotopically enriched diamond [60–62] and Si [59,63] has been reported.

Systematic work on the thermal conductivity of $\text{Si}_x\text{Ge}_{1-x}$ was carried out by Dismukes *et al.* [64] and the values they obtained for K and W are plotted in Figure 2.26. The solid lines represent the results calculated using Equations (2.25) and (2.26) with $C_{\text{SiGe}} = 50 \text{ cm K/W}$ [48]. The thermal resistivity markedly increased with alloying. The W value at $x \sim 0.5$ is about 28 times as large as those of Si and Ge. Such a feature was motivated by desire to obtain increased performance for thermoelectric power conversion since the figure of merit for such a device

Table 2.2 Room-temperature thermal conductivity K and resistivity W for some group-IV and III–V semiconductors, together with alloy disorder parameters $C_{\alpha\beta}$ used in the calculation of K and W .
 d = diamond; w = wurtzite; zb = zinc-blende

Material	K (W/cm K)	W (cm K/W)	$C_{\alpha\beta}$ (cm K/W)
Diamond (d)	22	0.045	$C_{\text{SiGe}} = 50$
Si (d)	1.56	0.64	$C_{\text{AlGa}} = 32$
Ge (d)	0.60	1.67	$C_{\text{AlIn}} = 15^a$
AlN (w)	3.19	0.31	$C_{\text{GaIn}} = 72$
AlP (zb)	0.90	1.1	$C_{\text{NP}} = 36^a$
AlAs (zb)	0.91	1.10	$C_{\text{NAs}} = 12^a$
AlSb (zb)	0.57	1.75	$C_{\text{NSb}} = 10^a$
GaN (w)	1.95	0.51	$C_{\text{PAs}} = 25$
GaP (zb)	0.77	1.30	$C_{\text{PSb}} = 16^a$
GaAs (zb)	0.45	2.22	$C_{\text{AsSb}} = 91$
GaSb (zb)	0.36	2.78	
InN (w)	0.45	2.22	
InP (zb)	0.68	1.47	
InAs (zb)	0.30	3.3	
InSb (zb)	0.175	5.71	

^aEstimated from Equation (2.31)

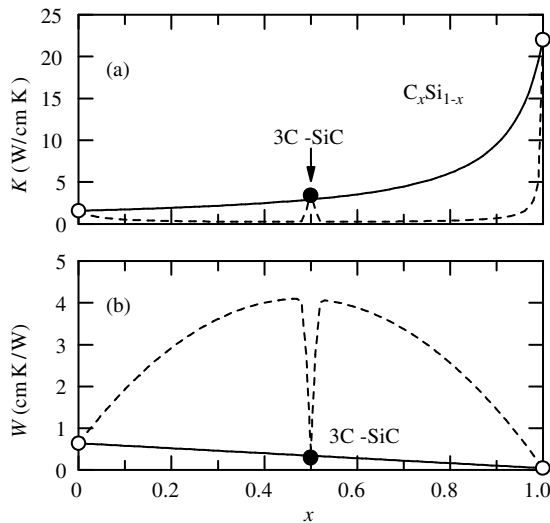


Figure 2.25 (a) Thermal conductivity K and (b) resistivity W versus x for $C_x\text{Si}_{1-x}$ at 300 K. The experimental data for diamond, Si and 3C-SiC ($x=0.5$) are taken from Table 2.2. The solid lines are calculated from Equations (2.25) and (2.26) without taking into account the contribution of alloy disorder (i.e. $C_{\text{CSi}} = 0$ cm K/W), while the dashed lines are obtained assuming $C_{\text{CSi}} = 15$ cm K/W and properly taking into account the alloy ordering effect at $x=0.5$ (3C-SiC). [Reprinted with permission from S. Adachi, *J. Appl. Phys.* **102**, 3502 (2007). Copyright (2007), American Institute of Physics]

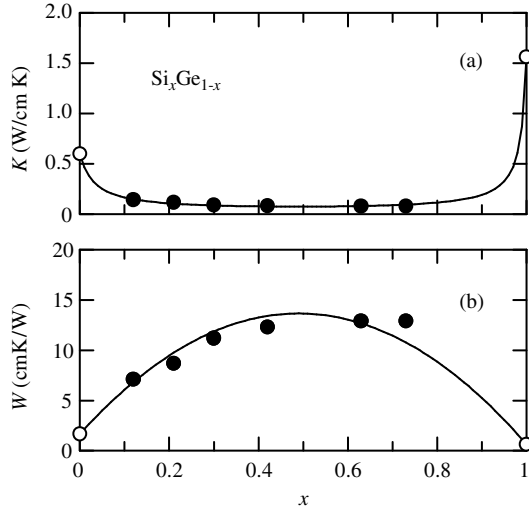


Figure 2.26 (a) Thermal conductivity K and (b) resistivity W versus x for $\text{Si}_x\text{Ge}_{1-x}$ at 300 K. The experimental data are taken from Dismukes *et al.* [64]. The solid lines are obtained from Equations (2.25) and (2.26) with $C_{\text{SiGe}} = 50 \text{ cm K/W}$. [Reprinted with permission from S. Adachi, *J. Appl. Phys.* **102**, 3502 (2007). Copyright (2007), American Institute of Physics]

application varies proportionally to W . One method of achieving a high value for W is by the use of a fine-grain SiGe technique, in which a decrease in thermal conductivity of up to 50% was attained by increasing grain-boundary scattering of phonons [65].

(c) III–V semiconductor alloy

Figure 2.27 shows the thermal conductivity K versus x for (Al, Ga)–V ternaries: (a) $w\text{-Al}_x\text{Ga}_{1-x}\text{N}$ and (b) $\text{Al}_x\text{Ga}_{1-x}\text{As}$ [48]. The experimental data are taken for $w\text{-Al}_x\text{Ga}_{1-x}\text{N}$ from Daly *et al.* [66] and Liu and Balandin [67] and for $\text{Al}_x\text{Ga}_{1-x}\text{As}$ from Afromowitz [68] and Pichardo *et al.* [69]. The solid lines represent the results calculated using Equation (2.26). The III–V binary data are taken from Table 2.2. The reduction in K from the binary value is much larger in $w\text{-Al}_x\text{Ga}_{1-x}\text{N}$ than in $\text{Al}_x\text{Ga}_{1-x}\text{As}$. However, these (Al, Ga)–V ternaries have the same disorder parameter $C_{\text{AlGa}} = 32 \text{ cm K/W}$ (solid lines). It was also found [66] that polycrystalline GaN has a thermal conductivity K , which is more than an order of magnitude lower than that of bulk GaN.

It should be noted that the thermal conductivity K (or thermal resistivity W) is a quantity given by a second-rank symmetric tensor [25]. The wurtzite-type III–N semiconductors thus have two tensor components, K_{\perp} and K_{\parallel} . However, the difference between K_{\perp} and K_{\parallel} usually appears to be less than the experimental uncertainty at room temperature [70].

Figure 2.28 shows the thermal conductivity K versus x for (Ga, In)–V ternaries: (a) $w\text{-Ga}_x\text{In}_{1-x}\text{N}$, (b) $\text{Ga}_x\text{In}_{1-x}\text{As}$ and (c) $\text{Ga}_x\text{In}_{1-x}\text{Sb}$ [48]. The experimental data in (a) are taken from Pantha *et al.* [71], in (b) from Abrahams *et al.* [72] and Arasly *et al.* [73] and in (c) from Magomedov *et al.* [74]. The solid lines in (a)–(c) represent the results calculated using Equation (2.26) with $C_{\text{GaIn}} = 72 \text{ cm K/W}$. It should be noted that the InN value $W_{\text{InN}} = 2.22 \text{ cm K/W}$ used in the calculation corresponds to that for InN ceramics, not the bulk crystalline value. The dashed line in Figure 2.28(a) shows the result calculated using Equation (2.26) and a

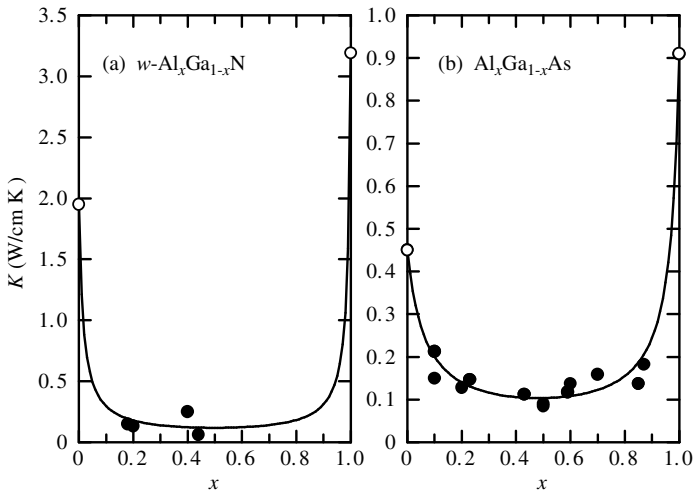


Figure 2.27 Thermal conductivity K versus x for (Al, Ga)-based III-V ternaries at 300 K: (a) $w\text{-Al}_x\text{Ga}_{1-x}\text{N}$ and (b) $\text{Al}_x\text{Ga}_{1-x}\text{As}$. The experimental data in (a) are taken from Daly *et al.* [66] and Liu and Balandin [67] and in (b) from Afromowitz [68] and Pichardo *et al.* [69]. The solid lines are obtained from Equation (2.26) with $C_{\text{AlGa}} = 32 \text{ cm K/W}$. [Reprinted with permission from S. Adachi, *J. Appl. Phys.* **102**, 3502 (2007). Copyright (2007), American Institute of Physics]

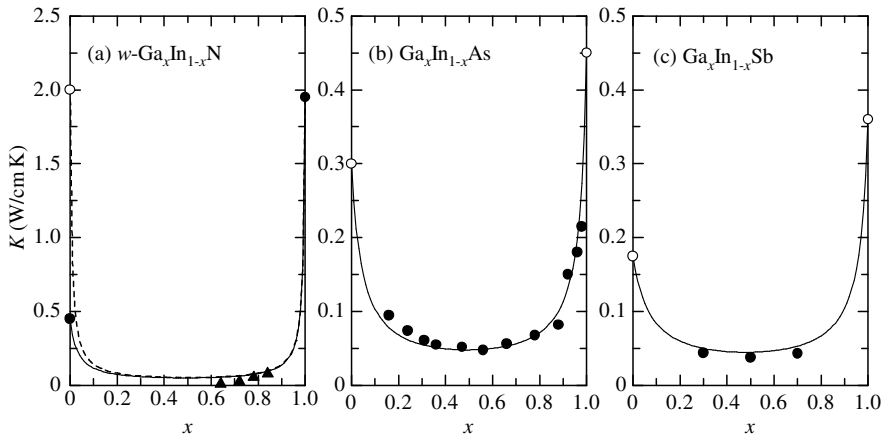


Figure 2.28 Thermal conductivity K versus x for (Ga, In)-based III-V ternaries at 300 K: (a) $w\text{-Ga}_x\text{In}_{1-x}\text{N}$, (b) $\text{Ga}_x\text{In}_{1-x}\text{As}$ and (c) $\text{Ga}_x\text{In}_{1-x}\text{Sb}$. The experimental data in (a) are taken from Pantha *et al.* [71] (solid triangles), in (b) from Abrahams *et al.* [72] and Arasly *et al.* [73] (solid circles) and in (c) from Magomedov *et al.* [74] (solid circles). The solid lines in (a)–(c) are obtained from Equation (2.26) with $C_{\text{GaIn}} = 72 \text{ cm K/W}$. The dashed line in (a) is also obtained from Equation (2.26) with a properly chosen value of $W_{\text{InN}} = 0.5 \text{ cm K/W}$ (open circle), instead of the ceramics InN value of $W_{\text{InN}} = 2.22 \text{ cm K/W}$ (solid line). [Reprinted with permission from S. Adachi, *J. Appl. Phys.* **102**, 3502 (2007). Copyright (2007), American Institute of Physics]

properly chosen value of $W_{\text{InN}} = 0.5 \text{ cm K/W}$, instead of the ceramics value $W_{\text{InN}} = 2.22 \text{ cm K/W}$ (solid line). The small W_{InN} effect is remarkable only in the limited region $x < 0.2$.

It is well known that dilute alloying of GaAs with InAs is a very effective technique for reducing the dislocation density of semiinsulating GaAs crystals grown by the liquid-encapsulated Czochralski method. Ohmer *et al.* [75] studied the effect of the addition of a small quantity of InAs on the thermal properties of GaAs. They reported that for $x = 0.005$ the thermal conductivity is reduced to 50% of the GaAs value. This region is in accordance with theory if the size difference is considered and combined coherently with the mass difference [76].

Values of K and W versus x for $\text{AlAs}_x\text{Sb}_{1-x}$ are shown in Figures 2.29(a) and 2.29(b), respectively [48]. The experimental data are taken from Borca-Tasciuc *et al.* [77]. The solid lines are calculated from Equations (2.25) and (2.26) with $C_{\text{AsSb}} = 91 \text{ cm K/W}$. The agreement between the calculated and experimental results was found to be very satisfactory.

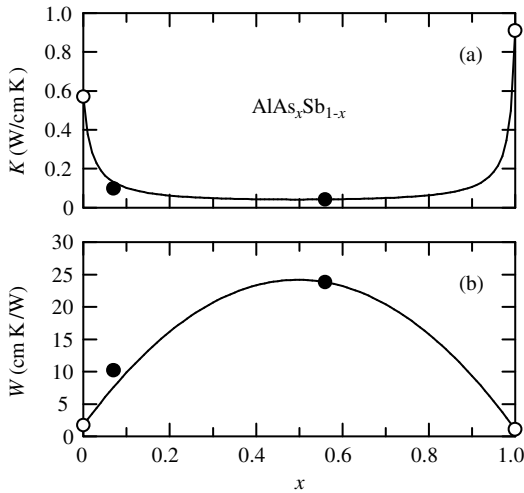


Figure 2.29 (a) Thermal conductivity K and (b) resistivity W versus x for $\text{AlAs}_x\text{Sb}_{1-x}$ at 300 K. The experimental data are taken from Borca-Tasciuc *et al.* [77]. The solid lines are obtained from Equations (2.25) and (2.26) with $C_{\text{AsSb}} = 91 \text{ cm K/W}$. [Reprinted with permission from S. Adachi, *J. Appl. Phys.* **102**, 3502 (2007). Copyright (2007), American Institute of Physics]

The lattice thermal conductivity K versus x plots for III–(P, As) ternaries $\text{GaP}_x\text{As}_{1-x}$ and $\text{InP}_x\text{As}_{1-x}$ are shown in Figures 2.30(a) and 2.30(b), respectively [48]. The experimental data for $\text{GaP}_x\text{As}_{1-x}$ are taken from Carlson *et al.* [78] and Maycock [79] and for $\text{InP}_x\text{As}_{1-x}$ from Maycock [79] and Bowers *et al.* [80]. The solid lines represent the results calculated using Equation (2.26) with $C_{\text{PAs}} = 25 \text{ cm K/W}$. The fit-determined disorder parameter $C_{\text{PAs}} = 25 \text{ cm K/W}$ is comparable to $C_{\text{AlGa}} = 32 \text{ cm K/W}$, but much smaller than $C_{\text{GaIn}} = 72 \text{ cm K/W}$ and $C_{\text{AsSb}} = 91 \text{ cm K/W}$.

The K values of some III–V quaternaries are shown in Figure 2.31 [48]. The experimental data for $\text{Al}_x\text{Ga}_{1-x}\text{As}_y\text{Sb}_{1-y}/\text{GaSb}$ are taken from Borca-Tasciuc *et al.* [77] and Both *et al.* [81], for $\text{Ga}_x\text{In}_{1-x}\text{P}_y\text{As}_{1-y}/\text{InP}$ from Both *et al.* [82] and for $\text{Ga}_x\text{In}_{1-x}\text{As}_y\text{Sb}_{1-y}/\text{GaSb}$ from Both *et al.* [81].

The theoretical curves in Figure 2.31 are obtained from Equation (2.27) with (a) $C_{\text{AlGa}} = 32 \text{ cm K/W}$ and $C_{\text{AsSb}} = 91 \text{ cm K/W}$, (b) $C_{\text{GaIn}} = 72 \text{ cm K/W}$ and $C_{\text{PAs}} = 25 \text{ cm K/W}$ and

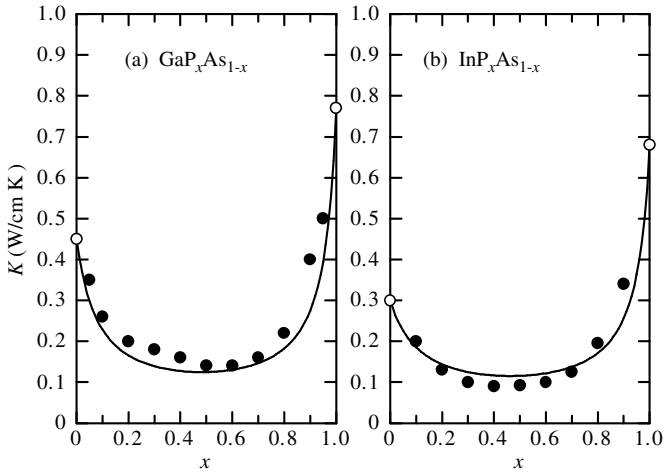


Figure 2.30 Thermal conductivity K versus x for (P, As)-based III-V ternaries at 300 K: (a) $\text{GaP}_x\text{As}_{1-x}$ and (b) $\text{InP}_x\text{As}_{1-x}$. The experimental data in (a) are taken from Carlson *et al.* [78] and Maycock [79] and in (b) from Maycock [79] and Bowers *et al.* [80]. The solid lines are obtained from Equation (2.26) with $C_{\text{PAs}} = 25 \text{ cm K/W}$. [Reprinted with permission from S. Adachi, *J. Appl. Phys.* **102**, 3502 (2007). Copyright (2007), American Institute of Physics]

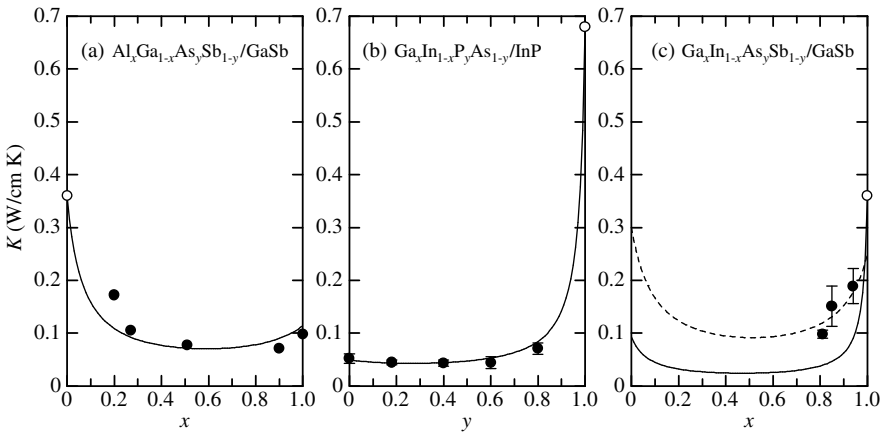


Figure 2.31 Thermal conductivity K versus x or y for III-V quaternaries at 300 K: (a) $\text{Al}_x\text{Ga}_{1-x}\text{As}_y\text{Sb}_{1-y}/\text{GaSb}$, (b) $\text{Ga}_x\text{In}_{1-x}\text{P}_y\text{As}_{1-y}/\text{InP}$ and (c) $\text{Ga}_x\text{In}_{1-x}\text{As}_y\text{Sb}_{1-y}/\text{GaSb}$. The experimental data for $\text{Al}_x\text{Ga}_{1-x}\text{As}_y\text{Sb}_{1-y}/\text{GaSb}$ are taken from Borca-Tasciuc *et al.* [77] and Both *et al.* [81], for $\text{Ga}_x\text{In}_{1-x}\text{P}_y\text{As}_{1-y}/\text{InP}$ from Both *et al.* [82] and for $\text{Ga}_x\text{In}_{1-x}\text{As}_y\text{Sb}_{1-y}/\text{GaSb}$ from Both *et al.* [81]. The solid lines are calculated from Equation (2.27) with (a) $C_{\text{AlGa}} = 32 \text{ cm K/W}$ and $C_{\text{AsSb}} = 91 \text{ cm K/W}$, (b) $C_{\text{GaIn}} = 72 \text{ cm K/W}$ and $C_{\text{PAs}} = 25 \text{ cm K/W}$ and (c) $C_{\text{GaIn}} = 72 \text{ cm K/W}$ and $C_{\text{AsSb}} = 91 \text{ cm K/W}$. The dashed line in (c) represents the result calculated using Equation (2.27) with the introduction of the very small disorder parameters $C_{\text{GaIn}} = 10 \text{ cm K/W}$ and $C_{\text{AsSb}} = 20 \text{ cm K/W}$. [Reprinted with permission from S. Adachi, *J. Appl. Phys.* **102**, 3502 (2007). Copyright (2007), American Institute of Physics]

(c) $C_{\text{GaIn}} = 72 \text{ cm K/W}$ and $C_{\text{AsSb}} = 91 \text{ cm K/W}$. The disorder parameters $C_{\alpha\beta}$ are obtained from the III–V ternary data analyses. The lattice-matching relationships between x and y are taken from Tables 1.9 and 1.10.

The agreement between the experimental and calculated data in Figures 2.31(a) and 2.31(b) is very good and successfully explains the composition dependence of K in the alloys. It should be noted, however, that the calculation in Figure 2.31(c) produces a K value considerably lower than the experimental value. The input of very small $C_{\alpha\beta}$ values into Equation (2.27) improves the fit very well; however, the endpoint ternary K value ($\text{InAs}_{0.91}\text{Sb}_{0.09}$) becomes very large and the binary K value (GaSb) very small, compared with the generally accepted values. The dashed line in Figure 2.31(c) shows an example of such a calculation. Putting $C_{\text{GaIn}} = 10 \text{ cm K/W}$ and $C_{\text{AsSb}} = 20 \text{ cm K/W}$ into Equation (2.27), we obtain $K = 0.30 \text{ W/cm K}$ for $x = 0$ ($\text{InAs}_{0.91}\text{Sb}_{0.09}$) and 0.25 W/cm K for $x = 1.0$ (GaSb), which are far from the generally accepted values.

If the endpoint K values and $C_{\alpha\beta}$ are available, the lattice thermal conductivity and its dependence on alloy composition can easily be calculated from Equation (2.26) or Equation (2.27). At the limit of weak scattering, the disorder parameter Γ in Equation (2.24) can be simply written as

$$\Gamma = \sum_i c_i \left(\frac{M_i - \bar{M}}{\bar{M}} \right)^2 \quad (2.30)$$

where c_i is the fractional concentration of the i th species, M_i is the atomic mass of the i th species and \bar{M} is the average atomic mass.

Figure 2.32 plots the obtained $C_{\alpha\beta}$ values versus Γ [48]. It can be seen that $C_{\alpha\beta}$ decreases with the increase in Γ . The solid line represents the least-squares fit of the III–V ternaries given by ($C_{\alpha\beta}$ in cm K/W)

$$C_{\alpha\beta} = \left(\frac{\Gamma}{7.7} \right)^{-0.90} \quad (2.31)$$

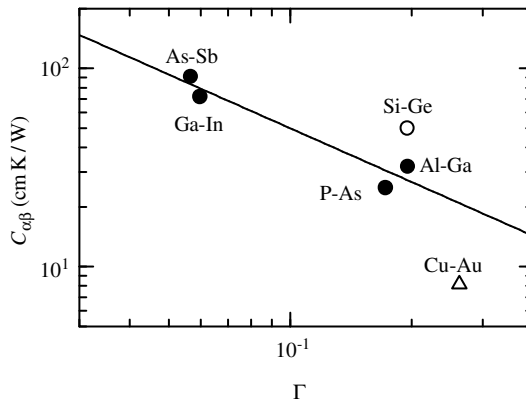


Figure 2.32 $C_{\alpha\beta}$ versus Γ determined for some group-IV binary and III–V ternary alloys and metallic Cu–Au alloy at 300 K. The solid line represents the least-squares fit (III–V ternary data) using Equation (2.31). [Reprinted with permission from S. Adachi, *J. Appl. Phys.* **102**, 3502 (2007). Copyright (2007), American Institute of Physics]

Using this expression, the unknown $C_{\alpha\beta}$ value can be estimated. For example, Γ of the cationic disorder system $i = (\text{Al}, \text{In})$ in Equation (2.30) is 0.384. Introducing this value into Equation (2.31), we obtain $C_{\text{AlIn}} = 15 \text{ cm K/W}$.

Figure 2.33 shows the lattice thermal conductivity as a function of x for (a) $\text{Ga}_x\text{In}_{1-x}\text{P}$ and (b) $\text{GaAs}_x\text{Sb}_{1-x}$ [48]. No experimental data are available for these alloys. The solid lines are calculated from Equation (2.26) with $C_{\text{GaIn}} = 72 \text{ cm K/W}$ in (a) and $C_{\text{AsSb}} = 95 \text{ cm K/W}$ in (b). As expected, the calculated K value markedly decreases with alloying and exhibits a minimum at $x \sim 0.5$.

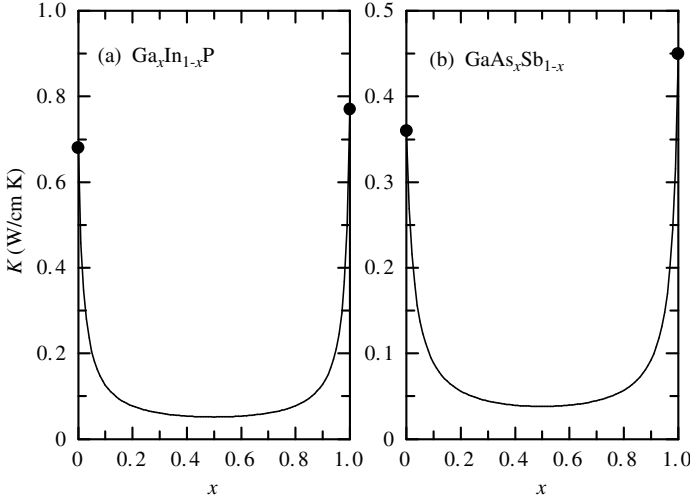


Figure 2.33 Thermal conductivity K versus x for some III-V ternaries at 300 K: (a) $\text{Ga}_x\text{In}_{1-x}\text{P}$ and (b) $\text{GaAs}_x\text{Sb}_{1-x}$. These values were estimated from Equation (2.26) with $C_{\text{GaIn}} = 72 \text{ cm K/W}$ (a) and $C_{\text{AsSb}} = 95 \text{ cm K/W}$ (b) (solid lines). The solid circles represent the experimental endpoint binary data. [Reprinted with permission from S. Adachi, *J. Appl. Phys.* **102**, 3502 (2007). Copyright (2007), American Institute of Physics]

In an $\text{A}_x\text{B}_y\text{C}_z\text{D}$ ($\text{AB}_x\text{C}_y\text{D}_z$) quaternary alloy, the lattice thermal conductivity K can be written as

$$K(x, y, z) = \frac{1}{W(x, y, z)} = \frac{1}{xW_{\text{AD}} + yW_{\text{BD}} + zW_{\text{CD}} + xyC_{\text{AB}} + xzC_{\text{AC}} + yzC_{\text{BC}}} \quad (2.32)$$

with

$$x + y + z = 1 \quad \text{or} \quad z = 1 - x - y \quad (2.33)$$

Since the thermal conductivity or resistivity in Equation (2.32) is specified in terms of the alloy composition x , y and z only, K or W of a quaternary alloy with arbitrary composition can easily be calculated. For example, the thermal conductivity of $\text{Al}_x\text{Ga}_y\text{In}_{1-x-y}\text{N}$ can be estimated from (in W/cm K)

$$K_{\text{AlGaInN}}(x, y, z) = \frac{1}{3.19x + 1.95y + 0.45z + 32xy + 15xz + 72yz} \quad (2.34)$$

Similarly, the K values for $(\text{Al}_x\text{Ga}_{1-x})_{0.53}\text{In}_{0.47}\text{P}/\text{GaAs}$ and $(\text{Al}_x\text{Ga}_{1-x})_{0.48}\text{In}_{0.52}\text{As}/\text{InP}$ can be estimated, as shown in Figure 2.34 [48]. The disorder parameters $C_{\alpha\beta}$ used are taken from Table 2.2. The lattice-matching relationships between x and y for these quaternaries are taken from Table 1.11.

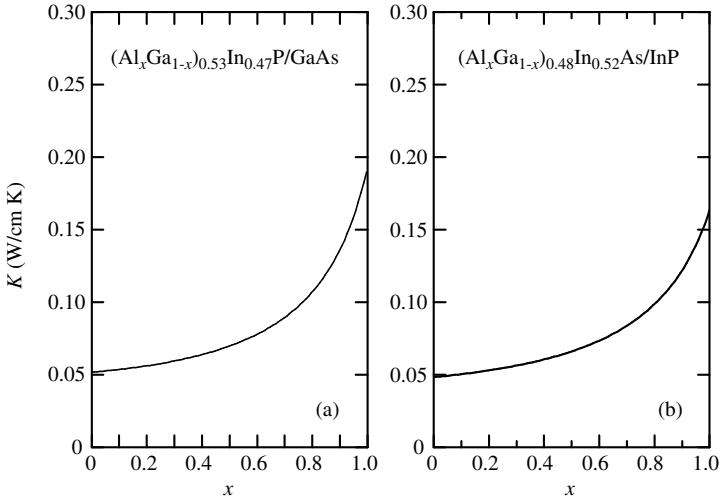


Figure 2.34 Thermal conductivity K versus x for some III–V quaternaries at 300 K: (a) $(\text{Al}_x\text{Ga}_{1-x})_{0.53}\text{In}_{0.47}\text{P}/\text{GaAs}$ and (b) $(\text{Al}_x\text{Ga}_{1-x})_{0.48}\text{In}_{0.52}\text{As}/\text{InP}$. These values were estimated from Equation (2.32) with $C_{\text{AlGa}} = 32 \text{ cm K/W}$, $C_{\text{AlIn}} = 15 \text{ cm K/W}$ and $C_{\text{GaIn}} = 72 \text{ cm K/W}$. [Reprinted with permission from S. Adachi, *J. Appl. Phys.* **102**, 3502 (2007). Copyright (2007), American Institute of Physics]

(d) II–VI semiconductor alloy

Ioffe and Ioffe [83] reported the thermal conductivity of ZnTe–CdTe, CdSe–HgSe, ZnSe–ZnTe, HgSe–HgTe, ZnSe–CdTe and ZnTe–CdSe alloys. Each of the starting materials was crushed into a fine powder, carefully blended in the required proportions, compressed under a pressure of $2\text{--}5 \text{ t/cm}^2$ at a temperature of about 300°C and then repeatedly annealed at higher temperatures until a stable value of thermal conductivity was attained. All the experimental data showed a marked decrease in thermal conductivity with alloying. Because of the ceramic-like nature of the samples, their absolute values may be much smaller than those of the bulk crystalline materials.

Aliev *et al.* [84] have reported the temperature dependence of K for $\text{Cd}_x\text{Hg}_{1-x}\text{Te}$ with $x = 0\text{--}0.2$. These results are shown in Figure 2.35. The data give a maximum K near 8 K. In the temperature range from 10 to 100 K, HgTe ($x = 0$) has a thermal conductivity proportional to $T^{-1.2}$. The alloys with $x > 0$ have lower thermal conductivities and the temperature exponents are also less. The experimentally determined exponents for various non-alloyed group-IV, III–V and II–VI semiconductors are summarized in Table 2.9 of Adachi [25].

The thermal conductivities K for $\text{Zn}_x\text{Hg}_{1-x}\text{Te}$ and $\text{Cd}_x\text{Hg}_{1-x}\text{Te}$ and their melts were reported by Sha *et al.* [85] and Su [86], respectively. These data were determined from the experimental diffusivities and theoretical specific heats (Section 2.5.2).

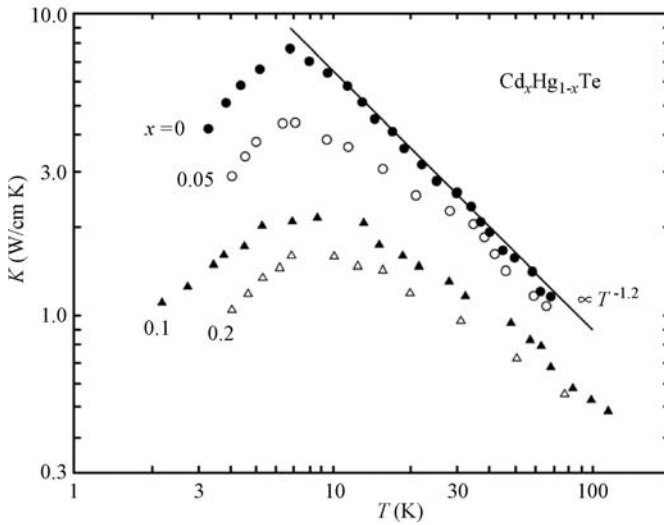


Figure 2.35 Thermal conductivity K for $\text{Cd}_x\text{Hg}_{1-x}\text{Te}$ with $x = 0, 0.05, 0.1$ and 0.2 . [Reprinted from *Sov. Phys Solid State* **2**, 719 (1960)] The solid line represents the exponential relationship, $K \propto T^{-1.2}$

2.5.2 Thermal Diffusivity

(a) General considerations

The thermal diffusivity D can be obtained from the thermal conductivity K by means of the definition

$$D = \frac{K}{C_p g} \quad (2.35)$$

where C_p and g represent the specific heat at constant pressure and crystal density, respectively. Thermal diffusivity D is measured in cm^2/s .

(b) Alloy value

Figure 2.36 shows the inverse plots of D versus x for (a) $\text{C}_x\text{Si}_{1-x}$ and (b) $\text{Al}_x\text{Ga}_{1-x}\text{As}$. The endpoint data are indicated by the open circles. The experimental data for 3C-SiC is also shown in Figure 2.36(a) by the solid circle. The solid line in Figure 2.36(b) is obtained from Equation (2.35) using the K and C_p values in Table 2.2 (Equation (2.26)) and Equation (2.10), respectively. The inverse thermal diffusivity D^{-1} of 3C-SiC is found to be well interpreted by the linear interpolation between the endpoint data.

Figure 2.37 shows the plot of K and D versus x for $(\text{GaAs})_x(\text{InP})_{1-x}$ quaternary. The K values are obtained from (in W/cm K)

$$K_{(\text{GaAs})(\text{InP})}(x) = \frac{1}{2.22x + 1.47(1-x) + 72x(1-x) + 25x(1-x)} \quad (2.36)$$

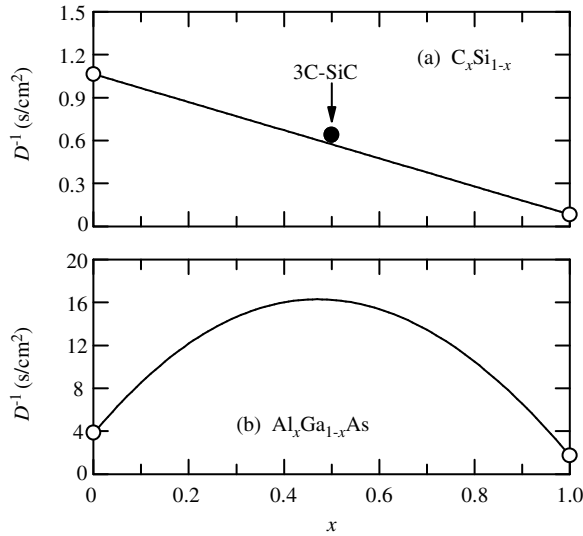


Figure 2.36 Inverse thermal diffusivity D versus x for (a) $\text{C}_x\text{Si}_{1-x}$ and (b) $\text{Al}_x\text{Ga}_{1-x}\text{As}$ at 300 K. The solid line in (a) represents the linear interpolation result between the endpoint data (open circles)

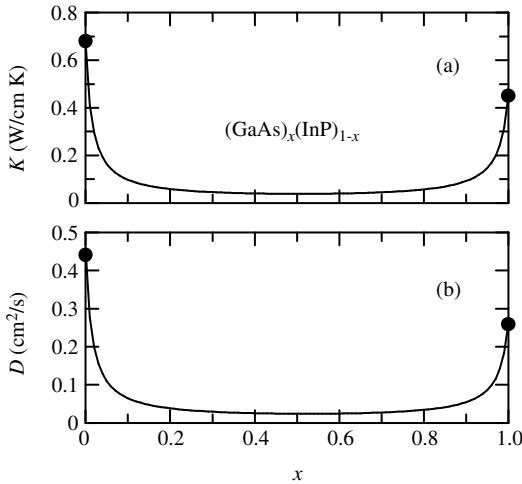


Figure 2.37 (a) Thermal conductivity K and (b) diffusivity D versus x for $(\text{GaAs})_x(\text{InP})_{1-x}$ quaternary at 300 K. The solid circles represent the experimental endpoint binary data

The C_p values used in the calculation of D are taken from Equation (2.9), while g is interpolated between GaAs and InP.

REFERENCES

[1] H. Stöhr and W. Klemm, *Z. Anorg. Allg. Chem.* **241**, 305 (1939).
 [2] T. Soma, *Phys. Status Solidi B* **111**, K23 (1982).

- [3] L. M. Foster and J. F. Woods, *J. Electrochem. Soc.* **118**, 1175 (1971).
- [4] G. B. Stringfellow, *J. Phys. Chem. Solids* **33**, 665 (1972).
- [5] M. B. Panish and M. Ilegems, *Prog. Solid State Chem.* **7**, 39 (1972).
- [6] S. Adachi, *J. Appl. Phys.* **58**, R1 (1985).
- [7] N. A. El-Masry, E. L. Piner, S. X. Liu, and S. M. Bedair, *Appl. Phys. Lett.* **72**, 40 (1998).
- [8] D. Doppalapudi, S. B. Basu, K. F. Ludwig, Jr., and T. D. Moustakas, *J. Appl. Phys.* **84**, 1389 (1998).
- [9] T. Saito and Y. Arakawa, *Phys. Rev. B* **60**, 1701 (1999).
- [10] T. Takeyama, M. Yuri, K. Itoh, T. Baba, and J. S. Harris, Jr., *J. Appl. Phys.* **88**, 1104 (2000).
- [11] L. K. Teles, J. Furthmüller, L. M. R. Scolfaro, J. R. Leite, and F. Bechstedt, *Phys. Rev. B* **62**, 2475 (2000).
- [12] M. Ferhat and F. Bechstedt, *Phys. Rev. B* **65**, 075213 (2002).
- [13] J. Adhikari and D. A. Kofke, *J. Appl. Phys.* **95**, 4500 (2004).
- [14] S. Y. Karpov, N. I. Podolskaya, I. A. Zhmakin, and A. I. Zhmakin, *Phys. Rev. B* **70**, 235203 (2004).
- [15] C. K. Gan, Y. P. Feng, and D. J. Srolovitz, *Phys. Rev. B* **73**, 235214 (2006).
- [16] S. Raghavan, J. P. Hajra, G. N. K. Iyengar, and K. P. Abraham, *Thermochim. Acta* **189**, 151 (1991).
- [17] V. L. Solozhenko, A. N. Baraov, and V. Z. Turkevich, *Solid State Commun.* **138**, 534 (2006).
- [18] J. Steininger, A. J. Strauss, and R. F. Brebrick, *J. Electrochem. Soc.* **117**, 1305 (1970).
- [19] A. G. Fischer and W. H. Fonger, Report No. 3 (1965), Contract No. AF 19 (628)-3866, US Air Force, Cambridge Research Laboratories, Bedford, Mass., USA.
- [20] A. J. Strauss and J. Steininger, *J. Electrochem. Soc.* **117**, 1420 (1970).
- [21] J. Steininger and A. J. Strauss, *J. Cryst. Growth* **13/14**, 657 (1972).
- [22] K. Ohata, J. Saraie, and T. Tanaka, *Jpn. J. Appl. Phys.* **12**, 1198 (1973).
- [23] D. A. Wood, K. D. Rogers, D. W. Lane, G. J. Conibeer, and D. Parton, *J. Mater. Sci. Lett.* **17**, 1511 (1998).
- [24] See, T. C. Harman, in *Physics and Chemistry of II–VI Compounds* (edited by M. Aven and J. S. Prener), North-Holland, Amsterdam, 1967, p. 767.
- [25] S. Adachi, *Properties of Group-IV, III–V and II–VI Semiconductors*, John Wiley & Sons, Ltd, Chichester, 2005.
- [26] H.-M. Kagaya, Y. Kitani, and T. Soma, *Solid State Commun.* **58**, 399 (1986).
- [27] A. N. N. Sirota, A. M. Antyukhov, and V. A. Fedorov, *Sov. Phys. Dokl.* **26**, 701 (1981).
- [28] A. N. N. Sirota, A. M. Antyukhov, V. V. Novikov, and A. A. Sidorov, *Sov. Phys. Dokl.* **27**, 754 (1982).
- [29] S. Adachi, *GaAs and Related Materials: Bulk Semiconducting and Superlattice Properties*. World Scientific, Singapore, 1994.
- [30] N. N. Sirota, N. P. Gavaleshko, V. V. Novikova, A. V. Novikova, and V. M. Frasunyak, *Russ. J. Phys. Chem.* **64**, 603 (1990).
- [31] M. Gambino, V. Vassiliev, and J. P. Bros, *J. Alloys Compounds* **176**, 304 (1987).
- [32] H. Maleki and L. R. Holland, in *Properties of Narrow Gap Cadmium-based Compounds*, EMIS Datareviews Series No. 10 (edited by P. Capper), INSPEC, London, 1994, p. 48.
- [33] C. G. Shirley, *Acta Cryst. A* **31**, 853 (1975).
- [34] V. N. Nikiforov and V. G. Sredin, *Rus. Phys. J.* **49**, 337 (2006).
- [35] V. V. Zhdanova, M. G. Kakna, and T. Z. Samadashvili, *Izv. Akad. Nauk. SSSR Neorg. Mater.* **3**, 1263 (1967).
- [36] N. S. Takahashi, in *Properties of Aluminium Gallium Arsenide*, EMIS Datareviews Series No. 7 (edited by S. Adachi), INSPEC, London, 1993, p. 3.
- [37] J. Bak-Misiuk, J. Domagała, W. Paszkowicz, J. Trela, Z. R. Żytkiewicz, M. Leszczyński, K. Regiński, J. Muszalski, J. Härtwig, and M. Ohler, *Acta Phys. Polonica A* **91**, 911 (1997).
- [38] I. Kudman and R. J. Paff, *J. Appl. Phys.* **43**, 3760 (1972).
- [39] M. Leszczyński, A. Kulik, and P. Ciepiewski, *Phys. Status Solidi A* **119**, 495 (1990).
- [40] M. E. Straumanis, J.-P. Krumme, and M. Rubenstein, *J. Electrochem. Soc.* **114**, 640 (1967).
- [41] S. Adachi, *Physical Properties of III–V Semiconductor Compounds: InP, InAs, GaAs, GaP, InGaAs, and InGaAsP*, John Wiley & Sons, Ltd, New York, 1992.

- [42] V. N. Bessolov, S. G. Konnikov, V. E. Umanskii, and Y. P. Yakoviev, *Sov. Phys. Tech. Phys.* **28**, 257 (1983).
- [43] D. Bagot, R. Granger, and S. Rolland, *Phys. Status Solidi B* **177**, 295 (1993).
- [44] J. R. Kim, R. M. Park, and K. S. Jones, *Mater. Res. Soc. Symp. Proc.* **340**, 475 (1994).
- [45] W.-T. Kim, *Phys. Rev. B* **59**, 4572 (1999).
- [46] B. Abeles, *Phys. Rev.* **131**, 1906 (1963).
- [47] S. Adachi, *J. Appl. Phys.* **54**, 1844 (1983).
- [48] S. Adachi, *J. Appl. Phys.* **102**, 063502 (2007).
- [49] W. Nakwaski, *J. Appl. Phys.* **64**, 159 (1988).
- [50] L. Nordheim, *Ann. Phys.* **401**, 607 (1931).
- [51] L. Nordheim, *Ann. Phys.* **401**, 641 (1931).
- [52] P. Jacobsson and B. Sundqvist, *J. Phys. Chem. Solids* **49**, 441 (1988).
- [53] A. Mascarenhas, *Spontaneous Ordering in Semiconductor Alloys*, Kluwer Academic, New York, 2002.
- [54] T. S. Kuan, T. F. Kuech, W. I. Wang, and E. L. Wilkie, *Phys. Rev. Lett.* **54**, 201 (1985).
- [55] A. Ourmazd and J. C. Bean, *Phys. Rev. Lett.* **55**, 765 (1985).
- [56] Y. K. Koh and D. G. Cahill, *Phys. Rev. B* **76**, 075207 (2007).
- [57] E. T. Croke, A. T. Hunter, C. C. Ahn, T. Laursen, D. Chandrasekhar, A. E. Bair, D. J. Smith, and J. W. Mayer, *J. Cryst. Growth* **175–176**, 486 (1997).
- [58] M. Asheghi, K. Kurabayashi, R. Kasnavi, and K. E. Goodson, *J. Appl. Phys.* **91**, 5079 (2002).
- [59] D. G. Cahill and F. Watanabe, *Phys. Rev. B* **70**, 235322 (2004).
- [60] T. R. Anthony, W. F. Banholzer, J. F. Fleischer, L. Wei, P. K. Kuo, R. L. Thomas, and R. W. Pryor, *Phys. Rev. B* **42**, 1104 (1990).
- [61] D. G. Onn, A. Witek, Y. Z. Wie, T. R. Anthony, and W. F. Banholzer, *Phys. Rev. Lett.* **68**, 2806 (1992).
- [62] J. R. Olson, R. O. Pohl, J. W. Vandersande, A. Zoltan, T. R. Anthony, and W. F. Banholzer, *Phys. Rev. B* **47**, 14850 (1993).
- [63] W. S. Capinski, H. J. Maris, E. Bauser, I. Silier, M. Asen-Palmer, T. Ruf, M. Cardona, and E. Gmelin, *Appl. Phys. Lett.* **71**, 2109 (1997).
- [64] J. P. Dismukes, L. Ekstrom, E. F. Steigmeier, I. Kudman, and D. S. Beers, *J. Appl. Phys.* **35**, 2899 (1964).
- [65] C. B. Vining, W. Laskow, J. O. Hanson, R. R. Van der Beck, and P. D. Gorsuch, *J. Appl. Phys.* **69**, 4333 (1991).
- [66] B. C. Daly, H. J. Maris, A. V. Nurmikko, M. Kuball, and J. Han, *J. Appl. Phys.* **92**, 3820 (2002).
- [67] W. Liu and A. A. Balandin, *Appl. Phys. Lett.* **85**, 5230 (2004).
- [68] M. A. Fromowitz, *J. Appl. Phys.* **44**, 1292 (1973).
- [69] J. L. Pichardo, J. J. Alvarado-Gil, A. Cruz, J. G. Mendoza, and G. Torres, *J. Appl. Phys.* **87**, 7740 (2000).
- [70] G. A. Slack and S. B. Austerman, *J. Appl. Phys.* **42**, 4713 (1971).
- [71] B. N. Pantha, R. Dahal, J. Li, J. Y. Lin, H. X. Jiang, and G. Pomrenko, *Appl. Phys. Lett.* **92**, 042112 (2008).
- [72] M. S. Abrahams, R. Braunstein, and F. D. Rosi, *J. Phys. Chem. Solids* **10**, 204 (1959).
- [73] D. G. Arasly, R. N. Ragimov, and M. I. Aliev, *Sov. Phys. Semicond.* **24**, 225 (1990).
- [74] Y. B. Magomedov, N. L. Kramynina, and S. M. Ismailov, *Sov. Phys. Solid State* **34**, 1486 (1992).
- [75] M. C. Ohmer, W. C. Mitchel, G. A. Graves, D. E. Holmes, H. Kuwamoto, and P. W. Yu, *J. Appl. Phys.* **64**, 2775 (1988).
- [76] F. Szmulowicz, F. L. Madarasz, P. G. Klemens, and J. Diller, *J. Appl. Phys.* **66**, 252 (1989).
- [77] T. Borca-Tasciuc, D. W. Song, J. R. Meyer, I. Vurgaftman, M.-J. Yang, B. Z. Nosho, L. J. Whitman, H. Lee, R. U. Martinelli, G. W. Turner, M. J. Manfra, and G. Chen, *J. Appl. Phys.* **92**, 4994 (2002).
- [78] R. O. Carlson, G. A. Slack, and S. J. Silverman, *J. Appl. Phys.* **36**, 505 (1965).
- [79] P. D. Maycock, *Solid-State Electron.* **10**, 161 (1967).
- [80] R. Bowers, J. E. Bauerle, and A. J. Cornish, *J. Appl. Phys.* **30**, 1050 (1959).

- [81] W. Both, A. E. Bochkarev, A. E. Drakin, and B. N. Sverdlov, *Cryst. Res. Technol.* **24**, K161 (1989).
- [82] W. Both, V. Gottschalch, and G. Wagner, *Cryst. Res. Technol.* **21**, K85 (1986).
- [83] A. V. Ioffe and A. F. Ioffe, *Sov. Phys. Solid State* **2**, 719 (1960).
- [84] S. A. Aliev, T. G. Gadzhive, and R. I. Selim-zade, *Sov. Phys. Solid State* **31**, 346 (1989).
- [85] Y.-G. Sha, C.-H. Su, K. Mazuruk, and S. L. Lehoczky, *J. Appl. Phys.* **80**, 752 (1996).
- [86] C.-H. Su, *J. Cryst. Growth* **78**, 51 (1986).

3 Elastic Properties

3.1 ELASTIC CONSTANT

3.1.1 General Considerations

The second-order elastic stiffness $[C]$ and compliance tensors $[S]$ are defined by the generalized Hooke's law: $[X] = [C][e]$ or $[e] = [S][X]$, where $[X]$ and $[e]$ are, respectively, the elastic stress and strain tensors which have six components. The elastic tensors $[C]$ and $[S]$ are second-order fourth-rank and have symmetric 6×6 components. Their explicit tensor forms are given in Adachi [1]. We present in Tables 3.1–3.3 the elastic stiffness and compliance constants for a number of group-IV, III–V and II–VI semiconductors used for obtaining alloy values.

3.1.2 Room-temperature Value

(a) Group-IV semiconductor alloy

Figure 3.1 shows the elastic constants C_{ij} of the metallic alloy Cu–Au. The solid and open circles represent the experimental ordered (CuAu₃ and Cu₃Au) and disordered phase data, respectively, gathered from various sources. The solid lines show the linear interpolation values between Au and Cu. No clear ordering effect can be found in the elastic properties of the metallic alloy.

Figure 3.2 shows the plots of experimental C_{ij} data for 3C-SiC ($x = 0.5$), together with those for diamond and Si. Note that 3C-SiC crystallizes in the zinc-blende structure and is a compound, not an alloy. The solid lines show the linear interpolation between diamond and Si. Because of the extremely large C_{ij} values of diamond, the linearly interpolated SiC values deviate considerably from the experimental values.

Mendik *et al.* [2] determined the elastic constants of a relaxed Si_{0.49}Ge_{0.51} film using Brillouin scattering and his data are shown in Figure 3.3, together with those of Si and Ge. The alloy value can be safely estimated using the linear interpolation scheme.

(b) III–V semiconductor alloy

Only a few reports of the direct measurement of elastic constants are available for III–V semiconductor alloys. The elastic constants C_{ij} of Ga_xIn_{1-x}Sb have been determined using a pulse echo method [3]. Figure 3.4 shows these results. The linearly interpolated values are shown by the solid lines and the experimental data are in good agreement with the linear interpolation results.

Figure 3.5 shows the elastic constants C_{ij} versus y or x for (a) Ga_xIn_{1-x}P_yAs_{1-y}/InP and (b) (Al_xGa_{1-x})_{0.53}In_{0.47}P/GaAs. The solid circles show the endpoint data determined by

Table 3.1 Elastic stiffness C_{ij} and compliance constants S_{ij} for a number of cubic group-IV, III-V and II-VI semiconductors at 300 K. d = diamond; zb = zinc-blende; rs = rocksalt

System	Material	C_{ij} (10^{11} dyn/cm ²)			S_{ij} (10^{-12} cm ² /dyn)		
		C_{11}	C_{12}	C_{44}	S_{11}	S_{12}	S_{44}
IV	Diamond (d)	107.9	12.4	57.8	0.0949	-0.00978	0.1730
	Si (d)	16.564	6.394	7.951	0.7691	-0.2142	1.2577
	Ge (d)	12.870	4.770	6.670	0.9718	-0.2628	1.499
	Sn (d) ^a	6.90	2.93	3.62	1.94	-0.578	2.76
	3C-SiC (zb)	39.0	14.2	25.6	0.318	-0.085	0.391
III-V	BN (zb)	82.0	19.0	48.0	0.134	-0.025	0.208
	BP (zb)	31.5	10	16	0.37	-0.09	1.00
	BAs (zb) ^b	27.9	12.0	11.3	0.484	-0.145	0.885
	AlN (zb) ^b	31.5	15.0	18.5	0.458	-0.148	0.541
	AlP (zb) ^b	15.0	6.42	6.11	0.897	-0.269	1.64
	AlAs (zb)	11.93	5.72	5.72	1.216	-0.394	1.748
	AlSb (zb)	8.769	4.341	4.076	1.697	-0.5618	2.453
	GaN (zb) ^b	29.1	14.8	15.8	0.523	-0.176	0.633
	GaP (zb)	14.050	6.203	7.033	0.9756	-0.2988	1.422
	GaAs (zb)	11.88	5.38	5.94	1.173	-0.366	1.684
	GaSb (zb)	8.838	4.027	4.320	1.583	-0.4955	2.315
	InN (zb) ^b	19.2	7.30	9.35	0.659	-0.182	1.07
	InP (zb)	10.22	5.73	4.42	1.639	-0.589	2.26
	InAs (zb)	8.329	4.526	3.959	1.945	-0.6847	2.526
InSb (zb)	6.608	3.531	3.027	2.410	-0.8395	3.304	
II-VI	BeS (zb) ^b	12.3	7.30	5.69	1.47	-0.55	1.76
	BeSe (zb) ^b	11.0	6.66	5.03	1.66	-0.63	1.99
	BeTe (zb) ^b	8.87	5.54	3.86	2.16	-0.83	2.59
	MgO (rs)	29.4	9.3	15.5	0.401	-0.096	0.647
	MgS (zb) ^b	8.88	5.53	3.87	2.16	-0.83	2.58
	MgSe (zb) ^b	7.58	4.86	3.17	2.64	-1.03	3.15
	MgTe (zb) ^b	5.28	3.66	1.93	4.38	-1.79	5.18
	ZnS (zb)	10.2	6.46	4.46	1.95	-0.76	2.25
	ZnSe (zb)	8.57	5.07	4.05	2.09	-0.78	2.47
	ZnTe (zb)	7.15	4.08	3.11	2.39	-0.85	3.25
	CdS (zb)	7.70	5.39	2.36	3.07	-1.26	4.24
	CdSe (zb)	6.67	4.63	2.23	3.48	-1.42	4.48
	CdTe (zb)	5.35	3.69	2.02	4.27	-1.74	4.95
	HgS (zb)	8.13	6.22	2.64	3.65	-1.58	3.79
	HgSe (zb)	6.08	4.46	2.23	4.34	-1.84	4.49
	HgTe (zb)	5.32	3.68	2.08	4.33	-1.77	4.80

^aObtained from an analysis of the phonon dispersion curves at 90 K^bCalculated or estimated

Table 3.2 Elastic stiffness constant C_{ij} for a number of hexagonal group-IV, III-V and II-VI semiconductors at 300 K (in 10^{11} dyn/cm²). w = wurtzite; h = hexagonal ($P6_3/mmc$ (D_{6h}))

System	Material	C_{11}	C_{12}	C_{13}	C_{33}	C_{44}	C_{66}^a
IV	2H-SiC (w) ^b	50.1	11.1	5.2	55.3	16.3	19.5
III-V	BN (h)	52.0	43.1	37.0	42.4	6.5	4.5
	AlN (w)	41.0	14.0	10.0	39.0	12.0	13.5
	GaN (w)	37.3	14.1	8.0	38.7	9.4	11.6
	InN (w)	19.0	10.4	12.1	18.2	0.99	4.3
II-VI	BeO (w)	46.1	12.6	8.85	49.2	14.8	16.8
	ZnO (w)	20.9	12.0	10.4	21.8	4.41	4.45
	ZnS (w)	12.2	5.8	4.2	13.8	2.87	3.2
	CdS (w)	8.65	5.40	4.73	9.44	1.50	1.63
	CdSe (w)	7.41	4.52	3.9	8.43	1.34	1.45

$$^a C_{66} = \frac{1}{2}(C_{11} - C_{12})$$

^bAssuming that the 2H-SiC values are the same as those for 6H-SiC within experimental error

Table 3.3 Elastic compliance constant S_{ij} for a number of hexagonal group-IV, III-V and II-VI semiconductors at 300 K (in 10^{-12} cm²/dyn). w = wurtzite; h = hexagonal ($P6_3/mmc$ (D_{6h}))

System	Material	S_{11}	S_{12}	S_{13}	S_{33}	S_{44}	S_{66}^a
IV	2H-SiC (w) ^b	0.211	-0.045	-0.016	0.184	0.614	0.512
III-V	BN (h)	0.726	-0.398	-0.286	0.735	1.54	2.25
	AlN (w)	0.285	-0.085	-0.051	0.283	0.833	0.740
	GaN (w)	0.320	-0.112	-0.043	0.276	1.06	0.864
	InN (w)	0.957	-0.206	-0.499	1.21	10.1	2.33
II-VI	BeO (w)	0.240	-0.060	-0.032	0.215	0.677	0.600
	ZnO (w)	0.782	-0.345	-0.210	0.664	2.24	2.254
	ZnS (w)	1.10	-0.45	-0.20	0.86	3.48	3.10
	CdS (w)	2.08	-1.00	-0.54	1.60	6.66	6.16
	CdSe (w)	2.32	-1.12	-0.55	1.69	7.47	6.88

$$^a S_{66} = 2(S_{11} - S_{12})$$

^bAssuming that the 2H-SiC values are the same as those for 6H-SiC within experimental error

Brillouin scattering for Ga_{0.47}In_{0.53}As [4] and Ga_{0.53}In_{0.47}P [5]. Since the lattice-matched quaternaries have the same lattice constants over the entire composition range ($a_{\text{InP}} = 5.8690$ Å or $a_{\text{GaAs}} = 5.65330$ Å), their elastic constants are not expected to show strong dependence on the alloy composition [1]. The solid lines in Figures 3.5(a) and 3.5(b) represent the results calculated using Equations (A.6) and (A.8), respectively.

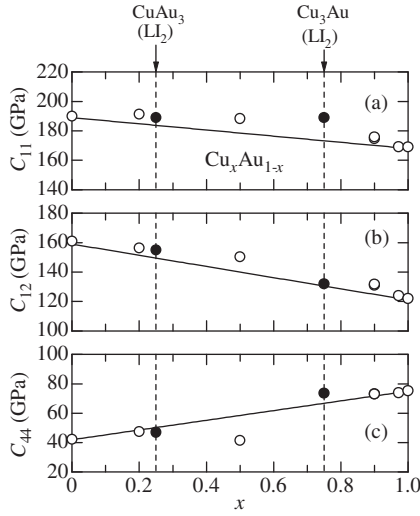


Figure 3.1 Elastic constants C_{ij} of Cu–Au. The solid and open circles represent the experimental ordered (L1_2 type) and disordered alloy data, respectively. The solid lines show the linear interpolation results between Au and Cu

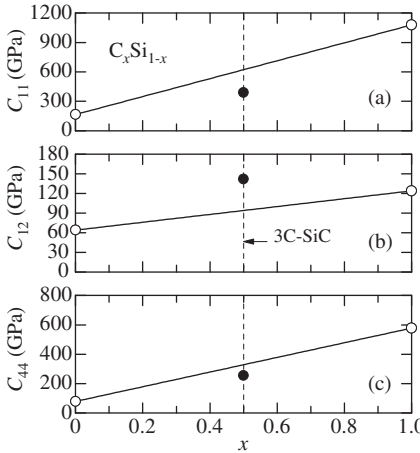


Figure 3.2 Elastic constants C_{ij} of $\text{C}_x\text{Si}_{1-x}$ at 300 K. The solid circles represent the 3C-SiC data ($x=0.5$). The solid lines show the linear interpolation results between the endpoint elemental data

(c) II–VI semiconductor alloy

The elastic constant C_{11} of MBE- $\text{Be}_x\text{Zn}_{1-x}\text{Se}$ on GaAs(100) has been determined using Brillouin scattering [6]. Figure 3.6 shows these results. The BeSe value is estimated from the simple $C_{ij}-a$ (lattice parameter) relationship described in Adachi [1]. The solid line is linearly interpolated between the endpoint binary data. The experimental data in Figure 3.6 suggest an upward bowing. Peiris *et al.* [6] determined C_{11} from the sound velocities v_s by measuring

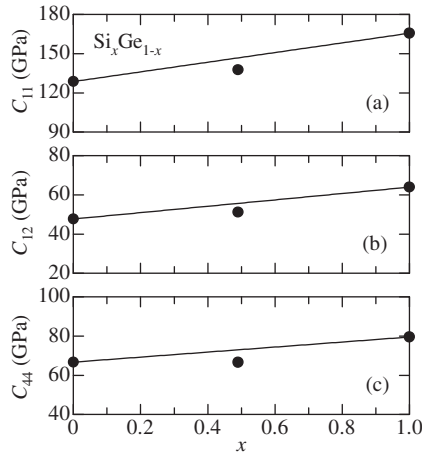


Figure 3.3 Elastic constants C_{ij} of $\text{Si}_x\text{Ge}_{1-x}$ at 300 K. The experimental data ($x=0.49$) are taken from Mendik *et al.* [2]. The solid lines show the linear interpolation results between the endpoint elemental data

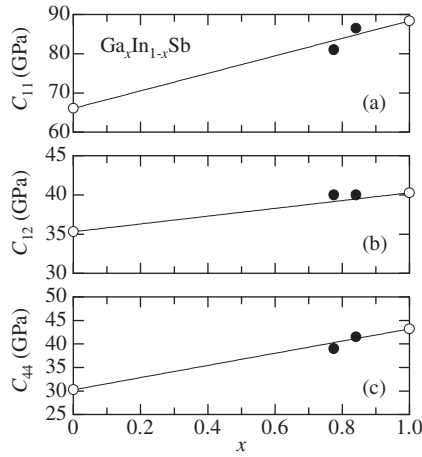


Figure 3.4 Elastic constants C_{ij} of $\text{Ga}_x\text{In}_{1-x}\text{Sb}$ at 300 K. The experimental data are taken from Galibert and Bougnot [3]. The solid lines show the linear interpolation results between the endpoint binary data

frequency shift $\Delta\omega$ of the Brillouin components using the relationship

$$\Delta\omega = \pm 2\omega_L n \frac{v_s}{c} \sin\left(\frac{\theta}{2}\right) \quad (3.1)$$

where ω_L is the frequency of the incident laser radiation, n is the refractive index of the material, c is the speed of light in vacuum and θ is the scattering angle (180°). Using a prism coupler technique, they also determined n for $\text{Be}_x\text{Zn}_{1-x}\text{Se}$.

Figure 3.7 shows the elastic constants C_{ij} versus x for $\text{Zn}_x\text{Cd}_{1-x}\text{Te}$. The experimental data are taken from Andrusiv *et al.* [7] ($x=0.35, 0.57$ and 0.71), from Maheswaranathan *et al.* [8]

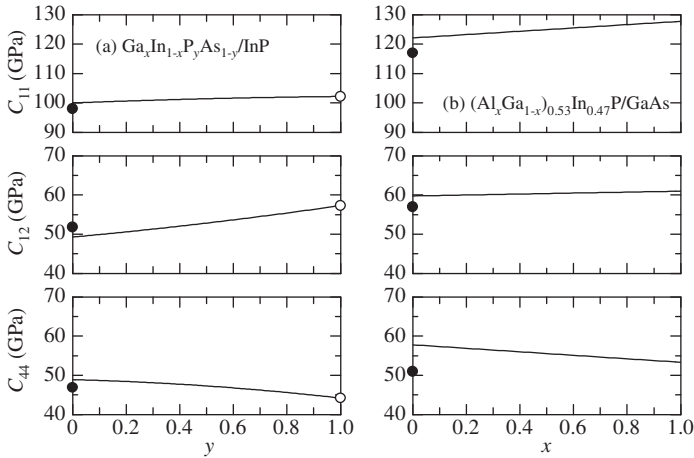


Figure 3.5 Elastic constants C_{ij} versus y or x for (a) $\text{Ga}_x\text{In}_{1-x}\text{P}_y\text{As}_{1-y}/\text{InP}$ and (b) $(\text{Al}_x\text{Ga}_{1-x})_{0.53}\text{In}_{0.47}\text{P}/\text{GaAs}$ at 300 K. The open circles in (a) represent the InP data, while the solid circles in (a) and (b) show the endpoint ternary data taken from Carlotti *et al.* [4] ($\text{Ga}_{0.47}\text{In}_{0.53}\text{As}$) and Hassine *et al.* [5] ($\text{Ga}_{0.53}\text{In}_{0.47}\text{P}$), respectively. The solid lines show the linear interpolation results of Equations (A.6) and (A.8)

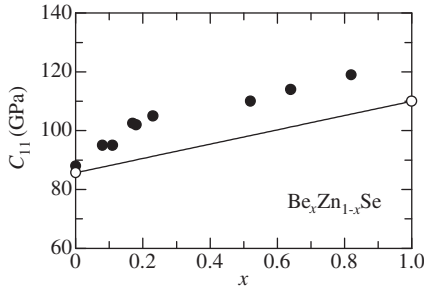


Figure 3.6 Elastic constant C_{11} of MBE-grown $\text{Be}_x\text{Zn}_{1-x}\text{Se}$ on GaAs(1 0 0) at 300 K. The experimental data are taken from Peiris *et al.* [6]. The solid line shows the linear interpolation result between the endpoint binary data

($x = 0.48$) and from Queheillalt and Wadley [9] ($x = 0.04$). These data are in agreement with the linearly interpolated values within experimental accuracy.

3.1.3 External Perturbation Effect

(a) Temperature effect

Only a few reports are available on the temperature dependence of C_{ij} for III–V and II–VI alloys [3,7,9]. Figure 3.8 shows the linearly interpolated dC_{ij}/dT versus y for $\text{Ga}_x\text{In}_{1-x}\text{P}_y\text{As}_{1-y}/\text{InP}$ calculated from Equation (A.6). The binary values used are taken from Table 3.8 in Adachi [1].

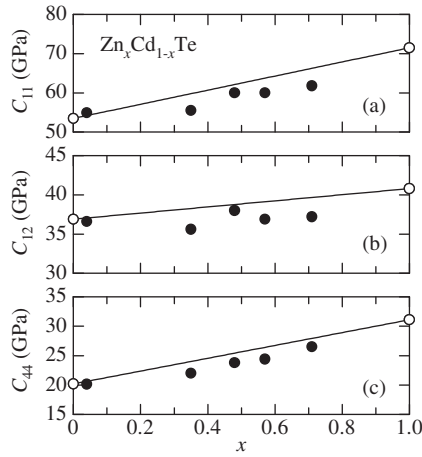


Figure 3.7 Elastic constants C_{ij} versus x for $\text{Zn}_x\text{Cd}_{1-x}\text{Te}$ at 300 K. The experimental data are taken from Andrusiv *et al.* [7] ($x=0.35, 0.57$ and 0.71), from Maheswaranathan *et al.* [8] ($x=0.48$) and from Queheillalt and Wadley [9] ($x=0.04$). The solid lines show the linear interpolation results between the endpoint binary data

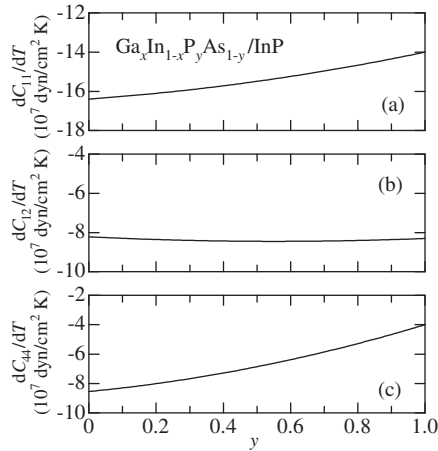


Figure 3.8 Linearly interpolated dC_{ij}/dT versus y for $\text{Ga}_x\text{In}_{1-x}\text{P}_y\text{As}_{1-y}/\text{InP}$ at 300 K. The binary dC_{ij}/dT data used in the calculation (Equation (A.6)) are taken from Adachi [1]

The temperature-dependent C_{ij} values of $\text{Zn}_x\text{Cd}_{1-x}\text{Te}$ have been determined from 78 to 300 K [7] and from 300 up to 1413 K [9]. The solid circles in Figure 3.9 show the dC_{ij}/dT data for $\text{Zn}_x\text{Cd}_{1-x}\text{Te}$ ($x=0.04$) [9]. The endpoint data taken from Table 3.8 in Adachi [1] are also shown by the open circles. The $x=0.04$ data are found to largely deviate from the linearly interpolated values. The temperature-dependent C_{ij} values for $\text{Ga}_x\text{In}_{1-x}\text{Sb}$ ($x=0.78-0.95$) were also measured using the pulse echo method between 4 and 300 K [3].

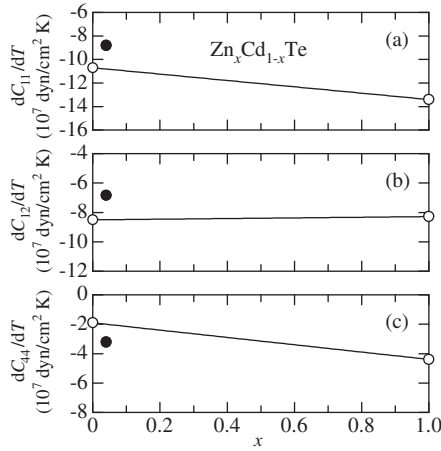


Figure 3.9 dC_{ij}/dT versus x for $Zn_xCd_{1-x}Te$ at 300 K. The data represented by solid circles are taken from Queheillalt and Wadley [9] ($x = 0.04$), while the open circles represent the endpoint binary data [1]

(b) Pressure effect

The pressure coefficient dC_{ij}/dp is a dimensionless quantity [1]. The linearly interpolated dC_{ij}/p values for $Ga_xIn_{1-x}P_yAs_{1-y}/InP$ are shown in Figure 3.10. The binary data are taken from Table 3.8 in Adachi [1]. Like dC_{ij}/dT in Figure 3.8, the dC_{ij}/dp versus y plots show very weak nonlinearity with respect to y .

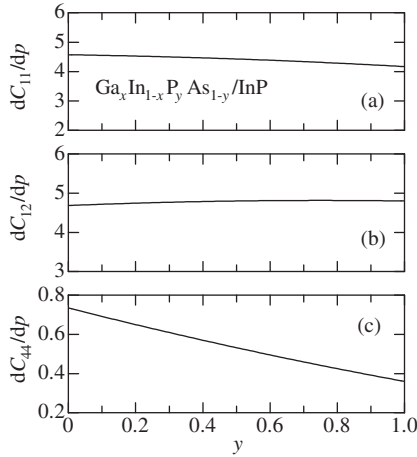


Figure 3.10 Linearly interpolated dC_{ij}/dp versus y for $Ga_xIn_{1-x}P_yAs_{1-y}/InP$ at 300 K. The binary dC_{ij}/dp values used in the calculation (Equation (A.6)) are taken from Adachi [1]

Maheswaranathan *et al.* [8] measured the pressure coefficients dC_{ij}/dp of CdTe and $Zn_xCd_{1-x}Te$ for p up to 4 kbar. They obtained $dC_{11}/dp = 3.6 \pm 0.1$, $dC_{12}/dp = 4.4 \pm 0.1$ (296 K) and $dC_{44}/dp = 1.99 \pm 0.01$ (196 K) for CdTe; $dC_{11}/dp = 4.0 \pm 0.1$, $dC_{12}/dp = 4.4 \pm 0.1$ (296 K) and $dC_{44}/dp = 2.38 \pm 0.02$ (196 K) for $Zn_{0.48}Cd_{0.52}Te$.

3.2 THIRD-ORDER ELASTIC CONSTANT

No experimental data has been reported on the third-order elastic constants (C_{ijk}) of group-IV, III–V or II–VI semiconductor alloys. This necessitates the use of some sort of an interpolation scheme. The reported C_{ijk} values for some non-alloyed group-IV, III–V and II–VI semiconductors are summarized in Tables 3.11 and 3.12 of Adachi [1].

3.3 YOUNG'S MODULUS, POISSON'S RATIO AND SIMILAR PROPERTIES

3.3.1 Group-IV Semiconductor Alloy

The general properties of various elastic moduli, such as Young's modulus and Poisson's ratio, are presented in Adachi [1]. The alloy C_{ij} values can be estimated with good accuracy using the linear interpolation scheme (Section 3.1.2). Thus, the various elastic moduli can be calculated from the linearly interpolated C_{ij} values. The expressions of the various elastic moduli can be found in Adachi [1].

As an example, the bulk moduli B_u calculated from the linearly interpolated C_{ij} values of C_xSi_{1-x} (dashed line) are illustrated in Figure 3.11. The endpoint and 3C-SiC data are shown by the open and solid circles, respectively [1]. These data show weak downward bowing (solid line).

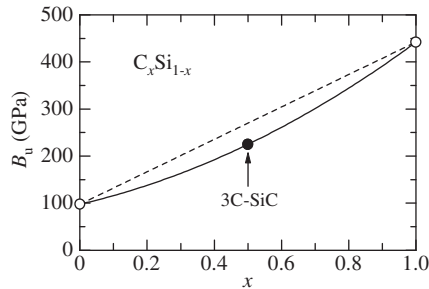


Figure 3.11 Bulk modulus B_u versus x for C_xSi_{1-x} at 300 K calculated using the linearly interpolated C_{ij} values (dashed line). The endpoint and 3C-SiC values are shown by the open and solid circles, respectively [1]. These experimental data exhibit weak downward bowing (solid line)

Using a Monte Carlo simulation, Kelires [10] found that C_xSi_{1-x} exhibits an accurate power-law dependence of B_u on the lattice constant a or, equivalently, on the 'average' nearest-neighbor distance d , over the whole composition range.

3.3.2 III–V Semiconductor Alloy

A technique using XRD was demonstrated for the simultaneous determination of Poisson's ratio P , lattice constant a and composition x for some III–V ternaries [11]. In Figure 3.12 P versus x has been plotted for (a) $Al_xIn_{1-x}As$, (b) $Ga_xIn_{1-x}P$ and (c) $Ga_xIn_{1-x}As$. The solid lines represent the results calculated from the linearly interpolated C_{ij} values.

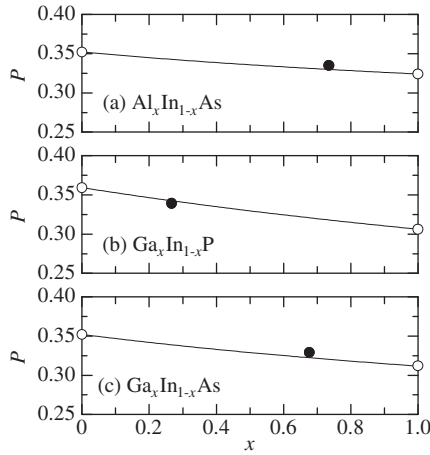


Figure 3.12 Poisson’s ratio P versus x for (a) $\text{Al}_x\text{In}_{1-x}\text{As}$, (b) $\text{Ga}_x\text{In}_{1-x}\text{P}$ and (c) $\text{Ga}_x\text{In}_{1-x}\text{As}$ at 300 K. The solid lines represent the P versus x curves calculated from the linearly interpolated C_{ij} values. The solid circles show the experimental data taken from Hoke *et al.* [11], while the open circles represent the endpoint binary data taken from Adachi [1]

Figure 3.13 shows the bulk modulus B_u as a function of y for $\text{Ga}_x\text{In}_{1-x}\text{P}_y\text{As}_{1-y}/\text{InP}$. The solid line represents the B_u versus y curve calculated from the linearly interpolated C_{ij} values. The experimental data plotted are taken from Prins and Dunstan [12]. The experimental B_u data are found to be the same as InP to within 1%, while $\text{Ga}_{0.47}\text{In}_{0.53}\text{As}$ ($y = 0$) is 5% lower.

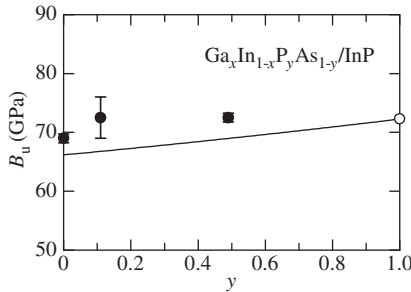


Figure 3.13 Bulk modulus B_u versus y for $\text{Ga}_x\text{In}_{1-x}\text{P}_y\text{As}_{1-y}/\text{InP}$ at 300 K. The solid line represents the B_u versus y curve calculated from the linearly interpolated C_{ij} values. The solid circles represent the experimental data taken from Prins and Dunstan [12]. The open circle also represents the InP data taken from Adachi [1]

Caro *et al.* [13] determined Poisson’s ratio P of $\text{Al}_x\text{Ga}_{1-x}\text{As}$ using a HRXRD. They concluded that both the lattice parameter a and Poisson’s ratio P are in agreement with Vegard law.

3.3.3 II–VI Semiconductor Alloy

The elastic constants C_{ij} for the Be-based II–VI semiconductors, BeS, BeSe and BeTe listed in Table 3.1, are estimated from the simple $C_{ij}-a$ (lattice parameter) relationship in Adachi [1].

These elastic constants yield the bulk moduli B_u of 90, 81 and 67 GPa for BeS, BeSe and BeTe, respectively. On the other hand, the experimental data were $B_u = 92.2 \pm 1.8$ GPa for BeSe and 66.8 ± 0.7 GPa for BeTe if the pressure derivatives dB_u/dp were fixed at 4 [14].

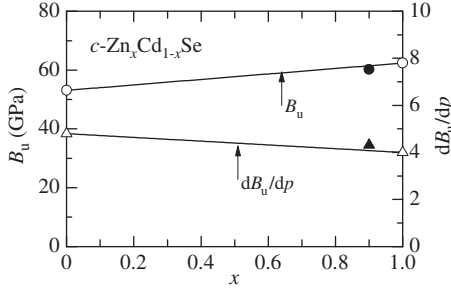


Figure 3.14 Bulk modulus B_u and pressure derivative dB_u/dp versus x for $c\text{-Zn}_x\text{Cd}_{1-x}\text{Se}$ at 300 K. The solid line represents the B_u versus y curve calculated using the linearly interpolated C_{ij} values. The solid line for dB_u/dp is also obtained from the linear interpolation scheme using the endpoint binary data in Adachi [1] (open triangles). The experimental data ($x=0.9$) are taken from Lin *et al.* [15]

The WDXS technique was employed to study the elastic properties of $\text{Zn}_x\text{M}_{1-x}\text{Se}$ ($M = \text{Cd}, \text{Fe}$ or Mn) [15]. Figure 3.14 shows the $\text{Zn}_x\text{Cd}_{1-x}\text{Se}$ data for $x=0.9$. The B_u versus x curve is calculated from the linearly interpolated C_{ij} values, while the dB_u/dp curve is simply obtained from the linear interpolation between the endpoint values in Adachi [1]. The pressure derivative of B_u can now be written as [1]

$$\frac{dB_u}{dp} = \frac{1}{3} \left(\frac{dC_{11}}{dp} \right) + \frac{2}{3} \left(\frac{dC_{12}}{dp} \right) \tag{3.2}$$

The bulk moduli B_u of $\text{ZnSe}_x\text{Te}_{1-x}$ ($0 \leq x \leq 1.0$) have been determined using the WDXS [16]. These data are presented in Figure 3.15. The solid line shows the linear least-squares fit given by

$$B_u(x) = 53.0 + 13.5x \tag{3.3}$$

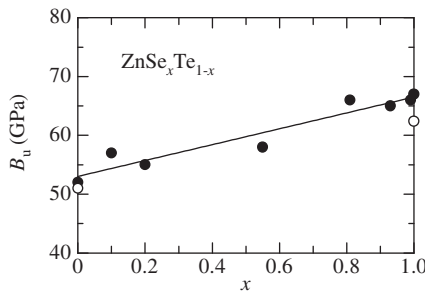


Figure 3.15 Bulk modulus B_u versus x for $\text{ZnSe}_x\text{Te}_{1-x}$ at 300 K. The experimental data are taken from Pellicer-Porres *et al.* [16]. The solid line represents the least-squares fit of Equation (3.3). The open circles show the endpoint binary data taken from Adachi [1]

The x -dependent Young's moduli Y have been determined for $\text{Be}_x\text{Zn}_{1-x}\text{Se}$ grown on GaP(100) and GaAs(100) by MBE [17]. The measured Y values increased almost linearly with increasing x . However, these data are slightly larger than the generally accepted values, e.g. about 10% larger for ZnSe.

3.4 MICROHARDNESS

3.4.1 Group-IV Semiconductor Alloy

No detailed studies relating to the microhardness of group-IV semiconductor alloys have been found in the literature. The hardness values H for Si, diamond and 3C-SiC are shown graphically in Figure 3.16. The experimental data are taken from Table 3.23 in Adachi [1]. The 3C-SiC value deviates slightly from the weighted average of diamond and Si.

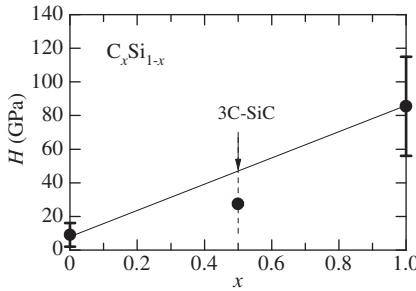


Figure 3.16 Microhardness H versus x for $\text{C}_x\text{Si}_{1-x}$ at 300 K. The endpoint and 3C-SiC values are plotted by the solid circles. These data are taken from Adachi [1]. The solid line represents the linear interpolation result between the endpoint elemental data

3.4.2 III-V Semiconductor Alloy

Several authors have carried out measurements on the microhardness H of III-V semiconductor alloys. The H values for some (Al, Ga)- and (Ga, In)-based ternaries are shown in Figures 3.17 and 3.18, respectively. The experimental data in Figure 3.17 are taken from Cáceres *et al.* [18] and Hjort *et al.* [19] and in Figure 3.18 from Bourhis and Patriarche [20] and Schenk and Silber [21]. The open circles represent the data taken from Adachi [1].

It can be seen from Figures 3.17 and 3.18 that the microhardness is almost linear with respect to x , except in the case of $\text{Ga}_x\text{In}_{1-x}\text{P}$. The considerable strengthening observed in $\text{Ga}_x\text{In}_{1-x}\text{P}$ ($x \sim 0.5$) was attributed to the high crystal friction as confirmed by the flow-stress values [20].

The microhardness anisotropy was determined for $\text{Ga}_x\text{In}_{1-x}\text{P}_y\text{As}_{1-y}/\text{InP}$. Figure 3.19 shows the 3D representation of the Knoop hardness anisotropy on the (100) surfaces of $\text{Ga}_x\text{In}_{1-x}\text{P}_y\text{As}_{1-y}/\text{InP}$ with y as a parameter [22]. The ternary ($y = 0$) and quaternary hardness anisotropy in Figure 3.19 share a general shape, which is fundamentally different from that of InP, having two or more maxima and one or more minima instead of one maximum and two minima. The major slip system in the diamond and zinc-blende structures is $1/2\langle 110 \rangle \{111\}$. Dislocations generated by plastic deformation, therefore, lie on the $\{111\}$ planes with

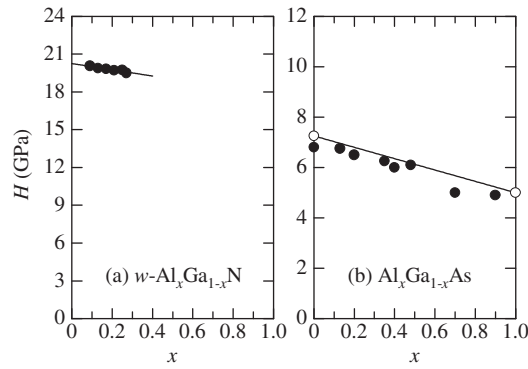


Figure 3.17 Microhardness H versus x for (a) $w\text{-Al}_x\text{Ga}_{1-x}\text{N}$ and (b) $\text{Al}_x\text{Ga}_{1-x}\text{As}$ at 300 K. The experimental data in (a) are taken from Cáceres *et al.* [18] and in (b) from Hjort *et al.* [19]. The solid line in (b) shows the linear interpolation result between the endpoint binary data [1]

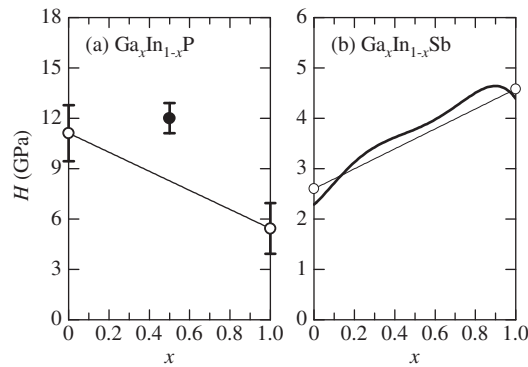


Figure 3.18 Microhardness H versus x for (a) $\text{Ga}_x\text{In}_{1-x}\text{P}$ and (b) $\text{Ga}_x\text{In}_{1-x}\text{Sb}$ at 300 K. The experimental data in (a) are taken from Bourhis and Patriarche [20] and in (b) from Schenk and Silber [21] (heavy solid line). The solid lines show the linear interpolation results between the endpoint binary data [1]

$1/2\langle 110 \rangle$ Burgers vectors. The radically different shape of the anisotropy curves observed may suggest significant differences between the deformation behavior of the alloys and InP, which might be associated with different dislocation dynamics and even, perhaps, a primary slip system different from the $\langle 110 \rangle$, $\{111\}$ system.

The composition dependence of the average Knoop hardness H in Figure 3.19 shows that H increases with increasing y from the ternary value (~ 5.2 GPa), peaking at $y \sim 0.5$ ($H \sim 5.4$ GPa), and decreasing with further increases of y ($H \sim 4$ GPa at $y = 1.0$) [22].

3.4.3 II–VI Semiconductor Alloy

The microhardness of BeO has been reported to be $H \sim 0.92\text{--}13$ GPa [23]. There has, however, been no experimental data for H in BeS, BeSe and BeTe. Alloying ZnSe with a more covalent II–VI compound such as BeSe may significantly alter the mechanical properties and eventually

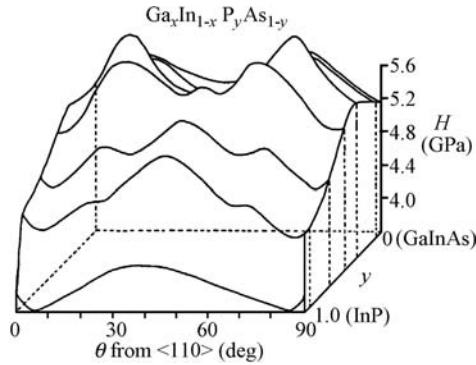


Figure 3.19 Three-dimensional representation of microhardness anisotropy observed on (100)-oriented $\text{Ga}_x\text{In}_{1-x}\text{P}_y\text{As}_{1-y}/\text{InP}$ with y as a parameter ($y = 0-1.0$) at 300 K. [Reproduced with permission from D. Y. Watts and A. F. W. Willoughby, *J. Mater. Sci.* **23**, 272 (1988), Copyright (1988) Springer]

lead to viable devices. In particular, both hardness and elastic modulus are expected to be enhanced by increasing the bond covalency. The composition dependence of H for $\text{Be}_x\text{Zn}_{1-x}\text{Se}$ has been investigated by several authors. We summarize these results in Figure 3.20. The experimental data are taken from Waag *et al.* [24] (open circles) and Paszkowicz *et al.* [25] (solid circles). The solid line also shows the experimental data of Grillo *et al.* [26]. Although there is a large difference in H , all these data show an increase in H with increasing x . The data of Grillo *et al.* [26] show a peak in H at $x \sim 0.7$.

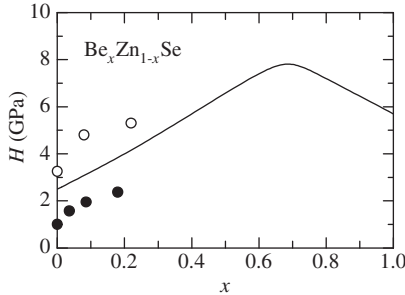


Figure 3.20 Microhardness H versus x for $\text{Be}_x\text{Zn}_{1-x}\text{Se}$ at 300 K. The experimental data are taken from Waag *et al.* [24] (open circles) and Paszkowicz *et al.* [25] (solid circles). The solid line also represents the experimental data by Grillo *et al.* [26]

The microhardness H for $\text{ZnSe}_x\text{Te}_{1-x}$ ($0 \leq x \leq 0.06$) and $\text{Be}_x\text{Zn}_{1-x}\text{Se}_y\text{Te}_{1-y}$ ($0 \leq x \leq 0.11$) has been measured by Maruyama *et al.* [27]. These data show an increase in H with increasing Se or Be concentration.

Figure 3.21 shows the experimental H data for $\text{Zn}_x\text{Hg}_{1-x}\text{Se}$ as measured by Fang *et al.* [28]. The open circles represent the endpoint data taken from Adachi [1]. The solid line represents the linearly interpolated result. The experimental curve shows a pronounced peak at

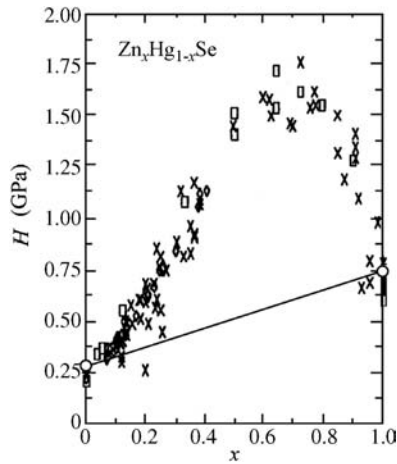


Figure 3.21 Microhardness H versus x for $\text{Zn}_x\text{Hg}_{1-x}\text{Se}$ at 300 K. [Reproduced with permission from S. Fang, L. J. Farthing, M.-F. S. Tang, and D. A. Stevenson, *J. Vac. Sci. Technol. A* **8**, 1120 (1990). Copyright (1990), American Vacuum Society]. The solid line shows the linear interpolation result between the endpoint binary data [1]

$x \sim 0.7$. Similarly, the experimental curve for $\text{Zn}_x\text{Cd}_{1-x}\text{Te}$ obtained by Schenk and Dunog [29] showed a peak at $x \sim 0.7$, as shown in Figure 3.22. A peak at $x \sim 0.7$ was also observed in $\text{Cd}_x\text{Hg}_{1-x}\text{Te}$ [28]. The microhardness at $x \sim 0.7$ in $\text{Zn}_x\text{Hg}_{1-x}\text{Se}$ is about 1.6 GPa, which is at least twice the value of that in $\text{Cd}_x\text{Hg}_{1-x}\text{Te}$. The microhardness H of $\text{Cd}_x\text{Hg}_{1-x}\text{Te}$ decreased with increasing temperature from 300 to 600 K, e.g. from $H \sim 0.7$ GPa at 300 K to ~ 0.2 GPa at 600 K for $x = 0.7$ [30].

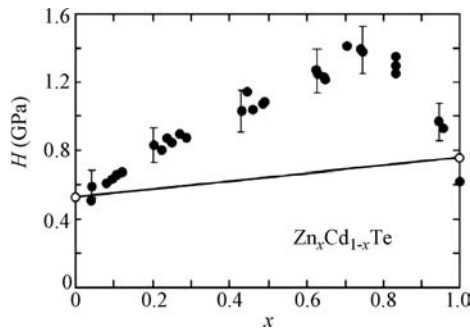


Figure 3.22 Microhardness H versus x for $\text{Zn}_x\text{Cd}_{1-x}\text{Te}$ at 300 K. [Reproduced with permission from M. Schenk and L. T. H. Dunog, *Semicond. Sci. Technol.* **13**, 335 (1998), Copyright (1998) Institute of Physics]. The solid line shows the linear interpolation result between the endpoint binary data [1]

Generally, isoelectronic doping in the order of ppm leads to a softening of the crystal lattice due to the vacancies in the lattice being filled with dopant atoms, and hence the etch-pit density is reduced, virtually without affecting the electrical properties of the material. Softening as a result of isoelectronic doping has been observed in In-doped GaAs [31] and in Zn-doped CdS [32].

In conclusion of this section, the microhardness H of some tetrahedral semiconductor alloys shows a liner relationship between H and the alloy composition. More ionic semiconductor alloys, namely, II–VI alloys, however, show not only a clear upward bowing, but also a deviation from the parabolic behavior of the microhardness H . Such deviations lead to a peak in H at $x \sim 0.7$ and not at $x \sim 0.5$.

3.5 SOUND VELOCITY

If the crystal density g and elastic stiffness C_{ij} of a solid are known, the sound velocity v can be calculated from the simple relationship

$$v = \sqrt{\frac{C_{ij}}{g}} \tag{3.4}$$

The detailed functional forms, in terms of C_{ij} , of Equation (3.4) are shown in Tables 3.25 and 3.27 of Adachi [1]. The alloy C_{ij} and g values can be approximated with good accuracy by the linear interpolation scheme. Thus, we can easily calculate the sound velocities propagating in the various crystallographic directions.

For example, Figure 3.23 shows the calculated sound velocities propagating in the [110] direction in (a) $\text{Al}_x\text{Ga}_{1-x}\text{As}$ and (b) $\text{Ga}_x\text{In}_{1-x}\text{P}_y\text{As}_{1-y}/\text{InP}$, where v_{LA} corresponds to the longitudinal mode and v_{TA1} and v_{TA2} correspond to the slow and fast transverse modes, respectively. It can be seen that the sound velocities propagating in these alloys exhibit a weak nonlinear dependence on x or y .

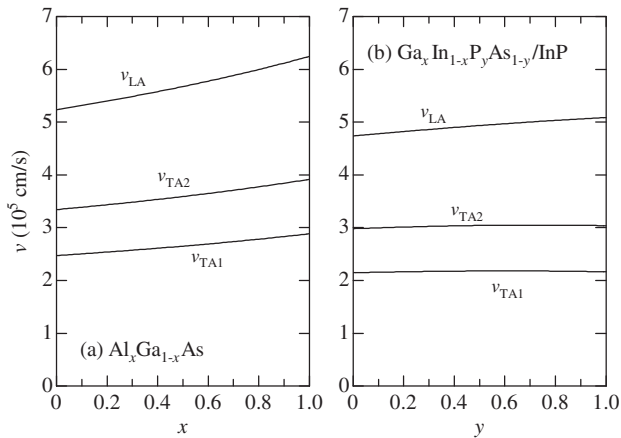


Figure 3.23 Sound velocities propagating in the [1 1 0] direction in (a) $\text{Al}_x\text{Ga}_{1-x}\text{As}$ and (b) $\text{Ga}_x\text{In}_{1-x}\text{P}_y\text{As}_{1-y}/\text{InP}$, where v_{LA} corresponds to the longitudinal mode and v_{TA1} and v_{TA2} correspond to the slow and fast transverse modes, respectively

Note that in piezoelectric semiconductors like GaAs and GaN, the sound velocity given by Equation (3.4) should be modified as

$$v = \sqrt{\frac{C_{ij} + K^2}{g}} \quad (3.5)$$

where K^2 is the electromechanical coupling constant [1], which leads to a piezoelectrically stiffened elastic constant if the sound wave is involved with piezoelectricity. The change in sound velocity due to piezoelectricity is only $\sim 0.1\%$ for GaAs, but is $\sim 0.5\%$ for GaN [33].

REFERENCES

- [1] S. Adachi, *Properties of Group-IV, III-V and II-VI Semiconductors*, John Wiley & Sons, Ltd, Chichester, 2005.
- [2] M. Mendik, M. Ospelt, H. von Känel, and P. Wachter, *Appl. Surf. Sci.* **50**, 303 (1991).
- [3] G. Galibert and G. Bougnot, *Mater. Res. Bull.* **9**, 167 (1974).
- [4] G. Carlotti, D. Fioretto, L. Palmieri, G. Socino, A. Verdini, and C. Rigo, *J. Phys.: Condens. Matter* **8**, 2265 (1996).
- [5] A. Hassine, J. Sapriel, P. L. Berre, P. Legay, F. Alexandre, and G. Post, *J. Appl. Phys.* **77**, 6569 (1995).
- [6] F. C. Peiris, U. Bindley, J. K. Furdyna, H. Kim, A. K. Ramdas, and M. Grimsditch, *Appl. Phys. Lett.* **79**, 473 (2001).
- [7] I. I. Andrusiv, G. M. Grigorovich, Y. V. Ilisavskiĭ, M. A. Ruvinskiĭ, and V. P. Shchetinin, *Sov. Phys. Solid State* **25**, 139 (1983).
- [8] P. Maheswaranathan, R. J. Sladek, and U. Debska, *Phys. Rev. B* **31**, 5212 (1985).
- [9] D. T. Queheillalt and H. N. G. Wadley, *J. Appl. Phys.* **83**, 4124 (1998).
- [10] P. C. Kelires, *Phys. Rev. B* **55**, 8784 (1997).
- [11] W. E. Hoke, T. D. Kennedy, and A. Torabi, *Appl. Phys. Lett.* **79**, 4160 (2001).
- [12] A. D. Prins and D. J. Dunstan, *Semicond. Sci. Technol.* **4**, 239 (1989).
- [13] L. D. Caro, C. Giannini, L. Tapfer, H.-P. Schönherr, L. Däweritz, and K. H. Ploog, *Solid State Commun.* **108**, 77 (1998).
- [14] H. Luo, K. Ghandehari, R. G. Greene, and A. L. Ruoff, *Phys. Rev. B* **52**, 7058 (1995).
- [15] C.-M. Lin, D.-S. Chuu, J. Xu, E. Huang, W.-C. Chou, J.-Z. Hu, and J.-H. Pei, *Phys. Rev. B* **58**, 16 (1998).
- [16] J. Pellicer-Porres, D. Martinez-Garcia, C. Ferrer-Roca, A. Segura, V. Muñoz-Sanjosé, J. P. Itié, A. Polian, and P. Munsch, *Phys. Rev. B* **71**, 035210 (2005).
- [17] S. E. Grillo, M. Ducarroir, M. Nadal, E. Tournié, and J.-P. Faurie, *J. Phys. D: Appl. Phys.* **35**, 3015 (2002).
- [18] D. Cáceres, I. Vergara, R. González, E. Monroy, F. Calle, E. Muñoz, and F. Omneès, *J. Appl. Phys.* **86**, 6773 (1999).
- [19] K. Hjort, F. Ericson, J.-Å. Schweitz, C. Hallin, and E. Janzén, *Thin Solid Films* **250**, 157 (1994).
- [20] E. L. Bourhis and G. Patriarche, *Philos. Mag. Lett.* **84**, 373 (2004).
- [21] M. Schenk and C. Silber, *J. Mater. Sci.: Mater. Electron.* **9**, 313 (1998).
- [22] D. Y. Watts and A. F. W. Willoughby, *J. Mater. Sci.* **23**, 272 (1988).
- [23] L. Garrato and A. Rucci, *Philos. Mag.* **35**, 1681 (1977).
- [24] A. Waag, F. Fischer, H.-J. Lugauer, T. Litz, T. Gerhard, J. Nürnberger, U. Lunz, U. Zehnder, W. Ossau, G. Landwehr, B. Roos, and H. Richter, *Mater. Sci. Eng. B* **43**, 65 (1997).

- [25] W. Paszkowicz, K. Godwod, J. Domagała, F. Firszt, J. Szatkowski, H. Męczyńska, S. Łęgowski, and M. Marczak, *Solid State Commun.* **107**, 735 (1998).
- [26] S. E. Grillo, M. Ducarroir, M. Nadal, E. Tournié, and J.-P. Faurie, *J. Phys. D: Appl. Phys.* **35**, 3015 (2002).
- [27] K. Maruyama, K. Suto, and J. Nishizawa, *Jpn. J. Appl. Phys.* **39**, 5180 (2000).
- [28] S. Fang, L. J. Farthing, M.-F. S. Tang, and D. A. Stevenson, *J. Vac. Sci. Technol. A* **8**, 1120 (1990).
- [29] M. Schenk and L. T. H. Dunog, *Semicond. Sci. Technol.* **13**, 335 (1998).
- [30] J. F. Barbot, G. Rivaud, H. Garem, C. Blanchard, J. C. Desoyer, D. Le-Scoul, J. L. Dessus, and A. Durand, *J. Mater. Sci.* **25**, 1877 (1990).
- [31] S. Koubaiti, C. Levade, J. J. Couderc, and G. Vanderschaeve, *Eur. Phys. J. Appl. Phys.* **1**, 141 (1998).
- [32] K. Balakrishnan, J. Kumar, and P. Ramasamy, *J. Mater. Sci. Lett.* **14**, 720 (1995).
- [33] C. Deger, E. Born, H. Angerer, O. Ambacher, M. Stutzmann, J. Hornsteiner, E. Riha, and G. Fischerauer, *Appl. Phys. Lett.* **72**, 2400 (1998).

4 Lattice Dynamic Properties

4.1 PHONON DISPERSION RELATIONSHIPS

Theoretical work on the lattice dynamics of semiconductor alloys has been carried out by several authors. For example, Myles [1] evaluated the spectral density of phonon states for 1D mass-disordered alloys using a generalized embedded-cluster method. Baroni *et al.* [2] studied the lattice vibronic properties of $\text{Al}_x\text{Ga}_{1-x}\text{As}$ using large supercells to simulate the disorder and *ab initio* interatomic force constants. They found that there are well-defined AlAs- and GaAs-like phonon dispersions for any concentration, in agreement with experimental evidence [3]. In addition to broadening phonon states with definite wavevectors, alloying also narrows the optical phonon branches and lowers the longitudinal modes more than the transverse modes, thus reducing the LO–TO splitting. The acoustic phonon bands are in contrast also found to be rather insensitive to the alloy composition.

4.2 PHONON FREQUENCY

4.2.1 General Considerations

Lattice vibronic properties in semiconductor alloys have received a great deal of attention over a long period of time [4]. The defect-induced local or gap modes for small concentrations of impurities are broadened into vibrational bands for high impurity concentrations as in solid solutions. In an $\text{A}_x\text{B}_{1-x}\text{C}$ alloy, such vibrational bands exhibit either ‘one-mode’ or ‘two-mode’ behavior (or more rigorously, three different types of mode behavior, namely, ‘one-’, ‘two-’ and ‘one-two-mode (mixed-mode)’ behaviors; see Figure 4.1). In a one-mode system (Figure 4.1(a)), such as most I–VII alloys, a single set of long-wavelength optical phonons appear. The one-mode phonon spectrum is approximately constant in strength but varies in energy as the alloy composition is varied from one end member to another. The two-mode system (Figure 4.1(b)), which is common for III–V ternaries, exhibits two distinct sets of optical modes with frequencies characteristic of each end member and strengths roughly proportional to the respective concentration. The one-two-mode system exhibits a single mode over only a part of the composition range, with two modes observed over the remaining range of composition (Figures 4.1(c) and 4.1(d)).

A number of models have been proposed to explain the so-called multi-mode behavior in solid solutions [5]. Of these different models, the MREI model of Chang and Mitra [5,6] appears to be the most successful. In the MREI model, if an alloy $\text{A}_x\text{B}_{1-x}\text{C}$ has the relationship

$$M_A < \mu_{BC} \quad (4.1)$$

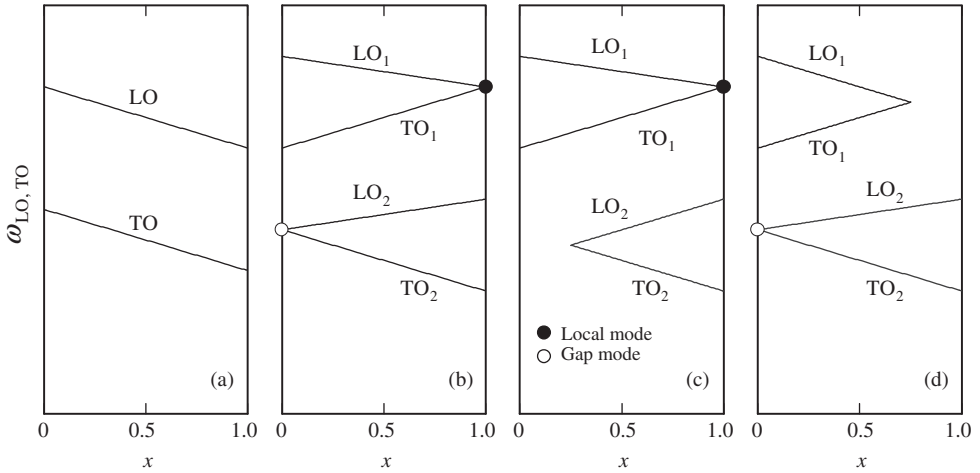


Figure 4.1 Four different types of long-wavelength phonon mode behavior in ternary alloy: (a) one-mode; (b) two-mode; (c) one-two-mode (1); (d) one-two-mode (2)

it exhibits two-mode behavior. Here, $\mu_{BC}^{-1} = M_B^{-1} + M_C^{-1}$ is the reduced mass of the binary material BC. The opposite is true for one-mode behavior. In other words, for an alloy to exhibit two-mode (one-mode) behavior it must (must not) have one substituting element whose mass is smaller than the reduced mass of the compound formed by the other two elements. Given the masses of the end members, the MREI model can predict whether an alloy will show one- or two-mode behavior and also the dependence of the optical phonon frequencies on x [5, 6].

Table 4.1 summarizes the long-wavelength optical phonon frequencies, $\hbar\omega_{LO}$ and $\hbar\omega_{TO}$, for a number of cubic group-IV, III-V and II-VI semiconductors at 300 K and Table 4.2 lists those for some hexagonal III-V and II-VI semiconductors at 300 K.

In an ordered alloy $\text{Ga}_{0.5}\text{In}_{0.5}\text{P}$, four additional phonon modes at 60, 205, 310 and 354 cm^{-1} , attributed to spontaneous ordering in this material, have been identified and explained using various experimental techniques [7]. However, a major obstacle to further enhancing the understanding of this subject is the lack of a theoretical model that can satisfactorily explain the experimental optical phonon frequencies and selection rules in ordered alloys. In the following, the data mainly refers to fully disordered semiconductor alloys.

4.2.2 Room-temperature Value

(a) Group-IV semiconductor alloy

The experimental long-wavelength optical phonon frequencies ω_{LO} and ω_{TO} for 3C-SiC, together with those for diamond and Si, are shown in Figure 4.2. 3C-SiC is considered to be an ordered alloy, or more succinctly, it is a compound, not an alloy. Note that for diamond-type structures the LO and TO branches are degenerate at $\mathbf{q} = 0$ and thus $\omega_{LO} = \omega_{TO}$. The solid line in Figure 4.2 shows the linear interpolation result between Si ($x = 0$) and diamond ($x = 1.0$). The 3C-SiC values can be satisfactorily interpreted by the average values of Si and diamond.

$\text{Si}_x\text{Ge}_{1-x}$ has three types of cell and consequently shows multi-mode behavior consisting of three main peaks due to the vibrations of Si-Si, Ge-Ge and Si-Ge pairs (Table 4.3). The composition dependence of the Si-Si, Si-Ge and Ge-Ge mode frequencies for $\text{Si}_x\text{Ge}_{1-x}$

Table 4.1 Long-wavelength optical phonon frequencies, $\hbar \omega_{\text{LO}}$ and $\hbar \omega_{\text{TO}}$, for some cubic group-IV, III–V and II–VI semiconductors at 300 K. d = diamond; zb = zinc-blende; rs = rocksalt

System	Material	$\hbar \omega_{\text{LO}}$ (cm ⁻¹)	$\hbar \omega_{\text{TO}}$ (cm ⁻¹)
IV	Diamond (d)	1332	1332
	Si (d)	519.2	519.2
	Ge (d)	301	301
	Sn (d)	200	200
	3C-SiC (zb)	972	796
III–V	BN (zb)	1305	1054.7
	BP (zb)	828.9	799
	AlN (zb)	902	655
	AlP (zb)	501.0	439.4
	AlAs (zb)	402	362
	AlSb (zb)	340.0	318.7
	GaN (zb)	739	553
	GaP (zb)	402.5	365.3
	GaAs (zb)	292	268
	GaSb (zb)	233	224
	InN (zb)	586	455
	InP (zb)	346.4	304.5
	InAs (zb)	241.4	219.6
	InSb (zb)	190.7	179.7
II–VI	BeSe (zb)	576	496
	BeTe (zb)	502	461
	MgO (rs)	725	401
	MgS (zb)	425	327
	MgSe (zb)	340	237
	MgTe (zb)	292	235
	ZnS (zb)	350.5	272.0
	ZnSe (zb)	252	205
	ZnTe (zb)	210	181
	CdO (rs)	478	262
	CdS (zb)	303 ^a	237 ^a
	CdSe (zb)	211 ^a	169 ^a
	CdTe (zb)	167	139
	HgS (zb)	224	177
	HgSe (zb)	174	132
	HgTe (zb)	135	116

^aCalculated or estimated

is shown in Figure 4.3(a). The experimental data were obtained from Pezzoli *et al.* [8]. The homopolar-bond frequencies vary almost linearly with x , while the heteropolar-bond frequency shows a maximum at $x \sim 0.5$. These can be written as (in cm⁻¹)

$$\omega_{\text{Si-Si}}(x) = 521 - 67x \quad (4.2a)$$

Table 4.2 Long-wavelength optical phonon frequencies for some hexagonal III–V and II–VI semiconductors at 300 K. h = hexagonal ($P6_3/mmc$ (D_{6h})); w = wurtzite

System	Material	Phonon frequency (cm^{-1})					
		E_2 low	A_1 (TO)	E_1 (TO)	E_2 high	A_1 (LO)	E_1 (LO)
III–V	BN (h)	49	770	1383	1367	778	1610
	AlN (w)	248	610	670	657	890	915
	GaN (w)	144	533	560	569	736	743
	InN (w)	87	457	490	475	588	582
II–VI	BeO (w)	340	680	724	684	1083	1098
	ZnO (w)	100	380	410	439	576	587
	ZnS (w)	65	270	273	281	350	350
	CdS (w)	41	233	239	255	301	304
	CdSe (w)	34	166	170		210	211

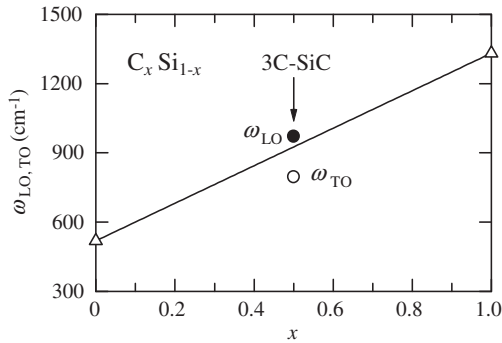


Figure 4.2 Long-wavelength optical phonon frequencies ω_{LO} and ω_{TO} for 3C-SiC at 300 K, together with those for diamond and Si. The solid line represents the linear interpolation result between the endpoint elemental data

Table 4.3 Long-wavelength optical phonon mode observed in some group-IV semiconductor alloys

Alloy	Phonon mode	Reference
SiGe	Si–Si, Ge–Ge, Si–Ge	<i>a</i>
CSiGe	Si–Si, Ge–Ge, C–Si, C–Ge (?), Si–Ge	<i>b</i>
SiGeSn	Si–Si, Ge–Ge, Si–Ge, Sn–Sn	<i>c</i>

^aF. Pezzoli *et al.*, *Mater. Sci. Eng. B* **124–125**, 127 (2005)

^bC ≤ 0.3 at% (M. Meléndez-Lira *et al.*, *Phys. Rev. B* **54**, 12866 (1996))

^cSi ≤ 20 at%, Sn ≤ 10 at% (V. R. D’Costa *et al.*, *Phys. Rev. B* **76**, 035211 (2007))

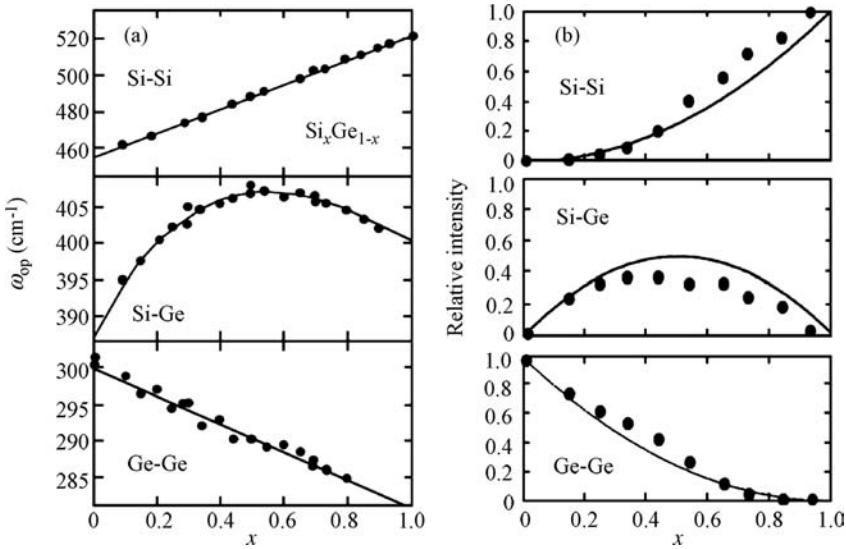


Figure 4.3 (a) Three main optical phonon frequencies due to the vibrations of Si–Si, Si–Ge and Ge–Ge pairs versus x for $\text{Si}_x\text{Ge}_{1-x}$ at 300 K. (b) Relative Raman intensities against x for $\text{Si}_x\text{Ge}_{1-x}$ at 300 K. [Reprinted with permission from *Mater. Sci. Eng. B*, Raman spectroscopy of $\text{Si}_{1-x}\text{Ge}_x$ epilayers by F. Pezzoli *et al.*, **124–125**, 127. Copyright (2005), Elsevier]

$$\omega_{\text{Ge-Ge}}(x) = 280 + 19x \quad (4.2b)$$

for the homopolar-bond modes and

$$\omega_{\text{Si-Ge}}(x) = 400 + 24.5x - 4.5x^2 - 33.5x^3 \quad (4.3)$$

for the heteropolar-bond mode.

The corresponding Raman intensities are plotted in Figure 4.3(b). The probability of finding Si–Si, Si–Ge and Ge–Ge vibrating pairs is proportional to the relative numbers of the bond types: x^2 , $2x(1-x)$ and $(1-x)^2$, respectively. The experimental data in Figure 4.3(b) follow this statistic very well.

The ordering effect and/or compositional fluctuation should influence the vibronic properties of alloys, and in particular, the relative intensities and linewidths of the Raman modes. Tsang *et al.* [9] measured the Raman spectra of compositionally ordered $\text{Si}_{0.5}\text{Ge}_{0.5}$ layers and compared them to the spectrum of a random alloy. They observed changes in the relative intensities of the different optical phonons, suggesting that the ordering is associated with an increase in the number of homopolar bonds and a decrease in the number of heteropolar bonds. The Raman scattering data also suggested that the ordering is not complete; the changes in the Raman intensities are quantitatively consistent with XRD-estimated ordering of $\sim 80\%$.

The effects of substitutional carbon in $\text{Si}_x\text{Ge}_{1-x}$ have been studied by several authors [10–12]. Because of the significant difference in covalent bond radii between Si and C atoms, the C defect in the Si lattice is surrounded by a considerable strain field, with substitutional defect bonds under tensile strain and interstitial bonds under compressive strain. A substitutional C defect in $\text{Si}_x\text{Ge}_{1-x}$ is expected to be surrounded by an even stronger strain field than

that in pure Si, due to the increase in the C bond lengths with the Ge atoms. Interstitial C defects will be under smaller compressive strain due to the increase in the average lattice constant with Ge. The experimental frequencies of the Si–Si, Ge–Ge and Si–Ge modes in $\text{Si}_x\text{Ge}_{1-x}$ increased as a function of C concentration, which can be explained qualitatively in terms of the large bond distortions caused by the lattice mismatch between $\text{Si}_x\text{Ge}_{1-x}$ and diamond [10]. A number of phonon modes associated with the substitutional C defects in $\text{Si}_x\text{Ge}_{1-x}$ have been detected and attributed to localized phonon modes of C defects with different nearest-neighbor configurations of Si and Ge atoms (Table 4.3).

(b) III–V semiconductor alloy

Most III–V ternaries exhibit two-mode behavior. Some III–V ternaries exhibit one- or one-two-mode behavior. These are summarized in Table 4.4. The long-wavelength optical phonon

Table 4.4 Behavior of the long-wavelength optical phonon modes in some III–V semiconductor alloys. zb = zinc-blende; w = wurtzite; O = one mode; T = two mode; O-T = one-two mode; Tr-F = three-four mode; Tr = three mode; F = four mode; T-Tr = two-three mode

Alloy	Material	Behavior	Reference
Ternary	AlGaN (zb)	O (LO), T (TO)	<i>a</i>
	AlGaN (w)	T ($E_1(\text{TO})$), O (others)	<i>b</i>
		O ($A_1(\text{LO}), E_1(\text{LO})$), T (others)	<i>c</i>
		O	<i>d</i>
		O ($E_1(\text{TO})$)	<i>e</i>
	AlInN (w)	O ($E_1(\text{TO})$)	<i>e</i>
	AlGaP (zb)	T	<i>f</i>
	AlGaAs (zb)	T	<i>g</i>
	AlGaSb (zb)	T	<i>h</i>
	AlInP (zb)	T	<i>i</i>
	AlInAs (zb)	T	<i>j</i>
	AlInSb (zb)	T	<i>k</i>
	GaInN (zb)	O	<i>l</i>
	GaInN (w)	O	<i>m</i>
	GaInP (zb)	T	<i>n</i>
	GaInAs (zb)	T	<i>o</i>
	GaInSb (zb)	O-T	<i>p</i>
	AlAsSb (zb)	O	<i>q</i>
	GaNP (zb)	T	<i>r</i>
	GaNAs (zb)	T	<i>s</i>
	GaPAs (zb)	T	<i>t</i>
	GaPSb (zb)	T	<i>u</i>
	GaAsSb (zb)	T	<i>v</i>
	InPAs (zb)	T	<i>w</i>
	InPSb (zb)	T	<i>x</i>
	InAsSb (zb)	O-T	<i>y</i>
Quaternary	AlGaPAs (zb)	Tr-F	<i>z</i>
	AlGaAsSb (zb)	Tr	<i>aa</i>
	GaInPSb (zb)	F	<i>ab</i>

Table 4.4 (Continued)

Alloy	Material	Behavior	Reference
	GaInPAs/InP (zb)	F	ac
	GaInPAs/GaAs (zb)	F	ad
	GaInAsSb (zb)	Tr	ae
	AlGaInP/GaAs (zb)	T-Tr	af
	AlGaInAs/InP (zb)	Tr	ag
	InPAsSb (zb)	Tr	ah

^aH. Harima *et al.*, *Appl. Phys. Lett.* **74**, 191 (1999)^bM. Kazan *et al.*, *J. Appl. Phys.*, **100**, 013508 (2006)^cV. Y. Davydov *et al.*, *Phys. Rev. B* **65**, 125203 (2002)^dM. S. Liu *et al.*, *J. Appl. Phys.* **90**, 1761 (2001)^eA. Kasic *et al.*, *Appl. Phys. Lett.* **78**, 1526 (2001)^fG. Armelles *et al.*, *Solid State Commun.* **65**, 779 (1988)^gD. J. Lockwood and Z. R. Wasilewski, *Phys. Rev. B* **70**, 155202 (2004)^hR. Ferrini *et al.*, *Phys. Rev. B* **56**, 7549 (1997)ⁱH. Asahi *et al.*, *J. Appl. Phys.* **65**, 5007 (1989)^jS. Emura *et al.*, *J. Appl. Phys.* **62**, 4632 (1987)^kV. P. Gnezdilov *et al.*, *J. Appl. Phys.* **74**, 6883 (1993)^lK. Torii *et al.*, *Appl. Phys. Lett.* **82**, 52 (2003)^mS. Hernández *et al.*, *J. Appl. Phys.* **98**, 013511 (2005)ⁿB. Jusserand and S. Slempek, *Solid State Commun.* **49**, 95 (1984)^oZ. S. Piao *et al.*, *Phys. Rev. B* **50**, 18644 (1994)^pZ. C. Feng *et al.*, *Can. J. Phys.* **69**, 386 (1991)^qH. C. Lin *et al.*, *Solid State Commun.* **107**, 547 (1998)^rG. Leibiger *et al.*, *Appl. Phys. Lett.* **79**, 3407 (2001)^sT. Prokofyeva *et al.*, *Appl. Phys. Lett.* **73**, 1409 (1998)^tG. Armelles *et al.*, *Appl. Phys. Lett.* **68**, 1805 (1996)^uY. T. Cherng *et al.*, *J. Appl. Phys.* **65**, 3285 (1989)^vT. C. McGlinn *et al.*, *Phys. Rev. B* **33**, 8396 (1986)^wD. J. Lockwood *et al.*, *J. Appl. Phys.* **102**, 033512 (2007)^xM. J. Jou *et al.*, *J. Appl. Phys.* **64**, 1472 (1988)^yN. L. Rowell *et al.*, *J. Vac. Sci. Technol. A* **22**, 935 (2004)^zP. N. Sen and G. Lucovsky, *Phys. Rev. B* **12**, 2998 (1975)^{aa}D. H. Jaw *et al.*, *J. Appl. Phys.* **69**, 2552 (1991)^{ab}D. H. Jaw and G. B. Stringfellow, *J. Appl. Phys.* **72**, 4265 (1992)^{ac}T. Sugiura *et al.*, *Jpn. J. Appl. Phys.* **37**, 544 (1998)^{ad}T. Sugiura *et al.*, *Jpn. J. Appl. Phys.* **32**, 2718 (1993)^{ae}D. H. Jaw *et al.*, *J. Appl. Phys.* **66**, 1965 (1989)^{af}T. Hofmann *et al.*, *Phys. Rev. B* **64**, 155206 (2001)^{ag}R. Manor *et al.*, *Phys. Rev. B* **56**, 3567 (1997)^{ah}L.-C. Chen *et al.*, *Jpn. J. Appl. Phys.* **37**, L1365 (1998)

frequencies ω_{LO} and ω_{TO} versus x for (a) $c\text{-Al}_x\text{Ga}_{1-x}\text{N}$ and (b) $c\text{-Ga}_x\text{In}_{1-x}\text{N}$ are shown in Figure 4.4. The experimental data for $c\text{-Al}_x\text{Ga}_{1-x}\text{N}$ are taken from Harima *et al.* [13] and for $c\text{-Ga}_x\text{In}_{1-x}\text{N}$ from Tabata *et al.* [14] and Torii *et al.* [15].

The LO phonon frequencies in Figure 4.4(a) exhibit one-mode behavior, while the two-mode behavior is observed for the TO phonon frequencies. The mass criterion of Equation (4.1) suggests that $\text{Al}_x\text{Ga}_{1-x}\text{N}$ may exhibit one-mode behavior ($M_{\text{Al,Ga}} > \mu_{\text{AlN,GaN}}$). Harima

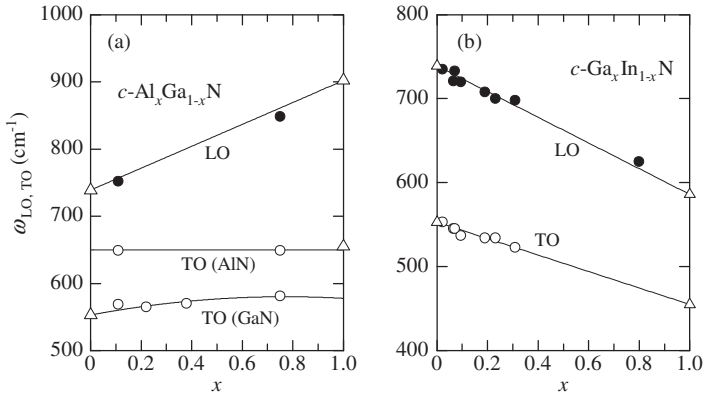


Figure 4.4 Long-wavelength optical phonon frequencies ω_{LO} and ω_{TO} versus x for (a) $c\text{-Al}_x\text{Ga}_{1-x}\text{N}$ and (b) $c\text{-Ga}_x\text{In}_{1-x}\text{N}$ at 300 K. The experimental data for $c\text{-Al}_x\text{Ga}_{1-x}\text{N}$ are taken from Harima *et al.* [13] and for $c\text{-Ga}_x\text{In}_{1-x}\text{N}$ from Tabata *et al.* [14] and Torii *et al.* [15]. The solid line in (a) shows the linear interpolation result between the endpoint binary data (LO). The solid lines in (b) represent the linear interpolation results of Equation (4.4)

et al. [13] calculated the phonon frequencies using the MREI model and considered that the two-mode behavior of ω_{TO} is a consequence of the different vibrating masses.

In Figure 4.4(b), clear one-mode phonon behavior of $c\text{-Ga}_x\text{In}_{1-x}\text{N}$ can be seen, in agreement with the criterion of Equation (4.1) ($M_{\text{Ga,In}} > \mu_{\text{GaN,InN}}$). The solid lines represent the linear interpolation results (in cm^{-1})

$$\omega_{\text{LO}}(x) = 739 - 153x \quad (4.4a)$$

$$\omega_{\text{TO}}(x) = 553 - 98x \quad (4.4b)$$

Figure 4.5 shows the LO and TO phonon frequencies as a function of x for $\text{Al}_x\text{Ga}_{1-x}\text{As}$. The experimental data are taken from Jusserand [16]. Only the AlAs-like LO mode exhibits weak nonlinearity with respect to x . Each phonon frequency can be expressed as (in cm^{-1})

$$\omega_{\text{LO,AlAs}}(x) = 354 + 81x - 33x^2 \quad (4.5a)$$

$$\omega_{\text{TO,AlAs}}(x) = 354 + 8x \quad (4.5b)$$

$$\omega_{\text{LO,GaAs}}(x) = 292 - 37x \quad (4.6a)$$

$$\omega_{\text{TO,GaAs}}(x) = 268 - 13x \quad (4.6b)$$

The two-mode behavior in $\text{Al}_x\text{Ga}_{1-x}\text{As}$ is the most prominent disorder-induced effect ($M_{\text{Al}} < \mu_{\text{GaAs}}$). Additional disorder-induced effects in $\text{Al}_x\text{Ga}_{1-x}\text{As}$ have been observed, i.e. an asymmetric line broadening and an activation of new phonon bands [16]. A low energy GaAs-like LO tail developed when the concentration of Al increased, and vice versa. When this concentration becomes very large, an additional line appears on the lower energy side. Apart from this broadening, additional phonon bands are observed in the TA ($\sim 100 \text{ cm}^{-1}$) and LA

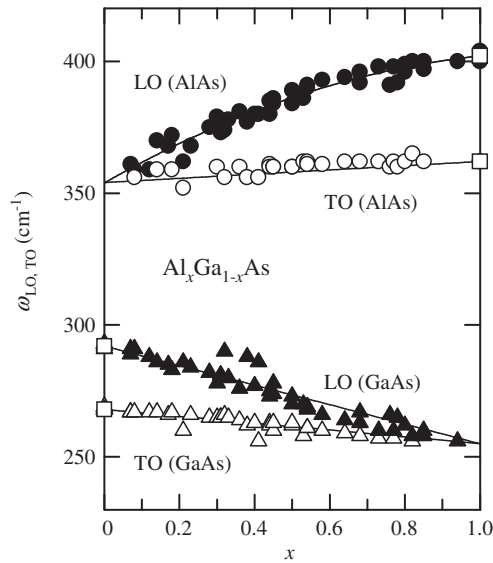


Figure 4.5 Long-wavelength optical phonon frequencies ω_{LO} and ω_{TO} versus x for $Al_xGa_{1-x}As$ at 300 K. The open squares represent the endpoint binary data. The solid lines show the results calculated using Equations (4.5) and (4.6)

range ($\sim 200 \text{ cm}^{-1}$). The asymmetric broadening and the emergence of additional phonon bands can be explained by a disorder activated relaxation of the $q = 0$ wavevector selection rule.

The LO and TO phonon frequencies for $Ga_xIn_{1-x}Sb$ determined by Raman scattering at 80 K by Feng *et al.* [17] are shown in Figure 4.6. They also reported the room-temperature data, which are essentially the same as those at 80 K. In Figure 4.6, the so-called one-two-mode behavior is observed; however, the mass criterion of Equation (4.1) indicates that the alloy will exhibit one-mode behavior ($M_{Ga,In} > \mu_{GaSb,InSb}$). The one-two-mode behavior was also confirmed using IR spectroscopy [18].

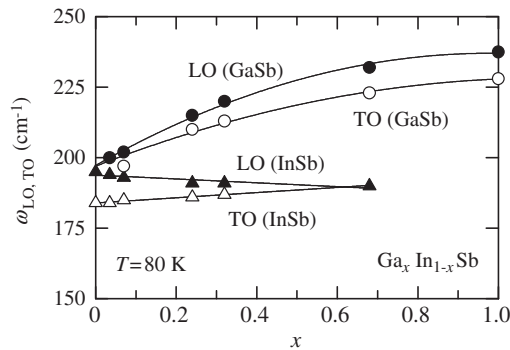


Figure 4.6 Long-wavelength optical phonon frequencies ω_{LO} and ω_{TO} versus x for $Ga_xIn_{1-x}Sb$ at 80 K. [Reproduced with permission from Z. C. Feng, S. Perkowitz, R. Rousina, and J. B. Webb, *Can. J. Phys.* **69**, 386–389 (1991), Copyright (1991) NRC Research Press]

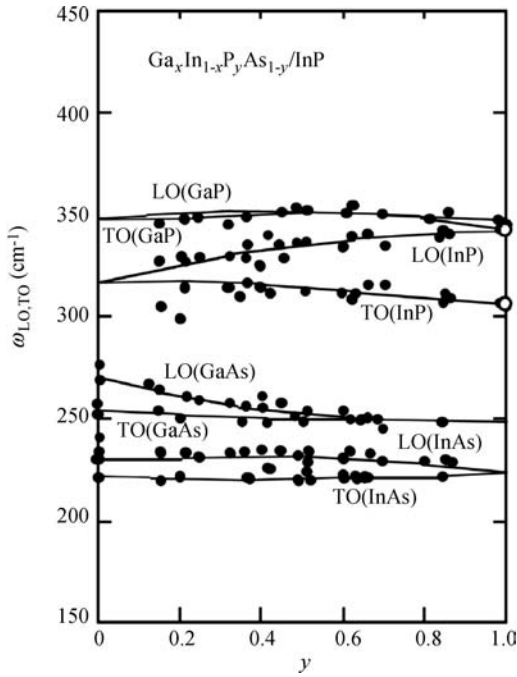


Figure 4.7 Long-wavelength optical phonon frequencies ω_{LO} and ω_{TO} versus y for $\text{Ga}_x\text{In}_{1-x}\text{P}_y\text{As}_{1-y}/\text{InP}$ at 300 K. [Reprinted with permission from *Jpn. J. Appl. Phys.*, Raman scattering study of InGaAsP quaternary alloys grown on InP in the immiscible region by T. Sugiura *et al.*, **37**, 544. Copyright (1998) Japanese Society of Pure and Applied Physics] The open circles represent the InP data

The long-wavelength optical phonon behaviors in $\text{Ga}_x\text{In}_{1-x}\text{P}_y\text{As}_{1-y}/\text{InP}$ have been studied by Raman and IR spectroscopy [19]. In Figure 4.7 the ω_{LO} and ω_{TO} frequencies versus y for $\text{Ga}_x\text{In}_{1-x}\text{P}_y\text{As}_{1-y}/\text{InP}$ are illustrated graphically. The experimental data are taken from Sugiura *et al.* [20]. The data fall into four separate bands, that is, a four-mode category, except for the GaAs mode at $y > 0.6$.

The composition dependence of ω_{LO} and ω_{TO} for $(\text{Al}_x\text{Ga}_{1-x})_{0.48}\text{In}_{0.52}\text{As}/\text{InP}$ is shown in Figure 4.8. The experimental data were obtained by Raman scattering [21]. Three modes, AlAs-, GaAs- and InAs-like modes, dominate the Raman spectra in $(\text{Al}_x\text{Ga}_{1-x})_{0.48}\text{In}_{0.52}\text{As}/\text{InP}$. The GaAs- and InAs-like modes vary almost linearly with x . The AlAs-like TO mode also varies linearly with x , but its LO branch exhibits weak nonlinearity with respect to x .

The one-mode behavior of $\text{AlAs}_x\text{Sb}_{1-x}$ and two-mode behavior of $\text{GaP}_x\text{As}_{1-x}$, $\text{GaP}_x\text{Sb}_{1-x}$ and $\text{InP}_x\text{As}_{1-x}$ in Table 4.4 agree with the mass criterion of Equation (4.1); however, the two-mode behavior observed in $\text{Ga}_x\text{In}_{1-x}\text{P}$ and $\text{GaAs}_x\text{Sb}_{1-x}$ is contrary to this criterion. Let us consider $\text{GaP}_x\text{As}_{1-x}$ and $\text{Ga}_x\text{In}_{1-x}\text{P}$, the former shows two-mode behavior, while the latter shows one-mode (or a very weak two-mode) behavior. These behaviors are easily understood by noting that the optical-phonon DOS of GaP and GaAs do not overlap unlike those of GaP and InP which do overlap (but in a narrow frequency range). Thus, the two-mode behavior of $\text{GaP}_x\text{As}_{1-x}$ is expected from Equation (4.1) ($M_P < \mu_{\text{GaAs}}$). Because $M_{\text{Ga}} > \mu_{\text{GaP,InP}}$ the MREI model predicts one-mode behavior in $\text{Ga}_x\text{In}_{1-x}\text{P}$.

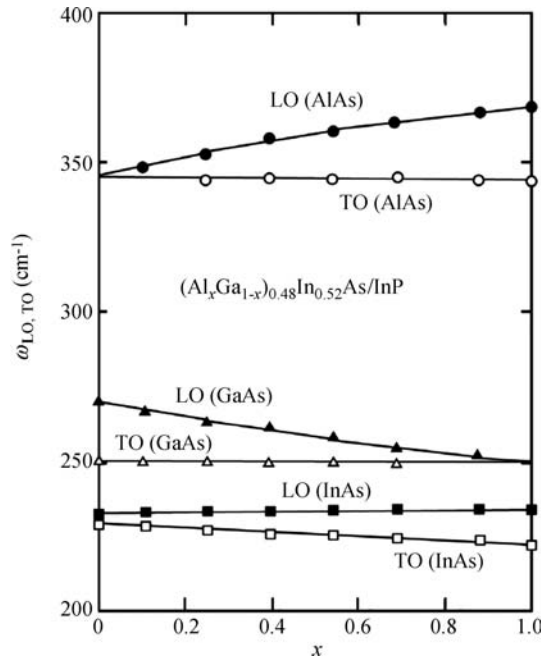


Figure 4.8 Long-wavelength optical phonon frequencies ω_{LO} and ω_{TO} versus x for $(Al_xGa_{1-x})_{0.48}In_{0.52}As/InP$ at 300 K. [Reproduced with permission from R. Manor, O. Brafman, and R. F. Kopf, *Phys. Rev. B* **56**, 3567–3570 (1997). Copyright (1997) American Physical Society]

(c) II–VI semiconductor alloy

II–VI ternaries grow either in the zinc-blende or wurtzite structure and mostly exhibit one- or two-mode behavior, as summarized in Table 4.5. Some II–VI ternaries exhibit a variation with composition that is intermediate between one- and two-mode.

Figure 4.9 shows the long-wavelength optical phonon frequencies ω_{LO} and ω_{TO} as a function of x for $Zn_xCd_{1-x}S$. The experimental data are taken from Lucovsky *et al.* [22]. Since $Zn_xCd_{1-x}S$ crystallizes in the wurtzite structure, the experimental data produced by Lucovsky *et al.* shows a small anisotropy splitting ($\sim 6\text{ cm}^{-1}$) between A_1 (LO, TO) and E_1 (LO, TO) modes for all values of x . For clarity, however, the averaged ω_{LO} and ω_{TO} values have been plotted in Figure 4.9. $Zn_xCd_{1-x}S$ serves a typical example of the one-mode phonon behavior.

Figure 4.10 shows the LO and TO phonon frequencies for $Cd_xHg_{1-x}Te$ measured by IR spectroscopy at 77 K [23]. Like $Zn_xHg_{1-x}Te$ [24], $Cd_xHg_{1-x}Te$ exhibits two-mode behavior. However, the ZnTe-like TO frequency in $Zn_xHg_{1-x}Te$ increased with increasing Zn content, while the CdTe-like TO phonon mode in $Cd_xHg_{1-x}Te$ (Figure 4.10) decreased with increasing Cd content. This could be due to the fact that the $Zn_xHg_{1-x}Te$ lattice constant decreases with increasing Zn content but the $Cd_xHg_{1-x}Te$ lattice constant increases with increasing Cd content. Note that the MREI model predicts $Zn_xHg_{1-x}Te$ to be of the two-mode type ($M_{Zn} < \mu_{HgTe}$) and $Cd_xHg_{1-x}Te$ to be of the one-mode type ($M_{Cd,Hg} > \mu_{CdTe,HgTe}$).

Both $Zn_xCd_{1-x}Se$ and $ZnSe_xTe_{1-x}$ exhibit an intermediate-mode behavior [25,26]. As an example, the data for $ZnSe_xTe_{1-x}$ is shown in Figure 4.11 [25]. Not only are the one-mode LO and TO phonons (LO_1 and TO_1) but also a new LO_2 – TO_2 pair inside the reststrahlen band.

Table 4.5 Behavior of the long-wavelength optical phonon modes in some II–VI semiconductor alloys. zb = zinc-blende; w = wurtzite; O = one mode; T = two mode; I = intermediate mode; Tr = three mode

Alloy	Material	Behavior	Reference
Ternary	BeZnSe	Tr	<i>a</i>
	BeZnTe	Tr	<i>b</i>
	MgZnO (zb)	T	<i>c</i>
	MgZnO (w)	O	<i>d</i>
	MgZnO (w)	T (E_1), O (A_1)	<i>e</i>
	MgZnS	O	<i>f</i>
	MgZnSe	T	<i>g</i>
	MgZnTe	T	<i>h</i>
	MgCdTe	T	<i>i</i>
	ZnCdS	O	<i>j</i>
	ZnCdSe	I	<i>k</i>
	ZnCdTe	T	<i>l</i>
	ZnHgTe	T	<i>m</i>
	CdHgTe	T	<i>n</i>
	ZnSSe	T	<i>o</i>
	ZnSTe	T	<i>p</i>
	ZnSeTe	I	<i>q</i>
	CdSSe	T	<i>o</i>
	CdSTe	T	<i>r</i>
	CdSeTe	T	<i>s</i>
Quaternary	MgZnSSe	Tr	<i>f</i>
	MgZnSeTe	T	<i>t</i>
	MgZnCdTe	Tr	<i>h</i>
	ZnCdHgTe	Tr	<i>u</i>
	CdSSeTe	Tr	<i>v</i>

^aShowing extra BeSe-like mode (O. Pagès *et al.*, *Phys. Rev. B* **70**, 155319 (2004))

^bShowing extra BeTe-like mode (O. Pagès *et al.*, *Appl. Phys. Lett.* **80**, 3081 (2002))

^cJ. Chen and W. Z. Shen, *Appl. Phys. Lett.* **83**, 2154 (2003)

^d $0 \leq x < 0.3$ (Z. P. Wei *et al.*, *Phys. Status Solidi C* **3**, 1168 (2006))

^e $x \sim 0.47-0.60$ (J. Chen and W. Z. Shen, *Appl. Phys. Lett.* **83**, 2154 (2003))

^fD. Wang *et al.*, *J. Appl. Phys.* **80**, 1248 (1996)

^gD. Huang *et al.*, *Appl. Phys. Lett.* **67**, 3611 (1995)

^hR. Vogelgesang *et al.*, *J. Raman Spectrosc.* **27**, 239 (1996)

ⁱE. Oh *et al.*, *Phys. Rev. B* **48**, 15040 (1993)

^jM. Ichimura *et al.*, *Phys. Rev. B* **46**, 4273 (1992)

^kR. G. Alonso *et al.*, *Phys. Rev. B* **40**, 3720 (1989)

^lD. N. Talwar *et al.*, *Phys. Rev. B* **48**, 17064 (1993)

^mM. P. Volz *et al.*, *Solid State Commun.* **75**, 943 (1990)

ⁿS. P. Kozyrev *et al.*, *Sov. Phys. Solid State* **34**, 1984 (1992)

^oI. F. Chang and S. S. Mitra, *Phys. Rev.* **172**, 924 (1968)

^pY.-M. Yu *et al.*, *J. Appl. Phys.* **95**, 4894 (2004)

^qT. R. Yang and C. C. Lu, *Physica B* **284-288**, 1187 (2000)

^rR. Pal *et al.*, *J. Phys. D: Appl. Phys.* **26**, 704 (1993)

^sZ. C. Feng *et al.*, *J. Cryst. Growth* **138**, 239 (1994)

^tH. Makino *et al.*, *J. Cryst. Growth* **214/215**, 359 (2000)

^uJ. Polit *et al.*, *Phys. Status Solidi B* **208**, 21 (1998)

^vV. M. Burlakov *et al.*, *Phys. Status Solidi B* **128**, 389 (1985)

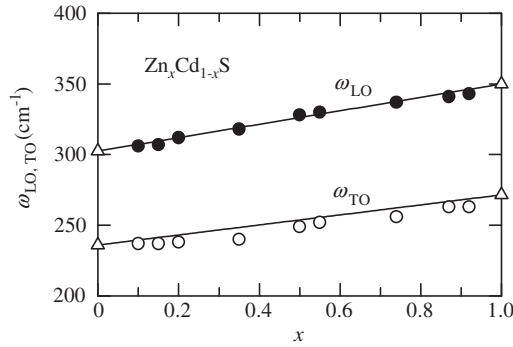


Figure 4.9 Long-wavelength optical phonon frequencies ω_{LO} and ω_{TO} versus x for $Zn_xCd_{1-x}S$ at 300 K. The experimental data are taken from Lucovsky *et al.* [22]. The solid lines show the linearly interpolated results between the endpoint binary data

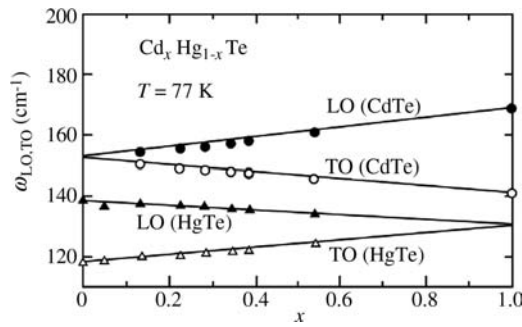


Figure 4.10 Long-wavelength optical phonon frequencies ω_{LO} and ω_{TO} versus x for $Cd_xHg_{1-x}Te$ at 77 K. [Reprinted with permission from J. Baars and F. Sorger, *Solid State Commun.* **10**, 875 (1972), Copyright (1972) Elsevier]

Pagès *et al.* [27, 28] investigated the Raman spectra of $Be_xZn_{1-x}Se$ and $Be_xZn_{1-x}Te$. The TO modes were of particular interest because they consist of quasi-independent oscillators and thereby carry clear information. In the LO symmetry, complexity arose due to coupling via the macroscopic polarization field. They observed the atypical TO one-bond \rightarrow two-mode behavior in the vibrational range of the stiff Be–VI bond in $Be_xZn_{1-x}Se$ and $Be_xZn_{1-x}Te$. This was explained by using a double-branch percolation picture which discriminates between vibrations within the randomly formed hard Be-rich host region and the soft Zn-rich region. The resulting phonon frequency versus composition plots showed that the (Be, Zn)–VI ternaries exhibit a three-mode (two usual modes plus one mode) behavior [27, 28].

The composition dependence of ω_{LO} and ω_{TO} for $Mg_xZn_{1-x}S_ySe_{1-y}/GaAs$ is shown in Figure 4.12. The experimental data were obtained by Raman scattering [29]. In brief, we can expect four-mode behavior (AB-, AC-, BC- and BD-like) in an $A_xB_{1-x}C_yD_{1-y}$ alloy. However, the data in Figure 4.12 reveal three-mode behavior (MgSe-, ZnSe- and MgZnS-like). Similarly,

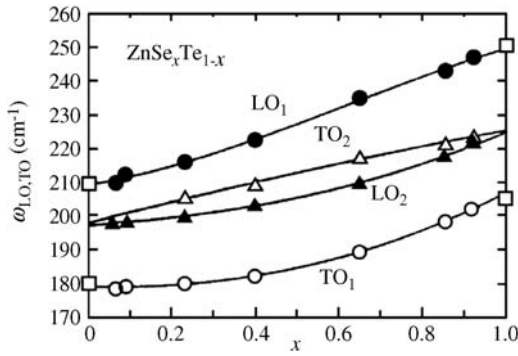


Figure 4.11 Long-wavelength optical phonon frequencies ω_{LO} and ω_{TO} versus x for $ZnSe_xTe_{1-x}$ at 300 K. [Reprinted with permission from *Physica B*, Infrared studies and optical characterization of $ZnSe_{1-x}Te_x$ molecular beam epitaxial films by T. R. Yang and C. C. Lu, **284–288**, 1187. Copyright (2000), Elsevier] The open circles represent the InP data

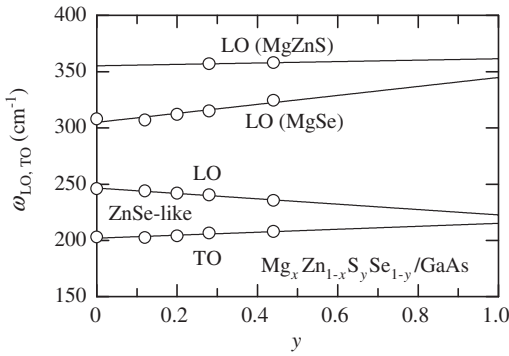


Figure 4.12 Long-wavelength optical phonon frequencies ω_{LO} and ω_{TO} versus y (S) for $Mg_xZn_{1-x}S_ySe_{1-y}/GaAs$ at 300 K. [Reprinted with permission from D. Wang *et al.*, *J. Appl. Phys.* **80**, 1248 (1996). Copyright (1996), American Institute of Physics]

$Mg_xZn_{1-x}S_yTe_{1-y}$ showed two-mode behavior (MgSeTe- and ZnSeTe-like), not four-mode behavior [30]. As expected, both $Zn_xCd_{1-x}Hg_{1-x-y}Te$ and $CdS_xSe_{1-x}Te_{1-x-y}$ exhibited three-mode behavior (Table 4.5).

4.2.3 External Perturbation Effect

(a) Group-IV semiconductor alloy

The phonon frequency is dependent both on temperature T and pressure p . The long-wavelength optical phonon frequency ω_{op} versus T can be expressed as [31]

$$\omega_{op}(T) = \omega_{op}(0) - \frac{\alpha T^2}{T + \beta} \tag{4.7}$$

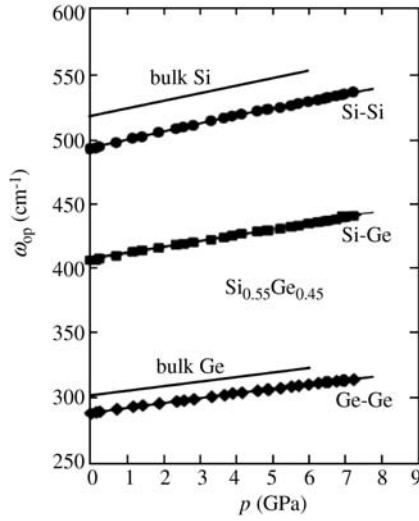


Figure 4.13 Hydrostatic-pressure dependence of the optical phonon frequency ω_{op} for $\text{Si}_{0.55}\text{Ge}_{0.45}$ at 300 K. The experimental data are taken from Sui *et al.* [32]. The bulk Si and Ge data are taken from Adachi [33]

where $\omega_{op}(0)$ is the $T=0$ K value, α is in cm^{-1} per degree Kelvin and β is a quantity proportional to the Debye temperature (in Kelvins). No detailed data on the temperature dependence of $\omega_{op} = \omega_{LO,TO}$ in group-IV semiconductor alloys has been reported.

The pressure dependence of ω_{op} in $\text{Si}_{0.55}\text{Ge}_{0.45}$ determined by Raman scattering is shown in Figure 4.13. The experimental data are taken from Sui *et al.* [32]. The pressure coefficients $d\omega/dp$ obtained from these plots are ~ 7 , ~ 5 and ~ 4 $\text{cm}^{-1}/\text{GPa}$ for the Si–Si, Si–Ge and Ge–Ge modes, respectively. The solid lines in Figure 4.13 show the bulk Si and Ge data [33].

(b) III–V semiconductor alloy

Figure 4.14 (a) shows the ω_{LO} versus T plots for the GaAs-like mode in $\text{Al}_x\text{Ga}_{1-x}\text{As}$. The experimental data are taken from Jiménez *et al.* [34]. The temperature variations are almost linear in the range between 300 and 650 K. The corresponding coefficient $d\omega_{LO}/dT$ for $\text{Al}_x\text{Ga}_{1-x}\text{As}$ is plotted in Figure 4.14 (b) [34]. The GaAs ($x=0$) and AlAs ($x=1.0$) data are also shown by the solid and open triangles, respectively [35]. It can be seen that the temperature coefficients are almost composition independent ($d\omega_{LO}/dT \sim 2 \times 10^{-2} \text{ cm}^{-1}/\text{K}$).

The pressure dependence of the LO phonon frequencies in $\text{Al}_{0.58}\text{Ga}_{0.42}\text{As}$ is shown in Figure 4.15. The LO phonon frequencies were measured by Raman scattering up to 7 GPa [36]. The pressure coefficients for the LO and TO modes in AlAs and GaAs were reported to be ~ 5 (AlAs) and ~ 4 $\text{cm}^{-1}/\text{GPa}$ (GaAs), respectively [36]. The slopes for the experimental $\text{Al}_{0.58}\text{Ga}_{0.42}\text{As}$ data in Figure 4.15 are nearly the same as those for AlAs and GaAs.

The pressure coefficients $d\omega_{LO,TO}/dp$ for the AlAs- and GaAs-like LO and TO modes for $\text{Al}_x\text{Ga}_{1-x}\text{As}$ are plotted as a function of x in Figure 4.16. The experimental data are taken from Holtz *et al.* [36]. Although the experimental data largely scatter, we can see that they fall in the range 5.3 ± 1.3 $\text{cm}^{-1}/\text{GPa}$, as shown by the vertical bar.

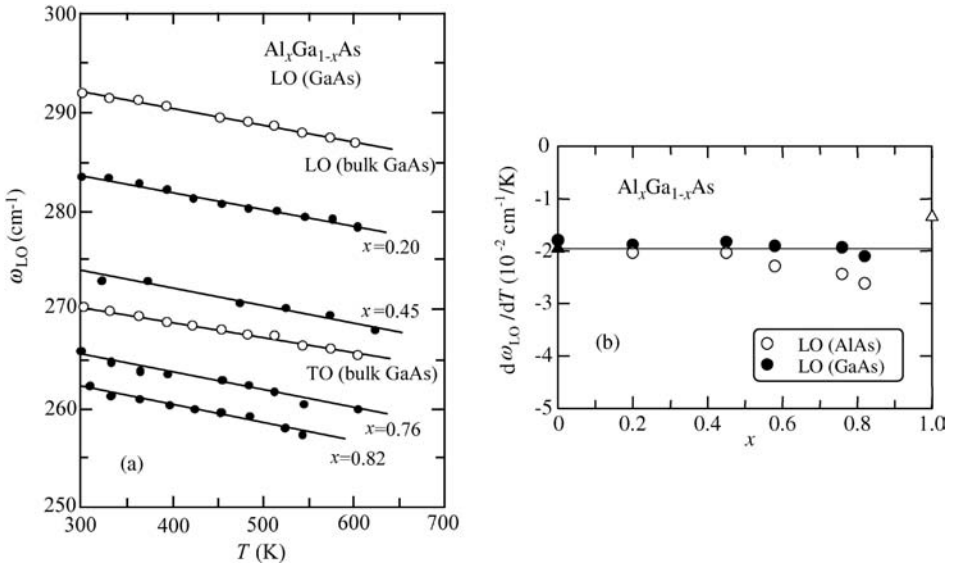


Figure 4.14 (a) Temperature dependence of the GaAs-like LO phonon frequency ω_{LO} for $Al_xGa_{1-x}As$. The data for bulk GaAs are also shown. [From J. Jiménez, E. Martín, A. Torres, and J. P. Landesman, *Phys. Rev. B* **58**, 10463–10469 (1998). Copyright (1998) American Physical Society.] (b) Temperature coefficient $d\omega_{LO}/dT$ versus x for $Al_xGa_{1-x}As$ at 300 K. The experimental data are taken from Jiménez *et al.* [34]. The solid and open triangles represent the endpoint binary data taken from Adachi [35]

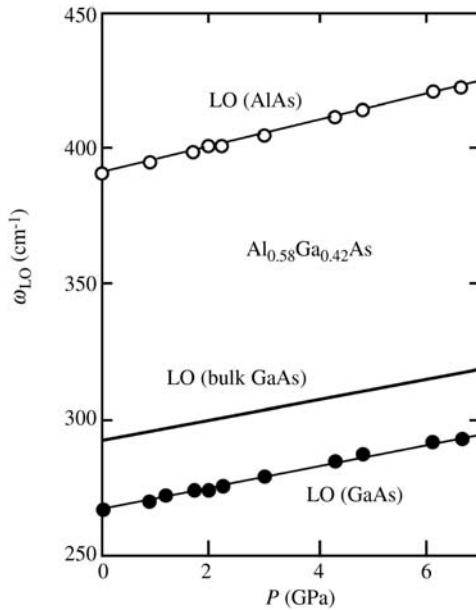


Figure 4.15 Hydrostatic-pressure dependence of the AlAs- and GaAs-like LO phonon frequencies for $Al_{0.58}Ga_{0.42}As$ at 300 K. The experimental data are taken from Holtz *et al.* [36]. The bulk GaAs data are also taken from Adachi [35]

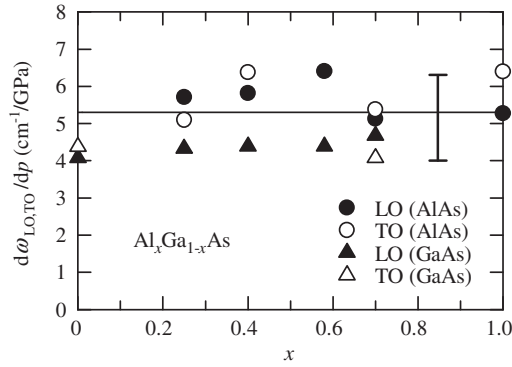


Figure 4.16 Pressure coefficients $d\omega_{\text{LO,TO}}/dT$ for the AlAs- and GaAs-like LO and TO modes in $\text{Al}_x\text{Ga}_{1-x}\text{As}$ at 300 K. The experimental data are taken from Holtz *et al.* [36]. The vertical bar indicates the range of the pressure-coefficient $5.3 \pm 1.3 \text{ cm}^{-1}/\text{GPa}$

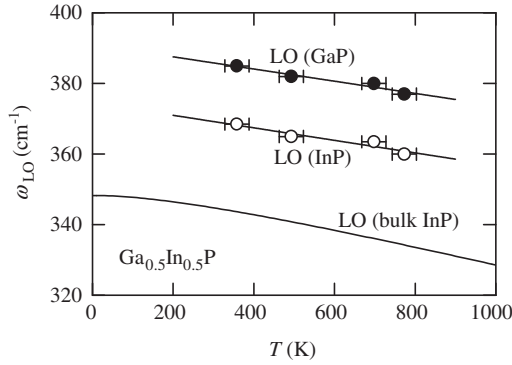


Figure 4.17 GaP- and InP-like LO phonon frequencies versus temperature T for $\text{Ga}_{0.5}\text{In}_{0.5}\text{P}$. The experimental data are taken from Shealy and Wicks [37]. The bulk InP data are also taken from Adachi [35]

The GaP- and InP-like LO phonon frequencies versus temperature T for $\text{Ga}_{0.5}\text{In}_{0.5}\text{P}$ are plotted in Figure 4.17. The experimental data were measured by Raman spectroscopy [37]. The bulk InP $\omega_{\text{LO}}(T)$ values which were calculated from Equation (4.7) with $\omega_{\text{LO}}(0) = 348.3 \text{ cm}^{-1}$, $\alpha = 2.8 \times 10^{-2} \text{ cm}^{-1}/\text{K}$ and $\beta = 420 \text{ K}$ are also shown [35]. The temperature variation in $\text{Ga}_x\text{In}_{1-x}\text{P}$ is found to be nearly the same as that in InP.

The pressure dependence of the GaP- and GaAs-like LO and TO data for $\text{GaP}_{0.11}\text{As}_{0.89}$ is shown in Figure 4.18. The experimental data are taken from Galtier *et al.* [38]. The solid lines represent the bulk LO and TO values versus p for GaP and GaAs taken from Adachi [35]. The $\text{GaP}_{0.11}\text{As}_{0.89}$ data are found to be very similar to those for GaP.

(c) II–VI semiconductor alloy

The temperature variations of the LO and TO phonon frequencies ω_{LO} and ω_{TO} for $c\text{-Zn}_x\text{Cd}_{1-x}\text{Se}$ are shown in Figure 4.19. The experimental data are taken from Valakh *et al.* [39]. The LO phonons in $c\text{-Zn}_x\text{Cd}_{1-x}\text{Se}$ exhibit one-mode behavior, while the

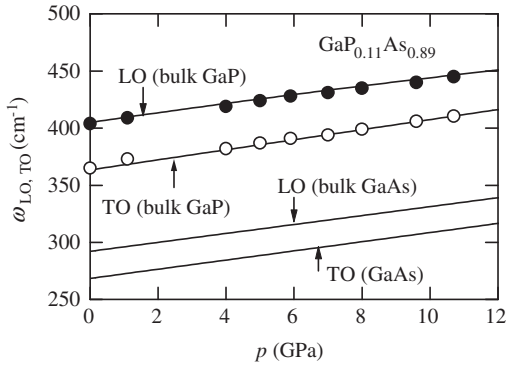


Figure 4.18 Hydrostatic-pressure dependence of the GaP-like LO (solid circles) and TO phonon frequencies (open circles) in $\text{GaP}_{0.11}\text{As}_{0.89}$ at 85 K. The experimental data are taken from Galtier *et al.* [38]. The solid lines represent the bulk GaP and GaAs data taken from Adachi [35]

TO phonon branch is much more complicated. The resulting optical phonon behavior in $c\text{-Zn}_x\text{Cd}_{1-x}\text{Se}$ is of the intermediate type, neither one-mode nor two-mode behavior.

The experimental ω_{LO} versus T behavior in Figure 4.19 can be found in many A^NB^{8-N} tetrahedral semiconductors. On the other hand, the effect of resonant interaction of the one-phonon (TO) and two-phonon (2TA) states in $c\text{-Zn}_x\text{Cd}_{1-x}\text{Se}$ [39] leads not only to the peculiar temperature dependence of intensity and line-shape of the bands, but also to the temperature

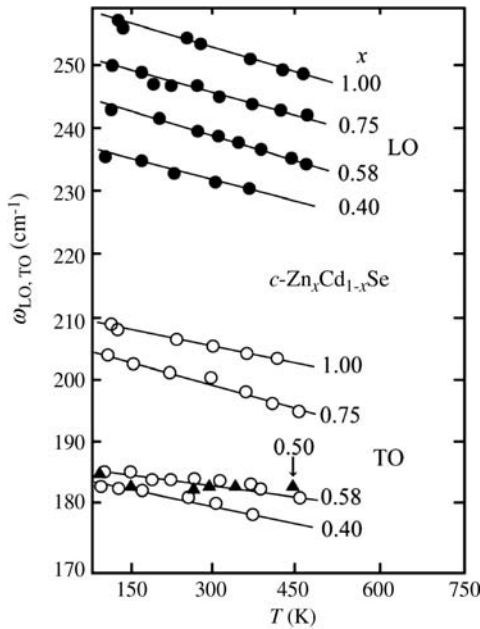


Figure 4.19 Temperature dependence of the LO and TO phonon frequencies ω_{LO} and ω_{TO} in $c\text{-Zn}_x\text{Cd}_{1-x}\text{Se}$. [Reprinted with permission from M. Y. Valakh *et al.*, *Phys. Status Solidi B* **113**, 635 (1982), Copyright (1982) Wiley-VCH]

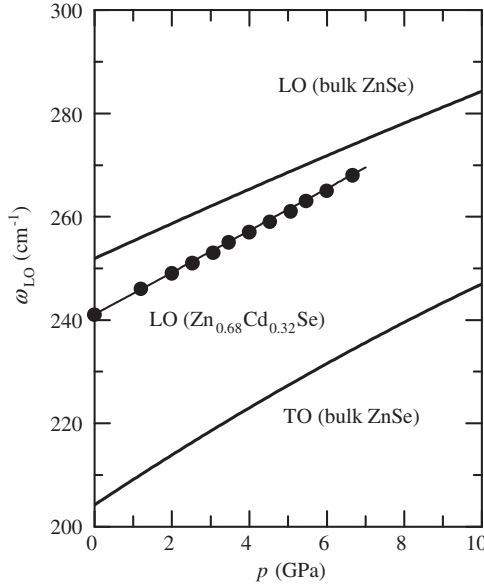


Figure 4.20 Hydrostatic-pressure dependence of the LO phonon frequency for $\text{Zn}_{0.68}\text{Cd}_{0.32}\text{Se}$ layer grown on GaAs(100) measured at 300 K. The experimental data are taken from Li *et al.* [40]. The solid line shows the result calculated using Equation (4.8) ($\text{Zn}_{0.68}\text{Cd}_{0.32}\text{Se}$). The bulk ZnSe LO and TO phonon frequencies are obtained from Adachi [41]

shift of the phonon frequencies. The latter can be easily identified in Figure 4.19. The ordinary temperature shift in ω_{LO} takes place for $x \geq 0.75$ for which the resonant interaction is small. When this interaction is significant ($0.4 < x < 0.6$), the phonon frequency ω_{TO} exhibits anomalous dependence on temperature; i.e. at $x = 0.50$ and 0.58 ω_{TO} is practically unchanged over a wide temperature range from 100 to 450 K (Figure 4.19). This is due to the strengthening of anharmonic coupling with increasing temperature and, as a result, to the stronger repulsion effect of the TO and 2TA bands [39].

The pressure dependence of ω_{LO} for $\text{Zn}_{0.68}\text{Cd}_{0.32}\text{Se}$ layer on GaAs(100) is shown in Figure 4.20. The Raman spectra were recorded up to 7 GPa [40]. The solid line represents the experimental data (ω_{LO} in cm^{-1} , p in GPa)

$$\omega_{\text{LO}}(p) = 241.07 + 4.066p \quad (4.8)$$

Also shown in Figure 4.20 are the experimental results for ZnSe [41] ($\omega_{\text{LO,TO}}$ in cm^{-1} , p in GPa)

$$\omega_{\text{LO}}(p) = 251.9 + 3.44p - 0.02p^2 \quad (4.9a)$$

$$\omega_{\text{TO}}(p) = 204.2 + 4.98p - 0.07p^2 \quad (4.9b)$$

The pressure dependence of the ZnSe-like LO and TO phonon frequencies for MBE-grown $\text{ZnSe}_{0.96}\text{Te}_{0.04}$ layer is shown in Figure 4.21. The optical phonon frequencies were obtained by

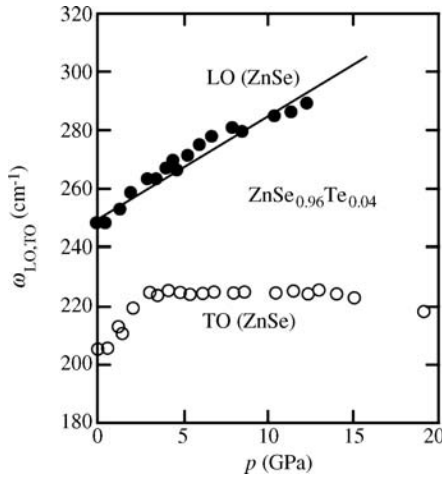


Figure 4.21 Hydrostatic-pressure dependence of the ZnSe-like LO and TO phonon frequencies for $\text{ZnSe}_{0.96}\text{Te}_{0.04}$ at 300 K. [Reprinted with permission from C. S. Yang *et al.*, *Phys. Rev. B* **59**, 8128–8131 (1999). Copyright (1999) American Physical Society]

Raman scattering and FTIR measurements under pressures of up to 20 GPa [42]. Both $\text{Zn}_x\text{Cd}_{1-x}\text{Se}$ (Figure 4.19) and $\text{ZnSe}_x\text{Te}_{1-x}$ exhibit an intermediate-mode behavior (Table 4.5). In addition to the usual ZnSe-like LO and TO modes, a new LO–TO phonon pair can therefore be identified inside the reststrahlen band in $\text{ZnSe}_x\text{Te}_{1-x}$ [25]. The ZnSe-like LO phonon frequency in Figure 4.21 can be approximated as (ω_{LO} in cm^{-1} , p in GPa)

$$\omega_{\text{LO}}(p) = 250 + 3.3p \quad (4.10)$$

On the other hand, the ZnSe-like TO phonon frequency exhibits anomalous dependence on p , i.e. it increases almost linearly up to ~ 3 GPa and tends to show a saturated value of $\sim 225 \text{ cm}^{-1}$ for $p > 3$ GPa. There have been many Raman peaks observed in $\text{ZnSe}_x\text{Te}_{1-x}$ for $0 < x < 1.0$ between the ZnSe-like LO and TO phonon frequency region. The anomalous pressure dependence of the ZnSe-like TO phonon frequency may be correlated with this fact [42].

Raman scattering has been used to investigate anharmonicity and disorder-induced effects in MBE- $\text{Be}_x\text{Zn}_{1-x}\text{Se}/\text{GaAs}(100)$ epilayers [43]. The anharmonicity is found to be higher in $\text{Be}_x\text{Zn}_{1-x}\text{Se}$ than in ZnSe, increasing with compositional disorder.

In conclusion of this section, the temperature and pressure coefficients of the long-wavelength optical phonon frequencies $d\omega_{\text{op}}/dT$ (or $\omega_{\text{op}}^{-1} d\omega_{\text{op}}/dT = d \ln \omega_{\text{op}}/dT$) and $d\omega_{\text{op}}/dp$ (or $\omega_{\text{op}}^{-1} d\omega_{\text{op}}/dp = d \ln \omega_{\text{op}}/dp$) in alloys of exhibiting one-mode behavior can be simply estimated from the linear interpolation between the endpoint values. In the case of two-mode (three- or four-mode) behavior in group-IV binaries and in III–V and II–VI ternaries (quaternaries), the temperature and pressure coefficients of the endpoint material values can be used, to a first approximation, as those for each phonon mode. For example, in an $\text{A}_x\text{B}_{1-x}\text{C}$ alloy, the temperature coefficient of the AC-like (BC-like) LO phonon frequency is the same as that of the bulk material AC (BC). These are schematically shown in Figure 4.22. A variety of the endpoint material data can be found in Adachi [33, 35, 41].

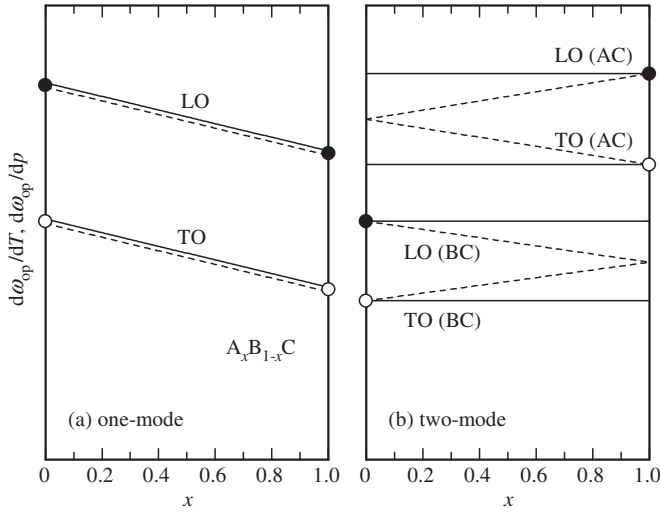


Figure 4.22 Schematic representations of the composition dependence of the temperature and pressure coefficients, $d\omega_{op}/dT$ and $d\omega_{op}/dp$, in an alloy of composition $A_xB_{1-x}C$ (solid lines). The solid and open circles represent the endpoint binary data. The dependence of ω_{op} on x is also schematically shown by the dashed lines. The schemes represented by the solid lines can also be used for estimating mode Grüneisen parameters and PDPs

4.3 MODE GRÜNEISEN PARAMETER

The anharmonic properties of solids are customarily described in terms of the Grüneisen parameter γ . As a measure of the volume dependence of the phonon frequency $\nu_i(\mathbf{q})$ of the i th mode, the mode Grüneisen parameter $\gamma_i(\mathbf{q})$ can be defined by

$$\gamma_i(\mathbf{q}) = -\frac{d[\ln\nu_i(\mathbf{q})]}{d[\ln V]} = -\frac{V}{\nu_i(\mathbf{q})} \frac{d\nu_i(\mathbf{q})}{dV} \quad (4.11)$$

where V is the crystal volume. The mode Grüneisen parameters for the long-wavelength ($\mathbf{q} = 0$) phonons in some non-alloyed group-IV, III-V and II-VI semiconductors are summarized in Tables 4.5 and 4.6 of Adachi [31].

Figure 4.23 shows the γ parameters for (a) Si–Si, (b) Si–Ge and (c) Ge–Ge modes in Si_xGe_{1-x} . The experimental data are taken from Sui *et al.* [32]. The Si and Ge values are also taken from Adachi [33]. The Si–Si (Ge–Ge) mode parameter slightly decreases (increases) with increasing x , while the Si–Ge mode parameter is nearly independent of x .

The LO and TO phonon γ parameters versus x for $Al_xGa_{1-x}As$ are plotted in Figure 4.24. The alloy data are taken from Holtz *et al.* [36]. The binary data are also taken from Adachi [35]. These data scatter relatively largely, but show no strong dependence on x . They fall in the range $\gamma_{LO,TO} = 1.1 \pm 0.3$, as indicated by the vertical bar.

Figure 4.25 plots the mode Grüneisen parameter γ versus x for c - GaN_xAs_{1-x} . The experimental data are taken from Güngerich *et al.* [44]. These authors used the pressure-dependent shift of the GaAs-like local vibrational mode to calculate the

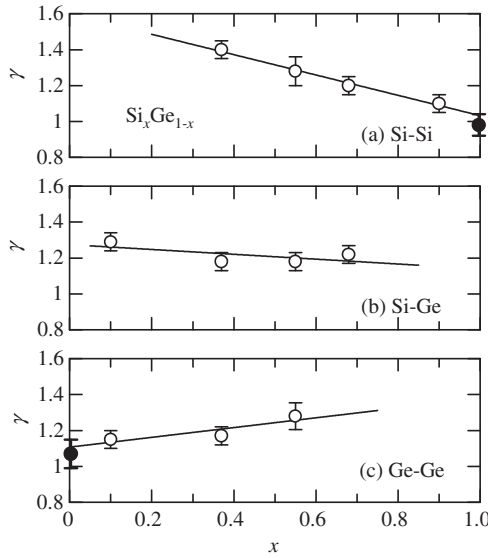


Figure 4.23 Mode Grüneisen parameters γ versus x for (a) Si–Si, (b) Si–Ge and (c) Ge–Ge phonon pairs in $\text{Si}_x\text{Ge}_{1-x}$ at 300 K. The experimental data are taken from Sui *et al.* [32]. The endpoint elemental data are also taken from Adachi [33]

anharmonicity of the Ga–N bond potential and qualitatively confirmed the simple picture in which the Ga–N bonds are significantly overstretched in Ga(N, As) with respect to their equilibrium length realized in GaN.

Finally, the composition dependence of the mode Grüneisen parameter in various semiconductor alloys can be estimated, to a first approximation, from the scheme shown in Figure 4.22. Using an $\text{A}_x\text{B}_{1-x}\text{C}$ alloy that exhibits the two-mode behavior as an example, the AC-like LO phonon mode has the same Grüneisen parameter as that of AC, irrespective of x . Similarly, the BC-like LO phonon mode has the same Grüneisen parameter as that of BC

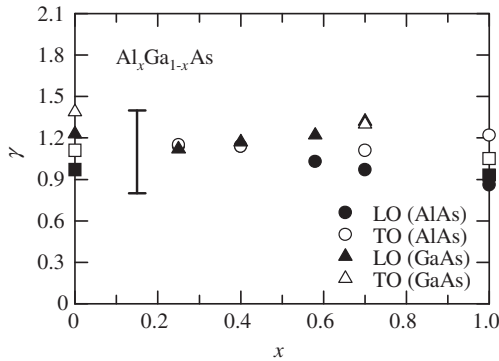


Figure 4.24 Mode Grüneisen parameter γ versus x for $\text{Al}_x\text{Ga}_{1-x}\text{As}$ at 300 K. The experimental data are taken from Holtz *et al.* [36]. The endpoint binary data are also taken from Adachi [35] (solid and open squares). The vertical bar indicates the range of $\gamma_{\text{LO,TO}} = 1.1 \pm 0.3$

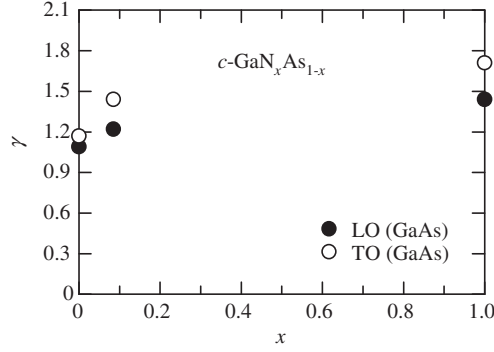


Figure 4.25 Mode Grüneisen parameter γ versus x for $c\text{-GaN}_x\text{As}_{1-x}$ at 300 K. The experimental data are taken from Güngerich *et al.* [44]

(Figure 4.22(b)). The endpoint γ values for some non-alloyed group-IV, III-V and II-VI semiconductors can be found in Adachi [31,33,35,41].

4.3.1 Phonon Deformation Potential

Strain- or stress-induced shift of the phonon frequency can be explained by the PDP [31]. The PDPs for some non-alloyed group-IV, III-V and II-VI semiconductors are summarized in Adachi [31, 33, 35, 41]. A very few data have, however, been reported on alloy materials. This necessitates the use of some sort of an interpolation scheme. The interpolation scheme in Figure 4.22 may be the simplest and most reliable way to estimate alloy PDP values. Indeed, the GaN- and AlN-like E_2 (high) phonon modes in $w\text{-Al}_x\text{Ga}_{1-x}\text{N}$ have the same PDPs as the relevant endpoint binary values ($w\text{-GaN}$ and $w\text{-AlN}$), respectively. [45].

The strain (ε)-induced shift of the LO phonon frequency can now be given by

$$\Delta\omega_{\text{LO}}\varepsilon = \omega_{\text{LO}} \left(K_{12}(\text{LO}) - \frac{C_{12}}{C_{11}} K_{11}(\text{LO}) \right) \varepsilon = \omega_{\text{LO}} \left(K_{12}(\text{LO}) + \frac{S_{12}}{S_{11} + S_{12}} K_{11}(\text{LO}) \right) \varepsilon \quad (4.12)$$

where K_{ij} is the dimensionless PDP and C_{ij} (S_{ij}) is the elastic stiffness (compliance) constant. The K_{ij} is usually defined, using p and q , as [31]

$$K_{11} = \frac{p}{\omega_{\text{LO}}^2}, \quad K_{12} = \frac{q}{\omega_{\text{LO}}^2} \quad (4.13)$$

Equation (4.12) can, then, be rewritten as

$$\Delta\omega_{\text{LO}}\varepsilon = \frac{1}{\omega_{\text{LO}}} \left(q(\text{LO}) - \frac{C_{12}}{C_{11}} p(\text{LO}) \right) \varepsilon = \frac{1}{\omega_{\text{LO}}} \left(q(\text{LO}) + \frac{S_{12}}{S_{11} + S_{12}} p(\text{LO}) \right) \varepsilon \equiv b\varepsilon \quad (4.14)$$

The b versus x data for $\text{Si}_x\text{Ge}_{1-x}$ are shown in Figure 4.26. The experimental data are taken from Lockwood and Baribeau [46] (open circles), Stoehr *et al.* [47] (open squares),

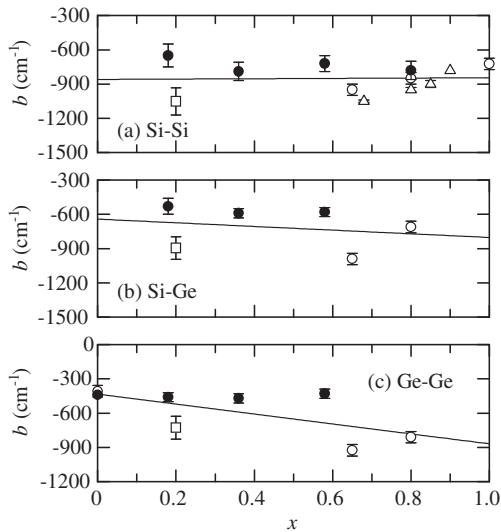


Figure 4.26 Optical-phonon strain-shift coefficient b versus x for $\text{Si}_x\text{Ge}_{1-x}$ at 300 K. The experimental data are taken from Lockwood and Baribeau [46] (open circles), Stoehr *et al.* [47] (open squares), Wong *et al.* [48] (open triangles) and Pezzoli *et al.* [49] (solid circles). The solid lines represent the linear least-squares fit of these data

Wong *et al.* [48] (open triangles) and Pezzoli *et al.* [49] (solid circles). It can be seen that the Si–Ge and Ge–Ge modes gradually decrease with increasing x , while the Si–Si mode is nearly independent of x . However, Reparaz *et al.* [50] were unable to observe any clear composition dependence of the Si-like, Ge-like and Si–Ge modes in $\text{Si}_x\text{Ge}_{1-x}$ between $x = 0$ and 0.6.

The GaP- and GaAs-like LO-phonon coefficients b for $\text{GaP}_x\text{As}_{1-x}$ are shown in Figure 4.27. The experimental data correspond to those for the (001) biaxial strain [51]. A much higher frequency shift of the GaAs-like mode than that of the GaP-like mode can be seen, suggesting

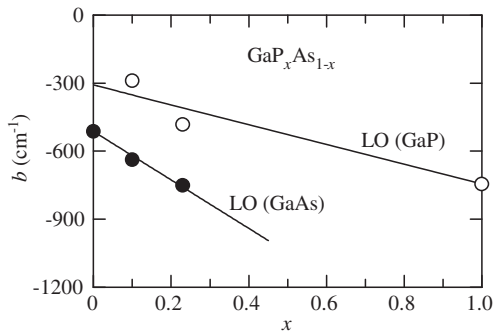


Figure 4.27 GaP- and GaAs-like LO-phonon strain-shift coefficients b versus x for $\text{GaP}_x\text{As}_{1-x}$ at 300 K. The experimental data are taken from Armelles *et al.* [51]. The solid lines represent the linear least-squares fit (in cm^{-1}): $b = -308 - 437x$ (GaP-like) and $-513 - 1069x$ (GaAs-like)

that the biaxial strain is not accommodated in the same way by the two types of bonds in $\text{GaP}_x\text{As}_{1-x}$.

REFERENCES

- [1] C. W. Myles, *Phys. Rev. B* **28**, 4519 (1983).
- [2] S. Baroni, S. de Gironcoli, and P. Giannozzi, *Phys. Rev. Lett.* **65**, 84 (1990).
- [3] J. A. Kash, J. M. Hvam, J. C. Tsang, and T. F. Kuech, *Phys. Rev. B* **38**, 5776 (1988).
- [4] G. P. Srivastava, *The Physics of Phonons*. Adam Hilger, Bristol, (1990).
- [5] I. F. Chang and S. S. Mitra, *Adv. Phys.* **20**, 359 (1971).
- [6] I. F. Chang and S. S. Mitra, *Phys. Rev.* **172**, 924 (1968).
- [7] A. Mascarenhas, H. M. Cheong, M. J. Seong, and F. Alsina, in *Spontaneous Ordering in Semiconductor Alloys* (edited by A. Mascarenhas), Kluwer Academic, New York, 2002, p. 391.
- [8] F. Pezzoli, L. Martinelli, E. Grilli, M. Guzzi, S. Sanguinetti, M. Bollani, H. D. Christina, G. Isella, H. von Känel, E. Wintersberger, J. Stangl, and G. Bauer, *Mater. Sci. Eng. B* **124–125**, 127 (2005).
- [9] J. C. Tsang, V. P. Kesan, J. L. Freeouf, F. K. LeGoues, and S. S. Iyer, *Phys. Rev. B* **46**, 6907 (1992).
- [10] M. Meléndez-Lira, J. Menéndez, W. Windl, O. F. Sankey, G. S. Spencer, S. Sego, R. B. Culbertson, A. E. Bair, and T. L. Alford, *Phys. Rev. B* **54**, 12866 (1996).
- [11] B.-K. Yang, M. Krishnamurthy, and W. H. Weber, *J. Appl. Phys.* **84**, 2011 (1998).
- [12] L. V. Kulik, C. Guedj, M. W. Dashiell, J. Kolodzey, and A. Hairie, *Phys. Rev. B* **59**, 15753 (1999).
- [13] H. Harima, T. Inoue, S. Nakamura, H. Okumura, Y. Ishida, S. Yoshida, T. Koizumi, H. Grille, and F. Bechstedt, *Appl. Phys. Lett.* **74**, 191 (1999).
- [14] A. Tabata, J. R. Leite, A. P. Lima, E. Silveira, V. Lemos, T. Frey, D. J. As, D. Schikora, and K. Lischka, *Appl. Phys. Lett.* **75**, 1095 (1999).
- [15] K. Torii, N. Usukura, A. Nakamura, T. Sota, S. F. Chichibu, T. Kitamura, and H. Okumura, *Appl. Phys. Lett.* **82**, 52 (2003).
- [16] B. Jusserand, in *Properties of Aluminium Gallium Arsenide*, EMIS Datareviews Series No. 7 (edited by S. Adachi), INSPEC, London, 1993, p. 30.
- [17] Z. C. Feng, S. Perkowitz, R. Rousina, and J. B. Webb, *Can. J. Phys.* **69**, 386 (1991).
- [18] M. H. Brodsky, G. Lucovsky, M. F. Chen, and T. S. Plaskett, *Phys. Rev. B* **2**, 3303 (1970).
- [19] S. Adachi, *Physical Properties of III–V Semiconductor Compounds: InP, InAs, GaAs, GaP, InGaAs, and InGaAsP*. John Wiley & Sons, Ltd, New York, 1992.
- [20] T. Sugiura, N. Hase, Y. Iguchi, and N. Sawaki, *Jpn. J. Appl. Phys.* **37**, 544 (1998).
- [21] R. Manor, O. Brafman, and R. F. Kopf, *Phys. Rev. B* **56**, 3567 (1997).
- [22] G. Lucovsky, E. Lind, and E. A. Davis, in *II–VI Semiconducting Compounds* (edited by D. G. Thomas), Benjamin, New York, 1967, p. 1150.
- [23] J. Baars and F. Sorger, *Solid State Commun.* **10**, 875 (1972).
- [24] M. P. Volz, F. R. Szofran, S. L. Lehoczky, and C. -H. Su, *Solid State Commun.* **75**, 943 (1990).
- [25] T. R. Yang and C. C. Lu, *Physica B* **284–288**, 1187 (2000).
- [26] R. G. Alonso, E.-K. Suh, A. K. Ramdas, N. Samarth, H. Luo, and J. K. Furdyna, *Phys. Rev. B* **40**, 3720 (1989).
- [27] O. Pagès, T. Tite, D. Bormann, O. Maksimov, and M. C. Tamargo, *Appl. Phys. Lett.* **80**, 3081 (2002).
- [28] O. Pagès, M. Ajjoun, T. Tite, D. Bormann, E. Tournié, and K. C. Rustagi, *Phys. Rev. B* **70**, 155319 (2004).
- [29] D. Wang, D. Huang, C. Jin, X. Liu, Z. Lin, J. Wang, and X. Wang, *J. Appl. Phys.* **80**, 1248 (1996).
- [30] H. Makino, H. Sasaki, J. H. Chang, and T. Yao, *J. Cryst. Growth* **214/215**, 359 (2000).
- [31] S. Adachi, *Properties of Group-IV, III–V and II–VI Semiconductors*, John Wiley & Sons, Ltd, Chichester, 2005.
- [32] Z. Sui, H. H. Burke, and I. P. Herman, *Phys. Rev. B* **48**, 2162 (1993).

- [33] S. Adachi, *Handbook on Physical Properties of Semiconductors: Volume 1 Group IV Semiconductors*, Kluwer Academic, Boston, 2004.
- [34] J. Jiménez, E. Martín, A. Torres, and J. P. Landesman, *Phys. Rev. B* **58**, 10463 (1998).
- [35] S. Adachi, *Handbook on Physical Properties of Semiconductors: Volume 2 III-V Compound Semiconductors*, Kluwer Academic, Boston, 2004.
- [36] M. Holtz, M. Seon, O. Brafman, R. Manor, and D. Fekete, *Phys. Rev. B* **54**, 8714 (1996).
- [37] J. R. Shealy and G. W. Wicks, *Appl. Phys. Lett.* **50**, 1173 (1987).
- [38] P. Galtier, J. Chevallier, M. Zigone, and G. Martinez, *Phys. Rev. B* **30**, 726 (1984).
- [39] M. Y. Valakh, M. P. Lisitsa, G. S. Pekar, G. N. Polysskii, V. I. Sidorenko, and A. M. Yaremko, *Phys. Status Solidi B* **113**, 635 (1982).
- [40] W. S. Li, Z. X. Shen, D. Z. Shen, and X. W. Fan, *J. Appl. Phys.* **84**, 5198 (1998).
- [41] S. Adachi, *Handbook on Physical Properties of Semiconductors: Volume 3 II-VI Compound Semiconductors*, Kluwer Academic, Boston, 2004.
- [42] C. S. Yang, W. C. Chou, D. M. Chen, C. S. Ro, J. L. Shen, and T. R. Yang, *Phys. Rev. B* **59**, 8128 (1999).
- [43] L. Y. Lin, C. W. Chang, W. H. Chen, Y. F. Chen, S. P. Guo, and M. C. Tamargo, *Phys. Rev. B* **69**, 075204 (2004).
- [44] M. Güngerich, P. J. Klar, W. Heimbrod, J. Koch, W. Stolz, M. P. Halsall, and P. Harmer, *Phys. Rev. B* **71**, 075201 (2005).
- [45] A. Sarua, M. Kuball, and J. E. Van Nostrand, *Appl. Phys. Lett.* **85**, 2217 (2004).
- [46] D. J. Lockwood and J.-M. Baribeau, *Phys. Rev. B* **45**, 8565 (1992).
- [47] M. Stoehr, D. Aubel, S. Juillaguet, J. L. Bischoff, L. Kubler, D. Bolmont, F. Hamdani, B. Fraisse, and R. Fourcade, *Phys. Rev. B* **53**, 6923 (1996).
- [48] L. H. Wong, C. C. Wong, J. P. Liu, D. K. Sohn, L. Chan, L. C. Hsia, H. Zang, Z. H. Ni, and Z. X. Shen, *Jpn. J. Appl. Phys.* **44**, 7922 (2005).
- [49] F. Pezzoli, E. Bonera, E. Grilli, M. Guzzi, S. Sanguinetti, D. Chrastina, G. Isella, H. von Känel, E. Wintersberger, J. Stangl, and G. Bauer, *J. Appl. Phys.* **103**, 093521 (2008).
- [50] J. S. Reparaz, A. Bernardi, A. R. Goñi, M. I. Alonso, and M. Garriga, *Appl. Phys. Lett.* **92**, 081909 (2008).
- [51] G. Armelles, M. J. Sanjuán, L. González, and Y. González, *Appl. Phys. Lett.* **68**, 1805 (1996).

5 Collective Effects and Some Response Characteristics

5.1 PIEZOELECTRIC CONSTANT

5.1.1 General Considerations

A crystal with a center of symmetry cannot be piezoelectric [1]. Thus, the diamond-type crystals (diamond, Si, Ge and α -Sn) cannot be piezoelectric. Tables 5.1 and 5.2 summarize the piezoelectric constants for some $A^N B^{8-N}$ tetrahedral semiconductors with cubic and hexagonal crystal structures, respectively. Note that the piezoelectric strain constant d_{ij} is connected reciprocally with the stress constant e_{ik} in the following manner

$$d_{ij} = \sum_k e_{ik} S_{kj} \quad (5.1)$$

or, vice versa

$$e_{ij} = \sum_k d_{ik} C_{kj} \quad (5.2)$$

where S_{kj} (C_{kj}) is the elastic compliance (stiffness) constant [1].

5.1.2 Alloy Value

Figure 5.1 shows the plot of e_{14} versus x for $C_x Si_{1-x}$. The theoretical e_{14} value for 3C-SiC is -0.345 C/m^2 [2]. However, no experimental e_{14} data for 3C-SiC has been reported. Similarly, $Si_x Ge_{1-x}$ will in principle have a nonzero e_{14} value at an ordered phase $x \sim 0.5$. In the fully disordered group-IV semiconductor alloys ($C_x Si_{1-x}$, $Si_x Ge_{1-x}$, etc.), we have zero e_{14} values over the whole alloy range $0 \leq x \leq 1.0$.

Using the endpoint binary data in Table 5.2, the linear interpolation scheme provides a set of the piezoelectric constants e_{ij} for $w\text{-Al}_x\text{Ga}_{1-x}\text{N}$ (in C/m^2)

$$e_{15}(x) = -0.33 - 0.15x \quad (5.3a)$$

$$e_{31}(x) = -0.55 - 0.03x \quad (5.3b)$$

$$e_{33}(x) = 1.12 + 0.43x \quad (5.3c)$$

Table 5.1 Piezoelectric stress and strain constants, e_{14} and d_{14} , for some cubic group-IV, III-V and II-VI semiconductors. d = diamond; zb = zinc-blende; rs = rocksalt

System	Material	e_{14} (C/m ²)	d_{14} (10 ⁻¹² m/V)
IV	Diamond (d) ^a	0	0
	Si (d) ^a	0	0
	Ge (d) ^a	0	0
	Sn (d) ^a	0	0
	3C-SiC (zb)	-0.345 ^b	-1.35 ^b
III-V	BN (zb)	-1.04 ^b	
	BP (zb)	-0.36 ^b	
	AlN (zb)	1.13 ^b	9.7 ^b
	AlP (zb)	-0.06 ^b	
	AlAs (zb)	-0.23 ^b	-3.9 ^b
	AlSb (zb)	0.068	1.7
	GaN (zb)	0.61 ^b	6.4 ^b
	GaP (zb)	0.10	1.42
	GaAs (zb)	-0.16	-2.7
	GaSb (zb)	0.126	2.92
	InN (zb)	0.71 ^b	
	InP (zb)	-0.083	-1.80
	InAs (zb)	0.045	1.14
InSb (zb)	0.071	2.4	
II-VI	MgO (rs) ^a	0	0
	ZnS (zb)	0.147	3.18
	ZnSe (zb)	0.049	1.10
	ZnTe (zb)	0.028	0.91
	CdO (rs) ^a	0	0
	CdS (zb)	0.37 ^b	
	CdSe (zb)	0.27 ^b	
	CdTe (zb)	0.0335	1.68
	HgS (zb)	0.14 ^b	5.3 ^b
	HgSe (zb)	0.058 ^b	2.6 ^b
	HgTe (zb)	0.029 ^b	1.4 ^b

^aPrincipally showing no piezoelectricity^bEstimated or calculated

The piezoelectric properties of ordered and disordered III-N alloys have been theoretically studied by several authors [3,4]. The piezoelectric constant e_{33} versus x for w -Ga _{x} In _{$1-x$} N is reproduced in Figure 5.2 [4]. The solid line shows the x dependence of e_{33} for disordered w -Ga _{x} In _{$1-x$} N, while the solid circles refer to ordered values. Four ordered structures, all exhibiting ordering along the c axis, will be considered. The first structure is denoted 1×1 and consists of a single Ga plane alternating with a simple In plane. This structure has also been studied by Bernardini and Fiorentini [3] and has an overall composition $x = 0.5$. The second structure, denoted 2×2 , also has an overall composition of 50 at% but

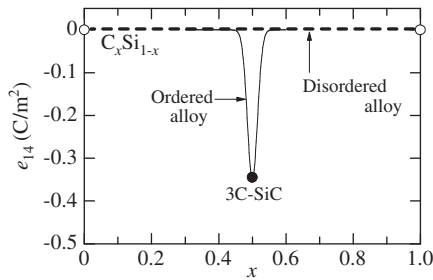
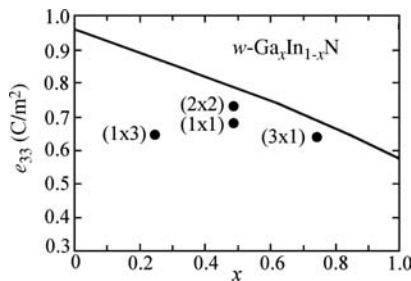
Table 5.2 Piezoelectric stress and strain constants e_{ij} and d_{ij} for some hexagonal group-IV, III-V and II-VI semiconductors. w = wurtzite; h = hexagonal ($P6_3/mmc$ (D_{6h}))

System	Material	e_{ij} (C/m ²)			d_{ij} (10 ⁻¹² m/V)		
		e_{15}	e_{31}	e_{33}	d_{15}	d_{31}	d_{33}
IV	2H-SiC (w)	-0.08 ^a		0.2 ^a			
III-V	BN (h) ^b	0	0	0	0	0	0
	AlN (w)	-0.48	-0.58	1.55	-4.07	-2.65	5.53
	GaN (w)	-0.33 ^c	-0.55	1.12	3.1	-1.9	3.7
	InN (w)		-0.41 ^c	0.81 ^c			4.7
II-VI	BeO (w)		-0.051	0.092		-0.12	0.24
	ZnO (w)	-0.37	-0.62	0.96	-8.3	-5.12	12.3
	ZnS (w)	-0.118	-0.238	0.265	-4.37	-2.14	3.66
	CdS (w)	-0.183	-0.262	0.385	-11.91	-5.09	9.71
	CdSe (w)	-0.138	-0.160	0.347	-10.51	-3.92	7.84

^aAssuming that the 2H-SiC values are the same as those for 6H-SiC within experimental error

^bPrincipally showing no piezoelectricity

^cEstimated or calculated

**Figure 5.1** Piezoelectric stress constant e_{14} versus x for C_xSi_{1-x} . The open circles show the endpoint elemental data ($e_{14}=0$), while the solid circle refers to the theoretical 3C-SiC ($x=0.5$) value**Figure 5.2** Theoretical piezoelectric stress constant e_{33} versus x for $w-Ga_xIn_{1-x}N$. The solid line shows the disordered alloy values, while the solid circles plot the ordered values. [Reprinted with permission from A. Al-Yacoub, L. Bellaiche, and S.-H. Wei, *Phys. Rev. Lett.* **89**, 7601–7604 (2002). Copyright (2002) American Physical Society]

differentiates itself from the 1×1 structure by exhibiting two pure Ga planes alternating with two pure In planes. The third (respectively, fourth) structure exhibits a succession of three (respectively, one) Ga and one (respectively, three) In planes. Consequently, it is denoted as 3×1 (respectively, 1×3) while having a Ga composition of 75 at% (respectively, 25 at%).

The theoretical results in Figure 5.2 indicate that the atomic ordering can have a large effect on the piezoelectricity and that e_{33} of disordered alloys is nearly linear with respect to x . The simple linear interpolation scheme, using the endpoint binary data in Table 5.2, provides e_{33} for $w\text{-Ga}_x\text{In}_{1-x}\text{N}$ (in C/m^2)

$$e_{33}(x) = 0.81 + 0.31x \quad (5.4)$$

Equation (5.4) indicates an increase in e_{33} with increasing x , in direct contrast to that obtained in Figure 5.2 [4].

Figure 5.3 shows the piezoelectric constant e_{14} as a function of x for $\text{Ga}_x\text{In}_{1-x}\text{As}$. The experimental data are taken from Sánchez-Rojas *et al.* [5] (solid circles), Chan *et al.* [6] (open square) and Izpura *et al.* [7] (open triangle). The solid line is obtained from the linear interpolation scheme between the endpoint data (open circles). It can be seen from Figure 5.3 that e_{14} passes through zero at $x \sim 0.2$ while undergoing a reversal in sign. The experimental data are slightly larger than the linearly interpolated values.

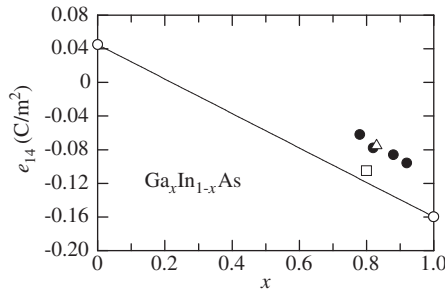


Figure 5.3 Piezoelectric stress constant e_{14} versus x for $\text{Ga}_x\text{In}_{1-x}\text{As}$. The experimental data are taken from Sánchez-Rojas *et al.* [5] (solid circles), Chan *et al.* [6] (open square) and Izpura *et al.* [7] (open triangle). The solid line represents the linearly interpolated result between the endpoint binary data

No experimental data on alloy e_{ij} values have been reported, except for $\text{Ga}_x\text{In}_{1-x}\text{As}$ (Figure 5.3). The piezoelectric constants e_{14} for $\text{Al}_x\text{Ga}_{1-x}\text{As}$ and $\text{Ga}_x\text{In}_{1-x}\text{P}_y\text{As}_{1-y}/\text{InP}$ in Figure 5.4 have been calculated from Equations (A.4) and (A.6), respectively, and can be given by

$$e_{14}(x) = -0.23 + 0.07x \quad (5.5)$$

for $\text{Al}_x\text{Ga}_{1-x}\text{As}$ and

$$e_{14}(y) = -0.05 + 0.15y - 0.18y^2 \quad (5.6)$$

for $\text{Ga}_x\text{In}_{1-x}\text{P}_y\text{As}_{1-y}/\text{InP}$.

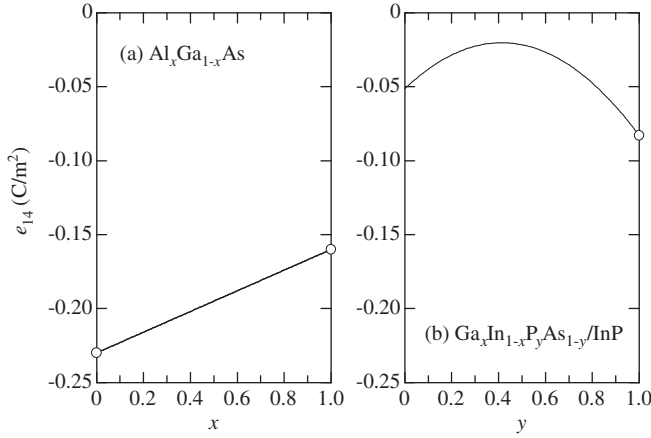


Figure 5.4 Piezoelectric stress constant e_{14} versus x or y for (a) $Al_xGa_{1-x}As$ and (b) $Ga_xIn_{1-x}P_yAs_{1-y}/InP$ calculated from the linear interpolation scheme. The open circles show the endpoint binary data

5.2 FRÖHLICH COUPLING CONSTANT

5.2.1 General Considerations

The theory of Fröhlich interaction in alloys of multi-mode phonon behaviors is very complex. Simply, it is possible to assume that there is a value for the Fröhlich coupling constant α_F for each phonon mode given by

$$\alpha_F = \frac{1}{2} \frac{e^2 / \sqrt{\hbar / 2m_c^\alpha \omega_{LO}}}{\hbar \omega_{LO}} \left(\frac{1}{\epsilon_\infty} - \frac{1}{\epsilon_s} \right) \quad (5.7)$$

where e is the electron charge, m_c^α is the electron effective mass (conductivity mass), ω_{LO} is the LO phonon frequency and ϵ_∞ and ϵ_s are the high-frequency and static dielectric constants, respectively. The final alloy α_F value can be obtained from the weighted average of each mode (i.e. Equation (5.7)).

Nash *et al.* [8] discussed the Fröhlich interaction in alloys of two-mode behavior based on a MREI model. They found that the electron–phonon coupling in $In_{0.53}Ga_{0.47}As$ is much weaker for the InAs-like mode than for the GaAs-like mode. The primary reason for this was considered to be the coupling of the LO distortions by the macroscopic electric field. A theory of the Fröhlich interaction in semiconductor alloys has also been proposed by several authors [9,10].

5.2.2 Alloy Value

Table 5.3 summarizes the Fröhlich coupling constant α_F for some non-alloyed group-IV, III–V and II–VI semiconductors. The simplest way to obtain the alloy value is to use the linear interpolation scheme using the endpoint data in Table 5.3.

Table 5.3 Fröhlich coupling constant α_F for some group-IV, III-V and II-VI semiconductors. d = diamond; zb = zinc-blende; w = wurtzite; rs = rocksalt

System	Material	α_F	System	Material	α_F
IV	Diamond (d) ^a	0	II-VI	ZnO (w)	1.19
	Si (d) ^a	0		ZnS (zb)	0.63
	Ge (d) ^a	0		ZnSe (zb)	0.432
	Sn (d) ^a	0		ZnTe (zb)	0.332
	3C-SiC (zb)	0.256		CdO (rs)	0.75
III-V	AlN (w)	0.65		CdS (w)	0.514
	AlAs (zb)	0.126		CdSe (w)	0.46
	AlSb (zb)	0.023		CdTe (zb)	0.35
	GaN (w)	0.48			
	GaP (zb)	0.201			
	GaAs (zb)	0.068			
	GaSb (zb)	0.025			
	InN (w)	0.24			
	InP (zb)	0.15			
	InAs (zb)	0.0454			
InSb (zb)	0.022				

^aPrincipally showing no Fröhlich coupling interaction

The x dependence of α_F for C_xSi_{1-x} is shown in Figure 5.5. The Fröhlich coupling constant α_F is strongly dependent on the ionic polarization of the crystal, which is related to the static and high-frequency dielectric constants ϵ_s and ϵ_∞ . Note that ϵ_s is equal to ϵ_∞ in such diamond-type crystals. Thus, no Fröhlich coupling occurs in diamond-type crystals ($\alpha_F = 0$, see Equation (5.7)).

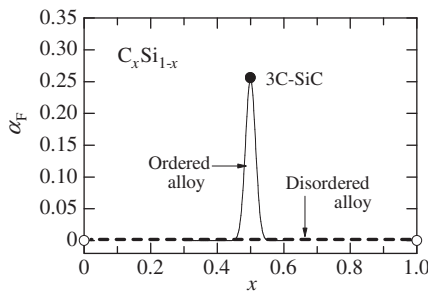


Figure 5.5 Fröhlich coupling constant α_F versus x for C_xSi_{1-x} . The open circles show the endpoint elemental data, while the solid circle refers to the experimental 3C-SiC ($x = 0.5$) value

The α_F value of 3C-SiC is 0.256 [11]. This means that the bond polarity of SiC resembles that of III-V and II-VI semiconductors ($\alpha_F \neq 0$) rather than that of Si or diamond ($\alpha_F = 0$). Similarly, an alloy of Si_xGe_{1-x} will have a nonzero α_F value near the ordered phase $x \sim 0.5$, although this has never been confirmed experimentally. In the fully disordered alloys (C_xSi_{1-x} , Si_xGe_{1-x} , etc.), a value of $\alpha_F = 0$ can be expected over the whole alloy range $0 \leq x \leq 1.0$.

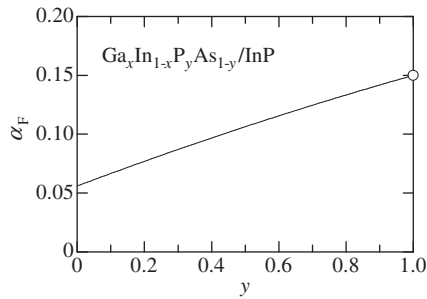


Figure 5.6 Fröhlich coupling constant α_F versus y for $\text{Ga}_x\text{In}_{1-x}\text{P}_y\text{As}_{1-y}/\text{InP}$. The solid line shows the linear interpolation result of Equation (A.6), which can be successfully approximated by the quadratic expression shown in Equation (5.8). The open circle shows the InP data

The linearly interpolated α_F value, obtained using Equation (A.6), is shown versus y for $\text{Ga}_x\text{In}_{1-x}\text{P}_y\text{As}_{1-y}/\text{InP}$ in Figure 5.6. This plot gives very weak upward bowing and can be expressed as

$$\alpha_F(y) = 0.056 + 0.107y - 0.013y^2 \quad (5.8)$$

REFERENCES

- [1] S. Adachi, *Properties of Group-IV, III-V and II-VI Semiconductors*, John Wiley & Sons, Ltd, Chichester, 2005.
- [2] A. P. Mirgorodsky, M. B. Smirnov, E. Abdelmounîm, T. Merle, and P. E. Quintard, *Phys. Rev. B* **52**, 3993 (1995).
- [3] F. Bernardini and V. Fiorentini, *Phys. Rev. B* **64**, 085207 (2001); erratum, *ibid.* **65**, 129903 (2002).
- [4] A. Al-Yacoub, L. Bellaïche, and S.-H. Wei, *Phys. Rev. Lett.* **89**, 057601 (2002).
- [5] J. L. Sánchez-Rojas, A. Sacedón, F. González-Sanz, E. Calleja, and E. Muñoz, *Appl. Phys. Lett.* **65**, 2042 (1994).
- [6] C. H. Chan, Y. F. Chen, M. C. Chen, H. H. Lin, and G. J. Jan, *J. Appl. Phys.* **84**, 1595 (1998).
- [7] I. Izpura, J. F. Valtueña, J. L. Sánchez-Rojas, A. Sacedón, E. Calleja, and E. Muñoz, *Solid-State Electron.* **40**, 463 (1996).
- [8] K. J. Nash, M. S. Skolnick, and S. J. Bass, *Semicond. Sci. Technol.* **2**, 329 (1987).
- [9] R. Zheng and M. Matsuura, *Phys. Rev. B* **59**, 15422 (1999).
- [10] X. X. Liang and S. L. Ban, *J. Lumin.* **94–95**, 781 (2001).
- [11] E. Kartheuser, in *Polarons in Ionic Crystals and Polar Semiconductors* (edited by J. T. Devreese), North-Holland, Amsterdam, 1972, p. 717.

6 Energy-band Structure: Energy-band Gaps

6.1 INTRODUCTORY REMARKS

6.1.1 Quasi-cubic Band Model

The review in this chapter is concerned with the most important band-gap energies as a function of alloy composition. They are: $E_0, E_0 + \Delta_0, E_1, E_1 + \Delta_1, E_2, E_g^X, E_g^L$, etc., and some of these gaps are shown in Figure 6.1 (see also Adachi [1]).

In Figure 6.1, the fundamental absorption refers to band-to-band or to excitonic transitions. The fundamental absorption manifests itself by a rapid rise in absorption and can be used to determine the band-gap energy of semiconductors and insulators. In most semiconductors, the lowest direct band-gap transitions occur at the E_0 edge, i.e. at the center of the BZ. Birman [2] discussed the relationship between the $k = 0$ (Γ) CB and VB states of the wurtzite structure and the corresponding states of the zinc-blende structure. The essential difference between the potential that an electron experiences in an ideal wurtzite lattice and that in a zinc-blende lattice is the relatively small difference in ‘crystal field’ due to sites beyond the next nearest neighbors.

Figure 6.2 shows the CB and VB states for (a) zinc-blende ($\Delta_{so} = \Delta_{cr} = 0$), (b) zinc-blende ($\Delta_{so} \neq 0, \Delta_{cr} = 0$) and (c) wurtzite semiconductors at $k = 0$. In the actual VB structure of a wurtzite crystal, the three VBs illustrated in Figure 6.2(c) can be thought of as arising from Figure 6.2(a) by the combined effect of both SO and crystal-field perturbations, while the wavefunction for each band may be written as a linear combination of p_x, p_y and p_z and spin functions, provided the interaction of the Γ_7 VB levels with the CB is neglected. This approach is known as the quasi-cubic model [3].

Under the SO interaction represented by the matrix element Δ_{so} and that of the crystal field represented by Δ_{cr} , the quasi-cubic model provides the difference in energies of the VBs

$$\Delta E_{BA} = E_{0B} - E_{0A} = \frac{\Delta_{so} + \Delta_{cr}}{2} - \sqrt{\left(\frac{\Delta_{so} + \Delta_{cr}}{2}\right)^2 - \frac{2}{3}\Delta_{so}\Delta_{cr}} \quad (6.1a)$$

$$\Delta E_{CA} = E_{0C} - E_{0A} = \frac{\Delta_{so} + \Delta_{cr}}{2} + \sqrt{\left(\frac{\Delta_{so} + \Delta_{cr}}{2}\right)^2 - \frac{2}{3}\Delta_{so}\Delta_{cr}} \quad (6.1b)$$

The lowest direct band-gap energies in wurtzite semiconductors can then be given by E_{0A}, E_{0B} and E_{0C} , as shown in Figure 6.2(c).

The lowest direct (E_0) and lowest indirect gap energies (E_g^X, E_g^L) for some group-IV, III–V and II–VI semiconductors are summarized in Table 6.1. Table 6.2 also lists the lowest direct

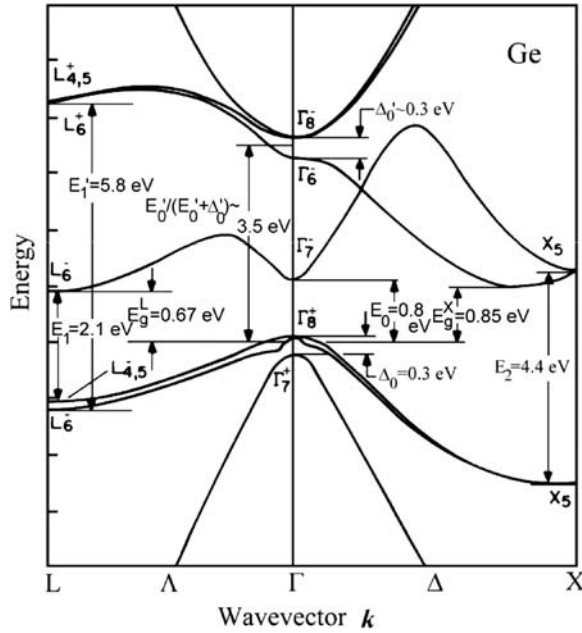


Figure 6.1 Electronic energy-band structure of Ge. The electronic states are labeled using the notation for the representations of the double group of the diamond structure. The main interband transitions are indicated by vertical arrows (at 300 K)

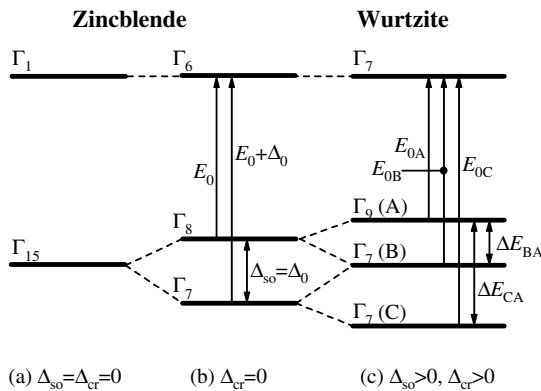


Figure 6.2 Relationships between the VB splitting at the Γ point in the zinc-blende ((a) $\Delta_{so} = \Delta_{cr} = 0$, (b) $\Delta_{so} \neq 0, \Delta_{cr} = 0$) and (c) wurtzite lattices ($\Delta_{so} \neq 0, \Delta_{cr} \neq 0$) and between the irreducible representations of the CB and VB in these lattices. (b) and (c) show the actual splitting found in the zinc-blende and wurtzite crystals, respectively

Table 6.1 E_0 , E_g^X and E_g^L for some cubic group-IV, III-V and II-VI semiconductors at 300 K.
d = diamond; zb = zinc-blende; rs = rocksalt

System	Material	E_0 (eV)	E_g^X (eV)	E_g^L (eV)
IV	Diamond (d)	15.3	5.50	7.26 ^a
	Si (d)	4.06	1.12	2.0
	Ge (d)	0.795	0.852	0.6657
	Sn (d)	-0.413 ^b		0.092 ^c
	3C-SiC (zb)	7.4	2.39	4.20
III-V	BN (zb)	7.9-11.40 ^d	6.27	
	BP (zb)	5	2.0	
	BAs (zb)	1.45 ^e		
	AlN (zb)	5.2	5.34	8.6 ^d
	AlP (zb)	3.91 ^f	2.48	3.57 ^d
	AlAs (zb)	3.01	2.15	2.37
	AlSb (zb)	2.27	1.615	2.211
	GaN (zb)	3.231 ^g	4.2 ^d	5.5 ^d
	GaP (zb)	2.76	2.261	2.63
	GaAs (zb)	1.43	1.911	1.72
	GaSb (zb)	0.72	1.05	0.76
	InN (zb)	0.56	3.0 ^d	5.8 ^d
	InP (zb)	1.35	2.21	2.05
	InAs (zb)	0.359	1.37	1.07
InSb (zb)	0.17	1.63	0.93	
II-VI	BeS (zb)	>5.5		
	BeSe (zb)	5.6	4-4.5	
	BeTe (zb)	4.1	2.63	
	MgO (rs)	7.8		
	MgS (zb)	4.45	3.6 ^d	
	MgSe (zb)	4.0	3.2 ^d	
	MgTe (zb)	3.4	2.5 ^d	
	ZnO (zb)	3.17		
	ZnS (zb)	3.726	5.14 ^d	
	ZnSe (zb)	2.721	3.4	3.8
	ZnTe (zb)	2.27	3.05	
	CdO (rs)	2.16		
	CdS (zb)	2.46	5.24 ^d	
	CdSe (zb)	1.675	4.37 ^d	
	CdTe (zb)	1.51	3.48 ^d	
	HgS (zb)	-0.04		
	HgSe (zb)	-0.08		
HgTe (zb)	-0.15			

^aEstimated

^bAt 1.5 K

^cAt 4.2 K

^dCalculated or estimated

^eTentative assignment

^fEstimated from $Al_xGa_{1-x}P$ data

^gGrown on MgO(100) substrate

gaps E_{0A} , E_{0B} and E_{0C} for some wurtzite-type group-IV, III–V and II–VI semiconductors. The Δ_{so} and Δ_{cr} values can be seen in Table 6.6 of Adachi [1].

6.1.2 Bowing Parameter

In a conventional band-structure calculation, the electrons are assumed to be independent particles interacting with some average potential due to positively charged ions and valence electrons, at an equilibrium lattice constant a . Since the electron wavefunction in a strictly periodic function must be of the form $\exp(i\mathbf{k}\cdot\mathbf{r})u_k(\mathbf{r})$, where $u_k(\mathbf{r})$ is a periodic function which satisfies the periodic boundary conditions, it is convenient to compute electron energies E as a function of \mathbf{k} . The computed energies are then drawn for various values of the wavevector lying along high symmetry lines in the first BZ (Figure 6.1). Though an alloy has no translational invariance, the VCA can recover it by replacing the potential by a periodic one, which is produced by ‘average’ atoms. For an $\text{Al}_x\text{Ga}_{1-x}\text{As}$ alloy, the potential is approximated by $u_{\text{VCA}}(\mathbf{r}) = xu_{\text{AlAs}}(\mathbf{r}) + (1-x)u_{\text{GaAs}}(\mathbf{r})$, which is periodic.

The band-gap energy is a typical case exhibiting nonlinearity with respect to alloy composition. Van Vechten and Bergstresser [4] developed a physical model for obtaining the bowing parameter of E_0 based on the Phillips’s dielectric theory of electronegativity [5]. The deviation from linearity is considered to be due to two terms involving c_i , the intrinsic bowing parameter due to the VCA, and c_e , the extrinsic bowing parameter due to aperiodicity in the alloy lattice

$$c = c_i + c_e \quad (6.2)$$

The extrinsic term c_e can be taken to be proportional to C_{A-B}^2 , i.e. to the square of the electronegativity difference C_{A-B} between the atoms A and B in an $\text{A}_x\text{B}_{1-x}\text{C}$ alloy.

6.1.3 Ordered Alloy

As mentioned in Section 1.3.2, it has become evidence that many cubic semiconductor alloys can exhibit spontaneous ordering. For example, $\text{Ga}_{0.5}\text{In}_{0.5}\text{P}$, when grown under proper conditions, forms the CuPt-B ordered structure. In this structure, an alternate GaP/InP monolayer SL is formed along the $\langle 111 \rangle$ direction. The effects of atomic ordering lead to many interesting effects, such as the band-gap reduction, VB splitting and polarization dependence of the optical transitions [6].

The schematic energy-band diagram of the disordered zinc-blende and ordered CuPt-B structures at the Γ point, where the electronic states are labeled in Slater–Koster notation [7] is shown in Figure 6.3. The essential difference between the potential that an electron experiences in an ideal zinc-blende lattice and that in an ordered CuPt-B structure is the relatively small differences in ‘crystal field (Δ_{cr}^s)’ due to sites beyond the next nearest neighbors. The detailed differences in the energy bands then arise from the difference in the crystal field and also from the SL nature in ordered materials. These can be briefly summarized as follows [6]:

1. The lowest CB Γ_4 in the CuPt-B structure corresponds to the CB Γ_6 in the zinc-blende structure, whereas the upper CB Γ_4 derives from the back-folded L-point CB minimum L_6 . Because of the same symmetry of these states their energies are shifted compared to those of

Table 6.2 $E_{0\alpha}$ ($\alpha = A, B$ or C) or related excitonic gap energy for some wurtzite group-IV, III-V and II-VI semiconductors at 300 K

System	Material	E_{0A} (eV)	E_{0B} (eV)	E_{0C} (eV)
IV	2H-SiC	3.330 ^a		
III-V	AlN	6.2		
	GaN	3.420	3.428	
	InN	0.70		
II-VI	BeO	10.6		
	MgSe	4.1 ^b		
	ZnO	3.45	3.40	3.55
	ZnS	3.75	3.78	3.87
	CdS	2.501	2.516	2.579
	CdSe	1.751	1.771	2.176
	CdTe	1.56 ^b		

^aAt 4.2 K^bEstimated

the ordered $\text{Ga}_{0.5}\text{In}_{0.5}\text{P}$ due to the level repulsion by a certain amount, the value of which increases with increasing order parameter η . This leads to a reduction in the gap between the upper VBs Γ_5, Γ_6 and the lowest CB Γ_4 , whereas the gap to the second lowest CB $\Gamma_4(L_6)$ increases.

- Due to reduction of symmetry with regard to the order direction $[11\bar{1}]$, the degeneracy of the $j = 3/2$ states at the Γ point is lifted. The Γ_5, Γ_6 states correspond to the $(3/2, \pm 3/2)$ HH and the Γ_4 state to the $(3/2, \pm 1/2)$ LH band. The VB splitting between the $\Gamma_5, \Gamma_6(A)$ and $\Gamma_4(B)$ states again increases with increasing order parameter η . The VB SO split-off band $\Gamma_4(C)$ shows a rather weak dependence on the order parameter for the usual values of $\eta < 0.5$.

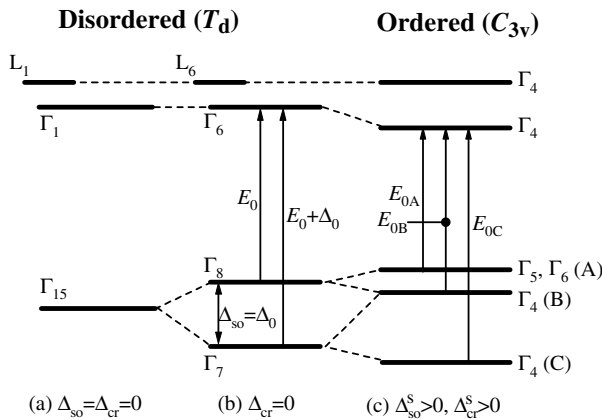


Figure 6.3 Schematic energy-band diagram of the disordered zinc-blende and ordered CuPt-B structures at the Γ point. Note that the upper CB Γ_4 in (c) derives from the back-folded L-point CB minimum L_6 in (b)

The triply degenerate Γ_{15} VB in Figure 6.3(a) is split into three states by the SO ($\Delta_{so}^s = \Delta_0^s$) and crystal-field interactions (Δ_{cr}^s). These three states can be described by the same model as that in Equation (6.1) by replacing Δ_{so} with Δ_{so}^s and Δ_{cr} with Δ_{cr}^s . The VB splitting at the top of the VB for CuPt-B ordering can then be given by

$$\Delta E_{BA}(\eta) = E_{0B}(\eta) - E_{0A}(\eta) = \frac{\Delta_{so}^s + \Delta_{cr}^s}{2} - \sqrt{\left(\frac{\Delta_{so}^s + \Delta_{cr}^s}{2}\right)^2 - \frac{2}{3}\Delta_{so}^s\Delta_{cr}^s} \quad (6.3a)$$

$$\Delta E_{CA}(\eta) = E_{0C}(\eta) - E_{0A}(\eta) = \frac{\Delta_{so}^s + \Delta_{cr}^s}{2} + \sqrt{\left(\frac{\Delta_{so}^s + \Delta_{cr}^s}{2}\right)^2 - \frac{2}{3}\Delta_{so}^s\Delta_{cr}^s} \quad (6.3b)$$

The quantities that are experimentally accessible are $\Delta E_{BA}(\eta)$, $\Delta E_{CA}(\eta)$ and $E_g(\eta) = E_{0A}(\eta)$ for partially ordered alloys and for random alloys. These values can be used to derive

$$\Delta_{so}^s(\eta) - \Delta_{so}^s(0) = \Delta_{so}^s(\eta) - \Delta_0 = \eta^2[\Delta_{so}^s(1) - \Delta_0] \quad (6.4a)$$

$$\Delta_{cr}^s(\eta) - \Delta_{cr}^s(0) = \Delta_{cr}^s(\eta) = \eta^2\Delta_{cr}^s(1) \quad (6.4b)$$

$$\Delta E_g(\eta) = E_g(\eta) - E_g(0) = \eta^2\Delta E_g(1) \quad (6.4c)$$

where $\eta=0$ and 1 describe perfectly disordered ($\Delta_{so}^s(0) = \Delta_0$ and $\Delta_{cr}^s(0) = 0$) and ordered materials, respectively, and $\Delta E_g(1)$ represents the maximum band-gap reduction for perfectly ordered material. However, since perfectly ordered ($\eta=1$) samples are unavailable, and also the degree of the order parameter η of a given sample is not usually determined directly, $\Delta_{so}^s(1)$, $\Delta_{cr}^s(1)$ and $\Delta E_g(1)$ cannot be found by this fitting procedure. Only the ratio

$$\xi = \frac{-\Delta E_g(1)}{\Delta_{so}^s(1) - \Delta_0} \quad (6.5a)$$

$$\zeta = \frac{-\Delta E_g(1)}{\Delta_{cr}^s(1)} \quad (6.5b)$$

can be determined from the measurement of $\Delta E_{BA}(\eta)$, $\Delta E_{CA}(\eta)$ and $E_g(\eta) = E_{0A}(\eta)$. On the other hand, if $(\Delta_{so}^s(1) - \Delta_0)$, $\Delta_{cr}^s(1)$ and $\Delta E_g(1)$ were known independently (e.g. from theoretical calculation), then experimental values for $\Delta E_{BA}(\eta)$, $\Delta E_{CA}(\eta)$ and $E_g(\eta)$ could be used to derive η from the above equations. The maximum band-gap reduction for perfectly ordered $\text{Ga}_{0.5}\text{In}_{0.5}\text{P}$ is reported to be 0.47 eV [8]. Perfectly ordered material has, of course, never been observed. In the most ordered $\text{Ga}_{0.5}\text{In}_{0.5}\text{P}$ structure, the highest order parameter η is ~ 0.6 [9] and the degree of ordering is nonuniform on the local scale.

In Figure 6.4 the band-gap energy reduction $\Delta E_g(\eta)$ has been plotted against the squared order parameter η^2 for $\text{Ga}_{0.5}\text{In}_{0.5}\text{P}$. The experimental data are taken from Forrest *et al.* [10]. It has been established that $\Delta E_g(\eta)$ increases almost linearly with increasing η^2 . The solid line in Figure 6.4 represents the relationship, $\Delta E_g(\eta) = 0.49\eta^2$ eV. From Equation (6.4c), the maximum band-gap reduction is found to be $\Delta E_g(1) = 0.49$ eV for perfectly ordered $\text{Ga}_{0.5}\text{In}_{0.5}\text{P}$.

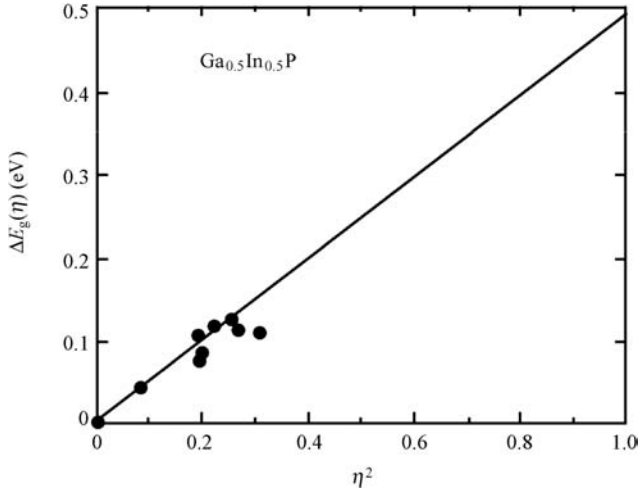


Figure 6.4 Band-gap energy reduction $\Delta E_g(\eta)$ against squared order parameter η^2 for $\text{Ga}_{0.5}\text{In}_{0.5}\text{P}$. The experimental data are taken from Forrest *et al.* [10]. The solid line shows the relationship, $\Delta E_g(\eta) = 0.49\eta^2$ eV

6.2 GROUP-IV SEMICONDUCTOR ALLOY

6.2.1 Binary Alloy

(a) CSi

The indirect and direct gap energies E_g^X and E_0 for diamond and Si, together with those for 3C-SiC ($x = 0.5$) are shown in Figure 6.5. The experimental data are taken from Table 6.1. The solid lines in Figure 6.5 show the best fit of these data using the parabolic expressions (in eV)

$$E_g^X(x) = 1.12 + 0.70x + 3.68x^2 \quad (6.6)$$

$$E_0(x) = 4.06 + 2.12x + 9.12x^2 \quad (6.7)$$

There is, however, some ambiguity about the band-gap energies and band lineups in $\text{C}_x\text{Si}_{1-x}/\text{Si}$ heterostructures. The large tensile strain in pseudomorphic $\text{C}_x\text{Si}_{1-x}$ layers on Si is expected to strongly affect the band edges (see Section 9.1.2).

The higher-lying CPs of supersaturated $\text{C}_x\text{Si}_{1-x}$ ($x < 0.02$) have become the origin of some controversy in the literature. Using ER and SE, Kissinger *et al.* [11] and Zollner *et al.* [12] found that the E_1 gap in $\text{C}_x\text{Si}_{1-x}$ increases linearly with increasing x , as shown in Figure 6.6. The slopes in Figure 6.6 at 300 K give $\Delta E_1 = 35$ meV/at%[C] and $\Delta E_0' = 7$ meV/at%[C]. On the other hand, Demkov and Sankey [13] argued that the band gaps of free-standing $\text{C}_x\text{Si}_{1-x}$ should decrease with increasing x . For strained pseudomorphic alloy, the lower of the two strain-split E_1 energies should decrease even more. Additional weak structures in the SE spectra of $\text{C}_x\text{Si}_{1-x}$ and $\text{C}_x\text{Si}_y\text{Ge}_{1-x-x}$ at 2.7 and 3.0 eV were, indeed, observed by Zollner *et al.* [12] and Lee *et al.* [14]. These structures were interpreted as previously unidentified optical transitions in the materials due to defects or C-related bands [14]. More recently, Zollner *et al.* [15] suggested

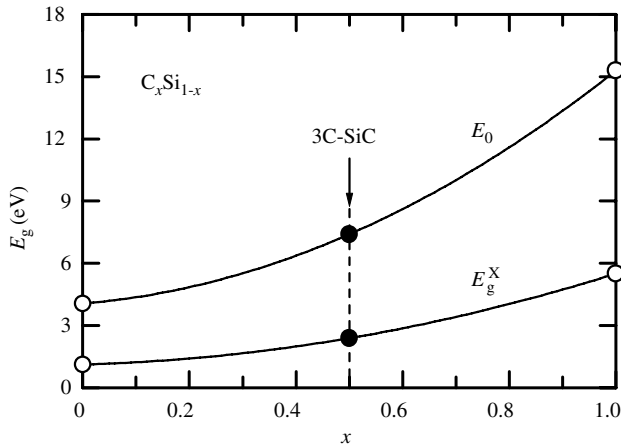


Figure 6.5 Energies of the indirect gap E_g^X and direct gap E_0 for diamond and Si at 300 K, together with those for 3C-SiC ($x = 0.5$). The open circles represent the endpoint elemental data in Table 6.1. The solid lines show the best-fit results of these data using Equations (6.6) and (6.7)

that the new structures are actually interference fringes originating from the reflection of light at the alloy/substrate interface.

(b) CGe

Figure 6.7 shows the lowest indirect gap energies E_g^X and E_g^L versus x for C_xGe_{1-x} . Kolodzey *et al.* [16] measured the optical absorption spectra of C_xGe_{1-x} grown on Si(1 0 0) by MBE. Schrader *et al.* [17] also carried out optical absorption measurements on C_xGe_{1-x}/Si deposited by hollow-cathode sputtering. The E_g^L values obtained from these studies are shown in Figure 6.7 by the open and solid circles. The linearly interpolated E_0 and E_g^X values using

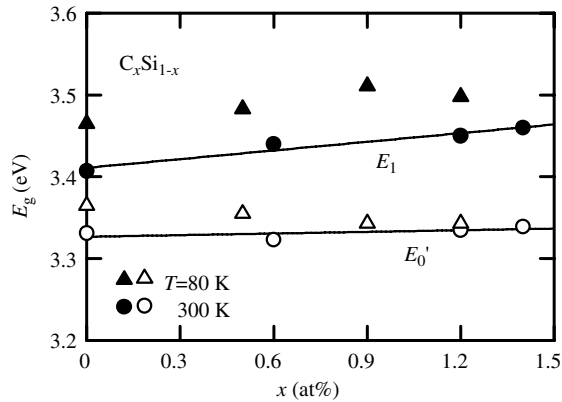


Figure 6.6 Energies of the $\Delta E_0'$ and E_1 CPs versus x for C_xSi_{1-x} at 300 K. The experimental data are taken from Kissinger *et al.* [11] (solid and open triangles) and Zollner *et al.* [12] (solid and open circles). The slopes shown by the solid lines give $\Delta E_1 = 35 \text{ meV/at\% [C]}$ and $\Delta E_0' = 7 \text{ meV/at\% [C]}$ (at 300 K)

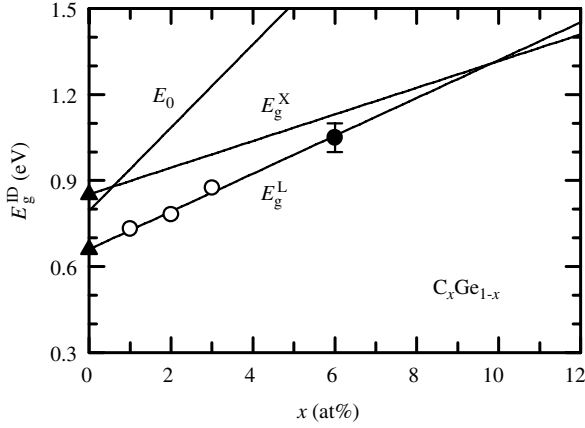


Figure 6.7 Energies of the lowest indirect gaps E_g^L and E_g^X and direct gap E_0 versus x for C_xGe_{1-x} at 300 K. The experimental data are taken from Kolodzey *et al.* [16] (open circles) and Schrader *et al.* [17] (solid circle). The solid triangles represent the endpoint elemental data in Table 6.1. The solid lines show the calculated results using data in Table 6.3

the endpoint data in Table 6.1 are shown by the solid lines. Table 6.3 summarizes the three main band-gap energies E_0 , E_g^X and E_g^L for C_xGe_{1-x} . From these results, we can expect the $E_g^X - E_g^L$ crossover to occur at $x \sim 0.1$. Extrapolation gives an E_g^L value of ~ 7.26 eV for diamond.

Table 6.3 Energies for some indirect and direct gaps in C_xGe_{1-x} at 300 K. LF = linear fit; LI = linear interpolation

Band Gap	Expression (eV)	Remark
E_g^L	$0.66 + 6.60x$	LF
E_0	$0.795 + 14.505x$	LI
E_g^X	$0.852 + 4.648x$	LI

The higher-lying CPs, such as E_1 , $E_1 + \Delta_1$, E'_0 and E_2 , for C_xGe_{1-x} have been determined using SE for x up to 0.03 [18]. These CPs are found to be roughly the same as those which do not contain C.

(c) SiGe

1. *Relaxed alloy*—The binary alloy of Si and Ge provides a continuous series of materials with gradually varying physical properties. The physical properties of Si_xGe_{1-x} grown on Si have been under extensive study stimulated by their potential for use in various device applications. Due to the large lattice mismatch ($\Delta a/a \sim 4\%$), however, the critical layer thickness for pseudomorphic Si_xGe_{1-x} growth decreases drastically with increasing x [19]. The lattice constant of ‘relaxed,’ or in other words ‘unstrained’ Si_xGe_{1-x} , has been measured and showed to obey Vegard law (Section 1.4.3).

The composition dependence of the fundamental absorption edge in Si_xGe_{1-x} was first determined by Braunstein *et al.* [20] using optical absorption and more recently by Weber

and Alonso [21] using PL measurements. Figure 6.8(a) shows the results obtained by Braunstein *et al.* [20]. The crossing-over of the lowest-lying CB states from the L point to the X point (or Δ direction) is found at $x \sim 0.15$. Thus, the conduction electron nature of $\text{Si}_x\text{Ge}_{1-x}$ changes from ‘Ge-like’ to ‘Si-like’ at $x \sim 0.15$. The solid lines in Figure 6.8(a) represent the results calculated from the data in Table 6.4.

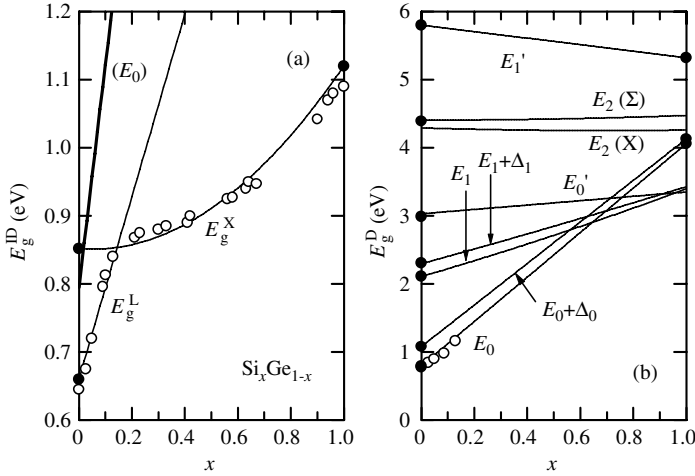


Figure 6.8 (a) Energies of the fundamental absorption edges E_g^L and E_g^X versus x for relaxed $\text{Si}_x\text{Ge}_{1-x}$ at 300 K. The experimental data are taken from Braunstein *et al.* [20]. (b) Energies of some CPs versus x for $\text{Si}_x\text{Ge}_{1-x}$ at 300 K. The solid circles in (a) and (b) represent the endpoint elemental data in Table 6.1 and Adachi [1]. The solid lines in (a) and (b) show the calculated results using the data in Table 6.4

The direct gap energies in relaxed $\text{Si}_x\text{Ge}_{1-x}$ have been determined using various measurement techniques, such as SE and ER. Table 6.4 summarizes the lowest direct and

Table 6.4 Energies for some indirect and direct gaps in relaxed $\text{Si}_x\text{Ge}_{1-x}$ at 300 K. LI = linear interpolation; QF = quadratic fit

Band Gap	Expression (eV)	Remark
E_g^L	$0.66 + 1.34x$	LI
E_0	$0.795 + 3.265x$	LI
E_g^X	$0.852 - 0.032x + 0.300x^2$	QF
$E_0 + \Delta_0$	$1.08 + 3.05x$	LI
E_1	$2.108 + 1.134x + 0.153x^2$	<i>a</i>
$E_1 + \Delta_1$	$2.296 + 1.070x + 0.062x^2$	<i>a</i>
E_0'	$3.03 + 0.32x$	<i>a</i>
$E_2(X)$	$4.291 - 0.116x + 0.084x^2$	<i>b</i>
$E_2(\Sigma)$	$4.406 - 0.005x + 0.072x^2$	<i>b</i>
E_1'	$5.80 - 0.48x$	LI

^aC. Pickering *et al.*, *Proc. SPIE* **1985**, 414 (1993)

^bJ. H. Bahng *et al.*, *J. Phys.: Condens. Matter* **13**, 777 (2001)

higher-lying direct gap energies in relaxed $\text{Si}_x\text{Ge}_{1-x}$ alloy. Note that the E_2 transitions in Si (and $\text{Si}_x\text{Ge}_{1-x}$) occur not only along the $\langle 110 \rangle$ direction (Σ) but also near the X point (or Δ direction). All these CPs, including E_0 and $E_0 + \Delta_0$, are plotted against x in Figure 6.8(b). Except for E_0' and E_2 , the band-gap energies in $\text{Si}_x\text{Ge}_{1-x}$ are found to be fairly sensitive to x .

2. *Strained alloy*—The band structure of pseudomorphical $\text{Si}_x\text{Ge}_{1-x}$ epilayers on Si(100) substrates is drastically altered by the built-in strain or stress. The remarkable effect of the biaxial or uniaxial stress on the band structure is to split the HH ($3/2, \pm 3/2$) and LH ($3/2, \pm 1/2$) degeneracy at the Γ point (see Figure 8.1 in Adachi [1]). The biaxial tetragonal distortion can also shift and split the CB edge, for example, the sixfold degenerate CB minima at the X point or along Δ in bulk Si split into twofold and fourfold minima under [001] compressive strain [1].

The fundamental absorption edge of strained $\text{Si}_x\text{Ge}_{1-x}/\text{Si}(100)$ has been investigated by several authors using photocurrent [22] and PL [23,24]. These results are summarized in Figure 6.9. The heavy gray lines show the theoretical results obtained by People [25]. The experimental data agree well with the theoretical values.

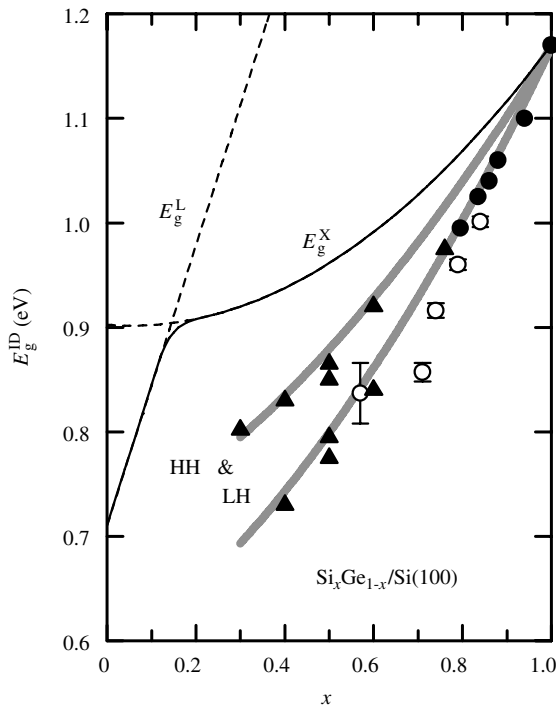


Figure 6.9 Energies of the fundamental absorption edges E_g^L and E_g^X versus x for strained $\text{Si}_x\text{Ge}_{1-x}/\text{Si}(100)$ epilayer. The experimental data are taken from Lang *et al.* [22] (solid triangles, at 90 K), Dutartre *et al.* [23] (solid circles, at 90 K) and Liu *et al.* [24] (at 77 K, open circles). The light solid line shows the low-temperature values of relaxed $\text{Si}_x\text{Ge}_{1-x}$ epilayer. The heavy gray lines show the theoretical results of People [25]

SE, ER and PR techniques have been used to determine the CP energies in strained $\text{Si}_x\text{Ge}_{1-x}/\text{Si}$ epilayers [26–30]. A decrease in the E_1 energy with increasing x , compared with that observed in relaxed $\text{Si}_x\text{Ge}_{1-x}$ samples, has been reported [26,27]. On the other hand, Bahng *et al.* [29] reported an increase in the $E_1/(E_1 + \Delta_1)$, $\Delta E'_0$ and E_2 energies with increasing in-built strain in strained $\text{Si}_{0.8}\text{Ge}_{0.2}/\text{Si}(100)$, where the strain was controlled by depositing different thickness of the $\text{Si}_{0.8}\text{Ge}_{0.2}$ epilayers from 35 to 350 nm. In the case of the externally applied uniaxial stress $X||[001]$, the E_1 energy in bulk Si decreased (increased) with increasing X for the light polarization $E||X$ ($E\perp X$) used in the SE measurements [31]. Therefore, attention must be paid to analyzing the effects of in-built strain on the electronic energy-band structure of strained materials based on the standard DP theory [1].

3. *External perturbation effect*—The temperature dependence of the fundamental absorption edge in relaxed $\text{Si}_x\text{Ge}_{1-x}$ alloy was measured by Braunstein *et al.* [20]. The experimental data were found to be essentially the same as those for bulk Si and Ge [1]. The temperature dependence of the higher-lying CPs in relaxed and strained $\text{Si}_x\text{Ge}_{1-x}$ has been measured by Humlíček *et al.* [32] and Ebner *et al.* [30], respectively. The relaxed alloy data obtained are: $dE_1/dT \sim (3 \pm 1) \times 10^{-4}$ eV/K and $dE_2/dT \sim (2-4) \times 10^{-4}$ eV/K ($x=0-1.0$). All strained-alloy CP data also satisfactorily fitted the phenomenological formulas of Varshni and Viña [1].

The influence of hydrostatic pressure on the ER spectra of relaxed $\text{Si}_x\text{Ge}_{1-x}$ alloy has been reported to be given by $dE_1/dp = 7.8 - 1.6x$ meV/kbar and $dE'_0/dp = 1.4 - 0.4x$ meV/kbar [33].

(d) *GeSn*

The fundamental absorption edge in $\text{Ge}_x\text{Sn}_{1-x}$ is expected to change from the Ge L_6^- indirect to the Sn Γ_7^- direct gap depending on x . The band structure near the direct–indirect transition region in relaxed or epitaxial $\text{Ge}_x\text{Sn}_{1-x}$ films has been studied using optical absorption [34,35], SE [36,37] and PR [37]. Figure 6.10(a) shows the E_0 and E_g^L energies versus x for nearly relaxed $\text{Ge}_x\text{Sn}_{1-x}$ ($1.0 > x \geq 0.85$) deposited on 10 nm thick relaxed Ge buffer layers on Si(100) substrates by MBE [34] and those obtained for epitaxial $\text{Ge}_x\text{Sn}_{1-x}$ films ($1.0 > x \geq 0.86$) deposited on Ge(100) substrates by rf magnetron sputtering [35]. Note that α -Sn (gray tin) is a zero gap semiconductor (i.e. semimetal) with degenerate valence and conduction bands at the center of the BZ. Thus, the lowest direct gap energy $E_0(\Gamma_8^+ \rightarrow \Gamma_7^-)$ in α -Sn has a negative value (-0.413 eV at 1.5 K, see Table 6.1). The solid lines in Figure 6.10(a) represent the quadratic fits of the experimental data. The resulting expressions are given in Table 6.5. These expressions predict that E_0 and E_g^L become zero at $x \sim 0.67$ and ~ 0.25 , respectively. $\text{Ge}_x\text{Sn}_{1-x}$ should therefore be a semimetal at up to $x \sim 0.7$. These expressions also predict that E_0 and E_g^L cross at $x \sim 0.88$.

The interband transition energies in $\text{Ge}_x\text{Sn}_{1-x}$ have been studied by D'Costa *et al.* [37]. Because of insufficient sensitivity of SE for energies below 1 eV, they carried out PR measurements at 15 K. Like E_0 (Figure 6.10(a)), $E_0 + \Delta_0$, $E_1/(E_1 + \Delta_1)$, E_0' and E_2 decreased with increasing Sn concentration. From the quadratic fits of the 15 K data, they determined the bowing parameter of each CP. Introducing these parameters and binary data into Equation (A.17), we obtain the CP energies of $\text{Ge}_x\text{Sn}_{1-x}$ at 300 K, as listed in Table 6.5. The numeric results of these expressions are shown in Figure 6.10(b).

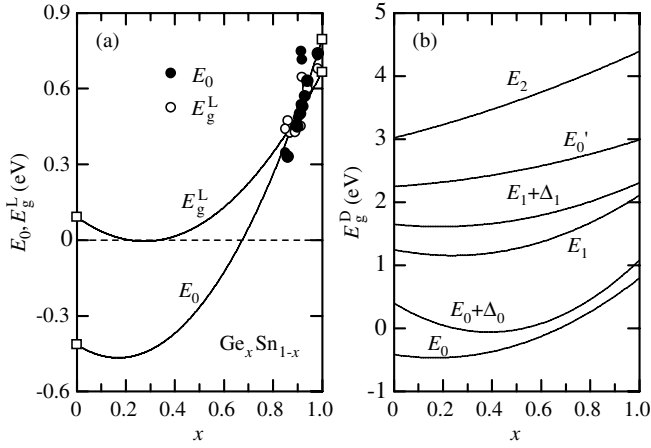


Figure 6.10 (a) Energies of the lowest direct E_0 (solid circles) and lowest indirect gap E_g^L (open circles) versus x for $\text{Ge}_x\text{Sn}_{1-x}$ at 300 K. The experimental data are taken from He and Atwater [34] and de Guevara *et al.* [35]. (b) Energies of some CPs versus x for $\text{Ge}_x\text{Sn}_{1-x}$ at 300 K. The solid lines in (a) and (b) show the calculated results using the data in Table 6.5

Table 6.5 Energies for some indirect and direct gaps in $\text{Ge}_x\text{Sn}_{1-x}$ at 300 K. QF = quadratic fit

Band Gap	Expression (eV)	Remark
E_0	$-0.413 - 0.617x + 1.826x^2$	QF
E_g^L	$0.092 - 0.702x + 1.275x^2$	QF
$E_0 + \Delta_0$	$0.40 - 2.36x + 3.04x^2$	<i>a</i>
E_1	$1.25 - 0.79x + 1.65x^2$	<i>a</i>
$E_1 + \Delta_1$	$1.65 - 0.39x + 1.05x^2$	<i>a</i>
E_0'	$2.25 + 0.25x + 0.49x^2$	<i>a</i>
E_2	$3.02 + 0.97x + 0.40x^2$	<i>a</i>

^aBowing parameter is obtained from V. R. D'Costa *et al.* (*Phys. Rev. B* **73**, 125207 (2006))

6.2.2 Ternary Alloy

(a) CSiGe

As mentioned in Section 1.4.3, $\text{C}_x\text{Si}_y\text{Ge}_{1-x-y}$ can be grown lattice-matched on Si substrate. The smaller C addition compensates the compressive strain in $\text{Si}_x\text{Ge}_{1-x}$ binary layers and thus relieves thickness limitations in $\text{Si}_x\text{Ge}_{1-x}$ growth. Furthermore, the major band offset in $\text{Si}_x\text{Ge}_{1-x}/\text{Si}$ heterojunction is in the CB, which, in connection with the VB offset in the $\text{Si}_x\text{Ge}_{1-x}/\text{Si}$, has already been opened up a wide variety of new electronic and optical properties within the $\text{Si}_x\text{Ge}_{1-x}/\text{Si}$ heterojunction system.

Amour *et al.* [38] have grown pseudomorphic $\text{C}_x\text{Si}_y\text{Ge}_{1-x-y}/\text{Si}(100)$ layers by rapid thermal CVD and measured PL spectra at temperatures between 2 and 77 K. We show in Figure 6.11 the lowest gap energy E_g^L versus biaxial compressive strain for pseudomorphic $\text{Si}_x\text{Ge}_{1-x}$ (adopted

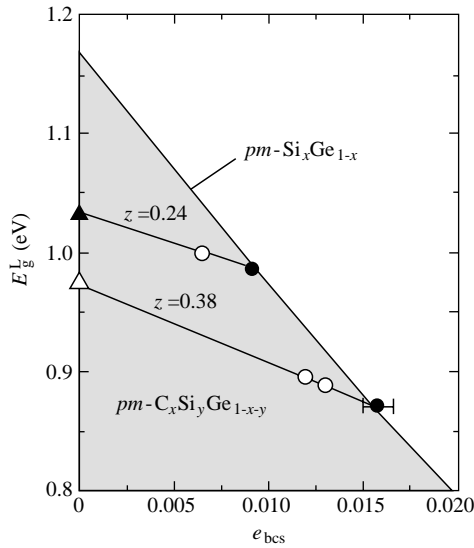


Figure 6.11 Energies of the fundamental absorption edge E_g^L versus biaxial compressive strain e_{bcs} for pseudomorphic (pm -) $\text{Si}_x\text{Ge}_{1-x}$ and $pm\text{-C}_x\text{Si}_y\text{Ge}_{1-x-y}$ ($z = 1-x-y$) at 77 K. The experimental data are taken from Amour *et al.* [38] (solid and open circles). The $pm\text{-Si}_x\text{Ge}_{1-x}$ line is taken from Van de Walle and Martin [39]. The $e_{\text{bcs}} = 0$ compositions are estimated to be $x = 0.05$ (0.03) and $y = 0.57$ (0.73) for $z = 0.38$ (0.24)

from Van de Walle and Martin [39]) and Amour's data. Adding C into $\text{Si}_x\text{Ge}_{1-x}$ and keeping the constant Ge content, the strain decreases and E_g^L increases, but the increase in E_g^L is much less than it would be if the strain was reduced simply by reducing the Ge content without adding C atoms. Amour *et al.* considered that for a given band gap, $\text{C}_x\text{Si}_y\text{Ge}_{1-x-y}$ has less strain than does $\text{Si}_x\text{Ge}_{1-x}$. The average slope of the $\text{C}_x\text{Si}_y\text{Ge}_{1-x-y}$ data, $\Delta E_g^L/\Delta e_{\text{bcs}} = -6.1$ eV/unit strain, corresponds to $\Delta E_g^L/\Delta x = +21$ meV/at% [C] [38]. Furthermore, by linearly extrapolating the $\text{C}_x\text{Si}_y\text{Ge}_{1-x-y}$ data to zero e_{bcs} , a significant band offset to Si for strain-free $\text{C}_x\text{Si}_y\text{Ge}_{1-x-y}$ films is obtained. For $z = 1-x-y = 0.38$, the band offset would be ~ 0.19 eV. From Table 1.8, we can estimate the $e_{\text{bcs}} = 0$ compositions to be $x = 0.05$ (0.03) and $y = 0.57$ (0.73) for $z = 0.38$ (0.24).

Schmidt and Eberl [40] grew strained, exactly strain compensated and compressively strained $\text{C}_x\text{Si}_y\text{Ge}_{1-x-y}$ layers on Si by MBE and measured their PL spectra at 8 K. In Figure 6.12 E_g^L has been plotted against Ge composition for exactly strain compensated, relaxed $\text{C}_x\text{Si}_y\text{Ge}_{1-x-y}$ layers obtained by Schmidt and Eberl. Note that the E_g^L energies plotted in Figure 6.12 were obtained from the zero-phonon PL peaks by adding the indirect-exciton binding energy to coincide with the value of $E_g^L = 1.17$ eV at 8 K for bulk Si [1]. These plots can be fitted by a linear decrease with $\Delta E_g^L/\Delta z = -8.4$ meV/at% [Ge], or equivalently, $\Delta E_g^L/\Delta x = -68$ meV/at% [C]. Schmidt and Eberl [40] also observed an initial increase in PL peak energies on the way from tensile strained $\text{C}_x\text{Si}_{1-x}$ as well as from compressively strained $\text{Si}_x\text{Ge}_{1-x}$ towards exactly strain compensated $\text{C}_x\text{Si}_y\text{Ge}_{1-x-y}$.

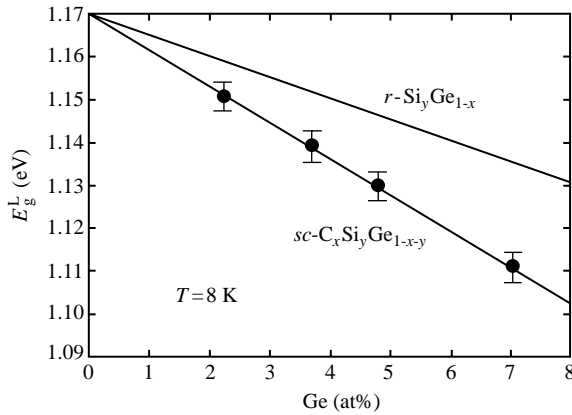


Figure 6.12 Energies of the fundamental absorption edge E_g^L versus Ge atomic composition for exactly strain compensated (sc -) $C_xSi_yGe_{1-x-y}$ layers at 8 K reported by Schmidt and Eberl [40]. The E_g^L energies were estimated from the zero-phonon PL peaks by adding the indirect-exciton binding energy to coincide with the band gap of $E_g^L = 1.17$ eV at 8 K for bulk Si. For comparison, the relaxed (r -) Si_yGe_{1-y} line is plotted against Ge atomic composition

The higher-lying CPs, such as E_1 and E_2 , in $C_xSi_yGe_{1-x-y}/Si(100)$ films were studied using SE and ER [18,41,42]. The E_1 gap increased and the E_2 gap decreased as x increased for Si-rich $C_xSi_yGe_{1-x-y}$ alloy [41,42]. For Ge-rich $C_xSi_yGe_{1-x-y}$ alloy, C had no detectable influence on the higher-lying CPs [18].

(b) SiGeSn

Single-phase $Si_xGe_ySn_{1-x-y}$ alloys with $x \leq 0.25$ and $y \geq 0.64$ were grown on Si(100) by CVD [43,44]. SE of selected samples yielded dielectric functions indicating a band structure consistent with highly crystalline semiconductors of diamond symmetry. Incorporation of Si into Ge_xSn_{1-x} led to an additional reduction of E_2 , as expected based on the E_2 values of Si and Ge [43].

6.2.3 Summary

We have discussed the energy band gaps in some group-IV semiconductor alloys. Figure 6.13 summarizes the fundamental absorption gap E_g versus lattice constant a for some binary alloys. We find that all binary gaps, except for Ge_xSn_{1-x} ($0 \leq x \leq 0.88$), are indirect. The Ge_xSn_{1-x} alloy for $0.67 \leq x \leq 0.88$ is a direct gap semiconductor, but becomes semimetallic for $x \leq 0.67$. We can thus suppose that almost all ternary gaps, like $C_xSi_yGe_{1-x-y}$, are indirect.

C_xSi_{1-x} is estimated to have an indirect gap at X (E_g^X) over the whole composition range, while C_xGe_{1-x} may have an indirect gap at L (E_g^L) for $0 \leq x \leq 0.09$ and at X for the rest. The band-gap energy of C_xGe_{1-x} lattice-matched to 3C-SiC can be derived from Figure 6.13. The lattice constant a of 3C-SiC is 4.3596 Å. The corresponding x and E_g^X for $C_xGe_{1-x}/3C$ -SiC are ~ 0.62 and ~ 3.7 eV, respectively. The fundamental absorption edge of 3C-SiC is ~ 2.39 eV (E_g^X , Table 6.1). Because of its wide band-gap nature, $C_{0.62}Ge_{0.38}$ can be used as a new gate or a

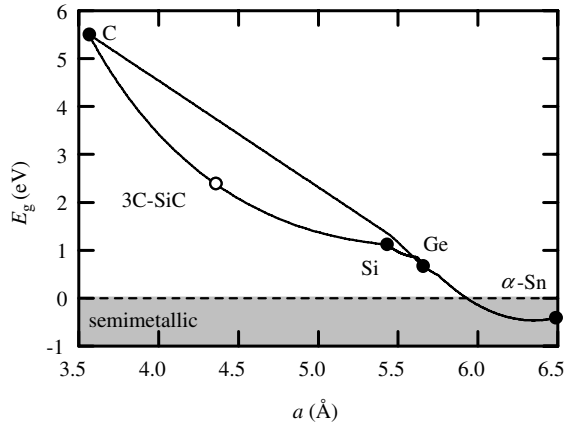


Figure 6.13 Lowest band-gap energy E_g versus cubic lattice constant a for some group-IV binary alloys at 300 K. The 3C-SiC data is plotted for comparison

barrier material for 3C-SiC FETs. It should be noted, however, that an interpolation scheme proposed by Soref [45] gives the nearly same E_g^X values between C_xGe_{1-x} /3C-SiC alloy and 3C-SiC.

The E_1 -gap bowing parameters c are determined to be 0.153 and 1.65 eV for Si_xGe_{1-x} and Ge_xSn_{1-x} , respectively (Tables 6.4 and 6.5). In Figure 6.14 these values are plotted against the product $\Delta a_{AB}\Delta X_{AB}$ of the lattice constant (Δa_{AB}) and electronegativity differences (ΔX_{AB}) between the elemental semiconductors A and B. The electronegativity values were taken from Phillips’s definition [46]. The bowing parameter c increases almost linearly with increasing product $\Delta a_{AB}\Delta X_{AB}$ (c in eV, $\Delta a_{AB}\Delta X_{AB}$ in ÅeV)

$$c = 9.93(\Delta a_{AB}\Delta X_{AB}) \tag{6.8}$$

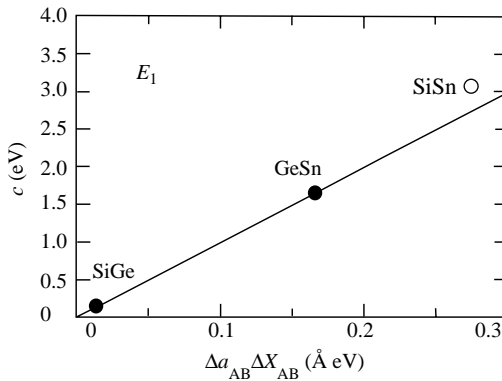


Figure 6.14 Bowing parameter c of the E_1 gap versus product $\Delta a_{AB}\Delta X_{AB}$ of the lattice-constant and electronegativity differences between the endpoint elements A and B in the binary alloy A_xB_{1-x} . The SiSn data (open circle) is taken from D’Costa *et al.* [44]. The solid line represents the calculated result using Equation (6.8)

D'Costa *et al.* [44] obtained $c \sim 3.05$ eV for $\text{Si}_x\text{Sn}_{1-x}$ from the SE analyses in the $E_1/(E_1 + \Delta_1)$ region of $\text{Si}_x\text{Ge}_y\text{Sn}_{1-x-y}$. The open circle in Figure 6.14 represents the data of D'Costa *et al.* We can conclude that the c values in the Si–Ge–Sn alloy system follows a simple scaling behavior that can be expressed in terms of the electronegativity and lattice mismatches (Equation (6.8)). It should be noted, however, that Equation (6.8) estimates in considerably large bowing parameters c for C-related alloys, ~ 20 , ~ 24 and ~ 39 eV for $\text{C}_x\text{Si}_{1-x}$, $\text{C}_x\text{Ge}_{1-x}$ and $\text{C}_x\text{Sn}_{1-x}$, respectively. Further study is, therefore, needed to elucidate this unexpected point.

6.3 III–V SEMICONDUCTOR TERNARY ALLOY

6.3.1 (III, III)–N Alloy

(a) c -AlGaN

Due to their metastable nature, the growth of single-phase cubic nitride films of sufficient homogeneity and crystal quality is still difficult and, in general the crystal quality of the cubic III–N layers grown so far is inferior to that of the hexagonal nitrides. The E_0 edge of c - $\text{Al}_x\text{Ga}_{1-x}\text{N}$ has been studied using SE [47–49]. These results are shown in Figure 6.15(a). We can see that the experimental data of Kasic *et al.* [49] gives larger E_0 values than those obtained by Suzuki *et al.* [48]. As a result, the linear interpolation scheme explains Kasic's data very well, as shown by the heavy solid line. The electronegativity and size mismatch

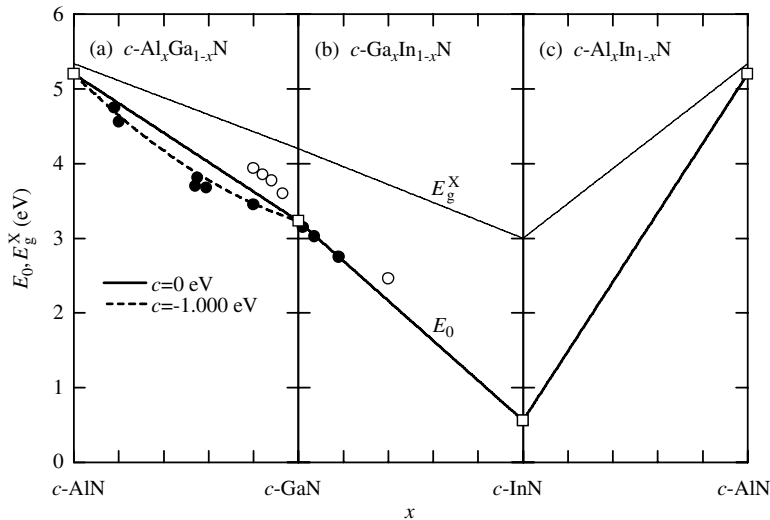


Figure 6.15 Energies of the lowest direct E_0 and indirect gaps E_g^X for (a) c - $\text{Al}_x\text{Ga}_{1-x}\text{N}$, (b) c - $\text{Ga}_x\text{In}_{1-x}\text{N}$ and (c) c - $\text{Al}_x\text{In}_{1-x}\text{N}$ at 300 K. The experimental data in (a) are taken from Suzuki *et al.* [48] (solid circles) and Kasic *et al.* [49] (open circles) and in (b) from Müllhäuser *et al.* [71] (open circle) and Goldhahn *et al.* [72] (solid circles). The theoretical curves are calculated from Table 6.6

product scale also predicts a very small bowing parameter $c \sim 0.07$ eV for $c\text{-Al}_x\text{Ga}_{1-x}\text{N}$ (Equation (6.23)).

No experimental data has been reported on the X- and L-valley gaps E_g^X and E_g^L for any binary nitrides or their alloys. All theoretical work, however, has suggested that in all III–N semiconductors the X-valley CB is located at a lower energy than the L-valley CB (i.e. $E_g^X < E_g^L$) [50]. Thompson *et al.* [51] carried out SE measurements on $c\text{-AlN}$ and concluded from the gradual onset of the absorption edge that $c\text{-AlN}$ is an indirect gap semiconductor. The gap that they obtained is ~ 5.34 eV (E_g^X). It should be noted, however, that it is very difficult to determine an indirect absorption edge, which usually has very weak transition strength, using SE. Thus, optical absorption or transmission measurements are needed to directly determine whether $c\text{-AlN}$ is a direct or an indirect gap semiconductor. The light solid line in Figure 6.15(a) shows the linear interpolation result of the theoretical E_g^X values for $c\text{-AlN}$ and $c\text{-GaN}$ [50]. The corresponding E_g^X and E_0 versus x formulas are listed in Table 6.6. The heavy dashed line also represents the result of Equation (A.5) with $c = 1.000$ eV. This value is recommended for $w\text{-Al}_x\text{Ga}_{1-x}\text{N}$ ($c = 1.00$ eV, see Table 6.7). The E_1 and E_2 CPs in $c\text{-Al}_x\text{Ga}_{1-x}\text{N}$ are also found to be blue- and red-shifted respectively, with increasing x for $x \leq 0.12$, [49].

(b) $w\text{-AlGaN}$

The experimental E_0 versus x data for $w\text{-Al}_x\text{Ga}_{1-x}\text{N}$ [52–55] are shown in Figure 6.16(a). The bowing parameter c of E_0 varies widely from upward to deep downward bowing [56,57]. Lee *et al.* [58] noted that the early findings of an upward bowing have generally not been duplicated. Although there have been many reports of c for $x < 0.4$, very few data have been reported for

Table 6.6 Energies for some direct and indirect gaps in cubic (III, III)–N ternaries at 300 K. LF = linear fit; LI = linear interpolation; QF = quadratic fit

Ternary	Band gap	Expression (eV)	Remark
$\text{Al}_x\text{Ga}_{1-x}\text{N}$	E_0	$3.231 + 1.969x$	LF (LI)
	E_0	$3.231 + 0.969x + 1.000x^2$	QF
	E_g^X	$4.20 + 1.14x$	LI
$\text{Al}_x\text{In}_{1-x}\text{N}$	E_0	$0.56 + 4.64x$	LI
	E_g^X	$3.00 + 2.34x$	LI
$\text{Ga}_x\text{In}_{1-x}\text{N}$	E_0	$0.560 + 2.671x$	LF (LI)
	E_g^X	$3.0 + 1.2x$	LI

Table 6.7 Energy for E_0 in some wurtzite (III, III)–N ternaries at 300 K. QF = quadratic

Ternary	E_0 (eV)	Remark
$\text{Al}_x\text{Ga}_{1-x}\text{N}$	$3.42 + 1.78x + 1.00x^2$	QF
$\text{Al}_x\text{In}_{1-x}\text{N}$	$0.70 + 1.80x + 3.70x^2$	QF
$\text{Ga}_x\text{In}_{1-x}\text{N}$	$0.700 + 1.080x + 1.640x^2$	QF

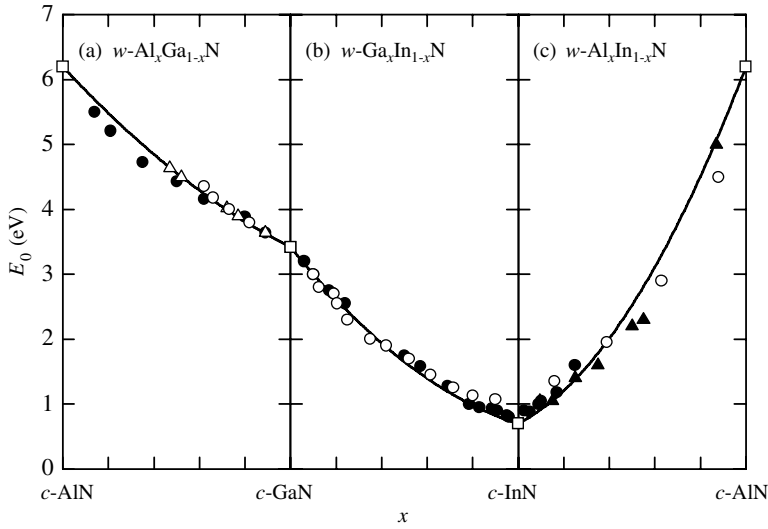


Figure 6.16 Energies of the lowest direct gap E_0 for (a) $w\text{-Al}_x\text{Ga}_{1-x}\text{N}$, (b) $w\text{-Ga}_x\text{In}_{1-x}\text{N}$ and (c) $w\text{-Al}_x\text{In}_{1-x}\text{N}$ at 300 K. The experimental data in (a) are taken from Brunner *et al.* [52] (solid circles), Muth *et al.* [53] (open circles), Meyer *et al.* [54] (solid triangles) and Buchheim *et al.* [55] (open triangles). The experimental data in (b) and (c) are taken from Wu and Walukiewicz [65] (solid circles), Androulidaki *et al.* [66] (open circles) and Terashima *et al.* [67] (solid triangles, (c)). The open squares in (a)–(c) represent the endpoint binary data taken from Table 6.2. The solid lines have been calculated from the data in Table 6.7

$x > 0.5$ [54,57,59]. It can be seen that such higher x samples tend to give smaller E_0 values, although the $w\text{-AlN}$ ($x = 1.0$) value is relatively large ($E_0 \sim 6.2$ eV, Figure 6.16(a)). The apparent observation of the stronger bowing in the higher x region is actually an artifact resulting from defect- or impurity-related transitions at energies below the band gap [60].

The solid line in Figure 6.16(a) shows the calculated E_0 curve using a recommended value of $c = -1.00$ eV, as summarized in Table 6.7. This value is in good agreement with the results of Yun *et al.* [61]. Wethkamp *et al.* [59] also reported the x dependence of the higher-lying CPs at $E_1 \sim 7$ eV and $E_2 \sim 8$ eV, together with an unidentified peak at $E_7 \sim 13$ eV.

The temperature and pressure dependence of the band-gap energies has been measured for III–N binaries [50]. There have, however, been relatively few studies on the III–N alloys. Malikova *et al.* [62] measured the temperature dependence of the excitonic A, B and C peaks in $w\text{-Al}_{0.05}\text{Ga}_{0.95}\text{N}$ in the 16–434 K range using contactless ER and analyzing the results with Varshni and Bose–Einstein expressions [1]. Brunner *et al.* [52] measured the absorption spectra of MBE-grown $w\text{-Al}_x\text{Ga}_{1-x}\text{N}$ ($0 \leq x \leq 1.0$) from 7 K up to room temperature, from which a negligible x dependence of the Varshni coefficients α and β was observed. More recently, Nepal *et al.* [63] employed deep-UV PL to study the temperature and composition dependence of the band-gap energies of MOCVD-grown $w\text{-Al}_x\text{Ga}_{1-x}\text{N}$ ($0 \leq x \leq 1.0$) in the range between 10 and 800 K. A quadratic dependence of the Varshni coefficients α and β with x was obtained, from which we can calculate the band-gap energy of $w\text{-Al}_x\text{Ga}_{1-x}\text{N}$ with optional x and T .

The pressure dependence of E_0 in $w\text{-Al}_x\text{Ga}_{1-x}\text{N}$ at $0 \leq x \leq 0.6$ grown by MOCVD on (0001)-sapphire substrates has been investigated by Shan *et al.* [64] for pressures of up to 9 GPa. They reported dE_0/dp to be ~ 40 meV/GPa.

(c) *c-AlInN*

No detailed experimental data has been reported on the band-gap energies in $c\text{-Al}_x\text{In}_{1-x}\text{N}$. We, therefore, show in Figure 6.15(c) the linearly interpolated results of E_0 and E_g^X using the experimental and theoretical endpoint data, respectively (Table 6.6).

(d) *w-AlInN*

The recent experimental studies which reported the E_0 of InN to be appreciably below 1 eV compared to the long-accepted value of ~ 2 eV, have initiated a continuing controversy concerning this fundamental quantity of the least studied III–N binary compound, InN. Also, obtaining high-quality Al-based semiconductors (AlN, AlP, AlAs, etc.) is very difficult as a consequence of its significantly higher contamination with residual impurities. Thus, the standard quadratic expression did not provide a reasonable fit to the compositional variation of E_0 in $w\text{-Al}_x\text{In}_{1-x}\text{N}$ [56].

The experimental E_0 versus x data for $w\text{-Al}_x\text{In}_{1-x}\text{N}$ is shown in Figure 6.16(c). The recent literature data are taken from Wu and Walukiewicz [65], Androulidaki *et al.* [66] and Terashima *et al.* [67]. These data suggest relatively large downward bowing. The solid line in Figure 6.16(c) shows the parabolic fit of these experimental data. The recommended bowing parameter is very large, $c \sim 3.70$ eV, as listed in Table 6.7.

Goldhahn *et al.* [68] measured the SE spectra of $w\text{-Al}_x\text{In}_{1-x}\text{N}$ at $0 \leq x \leq 0.29$ in the energy range up to 9.5 eV and determined the higher-lying CPs E_1 – E_4 , together with E_0 . They increased gradually with increasing x . The bowing parameters c determined for E_1 and E_2 are 1.8 and 2.7 eV, respectively.

The pressure dependence of E_0 in $w\text{-Al}_{0.25}\text{In}_{0.75}\text{N}$ has been studied by Li *et al.* [69]. They also estimated the pressure coefficients for $w\text{-Al}_x\text{In}_{1-x}\text{N}$ and expressed them as $dE_0/dp = 25 + 20x$ meV/GPa.

(e) *c-GaInN*

The E_0 gap in $c\text{-InN}$ grown on 3C-SiC(100) has been determined to be 0.56 eV by SE at 300 K [70]. The E_0 versus x data for $c\text{-Ga}_x\text{In}_{1-x}\text{N}$ has also been determined using SE [71,72]. These data together with the linearly interpolated E_g^X values are shown in Figure 6.15(b). The experimental E_0 values are in good agreement with the linearly interpolated E_0 result given by the heavy solid line (Table 6.6).

(f) *w-GaInN*

The recent crystal growth of high-quality $\text{Ga}_x\text{In}_{1-x}\text{N}$ epilayers with small x has considerably broadened the composition range over which the bowing could be determined reliably. The E_0 versus x data for $w\text{-Ga}_x\text{In}_{1-x}\text{N}$ are shown in Figure 6.16(b). The data are taken from Wu and Walukiewicz [65] and Androulidaki *et al.* [66]. A number of larger studies cast doubt on the small bowing parameter in $w\text{-Ga}_x\text{In}_{1-x}\text{N}$ [56]. For example, the experimental data of Parker *et al.* [73] implied a bowing of 3.42 eV (4.11 eV) for strained (relaxed) $\text{Ga}_x\text{In}_{1-x}\text{N}$ epilayers grown on (0001)-sapphire substrates with $x < 0.25$. However, recent studies of a broad

compositional range supported the findings of a smaller bowing of ~ 1.4 eV [65,74]. Our recommended bowing parameter in Figure 6.16(b) is 1.640 eV (Table 6.7).

Higher-lying CPs have been observed in $w\text{-Ga}_x\text{In}_{1-x}\text{N}$ using SE [75]. A total of five CPs (A , E_1 , E_2 , E_3 and E_4), together with E_0 , are observed in the spectral range of 0.5–10 eV. All these CPs showed a weak nonlinearity with x .

The E_0 gap of $w\text{-InN}$ is reported to be 0.70 ± 0.05 eV at 300 K [76]. The Varshni coefficients for $w\text{-InN}$ are also reported to be $\alpha = 0.41$ meV/K and $\beta = 454$ K [65]. An up-to-date compilation of various band parameters has been presented in Adachi [1] for group-IV elemental, III–V and II–VI binary semiconductors. By using an interpolation scheme, therefore, it is in principle, possible to estimate the band-gap energies for group-IV, III–V and II–VI semiconductor alloys at any temperature and also any pressure.

The temperature dependence of E_0 in $w\text{-Ga}_x\text{In}_{1-x}\text{N}$ has been determined for $x = 0.86$ [77] and 0.92 [78]. The Varshni coefficients $\alpha = 1.0$ meV/K and $\beta = 1196$ K for $x = 0.86$ [77] are nearly the same as those for $w\text{-GaN}$ ($\alpha \sim 1.3$ meV/K and $\beta \sim 1200$ K) [1].

The pressure dependence of E_0 in $w\text{-Ga}_x\text{In}_{1-x}\text{N}$ with $0.89 \leq x \leq 1.0$ grown by MOCVD has been investigated for pressures of up to 9 GPa [78]. The pressure coefficients dE_0/dp are 37.5 ± 2.5 meV/GPa ($T = 10\text{--}295$ K). The pressure coefficients for samples at $0.5 \leq x \leq 1.0$ have also been determined and found to be $dE_0/dp = 30 \pm 5$ meV/GPa [69].

6.3.2 (III, III)–P Alloy

(a) AlGaP

$\text{Al}_x\text{Ga}_{1-x}\text{P}$ has an indirect gap over the whole composition range. Figure 6.17(a) shows the lowest indirect and direct gap energies E_g^{ID} and E_0 as a function of x for $\text{Al}_x\text{Ga}_{1-x}\text{P}$. The experimental E_g^{X} data were obtained from optical absorption measurements [79]. The optical absorption at 6 K measured by Onton *et al.* [80] provided an indirect gap bowing of $c \sim 0.18$ eV. More recent CL data obtained at 14 K [81] support a small bowing of 0.13 eV for the lowest indirect gap E_g^{X} . However, Figure 6.17(a) shows that good agreement with the experimental data can be achieved by putting $c = 0$ eV into Equation (A.5).

The lowest and higher-lying CPs in $\text{Al}_x\text{Ga}_{1-x}\text{P}$ have been investigated using ER in early studies and SE more recently. The experimental E_0 data plotted in Figure 6.17(a) are taken from such studies (Rodríguez and Armelles [82], Choi *et al.* [83], etc.). The linear interpolation scheme provides good agreement with the experimental E_0 data, as shown by the solid line.

The composition dependence of the higher-lying CPs is shown in Figure 6.17(b). The experimental ER and SE data can be satisfactorily fitted by the linear expression against alloy composition x [83]. The corresponding formulas are listed in Table 6.8. Note that the SO split-off energies Δ_0 and Δ_1 are observed to be negligibly small in the III–P semiconductors. From Figure 6.17(b), we can expect crossing of E'_0 and E_2 at $x \sim 0.5$, which may be a unique characteristic of this alloy (cf. Figure 6.19). If we simply exchange an assignment of the CPs, namely $E'_0 \leftrightarrow E_2$, in AlP [83], no such crossing occurs, as demonstrated by the dashed lines in Figure 6.17(b). Note that the E'_0 and E_2 transitions occur at or near the Γ and X points in the BZ, respectively (Figure 6.1), and that identifying higher-lying CPs is a very difficult task.

(b) AlInP

$\text{Al}_x\text{In}_{1-x}\text{P}$ can be lattice-matched to GaAs at $x \sim 0.53$. Onton and Chicotka [84] grew bulk $\text{Al}_x\text{In}_{1-x}\text{P}$ by a modified Bridgman method and measured the CL spectra at 300 K. The open

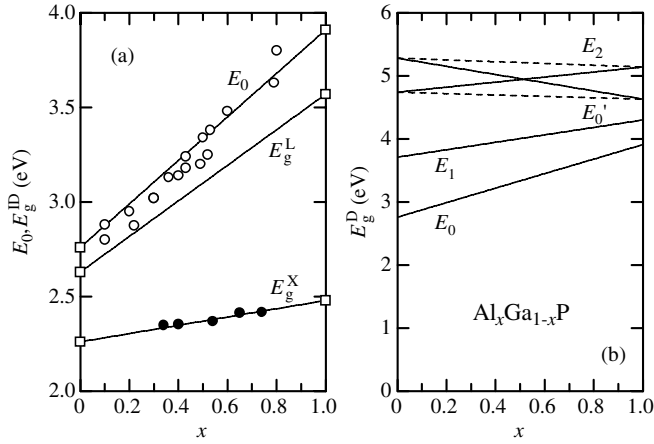


Figure 6.17 (a) Energies of the lowest direct E_0 and indirect gaps E_g^{ID} versus x for $\text{Al}_x\text{Ga}_{1-x}\text{P}$ at 300 K. The experimental data for E_0 are taken from Rodríguez and Armelles [82], Choi *et al.* [83], etc., and for E_g^{X} from Sonomura *et al.* [79]. (b) Energies of some CPs versus x for $\text{Al}_x\text{Ga}_{1-x}\text{P}$ at 300 K. The solid lines in (a) and (b) show the calculated results using the data in Table 6.8. The dashed lines were also obtained by exchanging the $E_0' \leftrightarrow E_2$ CP assignment in AlP

Table 6.8 Energies for some indirect and direct gaps in $\text{Al}_x\text{Ga}_{1-x}\text{P}$ at 300 K. LF = linear fit; LI = linear interpolation

Band gap	Expression (eV)	Remark
E_g^{X}	$2.261 + 0.219x$	LF
E_g^{L}	$2.63 + 0.94x$	LI
E_0	$2.76 + 1.15x$	LF
E_1	$3.71 + 0.59x$	LF
E_0'	$4.74 + 0.40x$	LF
E_2	$5.28 - 0.65x$	LF

circles in Figure 6.18(a) show these results. A Γ -X crossing is found to occur at $x \sim 0.45$. Bour *et al.* [85] also grew a series of $\text{Al}_x\text{In}_{1-x}\text{P}$ on GaAs (100) by MOCVD and determined the E_0 energies by ER. These results are also shown in Figure 6.18(a) by the solid circles. The quadratic fit of E_0 gives a value of $c \sim 0.40$ eV, as listed in Table 6.9.

No experimental data relating to the higher-lying CPs in $\text{Al}_x\text{In}_{1-x}\text{P}$ has been reported. We, therefore, show in Figure 8.18(b) the CP energies obtained from the linear interpolation scheme between the InP ($x = 0$) and AlP ($x = 1.0$) data in Adachi [1]. As in Figure 6.17(b) ($\text{Al}_x\text{Ga}_{1-x}\text{P}$), crossing of E_0' and E_2 occurs at $x \sim 0.4$ in $\text{Al}_x\text{In}_{1-x}\text{P}$. This crossing can be removed by simply exchanging the assignment of the CPs, $E_0' \leftrightarrow E_2$, in AlP [83], as demonstrated by the dashed lines in Figure 8.18(b).

The electron-HH and electron-LH transition energies in strained $\text{Al}_x\text{In}_{1-x}\text{P}$ layers grown on GaAs by MOCVD were investigated at 20 K using a PR technique [86]. The E_0 versus x data

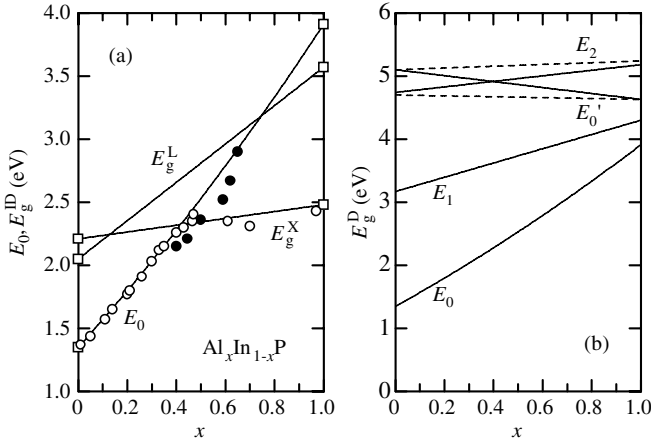


Figure 6.18 (a) Energies of the lowest direct E_0 and indirect gaps E_g^{ID} versus x for $\text{Al}_x\text{In}_{1-x}\text{P}$ at 300 K. The experimental data are taken from Onton and Chicotka [84] (open circles) and Bour *et al.* [85] (solid circles). (b) Energies of some CPs versus x for $\text{Al}_x\text{In}_{1-x}\text{P}$ at 300 K. The solid lines in (a) and (b) show the calculated results using the data in Table 6.9. The dashed lines are also obtained by exchanging the $E_0' \leftrightarrow E_2$ CP assignment in AlP

Table 6.9 Energies for some direct and indirect gaps in $\text{Al}_x\text{In}_{1-x}\text{P}$ at 300 K. QF = quadratic fit; LI = linear interpolation; LF = linear fit

Band gap	Expression (eV)	Remark
E_0	$1.35 + 2.16x + 0.40x^2$	QF
E_g^{L}	$2.05 + 1.52x$	LI
E_g^{X}	$2.21 + 0.27x$	LF
E_1	$3.71 + 1.13x$	LI
E_0'	$4.70 + 0.44x$	LI
E_2	$5.10 - 0.47x$	LI

were also measured for relaxed $\text{Al}_x\text{In}_{1-x}\text{P}$ at 20 K [86] and can be expressed as (in eV)

$$E_0(x) = 1.418 + 2.4x \quad (6.9)$$

(c) GaInP

$\text{Ga}_x\text{In}_{1-x}\text{P}$ exhibits some of the largest direct gaps among the non-nitride III-V semiconductors and can be grown lattice-matched to GaAs at $x \sim 0.52$. This alloy is widely used as a material for various optoelectronic and electronic devices. The lowest direct gap E_0 versus x for $\text{Ga}_x\text{In}_{1-x}\text{P}$ is shown graphically in Figure 6.19(a). The experimental data are taken from Onton *et al.* [87] (open circles) and Alibert *et al.* [88] (solid circles). The solid line represents the calculated E_0 versus x curve by putting $c = 0.65$ eV into Equation (A.5). This value is the same as that recommended in Vurgaftman *et al.* [89].

The Γ -X crossover is believed to occur at $x \sim 0.7$ in $\text{Ga}_x\text{In}_{1-x}\text{P}$. The indirect band-gap energies E_g^{X} for $x \geq 0.7$ are plotted against x in Figure 6.19(a) by the open triangles. They are

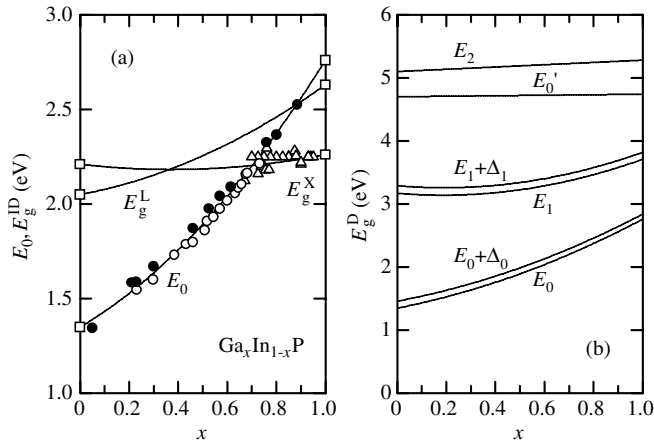


Figure 6.19 (a) Energies of the lowest direct E_0 and indirect gaps E_g^{ID} versus x for $\text{Ga}_x\text{In}_{1-x}\text{P}$ at 300 K. The experimental data for E_0 are taken from Onton *et al.* [87] (open circles) and Alibert *et al.* [88] (solid circle) and for E_g^{X} from Alibert *et al.* [88], Lange *et al.* [90], etc. (open triangles). (b) Energies of some CPs versus x for $\text{Ga}_x\text{In}_{1-x}\text{P}$ at 300 K. The solid lines in (a) and (b) show the calculated results using the data in Table 6.10

taken from Alibert *et al.* [88], Lange *et al.* [90], etc. The solid lines represent the calculated E_g^{X} and E_g^{L} curves using $c = 0.200$ and 0.34 eV, respectively. Early theoretical and experimental bowing parameters are summarized by Bugajski *et al.* [91] and more recent values by Vurgaftman *et al.* [89]. These results vary widely: $c = 0.39$ – 1.36 , 0 – 0.40 and 0.23 – 0.86 eV for E_0 , E_g^{X} and E_g^{L} , respectively. Clearly, the $c = 1.03$ eV value for E_g^{L} recommended by Vurgaftman *et al.* [89] is out of the reported range of 0.23 – 0.86 eV. If we assume here that $c = 0.34$ eV for E_g^{L} , which is exactly the same as Hill’s value [92], the $c = 0.200$ eV value for E_0 is also the same as that recommended by Vurgaftman *et al.* [89] ($c = 0.20$ eV). The expressions for such energy gaps are summarized in Table 6.10.

Table 6.10 Energies for some direct and indirect gaps in $\text{Ga}_x\text{In}_{1-x}\text{P}$ at 300 K. LI = linear interpolation

Band gap	Expression (eV)	Remark
E_0	$1.35 + 0.76x + 0.65x^2$	<i>a</i>
$E_0 + \Delta_0$	$1.46 + 0.73x + 0.65x^2$	<i>a</i>
E_g^{L}	$2.05 + 0.24x + 0.34x^2$	<i>b</i>
E_g^{X}	$2.210 - 0.149x + 0.200x^2$	<i>b</i>
E_1	$3.17 - 0.32x + 0.86x^2$	<i>c</i>
$E_1 + \Delta_1$	$3.29 - 0.33x + 0.86x^2$	<i>c</i>
E_0'	$4.70 + 0.04x$	LI
E_2	$5.10 + 0.18x$	LI

^aBowing parameter is obtained from I. Vurgaftman *et al.* (*J. Appl. Phys.* **89**, 5815 (2001))

^bBowing parameter is obtained from R. Hill (*J. Phys. C: Solid State Phys.* **7**, 516 (1974))

^cBowing parameter is obtained from C. Alibert *et al.* (*Phys. Rev. B* **6**, 1301 (1972))

The composition dependence of the higher-lying CPs for $\text{Ga}_x\text{In}_{1-x}\text{P}$ has been investigated using ER [88] and SE [93]. These studies observed remarkable bowing ($c \sim 0.9$ eV) for the E_1 and $E_1 + \Delta_1$ transitions. The $\text{Ga}_x\text{In}_{1-x}\text{P}$ samples used by Lee *et al.* [93] were epitaxially grown on GaAs and graded-GaInP/GaP substrates by various techniques, such as MOCVD, gas-source MBE, LPE or HT-VPE. They mainly investigated the strain and disorder effects of the electrical and optical properties. The general behavior of the $E_1/(E_1 + \Delta_1)$ peak shifts was explained in terms of the biaxial strain and strain relaxation caused by lattice mismatch. The solid lines in Figure 6.19(b) show the results calculated from Table 6.10. Since the SO split-off energies Δ_0 and Δ_1 are mainly characterized by the nature of the anion atom, the common anion alloys like $\text{Ga}_x\text{In}_{1-x}\text{P}$ and $\text{Zn}_x\text{Cd}_{1-x}\text{Te}$ have nearly the same Δ_0 or Δ_1 energies, irrespective of alloy composition x . Therefore, in such alloys the $E_0 + \Delta_0$ and $E_1 + \Delta_1$ gaps have nearly the same bowing parameters as the E_0 and E_1 gaps, respectively.

The temperature dependence of the fundamental absorption edge of $\text{Ga}_x\text{In}_{1-x}\text{P}$ ($x = 0-1.0$) has been investigated from 20 to 300 K by Ishitani *et al.* [94]. The same studies, but using samples lattice-matched to GaAs ($x \sim 0.5$), have also been carried out using PzR [95] and SE [96]. The measured data were analyzed using some empirical expressions, such as Varshni and Bose–Einstein formulas. Onton and Chicotka [97] also undertook PL measurements on $\text{Ga}_x\text{In}_{1-x}\text{P}$ at 2 K and obtained the x -dependent E_0 and E_g^X values given by (in eV)

$$E_0(x) = 1.409 + 0.695x + 0.758x^2 \quad (6.10)$$

$$E_g^X(x) = 2.321 + 0.017x \quad (6.11)$$

The pressure dependence of the fundamental absorption edge of $\text{Ga}_x\text{In}_{1-x}\text{P}$ has been determined by several authors [98,99]. The pressure coefficients dE_0/dp and dE_g^X/dp reported by Hakki *et al.* [98] were 125 ± 5 meV/GPa ($x \sim 0.5$) and -11.5 ± 1.5 meV/GPa ($x = 0-1.0$), respectively. Goñi *et al.* [99] found from optical absorption studies that Γ -X crossing occurred at 5.0 GPa for $x = 0.36$ and at 2.7 GPa for $x = 0.5$ at 300 K. PL measurements were also carried out to investigate Γ -X crossing as a function of pressure for $\text{Ga}_x\text{In}_{1-x}\text{P}$ epilayers grown on GaAs(100) substrates [100,101].

6.3.3 (III, III)–As Alloy

(a) AlGaAs

$\text{Al}_x\text{Ga}_{1-x}\text{As}$ is known to be the most important and the most investigated III–V semiconductor alloy. Figure 6.20(a) shows the lowest direct and indirect gaps E_0 , E_g^L and E_g^X versus x for $\text{Al}_x\text{Ga}_{1-x}\text{As}$. The experimental data for E_0 are taken from Aubel *et al.* [102] and Aspnes *et al.* [103], for E_g^L from Saxena [104] and for E_g^X from Monemar *et al.* [105]. The solid lines are calculated from the data in Table 6.11. The expression for E_0 is determined from the SE analysis [103]. This expression reveals that the bowing parameter is x -dependent in the manner (in eV) shown below

$$\begin{aligned} E_0(x) &= 1.430 + 1.707x - 1.437x^2 + 1.310x^3 \\ &= 1.430 + 1.580x + x(1-x)(0.127 - 1.310x) \end{aligned} \quad (6.12)$$

Using Equation (6.12), we can obtain good agreement with the experimental results. It should be noted, however, that almost all $\text{Al}_x\text{Ga}_{1-x}\text{As}$ data have been explained by the quadratic expression with c ranging from -0.25 to $+1.147$ eV [106].

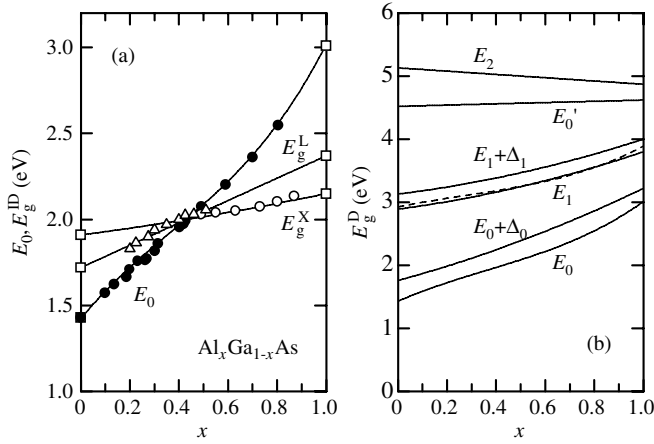


Figure 6.20 (a) Energies of the lowest direct E_0 and indirect gaps E_g^{ID} versus x for $Al_xGa_{1-x}As$ at 300 K. The experimental data for E_0 are taken from Aubel *et al.* [102] and Aspnes *et al.* [103] (open circles), for E_g^L from Saxena [104] (solid circles) and for E_g^X from Monemar *et al.* [105] (solid triangles). (b) Energies of some CPs versus x for $Al_xGa_{1-x}As$ at 300 K. The solid lines in (a) and (b) represent the calculated results using the data in Table 6.11. The dashed line in (b) also represents the result calculated using Equation (6.13)

Many reports support the hypothesis that the c value for E_g^L is almost equal to zero. Lee *et al.* [107], however, reported a value of $c = 0.055$ eV from PL measurements. The plots produced by Saxena [104] also suggested $c = 0$ eV for E_g^L , independent of temperature [108]. As seen from Figure 6.20(a), GaAs is a direct gap semiconductor with $\Gamma-L-X$ valley ordering, while AlAs is an indirect gap semiconductor with exactly the reverse ordering. The $\Gamma-X$ crossover composition x_c for $Al_xGa_{1-x}As$ was determined at various temperatures [106] and found to be ~ 0.4 at 300 K and ~ 0.38 at low temperatures.

The higher-lying CPs in $Al_xGa_{1-x}As$ have been determined by many authors [106]. The bowing parameter of $c \sim 0.39$ eV was reported for E_1 , while the E_2 gap showed an almost linear variation with x . Such results are shown in Figure 6.20(b) (see also Table 6.11). Aspnes

Table 6.11 Energies for some direct and indirect gaps in $Al_xGa_{1-x}As$ at 300 K. LI = linear interpolation

Band gap	Expression (eV)	Remark
E_0	$1.430 + 1.707x - 1.437x^2 + 1.310x^3$	<i>a</i>
E_g^L	$1.72 + 0.65x$	LI
$E_0 + \Delta_0$	$1.760 + 1.053x + 0.407x^2$	<i>b</i>
E_g^X	$1.910 + 0.185x + 0.055x^2$	<i>c</i>
E_1	$2.890 + 0.518x + 0.392x^2$	<i>b</i>
$E_1 + \Delta_1$	$3.130 + 0.479x + 0.391x^2$	<i>b</i>
E_0'	$4.52 + 0.10x$	LI
E_2	$5.13 - 0.26x$	LI

^aBowing parameter is obtained from D. E. Aspnes *et al.* (*J. Appl. Phys.* **60**, 754 (1986))

^bBowing parameter is obtained from J. L. Aubel *et al.* (*J. Appl. Phys.* **58**, 495 (1985))

^cBowing parameter is obtained from H. J. Lee *et al.* (*Phys. Rev. B* **21**, 659 (1980))

et al. [103] reported an expression analogous to Equation (6.12) for E_1 (in eV)

$$E_1(x) = 2.924 + 0.965x + x(1-x)(-0.157 - 0.935x) \quad (6.13)$$

The dashed line in Figure 6.20(b) represents the calculated result of this expression.

Traditionally, temperature variation of the band-gap energy E_g is expressed in terms of the Varshni formula [1]

$$E_g(T) = E_g(0) - \frac{\alpha T^2}{T + \beta} \quad (6.14)$$

where $E_g(0)$ is the band-gap energy at 0 K, α is in electron volts per Kelvin and β is closely related to the Debye temperature of the material (in Kelvin). The E_0 -gap Varshni parameters $E_0(0)$, α and β for $\text{Al}_x\text{Ga}_{1-x}\text{As}$ are shown in Figure 6.21(a). The experimental data were

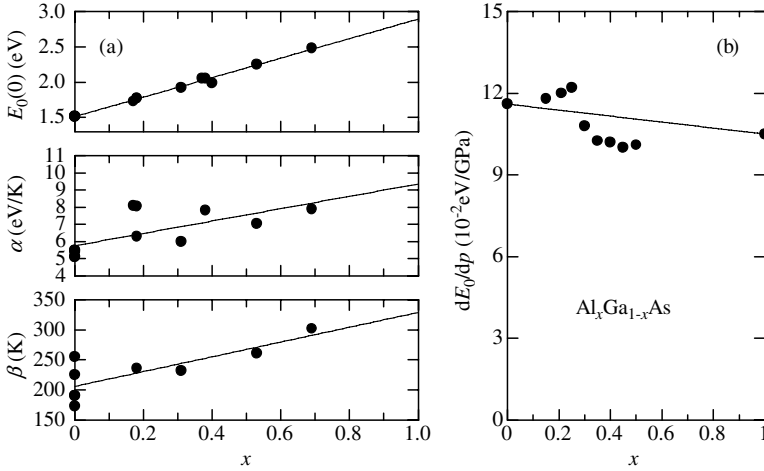


Figure 6.21 (a) Varshni parameters $E_g(0)$, α and β versus x for E_0 in $\text{Al}_x\text{Ga}_{1-x}\text{As}$. The solid lines represent the linear least-squares fits summarized in Table 6.12. (b) Pressure coefficient dE_0/dp versus x for $\text{Al}_x\text{Ga}_{1-x}\text{As}$. The experimental data are taken from Adachi [106]. The solid line shows the calculated result using Equation (6.15)

gathered from various sources. The solid lines represent the linear least-squares fits summarized in Table 6.12. The Varshni parameters for E_g^L and E_g^X are also listed in Table 6.12. Introducing such parameters into Equation (6.14), we obtain the E_0 , E_g^L and E_g^X energies for optional alloy compositions ($0 \leq x \leq 1.0$) and T from 0 up to at least 400 K. The Varshni parameters for the higher-lying CPs were reported in Adachi [106].

There is some considerable variation in the absolute pressure coefficients of E_0 and they are limited to $x \leq 0.5$ [106]. However, the literature data in Figure 6.21(b) can probably be best summarized by (in 10^{-2} eV/GPa)

$$\frac{dE_0(x)}{dp} = 11.6 - 1.1x \quad (6.15)$$

Table 6.12 Varshni parameters defined by Equation (6.14) for E_0 , E_g^L and E_g^X in $Al_xGa_{1-x}As$

Band gap	$E_g(0)$ (eV)	α (10^{-4} eV/K)	β (K)
E_0^a	$1.513 + 1.380x$	$5.8 + 3.6x$	$206 + 123x$
E_g^{Lb}	$1.775 + 0.792x$	6.1	204
E_g^{Xb}	$1.988 + 0.207x + 0.055x^2$	$4.6-1.0x$	204

^aObtained from Figure 6.21

^bS. Adachi, *GaAs and Related Materials: Bulk Semiconducting and Superlattice Properties*. World Scientific, Singapore, 1994

The E_g^L and E_g^X data showed no clear x -dependent pressure coefficients that can be approximated as $dE_g^L/dp \sim 5.5 \times 10^{-2}$ eV/GPa and $dE_g^X/dp \sim 1.5 \times 10^{-2}$ eV/GPa [106]. The pressure coefficients of E_1 and $E_1 + \Delta_1$ were approximated as $\sim(7-8) \times 10^{-2}$ eV/GPa [106].

(b) AlInAs

$Al_xIn_{1-x}As$ can be grown lattice-matched to InP at $x \sim 0.48$ and serve as a barrier layer in the important $Ga_{0.47}In_{0.53}As/Al_{0.48}Ga_{0.52}As/InP$ heterostructure system. Wakefield *et al.* [109] undertook CL measurements on $Al_xIn_{1-x}As/InP(100)$ at $x \sim 0.5$ and obtained a value of $c = 0.74$ eV for E_0 . More recently, Chou *et al.* [110] determined $c \sim 0$ eV from PR in the limited composition range $0.43 \leq x \leq 0.58$. The experimental data of Chou *et al.* (solid circles) are shown in Figure 6.22(a). The E_0 energy for $Al_{0.48}In_{0.52}As/InP$ was reported to be 1.439 ± 0.005 eV at 300 K [111]. The open circle in Figure 6.22(a) shows this data. From these data, we obtain a value of $c \sim 0.72$ eV, in good agreement with the earlier work of Wakefield *et al.* [109].

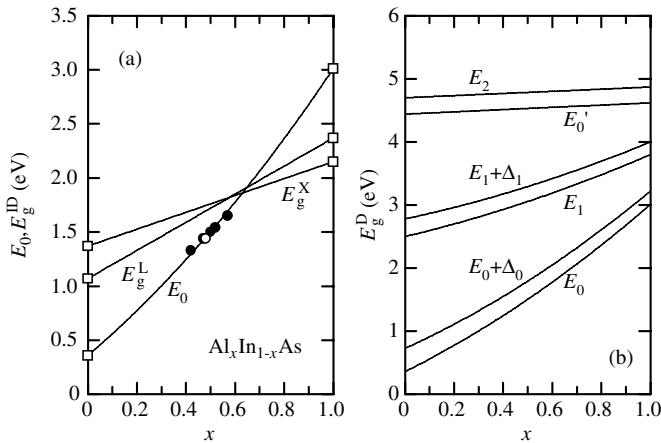


Figure 6.22 (a) Energies of the lowest direct E_0 and indirect gaps E_g^{ID} versus x for $Al_xIn_{1-x}As$ at 300 K. The experimental data are taken from Chou *et al.* [110] (solid circles) and Oertel *et al.* [111] (open circle). (b) Energies of some CPs versus x for $Al_xIn_{1-x}As$ at 300 K. The solid lines in (a) and (b) show the calculated results using the data in Table 6.13

The linear interpolation scheme, used to estimate the L- and X-valley minima, also implies Γ -X crossover occurring at $x \sim 0.63$ in Figure 6.22(a).

The higher-lying CPs in $\text{Al}_x\text{In}_{1-x}\text{As}$ have been studied using SE [82] and normal-incidence reflectivity [112]. These studies determined the E_1 -gap c value to be 0.86 and 0.38 eV, respectively. A value of $c = 0.39$ eV was also determined for $E_1 + \Delta_1$ [112]. The recommended band-gap expressions for $\text{Al}_x\text{In}_{1-x}\text{As}$ are summarized in Table 6.13.

Table 6.13 Energies for some direct and indirect gaps in $\text{Al}_x\text{In}_{1-x}\text{As}$ at 300 K. LI = linear interpolation

Band gap	Expression (eV)	Remark
E_0	$0.359 + 1.931x + 0.720x^2$	<i>a</i>
$E_0 + \Delta_0$	$0.726 + 1.774x + 0.720x^2$	<i>b</i>
E_g^L	$1.07 + 1.30x$	LI
E_g^X	$1.37 + 0.78x$	LI
E_1	$2.50 + 0.92x + 0.38x^2$	<i>c</i>
$E_1 + \Delta_1$	$2.78 + 0.83x + 0.39x^2$	<i>c</i>
E_0'	$4.44 + 0.18x$	LI
E_2	$4.70 + 0.17x$	LI

^aObtained from Figure 6.22

^bPostulated bowing parameter equal to that for E_0

^cBowing parameter is obtained from A. Convertino *et al.* (*J. Vac. Sci. Technol. B* **20**, 248 (2002))

(c) *GaInAs*

$\text{Ga}_x\text{In}_{1-x}\text{As}$ remains a direct gap material over the whole composition range. We show in Figure 6.23(a) the lowest direct and indirect gaps E_0 , E_g^L and E_g^X versus x for $\text{Ga}_x\text{In}_{1-x}\text{As}$. The E_0 versus x data are taken from Nahory *et al.* [113] (open circles) and Kim *et al.* [114] (solid circles). $\text{Ga}_{0.47}\text{In}_{0.53}\text{As}/\text{InP}$ has an energy $E_0 = 0.728 \pm 0.002$ eV at 300 K [115]. The open triangle in Figure 6.22(a) shows this value. From these data points, we obtain a value of $c \sim 0.58$ eV for E_0 , slightly larger than that recommended by Vurgaftman *et al.* [89] ($c = 0.477$ eV).

Singh [116] reviewed the E_0 gap in lattice-matched and strained $\text{Ga}_{0.47-\alpha}\text{In}_{0.53+\alpha}\text{As}$ grown on InP(100). He obtained the following expression for unstrained samples with small α at 300 K (in eV)

$$E_0(\alpha) = 0.75 - 1.05\alpha + 0.45\alpha^2 \quad (6.16)$$

with zero HH-LH splitting, while for strained samples (in eV)

$$E_0(\alpha) = 0.75 - 0.63\alpha + 0.45\alpha^2 \quad (6.17)$$

with HH-LH splitting of 0.42α eV.

There is no reliable experimental technique to determine the L- and X-valley gaps E_g^L and E_g^X in $\text{Ga}_x\text{In}_{1-x}\text{As}$. The c values in Table 6.14 are assumed to have a composite value in the range compiled by Vurgaftman *et al.* [89]. The dashed lines in Figure 6.22(a) represent the E_g^L and E_g^X values calculated using Vurgaftman's recommended c values.

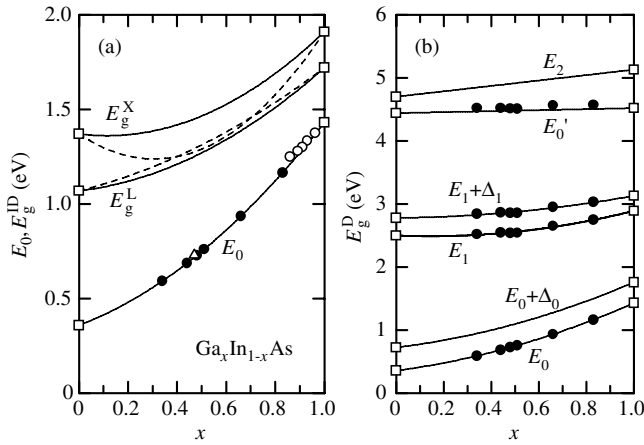


Figure 6.23 (a) Energies of the lowest direct E_0 and indirect gaps E_g^{ID} versus x for $\text{Ga}_x\text{In}_{1-x}\text{As}$ at 300 K. (b) Energies of some CPs versus x for $\text{Ga}_x\text{In}_{1-x}\text{As}$ at 300 K. The experimental data in (a) and (b) are taken from Nahory *et al.* [113] (open circles), Kim *et al.* [114] (solid circles) and Gaskill [115] (open triangle). The solid lines in (a) and (b) show the calculated results using the data in Table 6.14. The dashed lines in (a) are calculated using $c = 0.33$ and 1.4 eV for E_g^L and E_g^X , respectively

The higher-lying CPs in $\text{Ga}_x\text{In}_{1-x}\text{As}$ have been determined using SE [114]. These results are shown in Figure 6.23(b). The samples were grown on InP(100) at a thickness of $1 \mu\text{m}$, which exceeds the critical thicknesses of strain relaxation. Thus, the data presented in Figure 6.23 represent those for bulk materials. Andreani *et al.* [117] used PR and SE to investigate the optical response and energy-band structure of a series of strained and relaxed $\text{Ga}_x\text{In}_{1-x}\text{As}$ ($x > 0.85$) films on GaAs(100) substrates. They observed that the energy shifts in E_1 and $E_1 + \Delta_1$ due to built-in strain were in good agreement with those calculated from standard DP theory. The solid lines in Figure 6.23(b) were obtained by the analysis of Kim's data [114] or using the linear interpolation scheme. These results are summarized in Table 6.14.

Table 6.14 Energies for some direct and indirect gaps in $\text{Ga}_x\text{In}_{1-x}\text{As}$ at 300 K. LI = linear interpolation

Band gap	Expression (eV)	Remark
E_0	$0.359 + 0.491x + 0.580x^2$	<i>a</i>
$E_0 + \Delta_0$	$0.726 + 0.454x + 0.580x^2$	<i>b</i>
E_g^L	$1.07 + 0.15x + 0.50x^2$	<i>c</i>
E_g^X	$1.37 - 0.16x + 0.70x^2$	<i>c</i>
E_1	$2.50 - 0.16x + 0.55x^2$	<i>d</i>
$E_1 + \Delta_1$	$2.78 + 0.03x + 0.32x^2$	<i>d</i>
E_0'	$4.44 + 0.08x$	<i>d</i>
E_2	$4.70 + 0.43x$	LI

^aObtained from Figure 6.23

^bPostulated bowing parameter equal to that for E_0

^cEstimated from list by I. Vurgaftman *et al.* (*J. Appl. Phys.* **89**, 5815 (2001))

^dEstimated from data by T. Y. Kim *et al.* (*Phys. Rev. B* **68**, 115323 (2003))

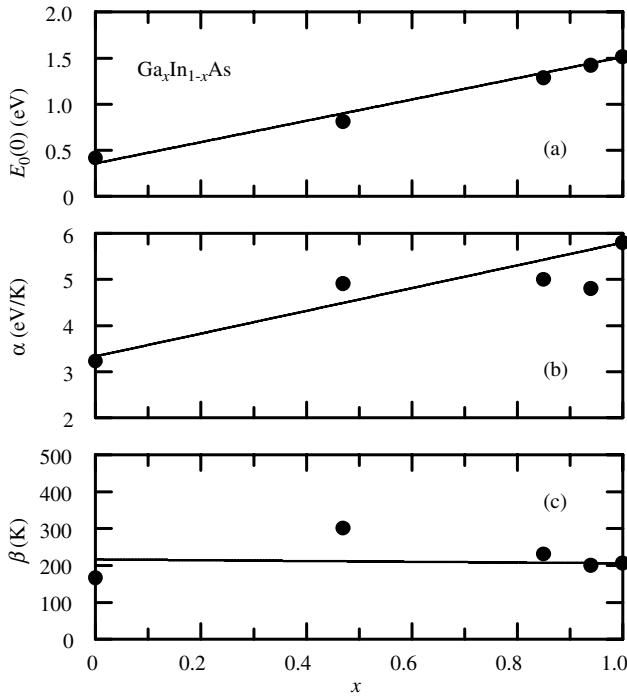


Figure 6.24 Varshni parameters $E_g(0)$, α and β versus x for E_0 in $\text{Ga}_x\text{In}_{1-x}\text{As}$. The solid lines represent the liner least-squares fits of Equation (6.18)

The Varshni parameters $E_0(0)$, α and β for E_0 in $\text{Ga}_x\text{In}_{1-x}\text{As}$ are plotted in Figure 6.24. The experimental data have been gathered from various sources (e.g. Hang *et al.* [118]). The solid lines show the liner least-squares fits given by

$$E_0(0)(x) = 0.359 + 1.154x \text{ eV} \quad (6.18a)$$

$$\alpha(x) = (3.3 + 2.5x) \times 10^{-4} \text{ eV/K} \quad (6.18b)$$

$$\beta(x) = 217 - 11x \text{ K} \quad (6.18c)$$

No detailed pressure dependence of the band-gap energies in $\text{Ga}_x\text{In}_{1-x}\text{As}$ has been reported. It should be noted, however, that the pressure dependence for GaAs and InAs can be given by $dE_0/dp = 107$ and 114 meV/GPa [1], respectively. Thus, we suggest the value of dE_0/dp for $\text{Ga}_x\text{In}_{1-x}\text{As}$ to be $\sim 110 \text{ meV/GPa}$, independent of x .

6.3.4 (III, III)–Sb Alloy

(a) AlGaSb

The bowing parameter c for E_0 in $\text{Al}_x\text{Ga}_{1-x}\text{Sb}$ was determined using various techniques, such as PL, optical absorption and ER [119–121]. The reported c values varied widely from -1.18

to + 0.69 eV [89]. Alibert *et al.* [119] obtained $c = 0.47$ and 0.48 eV at room temperature and low temperatures, respectively, and made a detailed comparison between these and previous results. More recently, Bignazzi *et al.* [120] obtained a better fit to the optical absorption data assuming a linear band-gap variation at low x . These results were confirmed by Bellani *et al.* [121] from TR measurements at $T = 90\text{--}300$ K. Consequently, a cubic expression was proposed for E_0 in $\text{Al}_x\text{Ga}_{1-x}\text{Sb}$

$$\begin{aligned} E_0(x) &= 0.723 + 1.547x + (0.044 - 1.220x)x(1-x) \\ &= 0.723 + 1.591x - 1.264x^2 + 1.220x^3 \end{aligned} \tag{6.19}$$

The calculated result of this expression is shown in Figure 6.25(a), together with the experimental data [119,121].

The experimental data in the higher x region in Figure 6.25(a) suggest that the X-valley gap E_g^X has no strong composition dependence. The experimental $\Gamma\text{--L}$ crossover composition also suggests that the bowing parameter may be negligibly small for E_g^L [89].

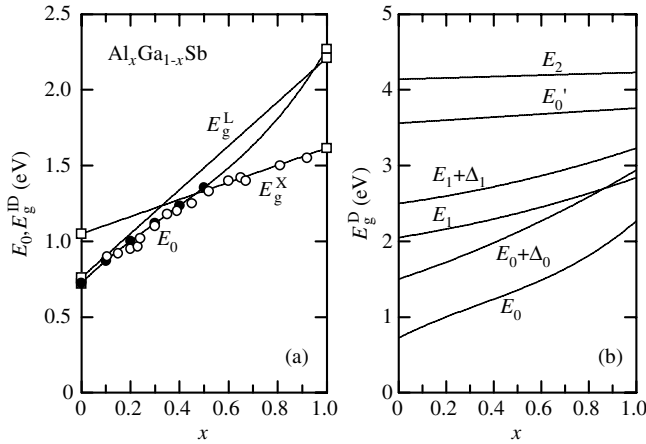


Figure 6.25 (a) Energies of the lowest direct E_0 and indirect gaps E_g^{ID} versus x for $\text{Al}_x\text{Ga}_{1-x}\text{Sb}$ at 300 K. The experimental data are taken from Anderson *et al.* (see Alibert *et al.* [119]) (open circles) and Bellani *et al.* [121] (solid circles). The solid line (E_0) shows the calculated result using Equation (6.19). (b) Energies of some CPs versus x for $\text{Al}_x\text{Ga}_{1-x}\text{Sb}$ at 300 K. The solid lines in (a) and (b) show the calculated results using the data in Table 6.15

The higher-lying CPs in $\text{Al}_x\text{Ga}_{1-x}\text{Sb}$ have been studied using modulation spectroscopy, such as PzR and ER [119,122] and SE [123,124]. The bowing parameters obtained from these studies are in the range 0.28–0.63 eV. Since the data of Choi *et al.* were limited to $0 \leq x \leq 0.39$ [124], they were fitted using a linear expression. The recommended band-gap expressions for $\text{Al}_x\text{Ga}_{1-x}\text{Sb}$ are summarized in Table 6.15.

The linear temperature coefficient dE_0/dT was reported to be $\sim 4 \times 10^{-4}$ eV/K for $0 \leq x \leq 1.0$ [121] and $x \leq 0.4$ [122]. The linear temperature coefficient dE_g^X/dT was also reported to be $-(3.1 \pm 0.2) \times 10^{-4}$ eV/K for $x > 0.52$ [119]. The Varshni parameters $E_0(0)$, α and β have been determined for $x = 0.12$ and 0.19 [125]. However, pressure studies have not been carried out on $\text{Al}_x\text{Ga}_{1-x}\text{Sb}$.

Table 6.15 Energies for some direct and indirect gaps in $\text{Al}_x\text{Ga}_{1-x}\text{Sb}$ at 300 K. LI = linear interpolation; LF = linear fit

Band gap	Expression (eV)	Remark
E_0	$0.723 + 1.591x - 1.264x^2 + 1.220x^3$	<i>a</i>
E_g^L	$0.760 + 1.451x$	LI
E_g^X	$1.050 + 0.565x$	LF
$E_0 + \Delta_0$	$1.50 + 1.04x + 0.40x^2$	<i>b</i>
E_1	$2.05 + 0.49x + 0.30x^2$	<i>c</i>
$E_1 + \Delta_1$	$2.50 + 0.43x + 0.30x^2$	<i>c</i>
E_0'	$3.56 + 0.20x$	LI
E_2	$4.14 + 0.09x$	LI

^aBowing parameter is obtained from V. Bellani *et al.* (*Phys. Rev. B* **59**, 12272 (1999))

^bEstimated from E_0 data

^cEstimated from various data

(b) AlInSb

Very limited data are available for $\text{Al}_x\text{In}_{1-x}\text{Sb}$ [126–128]. Isomura *et al.* [126] recorded the ER spectra for $\text{Al}_x\text{In}_{1-x}\text{Sb}$ at $0 \leq x \leq 1.0$. They determined the E_0 , $E_0 + \Delta_0$, E_1 and $E_1 + \Delta_1$ energies versus x at 300 K and their results are shown in Figure 6.26, together with those for E_g^L , E_g^X , E_0' and E_2 estimated from the linear interpolation scheme. The corresponding band-gap expressions are listed in Table 6.16. The data in Figure 6.26(a) suggest that $\text{Al}_x\text{In}_{1-x}\text{Sb}$ is a direct gap semiconductor at $x \leq 0.7$.

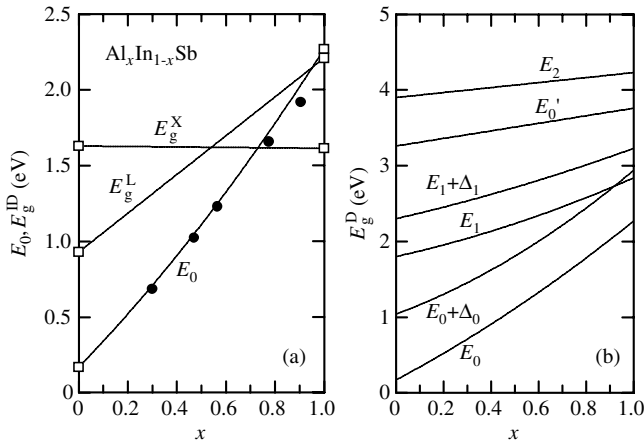


Figure 6.26 (a) Energies of the lowest direct E_0 and indirect gaps E_g^{ID} versus x for $\text{Al}_x\text{In}_{1-x}\text{Sb}$ at 300 K. The experimental data are taken from Isomura *et al.* [126] (solid circles). (b) Energies of some CBs versus x for $\text{Al}_x\text{In}_{1-x}\text{Sb}$ at 300 K. The solid lines in (a) and (b) represent the calculated results using the data in Table 6.16

Table 6.16 Energies for some direct and indirect gaps in $\text{Al}_x\text{In}_{1-x}\text{Sb}$ at 300 K. LI = linear interpolation

Band gap	Expression (eV)	Remark
E_0	$0.17 + 1.67x + 0.43x^2$	<i>a</i>
E_g^L	$0.930 + 1.281x$	LI
$E_0 + \Delta_0$	$1.04 + 1.16x + 0.74x^2$	<i>a</i>
E_g^X	$1.630 - 0.015x$	LI
E_1	$1.80 + 0.70x + 0.34x^2$	<i>a</i>
$E_1 + \Delta_1$	$2.30 + 0.72x + 0.21x^2$	<i>a</i>
E_0'	$3.26 + 0.50x$	LI
E_2	$3.90 + 0.33x$	LI

^aBowing parameter is estimated from data in S. Isomura *et al.* (*Phys. Status Solidi B* **65**, 213 (1974))

The bowing parameters obtained from Isomura *et al.* [126] are 0.34 and 0.21 eV for E_1 and $E_1 + \Delta_1$, respectively, while those obtained by Yaozhou *et al.* [127] are about a factor of 2 larger and are 0.752 and 0.723 eV for E_1 and $E_1 + \Delta_1$, respectively. The fundamental absorption edges in $\text{Al}_x\text{In}_{1-x}\text{Sb}$ layers ($0 \leq x \leq 0.25$) grown on GaAs substrates were studied by Dai *et al.* [128] using transmission spectroscopy from cryogenic to room temperature. A linear change of E_0 with lattice constant a (or x) was obtained.

(c) *GaInSb*

$\text{Ga}_x\text{In}_{1-x}\text{Sb}$ remains a direct gap semiconductor over $0 \leq x \leq 1.0$. The bowing parameters c for E_0 previously reported are $c = 0.413 - 0.43$ eV for bulk samples [129–131] and ~ 0.35 eV for epilayers [132]. A more recent study of a $\text{Ga}_x\text{In}_{1-x}\text{Sb}/\text{GaSb}(100)$ epilayer reports $c = 0.406 \pm 0.009$ eV [133], which is in much better agreement with the bulk results. The solid circles in Figure 6.27(a) show the PzR results obtained by Auvergne *et al.* [130], which give an E_0 bowing of 0.415 eV.

The considerable uncertainty for the indirect gaps in GaSb ($x=0$) and especially InSb ($x=1.0$) translates into a poor understanding of the L- and X-valley gap bowing. The c values of 0.40 and 0.33 eV for E_g^L and E_g^X in Table 6.17 are taken from Vurgaftman *et al.* [89].

The higher-lying CPs, E_1 , $E_1 + \Delta_1$, E_0' and E_2 , in $\text{Ga}_x\text{In}_{1-x}\text{Sb}$ have been studied using ER [129] and SE [134]. The bowing parameters determined from these studies are in reasonable agreement and are shown in Table 6.17 and Figure 6.27(b).

The linear temperature coefficient dE_0/dT obtained from PzR measurements [130] can be written as $-(2.75 - 1.05x) \times 10^{-4}$ eV/K. Therefore, the linear interpolation scheme can be safely used to obtain the temperature-dependent and may also be used to estimate the pressure-dependent band-gap energies in $\text{Ga}_x\text{In}_{1-x}\text{Sb}$. The necessary binary data are compiled from Adachi [1].

6.3.5 Dilute-nitride III–(V, V) Alloy

(a) *General Considerations*

Dilute-nitride III–V alloys, such as $\text{GaN}_x\text{As}_{1-x}$ and $\text{GaInN}_x\text{As}_{1-x}$, represent a new class of highly mismatched material systems, which have recently attracted great attention [135]. The ‘dilute’ nitrides now mean that a small N fraction of the order of a few percent can be added to a

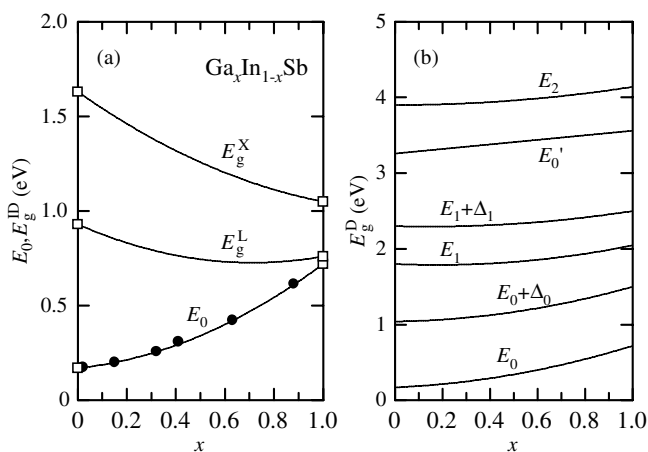


Figure 6.27 (a) Energies of the lowest direct E_0 and indirect gaps E_g^{ID} versus x for $\text{Ga}_x\text{In}_{1-x}\text{Sb}$ at 300 K. The experimental data are taken from Auvergne *et al.* [130] (solid circles). (b) Energies of some CPs versus x for $\text{Ga}_x\text{In}_{1-x}\text{Sb}$ at 300 K. The solid lines in (a) and (b) represent the calculated results using the data in Table 6.17

conventional non-nitride semiconductor, such as GaAs or GaInAs. Due to large differences in the lattice constant and ionicity between the host binary and N-related binary (Table 6.18), the dilute nitrides exhibit many unusual and fascinating physical properties. Among them the most prominent feature is the giant bowing in the band-gap energy. It is known that a single bowing parameter is inadequate even if the goal is only to describe the band-gap energy for a relatively wide range of compositions. For example, the bowing parameter c for E_0 in $\text{GaN}_x\text{As}_{1-x}$ reached 40 eV for a very low N incorporation ($x \sim 0.1$ at%), and strongly decreased with increasing N fraction [136]. Because of this, we do not recommend that the type of bowing parameter c be used to describe the dilute nitrides [56].

Table 6.17 Energies for some direct and indirect gaps in $\text{Ga}_x\text{In}_{1-x}\text{Sb}$ at 300 K

Band gap	Expression (eV)	Remark
E_0	$0.170 + 0.135x + 0.415x^2$	<i>a</i>
E_g^{L}	$0.93 - 0.57x + 0.40x^2$	<i>b</i>
$E_0 + \Delta_0$	$1.040 + 0.045x + 0.415x^2$	<i>c</i>
E_g^{X}	$1.63 - 0.91x + 0.33x^2$	<i>b</i>
E_1	$1.80 - 0.13x + 0.38x^2$	<i>d</i>
$E_1 + \Delta_1$	$2.30 - 0.08x + 0.28x^2$	<i>d</i>
E_0'	$3.26 + 0.30x$	<i>d</i>
E_2	$3.90 + 0.24x^2$	<i>d</i>

^aBowing parameter is obtained from D. Auvergne *et al.* (*J. Phys. Chem. Solids* **35**, 133 (1974))

^bBowing parameter is obtained from I. Vurgaftman *et al.* (*J. Appl. Phys.* **89**, 5815 (2001))

^cPostulated bowing parameter equal to that for E_0

^dBowing parameter is obtained from S. M. Vishnubhatla *et al.* (*Can. J. Phys.* **47**, 1661 (1969))

Table 6.18 Lattice mismatch $\Delta a/a$ and Phillips ionicity difference Δf_i for some III–(V, V) and (III, III)–V ternaries. Note that III–(N, V) ternaries exhibit ‘strongly perturbed’ characteristics

Alloy ^a	$ \Delta a/a $ (%)	$ \Delta f_i $	Alloy ^b	$ \Delta a/a $ (%)	$ \Delta f_i $
Al(N, P)	19.8	0.142	(Al, Ga)P	0.2	0.020
Al(N, As)	22.6	0.175	(Al, Ga)As	0.1	0.036
Al(N, Sb)	28.6	0.199	(Al, Ga)Sb	0.6	0.011
Ga(N, P)	17.1	0.173	(Ga, In)P	7.1	0.094
Ga(N, As)	20.0	0.190	(Ga, In)As	6.7	0.047
Ga(N, Sb)	34.9	0.239	(Ga, In)Sb	5.9	0.060
In(N, P)	15.0	0.157	Ga(P, As)	3.6	0.017
In(N, As)	21.5	0.221	Ga(P, Sb)	10.6	0.066
In(N, Sb)	23.0	0.257	Ga(As, Sb)	7.3	0.049
			In(P, As)	3.1	0.064
			In(P, Sb)	9.4	0.100
			In(As, Sb)	6.5	0.036

^aStrongly perturbed alloy^bWeakly perturbed alloy

The unexpected properties of various dilute nitrides are incompatible with standard models (e.g. VCA) describing semiconductor alloys. Many proposals have been developed, which can be summarized in the three main models: (1) impurity band formation [137,138], (2) BAC model [139,140] and (3) a polymorphous alloy model [141,142]. The subtle distinction between the three models lies in the evolution of the localized N states and the host CB states in the alloys [143]. The impurity band model argues that the CB minimum evolves from interacting N-related impurity states (isolated N centers, N pairs and clusters) and requires no participation of higher-lying host CB states [137,138]. The BAC model includes a mutual repulsion between the N level and Γ -valley CB state [139,140]. N-induced perturbed host states in the third model, on the other hand, covers all host CB states that are affected by the perturbation induced by nitrogen [141,142].

There is no perfect model to fully explain the unique properties of the dilute-nitride alloys; the dispute still continues [144–146]. It has, however, been well established that the electronic energy-band consequence of such materials can be simply parameterized in terms of the BAC model [56]. If the effect of the VB is completely neglected, the N states lead to a characteristic splitting of the CB into two subbands

$$E_{\pm}(\mathbf{k}) = \frac{1}{2} \left[(E^C(\mathbf{k}) + E_N) \pm \sqrt{(E^C(\mathbf{k}) - E_N)^2 + 4V^2x} \right] \quad (6.20)$$

where $E^C(\mathbf{k})$ is the CB dispersion of the unperturbed non-nitride semiconductor, E_N is the position of the N isoelectronic impurity level in that semiconductor, V is the interaction potential between the two subbands and x is the N fraction. The CB structure for $\text{GaN}_x\text{As}_{1-x}$ obtained from Equation (6.20) with $E^C(0) = 1.43$ eV (E_0), $E_N = 1.65$ eV and $V = 2.70$ eV is shown in Figure 6.28.

Any temperature dependence arises from the shift of the CB dispersion $E^C(0)$ in Equation (6.20), which is assumed to follow the Varshni, Bose–Einstein or other expression [1],

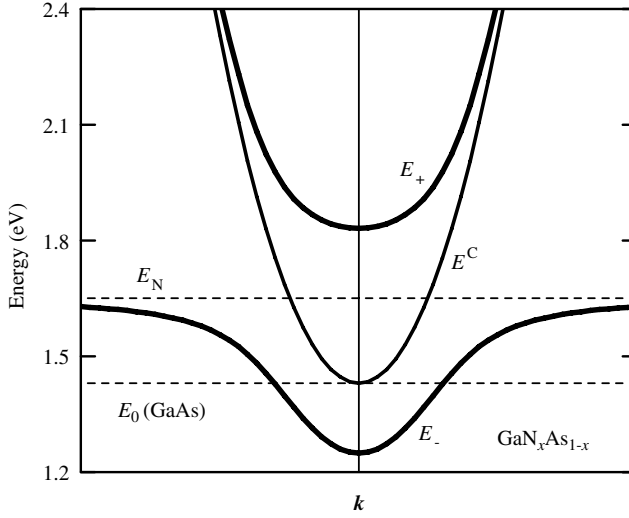


Figure 6.28 CB dispersion relationships for diluted-nitride $\text{GaN}_x\text{As}_{1-x}$ calculated from Equation (6.20). For comparison, the unperturbed GaAs CB (E^C) and the position of the N level (E_N) are shown

whereas E_N is assumed to be independent of T . In dilute-nitride alloys the DP interaction should be treated carefully, with a view to the much weaker shift of E_N with pressure. The pressure or strain dependence of the E_{\pm} transitions should be determined by substituting the appropriate DPs of the host semiconductor to obtain $E^C(\mathbf{k})$ and then deriving $E_{\pm}(\mathbf{k})$ from Equation (6.20) or an even more detailed formalism.

The effect of N incorporation on the electron effective mass is more subtle. In general, the smaller the E_0 gap, the smaller the CB effective mass m_e^{Γ} [1]. However, measurements on all diluted nitrides have shown an increase in the electron effective mass m_e^{Γ} . The band-anticrossing-induced enhancement of the DOS electron effective mass can be calculated from the dispersion relationship $E_-(\mathbf{k})$ in Equation (6.20) by [145]

$$m_{e-}^{\Gamma}(\mathbf{k}_F) = \hbar^2 \left| \frac{\mathbf{k}}{dE_-(\mathbf{k})/dk} \right|_{k=k_F} = m_e^{\Gamma} \left[1 + \frac{V^2 x}{(E_N - E_-(\mathbf{k}_F))^2} \right] \quad (6.21)$$

where m_e^{Γ} represents the host material value at $\mathbf{k} = 0$. The Fermi wavevector \mathbf{k}_F and Fermi energy $E_F = E_-(\mathbf{k}_F)$ can be determined from the free-electron concentration. Note that Equation (6.21) suggests an increase in m_{e-}^{Γ} with increasing x .

Since N incorporation mainly affects the CB states, the band anticrossing effect should not alter the VB structure, and as a result, the hole effective masses, appreciably. Similarly, since the band-gap bowing occurs mainly as a result of the lowering of the CB edge, a large CB offset and a small discontinuity in the VB edge should be expected. If we consider unstrained dilute nitride, the VB offset should be safely set equal to that of the host semiconductor material.

The electron mobility is expected to be lower in dilute nitrides due to strong alloy or impurity scattering and the enhanced electron effective mass. It is well known that the Γ -valley electron mobility decreases with increasing m_e^{Γ} [1]. Since reduced mobility of both electrons and holes has been observed, alloy or impurity scattering is likely the dominant effect governing carrier mobility, especially electron mobility.

(b) GaNP

Nitrogen is known to form a series of isoelectronic traps in GaP. The oscillator strength of the interband transitions in N-doped GaP can be strongly enhanced by increasing N concentrations up to the alloy limit, due to N-induced admixing of the Γ component to the lowest CB states of the alloy leading to the crossover from an indirect gap in GaP to a direct gap in $\text{GaN}_x\text{P}_{1-x}$ with a surprisingly low N concentration of around 0.5 at% [140,147–149].

Figure 6.29(a) shows the N concentration dependence of the CB edge E_- and Γ -point CB minimum E_+ in $\text{GaN}_x\text{P}_{1-x}$. The experimental data are taken from Buyanova *et al.* [150]. The horizontal arrows indicate the positions of E_0 , E_g^X and E_g^L in the host semiconductor GaP. The solid lines represent the results calculated according to Equation (6.20) using $E^C(\mathbf{k}=0) = 2.76$ eV (E_0), $E_N = 2.25$ eV and $V = 3.10$ eV (Table 6.19). Note that $E_N = 2.25$ eV is slightly smaller than the well-known isoelectronic NN states at 2.18 eV in GaP [151]. The determined N level $E_N = 2.25$ eV is placed nearly at the X-point CB minimum $E_g^X = 2.261$ eV (Table 6.1). The E_N and V values reported by Buyanova *et al.* [150] are, respectively, 2.25 and 2.76 eV, while those recommended by Vurgaftman and Meyer [56] are 2.18 eV (E_N) and 3.05 eV (V) respectively.

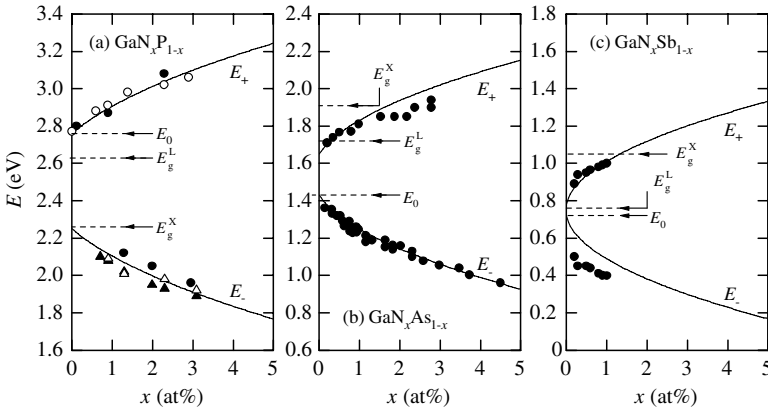


Figure 6.29 (a) N concentration dependence of the CB edge E_- and Γ -point CB minimum E_+ in $\text{GaN}_x\text{P}_{1-x}$ at 300 K. The experimental data are taken from Buyanova *et al.* [150]. (b) N concentration dependence of the CB edge E_- and Γ -point CB minimum E_+ in $\text{GaN}_x\text{As}_{1-x}$ at 300 K. The experimental data for E_- are taken from Wu *et al.* [160] and for E_+ from Gil [161]. (c) N concentration dependence of the CB edge E_- and Γ -point CB minimum E_+ in $\text{GaN}_x\text{Sb}_{1-x}$ at 300 K. The experimental data are taken from Jefferson *et al.* [178]. The solid lines in (a)–(c) represent the BAC results of Equation (6.20) using the model parameters in Table 6.19. The horizontal arrows indicate the positions of the E_0 , E_g^X and E_g^L gaps in the host semiconductor GaP, GaAs or GaSb

The CPs in $\text{GaN}_x\text{P}_{1-x}$ have been studied by Leibiger *et al.* [152] using SE at energies between 1 and 8.5 eV. They observed the Γ -point CPs E_0 and E_0' and Λ -direction CPs E_1 and E_1' , together with two additional CPs labeled E_2^1 and E_2^2 , which cannot be assigned unambiguously. A strong blueshift of E_0 and E_1 was observed with increasing N incorporation, in contrast to the well-known downshift of the CB edge. The E_0' , E_1' , E_2^1 and E_2^2 CPs did not significantly shift with increasing N concentration.

Table 6.19 BAC parameters E_N and V calculated from Equation (6.20) for some dilute-nitride III–V ternaries and quaternaries at 300 K.

Ternary	E_N (eV)	V (eV)	Remark
$\text{GaN}_x\text{P}_{1-x}$	2.25	3.10	<i>a</i>
$\text{GaN}_x\text{As}_{1-x}$	1.65	2.70	<i>b</i>
$\text{GaN}_x\text{Sb}_{1-x}$	0.78	2.60	<i>c</i>
$\text{InN}_x\text{P}_{1-x}$	2.00	3.50	<i>d</i>
$\text{InN}_x\text{As}_{1-x}$	1.45	2.00	<i>e</i>
$\text{InN}_x\text{Sb}_{1-x}$	0.74	2.10	<i>f</i>
$\text{Ga}_x\text{In}_{1-x}\text{N}_y\text{As}_{1-y}$	$1.44 + 0.21x$	$2.7 - 4.2x + 3.5x^2$	<i>g</i>

^aFlit-determined from Figure 6.29

^bW. Shan *et al.*, *Phys. Rev. Lett.* **82**, 1221 (1999)

^cP. H. Jefferson *et al.*, *Appl. Phys. Lett.* **89**, 111921 (2006)

^dK. M. Yu *et al.*, *J. Appl. Phys.* **90**, 2227 (2001)

^eFlit-determined from Figure 6.31

^fModeled result of *k-p* calculation shown in Figure 6.31

^gI. Vurgaftman and J. R. Meyer, *J. Appl. Phys.* **94**, 3675 (2003)

The CB edge E_- and Γ -point CB minimum E_+ versus temperature have been measured by Ruko *et al.* [149] and Buyanova *et al.* [150]. The pressure dependence of E_- has also been reported [140,153]. These studies ruled out the previous assertion that the Γ –X transitions dominate the band gap in $\text{GaN}_x\text{P}_{1-x}$ at low N concentrations [154].

(c) GaNAs

Among the dilute-nitride III–V alloys, $\text{GaN}_x\text{As}_{1-x}$ was first grown epitaxially and represented a relatively new material system with unusual physical properties and potential technological importance [155]. A huge bowing of 18 eV was found in $\text{GaN}_x\text{As}_{1-x}$, which is equivalent for small N concentrations to a linear model with that slope [156]. Few attempts have been made to quantify the strong composition dependence of the band-gap energy, assuming a composition-dependent bowing parameter [157], a two-level BAC model [139,140], in the form of an arbitrary function [136,158] or a $\Delta E_g \propto x^\alpha$ ($\alpha = 2/3$) scaling rule [159].

Figure 6.29(b) plots the fundamental gaps E_- and E_+ as a function of x for $\text{GaN}_x\text{As}_{1-x}$. The experimental data for E_- are taken from Wu *et al.* [160] and for E_+ from Gil [161]. The BAC results of Equation (6.20) are indicated by the solid lines. They are calculated using $E_N = 1.65$ eV and $V = 2.70$ eV (Table 6.19) and follow the parameterization of Shan *et al.* [139]. The increase in E_+ with increasing x is nearly equal to the band-gap reduction (ΔE_g), indicative of a N-induced level repulsion.

The CP energies versus x in $\text{GaN}_x\text{As}_{1-x}$ were determined using SE [162–167] and PR [167,168]. These studies reported the blueshifted E_1 and $E_1 + \Delta_1$ peaks, together with an uncommonly strong disorder-induced broadening, with increasing x . As in $\text{GaN}_x\text{P}_{1-x}$, no clear peak shift was observed for E_0' and E_2 CPs [164,165,168]. A strong dependence of Δ_0 on composition has also not been observed [169].

The linear temperature coefficient dE_0/dT is -4.4×10^{-4} eV/K for GaAs at $T \sim 300$ K [1]. A significant reduction in the temperature coefficient of the fundamental absorption edge has been reported for $\text{GaN}_x\text{As}_{1-x}$ [170–173]; typically $dE_-/dT = -3 \times 10^{-4}$ eV/K for $x \sim 3$

at% [170,172]. Similarly, the linear pressure coefficient dE_0/dp for GaAs is $\sim 1.2 \times 10^{-1}$ eV/GPa [1], while a value for dE_-/dp of $\sim 7 \times 10^{-2}$ eV/GPa was observed for $\text{GaN}_x\text{As}_{1-x}$ with $x = 0.1$ at% at $T = 33 - 130$ K [174]. Such weak external perturbation dependence of E_- in $\text{GaN}_x\text{As}_{1-x}$ is in good agreement with the BAC model [145].

The $\text{GaN}_x\text{As}_{1-x}$ alloy at high N concentration is an attractive material for extending the wavelength range of GaN-based optoelectronic devices toward the red/IR region. The fundamental absorption edges of such As-poor (N-rich) alloys have been studied by several authors [156,175,176]. These results are shown in Figure 6.30 together with those obtained in the As-rich region [160]. The solid line shows the quadratic fit given by (E_- in eV)

$$E_- = 1.43 - 11.7x + 13.5x^2 \tag{6.22}$$

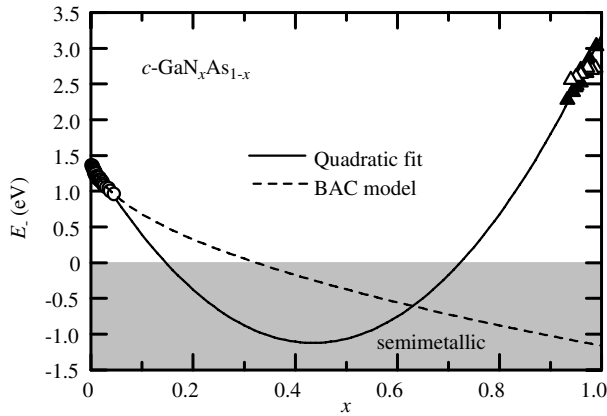


Figure 6.30 Lowest absorption edge E_- versus x for $c\text{-GaN}_x\text{As}_{1-x}$ at 300 K. The experimental data are taken from Wu *et al.* [160] (open circles), Kimura *et al.* [175] (solid triangles) and Wu *et al.* [176] (open squares). The solid line represents the quadratic least-squares fit of Equation (6.22), while the dashed line shows the BAC result of Equation (6.19) using the model parameters in Table 6.19

This fit provides huge bowing of $c = 13.5$ eV and thus results in a semimetallic overlap of the CB and VB at the intermediate compositions $0.15 \leq x \leq 0.73$. It should be noted, however, that the ~ 0.4 eV band-gap reduction observed with $x \sim 3$ at% in Figure 6.30 is similar to that measured with an N fraction of $x \sim 15$ at% [177]. No upper limit for the N concentrations for which the BAC model remains valid, has been identified so far [56].

(d) GaNSb

There has been only one experimental report on the structural and optoelectronic properties of $\text{GaN}_x\text{Sb}_{1-x}$ by MBE [178]. The $\text{GaN}_x\text{Sb}_{1-x}$ layers ($0.002 \leq x \leq 0.01$) were grown on GaAs substrates. The band-gap energies were determined from FTIR measurements. The band-gap reduction ΔE_g was solely due to the substitution of dilute amounts of highly electronegative N for Sb, and was greater than that observed in $\text{GaN}_x\text{As}_{1-x}$ with the same N concentration. The results obtained by Jefferson *et al.* are shown in Figure 6.29(c) [178]. The solid lines show the fits of these data with Equation (6.20). The parameters determined using the BAC model are listed in Table 6.19.

(e) *InNP*

Several experiments have been carried out on $\text{InN}_x\text{P}_{1-x}$ [179,180]. Bi and Tu [179] incorporated N atoms into InP by gas-source MBE using N radicals and observed the linear reduction ΔE_g with increasing N concentration. The value of ΔE_g is about 0.15 eV at $x = 1$ at%. More recently, Yu *et al.* [180] obtained dilute-nitride $\text{InN}_x\text{P}_{1-x}$ films by N^+ ion implantation into InP with N doses up to 4.8 at%. The $\text{InN}_x\text{P}_{1-x}$ layers were thermally stable up to an annealing temperature of 850 °C. The data of Yu *et al.* are shown in Figure 6.31(a) [180]. These data are nearly the same as those obtained by Bi and Tu [179]. The solid lines represent the BAC model results calculated using Equation (6.20) and the numeric parameters in Table 6.19.

(f) *InNAs*

There have been several experimental studies on the band-gap reduction in $\text{InN}_x\text{As}_{1-x}$ [181–184]. All these studies showed that the band gap was reduced with increasing x , as shown in Figure 6.31(b). The solid lines in Figure 6.31(b) represent the results calculated using

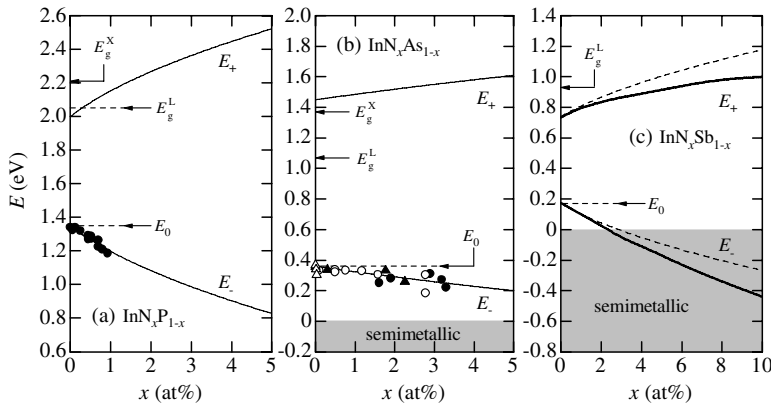


Figure 6.31 (a) N concentration dependence of the CB edge E_- and Γ -point CB minimum E_+ in $\text{InN}_x\text{P}_{1-x}$ at 300 K [180]. (b) N concentration dependence of the CB edge E_- and Γ -point CB minimum E_+ in $\text{InN}_x\text{As}_{1-x}$ at 300 K [181–184]. (c) N concentration dependence of the CB edge E_- and Γ -point CB minimum E_+ in $\text{InN}_x\text{Sb}_{1-x}$ at 300 K. The solid lines in (a) and (b) and dashed lines in (c) represent the BAC results of Equation (6.20) using the model parameters in Table 6.19, while the solid lines in (c) show $k\cdot p$ calculation made by Veal *et al.* [187]. The horizontal arrows indicate the positions of the E_0 , E_g^X and E_g^L gaps in the host semiconductor InP, InAs or InSb

Equation (6.20) with $E_N = 1.45$ eV and $V = 2.00$ eV (Table 6.19). The effective N level $E_N = 1.45$ eV is nearly equal to those reported by Shih *et al.* [182] and Veal *et al.* [184] (1.48 eV). The interaction potential $V = 2.00$ eV is slightly larger than those in Shih *et al.* [182] (1.68 eV), Kuroda *et al.* [183] (1.86 eV) and Veal *et al.* [184] (1.77 eV).

The higher-lying CPs E_1 and $E_1 + \Delta_1$ in $\text{InN}_x\text{As}_{1-x}$ were studied using SE [185]. They were blue-shifted at a rate of $\sim 20\text{--}25$ meV/at%[N].

(g) InNSb

Murdin *et al.* [186] measured the electron effective mass near the band anticrossing point by CR in $\text{InN}_x\text{Sb}_{1-x}$ with the absorption edge near $15 \mu\text{m}$. The observed results directly demonstrate band anticrossing and quantitatively confirm an increase in the effective mass predicted by a tight binding calculation for low N concentration ($x < 1$ at%).

More recently, Veal *et al.* [187] formed a thin $\text{InN}_x\text{Sb}_{1-x}$ layer by low-energy N implantation on InSb and found from XPS that N occupies ~ 6 at% of the anion sublattice sites. Using HREELS, they also observed the absence of a depletion layer, indicating that the Fermi level is located below the VB maximum. Consequently, the CB minimum is located below the VB maximum, meaning that a negative band-gap material has been formed. These results are consistent with the $k\cdot p$ calculation that predicts a semimetallic band structure, as shown by the solid lines in Figure 6.31(c) [187]. The dashed lines in Figure 6.31(c) show the parameterization fits of the $k\cdot p$ results (solid lines) using Equation (6.20). The resulting parameters are found to be $E_N = 0.74$ eV and $V = 2.10$ eV (Table 6.19).

Table 6.20 Energies for some indirect and direct gaps in some Al-(V, V) ternaries at 300 K

Ternary	Band gap	Expression (eV)	Remark
$\text{AlP}_x\text{As}_{1-x}$	E_g^X	$2.15 - 0.07x + 0.40x^2$	<i>a</i>
	E_g^L	$2.37 + 0.82x + 0.38x^2$	<i>a</i>
	E_0	$3.01 + 0.77x + 0.13x^2$	<i>b</i>
$\text{AlP}_x\text{Sb}_{1-x}$	E_g^X	$1.615 + 0.588x + 0.277x^2$	<i>a</i>
	E_g^L	$2.211 + 0.603x + 0.756x^2$	<i>a</i>
	E_0	$2.27 - 0.49x + 2.13x^2$	<i>b</i>
$\text{AlAs}_x\text{Sb}_{1-x}$	E_g^X	$1.615 + 0.285x + 0.250x^2$	<i>a</i>
	E_g^L	$2.211 - 0.315x + 0.474x^2$	<i>a</i>
	E_0	$2.27 - 0.45x + 1.19x^2$	<i>b</i>

^aBowing parameter is obtained from a theoretical study by A.-B. Chen and A. Sher (*Semiconductor Alloys*. Plenum, New York, 1995)

^bBowing parameter is estimated from Equation (6.23)

6.3.6 Al-(V, V) Alloy

The minimum gaps in the Al-based III-V ternaries $\text{AlP}_x\text{As}_{1-x}$, $\text{AlP}_x\text{Sb}_{1-x}$ and $\text{AlAs}_x\text{Sb}_{1-x}$ are an indirect band gaps throughout their whole composition range with the CB minimum located in the vicinity of the X point, as shown in Figure 6.32. The various curves have been calculated from the data in Table 6.20. The bowing parameters c for E_0 are estimated from the product of the lattice constant and electronegativity differences (Equation (6.23)). The bowing parameters c for E_g^L and E_g^X are obtained from the theoretical calculations by Chen and Sher [188].

Very few studies have been carried out on the determination of the energy-band structures for the Al-(V, V) ternaries. Saadallah *et al.* [189] have studied the photothermal properties of an MBE-grown $\text{AlAs}_{0.08}\text{Sb}_{0.92}/\text{GaSb}$ layer. From the absorption spectrum they obtained, we can

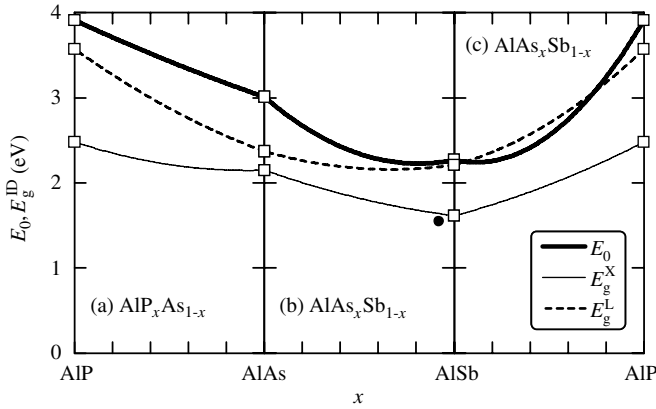


Figure 6.32 Energies of the lowest direct E_0 and indirect gaps E_g^{ID} versus x for (a) $\text{AlP}_x\text{As}_{1-x}$, (b) $\text{AlAs}_x\text{Sb}_{1-x}$ and (c) $\text{AlP}_x\text{Sb}_{1-x}$ at 300 K. The solid circle in (b) is estimated from an optical absorption spectrum by Saadallah *et al.* [189]. The various curves in (a)–(c) represent the calculated results using the data in Table 6.20

estimate an absorption edge at ~ 800 nm (~ 1.55 eV). The solid circle in Figure 6.32(b) represents this data.

6.3.7 Ga–(V, V) Alloy

(a) GaPAs

$\text{GaP}_x\text{As}_{1-x}$ remains a direct gap material in the composition range $0 \leq x \leq 0.48$ at room temperature. Above $x \sim 0.48$, the alloy becomes indirect because the X-valley minimum crosses below the Γ -valley minimum. The bowing parameter for E_0 reported previously lies within a relatively narrow range $c = 0.174\text{--}0.21$ eV [89]. The lowest direct and indirect gaps for $\text{GaP}_x\text{As}_{1-x}$ as determined by ER [190] and PL measurements [191], respectively, are shown in Figure 6.33(a). The $c = 0.24$ eV value for E_g^{X} recommended by Vurgaftman *et al.* [89] lies approximately in the middle of the previously reported range of $0.20\text{--}0.28$ eV. The same authors also recommended a value of $c = 0.16$ eV for E_g^{L} .

The higher-lying CPs, such as $E_1, E_1 + \Delta_1, E_0', E_0' + \Delta_0', E_2$ and $E_2 + \delta$, in $\text{GaP}_x\text{As}_{1-x}$ have been determined by ER [190], reflectivity [192] and SE [193]. The kinks in the slope of the composition dependence of E_1 and $E_1 + \Delta_1$ are found at $x \sim 0.5$ [190,192]. A recent SE study does not confirm such an anomaly, but observes some alloy disorder effects, i.e. a large positive bowing for E_0 and a large reduction in the $E_1/(E_1 + \Delta_1)$ strengths at $x \sim 0.5$ [193]. The large bowing reported is $c = 0.54$ eV, which is larger by more than a factor of 2 than the commonly accepted values ($0.20\text{--}0.28$ eV). This large bowing effect has not been verified and relies on only two data points with intermediates at $x = 0.4$ and 0.7 . All CPs higher than $E_1/(E_1 + \Delta_1)$ showed an almost linear increase with x [190,192,193], as shown in Figure 6.33(b). The recommended band-gap expressions are listed in Table 6.21.

The temperature effects on the fundamental absorption edge especially near the $E_0\text{--}E_g^{\text{X}}$ crossover region in $\text{GaP}_x\text{As}_{1-x}$ were studied using PL [191,194] and optical absorption [195]. As the temperature was increased to above 77 K, marked changes in PL were observed for both

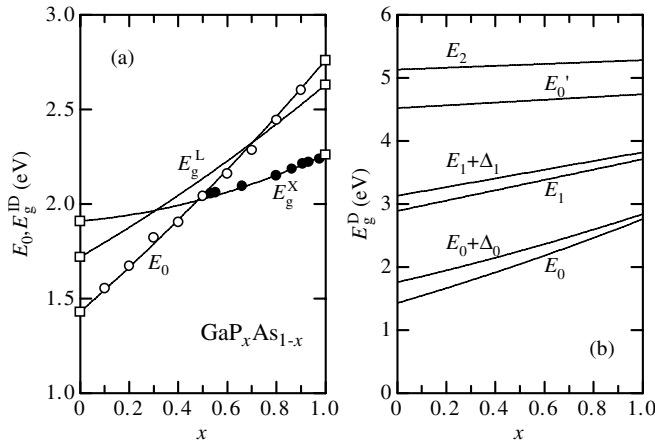


Figure 6.33 (a) Energies of the lowest direct E_0 and indirect gaps E_g^{ID} versus x for $\text{GaP}_x\text{As}_{1-x}$ at 300 K. The experimental data are taken for E_0 from Thompson *et al.* [190] (open circles) and for E_g^{X} from Craford *et al.* [191] (solid circles). (b) Energies of some CPs versus x for $\text{GaP}_x\text{As}_{1-x}$ at 300 K. The solid lines in (a) and (b) represent the calculated results using the data in Table 6.21

N-doped and N-free alloys [191]. In both cases the higher-energy or near-band-edge process dominated the emission as the temperature was increased. Zero-phonon as well as phonon-assisted transitions were identified in the intrinsic absorption edge [195].

(b) GaPSb

There are very few reports relating to $\text{GaP}_x\text{Sb}_{1-x}$ in the literature [196,197]. The intrinsic absorption edge in $\text{GaP}_x\text{Sb}_{1-x}$ as a function of x obtained by PL measurements is shown in

Table 6.21 Energies for some direct and indirect gaps in $\text{GaP}_x\text{As}_{1-x}$ at 300 K

Band gap	Expression (eV)	Remark
E_0	$1.43 + 1.14x + 0.19x^2$	<i>a</i>
E_g^{L}	$1.72 + 0.75x + 0.16x^2$	<i>a</i>
$E_0 + \Delta_0$	$1.76 + 0.90x + 0.18x^2$	<i>b</i>
E_g^{X}	$1.910 + 0.111x + 0.240x^2$	<i>a</i>
E_1	$2.89 + 0.82x$	<i>c</i>
$E_1 + \Delta_1$	$3.13 + 0.69x$	<i>c</i>
E_0'	$4.52 + 0.22x$	<i>c</i>
E_2	$5.13 + 0.15x^2$	<i>c</i>

^aBowing parameter is obtained from I. Vurgaftman *et al.* (*J. Appl. Phys.* **89**, 5815 (2001))

^bBowing parameter is fit-determined from experimental data reported by A. G. Thomson *et al.* (*Phys. Rev.* **146**, 601 (1966))

^cBowing parameter ($c = 0$ eV) is obtained from A. G. Thomson *et al.* (*Phys. Rev.* **146**, 601 (1966)) and K. J. Kim *et al.* (*J. Appl. Phys.* **84**, 3696 (1998))

Figure 6.34(a) [196,197]. The solid lines represent the E_0 , E_g^X and E_g^L versus x data obtained by putting $c = 2.7$ eV into Equation (A.5). This bowing parameter is taken from Vurgaftman *et al.* [89]. Although the experimental data scatter largely, the curves of the calculated results explain the experimental data very well. From Figure 6.34(a), we can expect the $E_0 - E_g^X$ crossover to occur at $x \sim 0.4$.

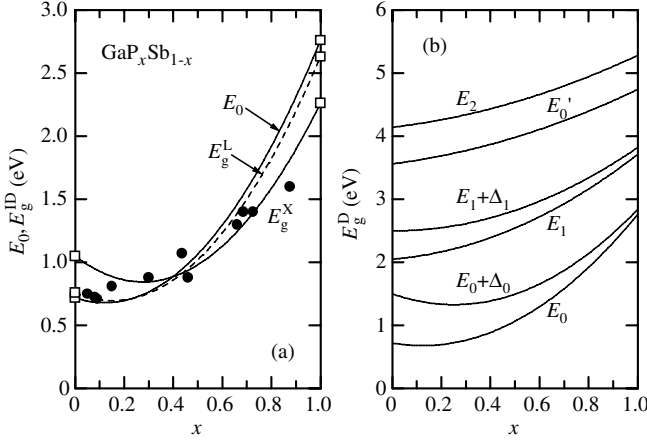


Figure 6.34 (a) Energies of the lowest direct E_0 and indirect gaps E_g^{ID} versus x for $\text{GaP}_x\text{Sb}_{1-x}$ at 300 K. The experimental data are taken from Jou *et al.* [196] and Loualiche *et al.* [197] (solid circles). (b) Energies of some CPs versus x for $\text{GaP}_x\text{Sb}_{1-x}$ at 300 K. The solid lines in (a) and (b) represent the calculated results using the data in Table 6.22

There have been no reports published concerning the higher-lying CPs in $\text{GaP}_x\text{Sb}_{1-x}$. We, therefore, assume the bowing parameters for E_1 and $E_1 + \Delta_1$ to be a half of that for E_0 and those for E_0' and E_2 to be a quarter of that for E_0 . Such trends can be found in some III-V ternary alloys (see e.g. $\text{GaAs}_x\text{Sb}_{1-x}$ in Table 6.23). The solid lines in Figure 6.34(b) show the calculated results using the data in Table 6.22.

Table 6.22 Energies for some direct and indirect gaps in $\text{GaP}_x\text{Sb}_{1-x}$ at 300 K

Band gap	Expression (eV)	Remark
E_0	$0.72 - 0.66x + 2.70x^2$	<i>a</i>
E_g^L	$0.76 - 0.83x + 2.70x^2$	<i>a</i>
E_g^X	$1.050 - 1.489x + 2.700x^2$	<i>a</i>
$E_0 + \Delta_0$	$1.50 - 1.36x + 2.70x^2$	<i>b</i>
E_1	$2.05 + 0.31x + 1.35x^2$	<i>c</i>
$E_1 + \Delta_1$	$2.50 - 0.03x + 1.35x^2$	<i>c</i>
E_0'	$3.56 + 0.50x + 0.68x^2$	<i>d</i>
E_2	$4.14 + 0.46x + 0.68x^2$	<i>d</i>

^aBowing parameter is obtained from I. Vurgaftman *et al.* (*J. Appl. Phys.* **89**, 5815 (2001))

^bPostulated bowing parameter equal to that for E_0

^cBowing parameter is assumed to be a half of that for E_0 ($c = 1.35$ eV)

^dBowing parameter is assumed to be a quarter of that for E_0 ($c = 0.68$ eV)

(c) *GaAsSb*

$\text{GaAs}_x\text{Sb}_{1-x}$ remains a direct gap material over the whole composition range, as shown in Figure 6.35(a). The E_0 -gap bowing parameter has been determined using various techniques [89]. The experimental data plotted in Figure 6.35(a) were obtained from PL results by Nahory *et al.* [198] (solid circles) and from optical absorption measurements by Yano *et al.* [199] (open circles) and McGlenn *et al.* [200] (solid triangles). The quadratic fit of these data provides $c = 1.25$ eV for E_0 . This value is slightly smaller than that recommended by Vurgaftman *et al.* [89] ($c = 1.43$ eV). No experimental data are available for the c values of E_g^X and E_g^L . In Figure 6.35(a), the x -dependent E_g^X and E_g^L curves are calculated by introducing $c = 1.20$ eV into Equation (A.5). These bowing parameters are recommended by Vurgaftman *et al.* [89].

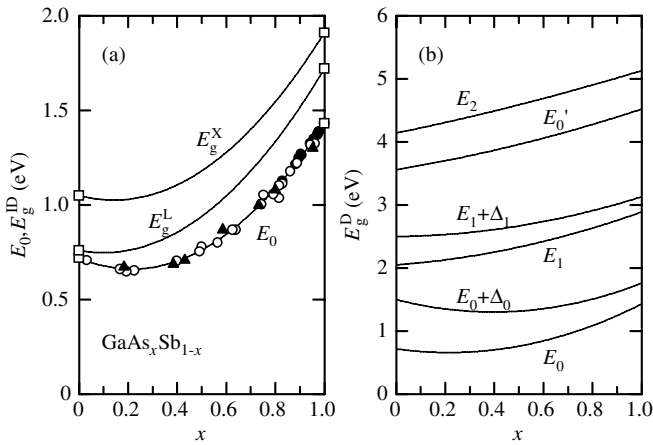


Figure 6.35 (a) Energies of the lowest direct E_0 and indirect gaps E_g^{ID} versus x for $\text{GaAs}_x\text{Sb}_{1-x}$ at 300 K. The experimental data are taken from Nahory *et al.* [198] (solid circles), Yano *et al.* [199] (open circles) and McGlenn *et al.* [200] (solid triangles). (b) Energies of some CPs versus x for $\text{GaAs}_x\text{Sb}_{1-x}$ at 300 K. The solid lines in (a) and (b) represent the calculated results using the data in Table 6.23

The higher-lying CPs have been investigated on MBE-grown $\text{GaAs}_x\text{Sb}_{1-x}$ ($0.56 \leq x \leq 1.0$) on GaAs(100) substrates using PR [201] and those ($0.35 \leq x \leq 0.78$) grown on InP(100) substrates by MOCVD using SE [202]. Serries *et al.* [203] determined strained and relaxed $E_1/(E_1 + \Delta_1)$ energies before and after correction for strain effects. The sample thickness used by Ferrini *et al.* [201] was in the range $0.6\text{--}1$ μm for complete strain release at each mole fraction. The results obtained by these authors [201,203], together with those for E_0 and $E_0 + \Delta_0$ (Table 6.23) are shown in Figure 6.35(b).

The temperature dependence of E_0 in $\text{GaAs}_x\text{Sb}_{1-x}$ has been studied by several authors [203–205]. Lukic-Zrnica *et al.* [204] obtained the Varshni parameters α and β , which describe not only their own data well, but also the previous data of Merkel *et al.* [203]. More recently, Chouaib *et al.* [205] obtained the Varshni parameters $\alpha = (4.0 \pm 0.1) \times 10^{-4}$ ($(3.9 \pm 0.1) \times 10^{-4}$) eV/K and $\beta = 143 \pm 18$ (140 ± 14) K for unintentionally doped (Si-doped) $\text{GaAs}_x\text{Sb}_{1-x}/\text{InP}$. These values are in reasonable agreement with those obtained by Lukic-Zrnica *et al.* [204]. Note that $\text{GaAs}_x\text{Sb}_{1-x}$ can be grown lattice-matched to InP at $x \sim 0.5$.

Table 6.23 Energies for some direct and indirect gaps in GaAs_xSb_{1-x} at 300 K

Band gap	Expression (eV)	Remark
E_0	$0.72 - 0.54x + 1.25x^2$	<i>a</i>
E_g^L	$0.76 - 0.24x + 1.20x^2$	<i>b</i>
E_g^X	$1.05 - 0.34x + 1.20x^2$	<i>b</i>
$E_0 + \Delta_0$	$1.50 - 0.99x + 1.25x^2$	<i>c</i>
E_1	$2.05 + 0.29x + 0.55x^2$	<i>d</i>
$E_1 + \Delta_1$	$2.50 + 0.04x + 0.59x^2$	<i>d</i>
E_0'	$3.56 + 0.64x + 0.32x^2$	<i>e</i>
E_2	$4.14 + 0.80x + 0.19x^2$	<i>e</i>

^aFlit-determined from Figure 6.35

^bBowing parameter is obtained from I. Vurgaftman *et al.* (*J. Appl. Phys.* **89**, 5815 (2001))

^cPostulated bowing parameter equal to that for E_0

^dBowing parameter is obtained from D. Serries *et al.* (*J. Appl. Phys.* **87**, 8522 (2000))

^eBowing parameter is obtained from R. Ferrini *et al.* (*J. Appl. Phys.* **86**, 4706 (1999))

6.3.8 In-(V, V) Alloy

(a) InPAs

Due to the high vapor pressure of As and P elements, growth of InP_xAs_{1-x} from the melt has received very little attention. Antypas and Yep [206] prepared InP_xAs_{1-x} ($0.735 \leq x \leq 1.0$) by LPE and undertook PL measurements. Nicholas *et al.* [207] also grew InP_xAs_{1-x} layers ($0 \leq x \leq 1.0$) by CVD and obtained their optical absorption spectra. More recently, Wada *et al.* [208] carried out both PL and absorption measurements on InP_xAs_{1-x} layers ($0.33 \leq x \leq 1.0$) grown by MOCVD on InP(100) substrates. The E_0 values for InP_xAs_{1-x} obtained by these authors have been plotted in Figure 6.36(a). From these data, the bowing parameter $c = 0.145$ eV for E_0 can be obtained. Note, however, that the most recent data produced by Bui *et al.* [209] using PR, showed clear upward bowing of $c = -0.22$ eV. Figure 6.36(a) also shows the composition dependence of E_g^X and E_g^L calculated from Equation (A.5) with the same c value as that for E_0 (0.145 eV).

ER measurements were carried out on InP_xAs_{1-x} by Vishnubhatla *et al.* [129] and Thompson *et al.* [210]. Choi *et al.* [211] also used SE to investigate the band structure of InP_xAs_{1-x} films on InP(100). The composition dependence of the higher-lying CPs, such as E_1 , $E_1 + \Delta_1$, E_0' and E_2 CPs, was determined from such investigations. Figure 6.36(b) shows the results of Vishnubhatla *et al.* [129]. Table 6.24 summarizes the numeric expressions.

The temperature variation of E_0 in InP_xAs_{1-x} has been studied by Wada *et al.* [208]. The linear temperature coefficient dE_0/dT for InP and InAs was reported to be -3.3×10^{-4} and -4.2×10^{-4} eV/K, respectively [1]. The InP_xAs_{1-x} value obtained by Wada *et al.* is approximately -3×10^{-4} eV/K and is independent of x .

(b) InPSb

InP_xSb_{1-x} may be an alternative material to Al-based semiconductor alloys, which commonly suffer from carbon and oxygen impurities. However, the predicted miscibility gap of this alloy

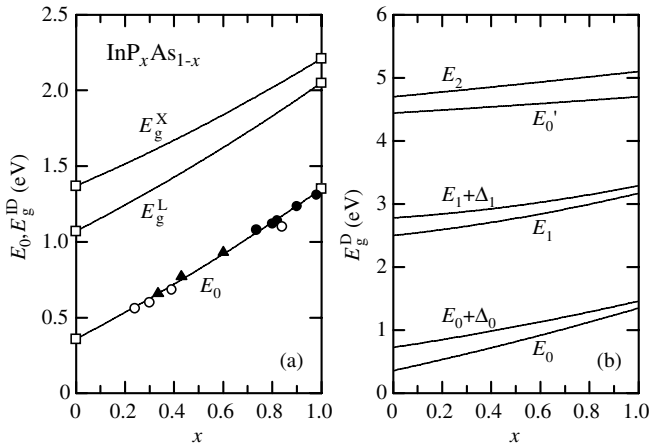


Figure 6.36 (a) Energies of the lowest direct E_0 and indirect gaps E_g^{ID} versus x for $\text{InP}_x\text{As}_{1-x}$ at 300 K. The experimental data are taken from Antypas and Yep [206] (solid circles), Nicholas *et al.* [207] (open circles) and Wada *et al.* [208] (solid triangles). (b) Energies of some CPs versus x for $\text{InP}_x\text{As}_{1-x}$ at 300 K. The solid lines in (a) and (b) represent the calculated results using the data in Table 6.24

could limit its usefulness in device applications. Reihlen *et al.* [212] succeeded in growing $\text{InP}_x\text{Sb}_{1-x}$ epilayers on InP, InAs and InSb by MOCVD and examined their optical properties. Duncan *et al.* [213] also grew an $\text{InP}_x\text{Sb}_{1-x}/\text{InP}$ epilayer and obtained $E_0 = 0.6$ eV at 300 K from PL measurements. These results are shown in Figure 6.37(a). The least-squares fit of these data gives a bowing parameter of $c = 1.60$ eV. This value is slightly smaller than $c = 1.9 \pm 0.1$ eV obtained at 10 K by Jou *et al.* [196].

The solid lines in Figure 6.37(a) show the composition dependence of E_g^{X} and E_g^{L} and have been obtained by putting the same c values for E_0 (1.60 eV) into Equation (A.5) since to date no alternative reliable data have been published.

Table 6.24 Energies for some direct and indirect gaps in $\text{InP}_x\text{As}_{1-x}$ at 300 K

Band gap	Expression (eV)	Remark
E_0	$0.359 + 0.846x + 0.145x^2$	<i>a</i>
$E_0 + \Delta_0$	$0.726 + 0.589x + 0.145x^2$	<i>b</i>
E_g^{L}	$1.070 + 0.835x + 0.145x^2$	<i>b</i>
E_g^{X}	$1.370 + 0.695x + 0.145x^2$	<i>b</i>
E_1	$2.50 + 0.42x + 0.25x^2$	<i>c</i>
$E_1 + \Delta_1$	$2.78 + 0.26x + 0.25x^2$	<i>c</i>
E_0'	$4.44 + 0.24x + 0.02x^2$	<i>c</i>
E_2	$4.70 + 0.37x + 0.03x^2$	<i>c</i>

^aFlit-determined from Figure 6.36

^bPostulated bowing parameter equal to that for E_0

^cBowing parameter is obtained from S. S. Vishnubhatla *et al.* (*Can. J. Phys.* **47**, 1661 (1969))

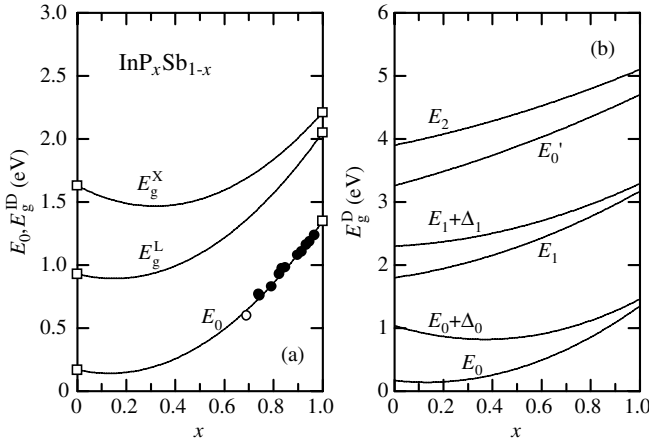


Figure 6.37 (a) Energies of the lowest direct E_0 and indirect gaps E_g^{ID} versus x for $\text{InP}_x\text{Sb}_{1-x}$ at 300 K. The experimental data are taken from Reihlen *et al.* [212] (solid circles) and Duncan *et al.* [213] (open circle). (b) Energies of some CPs versus x for $\text{InP}_x\text{Sb}_{1-x}$ at 300 K. The solid lines in (a) and (b) represent the calculated results using the data in Table 6.25

Since there have been no published reports relating to the higher-lying CPs in $\text{InP}_x\text{Sb}_{1-x}$, let us, therefore, assume the bowing parameters for E_1 and $E_1 + \Delta_1$ to be a half of that for E_0 and those for E_0' and E_2 to be a quarter of that for E_0 (see Section 6.3.7(b)). The solid lines in Figure 6.37(b) represent the calculated results using such bowing parameters. The recommended band-gap expressions are summarized in Table 6.25.

(c) *InAsSb*

InSb has the smallest band gap among the III–V binary semiconductors ($E_0 = 0.17$ eV at 300 K). The $\text{InAs}_x\text{Sb}_{1-x}$ alloy has the lowest band gap among all III–V semiconductors, with values as small as 0.1 eV at room temperature. The bowing parameter c for E_0 previously

Table 6.25 Energies for some direct and indirect gaps in $\text{InP}_x\text{Sb}_{1-x}$ at 300 K

Band gap	Expression (eV)	Remark
E_0	$0.17 - 0.42x + 1.60x^2$	<i>a</i>
E_g^{L}	$0.93 - 0.48x + 1.60x^2$	<i>b</i>
$E_0 + \Delta_0$	$1.04 - 1.18x + 1.60x^2$	<i>b</i>
E_g^{X}	$1.63 - 1.02x + 1.60x^2$	<i>b</i>
E_1	$1.80 + 0.57x + 0.80x^2$	<i>c</i>
$E_1 + \Delta_1$	$2.30 + 0.19x + 0.80x^2$	<i>c</i>
E_0'	$3.26 + 1.04x + 0.40x^2$	<i>d</i>
E_2	$3.90 + 0.80x + 0.40x^2$	<i>d</i>

^aFlit-determined from Figure 6.37

^bPostulated bowing parameter equal to that for E_0

^cBowing parameter is assumed to be a half of that for E_0 ($c = 0.80$ eV)

^dBowing parameter is assumed to be a quarter of that for E_0 ($c = 0.40$ eV)

reported for $\text{InAs}_x\text{Sb}_{1-x}$ is ~ 0.6 eV [89]. The values of E_0 as a function of x for $\text{InAs}_x\text{Sb}_{1-x}$ have been plotted in Figure 6.38(a). The experimental data have been obtained from Woolley and Warner [214], Stringfellow and Greene [215] and Dobbelaere *et al.* [216]. The least-squares fit of these data gives $c = 0.600$ eV. The composition dependence of E_g^X and E_g^L obtained from Equation (A.5) using the same bowing parameter as that for E_0 ($c = 0.60$ eV) have also been plotted in Figure 6.38(a).

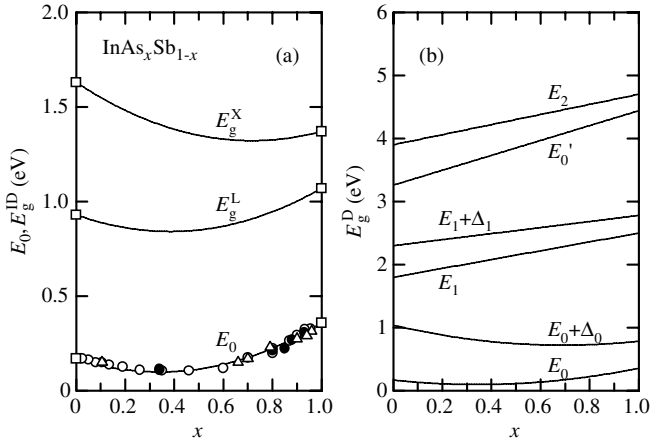


Figure 6.38 (a) Energies of the lowest direct E_0 and indirect gaps E_g^{ID} versus x for $\text{InAs}_x\text{Sb}_{1-x}$ at 300 K. The experimental data are taken from Woolley and Warner [214] (open circles), Stringfellow and Greene [215] (open triangles) and Dobbelaere *et al.* [216] (solid circles). (b) Energies of some CPs versus x for $\text{InAs}_x\text{Sb}_{1-x}$ at 300 K. The solid lines in (a) and (b) represent the calculated results using the data in Table 6.26

SE was used to investigate the higher-lying CPs in $\text{InAs}_x\text{Sb}_{1-x}$ [217]. The x -dependent E_1 , $E_1 + \Delta_1$ and E_2 CPs were determined from this study. These results, together with those for E_0 and $E_0 + \Delta_0$ CPs, are shown in Figure 6.38(b) and summarized in Table 6.26.

Table 6.26 Energies for some direct and indirect gaps in $\text{InAs}_x\text{Sb}_{1-x}$ at 300 K. LI = linear interpolation.

Band gap	Expression (eV)	Remark
E_0	$0.170 - 0.411x + 0.600x^2$	<i>a</i>
E_g^L	$0.93 - 0.46x + 0.60x^2$	<i>b</i>
$E_0 + \Delta_0$	$1.04 - 0.914x + 0.600x^2$	<i>b</i>
E_g^X	$1.63 - 0.86x + 0.60x^2$	<i>b</i>
E_1	$1.8 + 0.7x$	<i>c</i>
$E_1 + \Delta_1$	$2.30 + 0.48x$	<i>c</i>
E_0'	$3.26 + 1.18x$	LI
E_2	$3.9 + 0.8x$	<i>e</i>

^aFlit-determined from Figure 6.38

^bPostulated bowing parameter equal to that for E_0

^cBowing parameter ($c = 0$ eV) is obtained from H. Y. Deng and N. Dai (*Phys. Rev. B* **73**, 113102 (2006))

The Varshni parameters for E_0 in InAs (InSb) are reported to be $\alpha = 3.07 \times 10^{-4}$ eV/K (2.7×10^{-4} eV/K) and $\beta = 191$ K (106 K) [1]. The Varshni parameters for InAs_{*x*}Sb_{1-*x*} have also been determined by a number of authors, although the alloy composition was limited to a narrow region (see e.g. [218–222]). These data give the Varshni parameters of $\alpha \sim 2.4 \times 10^{-4}$ eV/K and $\beta \sim 180$ K both of which are nearly independent of x , although the alloy composition was in the limited range $x \leq 0.06$ or $x \geq 0.799$. Only the data of Bansal *et al.* [220] gave the extremely large values of $\alpha = 7.1 \times 10^{-4}$ eV/K and $\beta = 675$ K for $x = 0.05$.

6.3.9 Summary

This section has concentrated on reviewing the lowest direct and indirect gaps, together with some higher-lying CPs in III–V ternary alloys. These energy gaps have an approximately quadratic dependence on the mole fraction of one endpoint material x . The main emphasis is thus on the nonlinear or bowing parameter c .

The lowest direct (E_0) and indirect gaps (E_g^X) versus composition x for some cubic III–V ternary alloys are shown in Figure 6.39. The degree of bowing varies quite considerably depending on the band gap in question. The large, positive bowing effect obtained in the VCA is largely a volume effect [4]. An impressive plot of a large parabola composed of the individual E_0 versus x plots is shown in Figure 6.39 (AlAs–GaAs–...–GaSb–AlSb).

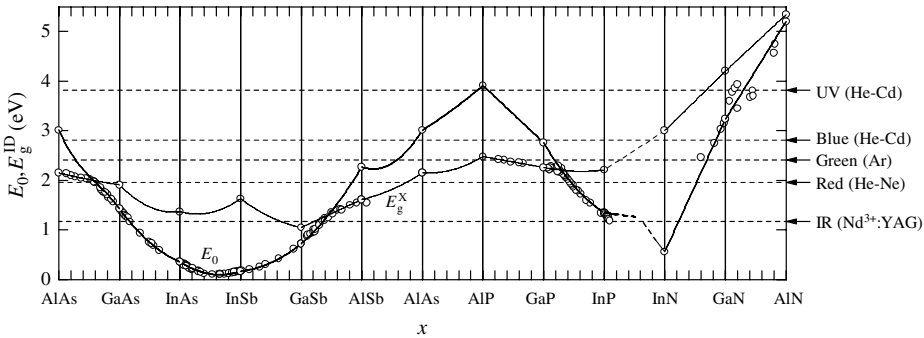


Figure 6.39 Lowest direct E_0 and indirect gaps E_g^X versus composition x for some cubic III–V semiconductor ternary alloys at 300 K. The experimental data are shown by the open circles

Table 6.27 summarizes the bowing parameters c for E_0 , E_g^X and E_g^L in some (III, III)–V and III–(V, V) ternary alloys. The degree of bowing does not appear to be directly related to the binary energy steps. Figure 6.40 shows these parameters plotted against the product $\Delta a_{\alpha\beta}\Delta X_{\alpha\beta}$ of the lattice constant and electronegativity differences between the endpoint binaries α and β . The electronegativity differences were obtained from Phillips' data [46]. The solid line in Figure 6.40 represents the least-squares fit given by (c in eV, $\Delta a_{\alpha\beta}\Delta X_{\alpha\beta}$ in ÅeV)

$$c = 9.62(\Delta a_{\alpha\beta}\Delta X_{\alpha\beta}) \quad (6.23)$$

Note that the proportionality factor 9.62 Å^{-1} in Equation (6.23) is slightly smaller than that (9.93 Å^{-1}) obtained in Equation (6.8). The c values for the Al–(V, V) ternary alloys shown in Table 6.20 are calculated from Equation (6.23).

Table 6.27 Bowing parameters c for E_0 , E_g^X and E_g^L in some (III, III)-V and III-(V, V) ternaries (in eV)

Ternary	E_0	E_g^X	E_g^L	Ternary	E_0	E_g^X	E_g^L
(Al, Ga)P	0	0	0	Al(P, As)	0.13 ^a	0.40	0.38
(Al, In)P	0.40	0	0	Al(P, Sb)	2.13 ^a	0.277	0.756
(Ga, In)P	0.65	0.200	0.34	Al(As, Sb)	1.19 ^a	0.250	0.474
(Al, Ga)As	0.127 ^b	0.055	0	Ga(P, As)	0.19	0.240	0.16
(Al, In)As	0.72	0	0	Ga(P, Sb)	2.70	2.700	2.70
(Ga, In)As	0.58	0.70	0.50	Ga(As, Sb)	1.25	1.20	1.20
(Al, Ga)Sb	0.044 ^b	0	0	In(P, As)	0.145	0.145	0.145
(Al, In)Sb	0.43	0	0	In(P, Sb)	1.60	1.60	1.60
(Ga, In)Sb	0.415	0.33	0.40	In(As, Sb)	0.60	0.60	0.60

^aEstimated from Equation (6.23)

^bIn the limit $x \rightarrow 0$ (see e.g. Equation (6.12))

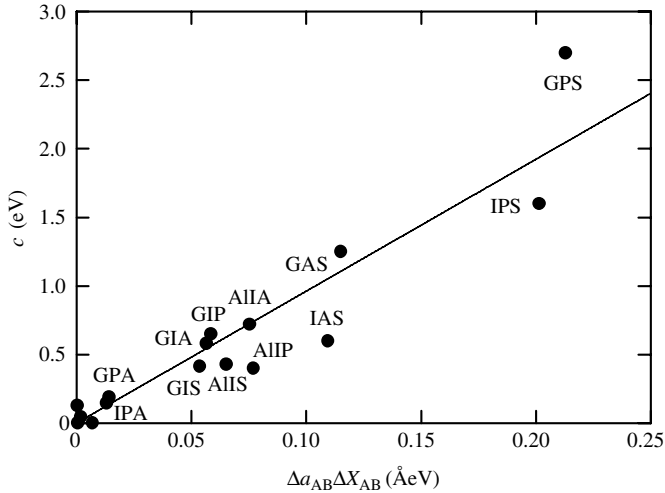


Figure 6.40 Bowing parameter c of the Γ -valley gap E_0 versus product $\Delta a_{\alpha\beta}\Delta X_{\alpha\beta}$ of the lattice-constant and electronegativity differences between the endpoint binary materials α and β in some III-V semiconductor ternary alloys. The solid line represents the calculated result using Equation (6.23). G = Ga; I = In; A = As; S = Sb

6.4 III-V SEMICONDUCTOR QUATERNARY ALLOY

6.4.1 Dilute-nitride Quaternary Alloy

(a) AlGaAs

The energy gaps in dilute-nitride $\text{Al}_x\text{Ga}_{1-x}\text{N}_y\text{As}_{1-y}$ have been investigated by Shan *et al.* [180]. The energy positions of E_- and E_+ can be explained by assuming an anticrossing interaction between states at the Γ minimum and located N state E_N whose energy depends on x in the

following manner $E_N(x) = 1.65 + 0.61x$ eV. The E_+ transitions lie above the Γ -valley CB minimum even in the indirect gap region of the $\text{Al}_x\text{Ga}_{1-x}\text{As}$ matrix. The results indicate that the N-induced interactions between the extended Γ , L and X CB states do not play a significant role in the modification of the CB structure of dilute-nitride III–V alloys.

(b) GaInNP

Some studies on $\text{Ga}_x\text{In}_{1-x}\text{N}_y\text{P}_{1-y}$ have been carried out using PL [223,224] and PR [225,226]. All these studies suggested that N incorporation reduces the fundamental absorption edge of $\text{Ga}_x\text{In}_{1-x}\text{P}$. The BAC parameters are $E_N = 2.1 \pm 0.1$ eV and $V = 1.7 \pm 0.2$ eV for $x = 0.44\text{--}0.49$ [224] and $E_N = 2.040$ eV and $V = 1.449 \pm 0.170$ eV for $x = 0.46$ [226]. A somewhat weaker temperature dependence of the band-gap energy was reported by Buyanova *et al.* [224], but Lin and Hwang [226] were unable to confirm such a weak temperature dependence.

(c) GaInNAs

Vurgaftman and Meyer [56] reviewed the results of studies on $\text{Ga}_x\text{In}_{1-x}\text{N}_y\text{As}_{1-y}$. The addition of N narrows the band gap for lower In concentrations, while at the same time providing tensile strain compensation. Samples with very low In compositions in the order of 10 at% showed no significant difference from $\text{GaN}_x\text{As}_{1-x}$ apart from the expected $\text{Ga}_x\text{In}_{1-x}\text{As}$ gap decrease including bowing [56,89]. However, for samples with larger In contents grown on GaAs and InP, an alternative parameterization with the BAC model was proposed [227]. The interaction potentials V recommended for $\text{GaN}_x\text{As}_{1-x}$ and $\text{InN}_x\text{As}_{1-x}$ are 2.70 and 2.00 eV, respectively (Table 6.19). Pan *et al.* [228] took E_N to be independent of the In concentration and used $V = 2.5$ eV for $\text{Ga}_x\text{In}_{1-x}\text{N}_y\text{As}_{1-y}$ with $x = 0.7\text{--}0.9$. Choulis *et al.* [229] made the same assumption regarding E_N , but the interaction potential was considerably lower ($V = 1.675$ eV). A similar value ($V = 1.7$ eV) was independently proposed by Polimeni *et al.* [230] for $x = 0.24\text{--}0.41$.

On the other hand, Sun *et al.* [231] used $V = 2.8\text{--}3.0$ eV to explain PL and PLE spectra in $\text{Ga}_x\text{In}_{1-x}\text{N}_y\text{As}_{1-y}/\text{GaAs}$ QWs ($x = 27.2$ at%). Serries *et al.* [232] also obtained the V values for high In-containing $\text{Ga}_x\text{In}_{1-x}\text{N}_y\text{As}_{1-y}/\text{InP}$ films and showed the QWs to be only slightly smaller than that reported for low In-content $\text{Ga}_x\text{In}_{1-x}\text{N}_y\text{As}_{1-y}/\text{GaAs}$ films. Vurgaftman and Meyer [56] suggested x -dependent E_N and V values for $\text{Ga}_x\text{In}_{1-x}\text{N}_y\text{As}_{1-y}$ and these values are summarized in Table 6.19.

The higher-lying CPs in $\text{Ga}_x\text{In}_{1-x}\text{N}_y\text{As}_{1-y}$ have been studied using SE [233]. In strong contrast to the behavior of E_- and E_+ , the higher-lying CPs such as E_1 and E_2 showed very weak liner nonlinearity with the N concentration. The temperature dependence of the fundamental absorption edge in $\text{Ga}_x\text{In}_{1-x}\text{N}_y\text{As}_{1-y}$ has also been studied by several authors [234–237] and found to exhibit weaker dependence than that observed in the N-free $\text{Ga}_x\text{In}_{1-x}\text{As}$ matrix [234,235]. The pressure dependence of the fundamental absorption edge in $\text{Ga}_x\text{In}_{1-x}\text{N}_y\text{As}_{1-y}$ has been studied experimentally by several authors [139,234,238]. These results show a very much weaker pressure dependence than those observed in the N-free $\text{Ga}_x\text{In}_{1-x}\text{As}$ alloy.

(d) GaNPAs

$\text{GaN}_x\text{P}_y\text{As}_{1-x-y}$ were synthesized by N ion implantation into a $\text{GaP}_y\text{As}_{1-y}$ epilayer ($y = 0\text{--}0.35$) followed by pulsed-laser melting and rapid thermal annealing techniques [239]. As

predicted from the BAC model, the incorporation of N split the CB in the bulk GaP_yAs_{1-y} substrate, and relatively strong optical transitions from the VB to the lower (E_-) and upper (E_+) conduction subbands were observed.

6.4.2 (III, III)–(V, V) Alloy

(a) AlGaPAs

Al_xGa_{1-x}P_yAs_{1-y} lattice-matches to GaAs with x and y are given in Table 1.10. The Al_xGa_{1-x}P_yAs_{1-y} layers can also be grown on commercially available GaP_{0.39}As_{0.61} epitaxial substrates. The lattice-matching relationship between x and y for the Al_xGa_{1-x}P_yAs_{1-y}/GaP_{0.39}As_{0.61} system can be written as

$$y = \frac{0.079 + 0.008x}{0.203 - 0.005x} \quad (0 \leq x \leq 1.0, 0.39 \leq y \leq 0.44) \quad (6.24)$$

No detailed experimental data relating to the x -dependent band-gap energies in Al_xGa_{1-x}P_yAs_{1-y} have been published thus far. The E_0 , E_g^X and E_g^L values obtained from Equation (A.15) are plotted in Figure 6.41 as a function of x for (a) Al_xGa_{1-x}P_yAs_{1-y}/GaAs and (b) Al_xGa_{1-x}P_yAs_{1-y}/GaP_{0.39}As_{0.61}. The ternary bowing parameters are taken from Table 6.27, while the quaternary parameter $D_{AlGaPAs}$ is assumed to be zero. We can see that the $E_0 - E_g^X$ crossing occurs at $x \sim 0.36$ (Figure 6.41(a)) and at ~ 0.07 (Figure 6.41(b)) (see also Table 6.28).

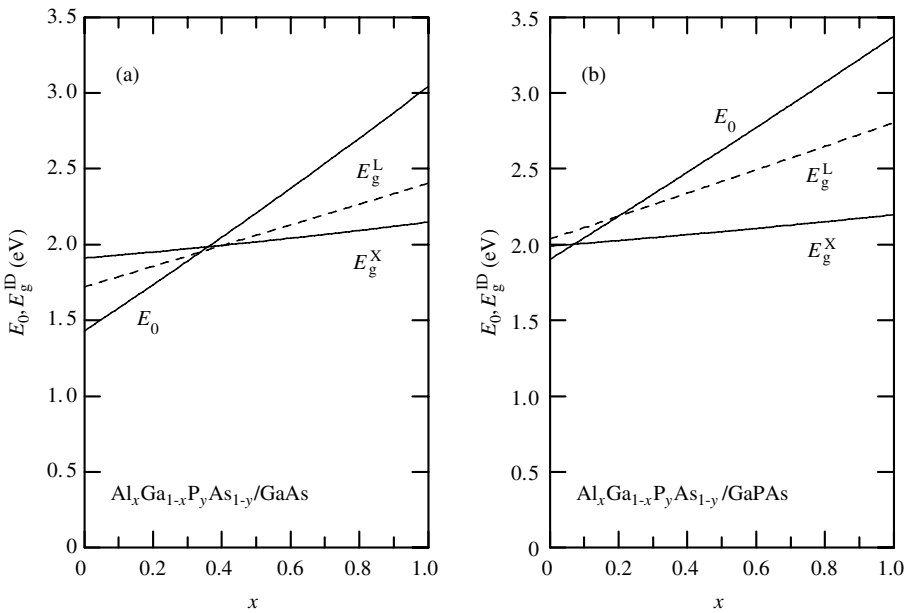


Figure 6.41 Energies of the lowest direct E_0 and indirect gaps E_g^{ID} versus x for (a) Al_xGa_{1-x}P_yAs_{1-y}/GaAs and (b) Al_xGa_{1-x}P_yAs_{1-y}/GaP_{0.39}As_{0.61} calculated from Equation (A.15) using the ternary bowing parameters in Table 6.27 and assuming $D_{AlGaPAs} = 0$ eV

Table 6.28 Energy for the fundamental absorption edge (E_g) in III–V quaternaries at 300 K. The expression gives the quadratic fit of Equation (A.15) with $D_{ABCD} = 0$ eV

Quaternary	Substrate	E_g	Expression (eV)	Remark
$Al_xGa_{1-x}P_yAs_{1-y}$	GaAs	E_0	$1.43 + 1.50x + 0.11x^2$	
		E_g^X	$1.91 + 1.93x + 0.04x^2$	
	GaPAs	E_0	$1.90 + 1.42x + 0.06x^2$	
		E_g^X	$1.99 + 0.18x + 0.03x^2$	
$Al_xGa_{1-x}As_ySb_{1-y}$	GaSb	E_0	$0.72 + 1.46x + 0.06x^2$	
		E_g^X	$1.05 + 0.54x + 0.05x^2$	
	InP	E_0	$0.77 + 1.53x + 0.09x^2$	
		E_g^X	$1.19 + 0.65x + 0.01x^2$	
	InAs	E_0	$0.68 + 1.48x + 0.07x^2$	
		E_g^X	$1.03 + 0.60x + 0.04x^2$	
$Al_xIn_{1-x}As_ySb_{1-y}$	GaSb	E_0	$0.30 + 1.17x + 0.77x^2$	
		E_g^X	$1.33 + 0.68x - 0.36x^2$	
	InP	E_0	$0.88 + 0.88x + 0.63x^2$	$0.48 \leq x \leq 1.0$
		E_g^L	$1.45 + 0.30x + 0.44x^2$	$0.48 \leq x \leq 1.0$
		E_g^X	$1.53 + 0.53x - 0.21x^2$	$0.48 \leq x \leq 1.0$
	InAs	E_0	$0.359 + 1.143x + 0.722x^2$	
E_g^X		$1.37 + 0.57x - 0.26x^2$		
$Ga_xIn_{1-x}P_yAs_{1-y}$	GaAs	E_0	$1.43 + 0.30y + 0.18y^2$	<i>a</i>
	InP	E_0	$0.75 + 0.46y + 0.14y^2$	<i>b</i>
$Ga_xIn_{1-x}As_ySb_{1-y}$	GaSb	E_0	$0.28 - 0.16x + 0.60x^2$	<i>c</i>
	InP	E_0	$0.97 - 0.84x + 0.64x^2$	$0.47 \leq x \leq 1.0$
	InAs	E_0	$0.359 - 0.415x + 0.718x^2$	
$(Al_xGa_{1-x})_{0.53}In_{0.47}P$	GaAs	E_0	$1.90 + 0.57x + 0.10x^2$	<i>d</i>
		E_g^X	$2.25 + 0.09x - 0.01x^2$	<i>d</i>
$(Al_xGa_{1-x})_{0.48}In_{0.52}As$	InP	E_0	$0.75 + 0.68x + 0.06x^2$	<i>e</i>
$InP_xAs_ySb_{1-x-y}$	InAs	E_0	$0.512 + 0.030y - 0.183y^2$	<i>f</i>

^aQuadratic-fit result of Equation (A.15) with $D_{AlInAsSb} = -0.11$ eV^bFit-determined from Figure 6.44^cFit-determined from Figure 6.47^dFit-determined from Figure 6.49^edit-determined from Figure 6.50^fFit-determined from Figure 6.51**(b) AlGaAsSb**

$Al_xGa_{1-x}As_ySb_{1-y}$ can be grown lattice-matched to GaSb, InP and InAs. The corresponding x and y relationships are presented in Table 1.10. This material system is attractive for optoelectronic applications in the near-IR wavelength range. However, very little data have so far been available on the composition-dependent band-gap energies in this alloy system. Herrera-Perez *et al.* [240] grew LPE- $Al_xGa_{1-x}As_ySb_{1-y}$ layers ($x = 0.27$, $y = 0.02$) on GaSb (100) and determined from PR measurements the energy gaps to be ~ 1.05 eV. Yacobi *et al.* [241] also obtained an absorption edge of 0.975 eV for $(x, y) = (0.15, 0.13)$ using a photothermal method. More recently, Saadallah *et al.* [189] undertook a photothermal study on an MBE- $Al_xGa_{1-x}As_ySb_{1-y}/GaSb$ layer ($x = 0.70$, $y = 0.08$) and obtained an absorption edge

of 1.57 eV. These data are plotted in Figure 6.42(a). The solid and dashed lines show the results calculated using Equation (A.15) together with the ternary bowing parameters shown in Table 6.27 and assuming $D_{\text{AlGaAsSb}} = 0$ eV. The quadratic fits of these curves are summarized in Table 6.28.

Filho *et al.* [242] measured the temperature-dependent PL peak energies for an MBE- $\text{Al}_x\text{Ga}_{1-x}\text{As}_y\text{Sb}_{1-y}/\text{InP}$ layer ($x = 0.12$, $y = 0.51$) at $T = 10 - 180$ K. By extrapolating these data, we can estimate the PL peak to be ~ 0.89 eV at 300 K. This data is shown in Figure 6.42(b), together with the calculated data from Equation (A.15) (see also Table 6.28).

The calculated E_0 , E_g^X and E_g^L values versus x curves for $\text{Al}_x\text{Ga}_{1-x}\text{As}_y\text{Sb}_{1-y}/\text{InAs}$ in Figure 6.42(c) are very similar to those in Figure 6.42(a). This is not surprising in view of the near equality of the InAs and GaSb lattice parameters. Yacobi *et al.* [241] found the As composition for $\text{Al}_x\text{Ga}_{1-x}\text{As}_y\text{Sb}_{1-y}$ at $x = 0.15$ grown on GaSb substrate to be $y = 0.13$. However, the exact lattice-matching relationship suggests that Yacobi's sample (x, y) = (0.15, 0.13) has y composition closely lattice-matched to InAs ($y = 0.10$) rather than to GaSb ($y = 0.01$). This data is, therefore, not only shown in Figure 6.42(a) but also in Figure 6.42(c).

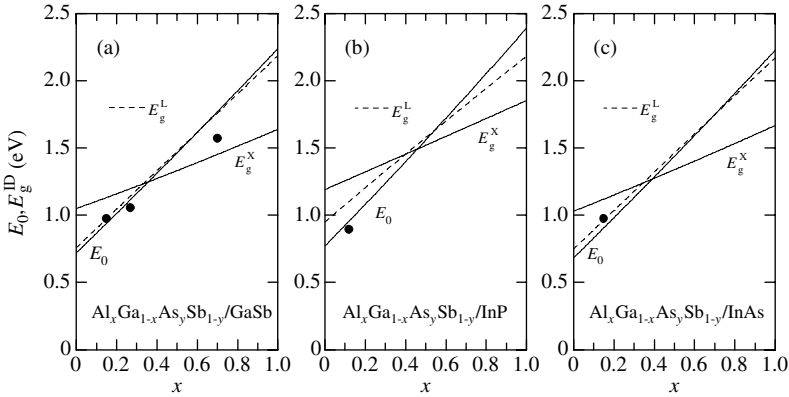


Figure 6.42 Energies of the lowest direct E_0 and indirect gaps E_g^{ID} versus x for (a) $\text{Al}_x\text{Ga}_{1-x}\text{As}_y\text{Sb}_{1-y}/\text{GaSb}$, (b) $\text{Al}_x\text{Ga}_{1-x}\text{As}_y\text{Sb}_{1-y}/\text{InP}$ and (c) $\text{Al}_x\text{Ga}_{1-x}\text{As}_y\text{Sb}_{1-y}/\text{InAs}$ calculated from Equation (A.15) using the ternary bowing parameters in Table 6.27 and assuming $D_{\text{AlGaAsSb}} = 0$ eV

No clear bowing can be seen for E_0 in Figure 6.42. The $\text{Al}_{0.5}\text{Ga}_{0.5}\text{As}_x\text{Sb}_{1-x}$ layers ($x = 0.3 - 0.7$) grown on GaAs by MBE have also been studied by PL [243]. A discrepancy of up to 0.2 eV from the predicted value using the established formalism indicates that an extra bowing factor needs to be included in the E_0 versus x expression for this quaternary system.

The temperature dependence of the fundamental absorption edges has been studied for $\text{Al}_x\text{Ga}_{1-x}\text{As}_y\text{Sb}_{1-y}/\text{GaSb}$ ($x = 0.27$, $y = 0.02$) [240] and $\text{Al}_x\text{Ga}_{1-x}\text{As}_y\text{Sb}_{1-y}/\text{InP}$ ($x = 0.12$, $y = 0.51$) [242]. The Varshni parameters for $\text{Al}_x\text{Ga}_{1-x}\text{As}_y\text{Sb}_{1-y}/\text{GaSb}$ were $\alpha = 3.6 \times 10^{-4}$ eV/K and $\beta = 78$ K [240], which are considerably smaller than the endpoint binary values $\alpha = (3.6 - 5.5) \times 10^{-4}$ eV/K and $\beta = 204 - 234$ K [1].

(c) *AllInAsSb*

$\text{Al}_x\text{In}_{1-x}\text{As}_y\text{Sb}_{1-y}$ can be grown lattice-matched to GaSb, InP and InAs (Table 1.10). However, no detailed study has been carried out on $\text{Al}_x\text{In}_{1-x}\text{As}_y\text{Sb}_{1-y}$ lattice-matched to GaSb and InP.

There is only one study by Charykov *et al.* [244] which reports PL measurements on LPE- $\text{Al}_x\text{In}_{1-x}\text{As}_y\text{Sb}_{1-y}/\text{InAs}$ epilayers. The composition range investigated corresponds to a wavelength from 3 ($x = 0$) to 2.5 μm ($x = 0.08$).

The solid and dashed lines in Figure 6.43 show the calculated E_0 , E_g^X and E_g^L gaps as a function of x for $\text{Al}_x\text{In}_{1-x}\text{As}_y\text{Sb}_{1-y}$ lattice-matched to GaSb, InP and InAs. These are obtained from Equation (A.15) using the ternary bowing parameters in Table 6.27 and assuming $D_{\text{AlInAsSb}} = 0 \text{ eV}$. The quadratic fits of these curves are summarized in Table 6.28. The solid circles in Figure 6.43(c) represent the experimental data taken from Charykov *et al.* [244]. The direct-indirect crossover occurs at $x_c = 0.77$ in (a), 0.70 in (b) and 0.77 in (c).

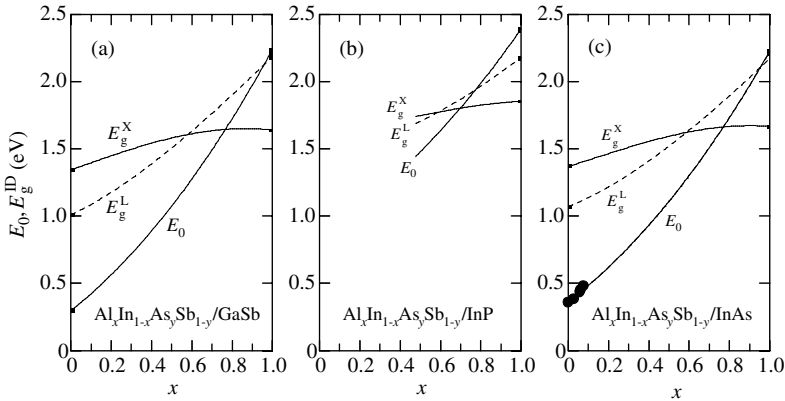


Figure 6.43 Energies of the lowest direct E_0 and indirect gaps E_g^{ID} versus x for (a) $\text{Al}_x\text{In}_{1-x}\text{As}_y\text{Sb}_{1-y}/\text{GaSb}$, (b) $\text{Al}_x\text{In}_{1-x}\text{As}_y\text{Sb}_{1-y}/\text{InP}$ and (c) $\text{Al}_x\text{In}_{1-x}\text{As}_y\text{Sb}_{1-y}/\text{InAs}$ calculated from Equation (A.15) using the ternary bowing parameters in Table 6.27 and assuming $D_{\text{AlInAsSb}} = 0 \text{ eV}$. The experimental data in (c) are taken from Charykov *et al.* [244]

(d) GaInPAs

A number of experimental studies have been published on E_0 versus composition for $\text{Ga}_x\text{In}_{1-x}\text{P}_y\text{As}_{1-y}$ quaternary alloy. These studies concentrated on the technologically important compositions which have lattice parameters equal to that of InP [245]. $\text{Ga}_x\text{In}_{1-x}\text{P}_y\text{As}_{1-y}$ can also be grown lattice-matched to GaAs. However, not very much is known about $\text{Ga}_x\text{In}_{1-x}\text{P}_y\text{As}_{1-y}/\text{GaAs}$.

Shirakata *et al.* [246] performed ER measurements on LPE-grown $\text{Ga}_x\text{In}_{1-x}\text{P}_y\text{As}_{1-y}/\text{GaAs}$ with $y = 0.70$ and 0.96 . These data are plotted versus y in Figure 6.44(a). The experimental data for $\text{Ga}_x\text{In}_{1-x}\text{P}_y\text{As}_{1-y}/\text{InP}$ are gathered from various sources and plotted in Figure 6.44(b). The solid and dashed lines in Figure 6.44 are obtained from Equation (A.15) using the ternary bowing parameters in Table 6.27 and inputting $D_{\text{AlInAsSb}} = -0.11 \text{ eV}$ (E_0) and 0 eV (E_g^X and E_g^L). The quaternary parameter $D_{\text{AlInAsSb}} = -0.11 \text{ eV}$ is taken from Donati *et al.* [247]. This parameter explains the E_0 data plotted in Figure 6.44(a), but not that in Figure 6.44(b). The heavy solid line in Figure 6.44(b) shows the quadratic least-squares fit of E_0 . The bowing parameter of $c = 0.14 \text{ eV}$ is determined from this fit (Table 6.28).

The higher-lying CPs, such as $E_0 + \Delta_0$, E_1 , $E_1 + \Delta_1$, E_0' and E_2 , for $\text{Ga}_x\text{In}_{1-x}\text{P}_y\text{As}_{1-y}/\text{InP}$ have been investigated by many authors [245,248,249]. The recommended higher-lying CPs are listed in Table 6.29 (see also Figure 6.45(a)).

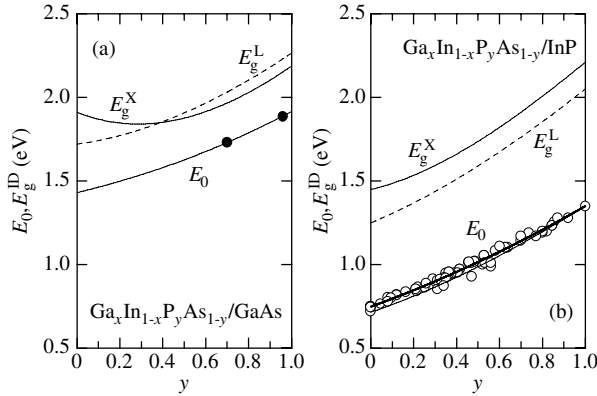


Figure 6.44 Energies of the lowest direct E_0 and indirect gaps E_g^{ID} versus y for (a) $\text{Ga}_x\text{In}_{1-x}\text{P}_y\text{As}_{1-y}/\text{GaAs}$ and (b) $\text{Ga}_x\text{In}_{1-x}\text{P}_y\text{As}_{1-y}/\text{InP}$ calculated from Equation (A.15) using the ternary bowing parameters in Table 6.27 and assuming $D_{\text{GaInPAs}} = -0.11$ (E_0) and 0 eV (E_g^X) and (E_g^L). The heavy solid line in (b) shows the quadratic least-squares fit listed in Table 6.28

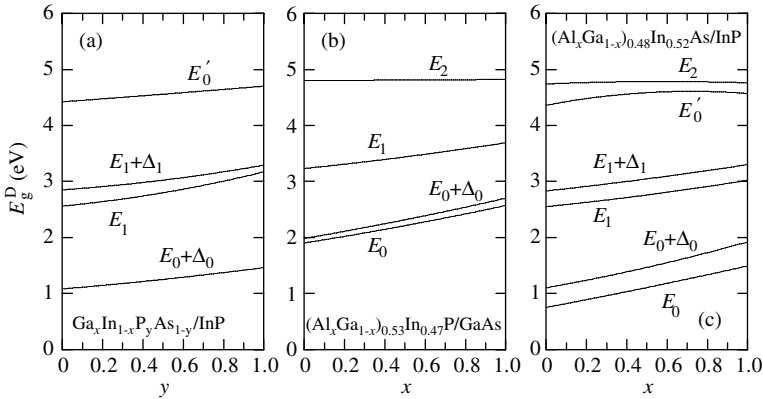


Figure 6.45 Energies of the higher-lying CPs versus y or x for (a) $\text{Ga}_x\text{In}_{1-x}\text{P}_y\text{As}_{1-y}/\text{InP}$, (b) $(\text{Al}_x\text{Ga}_{1-x})_{0.53}\text{In}_{0.47}\text{P}/\text{GaAs}$ and (c) $(\text{Al}_x\text{Ga}_{1-x})_{0.48}\text{In}_{0.52}\text{As}/\text{InP}$. The functional forms are summarized in Tables 6.28 and 6.29

The temperature dependence of E_0 for $\text{Ga}_x\text{In}_{1-x}\text{P}_y\text{As}_{1-y}/\text{InP}$ has been studied by several authors [245]. The experimental dE_0/dT versus y data are shown in Figure 6.46(a). These data give the slowly varying function of dE_0/dT versus y (in 10^{-4} eV/K)

$$-\frac{dE_0}{dT} = 3.6 + 0.5y \tag{6.25}$$

The pressure coefficient dE_0/dp for $\text{Ga}_x\text{In}_{1-x}\text{P}_y\text{As}_{1-y}/\text{InP}$ has been studied by several authors [245]. These results are summarized in Figure 6.46(b). The corresponding y dependence is written as (in 10^{-2} eV/GPa)

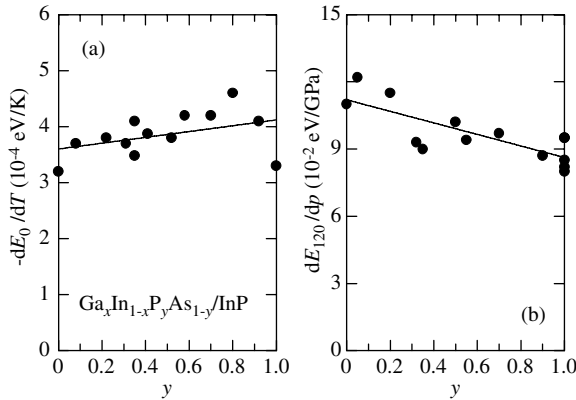
Table 6.29 Energies for the higher-lying CPs in some III–V quaternaries at 300 K

Quaternary	Substrate	CP	Expression (eV)
$\text{Ga}_x\text{In}_{1-x}\text{P}_y\text{As}_{1-y}$	InP	$E_0 + \Delta_0$	$1.08 + 0.30y + 0.08y^2$
		E_1	$2.56 + 0.34y + 0.27y^2$
		$E_1 + \Delta_1$	$2.85 + 0.25y + 0.19y^2$
		E'_0	$4.42 + 0.27y + 0.01y^2$
$(\text{Al}_x\text{Ga}_{1-x})_{0.53}\text{In}_{0.47}\text{P}$	GaAs	$E_0 + \Delta_0$	$1.98 + 0.62x + 0.10x^2$
		E_1	$3.23 + 0.37x + 0.09x^2$
		E_2	$4.80 + 0.02x$
$(\text{Al}_x\text{Ga}_{1-x})_{0.48}\text{In}_{0.52}\text{As}$	InP	$E_0 + \Delta_0$	$1.10 + 0.64x + 0.18x^2$
		E_1	$2.55 + 0.36x + 0.11x^2$
		$E_1 + \Delta_1$	$2.83 + 0.39x + 0.08x^2$
		E'_0	$4.36 + 0.69x - 0.48x^2$
		E_2	$4.74 + 0.15x - 0.13x^2$

$$\frac{dE_0}{dp} = 11.3 - 3.0y \quad (6.26)$$

(e) GaInAsSb

Figure 6.47 shows E_0 , E_{eg}^{X} and E_{eg}^{L} versus x for $\text{Ga}_x\text{In}_{1-x}\text{As}_y\text{Sb}_{1-y}$ lattice-matched to GaSb, InP and InAs. A distinguishing feature of $\text{Ga}_x\text{In}_{1-x}\text{As}_y\text{Sb}_{1-y}$ is the existence of a wide immiscibility range $0.24 < x < 0.75$, which means that the alloy can be prepared only in a narrow range of compositions either adjoining GaSb ($x = 1.0$) or InAs ($x = 0$). The solid and dashed lines in Figure 6.47 are calculated from Equation (A.15) using the ternary bowing parameters in Table 6.27 and assuming $D_{\text{GaInAsSb}} = 0$ eV.

**Figure 6.46** (a) Temperature and (b) pressure coefficients of E_0 as a function of y for $\text{Ga}_x\text{In}_{1-x}\text{P}_y\text{As}_{1-y}$ /InP. The solid lines in (a) and (b) are obtained from Equations (6.25) and (6.26), respectively

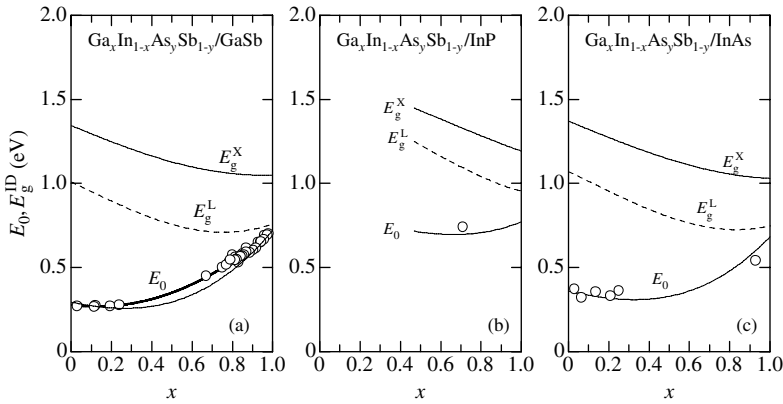


Figure 6.47 Energies of the lowest direct E_0 and indirect gaps E_g^{ID} versus x for (a) $\text{Ga}_x\text{In}_{1-x}\text{As}_y\text{Sb}_{1-y}/\text{GaSb}$, (b) $\text{Ga}_x\text{In}_{1-x}\text{As}_y\text{Sb}_{1-y}/\text{InP}$ and (c) $\text{Ga}_x\text{In}_{1-x}\text{As}_y\text{Sb}_{1-y}/\text{InAs}$ calculated from Equation (A.15) using the ternary bowing parameters in Table 6.27 and assuming $D_{\text{GaInAsSb}} = 0 \text{ eV}$. The heavy solid line in Figure 6.47(a) shows the quadratic least-squares fit listed in Table 6.28

The open circles in Figure 6.47 show the experimental data taken from various sources [250–254]. It can be seen that Equation (A.15) shows reasonable agreement with the available experimental data. However, Figure 6.47(a) shows poor agreement. We, therefore, tried to least-squares fit these data using a quadratic function. The heavy solid line in Figure 6.47(a) shows this result. The determined bowing parameter is $c = 0.60 \text{ eV}$ (Table 6.28).

The temperature dependence of the Γ -valley gap E_0 has been studied by Iyer *et al.* [255] and Muñoz *et al.* [256] for $\text{Ga}_x\text{In}_{1-x}\text{As}_y\text{Sb}_{1-y}$ grown on GaSb and by Gong *et al.* [257] for $\text{Ga}_x\text{In}_{1-x}\text{As}_y\text{Sb}_{1-y}$ grown on InAs. These results are shown in Figure 6.48. Although the data are somewhat sparse, they give values of $dE_0/dT \sim -3.8 \times 10^{-4}$ and $\sim -4.0 \times 10^{-4} \text{ eV/K}$ for samples grown on GaSb and InAs, respectively, near 300 K.

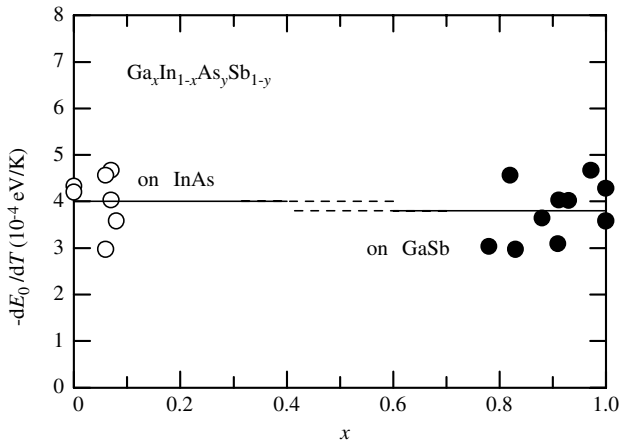


Figure 6.48 Temperature coefficient dE_0/dT as a function of x for $\text{Ga}_x\text{In}_{1-x}\text{As}_y\text{Sb}_{1-y}$ lattice-matched to GaSb and InAs

6.4.3 (III, III, III)–V Alloy

(a) AlGaInP

$\text{Al}_x\text{Ga}_y\text{In}_{1-x-y}\text{P}$ has the largest direct band gap of any semiconductor lattice-matched to GaAs. There have been many reports on $(\text{Al}_x\text{Ga}_{1-x})_{0.53}\text{In}_{0.47}\text{P}/\text{GaAs}$ (see e.g. [258–260]). The open circles in Figure 6.49 represent the experimental data at 300 K. They are taken from various sources, e.g. Asami *et al.* [261], Cao *et al.* [262] and Adachi *et al.* [263]. Data for E_0 , E_g^X and E_g^L for $(\text{Al}_x\text{Ga}_{1-x})_{0.53}\text{In}_{0.47}\text{P}/\text{GaAs}$ calculated from Equation (A.15) using the ternary bowing parameters in Table 6.27 and assuming $D_{\text{AlGaInP}} = 0$ eV have been plotted in Figure 6.49.

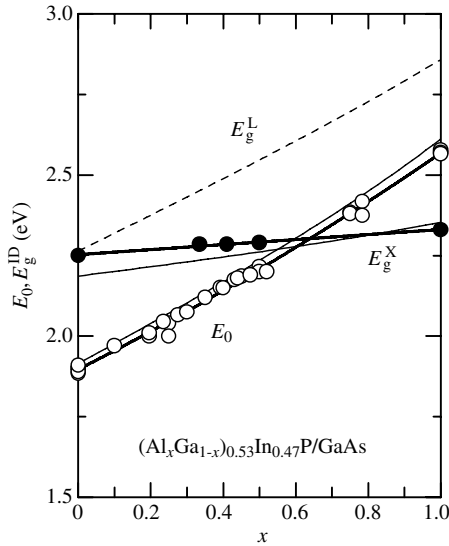


Figure 6.49 Energies of the lowest direct E_0 and indirect gaps E_g^{ID} versus x for $(\text{Al}_x\text{Ga}_{1-x})_{0.53}\text{In}_{0.47}\text{P}/\text{GaAs}$ calculated from Equation (A.15) using the ternary bowing parameters in Table 6.27 and assuming $D_{\text{AlGaInP}} = 0$ eV. The heavy solid lines show the quadratic least-squares fit listed in Table 6.28

Equation (A.15) predicts that the Γ – X crossover occurs at $x_c = 0.55$. However, excellent agreement can be never achieved with the experimental data even if $D_{\text{AlGaInP}} \neq 0$ eV is introduced into Equation (A.15). We, therefore, fit the experimental E_0 and E_g^X data using a quadratic function with respect to x . The heavy solid lines in Figure 6.49 show these results (see also Table 6.28) and predict that the Γ – X crossover point will be at $x_c = 0.64$. No experimental data has, however, been reported on the Γ – X crossover point.

The higher-lying CPs as a function of x for $(\text{Al}_x\text{Ga}_{1-x})_{0.53}\text{In}_{0.47}\text{P}/\text{GaAs}$ have been determined using various techniques, such as ER [261,263], TR [264] and SE [260,264,265]. The $E_0 + \Delta_0$, E_1 and E_2 energies versus x for $(\text{Al}_x\text{Ga}_{1-x})_{0.53}\text{In}_{0.47}\text{P}/\text{GaAs}$ have been plotted in Figure 6.45(b). They are obtained by averaging the published experimental data and are summarized in Table 6.29.

The pressure dependence of E_0 for $(\text{Al}_x\text{Ga}_{1-x})_{0.53}\text{In}_{0.47}\text{P}/\text{GaAs}$ has been investigated by several authors [266,267]. The experimental data reported by Harada *et al.* [267] can be written as

$$\frac{dE_0}{dp} = (1-0.29x) \frac{dE_0(0)}{dp} \quad (6.27)$$

where $dE_0(0)/dp = 9.5 \text{ eV/GPa}$ is the $\text{Ga}_{0.5}\text{In}_{0.5}\text{P}$ ($x = 0$) value estimated from the linear interpolation between GaP and InP [1].

(b) *AlGaInAs*

$\text{Al}_x\text{Ga}_y\text{In}_{1-x-y}\text{As}$ can be relatively easily grown on InP by MBE. This alloy system can also be prepared by MOCVD [268]. The E_0 , E_g^X and E_g^L gaps for $(\text{Al}_x\text{Ga}_{1-x})_{0.48}\text{In}_{0.52}\text{As}/\text{InP}$ are shown in Figure 6.50. The alloy system remains a direct gap material over the whole composition range $0 \leq x \leq 1.0$. The open circles in Figure 6.50 represent the experimental E_0 data taken from various sources (see e.g. [268–271]). These data are found to be slightly smaller than those calculated from Equation (A.15) assuming $D_{\text{AlGaInAs}} = 0 \text{ eV}$. The heavy solid line in Figure 6.50 represents the quadratic least-squares fit (Table 6.28).

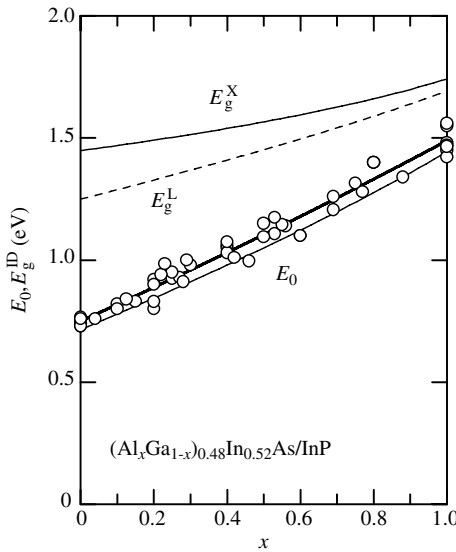


Figure 6.50 Energies of the lowest direct E_0 and indirect gaps E_g^{ID} versus x for $(\text{Al}_x\text{Ga}_{1-x})_{0.48}\text{In}_{0.52}\text{As}/\text{InP}$ calculated from Equation (A.15) using the ternary bowing parameters in Table 6.27 and assuming $D_{\text{AlGaInAs}} = 0 \text{ eV}$. The heavy solid line shows the quadratic least-squares fit listed in Table 6.28

The higher-lying CPs in $(\text{Al}_x\text{Ga}_{1-x})_{0.48}\text{In}_{0.52}\text{As}/\text{InP}$ have been studied using ER [272] and SE [273]. The $E_0 + \Delta_0$, E_1 , $E_1 + \Delta_1$, E_0' and E_2 versus x data for $(\text{Al}_x\text{Ga}_{1-x})_{0.48}\text{In}_{0.52}\text{As}/\text{InP}$ as determined by ER [272] has been plotted in Figure 6.45(c). The corresponding expressions are summarized in Table 6.29.

6.4.4 III–(V, V, V) Alloy

$\text{InP}_x\text{As}_y\text{Sb}_{1-x-y}/\text{InAs}$ is the only quaternary system that has been well studied in the literature. The E_0 versus y data for $\text{InP}_x\text{As}_y\text{Sb}_{1-x-y}/\text{InAs}$ are shown in Figure 6.51. They are taken from various sources [213,274–276]. The solid and dashed lines also show the E_0 , E_g^X and E_g^L versus y curves obtained from Equation (A.15) using the ternary bowing parameters in Table 6.27 and assuming $D_{\text{InPAsSb}} = 0 \text{ eV}$. The heavy solid line is obtained from the quadratic least-squares fit. This fit gives considerable upward bowing of $c = -0.183 \text{ eV}$ for E_0 (Table 6.28).

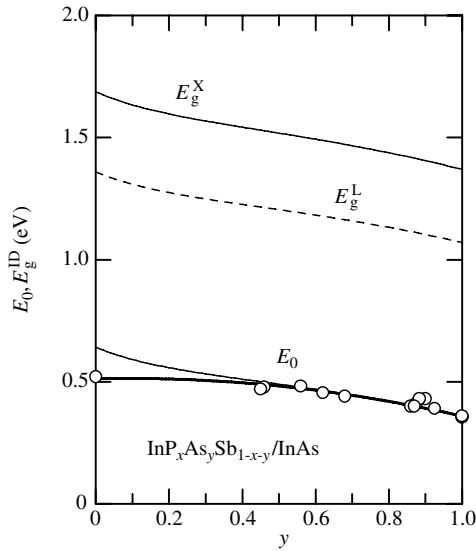


Figure 6.51 Energies of the lowest direct E_0 and indirect gaps E_g^{ID} versus y for $\text{InP}_x\text{As}_y\text{Sb}_{1-x-y}/\text{InAs}$ calculated from Equation (A.15) using the ternary bowing parameters in Table 6.27 and assuming $D_{\text{InPAsSb}} = 0 \text{ eV}$. The heavy solid line shows the quadratic least-squares fit listed in Table 6.28

The higher-lying CPs, $E_0 + \Delta_0$, E_1 and $E_1 + \Delta_1$, in $\text{InP}_x\text{As}_y\text{Sb}_{1-x-y}/\text{InAs}$ have been determined using ER [274,275]. Like E_0 , these CPs show no strong dependence on alloy composition. The temperature dependence of E_0 has also been determined to be $-(2.2-2.9) \times 10^{-4} \text{ eV/K}$ for $0.46 \leq y \leq 1.0$ [275], suggesting little dependence on alloy composition.

6.4.5 Summary

The lowest direct (E_0) and indirect gaps (E_g^X) for some III–V quaternary alloys lattice-matched to (a) GaAs, (b) GaSb, (c) InP and (d) InAs are summarized in Figure 6.52. The limits of applicability of the linear interpolation scheme using the binary data are apparent. The rationalized biquadratic interpolation algorithm, Equation (A.15), can be safely used to estimate the band-gap energies in quaternary alloys. However, it tends to give energies that are smaller (Figures 6.44, 6.47 and 6.50) or larger than the experimental data (Figures 6.49 and 6.51). These poorer fits can be improved to some extent, if the nonzero D_{ABCD} parameter is inserted into Equation (A.15). For example, introducing $D_{\text{GaInPAs}} = 0.5 \text{ eV}$ into Equation (A.15) improves the fit considerably, as demonstrated in Figure 6.53. It is, however, very difficult to explain the origin of such large upward bowing in this alloy system ($\text{Ga}_x\text{In}_{1-x}\text{P}_y\text{As}_{1-y}/\text{InP}$). The alloying effect in certain types of (III, III)–(V, V) quaternaries may be a secondary effect of the relatively strong cation–cation and anion–anion sublattice disorders which occur in ternary alloys. The triple cation or anion disorder effect may also be much smaller in alloys of the type (III, III, III)–V or III–(V, V, V). We can, therefore, expect that Equation (A.15) will become a good tool for obtaining reliable quaternary parameters when more exact ternary bowing parameters, which can be introduced into Equation (A.15), are required.

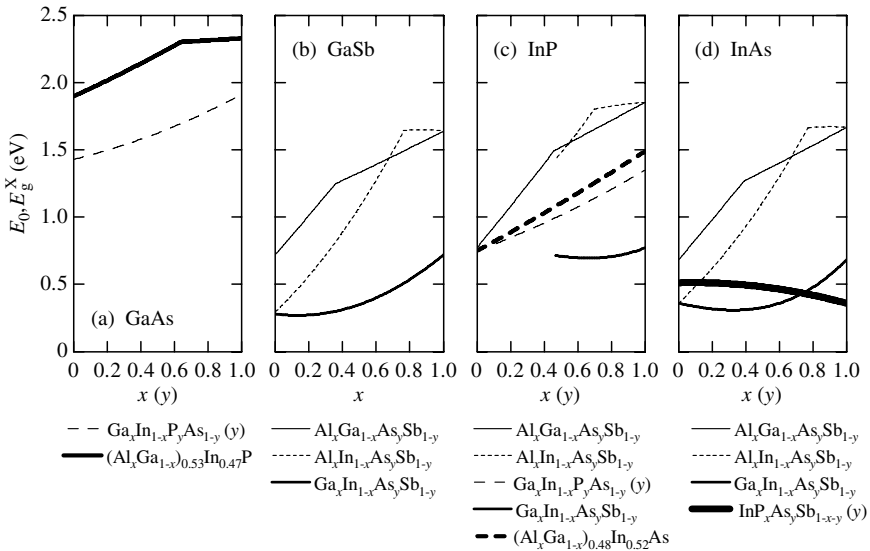


Figure 6.52 Energy of the lowest band gap E_0 or E_g^X versus x (or y) for some III–V quaternary alloys lattice-matched to (a) GaAs, (b) GaSb, (c) InP and (d) InAs. These curves are calculated from the data in Table 6.28

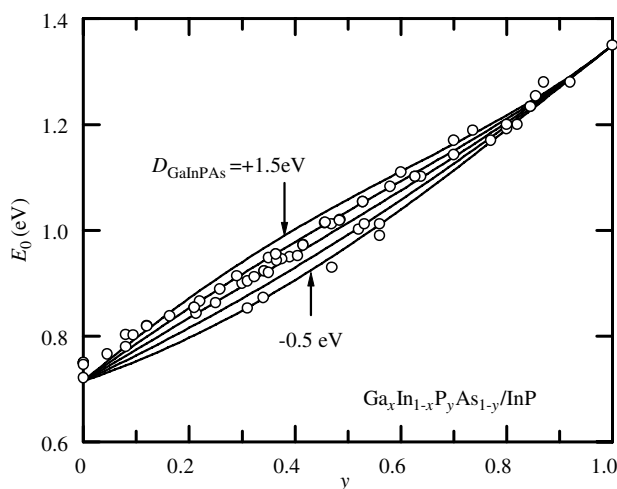


Figure 6.53 Lowest band-gap energy E_0 versus y for $\text{Ga}_x\text{In}_{1-x}\text{P}_y\text{As}_{1-y}/\text{InP}$ at 300 K. The solid lines are calculated from Equation (A.15) using the ternary bowing parameters in Table 6.27 and varying D_{GaInPAs} from -0.5 to $+1.5$ eV in steps of 0.5 eV

6.5 II–VI SEMICONDUCTOR ALLOY

6.5.1 (II, II)–O Ternary Alloy

(a) *BeZnO*

Beryllium chalcogenides attracted considerable attention because they exhibit covalent bonding, and appear to have very large band gaps. However, their optical and electronic properties have not yet been fully clarified.

Both BeO and ZnO usually crystallize in the wurtzite structure. BeO has a wide band gap ($E_0 = 10.6$ eV). Studies on $\text{Be}_x\text{Zn}_{1-x}\text{O}$ are very limited. Ryu *et al.* [277] deposited $\text{Be}_x\text{Zn}_{1-x}\text{O}$ layers on sapphire substrates using a hydride beam deposition method. They measured the transmittance spectra at 300 K and obtained E_0 for $0 \leq x \leq 0.69$. More recently, Han *et al.* [278] used the same crystal growth and measurement techniques, and obtained E_0 up to $x = 0.28$. These data are shown in Figure 6.54(a) (open circles [277], solid circles [278]). The solid line shows a rough fit of these data using the quadratic function shown in Table 6.30.

(b) *MgZnO*

MgO is the prototype of an ionic semiconductor crystallizing in the rocksalt structure, whereas ZnO crystallizes in the wurtzite structure. There have been many studies on the electronic energy-band structure of $\text{Mg}_x\text{Zn}_{1-x}\text{O}$. The E_0 versus x data taken from various sources (see e.g. [279–283]) are shown in Figure 6.54(b). It can be seen that the E_0 data for $x \leq 0.5$ are a good fit with the linear function of x , while those for $x > 0.4$ show quadratic dependence on x . The corresponding expressions are listed in Table 6.30. The wurtzite–cubic mixed phase region occurs at around $x \sim 0.4$.

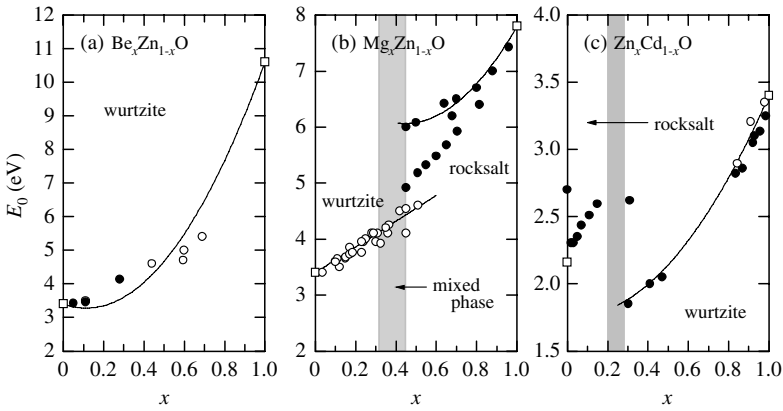


Figure 6.54 Energy of the E_0 gap versus x for some (II, II)-O ternaries at 300 K: (a) $\text{Be}_x\text{Zn}_{1-x}\text{O}$, (b) $\text{Mg}_x\text{Zn}_{1-x}\text{O}$ and (c) $\text{Zn}_x\text{Cd}_{1-x}\text{O}$. The solid lines represent the calculated results using the data in Table 6.30

The composition dependence of the higher-lying CPs in $w\text{-Mg}_x\text{Zn}_{1-x}\text{O}$ has been studied using SE [280]. E_1 and E_2 energies were observed at ~ 7 and ~ 9 eV, respectively, and showed little dependence on x .

The pressure dependence of E_0 has been measured using a diamond anvil cell for p up to 10 GPa [284]. The experimental pressure coefficient dE_0/dp increased at a rate of $40x$ meV/GPa ($0 \leq x \leq 0.13$).

(c) ZnCdO

There have been a few reports on $\text{Zn}_x\text{Cd}_{1-x}\text{O}$ [285,286]. The E_0 versus x data measured by Ishihara *et al.* [285] (solid circles) and Wang *et al.* [286] (open circles) have been plotted in Figure 6.54(c). These plots show that E_0 in the wurtzite region varies quadratically with x ($0.2 \leq x \leq 1.0$, see Table 6.30). The E_0 value in the rocksalt region decreases with decreasing x .

The E_0 versus x data at 2.1 K have been determined using PL [287]. The temperature dependence of E_0 has also been established by Makino [279] for $T = 5\text{--}300$ K ($x = 0.01$) and Wang *et al.* [286] for $T = 6\text{--}300$ K ($x = 0.022, 0.09$ and 0.157), illustrating nearly the same behavior as that for ZnO [279].

6.5.2 (II, II)-S Ternary Alloy

(a) MgZnS

Under normal conditions MgS crystallizes in the rocksalt structure, whereas ZnS crystallizes either in the wurtzite or zinc-blende structure. ZnS has the largest band gap among II-VI semiconductors except for Be- and Mg-chalcogenides. The E_0 gap in $w\text{-Mg}_x\text{Zn}_{1-x}\text{S}$ has been investigated by means of optical absorption [288]. The samples used were grown on (0001)-sapphire substrates by PLD. These data are shown in Figure 6.55(a) by the solid circles. It can

Table 6.30 Energy for E_0 in some II–VI ternaries and quaternaries at 300 K. w = wurtzite; rs = rocksalt; zb = zinc-blende

Alloy	E_0 (eV)	Remark
$\text{Be}_x\text{Zn}_{1-x}\text{O}$	$3.4 - 2.1x + 9.3x^2$	w ($0 \leq x \leq 1.0$)
$\text{Mg}_x\text{Zn}_{1-x}\text{O}$	$3.4 + 2.3x$	w ($0 \leq x \leq 0.5$)
	$7.2 - 5.0x + 5.6x^2$	rs ($0.4 \leq x \leq 1.0$)
$\text{Zn}_x\text{Cd}_{1-x}\text{O}$	$1.76 - 0.11x + 1.75x^2$	w ($0.2 \leq x \leq 1.0$)
$\text{Mg}_x\text{Zn}_{1-x}\text{S}$	$3.81 + 0.65x$	zb ($0 \leq x \leq 0.25$), $T = 10$ K
	$3.75 + 0.80x$	w ($0 \leq x \leq 0.25$)
$\text{Zn}_x\text{Cd}_{1-x}\text{S}$	$2.460 + 0.439x + 0.827x^2$	zb ($0 \leq x \leq 1.0$)
	$2.501 + 0.328x + 0.921x^2$	w ($0 \leq x \leq 1.0$)
$\text{Zn}_x\text{Hg}_{1-x}\text{S}$	$-0.040 + 2.770x + 0.996x^2$	zb ($0 \leq x \leq 1.0$)
$\text{Cd}_x\text{Hg}_{1-x}\text{S}$	$-0.040 + 2.541x$	w ($0.6 \leq x \leq 1.0$)
$\text{Be}_x\text{Zn}_{1-x}\text{Se}$	$2.721 + 1.846x + 1.033x^2$	zb ($0 \leq x \leq 1.0$)
$\text{Be}_x\text{Cd}_{1-x}\text{Se}$	$1.675 + 0.925x + 3.000x^2$	zb ($0 \leq x \leq 1.0$)
$\text{Mg}_x\text{Zn}_{1-x}\text{Se}$	$2.721 + 0.679x + 0.600x^2$	zb ($0 \leq x \leq 1.0$)
$\text{Mg}_x\text{Cd}_{1-x}\text{Se}$	$1.675 + 2.125x + 0.200x^2$	zb ($0 \leq x \leq 0.32$)
	$1.751 + 2.349x$	w ($0 \leq x \leq 1.0$)
$\text{Zn}_x\text{Cd}_{1-x}\text{Se}$	$1.675 + 0.659x + 0.387x^2$	zb ($0 \leq x \leq 1.0$)
$\text{Cd}_x\text{Hg}_{1-x}\text{Se}$	$-0.08 + 1.57x$	zb ($0 \leq x \leq 0.8$)
$\text{Be}_x\text{Zn}_{1-x}\text{Te}$	$2.27 + 1.83x$	zb ($0 \leq x \leq 1.0$)
$\text{Mg}_x\text{Zn}_{1-x}\text{Te}$	$2.27 + 0.67x + 0.46x^2$	zb ($0 \leq x \leq 1.0$)
$\text{Mg}_x\text{Cd}_{1-x}\text{Te}$	$1.51 + 1.35x + 0.54x^2$	zb ($0 \leq x \leq 1.0$)
$\text{Zn}_x\text{Cd}_{1-x}\text{Te}$	$1.51 + 0.45x + 0.31x^2$	zb ($0 \leq x \leq 1.0$)
$\text{Zn}_x\text{Hg}_{1-x}\text{Te}$	$-0.15 + 1.96x + 0.46x^2$	zb ($0 \leq x \leq 1.0$)
$\text{Cd}_x\text{Hg}_{1-x}\text{Te}$	$-0.15 + 1.45x + 0.21x^2$	zb ($0 \leq x \leq 1.0$)
$\text{ZnO}_x\text{S}_{1-x}$	$3.75 - 4.85x + 4.50x^2$	w ($0 \leq x \leq 1.0$)
$\text{ZnS}_x\text{Se}_{1-x}$	$2.721 + 0.425x + 0.580x^2$	zb ($0 \leq x \leq 1.0$)
$\text{ZnS}_x\text{Te}_{1-x}$	$2.270 - 2.294x + 3.750x^2$	zb ($0 \leq x \leq 1.0$)
$\text{ZnSe}_x\text{Te}_{1-x}$	$2.270 - 1.049x + 1.500x^2$	zb ($0 \leq x \leq 1.0$)
$\text{CdS}_x\text{Se}_{1-x}$	$1.751 + 0.050x + 0.700x^2$	w ($0 \leq x \leq 1.0$)
$\text{CdS}_x\text{Te}_{1-x}$	$1.51 - 0.85x + 1.80x^2$	zb ($0 \leq x \leq 1.0$)
	$1.560 - 0.859x + 1.800x^2$	w ($0 \leq x \leq 1.0$)
$\text{CdSe}_x\text{Te}_{1-x}$	$1.510 - 0.673x + 0.838x^2$	zb ($0 \leq x \leq 1.0$)
$\text{Mg}_x\text{Zn}_{1-x}\text{S}_y\text{Se}_{1-y}/\text{GaAs}$	$2.749 + 1.340x + 0.650x^2$	zb ($0 \leq x \leq 0.5$)
$\text{Mg}_x\text{Zn}_{1-x}\text{Se}_y\text{Te}_{1-y}/\text{InP}$	$2.13 + 1.59x + 0.37x^2$	zb ($0 \leq x \leq 0.84$)
$\text{Be}_x\text{Mg}_y\text{Zn}_{1-x-y}\text{Se}/\text{GaAs}$	$2.79 + 1.44y + 1.74y^2$	zb ($0 \leq y \leq 0.67$)
$\text{Mg}_x\text{Zn}_y\text{Cd}_{1-x-y}\text{Se}/\text{InP}$	$2.11 + 1.57x + 0.40x^2$	zb ($0 \leq x \leq 0.83$)

be seen that E_0 increases almost linearly at a rate of $\sim 0.8x$ eV from $E_0 = 3.75$ eV at $x = 0$ (w -ZnS). The detailed expression is given in Table 6.30.

The zinc-blende $\text{Mg}_x\text{Zn}_{1-x}\text{S}$ layers for x up to 0.24 have been grown on GaP(100) by MBE [289]. The E_0 gaps for these layers are determined by low-temperature (10 K) PL measurements. These results are shown in Figure 6.55(a) by the open circles. As in the case of w - $\text{Mg}_x\text{Zn}_{1-x}\text{S}$, the E_0 gap in c - $\text{Mg}_x\text{Zn}_{1-x}\text{S}$ increases at a rate of $\sim 0.7x$ eV from $E_0 = 3.81$ eV at $x = 0$ (c -ZnS). From the extrapolation scheme $E_0 \sim 4.5$ eV for c -MgS is estimated to occur at 10 K.

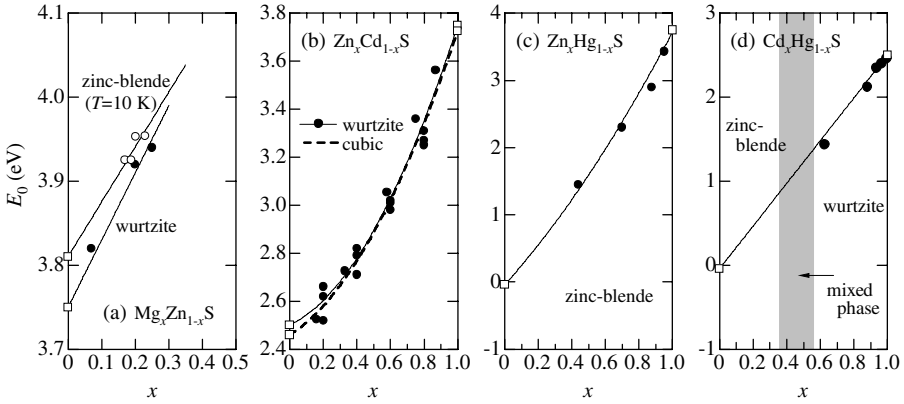


Figure 6.55 Energy of the E_0 gap versus x for some (II, II)-S ternaries at 300 K: (a) $\text{Mg}_x\text{Zn}_{1-x}\text{S}$, (b) $\text{Zn}_x\text{Cd}_{1-x}\text{S}$, (c) $\text{Zn}_x\text{Hg}_{1-x}\text{S}$ and (d) $\text{Cd}_x\text{Hg}_{1-x}\text{S}$. The solid and dashed lines represent the calculated results using the data in Table 6.30

(b) ZnCdS

$\text{Zn}_x\text{Cd}_{1-x}\text{S}$ can be grown both in the wurtzite and zinc-blende structures. The E_0 versus x data for $w\text{-Zn}_x\text{Cd}_{1-x}\text{S}$ reported in the literature [2–293] are shown in Figure 6.55(b). The experimental data largely scatter. The solid line shows the least-squares fit of these data (see Table 6.30). This fit gives a bowing parameter of $c \sim 0.921$ eV.

Yokogawa *et al.* [294] estimated $c \sim 0.827$ eV for E_0 in $c\text{-Zn}_x\text{Cd}_{1-x}\text{S}$. Introducing this value into Equation (A.5), the composition dependence of E_0 for $c\text{-Zn}_x\text{Cd}_{1-x}\text{S}$ can be calculated. The dashed line in Figure 6.55(b) represents the result of this calculation (see also Table 6.30).

The temperature coefficient of E_0 for $w\text{-Zn}_x\text{Cd}_{1-x}\text{S}$ has been studied by means of electro-absorption spectroscopy [295]. The experimental dE_0/dT is in the range of $-(3.8\text{--}6.0) \times 10^{-4}$ eV/K for $x = 0\text{--}1.0$. The pressure coefficient dE_0/dp in $w\text{-Zn}_x\text{Cd}_{1-x}\text{S}$ has also been determined for p up to 15 GPa [291]. The linear pressure coefficient, when plotted against the Cd concentration, displays a slow decrease up to 25 at% at which concentration a sudden drop appears. This behavior is reminiscent of ‘percolation-type’ phenomena.

(c) ZnHgS

The complete solid solution was obtained throughout the whole range for the ZnS–HgS alloy system [296]. The reflectance measurements revealed that the zinc-blende $\text{Zn}_x\text{Hg}_{1-x}\text{S}$ alloy appears to show a nearly linear increase of E_0 from $x \sim 0.44$ to 1.0. These results are shown in Figure 6.55(c) [296]. The solid line shows the quadratic fit of these data and those for $x = 0$ and 1.0 (see also Table 6.30).

(d) CdHgS

CdS and HgS form solid solutions over the whole range, but the crystal structure depends on the composition. The zinc-blende solid solution $c\text{-Cd}_x\text{Hg}_{1-x}\text{S}$ is obtained in the $x = 0\text{--}0.4$ range, while the wurtzite solid solution $w\text{-Cd}_x\text{Hg}_{1-x}\text{S}$ is obtained for $x \geq 0.6$. The cubic and wurtzite

structures can be present in the $x = 0.4\text{--}0.6$ range. As expected, the ratio of cubic to wurtzite solid solution increases continuously with increasing HgS concentration [296,297].

The dependence of E_0 on x for $\text{Cd}_x\text{Hg}_{1-x}\text{S}$ is shown in Figure 6.55(d) [296]. We can see that the E_0 versus x data are satisfactorily interpreted by the linear interpolation scheme between the CdS (2.541 eV) and HgS values (-0.04 eV), as shown by the solid line.

6.5.3 (II, II)–Se Ternary Alloy

(a) *BeZnSe*

Figure 6.56(a) shows the E_0 versus x data for $\text{Be}_x\text{Zn}_{1-x}\text{Se}$ obtained using SE by Wilmers *et al.* [298] (solid circles) and Bukaluk *et al.* [299] (open circles). The solid line represents the quadratic least-squares fit of these data. The bowing parameter c is determined to be 1.033 eV (Table 6.30).

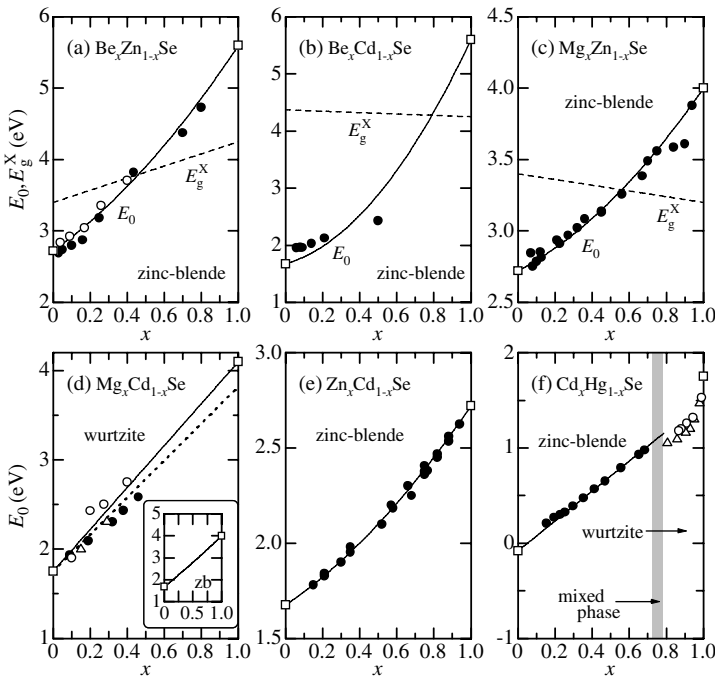


Figure 6.56 Energy of the E_0 gap versus x for some (II, II)–Se ternaries at 300 K: (a) $\text{Be}_x\text{Zn}_{1-x}\text{Se}$, (b) $\text{Be}_x\text{Cd}_{1-x}\text{Se}$, (c) $\text{Mg}_x\text{Zn}_{1-x}\text{Se}$, (d) $\text{Mg}_x\text{Cd}_{1-x}\text{Se}$, (e) $\text{Zn}_x\text{Cd}_{1-x}\text{Se}$ and (f) $\text{Cd}_x\text{Hg}_{1-x}\text{Se}$. The solid lines represent the calculated results using the data in Table 6.30. The dashed lines in (a)–(c) show the x dependence of E_g^X obtained by the linear interpolation between the endpoint binary data in Table 6.1. The dotted line in (d) represents the linear least-squares fit, which predicts a value of $E_0 \sim 3.8$ eV for w -MgSe ($x = 1.0$). The inset in (d) shows the x dependence of E_0 in c -Mg $_x$ Cd $_{1-x}$ Se (see also Table 6.30)

Beryllium chalcogenides BeX ($X = \text{S}, \text{Se}, \text{Te}$) are characterized by an indirect band gap with the CB minimum lying at the X point [300]. The direct and indirect gaps of these materials are listed in Table 6.1. The dashed line in Figure 6.56(a) shows the x dependence of E_g^X for

$\text{Be}_x\text{Zn}_{1-x}\text{Se}$ obtained by the linear interpolation between ZnSe ($x = 0$) and BeSe ($x = 1.0$). We can expect the Γ - X crossover to occur at $x \sim 0.4$. This agrees with an abrupt drop in the main PL peak intensity at $x \sim 0.45$ [301,302].

The SE spectra for $\text{Be}_x\text{Zn}_{1-x}\text{Se}$ have been measured in the 2–30 eV range [298], the 1.25–5 eV range [299] and the 1.5–6.0 eV range [303]. The higher-lying CPs assigned to $E_0 + \Delta_0$, E_1 , $E_1 + \Delta_1$, E_2 , E'_0 and E'_1 can be seen [298] and with increasing Be content their spectral positions are systematically shifted toward higher energies. Each CP has a different slope dE_g/dx , E_0 and $E_0 + \Delta_0$ having the steepest slope and, as a result, having the largest bowing parameter. The highest CP peak is at ~ 8.5 eV (E'_1) [298].

(b) *BeCdSe*

The zinc-blende-type $\text{Be}_x\text{Cd}_{1-x}\text{Se}$ alloy can be epitaxially grown on III-V semiconductor substrates. E_0 values for c - $\text{Be}_x\text{Cd}_{1-x}\text{Se}$ epilayers grown on $\text{GaAs}(100)$ [304] and on $\text{InP}(100)$ have been reported [305,306]. The experimental data obtained from these studies are shown in Figure 6.56(b). The solid line shows a quadratic dependence of E_0 on x (Table 6.30). The dashed line also shows the predicted E_g^X values obtained by the linear interpolation between c - CdSe ($x = 0$) and BeSe ($x = 1.0$). The Γ - X crossover is expected to occur at $x \sim 0.8$. The E_0 value in w - $\text{Be}_x\text{Cd}_{1-x}\text{Se}$ has also been measured by Huang *et al.* [306] and Wronkowska *et al.* [307].

(c) *MgZnSe*

Bulk $\text{Mg}_x\text{Zn}_{1-x}\text{Se}$ crystals grown by the Bridgman method are known to show the sphalerite-wurtzite phase transition at $x = 0.185 \pm 0.03$ [308]. On the other hand, c - $\text{Mg}_x\text{Zn}_{1-x}\text{Se}$ epilayer can be grown over the whole alloy range ($0 \leq x \leq 1.0$). The E_0 versus x data for c - $\text{Mg}_x\text{Zn}_{1-x}\text{Se}$ reported in the literature [309–312] are shown in Figure 6.56(c). The quadratic least-squares fit produces a bowing of $c \sim 0.600$ eV for E_0 (Table 6.30). The dashed line represents the x dependence of E_g^X obtained by the linear interpolation between ZnSe ($x = 0$) and MgSe ($x = 1.0$). It can be seen that the Γ - X crossover occurs at $x \sim 0.55$. No experimental determination has, however, been reported until now.

The higher-lying CPs in c - $\text{Mg}_x\text{Zn}_{1-x}\text{Se}$ have been studied using SE for $x \leq 0.37$ [303] and $x \leq 0.21$ [311]. The $E_0 + \Delta_0$, E_1 and $E_1 + \Delta_1$ CPs are reported to increase almost linearly with increasing x .

The temperature dependence of E_0 has been studied for both c - $\text{Mg}_x\text{Zn}_{1-x}\text{Se}$ [313,314] and w - $\text{Mg}_x\text{Zn}_{1-x}\text{Se}$ [315]. The experimental data have been analyzed using semi-empirical formulas, such as the Varshni and Pässler formulas [1]. An anomalous temperature dependence, i.e. showing a positive temperature coefficient at $T \leq 70$ K, has also been found in bulk w - $\text{Mg}_x\text{Zn}_{1-x}\text{Se}$ crystals grown by a closed-tube sublimation method and analyzed as originating from a volume dilution effect due to deep-level defects [315].

(d) *MgCdSe*

Under normal conditions bulk $\text{Mg}_x\text{Cd}_{1-x}\text{Se}$ crystallizes in the wurtzite structure. The E_0 versus x data for w - $\text{Mg}_x\text{Cd}_{1-x}\text{Se}$ obtained from Wronkowska *et al.* [316] (open circles), Firszt *et al.* [317] (open triangles) and Kim *et al.* [318] (solid circles) are shown in Figure 6.56(d); the experimental data scatter largely. The dotted line represents the linear least-squares fit of these data, which gives a change of E_0 at a rate of $dE_0/dx = 2.071$ eV and predicts a value of $E_0 \sim 3.8$ eV for w - MgSe . This value is considerably smaller than that of c - MgSe ($E_0 = 4.0$ eV,

Table 6.1). In III–V and II–VI semiconductors, the wurtzite polytype usually has a larger E_0 gap than the zinc-blende polytype (Tables 6.1 and 6.2). Thus, the E_0 value for w -MgSe should be larger than that for c -MgSe (~ 4.0 eV). The solid line in Figure 6.56(d) shows the linearly interpolated result assuming $E_0 = 4.1$ eV for w -MgSe.

The E_0 versus x data for c -Mg_xCd_{1-x}Se layers ($x \leq 0.32$) grown on InAs(100) have been determined using low-temperature (77 K) PL [319]. The bowing parameter $c \sim 0.2$ eV is estimated from this study. The inset in Figure 6.56(d) shows the E_0 versus x dependence at 300 K for c -Mg_xCd_{1-x}Se obtained by introducing $c = 0.200$ eV into Equation (A.5) (see also Table 6.30).

The composition dependence of E_0 at 11 K for w -Mg_xCd_{1-x}Se has been determined from PL measurements [320]. The temperature dependence of E_0 has also been reported by several authors [318,321]. Using SE, Wronkowska *et al.* [316] determined the higher-lying CPs for w -Mg_xCd_{1-x}Se. However, they explained these data using the notations of the zinc-blende lattice ($E_0 + \Delta_0$ and E_1), not those of the wurtzite lattice ($E_{0\alpha}$ and $E_{1\alpha}$ ($\alpha = A, B$ or C); see Adachi [1]).

(e) ZnCdSe

Zn_xCd_{1-x}Se is commonly used as QW material in ZnSe-based devices. In the bulk form, Zn_xCd_{1-x}Se has the zinc-blende structure at $0.7 \leq x \leq 1.0$, the wurtzite structure at $0 \leq x \leq 0.3$ and their mixed phases at $0.3 \leq x \leq 0.7$ [322]. On the other hand, MBE-grown Zn_xCd_{1-x}Se layers on GaAs(100) result in films of the zinc-blende structure over the whole composition range. The E_0 versus x data for c -Zn_xCd_{1-x}Se/GaAs(100) epilayers grown by MBE are shown in Figure 6.56(e) [323–326]. The solid line shows the quadratic least-squares fit of these data (see also Table 6.30).

The higher-lying CPs in c -Zn_xCd_{1-x}Se epilayers at $0 \leq x \leq 1.0$ have been studied using SE in the 1.5–6.0 eV range [324]. The $E_0 + \Delta_0$, E_1 and $E_1 + \Delta_1$ CPs have been observed and found to increase with increasing x . The corresponding bowing parameters are found to be $c = 0.38$ ($E_0 + \Delta_0$), 0.467 (E_1) and 0.351 eV ($E_1 + \Delta_1$).

The temperature dependence of E_0 for c -Zn_xCd_{1-x}Se layers grown by MBE has been determined by several authors [326–328]. Using SE, Lee *et al.* [326] obtained an expression that allows E_0 to be obtained for any composition and temperature within the ranges $0 \leq x \leq 0.34$ and $25 \leq T \leq 260$ °C. The E_0 versus T variation has also been determined by ER in the range $25 \leq T \leq 400$ K for $x = 0.56$ [327] and by PL in the range $15 \leq T \leq 250$ K for $0 \leq x \leq 1.0$ [328].

(f) CdHgSe

Cd_xHg_{1-x}Se crystallizes in the zinc-blende structure at $0 < x < 0.77$ and in the wurtzite structure at $x > 0.81$, while a mixed phase of both structures is observed at $0.77 < x < 0.81$ [329]. The composition dependence of E_0 for Cd_xHg_{1-x}Se is shown in Figure 6.56(f). The experimental data in the zinc-blende region are taken from Summers and Broerman [330] (solid circle), and those in the wurtzite region are taken from Himei and Muto [331] (open circles) and Pujari *et al.* [332] (open triangles). The E_0 versus x data in the zinc-blende region can be satisfactorily approximated by the linear expression. The corresponding slope dE_0/dx is given by 1.57 eV, as listed in Table 6.30. The experimental data in the wurtzite region differ largely among the literature, but clearly show nonlinear dependence on x .

The interband CPs in $\text{Cd}_x\text{Hg}_{1-x}\text{Se}$ have been determined using reflectance spectroscopy for x up to 0.79 [333] and SE for $0 \leq x \leq 0.30$ [334]. The E_1 and $E_1 + \Delta_1$ CPs are found to linearly increase with increasing x up to 0.4 [333,334] and show an abrupt increase for x above 0.4 [333].

The temperature dependence of E_0 for $c\text{-Cd}_x\text{Hg}_{1-x}\text{Se}$ has been studied by Summers and Broerman [330]. These results are shown in Figure 6.57(a). The experimental data suggest that the alloys at $x < 0.7$ have positive temperature coefficients. The solid line represents the dE_0/dT versus x plots obtained from the linear interpolation between the HgSe ($+7.4 \times 10^{-4}$ eV/K) and $w\text{-CdSe}$ values (-3.63×10^{-4} eV/K) [1]. It can be seen that the linear interpolation scheme explains the experimental data very well.

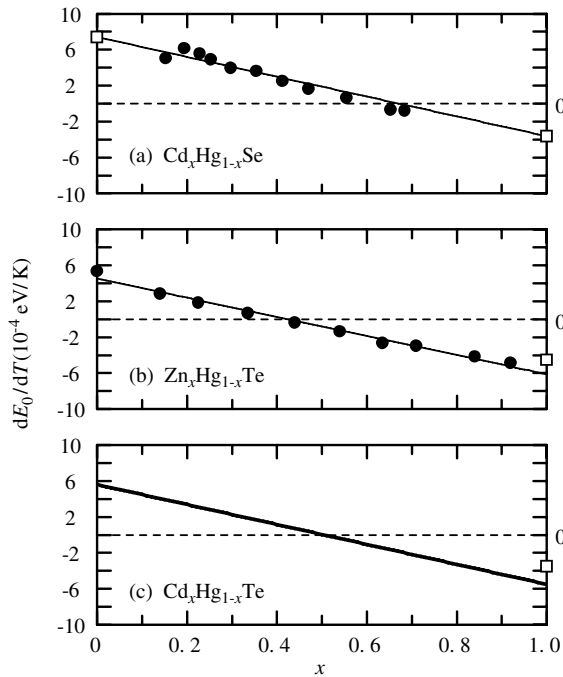


Figure 6.57 Temperature coefficient dE_0/dT as a function of x for (a) $\text{Cd}_x\text{Hg}_{1-x}\text{Se}$, (b) $\text{Zn}_x\text{Hg}_{1-x}\text{Te}$ and (c) $\text{Cd}_x\text{Hg}_{1-x}\text{Te}$. The experimental data are taken for (a) from Summers and Broerman [330] (solid circles), for (b) from Toulouse *et al.* [360] (solid circles) and for (c) from Hansen *et al.* [372] (solid line). The solid line in (a) represents the linearly interpolated values between the endpoint binary data taken from Adachi [1] (open squares). The solid line in (b) shows the linear least-squares fit of Equation (6.28)

6.5.4 (II, II)–Te Ternary Alloy

(a) *BeZnTe*

$\text{Be}_x\text{Zn}_{1-x}\text{Te}$ is a promising material for use as a p -type contact layer in various MgZnCdSe -based devices. The composition dependence of E_0 for $c\text{-Be}_x\text{Zn}_{1-x}\text{Te}$ is shown in Figure 6.58(a). The experimental data are taken from various sources [335–338]. The samples used were grown on $\text{InP}(100)$ by MBE [335–337] or from the melt using the high-pressure Bridgman

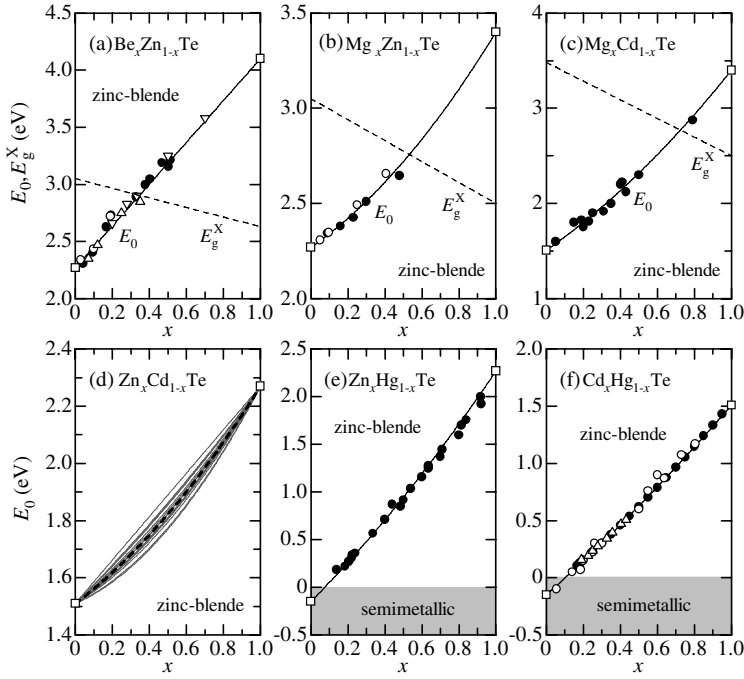


Figure 6.58 Energy of the E_0 gap versus x for some (II, II)–Te ternaries at 300 K: (a) $\text{Be}_x\text{Zn}_{1-x}\text{Te}$, (b) $\text{Mg}_x\text{Zn}_{1-x}\text{Te}$, (b) $\text{Mg}_x\text{Cd}_{1-x}\text{Te}$, (c) $\text{Zn}_x\text{Cd}_{1-x}\text{Te}$, (d) $\text{Zn}_x\text{Hg}_{1-x}\text{Te}$ and (e) $\text{Cd}_x\text{Hg}_{1-x}\text{Te}$. (f) The solid lines represent the calculated results using the data in Table 6.30. The dashed lines in (a)–(c) show the x dependence of E_g^X obtained by the linear interpolation between the endpoint binary data in Table 6.1. The gray lines in (d) represent the E_0 versus x curves calculated using the experimental c values listed in Table 6.31. The heavy dashed line in (d) shows the E_0 versus x curve calculated from the average c value of 0.27 eV

method [338]. These data suggest that the E_0 gap is almost linearly dependent upon Be content x . Indeed, the least-squares fit of these data can be described by $E_0(x) = 2.27 + 1.83x$ eV (solid line, see also Table 6.30). The dashed line in Figure 6.58(a) shows the x dependence of E_g^X for $c\text{-Be}_x\text{Zn}_{1-x}\text{Te}$ obtained by the linear interpolation between the ZnTe ($x=0$) and BeTe values ($x=1.0$) in Table 6.1. The Γ – X crossover is expected to occur at $x \sim 0.35$ ($E_0 = E_g^X \sim 2.9$ eV) for $c\text{-Be}_x\text{Zn}_{1-x}\text{Te}$.

The composition dependence of the higher-lying CPs, $E_0 + \Delta_0$, E_1 , $E_1 + \Delta_1$ and E_2 , for $c\text{-Be}_x\text{Zn}_{1-x}\text{Te}$ has been determined using SE [336,337]. The $E_0 + \Delta_0$, E_1 and $E_1 + \Delta_1$ CP energies increase at a rate of $\sim 0.8x$ eV, while E_2 is found to increase at a lower rate of $\sim 0.2x$ eV. It is interesting to note the absence of bowing in any of the CPs. This is in contrast to most of the II–VI ternary alloys, such as $\text{Be}_x\text{Zn}_{1-x}\text{Se}$ [303] and $\text{Zn}_x\text{Cd}_{1-x}\text{Se}$ [324], which all exhibit some degree of bowing about the CP energies.

(b) *MgZnTe*

$\text{Mg}_x\text{Zn}_{1-x}\text{Te}$ crystallizes in the zinc-blende structure at $0 \leq x \leq 0.53$ and in the wurtzite structure at $x \geq 0.53$ [339]. The E_0 versus x data for $c\text{-Mg}_x\text{Zn}_{1-x}\text{Te}$ determined by wavelength-modulation

(open circles) [340] and optical absorption spectroscopy (solid circle) are shown in Figure 6.58 (b) [341]. All samples used were grown by the Bridgman method. The solid line in Figure 6.58(b) shows the quadratic least-squares fit of these and *c*-MgTe ($x = 1.0$) data, providing a value of $c \sim 0.46$ eV.

The dashed line in Figure 6.58(b) shows the x dependence of E_g^X for *c*-Mg_{*x*}Zn_{1-*x*}Te obtained by the linear interpolation between ZnTe ($x = 0$) and MgTe ($x = 1.0$) as shown in Table 6.1. This result predicts the Γ -X crossover to occur at $x \sim 0.5$ ($E_0 = E_g^X \sim 2.75$ eV) for *c*-Mg_{*x*}Zn_{1-*x*}Te.

The higher-lying CPs in *c*-Mg_{*x*}Zn_{1-*x*}Te have been studied using SE by Franz *et al.* [342]. The samples were grown by MBE on GaAs(100) substrates ($0 \leq x \leq 0.52$). The experimental data obtained by these authors show that the E_1 and $E_1 + \Delta_1$ CPs increase almost linearly with increasing x , while a clear decrease in E_2 is observed from $x = 0$ (5.25 eV) to 0.52 (5.0 eV).

The temperature variation of E_0 for *c*-Mg_{*x*}Zn_{1-*x*}Te has been measured by Barbier *et al.* [340] and Chung *et al.* [341]. The dE_0/dT values near 300 K are given as $-(4.5 \pm 0.3) \times 10^{-4}$ ($0 \leq x \leq 0.41$) [340] and $-(5.9 \pm 0.2) \times 10^{-4}$ ($0 \leq x \leq 0.48$) eV/K [341], respectively, and are nearly independent of x .

(c) MgCdTe

Bulk Mg_{*x*}Cd_{1-*x*}Te alloy crystallizes in the zinc-blende structure at $0 \leq x \leq 0.6$ and in the wurtzite structure at $x \geq 0.75$ [343]. The E_0 versus x data for *c*-Mg_{*x*}Cd_{1-*x*}Te are plotted in Figure 6.58(c) [344–346]. The samples were grown by the Bridgman method [345] or by MBE on ZnCdTe [344] and GaAs substrates [346]. The solid line represents the quadratic least-squares fit of these and the *c*-MgTe ($x = 1.0$) data. This fit results in a bowing of $c \sim 0.54$ eV.

The composition dependence of E_g^X for *c*-Mg_{*x*}Cd_{1-*x*}Te obtained from the linear interpolation scheme between CdTe ($x = 0$) and MgTe ($x = 1.0$) in Table 6.1 is shown in Figure 6.58(c) by the dashed line. It can be seen that the Γ -X crossover occurs at $x \sim 0.7$ with $E_0 = E_g^X \sim 2.8$ eV, in good agreement with the theoretical prediction by Freytag [347].

The higher-lying CPs in *c*-Mg_{*x*}Cd_{1-*x*}Te have been measured using SE by Choi *et al.* [345] at $0 \leq x \leq 0.5$ and by Ihn *et al.* [346] at $0 \leq x \leq 0.43$. These studies observed the $E_0 + \Delta_0$, E_1 , $E_1 + \Delta_1$, E_2 and E_1' CPs. Some CPs, $E_0 + \Delta_0$, E_1 and $E_1 + \Delta_1$, increased almost linearly at a rate of $\sim(0.7 - 1.3)x$ eV, while E_2 and E_1' showed little dependence on x .

(d) ZnCdTe

Zn_{*x*}Cd_{1-*x*}Te crystallizes in the zinc-blende structure over the whole composition range $0 \leq x \leq 1.0$. The dependence of E_0 on x for Zn_{*x*}Cd_{1-*x*}Te has been determined by many authors. An overview of the bowing parameter c determined at 300 K is summarized in Table 6.31 and in Figure 6.58(d). The c values in Table 6.31 vary from 0 to 0.48 eV. The average c value is ~ 0.27 eV. The corresponding E_0 versus x plots are shown in Figure 6.58(d) by the heavy dashed line (see also Table 6.30).

The higher-lying CPs, such as E_1 , $E_1 + \Delta_1$ and E_2 , in Zn_{*x*}Cd_{1-*x*}Te have been studied by many authors. These CPs showed no or a very weak nonlinearity with respect to x [348–354]. Several studies, however, reported a clear nonlinearity with respect to x [355,356].

The temperature dependence of E_0 for Zn_{*x*}Cd_{1-*x*}Te has been studied using PR [357,358], reflectivity and PL [359]. The Varshni parameters have been determined as $\alpha = (4.7 \pm 0.1) \times 10^{-4}$ eV/K and $\beta = 166.5 \pm 6.5$ K for $0 \leq x \leq 0.3$ [357] and $\alpha = (4.7 \pm 0.2) \times 10^{-4}$ eV/K and

Table 6.31 Bowing parameter c for E_0 of $\text{Zn}_x\text{Cd}_{1-x}\text{Te}$ determined at 300 K. R = reflectance; ER = Electrorreflectance; PL = photoluminescence; OA = optical absorption; PR = photorelectance; SE = spectroscopic ellipsometry

c (eV)	Method	Reference
0.33	R	<i>a</i>
0.26	ER	<i>b</i>
0	R	<i>c</i>
0.139	PL	<i>d</i>
0.22890	OA	<i>e</i>
0.38	OA	<i>f</i>
0.11	PL	<i>g</i>
0.128	PR	<i>h</i>
0.46	OA	<i>i</i>
0.269	SE	<i>j</i>
0.48	OA	<i>k</i>
0.3156	OA	<i>l</i>
0.334	PR	<i>m</i>
0.33	R	<i>n</i>
0.197	SE	<i>o</i>
0.33	PR	<i>p</i>

^aA. Ebina *et al.*, *J. Appl. Phys.* **44**, 3659 (1973)

^bV. A. Tyagai *et al.*, *Sov. Phys. Solid State* **16**, 885 (1974)

^cV. V. Sobolev *et al.*, *Phys. Status Solidi B* **103**, 499 (1981)

^dD. J. Olego *et al.*, *Appl. Phys. Lett.* **47**, 1172 (1985)

^eS. M. Johnson *et al.*, *J. Vac. Sci. Technol. B* **9**, 1897 (1991)

^fA. Aydinli *et al.*, *Solid State Commun.* **80**, 465 (1991)

^gH. C. Poon *et al.*, *J. Phys.: Condens. Matter* **7**, 2783 (1995)

^hS. P. Tobin *et al.*, *J. Electron. Mater.* **24**, 697 (1995)

ⁱB. Samanta *et al.*, *Vacuum* **46**, 739 (1995)

^jO. Castaing *et al.*, *J. Phys.: Condens. Matter* **8**, 5757 (1996)

^kD. Ohlmann *et al.*, *J. Appl. Phys.* **82**, 1355 (1997)

^lJ. Franc *et al.*, *Semicond. Sci. Technol.* **15**, 561 (2000)

^mL. Tirado-Mejía *et al.*, *Phys. Status Solidi B* **220**, 255 (2000)

ⁿE. M. Larramendi *et al.*, *Semicond. Sci. Technol.* **17**, 8 (2002)

^oP. D. Paulson *et al.*, *J. Appl. Phys.* **95**, 3010 (2004)

^pO. Zelaya-Angel *et al.*, *J. Appl. Phys.* **95**, 6284 (2004)

$\beta = 110 \pm 30$ K for $0.551 \leq x \leq 0.944$ [359]. These parameters provide $dE_0/dT \sim -4 \times 10^{-4}$ eV/K near 300 K. The corresponding endpoint data are -4.53×10^{-4} eV/K (ZnTe) and -3.5×10^{-4} eV/K (CdTe) [1].

(e) ZnHgTe

$\text{Zn}_x\text{Hg}_{1-x}\text{Te}$ crystallizes in the zinc-blende structure over the whole composition range $0 \leq x \leq 1.0$. The E_0 versus x data for $\text{Zn}_x\text{Hg}_{1-x}\text{Te}$ determined by means of optical absorption [360,361] and SE [361,362] are shown in Figure 6.58(e). The samples used were grown by the THM [360,362,363] or from interdiffusion between the endpoint materials at high temperatures [361]. The quadratic least-squares fit of these data is shown in Figure 6.58(e)

by the solid line. The bowing parameter of $c \sim 0.46$ eV can be determined from this fit (see also Table 6.30). The semimetallic region is in the range $x < 0.08$ at 300 K.

The higher-lying CPs, $E_0 + \Delta_0$, E_1 , $E_1 + \Delta_1$ and E_2 , as a function of x for $\text{Zn}_x\text{Hg}_{1-x}\text{Te}$ have been determined using SE [363]. The bowing parameters obtained are $c = 0.860$ eV ($E_0 + \Delta_0$), 1.012 eV (E_1), 0.817 eV ($E_1 + \Delta_1$) and 0.428 eV (E_2).

The temperature dependence of E_0 for $\text{Zn}_x\text{Hg}_{1-x}\text{Te}$ has been investigated by Toulouse *et al.* [360]. The results obtained are plotted in Figure 6.57(b). It can be seen that the alloy at $x < 0.45$ has a positive temperature coefficient. The solid line shows the linear least-squares fit given by (in 10^{-4} eV/K)

$$\frac{dE_0}{dT} = 4.5 - 10.6x \quad (6.28)$$

(f) CdHgTe

$\text{Cd}_x\text{Hg}_{1-x}\text{Te}$ crystallizes in the zinc-blende structure over the whole composition range $0 \leq x \leq 1.0$. Figure 6.58(f) plots the experimental E_0 versus x data for $\text{Cd}_x\text{Hg}_{1-x}\text{Te}$ measured by Sredin *et al.* [364] (open circles), Laurenti *et al.* [365] (solid circles) and Chu *et al.* [366] (open triangles). The solid line shows the quadratic least-squares fit of these experimental data. The resulting bowing parameter is $c \sim 0.21$ eV (Table 6.30). The semimetallic region is expected at $x < 0.1$ and 300 K.

The higher-lying CPs, such as E_1 , $E_1 + \Delta_1$ and E_2 , as a function of x for $\text{Cd}_x\text{Hg}_{1-x}\text{Te}$ have been studied by fundamental reflectivity [364,367], ER [368] and SE [369,370]. They appeared at energies 2–3 (E_1), 3–4 ($E_1 + \Delta_1$) and 4.5–5 eV (E_2) and gradually increased with increasing x . The bowing parameters determined were $c \sim 0.7 - 0.9$ eV for E_1 and $\sim 0.5 - 0.6$ eV for $E_1 + \Delta_1$ [369]. The c value for E_2 was found to be negligibly small ($c = -0.06$ eV).

The temperature dependence of E_0 for $\text{Cd}_x\text{Hg}_{1-x}\text{Te}$ has been studied by several authors [365,366,371,372]. The result obtained by Hansen *et al.* [372] is shown in Figure 6.57 (c). The sign for dE_0/dT is positive at $x < 0.5$ and negative at $x > 0.5$. No temperature change in E_0 can be expected at $x \sim 0.5$ ($E_0 \sim 0.6$ eV, Figure 6.58(f)). The dE_0/dT value can then be given by (in 10^{-4} eV/K)

$$\frac{dE_0}{dT} = 5.5 - 11.0x \quad (6.29)$$

The temperature coefficients of the higher-lying CPs have been measured by several authors [367,373,374]. A dip in the dE_g/dT versus x data has been observed near $x \sim 0.5$ for E_1 , $E_1 + \Delta_1$, e_1 and $e_1 + \Delta_1$ [367]. The E_1 -gap Varshni parameters α and β have also been determined using ER [373].

6.5.5 Zn-(VI, VI) Ternary Alloy

(a) ZnOS

$\text{ZnO}_x\text{S}_{1-x}$ is one of the II-VI large size-mismatched alloys and may thus behave in a similar manner to $\text{GaN}_x\text{As}_{1-x}$ [375]. The E_0 gap as a function of x for $\text{ZnO}_x\text{S}_{1-x}$ has been determined from transmission measurements by Meyer *et al.* [376]. The alloy films ($0 \leq x \leq 1.0$) used were

grown by rf reactive sputtering on glass and (0001)-sapphire substrates and showed wurtzite structure with preferential c -axis orientation independent of whether glass or sapphire substrates were used. Figure 6.59(a) plots the E_0 versus x data measured by Meyer *et al.* [376]. The solid line shows the quadratic fit of these data and results in a huge bowing parameter of $c = 4.50$ eV (Table 6.30). This is in qualitative agreement with the fact that bowing parameters in large size-mismatched II–VI alloys increase as the size and chemical mismatches between the endpoint constituents increase [375].

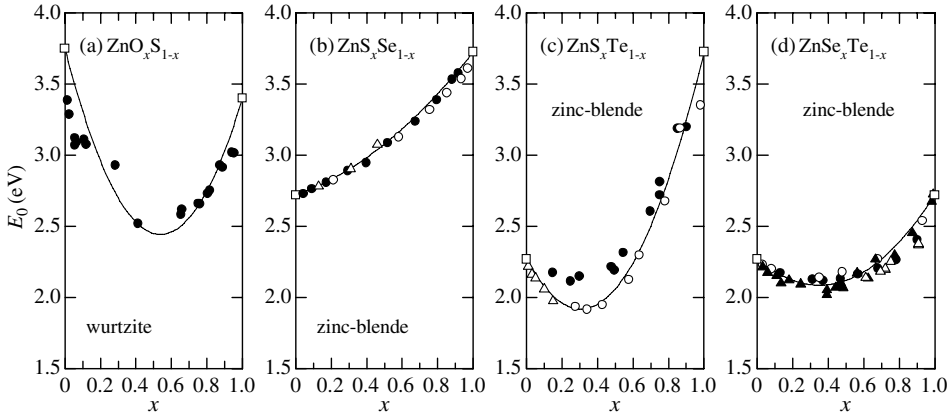


Figure 6.59 Energy of the E_0 gap versus x for some Zn–(VI, VI) ternaries at 300 K: (a) $\text{ZnO}_x\text{S}_{1-x}$, (b) $\text{ZnS}_x\text{Se}_{1-x}$, (c) $\text{ZnS}_x\text{Te}_{1-x}$ and (d) $\text{ZnSe}_x\text{Te}_{1-x}$. The solid lines represent the calculated results using the data in Table 6.30

(b) ZnOSe

$\text{ZnO}_x\text{Se}_{1-x}$ at $x = 0.35 - 1.3$ at% has been successfully grown on GaAs(100) by MBE in spite of the limited solubility of oxygen in ZnSe [377]. A large bowing parameter, as high as 8 eV has been obtained [377] and a reduced pressure coefficient has been successfully explained within the framework of the BAC model [378]. More recently, the temperature variation of E_0 in $\text{ZnO}_x\text{Se}_{1-x}$ ($x = 0.23 - 0.90$ at%) before and after hydrogen passivation was found to be similar to that for ZnSe and did not depend on the oxygen concentration [379]. Such a finding points toward the absence of a localized character in the $\text{ZnO}_x\text{Se}_{1-x}$ band edge.

(c) ZnSSe

c - $\text{ZnS}_x\text{Se}_{1-x}$ can be grown from the melt throughout the whole composition range $0 \leq x \leq 1.0$, although the alloy at $x \geq 0.9$ sometimes shows a short-range twin structure which is typically observed in ZnS grown from the melt [380].

We show in Figure 6.59(b) the x dependence of E_0 in $\text{ZnS}_x\text{Se}_{1-x}$ determined by fundamental reflectivity [380] (solid circles), CL [381] (open circles) and optical absorption measurements [382] (open triangles). The solid line shows the quadratic least-squares fit of these data. The resulting bowing parameter is $c = 0.580$ eV (Table 6.30). The low-temperature ($T \leq 6$ K) E_0 versus x data for $\text{ZnS}_x\text{Se}_{1-x}$ have also been reported [381,383]. The pressure coefficient dE_0/dp for p up to 12 GPa has been measured by Griebel *et al.* [382].

(d) ZnSTe

$\text{ZnS}_x\text{Te}_{1-x}$ is one of the II–VI large size-mismatched alloys and may have a large bowing of the E_0 gap. The E_0 versus x data reported by Hill and Richardson [384] (solid circles), Yu *et al.* [385] (open circles) and by Walukiewicz *et al.* [386] (open triangles) are shown in Figure 6.59(c). The samples were grown by vacuum evaporation [384], hot-wall epitaxy [385] or by the Bridgman method [386]. The solid line in Figure 6.59(c) shows the quadratic least-squares fit of the data of Yu *et al.* and Walukiewicz *et al.* The resulting bowing parameter is $c = 3.750$ eV (Table 6.30). The data of Hill and Richardson gave a value of $c \sim 3.0$ eV [384].

SE has been used by Bang *et al.* [387] on $\text{ZnS}_x\text{Te}_{1-x}$ epilayers ($0 \leq x \leq 1.0$) grown on GaAs (100) substrates by hot-wall epitaxy. The $E_0 + \Delta_0$ and E_1 structures merged into a single, broad structure for x larger than 0.3.

The pressure dependence of E_0 in $\text{ZnS}_x\text{Te}_{1-x}$ ($x = 0-0.1$) has been studied by Walukiewicz *et al.* [386] ($x = 0-0.1$) for p up to 10 GPa. A strong nonlinear dependence of E_0 on p was observed by optical absorption measurements. The results can be satisfactorily described by the BAC model.

(e) ZnSeTe

$\text{ZnSe}_x\text{Te}_{1-x}$ crystallizes in the zinc-blende structure over the whole composition range $0 \leq x \leq 1.0$. The composition dependence of E_0 has been studied by several authors. The E_0 versus x data measured by Larach *et al.* [388] (solid circles), Ebina *et al.* [389] (open circles), Brasil *et al.* [390] (solid triangles) and Su *et al.* [391] (open triangles) have been plotted in Figure 6.59(d). The quadratic least-squares fit of these data is shown by the solid line. The bowing parameter obtained is $c = 1.500$ eV (Table 6.30). This value is considerably larger than that for $\text{ZnS}_x\text{Se}_{1-x}$ ($c = 0.580$ eV, Figure 6.59(b)), but is much smaller than those for $\text{ZnO}_x\text{S}_{1-x}$ ($c = 4.50$ eV, Figure 6.59(a)) and $\text{ZnS}_x\text{Te}_{1-x}$ ($c = 3.750$ eV, Figure 6.59(c)).

The higher-lying CPs, such as $E_0 + \Delta_0$, E_1 , $E_1 + \Delta_1$ and E_2 , as a function of x for $\text{ZnSe}_x\text{Te}_{1-x}$ have been measured by fundamental reflectivity [389] and SE [392]. The bowing parameters determined were $c = 1.878$ eV (E_1), 1.458 eV ($E_1 + \Delta_1$) and -0.698 eV (E_2) [392]. Only the E_2 CP gives an upward bowing ($c < 0$ eV).

The high-energy PL line as a function of temperature T for $\text{ZnSe}_x\text{Te}_{1-x}$ ($0 \leq x \leq 0.30$) has been measured by Naumov *et al.* [393]. The experimental data could be fitted with the Varshni expression using the interpolated parameters between ZnTe ($x = 0$) and ZnSe ($x = 1.0$) [1]. The pressure dependence of E_0 has also been measured for p up to 10 GPa [394]. The first- and second-order pressure coefficients are reported as a function of x for $0 \leq x \leq 1.0$. The large deviation of dE_0/dp from the linear interpolation can be explained by the BAC model [394].

6.5.6 Cd–(VI, VI) Ternary Alloy**(a) CdSSe**

$\text{CdS}_x\text{Se}_{1-x}$ crystallizes in the wurtzite structure over the whole composition range $0 \leq x \leq 1.0$. The experimental E_0 value as a function of x for $w\text{-CdS}_x\text{Se}_{1-x}$ measured by Bondarenko *et al.* [395] (solid circles) and Perna *et al.* [396] are shown in Figure 6.60(a). The quadratic fit of these data gives a value of $c = 0.700$ eV (Table 6.30).

The higher-lying CPs, such as E_1 , E_2 and E'_1 , in w - $\text{CdS}_x\text{Se}_{1-x}$ have been determined from the fundamental reflectivity measurements for the ordinary ($E \perp c$) and extraordinary rays ($E \parallel c$) at 90 K [397].

The temperature dependence of E_0 in w - $\text{CdS}_x\text{Se}_{1-x}$ has been studied by Perna *et al.* [396]. These authors reported that the effects of the acoustic phonons are larger in alloy films than in the related binaries because of the compositional disorder.

(b) CdSTe

The CdS–CdTe phase diagram indicates that at low temperatures, $\text{CdS}_x\text{Te}_{1-x}$ has a zinc-blende structure for low S concentrations and a wurtzite structure for high S concentrations (Figure 2.7). These regions are separated by a miscibility gap where both phases exist, and optical transitions resulted from both wide band-gap wurtzite and narrow band-gap zinc-blende phases. Therefore, the two absorption edges would usually be detected, although their strengths would depend on the concentration of each phase.

Many authors have measured the E_0 versus x data for $\text{CdS}_x\text{Te}_{1-x}$ films (see Lane [398]). A small number of samples of different x have been studied generally, with the most widely accepted results relying on 19 data points from $x = 0$ to 1.0 reported by Ohata *et al.* [399]. From the quadratic fit of the previous data, we obtain a bowing parameter of $c \sim 1.8$ eV for both the zinc-blende and wurtzite phases (see also Figure 1 in Lane [398] and Figure 6.63). The curves plotted in Figure 6.60(b) show the quadratic fits of Equation (A.5) with $c \sim 1.8$ eV (Table 6.30).

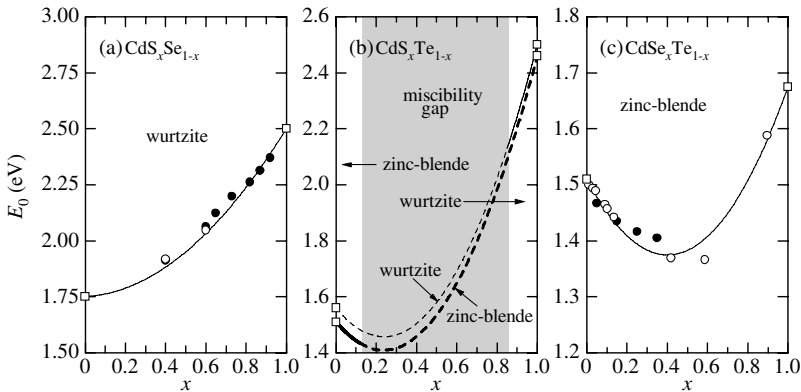


Figure 6.60 Energy of the E_0 gap versus x for some Cd–(VI, VI) ternaries at 300 K: (a) $\text{CdS}_x\text{Se}_{1-x}$, (b) $\text{CdS}_x\text{Te}_{1-x}$ and (c) $\text{CdSe}_x\text{Te}_{1-x}$. The solid and dashed lines represent the calculated results using the data in Table 6.30

The higher-lying CPs in c - $\text{CdS}_x\text{Te}_{1-x}$ ($x = 0 - 1.0$) have been determined using SE [400]. The samples used were deposited on borosilicate glass (Corning 7059) using a laser-deposition process. The XRD analysis suggested that the deposited films consisted of a single phase. The bowing parameter determined for the E_1 gap is $c \sim 0.8$ eV, while that for E_0 is 1.84 eV.

(c) CdSeTe

Since CdSe is a wurtzite crystal while CdTe is a zinc-blende crystal, it is reasonable to expect a phase change in crystal structure at some Se composition. This has been reported for alloys

grown on glass substrates with zinc-blende nucleation at $x < 0.60$ and wurtzite nucleation at $x > 0.60$ [401]. Similarly, melt-grown $\text{CdSe}_x\text{Te}_{1-x}$ was reported to nucleate as zinc-blende at $x \leq 0.45$ and as wurtzite at $x \geq 0.65$ with a mixed phase between $x = 0.45$ and 0.65 [402].

Figure 6.60(c) shows the plots of E_0 against x for $c\text{-CdSe}_x\text{Te}_{1-x}$ reported by Feng *et al.* [403] (solid circles) and Brill *et al.* [404] (open circles). The samples were grown by the Bridgman method ($x < 0.36$) [403] and by MBE on Si(211) ($0 \leq x \leq 1.0$) [404]. It could be clearly observed that the MBE-grown $\text{CdSe}_x\text{Te}_{1-x}/\text{Si}(211)$ films remained in the cubic phase throughout the entire composition range [404]. Note that CdSe can be grown in the cubic phase on GaAs and ZnSe substrates (see Brill *et al.* [404]). The solid line in Figure 6.60(c) represents the quadratic least-squares fit of the experimental data, yielding a value of $c = 0.838 \text{ eV}$ (Table 6.30).

6.5.7 (II, II)–(VI, VI) Quaternary Alloy

(a) MgZnSSe

$\text{Mg}_x\text{Zn}_{1-x}\text{S}_y\text{Se}_{1-y}$ can be grown lattice-matched to GaAs (Table 1.13) and has been used as an improved cladding material for ZnSe-based waveguiding devices [405]. The E_0 -gap energy as a function of x for $\text{Mg}_x\text{Zn}_{1-x}\text{S}_y\text{Se}_{1-y}/\text{GaAs}$ calculated from Equation (A.15) is shown in Figure 6.61(a). The experimental data shown are taken from Lunz *et al.* [406]

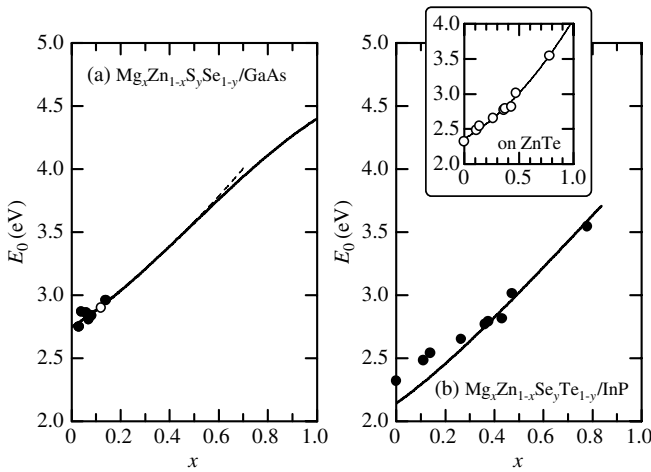


Figure 6.61 Energy of the E_0 gap versus x for (a) $\text{Mg}_x\text{Zn}_{1-x}\text{S}_y\text{Se}_{1-y}/\text{GaAs}$ and (b) $\text{Mg}_x\text{Zn}_{1-x}\text{Se}_y\text{Te}_{1-y}/\text{InP}$ calculated from Equation (A.15). The ternary bowing parameters are taken from Table 6.32. The unknown ternary and quaternary bowing parameters (c and D) are assigned to be 0 eV . The experimental data in (a) are taken from Lunz *et al.* [406] (solid circles) and Chen *et al.* [407] (open circle) and in (b) from Naniwae *et al.* [408] (300 K). The dashed line in (a) shows the quadratic approximation of Equation (A.15) for $0 \leq x \leq 0.5$ (see Table 6.30). The inset in (b) represents the E_0 versus x data for MBE-grown $\text{Mg}_x\text{Zn}_{1-x}\text{Se}_y\text{Te}_{1-y}/\text{ZnTe}$ reported by Shim *et al.* [409]. The solid line in the inset is calculated from Equation (6.30)

(solid circles) and Chen *et al.* [407] (open circle). It can be seen that the calculated E_0 varies from 2.749 eV ($x=0$, $y=0.06$) to 4.399 eV ($x=1.00$, $y=0.89$). This curve can be approximated by the quadratic expression as shown in Figure 6.61(a) by the dashed line (Table 6.30).

The temperature dependence of E_0 for $\text{Mg}_x\text{Zn}_{1-x}\text{S}_y\text{Se}_{1-y}/\text{GaAs}$ has been determined by Lunz *et al.* [406] from an optical absorption and by Chen *et al.* [407] from contactless ER. The dE_0/dT coefficient near 300 K is $\sim -6 \times 10^{-4}$ eV/K, while that for ZnSe is -4.7×10^{-4} eV/K [1].

(b) *MgZnSeTe*

$\text{Mg}_x\text{Zn}_{1-x}\text{Se}_y\text{Te}_{1-y}$ can be grown lattice-matched to InP (Table 1.13). The solid line in Figure 6.61(b) shows the E_0 versus x curve for $\text{Mg}_x\text{Zn}_{1-x}\text{Se}_y\text{Te}_{1-y}/\text{InP}$ obtained from Equation (A.15). The solid circles represent the experimental data measured by optical reflectivity [408]. The solid line can be approximated by the quadratic expression given in Table 6.30.

$\text{Mg}_x\text{Zn}_{1-x}\text{Se}_y\text{Te}_{1-y}$ can be grown lattice-matched to ZnTe. Shim *et al.* [409] grew $\text{Mg}_x\text{Zn}_{1-x}\text{Se}_y\text{Te}_{1-y}/\text{ZnTe}$ by MBE and determined E_0 from PL measurements. The inset in Figure 6.61(b) shows the E_0 versus x data of Shim *et al.* [409]. These data can be least-squares fit as (in eV)

$$E_0(x) = 2.36 + 0.89x + 0.82x^2 \quad (6.30)$$

6.5.8 (II, II, II)–VI Quaternary Alloy

(a) *BeMgZnSe*

$\text{Be}_x\text{Mg}_y\text{Zn}_{1-x-y}\text{Se}$ can be grown lattice-matched to GaAs (Table 1.14). The experimental E_0 versus y data for $\text{Be}_x\text{Mg}_y\text{Zn}_{1-x-y}\text{Se}/\text{GaAs}$ are plotted in Figure 6.62(a). These data are taken from Wagner *et al.* [410] (solid circles) and Godo *et al.* [411] (open circles). The solid line represents the E_0 versus y curve for $\text{Be}_x\text{Mg}_y\text{Zn}_{1-x-y}\text{Se}/\text{GaAs}$ calculated from Equation (A.15). This curve can be satisfactorily approximated by the quadratic expression shown in Table 6.30.

The $E_0/(E_0 + \Delta_0)$ structure of Bridgman-grown $\text{Be}_x\text{Mg}_y\text{Zn}_{1-x-y}\text{Se}$ alloy ($x=0.04$, $y=0.15$) has been investigated by PL, contactless ER and PR in the temperature range between 15 and 400 K [412]. The obtained data were analyzed using the Varshni and Bose–Einstein expressions.

(b) *BeZnCdSe*

Bulk $\text{Be}_x\text{Zn}_y\text{Cd}_{1-x-y}\text{Se}$ alloys were grown by the Bridgman method and investigated using ER, PR, SE and PL [413–415]. The samples were single wurtzite phase or wurtzite as the main phase in an admixture with another polytype ($x \leq 0.15$, $y \leq 0.45$). The temperature dependence of E_0 has been reported [413,415].

$\text{Be}_x\text{Zn}_y\text{Cd}_{1-x-y}\text{Se}$ can be epitaxially grown lattice-matched to InP. Hsieh *et al.* [416] have characterized the E_0 structure of MBE-grown $\text{Be}_x\text{Zn}_y\text{Cd}_{1-x-y}\text{Se}/\text{InP}$ using contactless ER and PzR in the temperature range between 15 and 450 K. The results show that Be incorporation can effectively reduce the rate of temperature variation of E_0 .

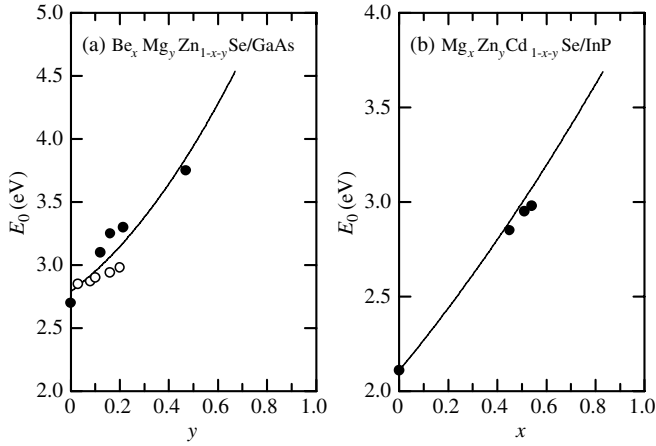


Figure 6.62 Energy of the E_0 gap versus y or x for (a) $\text{Be}_x\text{Mg}_y\text{Zn}_{1-x-y}\text{Se}/\text{GaAs}$ and (b) $\text{Mg}_x\text{Zn}_y\text{Cd}_{1-x-y}\text{Se}/\text{InP}$ calculated from Equation (A.15). The ternary bowing parameters are taken from Table 6.32 (see also Table 6.30). The unknown ternary and quaternary bowing parameters (c and D) are assigned to be 0 eV. The experimental data in (a) are taken from Wagner *et al.* [410] (solid circles) and Godo *et al.* [411] (open circles) (300 K). The solid circles in (b) are obtained from Maksimov *et al.* [417]. The solid lines show the quadratic approximations listed in Table 6.30

(c) MgZnCdSe

$\text{Mg}_x\text{Zn}_y\text{Cd}_{1-x-y}\text{Se}$ can be grown, together with those for the E_0 and $E_0 + \Delta_0$ CPs lattice-matched to InP (Table 1.14). Figure 6.62(b) plots the E_0 versus x data for $\text{Mg}_x\text{Zn}_y\text{Cd}_{1-x-y}\text{Se}/\text{InP}$ measured by Maksimov *et al.* [417]. The E_0 versus x curve calculated from Equation (A.15) is shown by the solid line. The corresponding quadratic expression is given in Table 6.30. The temperature dependence of E_0 has also been determined by Maksimov *et al.* [417] in the temperature range between 4.2 and 300 K.

6.5.9 Summary

Table 6.32 summarizes the bowing parameter c for E_0 in some II–VI ternary alloys. Figure 6.63 also shows the plots for the c value against the product $\Delta a_{\alpha\beta}\Delta X_{\alpha\beta}$ of the lattice constant and electronegativity differences between the endpoint binaries α and β . The electronegativity differences are obtained from Phillips [46]. The solid line in Figure 6.63 represents the least-squares fit obtained using the relationship (c in eV, $\Delta a_{\alpha\beta}\Delta X_{\alpha\beta}$ in ÅeV)

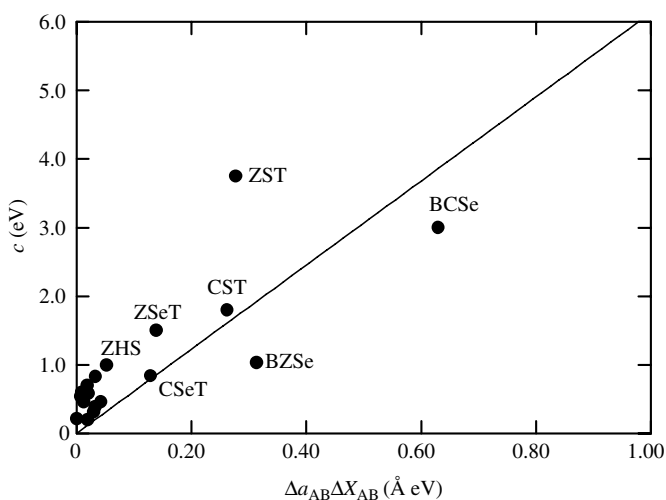
$$c = 6.13(\Delta a_{\alpha\beta}\Delta X_{\alpha\beta}) \tag{6.31}$$

Note that the proportionality factor 6.13 Å^{-1} obtained here is considerably smaller than the values 9.93 and 9.62 Å^{-1} for the group-IV binary and III–V ternary alloys, respectively (Equations (6.8) and (6.23)).

Finally, the relationships between the E_0 gap and lattice constant a_0 for various II–VI semiconductors are shown in Figure 6.64. It is clear that the lowest direct gap E_0 can be widely

Table 6.32 Bowing parameter c for E_0 in II–VI ternaries. w = wurtzite; zb = zinc-blende

(II, II)–VI	c (eV)	II–(VI, VI)	c (eV)
BeZnO (w)	9.3	ZnOS (w)	4.50
MgZnO (w)	0	ZnSSe (zb)	0.580
ZnCdO (w)	2.4	ZnSTe (zb)	3.750
MgZnS (zb)	0	ZnSeTe (zb)	1.500
MgZnS (w)	0	CdSSe (w)	0.700
ZnCdS (zb)	0.827	CdSTe (zb)	1.80
ZnCdS (w)	0.921	CdSTe (w)	1.800
ZnHgS (zb)	0.996	CdSeTe (zb)	0.838
CdHgS (w)	0		
BeZnSe (zb)	1.033		
BeCdSe (zb)	3.000		
MgZnSe (zb)	0.600		
MgCdSe (zb)	0.200		
MgCdSe (w)	0		
ZnCdSe (zb)	0.387		
CdHgSe (zb)	0		
BeZnTe (zb)	0		
MgZnTe (zb)	0.46		
MgCdTe (zb)	0.54		
ZnCdTe (zb)	0.31		
ZnHgTe (zb)	0.46		
CdHgTe (zb)	0.21		

**Figure 6.63** Bowing parameter c of the E_0 gap versus product $\Delta a_{\alpha\beta}\Delta X_{\alpha\beta}$ of the lattice-constant and electronegativity differences between the endpoint binary materials α and β in some II–VI semiconductor ternary alloys. The solid line represents the calculated result using Equation (6.31). B = Be; Z = Zn; C = Cd; T = Te

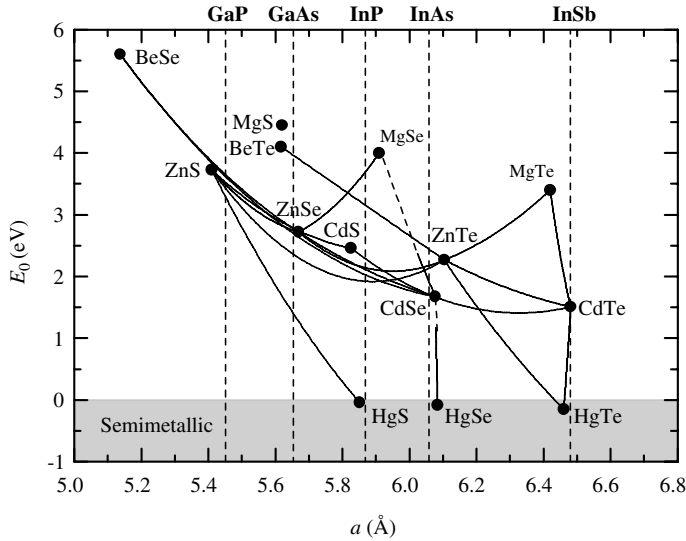


Figure 6.64 Relationships between the E_0 gap and lattice constant a_0 for II–VI semiconductor systems

varied by properly combining the binary materials when growing II–VI ternary and quaternary alloys. Such alloys can be epitaxially grown on commercially available III–V binary substrates, such as GaP, GaAs and InP.

REFERENCES

- [1] S. Adachi, *Properties of Group-IV, III–V and II–VI Semiconductors*, John Wiley & Sons, Ltd, Chichester, 2005.
- [2] J. L. Birman, *Phys. Rev.* **115**, 1493 (1959).
- [3] D. G. Thomas and J. J. Hopfield *Phys. Rev.* **116**, 573 (1959); J. J. Hopfield *J. Phys. Chem. Solids* **15**, 97 (1960).
- [4] J. A. Van Vechten and T. K. Bergstresser, *Phys. Rev. B* **1**, 3351 (1970).
- [5] J. C. Phillips and J. A. Van Vechten, *Phys. Rev. Lett.* **22**, 705 (1969).
- [6] P. Kiesel, T. Kippenberg, and G. H. Döhler, in *Spontaneous Ordering in Semiconductor Alloys* (edited by A. Mascarenhas), Kluwer Academic, New York, 2002, p. 365.
- [7] G. F. Koster, J. O. Dimmock, R. G. Wheeler, and H. Statz, *Properties of Thirty-Two Point Groups*, MIT Press, Cambridge, 1963.
- [8] P. Ernst, C. Geng, F. Scholz, H. Schweizer, Y. Zhang, and A. Mascarenhas, *Appl. Phys. Lett.* **67**, 2347 (1995).
- [9] B. T. McDermott, K. G. Reid, N. A. El-Masry, S. M. Bedair, W. M. Duncan, X. Yin, and F. H. Pollak, *Appl. Phys. Lett.* **56**, 1172 (1990).
- [10] R. L. Forrest, T. D. Golding, S. C. Moss, Z. Zhang, J. F. Geisz, J. M. Olson, A. Mascarenhas, P. Ernst, and C. Geng, *Phys. Rev. B* **58**, 15355 (1998).
- [11] W. Kissinger, M. Weidner, H. J. Osten, and M. Eichler, *Appl. Phys. Lett.* **65**, 3356 (1994).
- [12] S. Zollner, C. M. Herzinger, J. A. Woollam, S. S. Iyer, A. P. Powell, and K. Eberl, *Solid State Commun.* **96**, 305 (1995).
- [13] A. A. Demkov and O. F. Sankey, *Phys. Rev. B* **48**, 2207 (1993).

- [14] H. Lee, S. R. Kurtz, J. A. Floro, J. Strane, C. H. Seager, S. R. Lee, E. D. Jones, J. F. Nelson, T. Mayer, and S. T. Picraux, *Jpn. J. Appl. Phys.* **34**, L1340 (1995).
- [15] S. Zollner, K. E. Junge, R. Lange, and A. A. Affolder, *Jpn. J. Appl. Phys.* **35**, 5684 (1996).
- [16] J. Kolodzey, P. A. O'Neil, S. Zhang, B. A. Orner, K. Roe, K. M. Unruh, C. P. Swann, M. M. Waite, and S. I. Shah, *Appl. Phys. Lett.* **67**, 1865 (1995).
- [17] J. S. Schrader, J. L. Huguenin-Love, R. J. Soukup, N. J. Ianno, C. L. Exstrom, S. A. Darveau, R. N. Udey, and V. L. Dalal, *Sol. Ener. Mater. Sol. Cells* **90**, 2338 (2006).
- [18] K. E. Junge, N. R. Voss, R. Lange, J. M. Dolan, S. Zollner, M. Dashiell, D. A. Hits, B. A. Orner, R. Jonczyk, and J. Kolodzey, *Thin Solid Films* **313–314**, 172 (1998).
- [19] See, for example, *Semiconductors and Semimetals* (edited by R. K. Willardson and A. C. Beer), Academic, New York, 1991, Vol. 33 (Volume Editor, T. P. Pearsall).
- [20] R. Braunstein, A. R. Moore, and F. Herman, *Phys. Rev.* **109**, 695 (1958).
- [21] J. Weber and M. I. Alonso, *Phys. Rev. B* **40**, 5683 (1989).
- [22] D. V. Lang, R. People, J. C. Bean, and A. M. Sergent, *Appl. Phys. Lett.* **47**, 1333 (1985).
- [23] D. Dutartre, G. Brémond, A. Souifi, and T. Benyattou, *Phys. Rev. B* **44**, 11525 (1991).
- [24] C. W. Liu, J. C. Sturm, Y. R. J. Lacroix, M. L. W. Thewalt, and D. D. Perovic, *Appl. Phys. Lett.* **65**, 76 (1994).
- [25] R. People, *Phys. Rev. B* **32**, 1405 (1985); **34**, 2508 (1986).
- [26] F. Ferrieu, F. Beck, and D. Dutartre, *Solid State Commun.* **82**, 427 (1992).
- [27] R. T. Carline, C. Pickering, D. J. Robbins, W. Y. Leong, A. D. Pitt, and A. G. Cullis, *Appl. Phys. Lett.* **64**, 1114 (1994).
- [28] R. T. Carline, T. J. C. Hosea, and D. J. Hall, *J. Appl. Phys.* **78**, 4285 (1995).
- [29] J. H. Bahng, K. J. Kim, S. H. Ihm, and J. Y. Kim, *Solid State Commun.* **106**, 591 (1998).
- [30] T. Ebner, K. Thonke, R. Sauer, F. Schaeffler, and H. J. Herzog, *Phys. Rev. B* **57**, 15448 (1998).
- [31] P. Etchegoin, J. Kircher, and M. Cardona, *Phys. Rev. B* **47**, 10292 (1993).
- [32] J. Humlíček, F. Lukes, E. Schmidt, M. G. Kekoua, and E. Khoutsishvili, *Phys. Rev. B* **33**, 1092 (1986).
- [33] E. Schmidt and K. Vedam, *Solid State Commun.* **9**, 1187 (1971).
- [34] G. He and H. A. Atwater, *Phys. Rev. Lett.* **79**, 1937 (1997).
- [35] H. P. L. de Guevara, A. G. Rodríguez, H. Navarro-Contreras, and M. A. Vidal, *Appl. Phys. Lett.* **84**, 4532 (2004); **91**, 161909 (2007).
- [36] M. R. Bauer, J. Tolle, C. Bungay, A. V. G. Chizmeshya, D. J. Smith, J. Menéndez, and J. Kouvetakis, *Solid State Commun.* **127**, 355 (2003).
- [37] V. R. D'Costa, C. S. Cook, A. G. Birdwell, C. L. Littler, M. Canonico, S. Zollner, J. Kouvetakis, and J. Menéndez, *Phys. Rev. B* **73**, 125207 (2006).
- [38] A. S. Amour, C. W. Liu, J. C. Sturm, Y. Lacroix, and M. L. W. Thewalt, *Appl. Phys. Lett.* **67**, 3915 (1995).
- [39] C. G. Van de Walle and R. M. Martin, *Phys. Rev. B* **34**, 5621 (1986).
- [40] O. G. Schmidt and K. Eberl, *Phys. Rev. Lett.* **80**, 3396 (1998).
- [41] H. Lee, J. A. Floro, J. Strane, S. R. Lee, E. D. Jones, T. Mayer, and S. T. Picraux, *Mater. Res. Soc. Symp. Proc.* **379**, 211 (1995).
- [42] W. Kissinger, H. J. Osten, M. Weidner, and M. Eichler, *J. Appl. Phys.* **79**, 3016 (1996).
- [43] P. Aella, C. Cook, J. Tolle, S. Zollner, A. V. G. Chizmeshya, and J. Kouvetakis, *Appl. Phys. Lett.* **84**, 888 (2004).
- [44] V. R. D'Costa, C. S. Cook, J. Menéndez, J. Tolle, J. Kouvetakis, and S. Zollner, *Solid State Commun.* **138**, 309 (2006).
- [45] R. A. Soref, *J. Appl. Phys.* **70**, 2470 (1991).
- [46] J. C. Phillips, *Bonds and Bands in Semiconductors*, Academic, New York, 1973.
- [47] H. Okumura, T. Koizumi, Y. Ishida, H. Yaguchi, and S. Yoshida, *Phys. Status Solidi B* **216**, 211 (1999).
- [48] T. Suzuki, H. Yaguchi, H. Okumura, Y. Ishida, and S. Yoshida, *Jpn. J. Appl. Phys.* **39**, L497 (2000).

- [49] A. Kasic, M. Schubert, T. Frey, U. Köhler, D. J. As, and C. M. Herzinger, *Phys. Rev. B* **65**, 184302 (2002).
- [50] S. Adachi, *Handbook on Physical Properties of Semiconductors: Volume 2 III–V Compound Semiconductors*, Kluwer Academic, Boston, 2004.
- [51] M. P. Thompson, G. W. Auner, T. S. Zheleva, K. A. Jones, S. J. Simko, and J. N. Hilfiker, *J. Appl. Phys.* **89**, 3331 (2001).
- [52] D. Brunner, H. Angerer, E. Bustarret, F. Freudenberger, R. Höppler, R. Dimitrov, O. Ambacher, and M. Stutzmann, *J. Appl. Phys. Lett.* **82**, 5090 (1997).
- [53] J. F. Muth, J. D. Brown, M. A. L. Johnson, Z. Yu, R. M. Kolbas, J. W. Cook, Jr., and J. F. Schetzina, *Mater. Res. Soc. Symp. Proc.* **537**, G5.2 (1999).
- [54] B. K. Meyer, G. Steude, A. Göldner, A. Hoffmann, H. Amano, and I. Akasaki, *Phys. Status Solidi B* **216**, 187 (1999).
- [55] C. Buchheim, R. Goldhahn, M. Rakel, C. Cobet, N. Esser, U. Rossow, D. Fuhrmann, and A. Hangleiter, *Phys. Status Solidi B* **242**, 2610 (2005).
- [56] I. Vurgaftman and J. R. Meyer, *J. Appl. Phys.* **94**, 3675 (2003).
- [57] J. Wu, W. Walukiewicz, K. M. Yu, J. W. Ager III, S. X. Li, E. E. Haller, H. Lu, and W. J. Schaff, *Solid State Commun.* **127**, 411 (2003).
- [58] S. R. Lee, A. F. Wright, M. H. Crawford, G. A. Petersen, J. Han, and R. M. Biefeld, *Appl. Phys. Lett.* **74**, 3344 (1999).
- [59] T. Wethkamp, K. Wilmers, N. Esser, W. Richter, O. Ambacher, H. Angerer, G. Jungk, R. L. Johnson, and M. Cardona, *Thin Solid Films* **313–314**, 745 (1998).
- [60] W. Shan, J. W. Ager III, W. Walukiewicz, E. E. Haller, B. D. Little, J. J. Song, M. Schurman, Z. C. Feng, R. A. Stall, and B. Goldenberg, *Appl. Phys. Lett.* **72**, 2274 (1998).
- [61] F. Yun, M. A. Reshchikov, L. He, T. King, and H. Morkoç, *J. Appl. Phys.* **92**, 4837 (2002).
- [62] L. Malikova, Y. S. Huang, F. H. Pollak, Z. C. Feng, M. Schurman, and R. A. Stall, *Solid State Commun.* **103**, 273 (1997).
- [63] N. Nepal, J. Li, M. L. Nakarmi, J. Y. Lin, and H. X. Jiang, *Appl. Phys. Lett.* **87**, 242104 (2005).
- [64] W. Shan, J. W. Ager III, K. M. Yu, W. Walukiewicz, E. E. Haller, M. C. Martin, W. R. McKinney, and W. Yang, *J. Appl. Phys.* **85**, 8505 (1999).
- [65] J. Wu and W. Walukiewicz, *Superlatt. Microstruct.* **34**, 63 (2003).
- [66] M. Androulidaki, N. T. Pelekanos, K. Tsagaraki, E. Dimakis, E. Iliopoulos, A. Adikimenakis, E. Bellet-Amalric, D. Jalabert, and A. Georgakilas, *Phys. Status Solidi C* **3**, 1866 (2006).
- [67] W. Terashima, S.-B. Che, Y. Ishitani, and A. Yoshikawa, *Jpn. J. Appl. Phys.* **45**, L539 (2006).
- [68] R. Goldhahn, P. Schley, A. T. Winzer, G. Gobsch, V. Cimalla, O. Ambacher, M. Rakel, C. Cobet, N. Esser, H. Lu, and W. J. Schaff, *Phys. Status Solidi A* **203**, 42 (2006).
- [69] S. X. Li, J. Wu, E. E. Haller, W. Walukiewicz, W. Shan, H. Lu, and W. J. Schaff, *Appl. Phys. Lett.* **83**, 4963 (2003).
- [70] J. Schörmann, D. J. As, K. Lischka, P. Schley, R. Goldhahn, S. F. Li, W. Löffler, M. Hetterich, and H. Kalt, *Appl. Phys. Lett.* **89**, 261903 (2006).
- [71] J. R. Müllhäuser, O. Brandt, A. Trampert, B. Jenichen, and K. H. Ploog, *Appl. Phys. Lett.* **73**, 1230 (1998).
- [72] R. Goldhahn, J. Scheiner, S. Schokhovets, T. Frey, U. Köhler, D. J. As, and K. Lischka, *Appl. Phys. Lett.* **76**, 291 (2000).
- [73] C. A. Parker, J. C. Roberts, S. M. Bedair, M. J. Reed, S. X. Liu, N. A. El-Masry, and L. H. Robins, *Appl. Phys. Lett.* **75**, 2566 (1999).
- [74] C. Caetano, L. K. Teles, M. Marques, A. Dal Pino, Jr., and L. G. Ferreira, *Phys. Rev. B* **74**, 045215 (2006).
- [75] P. Schley, R. Goldhahn, A. T. Winzer, G. Gobsch, V. Cimalla, O. Ambacher, H. Lu, W. J. Schaff, M. Kurouchi, Y. Nanishi, M. Rakel, C. Cobet, and N. Esser, *Phys. Rev. B* **75**, 205204 (2007).
- [76] K. M. Yu, Z. Liliental-Weber, W. Walukiewicz, W. Shan, J. W. Ager III, S. S. Li, R. E. Jones, E. E. Haller, H. Lu, and W. J. Schaff, *Appl. Phys. Lett.* **86**, 071910 (2005).

- [77] W. Shan, B. D. Little, J. J. Song, Z. C. Feng, M. Schurman, and R. A. Stall, *Appl. Phys. Lett.* **69**, 3315 (1996).
- [78] W. Shan, W. Walukiewicz, E. E. Haller, B. D. Little, J. J. Song, M. D. McCluskey, N. M. Johnson, Z. C. Feng, M. Schurman, and R. A. Stall, *J. Appl. Phys.* **84**, 4452 (1998).
- [79] H. Sonomura, T. Nanmori, and T. Miyauchi, *Appl. Phys. Lett.* **24**, 77 (1974).
- [80] A. Onton, M. R. Lorenz, J. M. Woodall, and R. J. Chicotka, *J. Cryst. Growth* **27**, 166 (1974).
- [81] L. K. Vodop'yanov, V. I. Kozlovskii, and N. N. Mel'nik, *Sov. Phys. Semicond.* **34**, 405 (2000).
- [82] J. M. Rodríguez and G. Armelles, *J. Appl. Phys.* **69**, 965 (1991).
- [83] S. G. Choi, Y. D. Kim, S. D. Yoo, D. E. Aspnes, D. H. Woo, and S. H. Kim, *J. Appl. Phys.* **87**, 1287 (2000).
- [84] A. Onton and R. J. Chicotka, *J. Appl. Phys.* **41**, 4205 (1970).
- [85] D. P. Bour, J. R. Shealy, G. W. Wicks, and W. J. Schaff, *Appl. Phys. Lett.* **50**, 615 (1987).
- [86] Y. Ishitani, H. Hamada, S. Minagawa, H. Yaguchi, and Y. Shiraki, *Jpn. J. Appl. Phys.* **36**, 6607 (1997).
- [87] A. Onton, M. R. Lorenz, and W. Reuter, *J. Appl. Phys.* **42**, 3420 (1971).
- [88] C. Alibert, G. Bordure, A. Laugier, and J. Chevallier, *Phys. Rev. B* **6**, 1301 (1972).
- [89] I. Vurgaftman, J. R. Meyer, and L. R. Ram-Mohan, *J. Appl. Phys.* **89**, 5815 (2001).
- [90] H. Lange, J. Donecker, and H. Friedrich, *Phys. Status Solidi B* **73**, 633 (1976).
- [91] M. Bugajski, A. M. Kontkiewicz, and H. Mariette, *Phys. Rev. B* **28**, 7105 (1983).
- [92] R. Hill, *J. Phys. C: Solid State Phys.* **7**, 516 (1974).
- [93] H. Lee, D. Biswas, M. V. Klein, H. Morkoç, D. E. Aspnes, B. D. Choe, J. Kim, and C. O. Griffiths, *J. Appl. Phys.* **75**, 5040 (1994).
- [94] Y. Ishitani, H. Yaguchi, and Y. Shiraki, *Jpn. J. Appl. Phys.* **40**, 1183 (2001).
- [95] Y. C. Yeh, S. Chen, Y. S. Huang, C. H. Ho, and K. K. Tiong, *J. Phys.: Condens. Matter* **12**, 2183 (2000).
- [96] R. Ferrini, G. Guizzetti, M. Patrini, A. Parisini, L. Tarricone, and B. Valenti, *Eur. Phys. J. B* **27**, 449 (2002).
- [97] A. Onton and R. J. Chicotka, *Phys. Rev. B* **4**, 1847 (1971).
- [98] B. W. Hakki, A. Jayaraman, and C. K. Kim, *J. Appl. Phys.* **41**, 5291 (1970).
- [99] A. R. Goñi, K. Syassen, K. Strössner, and M. Cardona, *Phys. Rev. B* **39**, 3178 (1989).
- [100] J. Chen, D. Patel, J. R. Sites, I. L. Spain, M. J. Hafich, and G. Y. Robinson, *Solid State Commun.* **75**, 693 (1990).
- [101] J. Dong, G. Li, Z. Wang, D. Lu, X. Liu, X. Li, D. Sun, M. Kong, and Z. Wang, *J. Appl. Phys.* **79**, 7177 (1996).
- [102] J. L. Aubel, U. K. Reddy, S. Sundaram, W. T. Beard, and J. Comas, *J. Appl. Phys.* **58**, 495 (1985).
- [103] D. E. Aspnes, S. M. Kelso, R. A. Logan, and R. Bhat, *J. Appl. Phys.* **60**, 754 (1986).
- [104] A. K. Saxena, *Phys. Status Solidi B* **105**, 777 (1981).
- [105] B. Monemar, K. K. Shih, and G. D. Pettit, *J. Appl. Phys.* **47**, 2604 (1976).
- [106] S. Adachi, *GaAs and Related Materials: Bulk Semiconducting and Superlattice Properties*, World Scientific, Singapore, 1994.
- [107] H. J. Lee, L. Y. Jurel, J. C. Woolley, and A. J. Spring Thorpe, *Phys. Rev. B* **21**, 659 (1980).
- [108] J. C. M. Henning, J. P. M. Ansems, and P. J. Roksnoer, *J. Phys. C: Solid State Phys.* **19**, L335 (1986).
- [109] B. Wakefield, M. A. G. Halliwell, T. Kerr, D. A. Andrews, G. J. Davies, and D. R. Wood, *Appl. Phys. Lett.* **44**, 341 (1984).
- [110] W. Y. Chou, G. S. Chang, W. C. Hwang, and J. S. Hwang, *J. Appl. Phys.* **83**, 3690 (1998).
- [111] D. Oertel, D. Bimberg, R. K. Bauer, and K. W. Carey, *Appl. Phys. Lett.* **55**, 140 (1989).
- [112] A. Convertino, G. Padeletti, L. Cerri, and S. Viticoli, *J. Vac. Sci. Technol. B* **20**, 243 (2002).
- [113] R. E. Nahory, M. A. Pollack, and J. C. DeWinter, *J. Appl. Phys.* **46**, 775 (1975).
- [114] T. J. Kim, T. H. Ghong, Y. D. Kim, S. J. Kim, D. E. Aspnes, T. Mori, T. Yao, and B. H. Koo, *Phys. Rev. B* **68**, 115323 (2003).
- [115] D. K. Gaskill, N. Bottka, L. Aina, and M. Mattingly, *Appl. Phys. Lett.* **56**, 1269 (1990).

- [116] J. Singh, in *Properties of Lattice-matched and Strained Indium Gallium Arsenide*, EMIS Datareviews Series No. 8 (edited by P. Bhattacharya), INSPEC, London, 1993, p. 61.
- [117] L. C. Andreani, D. De Nova, S. Di Lernia, M. Geddo, G. Guizzetti, M. Patrini, C. Bocchi, A. Bosacchi, C. Ferrari, and S. Franchi, *J. Appl. Phys.* **78**, 6745 (1995).
- [118] Z. Hang, D. Yan, F. H. Pollak, G. D. Pettit, and J. M. Woodall, *Phys. Rev. B* **44**, 10546 (1991).
- [119] C. Alibert, A. Joullié, A. M. Joullié, and C. Ance, *Phys. Rev. B* **27**, 4946 (1983), and references cited therein.
- [120] A. Bignazzi, E. Grilli, M. Guzzi, C. Bocchi, A. Bosacchi, S. Franchi, and R. Magnanini, *Phys. Rev. B* **57**, 2295 (1998).
- [121] V. Bellani, M. Geddo, G. Guizzetti, S. Franchi, and R. Magnanini, *Phys. Rev. B* **59**, 12272 (1999).
- [122] H. Mathieu, D. Auvergne, P. Merle, and K. C. Rustagi, *Phys. Rev. B* **12**, 5846 (1975).
- [123] R. Ferrini, M. Patrini, and S. Franchi, *J. Appl. Phys.* **84**, 4517 (1998).
- [124] S. G. Choi, C. J. Palmstrøm, Y. D. Kim, S. L. Cooper, and D. E. Aspnes, *J. Appl. Phys.* **98**, 104108 (2005).
- [125] N. Kitamura, H. Yamamoto, and T. Wada, *Mater. Lett.* **15**, 89 (1992).
- [126] S. Isomura, F. G. D. Prat, and J. C. Woolley, *Phys. Status Solidi B* **65**, 213 (1974).
- [127] X. Yaozhou, Y. Beaulieu, and J. B. Webb, *Solid State Commun.* **87**, 9 (1993).
- [128] N. Dai, F. Brown, R. E. Doezema, S. J. Chung, K. J. Goldammer, and M. B. Santos, *Appl. Phys. Lett.* **73**, 3132 (1998).
- [129] S. M. Vishnubhatla, B. Eglunent, and J. C. Woolley, *Can. J. Phys.* **47**, 1661 (1969).
- [130] D. Auvergne, J. Camassel, H. Mathieu, and A. Joullie, *J. Phys. Chem. Solids* **35**, 133 (1974).
- [131] A. P. Roth and E. Fortin, *Can. J. Phys.* **56**, 1468 (1978).
- [132] R. Rousina, C. Halpin, and J. B. Webb, *J. Appl. Phys.* **68**, 2181 (1990).
- [133] S. Collins, A. G. Birdwell, R. Glosser, and B. R. Bennett, *J. Appl. Phys.* **91**, 1175 (2002).
- [134] S. Imai and S. Adachi, *Jpn. J. Appl. Phys.* **32**, 3860 (1993).
- [135] See, for example, M. Henini, *Dilute Nitride Semiconductors*, Elsevier, Amsterdam, 2005.
- [136] U. Tisch, E. Finkman, and J. Salzman, *Appl. Phys. Lett.* **81**, 463 (2002).
- [137] Y. Zhang, B. Fluegel, A. Mascarenhas, H. P. Xin, and C. W. Tu, *Phys. Rev. B* **62**, 4493 (2000).
- [138] Y. Zhang, B. Fluegel, M. C. Hanna, J. F. Geisz, L.-W. Wang, and A. Mascarenhas, *Phys. Status Solidi B* **240**, 396 (2003).
- [139] W. Shan, W. Walukiewicz, J. W. Ager III, E. E. Haller, J. F. Geisz, D. J. Friedman, J. M. Olson, and S. R. Kurtz, *Phys. Rev. Lett.* **82**, 1221 (1999).
- [140] W. Shan, W. Walukiewicz, K. M. Yu, J. Wu, J. W. Ager III, E. E. Haller, H. P. Xin, and C. W. Tu, *Appl. Phys. Lett.* **76**, 3251 (2000).
- [141] P. R. C. Kent and A. Zunger, *Phys. Rev. Lett.* **86**, 2613 (2001).
- [142] P. R. C. Kent and A. Zunger, *Phys. Rev. B* **64**, 115208 (2001).
- [143] I. A. Buyanova, M. Izadifard, W. M. Chen, H. P. Xin, and C. W. Tu, *Phys. Rev. B* **69**, 201303 (2004).
- [144] A. Mascarenhas, S. Francoeur, and S. Yoon, in *Dilute Nitride Semiconductors* (edited by M. Henini), Elsevier, Amsterdam, 2005, p. 179.
- [145] W. Walukiewicz, W. Shan, J. Wu, K. M. Yu, and J. W. Ager III, in *Dilute Nitride Semiconductors* (edited by M. Henini), Elsevier, Amsterdam, 2005, p. 325.
- [146] P. R. C. Kent, in *Dilute Nitride Semiconductors* (edited by M. Henini), Elsevier, Amsterdam, 2005, p. 393.
- [147] H. P. Xin, C. W. Tu, Y. Zhang, and A. Mascarenhas, *Appl. Phys. Lett.* **76**, 1267 (2000).
- [148] I. A. Buyanova, G. Pozina, J. P. Bergman, W. M. Chen, H. P. Xin, and C. W. Tu, *Appl. Phys. Lett.* **81**, 52 (2002).
- [149] G. Y. Rudko, I. A. Buyanova, W. M. Chen, H. P. Xin, and C. W. Tu, *Appl. Phys. Lett.* **81**, 3984 (2002).
- [150] I. A. Buyanova, M. Izadifard, A. Kasic, H. Arwin, W. M. Chen, H. P. Xin, Y. G. Hong, and C. W. Tu, *Phys. Rev. B* **70**, 085209 (2004).
- [151] D. G. Thomas, J. J. Hopfield, and C. J. Frosch, *Phys. Rev. Lett.* **15**, 857 (1965).

- [152] G. Leibiger, V. Gottschalch, M. Schubert, G. Benndorf, and R. Schwabe, *Phys. Rev. B* **65**, 245207 (2002).
- [153] J. Wu, W. Walukiewicz, K. M. Yu, J. W. Ager III, E. E. Haller, Y. G. Hong, H. P. Xin, and C. W. Tu, *Phys. Rev. B* **65**, 241303 (2002).
- [154] L. Bellaiche, S.-H. Wei, and A. Zunger, *Phys. Rev. B* **56**, 10233 (1997).
- [155] M. Weyers, M. Sato, and H. Ando, *Jpn. J. Appl. Phys.* **31**, L853 (1992).
- [156] G. Pozina, I. Ivanov, B. Monemar, J. V. Thordson, and T. G. Andersson, *J. Appl. Phys.* **84**, 3830 (1998).
- [157] R. Bhat, C. Caneau, L. Salamanca-Riba, W. Bi, and C. Tu, *J. Cryst. Growth* **195**, 427 (1998).
- [158] J. Šik, M. Schubert, G. Leibiger, V. Gottschalch, and G. Wagner, *J. Appl. Phys.* **89**, 294 (2001).
- [159] Y. Zhang, A. Mascarenhas, H. P. Xin, and C. W. Tu, *Phys. Rev. B* **63**, 161303 (2001).
- [160] J. Wu, W. Shan, and W. Walukiewicz, *Semicond. Sci. Technol.* **17**, 860 (2002).
- [161] B. Gil, *Solid State Commun.* **114**, 623 (2000).
- [162] G. Leibiger, V. Gottschalch, B. Rheinländer, J. Šik, and M. Schubert, *Appl. Phys. Lett.* **77**, 1650 (2000).
- [163] J. Wagner, K. Köhler, P. Ganser, and N. Herres, *Appl. Phys. Lett.* **77**, 3592 (2000).
- [164] S. Matsumoto, H. Yaguchi, S. Kashiwase, T. Hashimoto, S. Yoshida, D. Aoki, and K. Onabe, *J. Cryst. Growth* **221**, 481 (2000).
- [165] G. Leibiger, V. Gottschalch, B. Rheinländer, J. Šik, and M. Schubert, *J. Appl. Phys.* **89**, 4927 (2001).
- [166] U. Tisch, E. Finkman, and J. Salzman, *Phys. Rev. B* **65**, 153204 (2002).
- [167] A. Pulzara-Mora, E. Cruz-Hernández, J. Rojas-Ramirez, R. Contreras-Cuerrero, M. Meléndez-Lira, C. Falcony-Guajardo, M. A. Aguilar-Frutis, and M. López-López, *J. Cryst. Growth* **301–302**, 565 (2007).
- [168] W. K. Hung, M. Y. Chern, Y. F. Chen, Z. L. Yang, and Y. S. Huang, *Phys. Rev. B* **62**, 13028 (2000).
- [169] J. D. Perkins, A. Mascarenhas, Y. Zhang, J. F. Geisz, D. J. Friedman, J. M. Olson, and S. R. Kurtz, *Phys. Rev. Lett.* **82**, 3312 (1999).
- [170] K. Uesugi, I. Suemune, T. Hasegawa, T. Akutagawa, and T. Nakamura, *Appl. Phys. Lett.* **76**, 1285 (2000).
- [171] R. Chtourou, F. Bousbih, S. B. Bouzid, F. F. Charfi, J. C. Harmand, G. Ungaro, and L. Largeau, *Appl. Phys. Lett.* **80**, 2075 (2002).
- [172] A. Polimeni, M. Bissiri, A. Augieri, G. B. H. von Högersthal, M. Capizzi, D. Gollub, M. Fischer, M. Reinhardt, and A. Forchel, *Phys. Rev. B* **65**, 235325 (2002).
- [173] J. Plaza, J. L. Castaño, B. J. Garcia, H. Carrère, and E. Bedel-Pereira, *Appl. Phys. Lett.* **86**, 121918 (2005).
- [174] B. S. Ma, F. H. Su, K. Ding, G. H. Li, Y. Zhang, A. Mascarenhas, H. P. Xin, and C. W. Tu, *Phys. Rev. B* **71**, 045213 (2005).
- [175] A. Kimura, C. A. Paulson, H. F. Tang, and T. F. Kuech, *Appl. Phys. Lett.* **84**, 1489 (2004).
- [176] J. Wu, W. Walukiewicz, K. M. Yu, J. D. Denlinger, W. Shan, J. W. Ager III, A. Kimura, H. F. Tang, and T. F. Kuech, *Phys. Rev. B* **70**, 115214 (2004).
- [177] W. G. Bi and C. W. Tu, *Appl. Phys. Lett.* **70**, 1608 (1997).
- [178] P. H. Jefferson, T. D. Veal, L. F. J. Piper, B. R. Bennett, C. F. McConville, B. N. Murdin, L. Buckie, G. W. Smith, and T. Ashley, *Appl. Phys. Lett.* **89**, 111921 (2006).
- [179] W. G. Bi and C. W. Yu, *J. Appl. Phys.* **80**, 1934 (1996).
- [180] K. M. Yu, W. Walukiewicz, J. Wu, J. W. Beeman, J. W. Ager III, E. E. Haller, W. Shan, H. P. Xin, C. W. Tu, and M. C. Ridgway, *J. Appl. Phys.* **90**, 2227 (2001).
- [181] H. Naoi, Y. Naoi, and S. Sakai, *Solid-State Electron.* **41**, 319 (1997).
- [182] D.-K. Shih, H.-H. Lin, L.-W. Sung, T.-Y. Chu, and T.-R. Yang, *Jpn. J. Appl. Phys.* **42**, 375 (2003).
- [183] M. Kuroda, R. Katayama, S. Nishio, K. Onabe, and Y. Shiraki, *Phys. Status Solidi C* **0**, 2765 (2003).
- [184] T. D. Veal, L. F. J. Piper, P. H. Jefferson, I. Mahboob, C. F. McConville, M. Merrick, T. J. C. Hosea, B. N. Murdin, and M. Hopkinson, *Appl. Phys. Lett.* **87**, 182114 (2005).

- [185] J. Wagner, K. Köhler, P. Ganser, and M. Maier, *Appl. Phys. Lett.* **87**, 051913 (2005).
- [186] B. N. Murdin, A. R. Adams, P. Murzyn, C. R. Pidgeon, I. V. Bradley, J.-P. R. Wells, Y. H. Matsuda, N. Miura, T. Burke, and A. D. Johnson, *Appl. Phys. Lett.* **81**, 256 (2002).
- [187] T. D. Veal, I. Mahboob, and C. F. McConville, *Phys. Rev. Lett.* **92**, 13801 (2004).
- [188] A.-B. Chen and A. Sher, *Semiconductor Alloys: Physics and Materials Engineering*, Plenum, New York, 1995.
- [189] F. Saadallah, N. Yacoubi, F. Genty, and C. Alibert, *J. Appl. Phys.* **94**, 5041 (2003).
- [190] A. G. Thompson, M. Cardona, and K. L. Shaklee, *Phys. Rev.* **146**, 601 (1966).
- [191] M. G. Craford, R. W. Shaw, A. H. Herzog, and W. O. Groves, *J. Appl. Phys.* **43**, 4075 (1972).
- [192] A. G. Thompson, J. C. Woolley, and M. Rubenstein, *Can. J. Phys.* **44**, 2927 (1966).
- [193] K. J. Kim, M. H. Lee, J. H. Bahng, K. Shim, and B. D. Choe, *J. Appl. Phys.* **84**, 3696 (1998).
- [194] Z. I. Alferov, D. Z. Garbuzov, Y. V. Zhilyaev, and P. S. Kop'ev, *Sov. Phys. Semicond.* **6**, 589 (1992).
- [195] H. Mathieu, P. Merle, and E. L. Ameziane, *Phys. Rev. B* **15**, 2048 (1977).
- [196] M. J. Jou, Y. T. Cherng, H. R. Jen, and G. B. Stringfellow, *J. Cryst. Growth* **93**, 62 (1988).
- [197] S. Loualiche, A. L. Corre, S. Salaun, J. Caulet, B. Lambert, M. Gauneau, D. Lecrosnier, and B. Deveaud, *Appl. Phys. Lett.* **59**, 423 (1991).
- [198] R. E. Nahory, M. A. Pollack, J. C. DeWinter, and K. M. Williams, *J. Appl. Phys.* **48**, 1607 (1977).
- [199] M. Yano, Y. Suzuki, T. Ishii, Y. Matsushita, and M. Kimata, *Jpn. J. Appl. Phys.* **17**, 2091 (1978).
- [200] T. C. McGlenn, T. N. Krabach, and M. V. Klein, *Phys. Rev. B* **33**, 8396 (1986).
- [201] R. Ferrini, M. Geddo, G. Guizzetti, M. Patrini, S. Franchi, C. Bocchi, F. Germini, A. Baraldi, and R. Magnanini, *J. Appl. Phys.* **86**, 4706 (1999).
- [202] D. Serries, M. Peter, N. Herres, K. Winkler, and J. Wagner, *J. Appl. Phys.* **87**, 8522 (2000).
- [203] K. G. Merkel, V. M. Bright, M. A. Marciniak, C. L. A. Cerny, and M. O. Manasreh, *Appl. Phys. Lett.* **65**, 2442 (1994).
- [204] R. Lukic-Zrnica, B. P. Gorman, R. J. Cottier, T. D. Golding, C. L. Littler, and A. G. Norman, *J. Appl. Phys.* **92**, 6939 (2002).
- [205] H. Chouaib, C. Bru-Chevallier, G. Guillot, H. Lahreche, and P. Bove, *J. Appl. Phys.* **98**, 123524 (2005).
- [206] G. A. Antypas and T. O. Yep, *J. Appl. Phys.* **42**, 3201 (1971).
- [207] R. J. Nicholas, R. A. Stradling, and J. C. Ramage, *J. Phys. C: Solid State Phys.* **12**, 1641 (1979).
- [208] M. Wada, S. Araki, T. Kudou, T. Umezawa, S. Nakajima, and T. Ueda, *Appl. Phys. Lett.* **76**, 2722 (2000).
- [209] S. S. Bui, H. P. Lee, and K. M. Yu, *Appl. Phys. Lett.* **90**, 212113 (2007).
- [210] A. G. Thompson, J. E. Rowe, and M. Rubenstein, *Phys. Rev.* **40**, 3280 (1969).
- [211] S. G. Choi, C. J. Palmström, Y. D. Kim, D. E. Aspnes, H. J. Kim, and Y.-C. Chang, *Appl. Phys. Lett.* **91**, 041917 (2007).
- [212] E. H. Reihlen, M. J. Jou, Z. M. Fang, and G. B. Stringfellow, *J. Appl. Phys.* **68**, 4604 (1990).
- [213] W. J. Duncan, A. S. M. Ali, E. M. Marsh, and P. C. Spurdens, *J. Cryst. Growth* **143**, 155 (1994).
- [214] J. C. Woolley and J. Warner, *Can. J. Phys.* **42**, 1879 (1964).
- [215] G. B. Stringfellow and P. E. Greene, *J. Electrochem. Soc.* **118**, 805 (1971).
- [216] W. Dobbelaere, J. D. Boeck, and G. Borghs, *Appl. Phys. Lett.* **55**, 1856 (1989).
- [217] H. Y. Deng and N. Dai, *Phys. Rev. B* **73**, 113102 (2006).
- [218] S. Elies, A. Krier, I. R. Cleverley, and K. Singer, *J. Phys. D: Appl. Phys.* **26**, 159 (1993).
- [219] M. A. Marciniak, R. L. Hengehold, Y. K. Yeo, and G. W. Turner, *J. Appl. Phys.* **84**, 480 (1998).
- [220] B. Bansal, V. K. Dixit, V. Venkataraman, and H. L. Bhat, *Appl. Phys. Lett.* **82**, 4720 (2003).
- [221] V. K. Dixit, B. Bansal, V. Venkataraman, H. L. Bhat, K. S. Chandrasekharan, and B. M. Arora, *J. Appl. Phys.* **96**, 4989 (2004).
- [222] Y. Z. Gao, X. Y. Gong, Y. H. Chen, and T. Yamaguchi, *Proc. SPIE* **6029**, 60291I (2006).
- [223] Y. G. Hong, A. Nishikawa, and C. W. Tu, *Appl. Phys. Lett.* **83**, 5446 (2003).
- [224] I. A. Buyanova, M. Izadifard, W. M. Chen, Y. G. Hong, and C. W. Tu, *Appl. Phys. Lett.* **88**, 031907 (2006).

- [225] K. I. Lin, T. S. Wang, Y. T. Lu, and J. S. Hwang, *J. Appl. Phys.* **99**, 056103 (2006).
- [226] K. I. Lin and J. S. Hwang, *Appl. Phys. Lett.* **89**, 192116 (2006).
- [227] A. E. Zhukov, A. R. Kovsh, E. S. Semenova, V. M. Ustinov, L. Wei J.-S. Wang, and J. Y. Chi, *Semicond.* **36**, 899 (2002).
- [228] Z. Pan, L. H. Li, Y. W. Lin, B. Q. Sun, D. S. Jiang, and W. K. Ge, *Appl. Phys. Lett.* **78**, 2217 (2001).
- [229] S. A. Choulis, T. J. C. Hosea, S. Tomić, M. Kamal-Saadi, A. R. Adams, E. P. O'Reilly, B. A. Weinstein, and P. J. Klar, *Phys. Rev. B* **66**, 165321 (2002).
- [230] A. Polimeni, M. Capizzi, M. Geddo, M. Fischer, M. Reinhardt, and A. Forchel, *Phys. Rev. B* **63**, 195320 (2001).
- [231] H. D. Sun, M. D. Dawson, M. Othman, J. C. L. Yong, J. M. Rorison, P. Gilet, L. Grenouillet, and A. Million, *Appl. Phys. Lett.* **82**, 376 (2003).
- [232] D. Serries, T. Geppert, P. Ganser, M. Maier, K. Köhler, N. Herres, and J. Wagner, *Appl. Phys. Lett.* **80**, 2448 (2002).
- [233] C. Skierbiszewski, *Semicond. Sci. Technol.* **17**, 803 (2002), and references cited therein.
- [234] P. Perlin, S. G. Subramanya, and D. E. Mars, *Appl. Phys. Lett.* **73**, 3703 (1998).
- [235] C. Skierbiszewski, P. Erlin, P. Wisniewski, T. Suski, J. F. Geisz, K. Hingerl, W. Jantsch, D. E. Mars, and W. Walukiewicz, *Phys. Rev. B* **65**, 035207 (2001).
- [236] M. M. E. Fahmi, A. Khan, J. A. Griffin, G. L. Harris, L. H. Robins, A. G. Birdwell, Y.-S. Kang, D. J. Smith, T. Steiner, and S. N. Mohammad, *J. Appl. Phys.* **94**, 7576 (2003).
- [237] Y.-S. Kang, L. H. Robins, A. G. Birdwell, A. J. Shapiro, W. R. Thurber, M. D. Vaudin, M. M. E. Fahmi, D. Bryson, and S. N. Mohammad, *J. Appl. Phys.* **98**, 093714 (2005).
- [238] L. Bellaiche, *Appl. Phys. Lett.* **75**, 2578 (1999).
- [239] K. M. Yu, W. Walukiewicz, J. W. Ager III, D. Bour, R. Farshchi, O. D. Dubon, S. X. Li, I. D. Sharp, and E. E. Haller, *Appl. Phys. Lett.* **88**, 092110 (2005).
- [240] J. H. Herrera-Perez, M. B. Z. Morosini, and N. P. Patel, in *Proceedings of the 5th Brazilian School on Semiconductor Physics* (edited by J. R. Leite, A. Fazzio, and A. S. Chaves), World Scientific, Singapore, 1991, p. 395.
- [241] N. Yacoubi, A. Hafaiedh, and A. Joullié, *Appl. Opt.* **33**, 7171 (1994).
- [242] D. O. T. Filho, I. F. L. Dias, E. Laureto, J. L. Duarte, S. A. Lourenço, L. C. Poças, S. S. Prabhu, and J. Klem, *J. Appl. Phys.* **97**, 123702 (2005).
- [243] S. P. Svensson, D. M. Gill, and P. N. Uppal, *J. Appl. Phys.* **81**, 1422 (1997).
- [244] N. A. Charykov, A. M. Litvak, K. D. Moiseev, and Y. P. Yakovlev, *Proc. SPIE* **1512**, 198 (1991).
- [245] S. Adachi, *Physical Properties of III–V Semiconductor Compounds: InP, InAs, GaAs, GaP, InGaAs, and InGaAsP*, John Wiley & Sons, Ltd, New York, 1992.
- [246] S. Shirakata, M. Kondo, T. Nishino, and Y. Hamakawa, *Jpn. J. Appl. Phys.* **25**, 435 (1986).
- [247] G. P. Donati, R. Kaspi, and K. J. Malloy, *J. Appl. Phys.* **94**, 5814 (2003).
- [248] L. I. Kamlet and F. L. Terry, Jr., *J. Electron. Mater.* **24**, 2005 (1995).
- [249] C. Reh and G. Weiser, *Phys. Rev. B* **65**, 035321 (2001).
- [250] J. C. DeWinter, M. A. Pollack, A. K. Srivastava, and J. L. Zyskind, *J. Electron. Mater.* **14**, 729 (1985).
- [251] T. I. Voronina, T. S. Lagunova, M. P. Mikhailova, M. A. Sipovskaya, V. V. Sherstnev, and Y. P. Yakovlev, *Sov. Phys. Semicond.* **25**, 167 (1991).
- [252] M. P. Mikhailova and A. N. Titkov, *Semicond. Sci. Technol.* **9**, 1279 (1994).
- [253] M. J. Cherng, G. B. Stringfellow, D. W. Kisker, A. K. Srivastava, and J. L. Zyskind, *Appl. Phys. Lett.* **48**, 419 (1986).
- [254] T. Mei, *J. Appl. Phys.* **101**, 013520 (2007).
- [255] S. Iyer, S. Hegde, K. K. Bajaj, A. Abul-Fadl, and W. Mitchel, *J. Appl. Phys.* **73**, 3958 (1993).
- [256] M. Muñoz, F. H. Pollak, M. B. Zakia, N. B. Patel, and J. L. Herrera-Pérez, *Phys. Rev. B* **62**, 16600 (2000).
- [257] X. Gong, H. Kan, T. Yamaguchi, I. Suzuki, M. Aoyama, M. Kumagawa, N. L. Rowell, A. Wang, and R. Rinfret, *Jpn. J. Appl. Phys.* **33**, 1740 (1994).

- [258] D. J. Mowbray, O. P. Kowalski, M. Hopkinson, and J. P. R. David, *Appl. Phys. Lett.* **65**, 213 (1994).
- [259] S. P. Najda, A. H. Kean, M. D. Dawson, and G. Duggan, *J. Appl. Phys.* **77**, 3412 (1995).
- [260] M. Schubert, J. A. Woollam, G. Leibiger, B. Rheinländer, I. Pietzonka, T. Saß, and V. Gottschalch, *J. Appl. Phys.* **86**, 2025 (1999).
- [261] K. Asami, H. Asahi, S. Gonda, Y. Kawamura, and H. Tanaka, *Solid State Commun.* **70**, 33 (1989).
- [262] D. S. Cao, A. W. Kimball, and G. B. Stringfellow, *J. Appl. Phys.* **67**, 739 (1990).
- [263] S. Adachi, S. Ozaki, M. Sato, and K. Ohtsuka, *Jpn. J. Appl. Phys.* **35**, 537 (1996).
- [264] S. Ozaki, S. Adachi, M. Sato, and K. Ohtsuka, *J. Appl. Phys.* **79**, 439 (1996).
- [265] H. Lee, M. V. Klein, D. E. Aspnes, C. P. Kuo, M. Peanasky, and M. G. Craford, *J. Appl. Phys.* **73**, 400 (1993).
- [266] A. D. Prins, J. L. Sly, A. T. Meney, D. J. Dunstan, E. P. O'Reilly, A. R. Adams, and A. Valster, *J. Phys. Chem. Solids* **56**, 349 (1995).
- [267] J. Harada, T. Kobayashi, A. D. Prins, and D. J. Dunstan, *Phys. Status Solidi B* **235**, 505 (2003).
- [268] J. I. Davies, A. C. Marshall, M. D. Scott, and R. J. M. Griffiths, *Appl. Phys. Lett.* **53**, 276 (1988).
- [269] C. Cacciatore, D. Campi, C. Coriasso, C. Rigo, and C. Alibert, *Thin Solid Films* **197**, 1 (1991).
- [270] W. F. Tseng, J. Comas, B. Steiner, G. Metze, A. Cornfeld, P. B. Klein, D. K. Gaskill, W. Xia, and S. S. Lau, *Mater. Res. Soc. Symp. Proc.* **240**, 117 (1992).
- [271] R. F. Kopf, H. P. Wei, A. P. Perley, and G. Livescu, *Appl. Phys. Lett.* **60**, 2386 (1992).
- [272] P. Parayanthal, C. S. Ro, F. H. Pollak, C. R. Stanley, G. W. Wicks, and L. F. Eastman, *Appl. Phys. Lett.* **43**, 109 (1983).
- [273] J.-W. Pan, J.-L. Shieh, J.-H. Gau, J.-I. Chyi, J.-C. Lee, and K.-J. Ling, *J. Appl. Phys.* **78**, 442 (1995).
- [274] S. N. Grinyaev, L. M. Dolginov, M. A. Il'in, Y. N. Korchagin, A. I. Lukomskii, and V. A. Chaldyshev, *Sov. Phys. Semicond.* **16**, 467 (1982).
- [275] H. Mani, E. Tournié, J. L. Lazzari, C. Alibert, A. Joullié, and B. Lambert, *J. Cryst. Growth* **121**, 463 (1992).
- [276] L.-C. Chen, W.-J. Ho, and M.-C. Wu, *Jpn. J. Appl. Phys.* **38**, 1314 (1999).
- [277] Y. R. Ryu, T. S. Lee, J. A. Lubguban, A. B. Corman, H. W. White, J. H. Leem, M. S. Han, Y. S. Park, C. J. Youn, and W. J. Kim, *Appl. Phys. Lett.* **88**, 052103 (2006).
- [278] M. S. Han, J. H. Kim, T. S. Jeong, J. M. Park, C. J. Youn, J. H. Leem, and Y. R. Ryu, *J. Cryst. Growth* **303**, 506 (2007).
- [279] T. Makino, Y. Segawa, M. Kawasaki, A. Ohtomo, R. Shiroki, K. Tamura, T. Yasuda, and H. Koinuma, *Appl. Phys. Lett.* **78**, 1237 (2001).
- [280] R. Schmidt-Grund, M. Schubert, B. Rheinländer, D. Fritsch, H. Schmidt, E. M. Kaidashev, M. Lorenz, C. M. Herzinger, and M. Grundmann, *Thin Solid Films* **455–456**, 500 (2004).
- [281] K. Koike, K. Hama, I. Nakashima, G. Takada, K. Ogata, S. Sasa, M. Inoue, and M. Yano, *J. Cryst. Growth* **278**, 288 (2005).
- [282] R. Schmidt-Grund, A. Carstens, B. Rheinländer, D. Spemann, H. Hochmut, G. Zimmermann, M. Lorenz, and M. Grundmann, *J. Appl. Phys.* **99**, 123701 (2006).
- [283] N. B. Chen and C. H. Sui, *Mater. Sci. Eng. B* **126**, 16 (2006).
- [284] J. A. Sans and A. Segura, *High Pressure Res.* **24**, 119 (2004).
- [285] J. Ishihara, A. Nakamura, S. Shigemori, T. Aoki, and J. Temmyo, *Appl. Surf. Sci.* **244**, 381 (2005), and references cited therein.
- [286] X. J. Wang, I. A. Buyanova, W. M. Chen, M. Izadifard, S. Rawal, D. P. Norton, S. J. Pearton, A. Osinsky, J. W. Dong, and A. Dabiran, *Appl. Phys. Lett.* **89**, 151909 (2006).
- [287] H. S. Kang, J. W. Kim, J. H. Kim, S. Y. Lee, Y. Li, J.-S. Lee, J. K. Lee, M. A. Nastasi, S. A. Crooker, and Q. X. Jia, *J. Appl. Phys.* **99**, 066113 (2006).
- [288] H. C. Ong and J. Y. Dai, *Appl. Phys. Lett.* **81**, 1444 (2002).
- [289] K. Ichino, K. Ueyama, M. Yamamoto, H. Kariya, H. Miyata, H. Misasa, M. Kitagawa, and H. Kobayashi, *J. Appl. Phys.* **87**, 4249 (2000).
- [290] G. K. Padam, G. L. Malhotra, and S. U. M. Rao, *J. Appl. Phys.* **63**, 770 (1988).
- [291] A. Béliveau and C. Carlone, *Phys. Rev. B* **41**, 9860 (1990).

- [292] V. Kumar, V. Singh, S. K. Sharma, and T. P. Sharma, *Opt. Mater.* **11**, 29 (1998).
- [293] A. M. Salem, *Appl. Phys. A* **74**, 205 (2002).
- [294] T. Yokogawa, T. Ishikawa, J. L. Merz, and T. Taguchi, *J. Appl. Phys.* **75**, 2189 (1994).
- [295] M. R. Muhamad, *Jpn. J. Appl. Phys.* **32**, 3385 (1993).
- [296] A. Krehmeller, A. K. Levine, and G. Gashurov, *J. Electrochem. Soc.* **107**, 12 (1960).
- [297] E. S. Rittner and J. H. Schulman, *J. Phys. Chem.* **47**, 537 (1943).
- [298] K. Wilmers, T. Wethkamp, N. Esser, C. Cobet, W. Richter, V. Wagner, H. Lugauer, F. Fischer, T. Gerhard, M. Keim, and M. Cardona, *J. Electron. Mater.* **28**, 670 (1999).
- [299] A. Bukaluk, A. A. Wronkowska, A. Wronkowski, H. Arwin, F. Firszt, S. Łęgowski, H. Męczyńska, and J. Szatkowski, *Appl. Surf. Sci.* **175–176**, 531 (2001).
- [300] G. P. Srivastava, H. M. Tütüncü, and N. Günhan, *Phys. Rev. B* **70**, 085206 (2004).
- [301] C. Chauvet, E. Tournié, and J.-P. Faurie, *Phys. Rev. B* **61**, 5332 (2000).
- [302] C. Chauvet, E. Tournié, and J.-P. Faurie, *J. Cryst. Growth* **214/215**, 95 (2000).
- [303] H. Lee, I.-Y. Kim, J. Powell, D. E. Aspnes, S. Lee, F. Peiris, and J. K. Furdyna, *J. Appl. Phys.* **88**, 878 (2000).
- [304] S. V. Ivanov, O. V. Nekrutkina, S. V. Sorokin, V. A. Kaygorodov, T. V. Shubina, A. A. Toropov, P. S. Kop'ev, G. Reuscher, V. Wagner, J. Geurts, A. Waag, and G. Landwehr, *Appl. Phys. Lett.* **78**, 404 (2001).
- [305] O. Maksimov, M. Muñoz, and M. C. Tamargo, *Microelectron. J.* **37**, 19 (2006).
- [306] P. J. Huang, P. Sitarek, Y. S. Huang, O. Maksimov, M. C. Tamargo, F. Firszt, and H. Męczyńska, *Phys. Status Solidi C* **3**, 738 (2006).
- [307] A. A. Wronkowska, A. Wronkowski, F. Firszt, S. Łęgowski, H. Męczyńska, A. Marasek, and W. Paszkowicz, *Phys. Status Solidi C* **1**, 641 (2004).
- [308] F. Firszt, S. Łęgowski, H. Męczyńska, H. L. Oczkowski, W. Osińska, J. Szatkowski, W. Paszkowicz, and Z. M. Spolnik, *J. Cryst. Growth* **159**, 167 (1996).
- [309] B. Jobst, D. Hommel, U. Lunz, T. Gerhard, and G. Landwehr, *Appl. Phys. Lett.* **69**, 97 (1996).
- [310] H. Okuyama, Y. Kishita, and A. Ishibashi, *Phys. Rev. B* **57**, 2257 (1998).
- [311] K. J. Kim, M. H. Lee, J. H. Bahng, C. Y. Kwak, and E. Oh, *Solid State Commun.* **105**, 17 (1998).
- [312] M. Sohel, M. Muñoz, and M. C. Tamargo, *Appl. Phys. Lett.* **85**, 2794 (2004).
- [313] R. Pässler, F. Blaschta, E. Griehl, K. Papagelis, B. Haserer, T. Reisinger, S. Ves, and W. Gebhardt, *Phys. Status Solidi B* **204**, 685 (1997).
- [314] A. Gapiński and W. Bała, *Proc. SPIE* **3725**, 72 (1999).
- [315] W.-T. Kim, *Phys. Rev. B* **59**, 4572 (1999).
- [316] A. A. Wronkowska, A. Wronkowski, H. Arwin, F. Firszt, S. Łęgowski, H. Męczyńska, and J. Szatkowski, *Vacuum* **63**, 233 (2001).
- [317] F. Firszt, A. A. Wronkowska, A. Wronkowski, S. Łęgowski, A. Marasek, H. Męczyńska, M. Pawlak, W. Paszkowicz, K. Strzałkowski, and A. J. Zakrzewski, *Cryst. Res. Technol.* **40**, 386 (2005).
- [318] D.-T. Kim, S.-A. Park, W.-J. Jeong, C.-C. Park, M.-S. Jin, and C.-D. Kim, *Phys. Status Solidi C* **3**, 2665 (2006).
- [319] V. A. Kaygorodov, I. V. Sedova, S. V. Sorokin, A. A. Sitnikova, O. V. Nekrutkina, T. V. Shubina, A. A. Toropov, V. S. Sorokin, and S. V. Ivanov, *Phys. Status Solidi B* **229**, 19 (2002).
- [320] C.-D. Kim, D.-H. Shin, H.-H. Jang, H.-M. Jeong, D.-T. Kim, C.-S. Yoon, H.-L. Park, and W.-T. Kim, *J. Appl. Phys.* **85**, 7972 (1999).
- [321] P. J. Huang, Y. S. Huang, F. Firszt, S. Łęgowski, H. Męczyńska, and K. K. Tiong, *J. Phys.: Condens. Matter* **19**, 266002 (2007).
- [322] A. S. Nasibov, Y. V. Korostelin, P. V. Shapkin, L. G. Suslina, D. L. Fedorov, and L. S. Markov, *Solid State Commun.* **71**, 867 (1989).
- [323] N. Samarth, H. Luo, J. K. Furdyna, R. G. Alonso, Y. R. Lee, A. K. Ramdas, S. B. Qadri, and N. Otsuka, *Appl. Phys. Lett.* **56**, 1163 (1990).
- [324] Y. D. Kim, M. V. Klein, S. F. Ren, Y. C. Chang, H. Luo, N. Samarth, and J. K. Furdyna, *Phys. Rev. B* **49**, 7262 (1994).

- [325] U. Lunz, J. Kuhn, F. Goschenhofer, U. Schüssler, S. Einfeldt, C. R. Becker, and G. Landwehr, *J. Appl. Phys.* **80**, 6861 (1996).
- [326] J. Lee, F. Flack, N. Samarth, and R. W. Collins, *Appl. Opt.* **36**, 5372 (1997).
- [327] L. Malikova, W. Krystek, F. H. Pollak, N. Dai, A. Cavus, and M. C. Tamargo, *Phys. Rev. B* **54**, 1819 (1996).
- [328] M.-C. Kuo, K.-C. Chiu, T.-H. Shin, Y.-J. Lai, C.-S. Yang, W.-K. Chen, D.-S. Chuu, M.-C. Lee, W.-C. Chou, S.-Y. Jeng, Y.-T. Shin, and W.-H. Lan, *Jpn. J. Appl. Phys.* **43**, 5145 (2004).
- [329] A. Kalb and V. Leute, *Phys. Status Solidi A* **5**, K199 (1971).
- [330] C. J. Summers and J. G. Broerman, *Phys. Rev. B* **21**, 559 (1980).
- [331] N. Himei and J. Muto, *J. Mater. Sci.: Mater. Electron.* **11**, 145 (2000).
- [332] V. B. Pujari, S. H. Mane, V. S. Karande, J. S. Dargad, and L. P. Deshmukh, *Mater. Chem. Phys.* **83**, 10 (2004).
- [333] I. N. Borisov, P. S. Kireev, V. V. Mikhailin, and V. M. Bezborodova, *Sov. Phys. Semicond.* **5**, 734 (1971).
- [334] K. Kumazaki, L. Viña, C. Umbach, and M. Cardona, *Phys. Status Solidi B* **156**, 371 (1989).
- [335] O. Maksimov and M. C. Tamargo, *Appl. Phys. Lett.* **79**, 782 (2001).
- [336] M. R. Buckley, F. C. Peiris, O. Maksimov, M. Muñoz, and M. C. Tamargo, *Appl. Phys. Lett.* **81**, 5156 (2002).
- [337] M. Muñoz, O. Maksimov, M. C. Tamargo, M. R. Buckley, and F. C. Peiris, *Phys. Status Solidi C* **1**, 706 (2004).
- [338] J. Zakrzewski, *Proc. SPIE* **5953**, 595307 (2005).
- [339] S. G. Parker, A. R. Reinberg, J. E. Pinnell, and W. C. Holton, *J. Electrochem. Soc.* **118**, 979 (1971).
- [340] D. Barbier, B. Montegu, and A. Laugier, *Solid State Commun.* **28**, 525 (1978).
- [341] S.-J. Chung, Y. Kwon, C.-S. Yoon, B.-H. Kim, D. Cha, C.-D. Kim, W.-T. Kim, and C. U. Hong, *J. Phys. Chem. Solids* **60**, 799 (1999).
- [342] A. J. Franz, F. C. Peiris, X. Liu, U. Bindley, and J. K. Furdyna, *Phys. Status Solidi B* **241**, 507 (2004).
- [343] K. Itoh, *J. Phys. Soc. Jpn* **22**, 1119 (1967).
- [344] M. Luttmann, F. Bertin, and A. Chabli, *J. Appl. Phys.* **78**, 3387 (1995).
- [345] S. G. Choi, Y. D. Kim, S. D. Yoo, D. E. Aspnes, I. Miotkowski, and A. K. Ramdas, *Appl. Phys. Lett.* **71**, 249 (1997).
- [346] Y. S. Ihn, T. J. Kim, T. H. Ghong, Y. D. Kim, D. E. Aspnes, and J. Kossut, *Thin Solid Films* **455–456**, 222 (2004).
- [347] B. Freytag, *J. Phys.: Condens. Matter* **6**, 9875 (1994).
- [348] K. Saito, A. Ebina, and T. Takahashi, *Solid State Commun.* **11**, 841 (1972).
- [349] V. A. Tyagai, O. V. Snitko, V. N. Bondarenko, N. I. Vitrikhovskii, V. B. Popov, and A. N. Krasiko, *Sov. Phys. Solid State* **16**, 885 (1974).
- [350] V. V. Sobolev, O. G. Maksimova, and S. G. Kroitoru, *Phys. Status Solidi B* **499** (1981).
- [351] S. Adachi and T. Kimura, *Jpn. J. Appl. Phys.* **32**, 3496 (1993).
- [352] O. Castaing, R. Granger, J. T. Benhlal, and R. Triboulet, *J. Phys.: Condens. Matter* **8**, 5757 (1996).
- [353] K. P. Rao, O. M. Hussain, K. T. R. Reddy, P. S. Reddy, S. Uthanna, B. S. Naidu, and P. J. Reddy, *Opt. Mater.* **5**, 63 (1996).
- [354] P. D. Paulson, B. E. McCandless, and R. W. Birkmire, *J. Appl. Phys.* **95**, 3010 (2004).
- [355] A. Kisiel, *Acta Phys. Polon. A* **38**, 691 (1970).
- [356] E. M. Larramendi, E. Purón, and O. de Melo, *Semicond. Sci. Technol.* **17**, 8 (2002).
- [357] F. G. Sánchez-Almazan, H. Navarro-Contreras, G. Ramírez-Flores, M. A. Vidal, O. Zelaya-Angel, M. E. Rodríguez, and R. Baquero, *J. Appl. Phys.* **79**, 7713 (1996).
- [358] O. Zelaya-Angel, J. G. Mendoza-Alvarez, M. Becerril, H. Navarro-Contreras, and L. Tirado-Mejia, *J. Appl. Phys.* **95**, 6284 (2004).
- [359] Y. T. Shih, W. C. Fan, C. S. Yang, M. C. Kuo, and W. C. Chou, *J. Appl. Phys.* **94**, 3791 (2003).
- [360] B. Toulouse, R. Granger, S. Rolland, and R. Triboulet, *J. Phys.* **48**, 247 (1987).

- [361] D. Lemoine, K. H. Khelladi, O. Castaing, J. Benhlal, A. Quémerais, I. Pollini, R. Triboulet, and R. Granger, *Mater. Sci. Eng. B* **28**, 39 (1994).
- [362] F. El-Akkad and A. R. Farhan, *J. Phys. D: Appl. Phys.* **28**, 1958 (1995).
- [363] O. Casting, J. T. Benhlal, R. Granger, and R. Triboulet, *J. Phys. I France* **6**, 907 (1996).
- [364] V. G. Sredin, V. G. Savitskii, Y. V. Danilyuk, M. V. Miliyanchuk, and I. V. Petrovich, *Sov. Phys. Semicond.* **15**, 249 (1981).
- [365] J. P. Laurenti, J. Camassel, A. Bouhemadou, B. Toulouse, R. Legros, and A. Lusso, *J. Appl. Phys.* **67**, 6454 (1990).
- [366] J. Chu, Z. Mi, and D. Tang, *Infrared Phys.* **32**, 195 (1991).
- [367] A. Rodzik and A. Kisiel, *J. Phys. C: Solid State Phys.* **16**, 203 (1983).
- [368] A. Moritani, K. Taniguchi, C. Hamaguchi, J. Nakai, R. Ueda, and O. Ohtsuki, *J. Phys. Soc. Jpn.* **31**, 945 (1971).
- [369] L. Viña, C. Umbach, M. Cardona, and L. Vodopyanov, *Phys. Rev. B* **29**, 6752 (1984).
- [370] H. Arwin and D. E. Aspnes, *J. Vac. Sci. Technol. A* **2**, 1316 (1984).
- [371] M. W. Scott, *J. Appl. Phys.* **40**, 4077 (1969).
- [372] G. L. Hansen, J. L. Schmit, and T. N. Casselman, *J. Appl. Phys.* **53**, 7099 (1982).
- [373] A. Ksendzov, F. H. Pollak, J. A. Wilson, and V. A. Cotton, *J. Appl. Phys.* **66**, 5528 (1989).
- [374] C. C. Kim and S. Sivananthan, *J. Electron. Mater.* **26**, 561 (1997).
- [375] C.-Y. Moon, S.-H. Wei, Y. Z. Zhu, and G. D. Chen, *Phys. Rev. B* **74**, 233202 (2006).
- [376] B. K. Meyer, A. Polity, B. Farangis, Y. He, D. Hasselkamp, T. Krämer, and C. Wang, *Appl. Phys. Lett.* **85**, 4929 (2004).
- [377] Y. Nabetani, T. Mukawa, Y. Ito, T. Kato, and T. Matsumoto, *Appl. Phys. Lett.* **83**, 1148 (2003).
- [378] W. Shan, W. Walukiewicz, J. W. Ager III, K. M. Yu, J. Wu, E. E. Haller, Y. Nabetani, T. Murakawa, Y. Ito, and T. Matsumoto, *Appl. Phys. Lett.* **83**, 299 (2003).
- [379] A. Polimeni, M. Capizzi, Y. Nabetani, Y. Ito, K. Kato, T. Matsumoto, and T. Hirai, *Appl. Phys. Lett.* **84**, 3304 (2004).
- [380] A. Ebina, E. Fukunaga, and T. Takahashi, *Phys. Rev. B* **10**, 2495 (1974).
- [381] H. Araki, H. Kanie, and M. Sano, *Jpn. J. Appl. Phys.* **33**, 235 (1994).
- [382] E. Griebel, G. F. Schötz, C. Birzer, W. Kerner, T. Reisinger, B. Hahn, and W. Gebhardt, *Acta Phys. Polon. A* **88**, 995 (1995).
- [383] P. R. Newbury, K. Shahzad, J. Petruzzello, and D. A. Cammack, *J. Appl. Phys.* **66**, 4950 (1989).
- [384] R. Hill and D. Richardson, *J. Phys. C: Solid State Phys.* **6**, L115 (1973).
- [385] Y.-M. Yu, S. Nam, J.-K. Rhee, B. O. K.-S. Lee, and Y. D. Choi, *J. Cryst. Growth* **210**, 521 (2000).
- [386] W. Walukiewicz, W. Shan, K. M. Yu, J.W. Ager III, E. E. Haller, I. Miotkowski, M. J. Seong, H. Alawadhi, and A. K. Ramdas, *Phys. Rev. Lett.* **85**, 1552 (2000).
- [387] C. Y. Bang, M. S. Lee, T. J. Kim, Y. D. Kim, D. E. Aspnes, Y. M. Yu, B. O., and Y. D. Choi, *J. Kor. Phys. Soc.* **39**, 462 (2001).
- [388] S. Larach, R. E. Shrader, and C. F. Stocker, *Phys. Rev.* **108**, 587 (1957).
- [389] A. Ebina, M. Yamamoto, and T. Takahashi, *Phys. Rev. B* **6**, 3786 (1972).
- [390] M. J. S. P. Brasil, R. E. Nahory, F. S. Turco-Sandroff, H. L. Gilchrist, and R. J. Martin, *Appl. Phys. Lett.* **58**, 2509 (1991).
- [391] C.-H. Su, S. Feth, S. Zhu, S. L. Lehoczky, and L. J. Wang, *J. Appl. Phys.* **88**, 5148 (2000).
- [392] H. Lee, S. M. Kim, B. Y. Seo, E. Z. Seong, S. H. Choi, S. Lee, and J. K. Furdyna, *Appl. Phys. Lett.* **77**, 2997 (2000).
- [393] A. Naumov, H. Stanzl, K. Wolf, S. Lankes, and W. Gebhardt, *J. Appl. Phys.* **74**, 6178 (1993).
- [394] J. Wu, W. Walukiewicz, K. M. Yu, W. Shan, J. W. Ager III, E. E. Haller, I. Miotkowski, A. K. Ramdas, and C.-H. Su, *Phys. Rev. B* **68**, 033206 (2003).
- [395] V. N. Bondarenko, N. I. Vitrikhovskii, and V. A. Tyagai, *Sov. Phys. Solid State* **13**, 1854 (1972).
- [396] G. Perna, S. Pagliara, V. Capozzi, M. Ambrico, and M. Pallara, *Solid State Commun.* **114**, 161 (2000).
- [397] R. L. Hengehold and C. R. Fraime, *Phys. Rev.* **174**, 808 (1968).

- [398] D. W. Lane, *Sol. Ener. Mater. Sol. Cells* **90**, 1169 (2006).
- [399] K. Ohata, J. Saraie, and T. Tanaka, *Jpn. J. Appl. Phys.* **12**, 1641 (1973).
- [400] K. Wei, F. H. Pollak, J. L. Freeouf, D. Shvydka, and A. D. Compaan, *J. Appl. Phys.* **85**, 7418 (1999).
- [401] P. J. Sebastian and V. Sivaramakrishnan, *J. Cryst. Growth* **112**, 421 (1991).
- [402] M. Schenk and C. Silber, *J. Mater. Sci.: Mater. Electron.* **9**, 295 (1998).
- [403] Z. C. Feng, P. Becla, L. S. Kim, S. Perkowitz, Y. P. Feng, H. C. Poon, K. P. Williams, and G. D. Pitt, *J. Cryst. Growth* **138**, 239 (1994).
- [404] G. Brill, Y. Chen, P. M. Amirtharaj, W. Sarney, D. Chandler-Horowitz, and N. K. Dhar, *J. Electron. Mater.* **34**, 655 (2005).
- [405] J. M. Gaines, R. R. Drenten, K. W. Haberern, T. Marshall, P. Mensz, and J. Petruzzello, *Appl. Phys. Lett.* **62**, 2462 (1993).
- [406] U. Lunz, B. Jobst, S. Einfeldt, C. R. Becker, D. Hommel, and G. Landwehr, *J. Appl. Phys.* **77**, 5377 (1995).
- [407] H. J. Chen, D. Y. Lin, Y. S. Huang, R. C. Tu, Y. K. Su, and K. K. Tiong, *Semicond. Sci. Technol.* **14**, 85 (1999).
- [408] K. Naniwae, H. Iwata, and K. Yashiki, *Appl. Phys. Lett.* **74**, 3984 (1999).
- [409] K. Shim, H. Rabitz, J.-H. Chang, and T. Yao, *J. Cryst. Growth* **214/215**, 350 (2000).
- [410] V. Wagner, A. Fleszar, J. Geurts, G. Reuser, M. Keim, A. Waag, G. Landwehr, K. Wilmers, N. Esser, and W. Richter, *J. Cryst. Growth* **214/215**, 340 (2000).
- [411] K. Godo, H. Makino, M. W. Cho, J. H. Chang, Y. Yamazaki, T. Yao, M. Y. Shen, and T. Goto, *Appl. Phys. Lett.* **79**, 4168 (2001).
- [412] P. J. Huang, H. P. Hsu, Y. S. Huang, F. Firszt, S. Łęgowski, H. Męczyńska, A. Marasek, and K. K. Tiong, *J. Appl. Phys.* **102**, 083515 (2007).
- [413] Y. T. Liu, P. Sitarek, Y. S. Huang, F. Firszt, S. Łęgowski, H. Męczyńska, A. Marasek, W. Paszkowicz, and K. K. Tiong, *J. Appl. Phys.* **98**, 083519 (2005).
- [414] A. A. Wronkowska, F. Firszt, H. Arwin, A. Wronkowski, M. Wakula, K. Strzalkowski, and W. Paszkowicz, *Phys. Status Solidi C* **3**, 1193 (2006).
- [415] J. W. Wang, P. J. Huang, H. P. Hsu, Y. S. Huang, F. Firszt, S. Łęgowski, H. Męczyńska, A. Marasek, and K. K. Tiong, *J. Appl. Phys.* **101**, 103539 (2007).
- [416] C.-H. Hsieh, Y.-S. Huang, C.-H. Ho, K.-K. Tiong, M. Muñoz, O. Maksimov, and M. C. Tamargo, *Jpn. J. Appl. Phys.* **43**, 459 (2004).
- [417] O. Maksimov, M. Muñoz, W. H. Wang, M. C. Tamargo, and N. Samarth, *Phys. Status Solidi B* **241**, R5 (2004).

7 Energy-band Structure: Effective Masses

7.1 INTRODUCTORY REMARKS

7.1.1 Electron Effective Mass

The constant-energy surface in semiconductors can be defined by

$$E = \frac{\hbar^2 k_x^2}{2m_x} + \frac{\hbar^2 k_y^2}{2m_y} + \frac{\hbar^2 k_z^2}{2m_z} \quad (7.1)$$

where the electron at the center of the BZ has a spherical constant-energy surface (i.e. $m_x = m_y = m_z$), while there are six constant-energy ellipsoids along the principal diagonal [100] and its equivalent directions and eight ellipsoids along the $\langle 111 \rangle$ directions [1]. In such ellipsoidal constant-energy surfaces, Equation (7.1) can be simply written as

$$E = \frac{\hbar^2 k_l^2}{m_l} + \frac{\hbar^2 k_t^2}{2m_t} \quad (7.2)$$

The two masses m_l and m_t in Equation (7.2) are the longitudinal mass and transverse mass, respectively, because m_l (m_z) is defined along the $\langle 100 \rangle$ axis (X valley) and along the $\langle 111 \rangle$ axis (L valley), whereas m_t ($m_x = m_y$) is defined in a plane transverse to the said axis. The longitudinal effective mass, m_l , is usually much larger than its counterparts m_t .

The DOS effective mass m_c^α for electrons in the CB minima $\alpha = \Gamma, X$ or L is given by

$$m_c^\alpha = N^{2/3} m_{l\alpha}^{2/3} m_{t\alpha}^{1/3} \quad (7.3)$$

where N is the number of equivalent α minima ($N = 1$ for the Γ minimum, $N = 3$ for the X minima and $N = 4$ for the L minima). The DOS mass can be used for DOS calculations.

The conductivity effective mass m_c^α , which can be used for conductivity or mobility calculations, is written as

$$m_c^\alpha = \frac{3m_{l\alpha}m_{t\alpha}}{m_{l\alpha} + 2m_{t\alpha}} \quad (7.4)$$

Since $m_{l\Gamma} = m_{l\Gamma}$, we have the relationship $m_c^\Gamma = m_c^\Gamma$ at the $\alpha = \Gamma$ minimum.

In hexagonal semiconductors, the CB electron has an ellipsoidal constant-energy surface, not a spherical surface, even at the zone center (Γ)

$$m_e^\perp \equiv m_x = m_y \neq m_z \equiv m_e^\parallel \quad (7.5)$$

Thus, $m_e^\Gamma \neq m_e^\Gamma$ holds in such anisotropic semiconductors, but its difference is very small.

We summarize in Table 7.1 the Γ -valley electron effective mass m_e^Γ for a number of cubic group-IV, III-V and II-VI semiconductors. Table 7.2 also summarizes the Γ -valley electron effective masses for some wurtzite III-V and II-VI semiconductors. The m_e^Γ values for InN, BeSe and BeTe in Table 7.1 and those for InN, BeO, BeSe and CdTe in Table 7.2 are obtained using the m_e^Γ versus E_0 relationships described in Section 7.1.2 of Adachi [1]. The InN values in Table 7.2 are taken from Hofmann *et al.* [2].

The electron effective masses in the X (Δ) and L minima for some cubic group-IV and III-V semiconductors are listed in Table 7.3. The corresponding DOS and conductivity masses are listed in Table 7.4.

7.1.2 Hole Effective Mass

The effective Hamiltonian is generally derived from a $k \cdot p$ theory or from the theory of invariants developed by Bir and Pikus. The effective Hamiltonians for the CB and VB in the

Table 7.1 Electron effective mass m_e^Γ for some cubic group-IV, III-V and II-VI semiconductors. d = diamond; zb = zinc-blende; rs = rocksalt

System	Material	m_e^Γ/m_0	System	Material	m_e^Γ/m_0
IV	Diamond (d)	0.36–2.030 ^a	II-VI	BeSe (zb)	0.28 ^a
	Si (d)	0.188 ^a		BeTe (zb)	0.21 ^a
	Ge (d)	0.038		MgO (rs)	0.35 ^a
	Sn (d)	–0.058 ^b		MgS (zb)	0.225 ^a
	3C-SiC (zb)	0.449 ^a		MgSe (zb)	0.20 ^a
III-V	BN (zb)	0.752 ^a		MgTe (zb)	0.17 ^a
	BP (zb)	0.150 ^a		ZnS (zb)	0.20
	BAs (zb)	0.0499 ^a		ZnSe (zb)	0.137
	AlN (zb)	0.26 ^a		ZnTe (zb)	0.117
	AlP (zb)	0.220 ^a		CdO (rs)	0.21
	AlAs (zb)	0.124		CdS (zb)	0.14 ^a
	AlSb (zb)	0.14	CdSe (zb)	0.112	
	GaN (zb)	0.15	CdTe (zb)	0.090	
	GaP (zb)	0.114	HgS (zb)	–0.006 ^{a,c}	
	GaAs (zb)	0.067	HgSe (zb)	–0.042 ^{a,c}	
	GaSb (zb)	0.039	HgTe (zb)	–0.028 ^c	
	InN (zb)	0.03 ^a			
	InP (zb)	0.07927			
	InAs (zb)	0.024			
	InSb (zb)	0.013			

^aCalculated or estimated

^bThe sign is chosen positive for a normal band structure like that of Ge

^cThe sign is chosen positive for a normal band structure like that of CdTe

Table 7.2 Γ -valley electron effective masses, m_e^\perp , m_e^\parallel and m_e^Γ , for some wurtzite III–V and II–VI semiconductors. $m_e^\Gamma = (m_e^{\perp 2} m_e^\parallel)^{1/3}$: DOS effective mass

System	Material	m_e^\perp/m_0	m_e^\parallel/m_0	m_e^Γ/m_0
III–V	AlN	0.29 ^a	0.30 ^a	0.29–0.45 (0.29 ^a)
	GaN	0.21	0.22	0.21
	InN	0.047	0.039	0.044
II–VI	BeO			0.7 ^a
	MgSe			0.3 ^a
	ZnO			0.234
	ZnS	0.28	0.28	0.28
	CdS	0.150	0.152	0.151
	CdSe	0.127	0.122	0.125
	CdTe			0.11 ^a

^aCalculated or estimated

zinc-blende- and wurtzite-type semiconductors are shown in Section 6.2.1 of Adachi [1]. The expressions for the hole effective masses in terms of the Luttinger's VB parameters γ (cubic) and A (hexagonal) have been described in Section 7.3.1 of Adachi [1].

The γ and A values for some cubic and wurtzite semiconductors are summarized in Tables 7.5 and 7.6, respectively. Table 7.7 also lists the effective HH and LH band masses,

Table 7.3 Electron effective mass in the X (Δ) and L minima for some cubic group-IV and III–V semiconductors. d = diamond; zb = zinc-blende

System	Material	X		L	
		m_{iX}/m_0	m_{iX}/m_0	m_{iL}/m_0	m_{iL}/m_0
IV	Diamond (d)	0.36	1.4		
	Si (d)	0.1905	0.9163	0.130 ^a	1.418 ^a
	Ge (d)	0.29	1.35	0.081	1.61
	Sn (d)	0.086 ^a	0.89 ^a	0.075 ^a	1.478 ^a
	3C-SiC (zb)	0.25	0.67		
III–V	BN (zb)	0.23 ^a	0.94 ^a		
	BP (zb)	0.204 ^a	1.125 ^a		
	AlN (zb)	0.32 ^a	0.52 ^a		
	AlP (zb)	0.212 ^a	3.67 ^a		
	AlAs (zb)	0.19	1.1	0.15 ^a	1.32 ^a
	AlSb (zb)	0.21	1.50	0.20 ^a	1.82 ^a
	GaN (zb)	0.30 ^a	0.58 ^a		
	GaP (zb)	0.252	6.9	0.150 ^a	1.184 ^a
	GaAs (zb)	0.23	1.3	0.0754	1.9
	GaSb (zb)	0.33 ^a	1.30 ^a	0.085	1.4
	InP (zb)	0.34 ^a	1.26 ^a	0.13 ^a	1.64 ^a
	InAs (zb)	0.28 ^a	1.32 ^a	0.12 ^a	3.57 ^a

^aTheoretical

Table 7.4 Electron DOS mass $m_c^{X,L}$ and conductivity mass $m_c^{X,L}$ in the X and L minima for some cubic group-IV and III-V semiconductors. d = diamond; zb = zinc-blende

System	Material	Density-of-states mass		Conductivity mass	
		m_c^X/m_0	m_c^L/m_0	m_c^X/m_0	m_c^L/m_0
IV	Diamond (d)	1.18		0.48	
	Si (d)	0.669	0.73	0.259	0.19
	Ge (d)	1.01	0.553	0.39	0.119
	α -Sn (d)	0.39 ^a	0.51 ^a	0.12 ^a	0.11 ^a
	3C-SiC (zb)	0.72		0.32	
III-V	BN (zb)	0.76 ^a		0.31 ^a	
	BP (zb)	0.75 ^a		0.28 ^a	
	AlN (zb)	0.78 ^a		0.37 ^a	
	AlP (zb)	1.14 ^a		0.31 ^a	
	AlAs (zb)	0.71	0.78	0.26 ^a	0.21 ^a
	AlSb (zb)	0.84	1.05 ^a	0.29	0.28 ^a
	GaN (zb)	0.78 ^a		0.36 ^a	
	GaP (zb)	1.58	0.75 ^a	0.37	0.21 ^a
	GaAs (zb)	0.85	0.56	0.32	0.11
	GaSb (zb)	1.08 ^a	0.54	0.44 ^a	0.12
	InP (zb)	1.09 ^a	0.76 ^a	0.45 ^a	0.19 ^a
	InAs (zb)	0.98 ^a	0.94 ^a	0.38 ^a	0.18 ^a

^aTheoretical

m_{HH} and m_{LH} , along the [001] and [111] directions for some cubic semiconductors. The DOS HH (m_{HH}^*), averaged LH (m_{LH}^*) and SO split-off hole effective masses (m_{SO}) are summarized in Table 7.8. The c -InN γ values in Table 7.5 are taken from Fritsch *et al.* [3].

7.1.3 Interpolation Scheme

Let us consider a linear interpolation representation for the composition dependence of the effective mass $m(x)$ for a semiconductor alloy A_xB_{1-x} ($A_xB_{1-x}C$). The simplest linear interpolation scheme is the use of the equation

$$m_{AB}(x) = xm_A + (1-x)m_B \quad (7.6)$$

where m_A and m_B represent the masses of elemental (binary) semiconductors A (AC) and B (BC), respectively.

If any material parameter can be given by a specific expression owing to some physical basis, it is natural to consider that the corresponding interpolation scheme may also obey this specific expression. The effective mass representation can then be written as

$$\frac{1}{m_{AB}(x)} = \frac{x}{m_A} + \frac{1-x}{m_B} \quad (7.7)$$

Table 7.5 Luttinger's VB parameter γ_i for some cubic group-IV, III-V and II-VI semiconductors (in $\hbar^2/2m_0$). d = diamond; zb = zinc-blende

System	Material	γ_1	γ_2	γ_3
IV	Diamond (d)	4.24	0.82	1.71
	Si (d)	4.285	0.339	1.446
	Ge (d)	13.38	4.24	5.69
	Sn (d)	-15.0	-11.5	-8.6
	3C-SiC (zb)	2.817	0.508	0.860
III-V	BN (zb)	1.92 ^a	0.02 ^a	0.56 ^a
	AlN (zb)	1.73 ^a	0.43 ^a	0.65 ^a
	AlP (zb)	3.47 ^a	0.06 ^a	1.15 ^a
	AlAs (zb)	3.76 ^a	0.90 ^a	1.42 ^a
	AlSb (zb)	4.15 ^a	1.01 ^a	1.75 ^a
	GaN (zb)	2.84 ^a	0.82 ^a	1.12 ^a
	GaP (zb)	4.04	0.53	1.26
	GaAs (zb)	7.10	2.02	2.91
	GaSb (zb)	13.3	4.4	5.7
	InN (zb)	5.381 ^a	2.294 ^a	2.508 ^a
	InP (zb)	5.33	1.57	2.11
	InAs (zb)	20.4	8.3	9.1
	InSb (zb)	36.3	16.1	17.2
	II-VI	MgS (zb)	2.62 ^a	0.38 ^a
MgSe (zb)		2.84 ^a	0.43 ^a	1.00 ^a
MgTe (zb)		3.21 ^a	0.52 ^a	1.15 ^a
ZnS (zb)		1.77 ^a	0.30 ^a	0.62 ^a
ZnSe (zb)		3.94	1.00	1.52
ZnTe (zb)		3.96	0.86	1.39
CdS (zb)		4.11 ^a	0.77 ^a	1.53 ^a
CdSe (zb)		5.51 ^a	1.24 ^a	2.14 ^a
CdTe (zb)		4.14	1.09	1.62
HgS (zb)		-41.28 ^a	-21.00 ^a	-20.73 ^a
HgSe (zb)		-25.96 ^a	-13.69 ^a	-13.20 ^a
HgTe (zb)		-15.6	-9.6	-8.6

^aCalculated or estimated

Similarly, for quaternary semiconductor alloys of types $A_xB_{1-x}C_yD_{1-y}$ and $A_xB_yC_{1-x-y}D$ ($AB_xC_yD_{1-x-y}$) we obtain

$$\frac{1}{m_{ABCD}(x,y)} = \frac{xy}{m_{AC}} + \frac{x(1-y)}{m_{AD}} + \frac{(1-x)y}{m_{BC}} + \frac{(1-x)(1-y)}{m_{BD}} \quad (7.8a)$$

$$\frac{1}{m_{ABCD}(x,y)} = \frac{x}{m_{AD}} + \frac{y}{m_{BD}} + \frac{1-x-y}{m_{CD}} \quad (7.8b)$$

Table 7.6 Theoretically obtained Luttinger's VB parameter A_i for some wurtzite III–V and II–VI semiconductors

System	Material	A_1	A_2	A_3	A_4	A_5	A_6	$ A_7 $
III–V	AlN	–4.15	–0.39	3.76	–1.61	–1.76	–2.07	0.10
	GaN	–6.87	–0.68	6.27	–2.98	–3.05	–4.25	0.23
	InN	–9.15	–0.66	8.50	–4.52	–4.47	–5.74	0.33
II–VI	ZnO	–3.78	–0.44	3.45	–1.63	1.68	–2.23	0.025
	ZnS	–4.58	–0.53	4.14	–2.34	–2.34	–3.69	
	CdS	–5.92	–0.70	5.37	–1.82	–1.82	–1.36	
	CdSe	–10.2	–0.76	9.53	–3.2	–3.2	–2.31	

Justification for Equation (7.7) is supported by the effective-mass transformation of the Schrödinger equation

$$\left[-\frac{\hbar^2 \nabla^2}{2m_0} + \sum_r U(r-\tau) \right] \rightarrow -\frac{\hbar^2 \nabla^2}{2m_{AB}(x)} \quad (7.9)$$

Figure 7.1 shows the effective HH band mass m_{HH} as a function of x for $Al_xGa_{1-x}As$. The solid and dashed lines are obtained by introducing the GaAs ($x=0$) and AlAs values ($x=1.0$) from Table 7.7 into Equations (7.6) and (7.7), respectively. The dotted lines are obtained by introducing the linearly interpolated γ values from Table 7.5 into the following equations (see Table 7.7 in Adachi [1])

$$m_{HH[001]}(x) = \frac{1}{\gamma_1(x) - 2\gamma_2(x)} \quad (7.10a)$$

$$m_{HH[111]}(x) = \frac{1}{\gamma_1(x) - 2\gamma_3(x)} \quad (7.10b)$$

It can be seen from Figure 7.1 that the dashed (Equation (7.7)) and dotted lines (Equation (7.10)) agree with each other.

7.2 GROUP-IV SEMICONDUCTOR ALLOY

7.2.1 CSi Binary Alloy

The lowest CB valleys in diamond and Si are located at the X (Δ) point in the BZ [1]. Figure 7.2 (a) plots the X-valley DOS and conductivity masses m_c^X and m_c^X for C_xSi_{1-x} . The solid and dashed lines show the linear interpolation results between diamond and Si listed in Table 7.4 using Equations (7.6) and (7.7), respectively. The solid circles also show the effective masses for 3C-SiC ($x=0.5$) taken from Table 7.4.

Table 7.7 HH and LH effective band masses, m_{HH} and m_{LH} , along the [001] and [111] directions for some cubic group-IV, III-V and II-VI semiconductors. d = diamond; zb = zinc-blende; rs = rocksalt

System	Material	m_{HH}/m_0		m_{LH}/m_0	
		[001]	[111]	[001]	[111]
IV	Diamond (d)	0.38	1.22	0.17	0.13
	Si (d)	0.277	0.718	0.202	0.139
	Ge (d)	0.204	0.500	0.0457	0.0404
	Sn (d)	0.125	0.46	-0.026 ^a	-0.031 ^a
	3C-SiC (zb)	0.56	0.91	0.26	0.22
III-V	BN (zb)	0.53 ^b	1.25 ^b	0.51 ^b	0.33 ^b
	BP (zb)	0.375 ^b	0.926 ^b	0.150 ^b	0.108 ^b
	AlN (zb)	1.15 ^b	2.33 ^b	0.39 ^b	0.33 ^b
	AlP (zb)	0.30 ^b	0.85 ^b	0.28 ^b	0.17 ^b
	AlAs (zb)	0.51 ^b	1.09 ^b	0.18 ^b	0.15 ^b
	AlSb (zb)	0.47 ^b	1.54 ^b	0.16 ^b	0.13 ^b
	GaN (zb)	0.83 ^b	1.67 ^b	0.22 ^b	0.20 ^b
	GaP (zb)	0.34	0.66	0.20	0.15
	GaAs (zb)	0.33	0.78	0.090	0.077
	GaSb (zb)	0.22	0.53	0.045	0.040
	InN (zb)	1.261	2.740	0.100	0.096
	InP (zb)	0.46	0.90	0.12	0.11
	InAs (zb)	0.26	0.45	0.027	0.026
InSb (zb)	0.24	0.53	0.015	0.014	
II-VI	MgO (rs)	1.60 ^b	2.77 ^b	0.35 ^b	0.31 ^b
	MgS (zb)	0.54 ^b	1.25 ^b	0.30 ^b	0.23 ^b
	MgSe (zb)	0.51 ^b	1.19 ^b	0.27 ^b	0.21 ^b
	MgTe (zb)	0.46 ^b	1.10 ^b	0.24 ^b	0.18 ^b
	ZnS (zb)	0.85 ^b	1.9 ^b	0.42 ^b	0.33 ^b
	ZnSe (zb)	0.52	1.11	0.168	0.143
	ZnTe (zb)	0.45	0.85	0.176	0.148
	CdS (zb)	0.39 ^b	0.95 ^b	0.18 ^b	0.14 ^b
	CdSe (zb)	0.33 ^b	0.81 ^b	0.13 ^b	0.10 ^b
	CdTe (zb)	0.51	1.11	0.158	0.136
	HgS (zb)	1.39 ^b	5.56 ^b	-0.012 ^{b,c}	-0.012 ^{b,c}
	HgSe (zb)	0.70 ^b	2.27 ^b	-0.019 ^{b,c}	-0.019 ^{b,c}
	HgTe (zb)	0.28	0.63	-0.029 ^c	-0.030 ^c

^aThe sign is chosen positive for a normal band structure like that of Ge^bCalculated or estimated^cThe sign is chosen positive for a normal band structure like that of CdTe

Figure 7.2(b) shows the HH and LH masses m_{HH} and m_{LH} along the [001] and [111] directions for $\text{C}_x\text{Si}_{1-x}$. The solid lines represent the results calculated from Equation (7.6) using the diamond and Si values in Table 7.7. The 3C-SiC ($x=0.5$) values are also plotted in Figure 7.2(b). These values are calculated from a set of the Luttinger's VB parameters derived by a five-level $k\text{-}p$ analysis [4]. Note that the HH and LH bands are anisotropic even in the

Table 7.8 DOS HH (m_{HH}^*), averaged LH (m_{LH}^*) and SO split-off hole effective masses (m_{SO}) for some cubic group-IV, III-V and II-VI semiconductors. d = diamond; zb = zinc-blende

System	Material	m_{HH}^*/m_0	m_{LH}^*/m_0	m_{SO}/m_0
IV	Diamond (d)	0.78	0.14	0.394 ^a
	Si (d)	0.528	0.157	0.29
	Ge (d)	0.345	0.0427	0.095
	Sn (d)	-0.029 ^b	0.19	0.041
	3C-SiC (zb)	0.76	0.24	0.51
III-V	BN (zb)	0.99 ^a	0.37 ^a	0.52 ^a
	BAAs (zb)		0.0800 ^a	0.2220 ^a
	AlN (zb)	1.77 ^a	0.35 ^a	0.58 ^a
	AlP (zb)	0.63 ^a	0.20 ^a	0.29 ^a
	AlAs (zb)	0.81 ^a	0.16 ^a	0.30 ^a
	AlSb (zb)	0.9	0.13	0.317 ^a
	GaN (zb)	1.27 ^a	0.21 ^a	0.35 ^a
	GaP (zb)	0.52	0.17	0.34
	GaAs (zb)	0.55	0.083	0.165
	GaSb (zb)	0.37	0.043	0.12
	InN (zb)	1.959	0.098	0.186
	InP (zb)	0.69	0.11	0.21
	InAs (zb)	0.36	0.026	0.14
	InSb (zb)	0.38	0.014	0.10
II-VI	MgS (zb)	0.93 ^a	0.25 ^a	0.38 ^a
	MgSe (zb)	0.88 ^a	0.23 ^a	0.35 ^a
	MgTe (zb)	0.80 ^a	0.20 ^a	0.31 ^a
	ZnS (zb)	1.42 ^a	0.36 ^a	0.56 ^a
	ZnSe (zb)	0.82	0.154	0.24
	ZnTe (zb)	0.67	0.159	0.25
	CdS (zb)	0.68 ^a	0.15 ^a	0.24 ^a
	CdSe (zb)	0.57 ^a	0.11 ^a	0.18 ^a
	CdTe (zb)	0.82	0.145	0.24
	HgS (zb)	-0.012 ^{a,c}	2.22 ^a	-0.013 ^{a,c}
	HgSe (zb)	-0.019 ^{a,c}	1.07 ^a	0.031 ^a
	HgTe (zb)	-0.030 ^c	0.38	0.102 ^a

^aCalculated or estimated^bThe sign is chosen positive for a normal band structure like that of Ge^cThe sign is chosen positive for a normal band structure like that of CdTe

diamond- and zinc-blende-type semiconductors [1]. As can be easily seen from Figure 7.2(b), the anisotropic effect is most pronounced for the HH band, which has a strongly directionally-dependent effective mass, with a larger mass along the [111] direction than along the [001] direction.

Using the linear interpolation scheme, we can obtain the plausible effective mass values for 3C-SiC. Note, however, that it is very difficult to accurately measure the effective masses in semiconductors. This is especially true for the hole effective masses and also for the $k \neq 0$

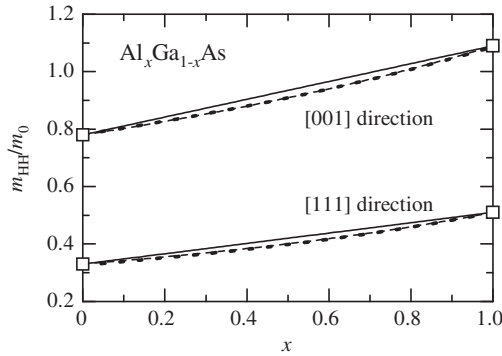


Figure 7.1 Effective HH band mass m_{HH} in the [001] and [111] directions as a function of x for $\text{Al}_x\text{Ga}_{1-x}\text{As}$. The solid and dashed lines are calculated from Equations (7.6) and (7.7), respectively. The dotted lines are obtained by introducing the linearly interpolated γ values in Table 7.5 into Equation (7.10)

(e.g. X and L valleys) electron masses in semiconductors (and even for the $\mathbf{k} = 0$ (Γ -valley) electron masses in wide band-gap semiconductors).

7.2.2 SiGe Binary Alloy

The transition from a Ge-like CB edge (X (Δ) valley) to a Si-like edge (L valley) was verified by CR to occur between $x = 0.115$ and 0.19 [5]. In $\text{Si}_x\text{Ge}_{1-x}$, the CB edge mass ratios are predicted from Table 7.3 to be $m_{\text{IX}}/m_{\text{IX}} = 10.9 + 9.0x$ (Ge-like) and $m_{\text{L}}/m_{\text{L}} = 4.8 - 0.1x$ (Si-like). Fink and Braunstein [5] carried out CR measurements on the CB of Si–Ge alloy at 891 GHz ($337 \mu\text{m}$) using an IR laser. The IR laser enabled measurements of the longitudinal and transverse effective masses to within 4% of each side of the alloy composition at which the CB edge switches from the [111] to the [001] direction (15 at% Si in Ge). The measured mass

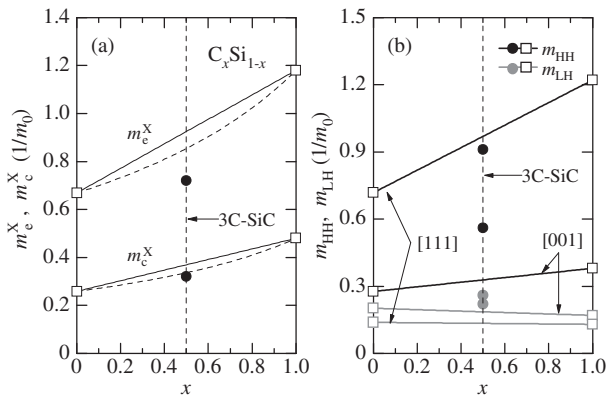


Figure 7.2 (a) X-valley DOS and conductivity masses m_c^{X} and m_c^{X} for $\text{C}_x\text{Si}_{1-x}$. The solid and dashed lines represent the linear interpolation results derived from Equations (7.6) and (7.7), respectively. The solid circles show the effective masses for 3C-SiC ($x = 0.5$) taken from Table 7.4. (b) Effective HH and LH band masses m_{HH} and m_{LH} in the [001] and [111] directions for $\text{C}_x\text{Si}_{1-x}$. The solid lines represent the linear interpolation results using Equation (7.6)

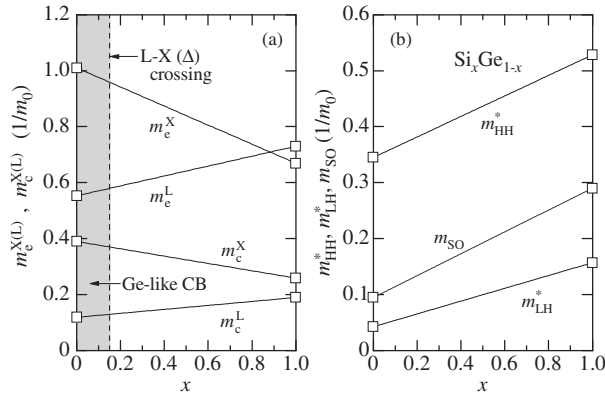


Figure 7.3 (a) X- and L-valley DOS and conductivity masses $m_c^{X,L}$ and $m_c^{X,L}$ for $\text{Si}_x\text{Ge}_{1-x}$. (b) DOS HH (m_{HH}^*), averaged LH (m_{LH}^*) and SO split-off hole effective masses (m_{SO}) for $\text{Si}_x\text{Ge}_{1-x}$. The solid lines in (a) and (b) are calculated from Equation (7.6). The dashed line in (a) indicates the CB L–X (Δ) crossing composition $x_c \sim 0.15$

did not appear to change from their values in the pure constituents, although only the transverse mass of the [111], Ge-like minimum could be measured with reliable accuracy. More recent CR measurements on high-mobility 2D electron gas in strained $\text{Si}_{0.94}\text{Ge}_{0.06}$ showed an in-plane mass of $0.193m_0$ [6], in good agreement with the expectations of Table 7.3. The X- and L-valley DOS and conductivity masses $m_c^{X,L}$ and $m_c^{X,L}$ for $\text{Si}_x\text{Ge}_{1-x}$ calculated from Equation (7.6) are shown in Figure 7.3(a).

Experimental hole masses based on CR are available from measurements of 2D samples for pseudomorphic $\text{Si}_x\text{Ge}_{1-x}$ channels on Si [7]. The results gave insight into the complexity of the VB structure. The DOS HH (m_{HH}^*), averaged LH (m_{LH}^*) and SO split-off hole effective masses (m_{SO}) for $\text{Si}_x\text{Ge}_{1-x}$ calculated from Equation (7.6) using the Si and Ge values in Table 7.8 are shown in Figure 7.3(b).

7.3 III–V SEMICONDUCTOR TERNARY ALLOY

7.3.1 (III, III)–N Alloy

Unfortunately, there is no experimental information on the carrier effective masses in III–N alloys. This necessitates the use of some type of interpolation scheme. The Γ -valley electron mass m_c^Γ versus composition x for c - and w -(III, III)–N ternaries are shown in Figure 7.4. Equation (7.6) is used as the linear interpolation expression. The corresponding endpoint binary data are taken from Tables 7.1 and 7.2.

7.3.2 (III, III)–P Alloy

Figure 7.5 shows the Γ -valley electron mass m_c^Γ for some P-based ternaries. No experimental determinations of the effective masses in $\text{Al}_x\text{Ga}_{1-x}\text{P}$ and $\text{Al}_x\text{In}_{1-x}\text{P}$ appear to be available. Therefore, the electron effective masses m_c^Γ in Figure 7.5 were obtained from Equation (7.6). The m_c^Γ mass in a random $\text{Ga}_{0.5}\text{In}_{0.5}\text{P}$ alloy was determined to be $(0.092 \pm 0.003)m_0$ by

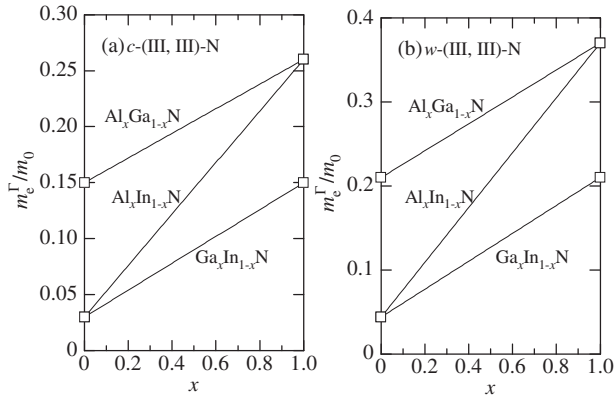


Figure 7.4 Γ -valley electron effective mass m_e^Γ versus x for (a) c - and (b) w -(III, III)-N alloys. The solid lines are calculated from Equation (7.6)

Emanuelsson *et al.* [8]. This value is somewhat lower than the linearly interpolated value obtained using Equation (7.6), but is in reasonable agreement with that obtained from Equation (7.7). The quadratic least-squares fit of the $x = 0.5$ and endpoint data gives a bowing parameter of $c = 0.01854m_0$ (heavy solid line, see also Table 7.9). Emanuelsson *et al.* [8] found the Γ -valley electron mass in an ordered $\text{Ga}_{0.5}\text{In}_{0.5}\text{P}$ alloy to be $(0.088 \pm 0.003)m_0$, which was slightly smaller than the random alloy value $(0.092m_0)$.

7.3.3 (III, III)-As Alloy

(a) AlGaAs

An important description of the carrier effective masses in semiconductors was presented by Adachi [9,10] who reviewed many carried out on GaAs, AlAs and $\text{Al}_x\text{Ga}_{1-x}\text{As}$. We have already shown in Figure 7.1 the HH masses m_{HH} in the [001] and [111] directions for

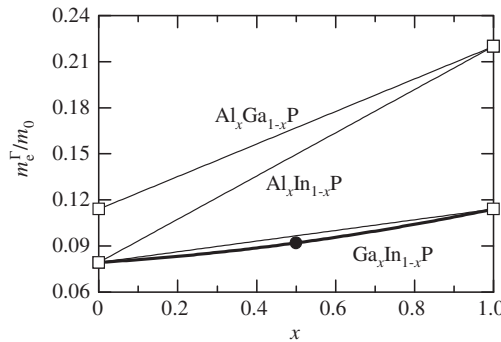


Figure 7.5 Γ -valley electron effective mass m_e^Γ versus x for (III, III)-P alloys obtained from the linear interpolation scheme in Equation (7.6) (solid lines). The solid circle represents the CR data for a random $\text{Ga}_{0.5}\text{In}_{0.5}\text{P}$ alloy obtained by Emanuelsson *et al.* [8]. The heavy solid line shows the quadratic least-squares fit of the endpoint binary data and Emanuelsson's data (see Table 7.9)

Table 7.9 Γ -valley electron effective mass m_e^Γ determined experimentally for some cubic III-V semiconductor alloys

Alloy	m_e^Γ/m_0	Remark
$\text{Ga}_x\text{In}_{1-x}\text{P}$	$0.07927 + 0.01619x + 0.01854x^2$	$0 \leq x \leq 1.0$
$\text{Al}_x\text{Ga}_{1-x}\text{As}$	$0.067 + 0.057x$	$0 \leq x \leq 1.0$
$\text{Al}_x\text{In}_{1-x}\text{As}$	$0.024 + 0.088x + 0.012x^2$	$0 \leq x \leq 1.0$
$\text{Ga}_x\text{In}_{1-x}\text{As}$	$0.024 + 0.035x + 0.008x^2$	$0 \leq x \leq 1.0$
$\text{Ga}_x\text{In}_{1-x}\text{Sb}$	$0.013 + 0.016x + 0.010x^2$	$0 \leq x \leq 1.0$
$\text{GaN}_x\text{As}_{1-x}$	$0.0067 + 0.047x$ (x in at%)	$0 \leq x \leq 2$ at%
$\text{GaP}_x\text{As}_{1-x}$	$0.067 + 0.047x$	$0 \leq x \leq 1.0$
$\text{GaAs}_x\text{Sb}_{1-x}$	$0.039 + 0.014x + 0.014x^2$	$0 \leq x \leq 1.0$
$\text{InP}_x\text{As}_{1-x}$	$0.02400 + 0.05572x$	$0 \leq x \leq 1.0$
$\text{In}_x\text{As}_{1-x}\text{Sb}$	$0.013 - 0.016x + 0.027x^2$	$0 \leq x \leq 1.0$
$\text{Ga}_x\text{In}_{1-x}\text{P}_y\text{As}_{1-y}/\text{InP}$	$0.04084 + 0.03384y + 0.00459y^2$	$0 \leq y \leq 1.0$
$(\text{Al}_x\text{Ga}_{1-x})_{0.48}\text{In}_{0.52}\text{As}/\text{InP}$	$0.043 + 0.031x$	$0 \leq x \leq 1.0$

$\text{Al}_x\text{Ga}_{1-x}\text{As}$. The Γ -, X- and L-valley electron conductivity masses m_e^Γ , m_e^X and m_e^L for $\text{Al}_x\text{Ga}_{1-x}\text{As}$ have been plotted in Figure 7.6(a). The solid lines represent the linear interpolation results of Equation (7.6) using the endpoint binary data in Tables 7.1 and 7.4. The solid circles show the experimental m_e^Γ data taken from Adachi [10]. The corresponding linear least-squares fit is represented by the heavy solid line (see also Table 7.9).

Figure 7.6(b) plots the cyclotron HH and LH masses m_{Hc} and m_{Lc} in the [001] direction as a function of x for $\text{Al}_x\text{Ga}_{1-x}\text{As}$. The experimental data are taken from Adachi [10]. The cyclotron masses m_{Hc} and m_{Lc} result from averaging the band effective masses in Equation (47) in Hensel and Suzuki [11]. The solid lines in Figure 7.6(b) show the linear interpolation results between AlAs and GaAs using Equation (7.6), while the heavy solid lines represent the results

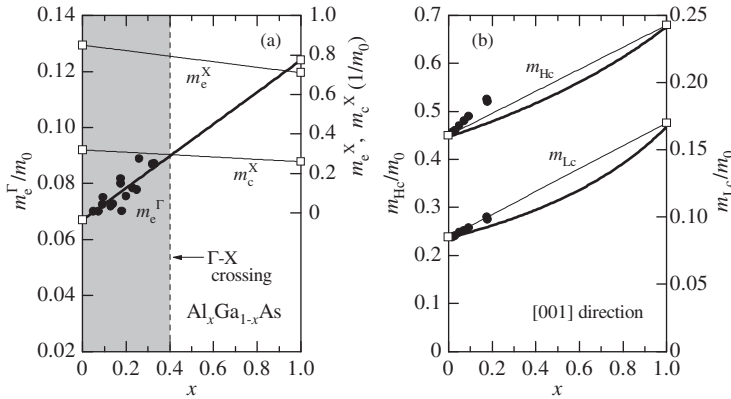


Figure 7.6 (a) Γ - and X-valley electron effective masses m_e^Γ , m_e^X and m_e^L for $\text{Al}_x\text{Ga}_{1-x}\text{As}$. The solid lines show the linearly interpolated results using Equation (7.6). The heavy solid line represents the linear least-squares fit (see Table 7.9). The dashed line indicates the CB Γ -X crossing composition $x_c \sim 0.4$. (b) Cyclotron HH and LH masses m_{Hc} and m_{Lc} in the [001] direction for $\text{Al}_x\text{Ga}_{1-x}\text{As}$. The solid lines show the linear interpolation results using Equation (7.6). The heavy solid lines are obtained by introducing the linearly interpolated γ values into Equation (47) of Hensel and Suzuki [11]. The experimental data in (a) and (b) are taken from Adachi [10] (solid circles)

calculated by introducing the linearly interpolated γ values (Equation (7.6)) into Equation (47) of Hensel and Suzuki [11].

(b) *AlInAs*

Matyas and Karoza [12] determined the Γ -valley electron mass m_e^Γ from a plasma resonance minimum in the IR reflectance spectra for bulk $\text{Al}_x\text{In}_{1-x}\text{As}$ alloy. Their results (solid circles), together with the linearly interpolated m_e^Γ , m_e^X and m_c^X using Equation (7.6) (solid lines) are shown in Figure 7.7. The experimental m_e^Γ data for $x > 0.08$ are considerably larger than the linearly interpolated values. Similarly, Wright *et al.* [13] obtained from optically detected CR a considerably larger value of $m_e^\Gamma = (0.10 \pm 0.01)m_0$ for $\text{Al}_{0.48}\text{In}_{0.52}\text{As}$ grown by MBE on InP. On the other hand, Cury *et al.* [14] measured a much smaller mass of $m_e^\Gamma = 0.069m_0$ which is only a little lower than the linearly interpolated value obtained using Equation (7.6) ($0.072m_0$). The smaller result is supported by the optically detected CR measurements by Chen *et al.* [15]. The heavy solid line in Figure 7.7 shows the quadratic least-squares fit of the endpoint and Cury's data (see also Table 7.9).

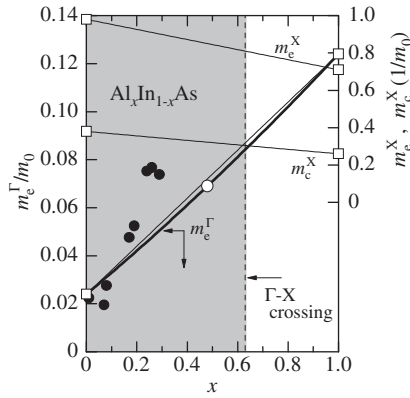


Figure 7.7 Γ - and X-valley electron effective masses m_e^Γ , m_e^X and m_c^X for $\text{Al}_x\text{In}_{1-x}\text{As}$. The solid and open circles represent the experimental data taken from Matyas and Karoza [12] and Cury *et al.* [14], respectively. The solid lines show the linear interpolation results using Equation (7.6). The heavy solid line shows the quadratic least-squares fit of the endpoint binary data and Cury's data (see Table 7.9). The dashed line indicates the CB Γ -X crossing composition $x_c \sim 0.63$

(c) *GaInAs*

The Γ -valley electron mass m_e^Γ in $\text{Ga}_x\text{In}_{1-x}\text{As}$ has been measured by a number of authors [16–20]. These results are shown in Figure 7.8(a). The solid and dashed lines represent the linear interpolation results of Equations (7.6) and (7.7) using the endpoint binary data in Table 7.1, respectively. The heavy solid line shows the quadratic least-squares fit of the experimental data, yielding a small bowing value of $c = 0.008m_0$ (Table 7.9).

A set of the Luttinger's VB parameters γ for $\text{Ga}_x\text{In}_{1-x}\text{As}$ have been measured by several authors [21–23]. Traynor *et al.* [23] observed a significant bowing in κ defined by

$$\kappa = -\frac{1}{3}\gamma_1 + \frac{2}{3}\gamma_2 + \gamma_3 - \frac{2}{3} \quad (7.11)$$

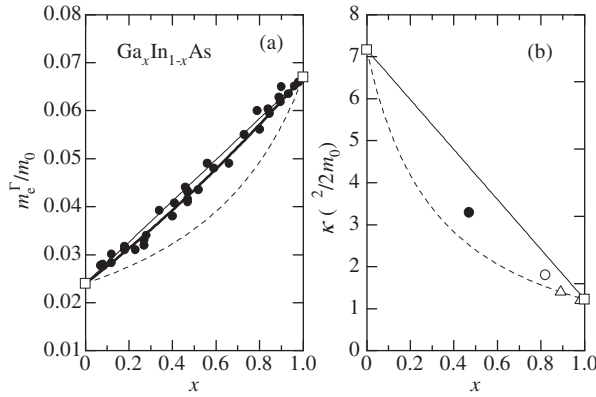


Figure 7.8 (a) Γ -valley electron effective mass m_e^Γ for $\text{Ga}_x\text{In}_{1-x}\text{As}$. The solid and dashed lines show the linear interpolation results of Equations (7.6) and (7.7), respectively. The heavy solid line represents the quadratic least-squares fit (see Table 7.9). (b) Plots of κ values for $\text{Ga}_x\text{In}_{1-x}\text{As}$. The symbols represent the experimental data taken from various sources (see text). The solid and dashed lines are obtained by introducing the linearly interpolated γ values of Equations (7.6) and (7.7) into Equation (7.11), respectively

which is a parameter introduced by Luttinger and necessary to describe the magnetic levels, although it is not measured in classical CR experiments. The κ values reported by Traynor *et al.* [23] are plotted against $x = 0.08$ and 0.11 in Figure 7.8(b) (open triangles), together with those obtained from the Luttinger’s VB parameters by Alavi *et al.* [21] for $x = 0.47$ (solid circle) and Warburton *et al.* [22] for $x = 0.82$ (open circle). The solid and dashed lines in Figure 7.8(b) show the κ values obtained by introducing the linearly interpolated γ values from Equations (7.6) and (7.7) into Equation (7.11), respectively.

7.3.4 (III, III)–Sb Alloy

No experimental data are available for the effective masses in $\text{Al}_x\text{Ga}_{1-x}\text{Sb}$ and $\text{Al}_x\text{In}_{1-x}\text{Sb}$. It can be expected however, that the Γ -valley mass m_e^Γ will be satisfactorily represented by the linear interpolation scheme. That is, any nonlinearity in the composition dependence of the effective mass stems entirely from the bowing of the energy band gap (see Figure 7.26). Very little strong bowing in the E_0 gap has been observed experimentally for $\text{Al}_x\text{Ga}_{1-x}\text{Sb}$ and $\text{Al}_x\text{In}_{1-x}\text{Sb}$ (Figures 6.25 and 6.26).

Figure 7.9(a) shows the Γ -valley electron mass m_e^Γ in $\text{Ga}_x\text{In}_{1-x}\text{Sb}$ measured by Aubin *et al.* [24]. The solid and dashed lines are obtained by introducing the InSb ($x = 0$) and GaSb values ($x = 1.0$) in Table 7.1 into Equations (7.6) and (7.7), respectively. The heavy solid line represents the quadratic least-squares fit of the experimental data.

The VB structure of $\text{Ga}_x\text{In}_{1-x}\text{Sb}$ was investigated by Roth and Fortin [25] using an interband magneto-optical technique. All the fundamental band parameters obtained by these authors exhibited a nonlinear dependence on x . The HH and LH band masses m_{HH} and m_{LH} in the [001] direction for $\text{Ga}_x\text{In}_{1-x}\text{Sb}$ have been plotted in Figure 7.9(b) as examples. These plots are obtained by introducing the nonlinear γ values into the expressions shown in Table 7.7 of Adachi [1] (see also an expression for m_{HH} in Equation (7.10a)). The results can be expressed as

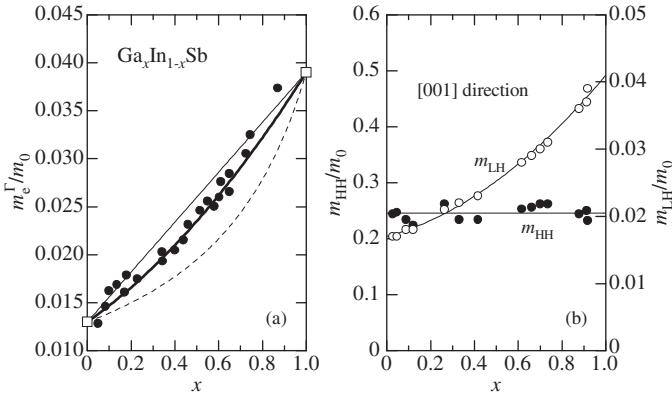


Figure 7.9 (a) Γ -valley electron effective mass m_e^Γ in $\text{Ga}_x\text{In}_{1-x}\text{Sb}$. The experimental data are taken from Aubin *et al.* [24]. The solid and dashed lines are obtained from Equations (7.6) and (7.7), respectively. The heavy solid line shows the quadratic least-squares fit (see Table 7.9). (b) Effective HH and LH band masses m_{HH} and m_{LH} in the [001] direction for $\text{Ga}_x\text{In}_{1-x}\text{Sb}$. These plots are obtained by introducing the Luttinger's VB parameters γ determined experimentally by Roth and Fortin [25] into the expressions in Table 7.7 of Adachi [1] (see also Equation (7.12))

$$\frac{m_{\text{HH}}}{m_0} = 0.246 \quad (7.12a)$$

$$\frac{m_{\text{LH}}(x)}{m_0} = 0.017 + 0.009x + 0.015x^2 \quad (7.12b)$$

7.3.5 Dilute-nitride III–(V, V) Alloy

(a) Ga–(N, V) alloy

The conductivity masses at the lowest direct and indirect conduction minima of GaP are $m_e^\Gamma = 0.114m_0$ (Table 7.1) and $m_c^X = 0.37m_0$ (Table 7.4), respectively. A large CB effective mass of $\sim 0.9m_0$ has been estimated by analyzing PL spectra for $\text{GaN}_x\text{P}_{1-x}/\text{GaP}$ MQWs of various well thicknesses [26]. The results may indicate a mixing of the Γ - and X-valley wavefunctions in the CB.

The electron effective mass in dilute-nitride $\text{GaN}_x\text{As}_{1-x}$ has been measured using various techniques, such as optically detected CR [27], PR [28] and magneto-PL measurements [29–31]. These results have been plotted in Figure 7.10. Since the band structure of dilute nitrides is still unclear, let us use a new symbol m_e^* for the free-electron effective mass. There is a large scatter in m_e^* . The solid line represents the linear least-squares fit of these data (see also Table 7.9).

Zhang and Mascarenhas [32] investigated quantum-confinement phenomena in $\text{GaN}_x\text{As}_{1-x}/\text{GaAs}$ QWs ($0.009 \leq x \leq 0.045$) using an ER technique. They demonstrated formation of an impurity band due to heavy N doping and the quantum confinement of an electron belonging to such an impurity band. The resulting electron effective masses are much larger than those shown in Figure 7.10 (e.g. $m_e^* \sim 0.55m_0$ at $x = 0.009$ and $\sim 0.4m_0$ at $x = 0.023$). The extremely large m_e^* value with N incorporation and its subsequent decrease can be expected to be a result of the impurity band formation.

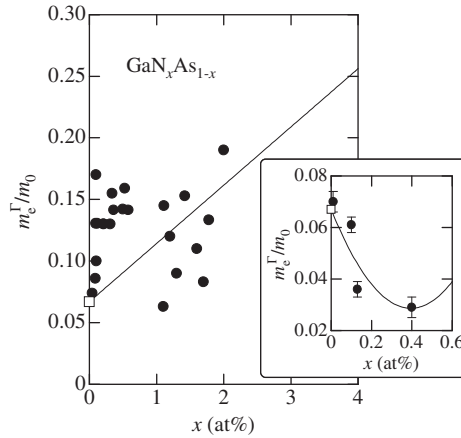


Figure 7.10 Electron effective mass m_e^* in dilute-nitride $\text{GaN}_x\text{As}_{1-x}$. The solid line represents the linear least-squares fit (see Table 7.9). The inset shows the experimental results of Young *et al.* [33] for x from 0 up to 0.4 at%. The solid line in the inset also shows the quadratic least-squares fit of Equation (7.13)

In contrast, by analyzing carrier transport properties Young *et al.* [33] observed a decrease in m_e^* with increasing x from 0 up to 0.4 at% in $\text{GaN}_x\text{As}_{1-x}$. Their results are reproduced in the inset of Figure 7.10. The solid line shows the quadratic least-squares fit of these data (x in at%)

$$\frac{m_e^*(x)}{m_0} = 0.067 - 0.194x + 0.246x^2 \quad (7.13)$$

The traditional $k \cdot p$ theory predicts that the CB mass should decrease with decreasing band-gap energy [1] (Figure 7.26). We have shown that adding N to GaAs reduces its band-gap energy considerably (Figure 6.29), so this effect alone may be expected to reduce the effective mass. On the other hand, any effect of N incorporation on the CB wavefunction admixture will increase the electron effective mass [34]. Young *et al.* [33] considered that their samples lay at the limit of dilute alloy where there are minor perturbations of the CB. The observed m_e^* reduction is thus thought to be due to the band-gap reduction. The large increase in m_e^* observed in the intermediate or higher N concentration region [27–31] is due to the mixing effect of the CB states (Γ , X and L).

The effect of N incorporation on the electron effective mass is more subtle and it may represent a more stringent test for the validity of different theoretical models aimed at explaining the puzzling effects of N in various III–V semiconductors [34]. Unfortunately, the experimental m_e^* data reported do not show a common and clear trend with increasing N concentration, as can be seen from Figure 7.10.

(b) In–(N, V) alloy

The electron effective mass m_e^* in dilute-nitride $\text{InN}_x\text{As}_{1-x}$ has been measured by several authors [35–37]. Figure 7.11 plots the results obtained by these authors (solid circles: Huang *et al.* [35]; open circle: Hang *et al.* [36]; open triangles: Shih *et al.* [37]). The heavy solid line shows the quadratic least-squares fit of these data (x in at%)

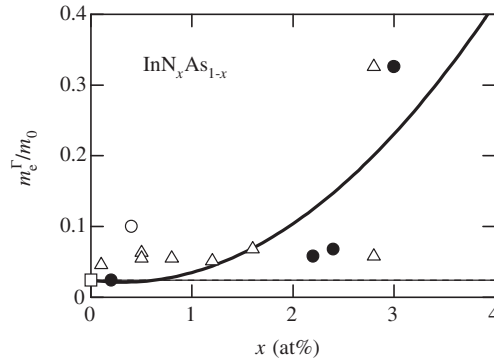


Figure 7.11 Electron effective mass m_e^* in dilute-nitride $\text{InN}_x\text{As}_{1-x}$. The solid and dashed lines are calculated by introducing the endpoint binary data into Equations (7.6) and (7.7), respectively. Note that these lines completely overlap in the region of $x \leq 4$ at%. The heavy solid line shows the quadratic least-squares fit of Equation (7.14)

$$\frac{m_e^*(x)}{m_0} = 0.024 - 0.018x + 0.029x^2 \quad (7.14)$$

The solid and dashed lines are obtained by introducing the InAs ($x=0$) and c -InN values ($x=1.0$) in Table 7.1 into Equations (7.6) and (7.7), respectively.

The effective mass m_e^* in dilute-nitride $\text{InN}_x\text{Sb}_{1-x}$ has been measured by Murdin *et al.* [38] using the CR technique. The experimental m_e^* value for $x=0.044$ at $5.53 \mu\text{m}$ exciting laser wavelength was 0.044, which was compared with 0.033 for InSb ($x=0$) at the same wavelength.

Since N incorporation mainly affects the CB states [34], the dilute-nitride hole effective masses can be compared with those of the hole masses in the nitride-free III–V host semiconductors, such as GaP, GaAs, InAs and InSb.

7.3.6 Al–(V, V) Alloy

No experimental data are available on the effective masses of Al-based ternary alloys. Therefore, the linearly interpolated m_e^Γ values for $\text{AlP}_x\text{As}_{1-x}$, $\text{AlP}_x\text{Sb}_{1-x}$ and $\text{AlAs}_x\text{Sb}_{1-x}$ using Equation (7.6) are shown in Figure 7.12. The endpoint binary masses are taken from Table 7.1.

7.3.7 Ga–(V, V) Alloy

(a) GaPAs

Figure 7.13(a) shows the Γ -valley electron effective mass m_e^Γ in $\text{GaP}_x\text{As}_{1-x}$ measured by Wetzter *et al.* [39] using an optical detection CR technique. The solid and dashed lines represent the linear interpolation results obtained by introducing the GaAs ($x=0$) and GaP values ($x=1.0$) in Table 7.1 into Equations (7.6) and (7.7), respectively.

There is a tendency for upward bowing in the experimental m_e^Γ versus x plots; however, the same alloy showed a weak downward bowing in E_0 (Figure 6.33). It can, therefore, be concluded that $\text{GaP}_x\text{As}_{1-x}$ has an almost linear dependence of m_e^Γ on x . The resulting expression is given in Table 7.9.

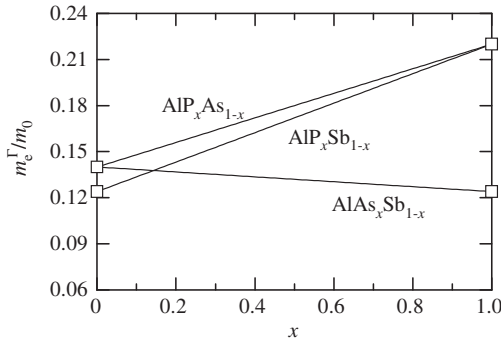


Figure 7.12 Γ -valley electron effective mass m_e^Γ versus x for Al-(V, V) alloys obtained from the linear interpolation scheme of Equation (7.6)

(b) GaAsSb

Filion and Fortin [40] determined the Γ -valley electron effective mass m_e^Γ in $\text{GaAs}_x\text{Sb}_{1-x}$ by measuring intrinsic photoconductivity under magnetic fields of up to 65 kG. The data they obtained for m_e^Γ , together with the linearly interpolated results using Equations (7.6) and (7.7) are shown in Figure 7.13(b). The result calculated using Equation (7.7), shown by the dashed line, explains the peculiar experimental data very well and can be approximated by the quadratic expression given in Table 7.9.

7.3.8 In-(V, V) Alloy

(a) InPAs

The electron effective mass m_e^Γ in $\text{InP}_x\text{As}_{1-x}$ has been measured by various authors [41–45]. The solid line in Figure 7.14 represents the linear least-squares fit of these data (see Table 7.9).

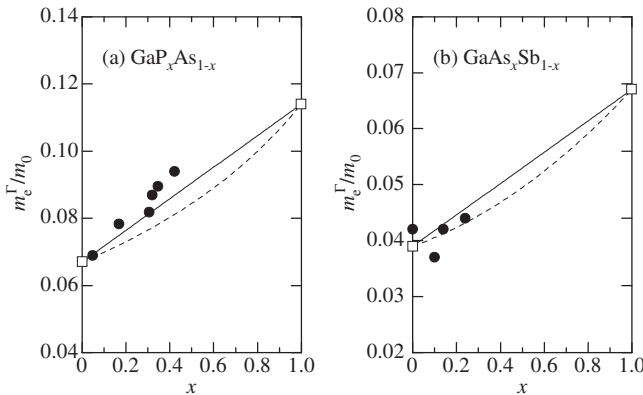


Figure 7.13 Γ -valley electron effective mass m_e^Γ versus x for (a) $\text{GaP}_x\text{As}_{1-x}$ and (b) $\text{GaAs}_x\text{Sb}_{1-x}$. The experimental data in (a) are taken from Wetzel *et al.* [39] and in (b) from Filion and Fortin [40] (solid circles). The solid and dashed lines are obtained by introducing the endpoint binary data into Equations (7.6) and (7.7), respectively. The expressions used to obtain these lines are listed in Table 7.9

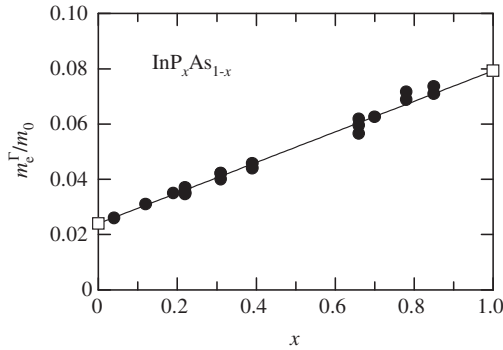


Figure 7.14 Γ -valley electron effective mass m_e^Γ in $\text{InP}_x\text{As}_{1-x}$. The solid line represents the linear least-squares fit (see Table 7.9)

(b) InAsSb

The electron effective mass m_e^Γ in $\text{InAs}_x\text{Sb}_{1-x}$ obtained from Thomas and Woolley [46] is shown in Figure 7.15(a). The solid and dashed lines represent the linear interpolation results obtained by introducing the InSb ($x=0$) and InAs data ($x=1.0$) in Table 7.1 into Equations (7.6) and (7.7), respectively. The heavy solid line also shows the quadratic least-squares fit of the experimental data. The bowing parameter c obtained from this fit is $0.027m_0$, which is much larger than the endpoint values $m_e^\Gamma = 0.013m_0$ (InSb) and $0.024m_0$ (InAs). The resulting m_e^Γ versus x curve exhibits considerably large downward bowing, as shown in Figure 7.15(a).

A full set of the Luttinger's VB parameters for $\text{InAs}_x\text{Sb}_{1-x}$ have been determined by Smith *et al.* [47] from interband magnetoabsorption measurements. The results they obtained have been plotted in Figure 7.15(b). These parameters show almost linear dependence on x .

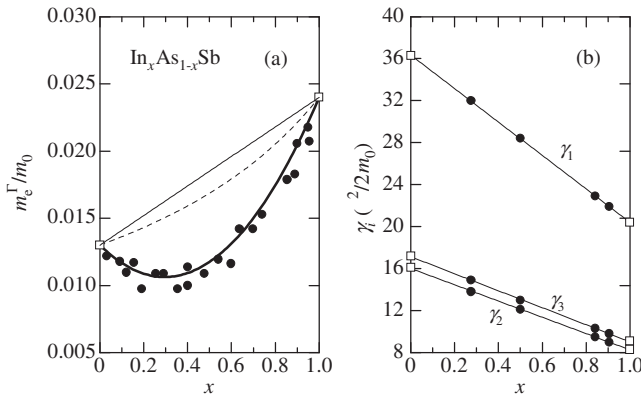


Figure 7.15 (a) Γ -valley electron effective mass m_e^Γ in $\text{InAs}_x\text{Sb}_{1-x}$. The experimental data are taken from Thomas and Woolley [46]. The solid and dashed lines are obtained by introducing the endpoint binary data into Equations (7.6) and (7.7), respectively. The heavy solid line shows the quadratic least-squares fit (see Table 7.9). (b) Luttinger's VB parameters for $\text{InAs}_x\text{Sb}_{1-x}$ determined by Smith *et al.* [47]

7.4 III–V SEMICONDUCTOR QUATERNARY ALLOY

7.4.1 Dilute-nitride Quaternary Alloy

As mentioned in Section 7.3.5, the electron effective mass m_e^* in dilute-nitride III–V ternaries is usually larger than the electron effective mass m_e^Γ in the host materials, possibly due to the interaction of the CB with N-related resonant states. The same conclusion can be drawn for dilute-nitride III–V quaternaries. The electron effective mass m_e^* in dilute-nitride $\text{Ga}_x\text{In}_{1-x}\text{N}_y\text{As}_{1-y}$ obtained by Pan *et al.* [48] and Héroux *et al.* [49] is shown in Figure 7.16. These data show a clear increase in m_e^* with increasing N concentration. A number of groups also observed an increase in the electron effective mass by incorporating N atoms into $\text{Ga}_x\text{In}_{1-x}\text{As}$ [50–54].

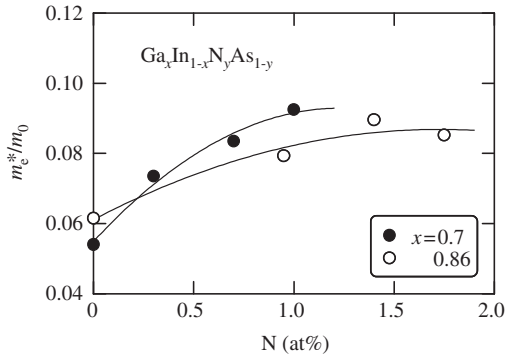


Figure 7.16 Electron effective mass m_e^* in dilute-nitride $\text{Ga}_x\text{In}_{1-x}\text{N}_y\text{As}_{1-y}$ reported by Pan *et al.* [48] (solid circles) and Héroux *et al.* [49] (open circles)

Polimeni *et al.* [55] found that there was dependence of the in-plane hole effective masses in $\text{Ga}_x\text{In}_{1-x}\text{N}_y\text{As}_{1-y}$ QWs on the In concentration by PL measurements after picosecond excitation and under a magnetic field \mathbf{B} . These results suggest that the dilute-nitride hole effective masses are nearly the same as those for nitride-free $\text{Ga}_x\text{In}_{1-x}\text{As}$ host semiconductor. This agrees with the fact that N incorporation mainly affects the CB states [34].

7.4.2 (III, III)–(V, V) Alloy

(a) GaInPAs

Adachi [56] has reviewed the carrier effective masses in $\text{Ga}_x\text{In}_{1-x}\text{P}_y\text{As}_{1-y}$. The Γ -valley electron effective mass m_e^Γ versus y for $\text{Ga}_x\text{In}_{1-x}\text{P}_y\text{As}_{1-y}/\text{InP}$ has been plotted in Figure 7.17(a). The solid and dashed lines represent the linear interpolation results obtained from Equations (A.6) and (7.8) respectively, using the binary data in Table 7.1. The solid circles show the experimental data taken from Adachi [56]. The corresponding quadratic least-squares fit is given by the heavy solid line (see also Table 7.9).

The LH effective mass in $\text{Ga}_x\text{In}_{1-x}\text{P}_y\text{As}_{1-y}/\text{InP}$ versus y is plotted in Figure 7.17(b). The experimental data are taken from Adachi [56]. The solid and dashed lines represent the linear interpolation results obtained from Equations (A.6) and (7.8) respectively, using the binary data in Table 7.7. The heavy solid line shows the quadratic best-fit expression

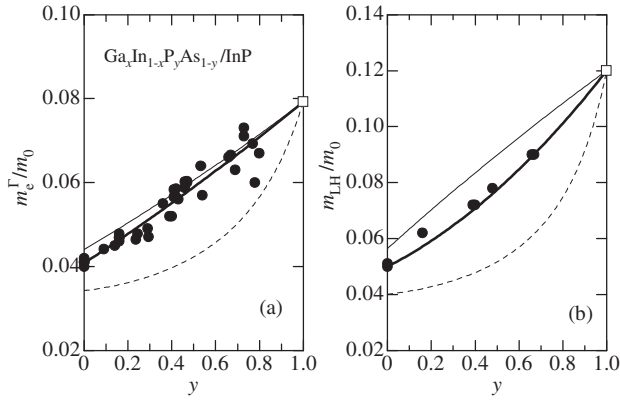


Figure 7.17 (a) Γ -valley electron effective mass m_c^Γ and (b) LH effective mass m_{LH} versus y for $\text{Ga}_x\text{In}_{1-x}\text{P}_y\text{As}_{1-y}/\text{InP}$. The solid and dashed lines are obtained by introducing the binary data into Equations (A.6) and (7.8), respectively. The solid circles show the experimental data taken from Adachi [56]. The heavy solid lines represent the quadratic least-squares fit in Table 7.9 (m_c^Γ) and the result obtained using Equation (7.15) (m_{LH}). The open squares correspond to the InP ($y = 1.0$) data

$$\frac{m_{LH}(y)}{m_0} = 0.05 + 0.04y + 0.03y^2 \quad (7.15)$$

(b) *GaInAsSb*

No experimental data on the carrier effective masses in $\text{Ga}_x\text{In}_{1-x}\text{As}_y\text{Sb}_{1-y}$ has been reported. The linearly interpolated m_c^Γ values for $\text{Ga}_x\text{In}_{1-x}\text{As}_y\text{Sb}_{1-y}$ lattice-matched to GaSb and InAs have therefore been plotted in Figure 7.18. The solid and dashed lines represent the linear interpolation results of Equations (A.6) and (7.8) respectively, using the binary data in

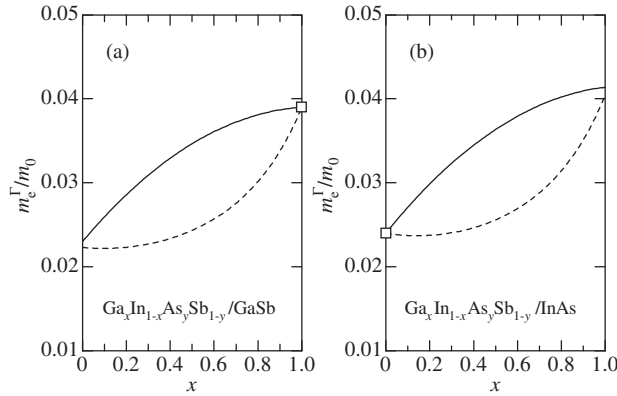


Figure 7.18 Γ -valley electron effective mass m_c^Γ versus x for (a) $\text{Ga}_x\text{In}_{1-x}\text{As}_y\text{Sb}_{1-y}/\text{GaSb}$ and (b) $\text{Ga}_x\text{In}_{1-x}\text{As}_y\text{Sb}_{1-y}/\text{InAs}$. The solid and dashed lines are obtained by introducing the binary data into Equations (A.6) and (7.8), respectively

Table 7.1. The results of $\text{Ga}_x\text{In}_{1-x}\text{P}_y\text{As}_{1-y}/\text{InP}$ in Figure 7.17 support the use of Equation (A.6) for providing more plausible effective masses for III–V semiconductor alloys.

7.4.3 (III, III, III)–V Alloy

(a) AlGaInP

The electron effective mass m_e^Γ in $(\text{Al}_x\text{Ga}_{1-x})_{0.53}\text{In}_{0.47}\text{P}/\text{GaAs}$ has been measured by Emanuelsson *et al.* [8] using conventional and optically detected CR measurements. The result they obtained $m_e^\Gamma/m_0 = 0.14 \pm 0.01$ ($x = 0.3$) is shown in Figure 7.19, together with those calculated from Equations (A.6) and (7.8) using the binary data in Table 7.1 (solid and dashed lines). The experimental data is found to be slightly larger than the interpolated value obtained using Equation (A.6) (solid line). This may be due to X-valley interactions (see Figure 6.49) and/or any effect of band nonparabolicity.

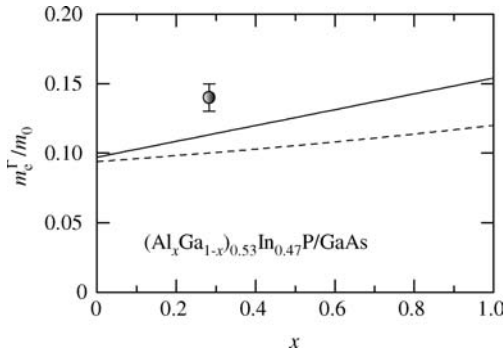


Figure 7.19 Γ -valley electron effective mass m_e^Γ versus x for $(\text{Al}_x\text{Ga}_{1-x})_{0.53}\text{In}_{0.47}\text{P}/\text{GaAs}$. The solid circle represents the experimental data taken from Emanuelsson *et al.* [8]. The solid and dashed lines are obtained by introducing the binary data into Equations (A.6) and (7.8), respectively

(b) AlGaInAs

The Γ -valley electron effective mass m_e^Γ in $(\text{Al}_x\text{Ga}_{1-x})_{0.48}\text{In}_{0.52}\text{As}/\text{InP}$ has been measured by several authors [14,15,57,58]. Figure 7.20 shows these results (solid circles), together with those obtained from Equations (A.6) and (7.8) using the binary data in Table 7.1 (solid and dashed lines). The linear least-squares fit of the experimental data is also shown by the heavy solid line (see also Table 7.9). Equation (A.6) has been found to estimate m_e^Γ more reliably than Equation (7.8).

7.4.4 III–(V, V, V) Alloy

The electron effective mass m_e^Γ in $\text{InP}_x\text{As}_y\text{Sb}_{1-x-y}/\text{InAs}$ has been measured by Voronina *et al.* [59] using various techniques, such as the Shubnikov–de Haas effect, Hall effect, magnetoresistance and photoconductivity. This result is plotted in Figure 7.21 ($x = 0.26, y = 0.62$). The solid and dashed lines show the linear interpolation results of Equations (A.6) and (7.8) respectively, using the binary data in Table 7.1. It can be seen that the experimental data is slightly smaller than the linearly interpolated value derived using Equation (A.6) (solid line).

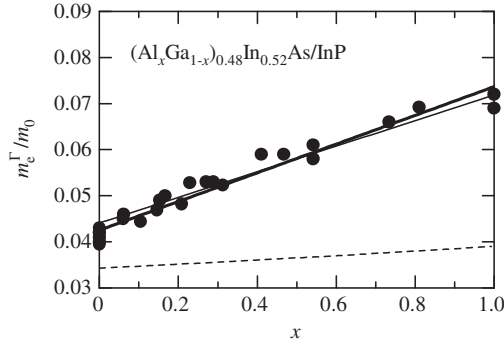


Figure 7.20 Γ -valley electron effective mass m_e^Γ versus x for $(\text{Al}_x\text{Ga}_{1-x})_{0.48}\text{In}_{0.52}\text{As}/\text{InP}$. The solid and dashed lines are obtained by introducing the binary data into Equations (A.6) and (7.8), respectively. The heavy solid line shows the quadratic least-squares fit (see Table 7.9)

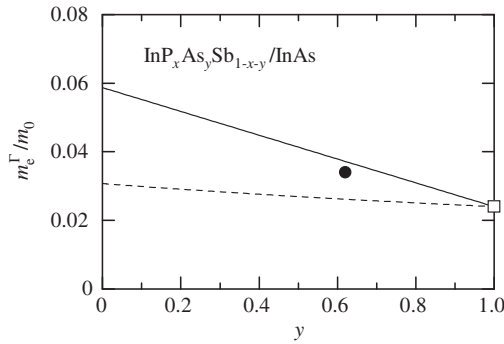


Figure 7.21 Γ -valley electron effective mass m_e^Γ versus x for $\text{InP}_x\text{As}_y\text{Sb}_{1-x-y}/\text{InAs}$. The solid circle represents the experimental data taken from Voronina *et al.* [59]. The solid and dashed lines are obtained by introducing the binary data into Equations (A.6) and (7.8), respectively

7.5 II–VI SEMICONDUCTOR ALLOY

7.5.1 (II, II)–VI Ternary Alloy

Lu *et al.* [60] obtained the electron effective mass m_e^Γ in $\text{Mg}_x\text{Zn}_{1-x}\text{O}$ from analyzing the Burstein–Moss shift. The mass values they obtained are plotted in Figure 7.22(a). The electron effective mass increased with increasing x from $0.30m_0$ ($x=0$) to $0.49m_0$ ($x=0.21$). Note, however, that the ZnO ($x=0$) value is slightly larger than that estimated from the generalized m_e^Γ versus E_0 relationship ($\sim 0.23m_0$) [1].

Figure 7.22(b) shows the Γ -valley electron effective mass m_e^Γ in $c\text{-Zn}_x\text{Cd}_{1-x}\text{Se}$ reported by Imanaka and Miura [61] (solid circle), Lo *et al.* [62] (open circle) and Ng *et al.* [63] (open triangles). We can see that the data of Lo *et al.* is considerably larger than that estimated from the linear interpolation scheme (solid and dashed lines). Shao *et al.* [64] also determined the m_e^Γ value in $\text{Zn}_{0.80}\text{Cd}_{0.20}\text{Se}/\text{ZnS}_{0.06}\text{Se}_{0.94}$ QW by Shubnikov–de Haas oscillations. The

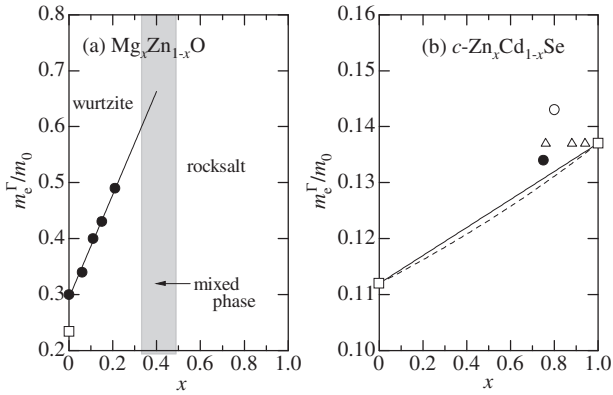


Figure 7.22 (a) Γ -valley electron effective mass m_e^Γ in $Mg_xZn_{1-x}O$. The experimental data are taken from Lu *et al.* [60]. (b) Γ -valley electron effective mass m_e^Γ in $c\text{-}Zn_xCd_{1-x}Se$. The experimental data are taken from Imanaka and Miura [61] (solid circle), Lo *et al.* [62] (open circle) and Ng *et al.* [63] (open triangles). The solid and dashed lines in (b) are obtained by introducing the endpoint binary data into Equations (7.6) and (7.7), respectively. The open squares in (a) and (b) show the endpoint binary data in Table 7.1

value they obtained, $0.17m_0$ ($x = 0.80$) is, however, much larger than the endpoint binary data. The larger m_e^Γ value was considered to be due to the effect of a parallel conduction layer in the sample measured [64].

The Hg-based ternaries $Zn_xHg_{1-x}Te$ and $Cd_xHg_{1-x}Te$ exhibit a semimetallic nature at low x compositions ($E_0 < 0$ eV, see Figure 6.58). The corresponding CB electrons have a negative mass value. The Γ -valley electron effective masses m_e^Γ in $Zn_xHg_{1-x}Te$ and $Cd_xHg_{1-x}Te$ are shown in Figure 7.23. The experimental data for $Zn_xHg_{1-x}Te$ are taken from Shneider and Tsiutsiura [65] and for $Cd_xHg_{1-x}Te$ from Kim and Narita [66] (open triangles) and Laurenti

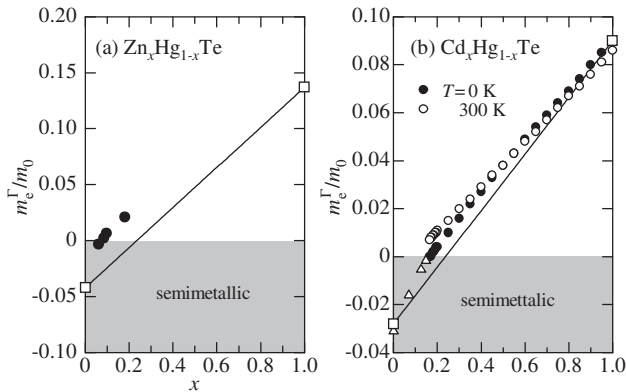


Figure 7.23 Γ -valley electron effective mass m_e^Γ in (a) $Zn_xHg_{1-x}Te$ and (b) $Cd_xHg_{1-x}Te$. The experimental data in (a) are taken from Shneider and Tsiutsiura [65] and in (b) from Kim and Narita [66] (at 4.2 K, open triangles) and Laurenti *et al.* [67] (at 0 K (solid circles) and 300 K (open circles)). The solid lines in (a) and (b) are obtained by introducing the endpoint binary data into Equation (7.6)

et al. [67] ($T = 0$ K (solid circles), 300 K (open circles)). A large difference can be seen between the experimental and linearly interpolated values for $\text{Zn}_x\text{Hg}_{1-x}\text{Te}$. Note that the Hg-based alloys have positive and strongly x -dependent coefficients dE_0/dT at high Hg concentrations (Figure 6.57). The semimetal/semiconductor crossing composition and free-electron concentration then show strong temperature dependence [67–69]. These facts make it difficult to accurately determine the electron effective mass at high Hg concentration. Note also that the lowest CB minimum in a semiconductor region is at the Γ_6 state while that in a semimetal region is at the Γ_8 state (i.e. the LH band in the cubic, zinc-blende semiconductors).

7.5.2 II–(VI, VI) Ternary Alloy

The Γ -valley electron effective mass m_e^Γ in $w\text{-CdS}_x\text{Se}_{1-x}$ has been determined by analyzing optical absorption spectra using a $k\cdot p$ method [70]. These results have been plotted in Figure 7.24. The solid line also shows the linear interpolation result obtained by introducing the endpoint binary data in Table 7.1 into Equation (7.6).

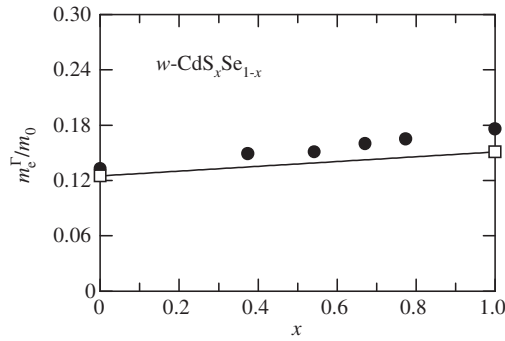


Figure 7.24 Γ -valley electron effective mass m_e^Γ in $w\text{-CdS}_x\text{Se}_{1-x}$. The experimental data are taken from Brodin *et al.* [70]. The solid line is obtained by introducing the endpoint binary data into Equation (7.6)

Brodin *et al.* [70] reported the x -dependent hole effective masses at the three VB states (Γ_9 , Γ_7 and Γ_7). All these hole masses and m_e^Γ (Figure 7.24) increased almost linearly from CdSe ($x = 0$) to CdS ($x = 1.0$).

7.5.3 (II, II)–(VI, VI) Quaternary Alloy

No detailed experimental determinations of the electron or hole effective mass in II–VI quaternary alloys have been carried out. Therefore, the Γ -valley electron effective mass m_e^Γ in $\text{Mg}_x\text{Zn}_{1-x}\text{S}_y\text{Se}_{1-y}/\text{GaAs}$ obtained from the linear interpolation scheme is shown in Figure 7.25. The solid and dashed lines were obtained from Equations (A.6) and (7.8), respectively. The interpolated values show upward bowing. For example, the solid line can be expressed as

$$\frac{m_e^\Gamma(x)}{m_0} = 0.14 + 0.12x - 0.04x^2 \quad (7.16)$$

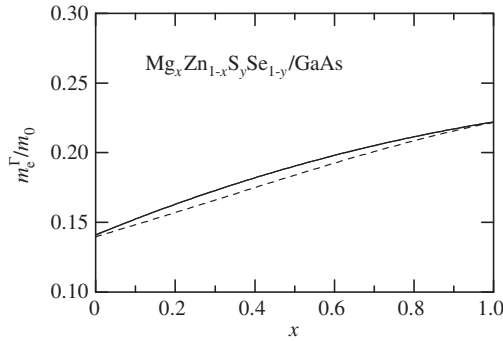


Figure 7.25 Γ -valley electron effective mass m_e^Γ in $\text{Mg}_x\text{Zn}_{1-x}\text{S}_y\text{Se}_{1-y}/\text{GaAs}$. The solid and dashed lines are calculated by introducing the binary data into Equations (A.6) and (7.8), respectively

7.6 CONCLUDING REMARKS

7.6.1 Composition Dependence

The simple three-band $k\cdot p$ theory gives

$$\frac{m_0}{m_e^\Gamma} = 1 + \frac{P^2}{3} \left(\frac{2}{E_0} + \frac{1}{E_0 + \Delta_0} \right) + C \approx \frac{P^2}{E_0} + C' \propto \frac{P^2}{E_0} \quad (7.17)$$

where P is the momentum matrix element relating the p -like VB to the s -like CB and C (C') is a correction for all higher-lying bands. Thus, the Γ -valley electron effective mass m_e^Γ is expected to be proportional to E_0 (see Equations (7.8) and (7.9) in Adachi [1]).

Figure 7.26 plots the E_0 and m_e^Γ versus x for some cubic III–V ternaries. It can be seen that the smaller E_0 -gap material has a smaller m_e^Γ value, as predicted by Equation (7.17). The results in Sections 7.2–7.5 also indicate that linear interpolation (especially Equation (7.6) or Equation (A.6)) is an easy and effective means to obtain the electron and hole effective masses in semiconductor alloys.

7.6.2 External Perturbation Effect

Like the Γ -point energy gaps (E_0 and $E_0 + \Delta_0$), the electron and hole effective masses at the Γ point of non-alloyed semiconductors decrease with increasing temperature (T) and also increase with increasing pressure p [1]. The same tendency can be expected in semiconductor alloys. Laurenti *et al.* [67] observed that increasing T from 0 to 500 K leads to a gradual decrease in the m_e^Γ value of $\text{Cd}_x\text{Hg}_{1-x}\text{Te}$ for $x \geq 0.5$. Similarly, Nicholas *et al.* [42] found that for $\text{InP}_x\text{As}_{1-x}$ ($0 \leq x \leq 1.0$) the value of m_e^Γ was relatively constant from low T up to $T \sim 100$ K and that further increases in T decreased m_e^Γ in an almost proportional manner. The change in the electron effective mass Δm_e^Γ from $T = 0$ to 300 K was less than 8%.

The pressure dependence of the electron effective mass m_e^Γ in $\text{InP}_x\text{As}_{1-x}$ has been measured by Torres and Stradling [44]. These results have been plotted in Figure 7.27. It can be seen that m_e^Γ increases almost linearly with increasing p . Similarly, an increase in m_e^Γ has been observed in $\text{Ga}_{0.47}\text{In}_{0.53}\text{As}$ [71,72] and also in dilute-nitride $\text{Ga}_x\text{In}_{1-x}\text{N}_y\text{As}_{1-y}$ (m_e^*) [73,74].

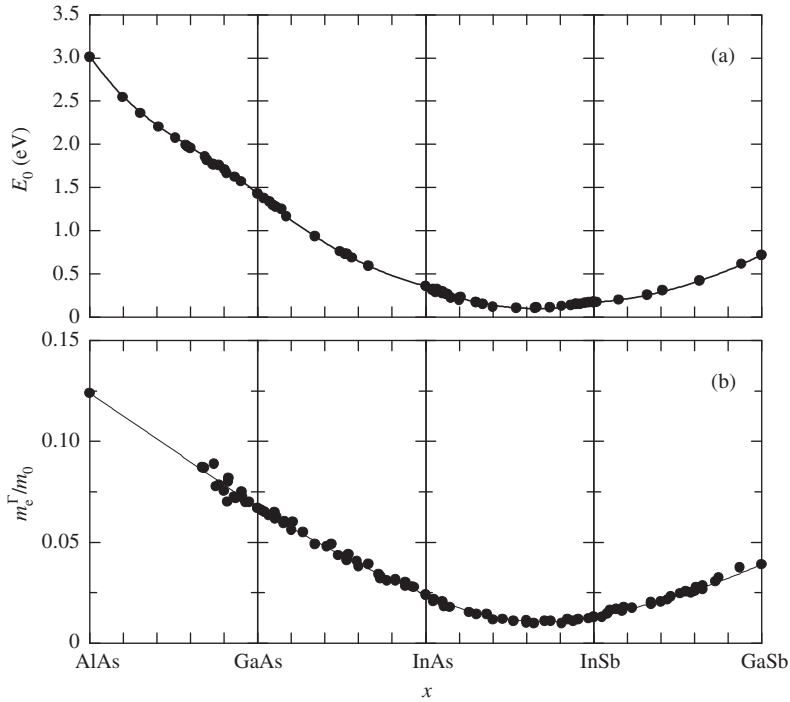


Figure 7.26 (a) Lowest direct gap (E_0) at 300 K and (b) Γ -valley electron effective mass (m_e^Γ) versus composition x for some III-V ternaries. The experimental data are plotted by the solid circles

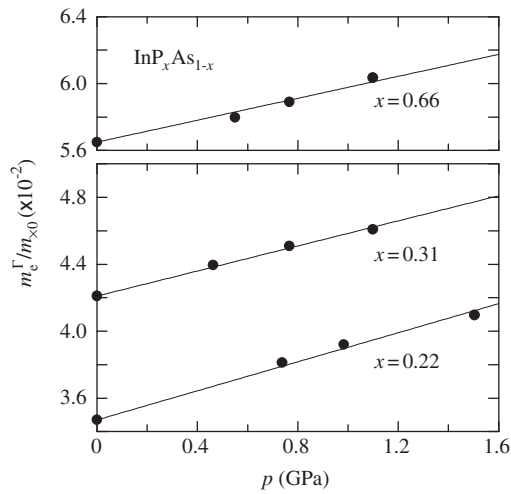


Figure 7.27 Pressure dependence of m_e^Γ in $\text{InP}_x\text{As}_{1-x}$. The experimental data are taken from Torres and Stradling [44]

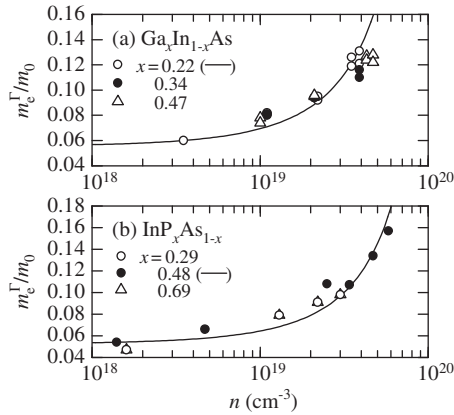


Figure 7.28 Free-electron concentration dependence of m_e^Γ in (a) $\text{Ga}_x\text{In}_{1-x}\text{As}$ and (b) $\text{InP}_x\text{As}_{1-x}$. The experimental data are taken from Metzger *et al.* [75]. The solid lines show the least-squares fits given by (a) $\ln(m_e^\Gamma/m_0) = (2.24 \times 10^{-20})n - 2.89$ ($x = 0.22$) and (b) $\ln(m_e^\Gamma/m_0) = (2.04 \times 10^{-20})n - 2.95$ ($x = 0.48$) with n in cm^{-3} , respectively

The highest VBs and lowest CB of III–V and II–VI semiconductors are nonparabolic. Since the band nonparabolicity becomes significant as the Fermi level moves deep in the band, the electron effective mass in semiconductors increases with doping level for carrier concentrations larger than $\sim 10^{18} \text{ cm}^{-3}$. The dependence of the electron effective mass m_e^Γ on electron concentration in $\text{Ga}_x\text{In}_{1-x}\text{As}$ and $\text{InP}_x\text{As}_{1-x}$ has been reported by Metzger *et al.* [75]. Their results are reproduced in Figure 7.28. The electron effective masses increase abruptly as a function of free-electron density and converge at $n \sim 5 \times 10^{19} \text{ cm}^{-3}$. They concluded that the Kane's band model offers an accurate description of CB nonparabolicity. An increase in m_e^* with increasing free-electron density has also been observed in dilute-nitride $\text{Ga}_x\text{In}_{1-x}\text{N}_y\text{As}_{1-y}$ [74].

REFERENCES

- [1] S. Adachi, *Properties of Group-IV, III–V and II–VI Semiconductors*, John Wiley & Sons, Ltd, Chichester, 2005.
- [2] T. Hofmann, T. Chavdarov, V. Darakchieva, H. Lu, W. J. Schaff, and M. Schubert, *Phys. Status Solidi C* **3**, 1854 (2006).
- [3] D. Fritsch, H. Schmidt, and M. Grundmann, *Phys. Rev. B* **69**, 165204 (2004).
- [4] D. Bimberg, M. Altarelli, and N. O. Lipari, *Solid State Commun.* **40**, 437 (1981).
- [5] D. Fink and R. Braunstein, *Phys. Status Solidi B* **73**, 361 (1976).
- [6] C. W. Liu and V. Venkataraman, *Mater. Chem. Phys.* **49**, 29 (1997).
- [7] J. F. Nützel, C. M. Engelhardt, and G. Abstreiter, in *Properties of Strained and Relaxed Silicon Germanium*, EMIS Datareviews Series No. 12 (edited by E. Kasper), INSPEC, London, 1995, p. 103.
- [8] P. Emanuelsson, M. Drechsler, D. M. Hofmann, and B. K. Meyer, *Appl. Phys. Lett.* **64**, 2849 (1994).
- [9] S. Adachi, in *Properties of Aluminium Gallium Arsenide*, EMIS Datareviews Series No. 7 (edited by S. Adachi), INSPEC, London, 1993, pp. 58–72.

- [10] S. Adachi, *GaAs and Related Materials: Bulk Semiconducting and Superlattice Properties*, World Scientific, Singapore, 1994.
- [11] J. C. Hensel and K. Suzuki, *Phys. Rev. B* **9**, 4219 (1974).
- [12] E. E. Matyas and A. G. Karoza, *Phys. Status Solidi B* **111**, K45 (1982).
- [13] M. G. Wright, A. Kana'ah, B. C. Cavenett, G. R. Johnson, and S. T. Davey, *Semicond. Sci. Technol.* **4**, 590 (1989).
- [14] L. A. Cury, J. Beerens, and J. P. Praseuth, *Appl. Phys. Lett.* **63**, 1804 (1993).
- [15] Y. F. Chen, Y. T. Dai, J. C. Fan, T. L. Lee, and H. H. Lin, *Appl. Phys. Lett.* **67**, 1256 (1995).
- [16] M. B. Thomas and J. C. Woolley, *Can. J. Phys.* **49**, 2052 (1971).
- [17] H. Fetterman, J. Waldman, and C. M. Wolfe, *Solid State Commun.* **11**, 375 (1972).
- [18] C. K. Sarkar, R. J. Nicholas, J. C. Portal, M. Razeghi, J. Chevrier, and J. Massies, *J. Phys. C: Solid State Phys.* **18**, 2667 (1985).
- [19] Y. T. Dai, J. L. Shen, Y. F. Chen, S. Z. Chang, and S. C. Lee, *Chin. J. Phys.* **36**, 20 (1998).
- [20] J. L. Shen, Y. D. Dai, Y. F. Chen, S. Z. Chang, and S. C. Lee, *Phys. Rev. B* **51**, 17648 (1995).
- [21] K. Alavi, R. L. Aggarwal, and S. H. Groves, *Phys. Rev. B* **21**, 1311 (1980).
- [22] R. J. Warburton, R. W. Martin, R. J. Nicholas, L. K. Howard, and M. T. Emeny, *Semicond. Sci. Technol.* **6**, 359 (1991).
- [23] N. J. Traynor, R. J. Warburton, M. J. Snelling, and R. T. Harley, *Phys. Rev. B* **55**, 15701 (1997).
- [24] M. J. Aubin, M. B. Thomas, E. H. van Tongerloo, and J. C. Woolley, *Can. J. Phys.* **47**, 631 (1969).
- [25] A. P. Roth and E. Fortin, *Can. J. Phys.* **56**, 1468 (1978).
- [26] H. P. Xin and C. W. Tu, *Appl. Phys. Lett.* **77**, 2180 (2000).
- [27] P. N. Hai, W. M. Chen, I. A. Buyanova, H. P. Xin, and C. W. Tu, *Appl. Phys. Lett.* **77**, 1843 (2000).
- [28] J. Wu, W. Shan, W. Walukiewicz, K. M. Yu, J. W. Ager III, E. E. Haller, H. P. Xin, and C. W. Tu, *Phys. Rev. B* **64**, 085320 (2001).
- [29] Y. J. Wang, X. Wei, Y. Zhang, A. Mascarenhas, H. P. Xin, Y. G. Hong, and C. W. Tu, *Appl. Phys. Lett.* **82**, 4453 (2003).
- [30] F. Masia, A. Polimeni, G. B. H. von Högersthal, M. Bissiri, P. J. Klar, and W. Stolz, *Appl. Phys. Lett.* **82**, 4474 (2003).
- [31] F. Masia, G. Pettinari, A. Polimeni, M. Felici, A. Miriametro, M. Capizzi, A. Lindsay, S. B. Healy, E. P. O'Reilly, A. Cristofoli, G. Bais, M. Piccin, S. Rubini, F. Martelli, A. Faranciosi, P. J. Klar, K. Volz, and W. Stolz, *Phys. Rev. B* **73**, 073201 (2006).
- [32] Y. Zhang and A. Mascarenhas, *Phys. Rev. B* **61**, 7479 (2000).
- [33] D. L. Young, J. F. Geisz, and T. J. Coutts, *Appl. Phys. Lett.* **82**, 1236 (2003).
- [34] See, for example, M. Henini, *Dilute Nitride Semiconductors*, Elsevier, Amsterdam, 2005.
- [35] W. K. Hung, K. S. Cho, M. Y. Chern, Y. F. Chen, D. K. Shih, H. H. Lin, C. C. Lu, and T. R. Yang, *Appl. Phys. Lett.* **80**, 796 (2002).
- [36] D. R. Hang, C. F. Huang, W. K. Hung, Y. H. Chang, J. C. Chen, H. C. Yang, Y. F. Chen, D. K. Shih, T. Y. Chu, and H. H. Lin, *Semicond. Sci. Technol.* **17**, 999 (2002).
- [37] D. -K. Shih, H. -H. Lin, L. -W. Sung, T. -Y. Chu, and T. -R. Yang, *Jpn. J. Appl. Phys.* **42**, 375 (2003).
- [38] B. N. Murdin, A. R. Adams, P. Murzyn, C. R. Pidgeon, I. V. Bradley, J. -P. R. Wells, Y. H. Matsuda, N. Miura, T. Burke, and A. D. Johnson, *Appl. Phys. Lett.* **81**, 256 (2002).
- [39] C. Wetzel, B. K. Meyer, and P. Omling, *Phys. Rev. B* **47**, 15588 (1993).
- [40] A. Filion and E. Fortin, *Can. J. Phys.* **52**, 743 (1974).
- [41] R. J. Nicholas, R. A. Stradling, and J. C. Ramage, *J. Phys. C: Solid State Phys.* **12**, 1641 (1979).
- [42] R. J. Nicholas, R. A. Stradling, J. C. Portal, and S. Askenazy, *J. Phys. C: Solid State Phys.* **12**, 1653 (1979).
- [43] V. V. Kruzhaev, G. M. Min'kov, and O. É. Rut, *Sov. Phys. Semicond.* **16**, 596 (1982).
- [44] C. M. S. Torres and R. A. Stradling, *Semicond. Sci. Technol.* **2**, 323 (1987).
- [45] T. W. Kim, D. C. Choo, D. U. Lee, M. Jung, and S. O. Kang, *J. Phys. Chem. Solids* **63**, 875 (2002).
- [46] M. B. Thomas and J. C. Woolley, *Can. J. Phys.* **49**, 2056 (1971).

- [47] S. N. Smith, C. C. Phillips, R. H. Thomas, R. A. Stradling, I. T. Ferguson, A. G. Norman, B. N. Murdin, and C. R. Pidgeon, *Semicond. Sci. Technol.* **7**, 900 (1992).
- [48] Z. Pan, L. H. Li, Y. W. Lin, B. Q. Sun, and D. S. Jiang, *Appl. Phys. Lett.* **78**, 2217 (2001).
- [49] J. B. Hérouz, X. Yang, and W. I. Wang, *J. Appl. Phys.* **92**, 4361 (2002).
- [50] M. Hetterich, M. D. Dawson, A. Y. Egorov, D. Bernkiau, and H. Riechert, *Appl. Phys. Lett.* **76**, 1030 (2000).
- [51] C. Skierbiszewski, P. Perlin, P. Wisniewski, W. Knap, T. Suski, W. Walukiewicz, W. Shan, K. M. Yu, J. W. Ager, E. E. Haller, J. F. Geisz, and J. M. Olson, *Appl. Phys. Lett.* **76**, 2409 (2000).
- [52] J. -Y. Duboz, J. A. Gupta, M. Byloss, G. C. Aers, H. C. Liu, and Z. R. Wasilewski, *Appl. Phys. Lett.* **81**, 1836 (2002).
- [53] C. Skierbiszewski and J. Łusakowski, *J. Phys.: Condens. Matter* **16**, S3319 (2004).
- [54] M. H. Gass, A. J. Papworth, T. B. Joyce, T. J. Bullough, and P. R. Chalker, *Appl. Phys. Lett.* **84**, 1453 (2004).
- [55] A. Polimeni, F. Masia, A. Vinattieri, G. B. H. von Högersthal, and M. Capizzi, *Appl. Phys. Lett.* **84**, 2295 (2004).
- [56] S. Adachi, *Physical Properties of III–V Semiconductor Compounds: InP, InAs, GaAs, GaP, InGaAs, and InGaAsP*, John Wiley & Sons, Ltd, New York, 1992.
- [57] D. Olego, T. Y. Chang, E. Silberg, E. A. Caridi, and A. Pinczuk, *Appl. Phys. Lett.* **41**, 476 (1982).
- [58] R. F. Kopf, H. P. Wei, A. P. Perley, and G. Livescu, *Appl. Phys. Lett.* **60**, 2386 (1992).
- [59] T. I. Voronina, T. S. Lagunova, K. D. Moiseev, M. A. Sipovskaya, I. N. Timchenko, and Y. P. Yakovlev, *Semicond.* **27**, 978 (1993).
- [60] J. G. Lu, S. Fujita, T. Kawaharamura, H. Nishinaka, Y. Kamada, and T. Ohshima, *Appl. Phys. Lett.* **89**, 262107 (2006).
- [61] Y. Imanaka and N. Miura, *Physica B* **249–251**, 932 (1998).
- [62] I. Lo, S. J. Chen, L. -W. Tu, W. C. Mitchel, R. C. Tu, and Y. K. Su, *Phys. Rev. B* **60**, R11281 (1999).
- [63] H. K. Ng, Y. A. Leem, R. Knobel, I. P. Smorchkova, A. A. Sirenko, and N. Samarth, *Appl. Phys. Lett.* **75**, 3662 (1999).
- [64] H. Shao, S. Scholl, H. Schäfer, J. Gerschütz, B. Jobst, D. Hommel, and G. Landwehr, *Solid State Commun.* **100**, 739 (1996).
- [65] A. D. Shneider and D. I. Tsiutsiura, *Phys. Status Solidi A* **5**, K39. (1971).
- [66] R. S. Kim and S. Narita, *Phys. Status Solidi B* **73**, 741 (1976).
- [67] J. P. Laurenti, J. Camassel, A. Bouhemadou, B. Toulouse, R. Legros, and A. Lussion, *J. Appl. Phys.* **67**, 6454 (1990).
- [68] J. Chu, Z. Mi, and D. Tang, *Infrared Phys.* **32**, 195 (1991).
- [69] Y. -G. Sha, C. -H. Su, and S. L. Lehoczky, *J. Appl. Phys.* **81**, 2245 (1997).
- [70] M. S. Brodin, M. V. Kurik, and S. P. Yurtsenyuk, *Sov. Phys. Solid State* **7**, 2516 (1966).
- [71] D. Gauthier, L. Dmowski, J. C. Portal, D. Leadley, M. A. Hopkins, M. A. Brummell, R. J. Nicholas, M. Razeghi, and P. Maurel, *Superlatt. Microstruct.* **4**, 201 (1988).
- [72] S. Charlebois, J. Beerens, C. J. Miner, and N. Puetz, *Phys. Rev. B* **54**, 13456 (1996).
- [73] C. Skierbiszewski, P. Erlin, P. Wisniewski, T. Suski, J. F. Geisz, K. Hingerl, W. Jantsch, D. E. Mars, and W. Walukiewicz, *Phys. Rev. B* **65**, 035207 (2001).
- [74] C. Skierbiszewski, *Semicond. Sci. Technol.* **17**, 803 (2002).
- [75] W. K. Metzger, M. W. Wanlass, L. M. Gedvilas, J. C. Verley, J. J. Carapella, and R. K. Ahrenkiel, *J. Appl. Phys.* **92**, 3524 (2002).

8 Deformation Potentials

8.1 INTRAVALLEY DEFORMATION POTENTIAL: Γ POINT

8.1.1 Group-IV Semiconductor Alloy

A review of the various DPs is given in Adachi [1]. The Γ -valley DPs ($a_c^\Gamma = E_1^\Gamma$ and D_i) in the CB of some non-alloyed $A^N B^{8-N}$ tetrahedral semiconductors are summarized in Tables 8.1 and 8.2. Tables 8.3 and 8.4 also summarize the Γ -point DPs a , b , d and C_i in the VB for some cubic and wurtzite semiconductors, respectively.

Table 8.1 Intravalley deformation potential, $a_c^\Gamma = E_1^\Gamma$, for electrons at the Γ point of some cubic group-IV, III-V and II-VI semiconductors. d = diamond; zb = zinc-blende

System	Material	a_c^Γ (eV)	System	Material	a_c^Γ (eV)
IV	Diamond (d)	-30.7 ^{a,b}	II-VI	ZnS (zb)	-4.09 ^b
	Si (d)	-15.3 ^{a,b}		ZnSe (zb)	-4.17 ^b
	Ge (d)	-8.24 ^{a,b}		ZnTe (zb)	-5.83 ^b
	α -Sn (d)	-13.7 ^{a,b}		CdS (zb)	-27.1 ^b
	3C-SiC (zb)	-7.50 ^b		CdSe (zb)	-11.0 ^b
				CdTe (zb)	-3.96 ^b
III-V	BN (zb)	-36.5 ^b		HgTe (zb)	-4.60 ^b
	BP (zb)	-13.3 ^b			
	AlN (zb)	-11.7 ^b			
	AlP (zb)	-5.54 ^b			
	AlAs (zb)	-5.64 ^b			
	AlSb (zb)	-6.97 ^b			
	GaN (zb)	-21.3 ^b			
	GaP (zb)	-7.14 ^b			
	GaAs (zb)	-11.0			
	GaSb (zb)	-9			
	InP (zb)	-11.4			
	InAs (zb)	-10.2			
	InSb (zb)	-15			

^a $\Gamma_{2'}$ -conduction band

^bCalculated

No experimental determinations of the intravalley DPs in the Γ valley for group-IV semiconductor alloys appear to be available. The interpolated DPs for $\text{Si}_x\text{Ge}_{1-x}$ obtained by

Table 8.2 Intravalley deformation potentials, D_1 and D_2 , for electrons at the Γ point of some wurtzite III–V semiconductors

System	Material	D_1 (eV)	D_2 (eV)
III–V	AlN	-10.23^a	-9.65^a
	GaN	-9.47^a	-7.17^a

^aCalculated**Table 8.3** Deformation potentials, a , b and d , for holes at the Γ point of some cubic group-IV, III–V and II–VI semiconductors. d = diamond; zb = zinc-blende

System	Material	a (eV)	b (eV)	d (eV)
IV	Diamond (d)	-36.1^a	-11.1^a	
	Si (d)	-5	-2.3	-5.3
	Ge (d)	-5.2	-2.4	-4.8
	α -Sn (d)	-3.3^a	-2.3	-4.1
	3C-SiC (zb)	4.30^a	-2.20^a	-6.26^a
III–V	BN (zb)	-7.3^a	-3.41^a	-3.75^a
	BP (zb)	4.2^a	-4.9^a	
	BAs (zb)		-4.5^a	
	AlN (zb)	-5.9^a	-1.7^a	-4.4^a
	AlP (zb)	3.15^a	-1.5^a	
	AlAs (zb)	-2.6^a	-2.3^a	
	AlSb (zb)	1.38^a	-1.35	-4.3
	GaN (zb)	-13.33^a	-2.09^a	-1.75^a
	GaP (zb)	1.70^a	-1.7	-4.4
	GaAs (zb)	-0.85	-1.85	-5.1
	GaSb (zb)	0.79^a	-2.4	-5.4
	InP (zb)	-0.6	-1.7	-4.3
	InAs (zb)	1.00^a	-1.8	-3.6
	InSb (zb)	0.36^a	-2.0	-5.4
II–VI	MgSe (zb)	-1.0^a	-1.27^a	
	ZnS (zb)	2.31^a	-1.1	-4.4
	ZnSe (zb)	1.65^a	-1.8	-5.0
	ZnTe (zb)	0.79^a	-1.4	-4.4
	CdS (zb)	0.92^a	-4.7	
	CdSe (zb)	-8.9^a	-0.8	
	CdTe (zb)	0.55^a	-1.0	-4.4
	HgS (zb)		-1.24^a	
	HgSe (zb)		-1.16^a	
	HgTe (zb)	-0.13^a	-1.5	-8.0

^aCalculated

Table 8.4 Deformation potential C_i for holes at the Γ point of some wurtzite III–V and II–VI semiconductors (in eV)

System	Material	C_1	D_1-C_1	C_2	D_2-C_2	C_3	C_4	C_5	C_6
III–V	AlN	-12.9^a		-8.4^a		4.5^a	-2.2^a	-2.6^a	-4.1^a
	GaN	-41.4	-3.1	-33.3	-11.2	8.2	-4.1	-4.7	
	InN		-4.05^a		-6.67^a	4.92^a	-1.79^a		
II–VI	ZnO		-3.90		-4.13	1.15	-1.22	-1.53	2.88
	CdS		-1.36		-2.28	1.54	-2.34	-1.20	
	CdSe		-0.76		-3.7	4.0	-2.2	1.2	3.0

^aCalculated

introducing the Si and Ge values in Tables 8.1 and 8.3 into Equation (A.16) are therefore plotted in Figure 8.1. The solid circles in Figure 8.1(b) show the theoretical b values obtained by Schmid *et al.* [2]. Rieger and Vogl [3] also reported the theoretical b versus x data for $\text{Si}_x\text{Ge}_{1-x}$, which vary from -2.1 ($x = 0$) to -2.3 eV ($x = 1.0$).

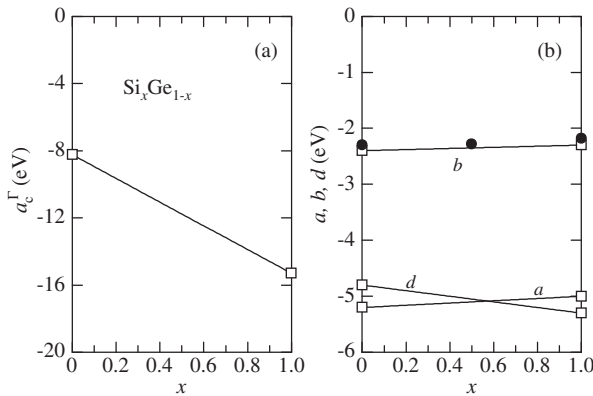


Figure 8.1 (a) CB DP a_c^Γ and (b) VB DPs a , b and d for $\text{Si}_x\text{Ge}_{1-x}$. The solid lines are obtained by introducing the endpoint elemental data into Equation (A.16). The solid circles in (b) show the theoretical b values calculated by Schmid *et al.* [2]

The E_0 -gap DP a_0^Γ for some non-alloyed group-IV, III–V and II–VI semiconductors is listed in Table 8.5. Schmid *et al.* [2] reported a theoretical a_0^Γ value of -11.5 eV for $\text{Si}_{0.5}\text{Ge}_{0.5}$. No experimental data are available for group-IV semiconductor alloys.

8.1.2 III–V Semiconductor Ternary Alloy

(a) AlGaN

The E_0 -gap DP a_0^Γ can be simply obtained if the pressure coefficient dE_0/dp and bulk modulus B_u are available [1]. The pressure coefficient for $w\text{-Al}_x\text{Ga}_{1-x}\text{N}$ has been measured by

Table 8.5 Hydrostatic deformation potential a_0^Γ for the E_0 gap of some cubic and hexagonal semiconductors. d = diamond; zb = zinc-blende; w = wurtzite

System	Material	a_0^Γ (eV)	System	Material	a_0^Γ (eV)
IV	Diamond (d)	$-27^{a,b}$	II-VI	MgSe (zb)	-4.2^b
	Si (d)	$-11.84^{a,b}$		ZnO (w)	-3.51 (A)
	Ge (d)	-9.8^a			-3.59 (B)
	α -Sn (d)	$-7.04^{a,b}$			-3.81 (C)
	3C-SiC (zb)	-11.5^b		ZnS (zb)	-5.2
		ZnS (w)		-4.7^b	
III-V	BP (zb)	-17.5^b		ZnSe (zb)	-5.1
	AlN (zb)	-9.5^b		ZnTe (zb)	-5.3
	AlN (w)	-10.3^b		CdS (zb)	0.43^b
	AlP (zb)	-9.52^b		CdS (w)	-2.9
	AlAs (zb)	-8.93^b	CdSe (zb)	0.80^b	
	AlSb (zb)	-5.9	CdSe (w)	-2.3	
	GaN (zb)	-9.0^b	CdTe (zb)	-2.9	
	GaN (w)	-8.8	HgS (zb)	-2.16^b	
	GaP (zb)	-9.3	HgSe (zb)	-2.15^b	
	GaAs (zb)	-8.8	HgTe (zb)	-3.69	
	GaSb (zb)	-8.3			
	InN (w)	-4.2^b			
	InP (zb)	-6.0			
	InAs (zb)	-6.3			
	InSb (zb)	-7.0			

 $a_{25}^{\Gamma_2} - \Gamma_2^c$ gap^bCalculated or estimated

Shan *et al.* [4]. The x -dependent B_u value for this alloy can be easily obtained by introducing the AlN and GaN values in Table 3.22 of Adachi [1] into the linear interpolation expression. The results obtained are shown in Figure 8.2(a).

(b) GaInN

The pressure coefficient dE_0/dp for w -Ga _{x} In _{$1-x$} N has been measured by Li *et al.* [5] and also discussed both theoretically and experimentally by Franssen *et al.* [6]. Figure 8.2(b) shows the a_0^Γ versus x plots for w -Ga _{x} In _{$1-x$} N obtained using the same procedure as in Figure 8.2(a).

(c) AlInP

Figure 8.3(a) shows the shear DPs b and d versus x for Al _{x} In _{$1-x$} P. Ishitani *et al.* [7] determined the shear DP $b = -1.67 \pm 0.26$ eV for Al _{x} In _{$1-x$} P ($0.43 \leq x \leq 0.62$) grown on GaAs(100) by MOCVD using PR. This value is plotted in Figure 8.3(a) by the solid circle. The linear interpolation scheme is found to give satisfactory agreement with the experimental data.

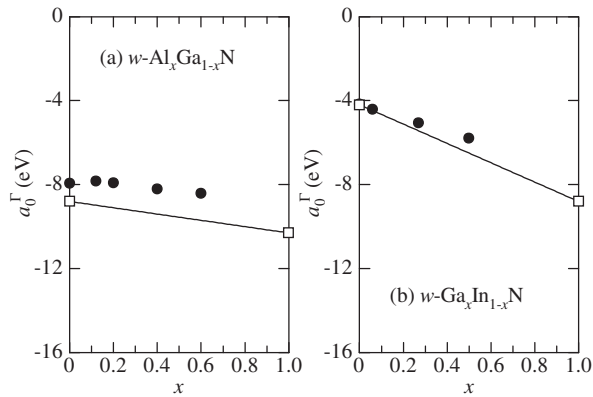


Figure 8.2 a_0^Γ for (a) $w\text{-Al}_x\text{Ga}_{1-x}\text{N}$ and (b) $w\text{-Ga}_x\text{In}_{1-x}\text{N}$. The solid circles are deduced from the experimental dE_0/dp data of (a) Shan *et al.* [4] and (b) Li *et al.* [5]. The solid lines are obtained by introducing the endpoint binary data into Equation (A.4)

(d) GaInP

The shear DPs b and d versus x for $\text{Ga}_x\text{In}_{1-x}\text{P}$ are shown plot in Figure 8.3(b). The solid circle represents the experimental data $d = -4.0 \pm 0.2$ eV taken from Bolkhovityanov *et al.* [8]. This data deviates slightly from the linear interpolation result.

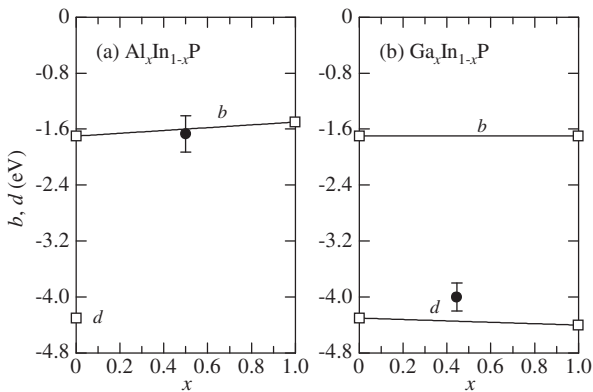


Figure 8.3 Shear DPs b and d for (a) $\text{Al}_x\text{In}_{1-x}\text{P}$ and (b) $\text{Ga}_x\text{In}_{1-x}\text{P}$. The experimental data in (a) are taken from Ishitani *et al.* [7] and in (b) from Bolkhovityanov *et al.* [8]. The solid lines are obtained by introducing the endpoint binary data into Equation (A.4)

(e) AlGaAs

Figure 8.4(a) shows the DPs a , b and d for $\text{Al}_x\text{Ga}_{1-x}\text{As}$. The experimental data are taken from Qiang *et al.* [9,10]. The solid lines (a and b) show the linear interpolation results obtained by introducing the GaAs ($x=0$) and AlAs ($x=1.0$) values in Table 8.3 into Equation (A.4).

Figure 8.4(b) shows the E_0 -gap DP a_0^Γ for $\text{Al}_x\text{Ga}_{1-x}\text{As}$. The solid circles are obtained from the experimental data for dE_0/dp (Figure 6.21(b)) using the same procedure as in Figure 8.2(a). The a_0^Γ value is found to be -8.9 eV, i.e. independent of x .

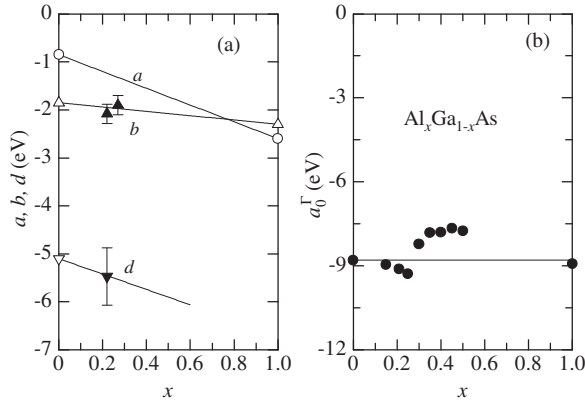


Figure 8.4 (a) DPs a , b and d and (b) a_0^Γ for $\text{Al}_x\text{Ga}_{1-x}\text{As}$. The experimental data in (a) are taken from Qiang *et al.* [9,10]. The a_0^Γ values in (b) are deduced from the experimental dE_0/dp data in Figure 6.21(b). The solid lines for a and b in (a) are obtained by introducing the endpoint binary data into Equation (A.4)

(f) *AllnAs*

The DPs a , b and d for $\text{Al}_x\text{In}_{1-x}\text{As}$ are shown in Figure 8.5(a). The experimental data are taken from Yeh *et al.* [11] (open circle) and Pavesi *et al.* [12] (solid circle). The E_0 -gap DP values a_0^Γ measured by Pavesi *et al.* [12] (solid circle) and Ferguson *et al.* [13] (solid triangle) are also shown in Figure 8.5(b), together with the endpoint binary data (open squares).

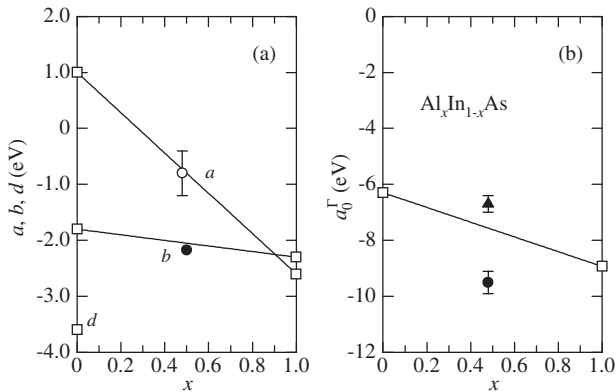


Figure 8.5 (a) DPs a , b and d and (b) a_0^Γ for $\text{Al}_x\text{In}_{1-x}\text{As}$. The solid lines in (a) and (b) are obtained by introducing the endpoint binary data into Equation (A.4). The open circle in (a) represents the experimental data of Yeh *et al.* [11], while the solid circles in (a) and (b) are taken from Pavesi *et al.* [12]. The solid triangle in (b) also shows the experimental data of Ferguson *et al.* [13]

(g) GaInAs

Figure 8.6 shows the E_0 -gap DP a_0^Γ versus x for $\text{Ga}_x\text{In}_{1-x}\text{As}$. The experimental data obtained by People *et al.* [14] for $x = 0.47$ is shown in Figure 8.5(b) by the solid circle, together with the endpoint binary data (open squares). These data give the following quadratic least-squares fit (in eV)

$$a_0^\Gamma(x) = -6.3 - 3.8x + 1.3x^2 \quad (8.1)$$

Wilkinson *et al.* [15] reported the x -dependent a_0^Γ value for $\text{Ga}_x\text{In}_{1-x}\text{As}$ to be $a_0^\Gamma = -7.99 - 3.76x$ eV. However, the InAs value, $a_0^\Gamma = -7.99$ eV, obtained from this expression predicts a considerably large pressure coefficient $dE_0/dp \sim 1.4 \times 10^{-1}$ eV/GPa. A pressure coefficient as large as this has never been reported in the literature. (Only values in the range of $dE_0/dp = -(9.56-11.4) \times 10^{-2}$ eV/GPa have been reported in the literature [16]).

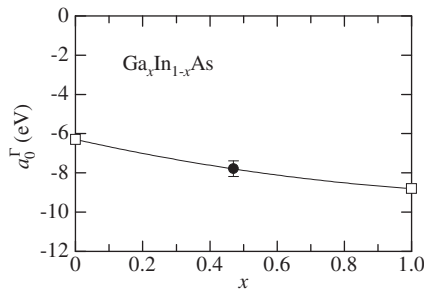


Figure 8.6 a_0^Γ for $\text{Ga}_x\text{In}_{1-x}\text{As}$. The solid circle shows the experimental data of People *et al.* [14]. The solid line represents the calculated result using Equation (8.1)

(h) GaNAs

The shear DP b for dilute-nitride $\text{GaN}_x\text{As}_{1-x}$ has been determined using ER [17] and PR [18]. The data obtained by Zhang *et al.* [17] (solid circles) and Ya *et al.* [18] (open circles) are shown in Figure 8.7. These data show a surprising bowing in a small range of alloy compositions and exhibit a minimum at $x \sim 1.7$ at%. The quadratic least-squares fit of these data can be written as

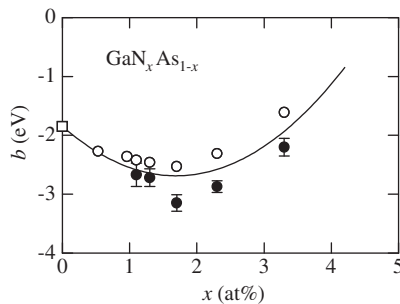


Figure 8.7 Shear DP b for dilute-nitride $\text{GaN}_x\text{As}_{1-x}$. The experimental data are obtained from Zhang *et al.* [17] (solid circles) and Ya *et al.* [18] (open circles). The solid line shows the calculated result using Equation (8.2)

(b in eV, x in at%)

$$b(x) = -1.85 - 0.99x + 0.29x^2 \tag{8.2}$$

The results contradict the currently held view that the CB is greatly altered but the VB is only weakly perturbed by dilute N doping of III–V semiconductors.

(i) *GaPAs*

The DPs a , b and d for $\text{GaP}_x\text{As}_{1-x}$ are shown in Figure 8.8. The solid circles represent the experimental b values obtained by González *et al.* [19]. It can be seen that the linear interpolation scheme traces the experimental DP data very well.

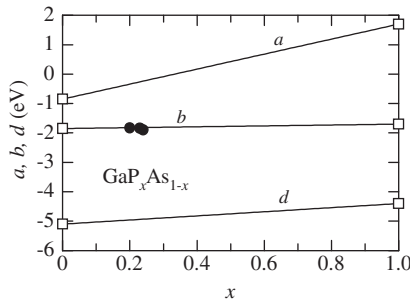


Figure 8.8 DPs a , b and d for $\text{GaP}_x\text{As}_{1-x}$. The solid circles show the experimental data reported by González *et al.* [19]. The solid lines are obtained by introducing the endpoint binary data into Equation (A.4)

8.1.3 III–V Semiconductor Quaternary Alloy

There has been no detailed experimental data relating to a , b or d for any III–V quaternary. Therefore, the linearly interpolated a , b and d values for $\text{Ga}_x\text{In}_{1-x}\text{P}_y\text{As}_{1-y}/\text{InP}$ using Equation (A.6) are plotted in Figure 8.9(a). The DPs a and d show upward bowing against y , while b varies almost linearly with y .

Figure 8.9(b) shows the E_0 -gap DP a_0^Γ versus y for $\text{Ga}_x\text{In}_{1-x}\text{P}_y\text{As}_{1-y}/\text{InP}$. The solid circles represent the experimental data obtained from the pressure coefficients dE_0/dp (Figure 6.46(b)) using the same procedure as in Figure 8.2(a). The solid line represents the linearly interpolated a_0^Γ values obtained by introducing the binary data into Equation (A.6). The experimental a_0^Γ values for $\text{Ga}_x\text{In}_{1-x}\text{P}_y\text{As}_{1-y}/\text{InP}$ are found to be well interpreted by the linear interpolation expression (in eV)

$$a_0^\Gamma(x) = -7.6 + 1.6x \tag{8.3}$$

8.1.4 II–VI Semiconductor Alloy

The shear DPs b and d versus x for $\text{Zn}_x\text{Cd}_{1-x}\text{Te}$ are shown in Figure 8.10. The solid circle shows the experimental value $b = -1.07 \pm 0.06$ eV for $x = 0.605$ determined by Pelhos *et al.* [20].

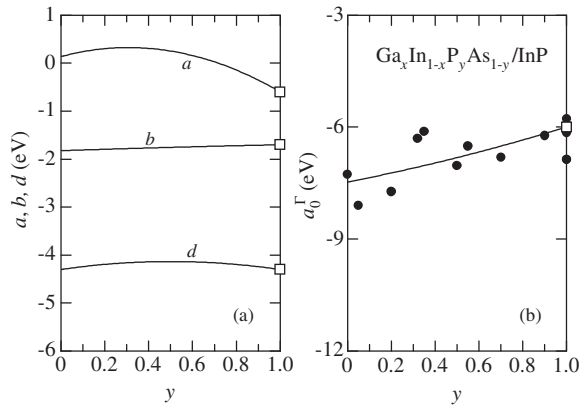


Figure 8.9 (a) DPs a , b and d and (b) a_0^Γ for $\text{Ga}_x\text{In}_{1-x}\text{P}_y\text{As}_{1-y}/\text{InP}$. The solid circles in (b) are deduced from the experimental dE_0/dp data in Figure 6.46(b). The solid lines in (a) and (b) are obtained by introducing the binary data into Equation (A.6)

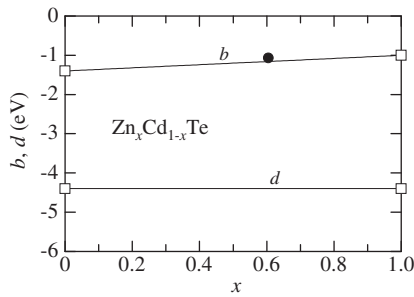


Figure 8.10 Shear DPs b and d for $\text{Zn}_x\text{Cd}_{1-x}\text{Te}$. The solid circle shows the experimental data reported by Pelhos *et al.* [20]. The solid lines are obtained by introducing the endpoint binary data into Equation (A.4)

The pressure coefficient dE_0/dp has been measured on some II–VI semiconductor alloys, such as w - $\text{Mg}_x\text{Zn}_{1-x}\text{O}$ [21], w - $\text{Zn}_x\text{Cd}_{1-x}\text{S}$ [22], c - $\text{ZnO}_x\text{Se}_{1-x}$ [23], $\text{ZnS}_x\text{Se}_{1-x}$ [24], $\text{ZnS}_x\text{Te}_{1-x}$ [25] and $\text{ZnSe}_x\text{Te}_{1-x}$ [26]. By introducing these pressure coefficients and interpolated B_u values (Tables 3.17 and 3.22 in Adachi [1]) into Equation (8.14) of Adachi [1], a_0^Γ for such II–VI semiconductor alloys can be obtained.

8.2 INTRAVALLEY DEFORMATION POTENTIAL: HIGH-SYMMETRY POINTS

8.2.1 Group-IV Semiconductor Alloy

The L-valley DPs for some non-alloyed A^NB^{8-N} tetrahedral semiconductors are summarized in Tables 8.6–8.8. Table 8.9 also summarizes the X (Δ)-valley DPs for some non-alloyed group-IV and III–V semiconductors.

Table 8.6 Hydrostatic E_1 and shear deformation potentials E_2 for electrons at the L point of some cubic group-IV and III-V semiconductors

System	Material	E_1 (eV)	E_2 (eV)	System	Material	E_1 (eV)	E_2 (eV)
IV	Si	-3.1 ^a	18.0 ^a	III-V	c-BN		27.9 ^a
	Ge	-3.8	15.9		c-AlN		25.5 ^a
			AlAs		-4.2 ^b		
			β -GaN			27.5 ^a	
			GaAs		-2	14.5	
			GaSb		-3.2	17.5	

^aCalculated

^bEstimated

Table 8.7 Deformation potentials, D_3^5 and D_3^3 , for holes at the L point of some cubic group-IV, III-V and II-VI semiconductors determined experimentally

System	Material	D_3^5 (eV)	D_3^3 (eV)	System	Material	D_3^5 (eV)	D_3^3 (eV)
IV	Si	4.3	4.6	II-VI	ZnSe	-27	-17
	Ge	3.7	-5.6 (E_1) -6.2 ($E_1 + \Delta_1$)		ZnTe	-15	-29
III-V	GaAs	-6.4	-5.4				
	InP	-12.9	-4.1				

Table 8.8 Hydrostatic D_1^1 ($= \sqrt{3}a_1^L$) and interband deformation potentials D_1^5 for the E_1 and $E_1 + \Delta_1$ gaps of some cubic group-IV, III-V and II-VI semiconductors determined experimentally

System	Material	D_1^1 (eV)	D_1^5 (eV)
IV	Si	-9.0	9
	Ge	-8.7	12.2
III-V	GaAs	-8.3	12.0
	GaSb	-12.3 (E_1) -17.7 ($E_1 + \Delta_1$)	7.4 (E_1)
	InP	-9.2	20.4
	InSb	-7.4 (E_1) -8.5 ($E_1 + \Delta_1$)	-7.4 (E_1) -6.5 ($E_1 + \Delta_1$)
II-VI	ZnSe	-5.8	30
	ZnTe	-5.5	40

Table 8.9 Hydrostatic E_1 and shear deformation potentials E_2 for electrons at the X point of some cubic group-IV and III–V semiconductors

System	Material	E_1 (eV)	E_2 (eV)	System	Material	E_1 (eV)	E_2 (eV)
IV	Si	4.2	9.6	III–V	<i>c</i> -BN		17.9 ^a
	Ge	5.75 ^a	9.75 ^a		<i>c</i> -AlN	-5.5 ^a	6.6 ^a
			AlP		1.81 ^a	6.75 ^a	
			AlAs		1.20	6.9	
			AlSb			5.4	
			β -GaN		-6.8 ^a	7.1 ^a	
			GaP		2.7	6.3	
			GaAs		1.05 ^b	6.5	
			GaSb		1.99 ^a	6.46 ^a	
			InP		1.85 ^a	3.3 ^a	
			InAs		1.59 ^a	3.7 ^a	
			InSb		1.56 ^a	4.53 ^a	

^aCalculated

^bEstimated

Although there have been several theoretical studies on the DPs at the high-symmetry points of $\text{Si}_x\text{Ge}_{1-x}$ [2,3], no experimental determinations appear to be available for any group-IV semiconductor alloy. Figure 8.11 shows the linearly interpolated L- and X-valley DPs $E_1(\text{L})$ and $E_1(\text{X})$ at the CB, respectively, obtained by introducing the Si and Ge values in Tables 8.6 and 8.9 into Equation (A.16). The crossing of the lowest-lying CB states from the L point to the X (Δ) point can be seen at $x \sim 0.15$ (Figure 6.8). Thus, the nature of the conduction electron in $\text{Si}_x\text{Ge}_{1-x}$ changes from ‘Ge-like’ to ‘Si-like’ at $x \sim 0.15$.

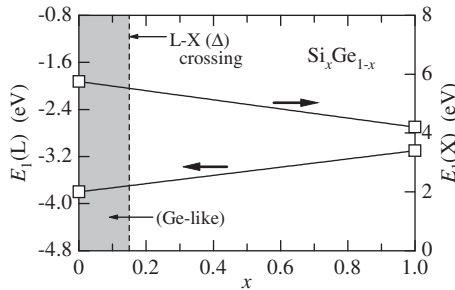


Figure 8.11 L- and X-valley DPs $E_1(\text{L})$ and $E_1(\text{X})$ at the CB for $\text{Si}_x\text{Ge}_{1-x}$. The solid lines are obtained by introducing the endpoint elemental data into Equation (A.16). The dashed line indicates the L–X (Δ) crossing composition $x_c \sim 0.15$

8.2.2 III–V Semiconductor Alloy

Figure 8.12 shows the X-valley DP E_1 in the CB versus x for $\text{Al}_x\text{Ga}_{1-x}\text{As}$. The experimental data are taken from Adachi [27]. These data provide the following x variation: $E_1 = 1.05 + 0.15x$ eV. The solid line in Figure 8.12 shows the result of this variation.

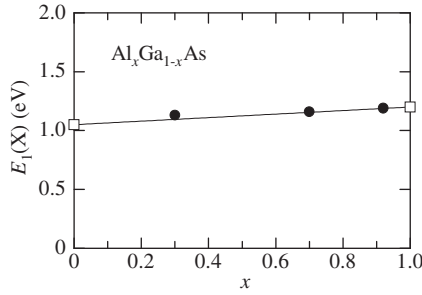


Figure 8.12 X-valley DP E_1 in the CB for $\text{Al}_x\text{Ga}_{1-x}\text{As}$. The experimental data are taken from Adachi [27]. The solid line shows the linearly interpolated result using the endpoint binary data

Figure 8.13 plots the L-valley DP D_3^3 in the VB for $\text{GaP}_x\text{As}_{1-x}$. The solid circles show the experimental data obtained by González *et al.* [19] determined using ER. The solid line represents the calculated result of $D_3^3 = -5.4 + 5.0x$ eV. This expression predicts a GaP ($x = 1.0$) value of -0.4 eV. The experimental D_3^5 and D_3^3 values reported for non-alloyed A^NB^{8-N} tetrahedral semiconductors are limited to Si, Ge, GaAs, InP, ZnSe and ZnTe (Table 8.7, see also Adachi [16,28,29]).

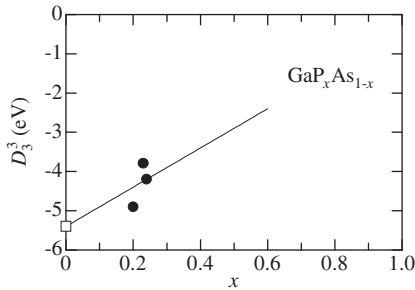


Figure 8.13 L-valley DP D_3^3 in the VB for $\text{GaP}_x\text{As}_{1-x}$. The solid circles show the experimental data of González *et al.* [19]. The solid line represents the calculated result of $D_3^3 = -5.4 + 5.0x$ eV

8.2.3 II–VI Semiconductor Alloy

No detailed data are available for II–VI semiconductor alloys.

8.3 INTERVALLEY DEFORMATION POTENTIAL

8.3.1 Group-IV Semiconductor Alloy

The intervalley DPs for some non-alloyed group-IV, III–V and II–VI semiconductors are summarized in Tables 8.10 and 8.11. Unfortunately, no detailed data are available for group-IV semiconductor alloys.

Table 8.10 Intervalley deformation potential D_{ij} for electrons in some cubic group-IV, III-V and II-VI semiconductors (in eV/Å)

System	Material	$D_{\Gamma L}$	$D_{\Gamma X}^a$	D_{LL}	D_{XX}	D_{LX}
IV	Diamond				8.0	
	Si			2.63	0.15–4.0	4.0
	Ge	2.0	10.0	0.2–3.0	0.79–9.5	4.1
III-V	AlP	5.0	5.0	0.3–1.0	8.1	
	AlAs	1.6–2.3	3.1	1.6	4.7	0.4–1.7
	AlSb	2.3–3.4	1.3–4.9	0.5–0.6	9.5	0.8–3.7
	GaP	0.7–1.1	0.8–1.1	0.6	3.0	0.4–1.6
	GaAs	1.5–9.5	5.2–15	5	10	2.75–3.1
	GaSb	2.7–2.8	2.5–4.5	0.6–1.2	6.0	1.0–2.2
	InP	1.3–2.7	1.6	0.3–0.9	3.6	0.7–3.3
	InAs	1.0–2.0	2.0–2.2	1.1	2.5	0.6–1.9
	InSb	1.1–4.3	3.3–4.9	0.3–0.6	6.8	0.2–2.9
II-VI	β -ZnS	2.18–4.13	1.10–1.89			
	ZnSe	2.17–2.71	0.72–1.37			
	ZnTe	3.19–3.31	1.17–1.43			
	CdTe	1.68–1.76	0.40–1.23			

^a $D_{\Gamma X(1)}$ and $D_{\Gamma X(3)}$

Table 8.11 Intervalley deformation potential D_{ij} for electrons in some hexagonal III-V semiconductors

Material	D_{ij} (eV/Å)	
	Equivalent valley	Nonequivalent valley
w-AlN	10	10
α -GaN	5–10	10
InN	10	10

8.3.2 III-V Semiconductor Alloy

Parker *et al.* [30] observed field-assisted emission from a heterostructure with a GaAs–Al_{0.25}Ga_{0.75}As emitter layer and derived information on hot-electron energy distributions at the low electron density limit. From computer-modeled analysis, they deduced the intervalley coupling constants D_{ij} for Al_{0.25}Ga_{0.75}As. These results are shown in Figure 8.14 together with those for AlAs and GaAs (Table 8.10).

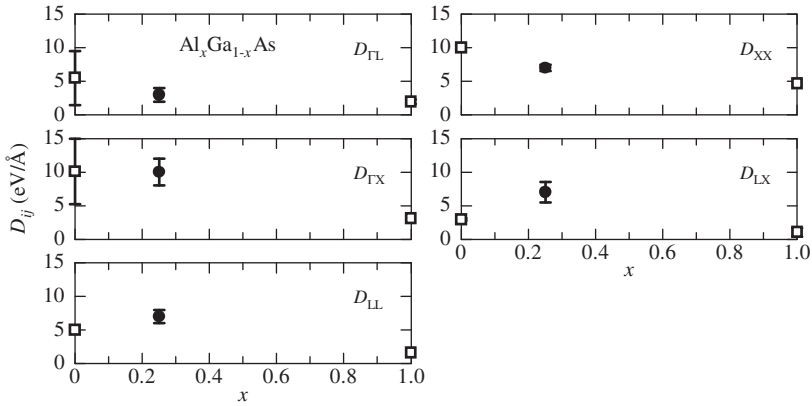


Figure 8.14 Intervalley coupling constants D_{ij} for $Al_xGa_{1-x}As$. The solid circles show the $Al_{0.25}Ga_{0.75}As$ values deduced from field-assisted emission data reported by Parker *et al.* [30]

8.3.3 II–VI Semiconductor Alloy

No detailed data are available for II–VI semiconductor alloys.

REFERENCES

- [1] S. Adachi, *Properties of Group-IV, III–V and II–VI Semiconductors*, John Wiley & Sons, Ltd, Chichester, 2005.
- [2] U. Schmid, N.E. Christensen, and M. Cardona, *Solid State Commun.* **75**, 39 (1990).
- [3] M.M. Rieger and P. Vogl, *Phys. Rev. B* **48**, 14276 (1993).
- [4] W. Shan, J.W. Ager III, K.M. Yu, W. Walukiewicz, E.E. Haller, M.C. Martin, W.R. McKinney, and W. Yang, *J. Appl. Phys.* **85**, 8505 (1999).
- [5] S.X. Li, J. Wu, W. Walukiewicz, W. Shan, E.E. Haller, H. Lu, W.J. Schaff, Y. Saito, and Y. Nanishi, *Phys. Status Solidi B* **241**, 3107 (2004).
- [6] G. Fransen, I. Gorczyca, T. Suski, A. Kamińska, J. Pereiro, E. Muñoz, E. Iliopoulos, A. Georgakilas, S.B. Che, Y. Ishitani, A. Yoshikawa, N.E. Christensen, and A. Svane, *J. Appl. Phys.* **103**, 033514 (2008).
- [7] Y. Ishitani, H. Hamada, S. Minagawa, H. Yaguchi, and Y. Shiraki, *Jpn. J. Appl. Phys.* **36**, 6607 (1997).
- [8] Y.B. Bolkhovityanov, A.S. Jaroshevich, M.A. Revenko, H.E. Scheibler, and A.S. Terekhov, *Semicond. Sc. Technol.* **11**, 1847 (1996).
- [9] H. Qiang, F.H. Pollak, and G. Hickman, *Solid State Commun.* **76**, 1087 (1990).
- [10] H. Qiang, F.H. Pollak, and R.N. Sacks, *Solid State Commun.* **84**, 51 (1992).
- [11] C.N. Yeh, L.E. McNeil, R.E. Nahory, and R. Bhat, *Phys. Rev. B* **52**, 14682 (1995).
- [12] L. Pavesi, R. Houdré, and P. Giannozzi, *J. Appl. Phys.* **78**, 470 (1995).
- [13] I.T. Ferguson, T.P. Beales, T.S. Cheng, C.M. Sotomayor-Torres, and E.G. Scott, *Semicond. Sci. Technol.* **4**, 243 (1989).
- [14] R. People, A. Jayaaraman, K.W. Wecht, D.L. Sivco, and A.Y. Cho, *Appl. Phys. Lett.* **52**, 2124 (1988).
- [15] V.A. Wilkinson, A.D. Prins, J.D. Lambkin, E.P. O'Reilly, D.J. Dunstan, L.K. Howard, and M.T. Emeny, *Phys. Rev. B* **42**, 3113 (1990).

- [16] S. Adachi, *Handbook on Physical Properties of Semiconductors: Volume 2 III–V Compound Semiconductors*, Kluwer Academic, Boston, 2004.
- [17] Y. Zhang, A. Mascarenhas, H.P. Xin, and C.W. Tu, *Phys. Rev. B* **61**, 4433 (2000).
- [18] M.H. Ya, Y.F. Chen, and Y.S. Huang, *J. Appl. Phys.* **92**, 1446 (2002).
- [19] Y. González, G. Armelles, and L. González, *J. Appl. Phys.* **76**, 1951 (1994).
- [20] K. Pelhos, S.A. Lee, Y. Rajakarunanyake, and J.L. Reno, *Phys. Rev. B* **51**, 13256 (1995).
- [21] J.A. Sans and A. Segura, *High Pressure Res.* **24**, 119 (2004).
- [22] A. Béliveau and C. Carlone, *Phys. Rev. B* **41**, 9860 (1990).
- [23] W. Shan, W. Walukiewicz, J.W. Ager III, K.M. Yu, J. Wu, E.E. Haller, Y. Nabetani, T. Murakawa, Y. Ito, and T. Matsumoto, *Appl. Phys. Lett.* **83**, 299 (2003).
- [24] E. Griehl, G.F. Schötz, C. Birzer, W. Kerner, T. Reisinger, B. Hahn, and W. Gebhardt, *Acta Phys. Polon. A* **88**, 995 (1995).
- [25] W. Walukiewicz, W. Shan, K.M. Yu, J.W. Ager III, E.E. Haller, I. Miotkowski, M.J. Seong, H. Alawadhi, and A.K. Ramdas, *Phys. Rev. Lett.* **85**, 1552 (2000).
- [26] J. Wu, W. Walukiewicz, K.M. Yu, W. Shan, J.W. Ager III, E.E. Haller, I. Miotkowski, A.K. Ramdas, and C.-H. Su, *Phys. Rev. B* **68**, 033206 (2003).
- [27] S. Adachi, *GaAs and Related Materials: Bulk Semiconducting and Superlattice Properties*, World Scientific, Singapore, 1994.
- [28] S. Adachi, *Handbook on Physical Properties of Semiconductors: Volume 1 Group IV Semiconductors*, Kluwer Academic, Boston, 2004.
- [29] S. Adachi, *Handbook on Physical Properties of Semiconductors: Volume 3 II–VI Compound Semiconductors*, Kluwer Academic, Boston, 2004.
- [30] T.R. Parker, C.C. Phillips, and P.C. May, *Phys. Rev. B* **51**, 4264 (1995).

9 Heterojunction Band Offsets and Schottky Barrier Height

9.1 HETEROJUNCTION BAND OFFSETS

9.1.1 General Considerations

One of the most important parameters for the design and analysis of heterojunction and QW electronic and optoelectronic devices is the heterojunction band offset. The band offset is a consequence of the difference between the band-gap energies of two semiconductors. As shown in Figure 9.1, the energy difference is distributed between a CB offset ΔE_c and a VB offset ΔE_v . In a type I (straddling lineup), we obtain

$$\Delta E_g = \Delta E_c + \Delta E_v \quad (9.1)$$

while for type II (broken-gap and staggered lineups) the relationship is given by

$$\Delta E_g = |\Delta E_c - \Delta E_v| \quad (9.2)$$

where $\Delta E_g = |E_{g1} - E_{g2}|$ is the band-gap energy difference.

Since the temperature variations of the band-gap energies are very similar among various semiconductors [1], the band offsets and offset ratio can usually be assumed to be independent of temperature.

9.1.2 Group-IV Semiconductor Heterostructure System

(a) C_xSi_{1-x}/Si

The C_xSi_{1-x}/Si heterostructure shows a biaxial tensile strain in the alloy layer. The biaxial strain or stress in the coherently strained QW layers splits the LH and HH bands so that the LH band is highest in C_xSi_{1-x} layer. Similarly, for C_xSi_{1-x} layers with smaller x compositions, the lowest CB is at the X (Δ) band. Brunner *et al.* [2] measured near-band-edge emission from pseudomorphic C_xSi_{1-x}/Si QW structures with x up to ~ 2 at%. They found a linear decrease in the PL emission peak with increasing x , which is about 30% larger than the expected band-gap reduction induced by strain. This might indicate that incorporation of C reduces the intrinsic band-gap energy. The trend for decreasing C_xSi_{1-x} band-gap energy was also proposed by detailed binding calculations [3].

The band-offset values for C_xSi_{1-x}/Si heterostructure have been determined experimentally by several authors [4, 5]. Houghton *et al.* [4] confirmed a type-I alignment in C_xSi_{1-x}/Si with $x = 0.5 - 1.7$ at% and also observed an elastic-strain-induced transition from type I to type II in

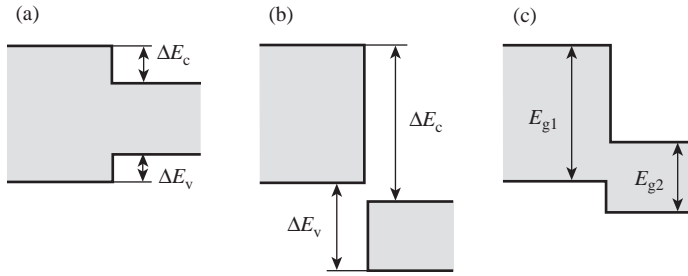


Figure 9.1 Schematic energy-band diagrams showing three representative types of heterostructure interfaces: (a) type I (straddling lineup), (b) type II-misaligned (broken-gap lineup) and (c) type II-staggered (staggered lineup)

C_xSi_{1-x}/Si QWs. The band-offset ratio obtained by these authors is $\Delta E_c : \Delta E_v = 65 : 35$ with $E_g(Si) \geq E_g(C_xSi_{1-x})$. Williams *et al.* [5] also obtained a band-offset ratio of about 70 : 30

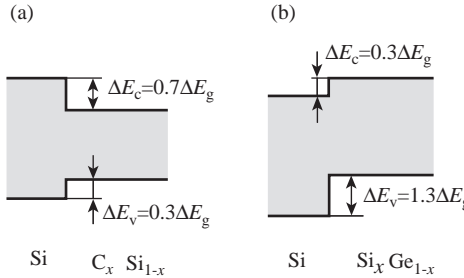


Figure 9.2 Schematic energy-band alignments for (a) C_xSi_{1-x}/Si and (b) Si_xGe_{1-x}/Si heterostructures obtained by Williams *et al.* [5] and Cheng *et al.* [12], respectively

for $x = 0.5 - 1.7$ at%. The corresponding band lineup is shown schematically in Figure 9.2(a). An *ab initio* calculation confirms the offset ratio of 70 : 30 [6].

(b) SiGe/Si

Previous studies on the band alignment of the Si_xGe_{1-x}/Si heterostructure suggest type-I [7, 8] or type-II behavior [9–12]. By employing a wafer bending technique, Thewalt *et al.* [11] observed both type-I and type-II behaviors respectively, in PL of an UHV-CVD-grown $Si_{0.7}Ge_{0.3}/Si(100)$ QW at high and low laser powers. They concluded that a determination of type-I alignment [7, 8] is a result of the band-bending effects due to high excitation. More recently, Cheng *et al.* [12] made PL measurements on UHV-CVD-grown and MBE-grown Si_xGe_{1-x}/Si MQWs and concluded that the band alignment was type II with $\Delta E_c = 0.3\Delta E_g$ and $\Delta E_v = 1.3\Delta E_g$, as shown in Figure 9.2(b).

(c) CSiGe/Si

The incorporation of C into Si_xGe_{1-x} can compensate for some of the biaxial compressive strain in the Si_xGe_{1-x}/Si heterostructure. The incorporation of C evidently lowers the CB and VB energies and decreases the intrinsic band gap in Si_xGe_{1-x} . The intrinsic band alignment of Si_xGe_{1-x}/Si is always type-II in character. Neglecting the effect of strain, therefore, we can

expect a transition from type II to type I by incorporating C into $\text{Si}_x\text{Ge}_{1-x}$. In fact, Stein *et al.* [13, 14] and Hartmann *et al.* [15] concluded that the band alignment in the $\text{C}_x\text{Si}_y\text{Ge}_{1-x-y}/\text{Si}$ heterostructure is type I, regardless of whether the strain is compensated or not. However, a staggered type-II alignment has been reported in strain-relaxed Ge-rich $\text{C}_x\text{Si}_y\text{Ge}_{1-x-y}/\text{Si}$ heterostructures ($x = 0.01 - 0.02$ and $y = 0.10 - 0.13$), with electrons (holes) localized in the Si ($\text{C}_x\text{Si}_y\text{Ge}_{1-x-y}$) layer [16]. The band offsets ΔE_c and ΔE_v determined were typically ~ 0.4 and ~ 0.6 eV, respectively.

(d) *CSi/SiGe*

Using a wafer bonding technique, Houghton *et al.* [4] obtained a type-II transition in a $\text{C}_{0.01}\text{Si}_{0.99}/\text{Si}_{0.84}\text{Ge}_{0.16}/\text{Si}$ heterostructure, with electrons (holes) localized in the $\text{C}_{0.01}\text{Si}_{0.99}$ ($\text{Si}_{0.84}\text{Ge}_{0.16}$) layer.

9.1.3 III–V Semiconductor Heterostructure System: Lattice-matched Ternary-alloy System

(a) *GaInP/GaAs*

The band-offset ratio $\Delta E_c : \Delta E_v$ determined experimentally for the $\text{Ga}_{0.52}\text{In}_{0.48}\text{P}/\text{GaAs}$ heterostructure ranges widely from 13:87 to 63:37 [17]. The mean offset ratio gives $\Delta E_c : \Delta E_v = 33 : 67$. The corresponding band offsets are $\Delta E_c \sim 0.16$ eV and $\Delta E_v \sim 0.33$ eV.

The existence of spontaneous ordering in the $\text{Ga}_{0.52}\text{In}_{0.48}\text{P}$ layer could significantly alter the band offset [17]. Thus, it appears that the ordering effect itself might have contributed to the larger scatter in the reported values, at least to some extent. The ordering effect can also change the band alignment from type I to type II, as schematically shown in Figure 9.3.

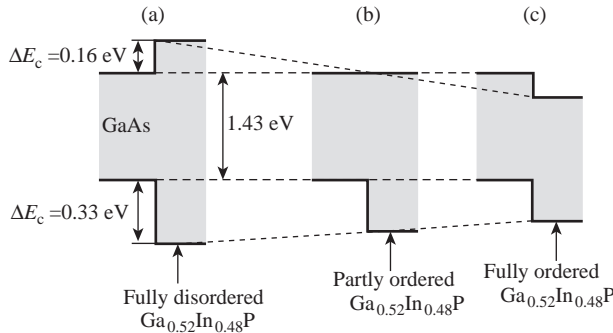


Figure 9.3 Schematic energy-band diagram showing the effect of spontaneous ordering for $\text{Ga}_{0.52}\text{In}_{0.48}\text{P}/\text{GaAs}$ heterostructure

Zhang *et al.* [17] obtained theoretically a transition from type I to type II at $\eta = 0.46$ (0.54) in the $\text{Ga}_x\text{In}_{1-x}\text{P}/\text{GaAs}$ heterostructure with $x = 0.50$ (0.52), where η is the so-called order parameter.

(b) *GaInP/AlInP*

Patel *et al.* [18] obtained the band-offset ratio $\Delta E_c : \Delta E_v = 52 : 48$ in the $\text{Ga}_{0.52}\text{In}_{0.48}\text{P}/\text{Al}_{0.5}\text{In}_{0.5}\text{P}$ heterostructure, where the CB minimum is in the X valley for $\text{Al}_{0.5}\text{In}_{0.5}\text{P}$ and in

the Γ valley for $\text{Ga}_{0.52}\text{In}_{0.48}\text{P}$ (i.e. $\Delta E_c = E_c^X(\text{Al}_{0.5}\text{In}_{0.5}\text{P}) - E_c^\Gamma(\text{Ga}_{0.52}\text{In}_{0.48}\text{P})$). More recently, Dawson *et al.* [19] revised the offset ratio to $\Delta E_c : \Delta E_v = 67 : 33$ from low-temperature PL measurements.

(c) *GaInP/AlGaAs*

The band alignment in the $\text{Ga}_{0.52}\text{In}_{0.48}\text{P}/\text{Al}_x\text{Ga}_{1-x}\text{As}$ heterostructure is expected to change from a straddling to a staggered type as the Al content x increases from $x=0$ (GaAs), as shown in Figure 9.4. Kim *et al.* [20] reported a transition occurring at about $x=0.12$ (Figure 9.4(b)).

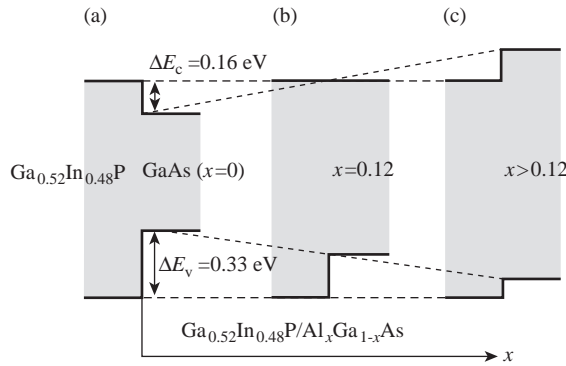


Figure 9.4 Schematic energy-band diagram for $\text{Ga}_{0.52}\text{In}_{0.48}\text{P}/\text{Ga}_x\text{Al}_{1-x}\text{As}$ heterostructure with (a) $x=0$, (b) $x=0.12$ and (c) $x > 0.12$

(d) *AlGaAs/GaAs*

The pioneering work of Dingle *et al.* [21, 22] on the $\text{Al}_x\text{Ga}_{1-x}\text{As}/\text{GaAs}$ MQW structure gave the offset ratio of $\Delta E_c : \Delta E_v = 85 : 15$. Although this ratio had long been accepted, some studies required different ratios in the range of $(0.62 - 0.66) : (0.38 - 0.34)$ to explain electrical and photoelectric data. The discrepancy with Dingle's result was attributed to compositional grading or any interface states at the $\text{Al}_x\text{Ga}_{1-x}\text{As}/\text{GaAs}$ heterojunction.

However, in 1984 Miller *et al.* [23, 24] reported values of $51 : 49$ and $57 : 43$ using PL from parabolic and rectangular QWs. Subsequently, Dugan *et al.* [25] arrived at $65 : 35$. By averaging the recently published data, we recommend an offset ratio of $\Delta E_c^\Gamma : \Delta E_v = 63 : 37$. Using this ratio and the E_0 and E_g^X values shown in Table 6.11, we obtain the ΔE_c and ΔE_v versus x plots for the $\text{Al}_x\text{Ga}_{1-x}\text{As}/\text{GaAs}$ heterostructure. Figure 9.5 shows these results. We can see that the band lineup is type I over the whole composition range $0 \leq x \leq 1.0$ [26]. Note, however, that the CB minimum changes from the Γ point (ΔE_c^Γ) to the X point (ΔE_c^X) at $x \sim 0.43$. The band offsets can be finally approximated for $x \leq 0.8$ as (in eV)

$$\Delta E_c^\Gamma(x) = 0.85x \quad (9.3a)$$

$$\Delta E_c^X(x) = 0.48 - 0.30x \quad (9.3b)$$

$$\Delta E_v(x) = 0.50x \quad (9.3c)$$

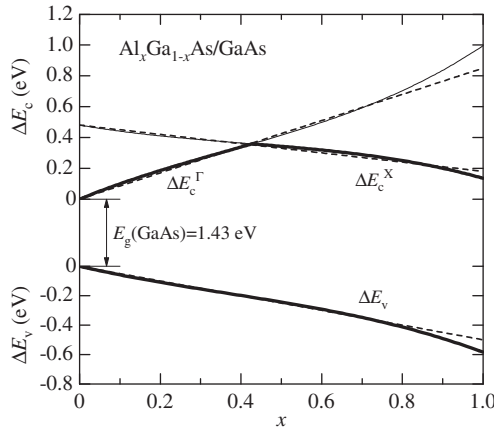


Figure 9.5 A full $\text{Al}_x\text{Ga}_{1-x}\text{As}/\text{GaAs}$ heterostructure band diagram obtained by assuming a band-offset ratio of $\Delta E_c^\Gamma : \Delta E_v = 63 : 37$ and using E_0 and E_g^X in Table 6.11 (solid lines). The dashed lines represent the linear variations of ΔE_c and ΔE_v given by Equation (9.3)

(e) AlInAs/InP

The $\text{Al}_{0.48}\text{In}_{0.52}\text{As}/\text{InP}$ interface is the least well characterized [27]. The staggered type-II alignment with holes localized in the $\text{Al}_{0.48}\text{In}_{0.52}\text{As}$ layer is generally agreed upon. A CB offset of $\Delta E_c = 2.86\Delta E_g$ has been reported by Böhler *et al.* [28].

The direct and inverse heterointerface properties have been studied for the $\text{Al}_{0.48}\text{In}_{0.52}\text{As}/\text{InP}$ heterostructure ($\text{Al}_{0.48}\text{In}_{0.52}\text{As}$ layer grown on InP versus InP layer grown on $\text{Al}_{0.48}\text{In}_{0.52}\text{As}$) [29, 30]. The clear noncommutativity of $100 \pm 20 \text{ meV}$ [29] and $53 \pm 10 \text{ meV}$ [30] has been observed for ΔE_c .

(f) GaInAs/InP

The band offsets in the $\text{Ga}_{0.47}\text{In}_{0.53}\text{As}/\text{InP}$ heterostructure have been studied both theoretically and experimentally [27]. We obtain an averaged experimental offset ratio of $\Delta E_c : \Delta E_v = 38 : 62$. The corresponding band alignment is shown in Figure 9.6(a).

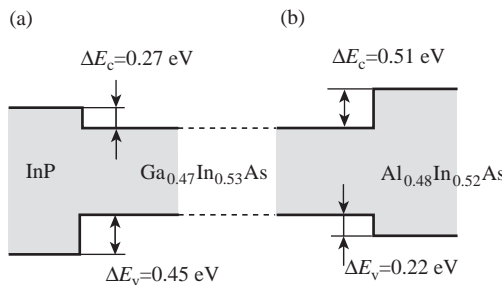


Figure 9.6 Schematic energy-band alignments for (a) $\text{Ga}_{0.47}\text{In}_{0.53}\text{As}/\text{InP}$ and (b) $\text{Ga}_{0.47}\text{In}_{0.53}\text{As}/\text{Al}_{0.48}\text{In}_{0.52}\text{As}$ heterostructures. The band offsets ΔE_c and ΔE_v are obtained by averaging the literature data

The direct and inverse heterointerface properties have been studied on the $\text{Ga}_{0.47}\text{In}_{0.53}\text{As}/\text{InP}$ heterointerface [30, 31]. Substantially large noncommutativity has been reported. The cause of the noncommutativity is attributed to a difference in the chemical nature of the direct and inverse interfaces [31]. A significant nontransitivity for the average band offsets has also been found in the $\text{InP}-\text{Al}_x\text{In}_{1-x}\text{As}-\text{Ga}_x\text{In}_{1-x}\text{As}$ family [29, 30].

(g) GaInAs/AlInAs

Like $\text{Ga}_{0.47}\text{In}_{0.53}\text{As}$, $\text{Al}_{0.48}\text{In}_{0.52}\text{As}$ can be grown lattice-matched to InP. The band-gap difference ΔE_g between these ternaries is about 0.73 eV. The band offsets in the $\text{Ga}_{0.47}\text{In}_{0.53}\text{As}/\text{Al}_{0.48}\text{In}_{0.52}\text{As}$ heterostructure have been determined by several authors [27, 32–34]. Averaging these results produces the offset ratio of $\Delta E_c : \Delta E_v = 70 : 30$. The corresponding band lineup is shown in Figure 9.6(b).

(h) InAsSb/GaSb

$\text{InAs}_{0.91}\text{Sb}_{0.09}$ can be grown lattice-matched to GaSb. A broken type of band lineup is accepted for the $\text{InAs}_{0.91}\text{Sb}_{0.09}/\text{GaSb}$ heterostructure [35–37]. Mebarki *et al.* [36] reported band offsets of $\Delta E_c = 0.82$ eV and $\Delta E_v = 0.36$ eV, respectively. The band lineup for this heterojunction system is illustrated in Figure 9.7.

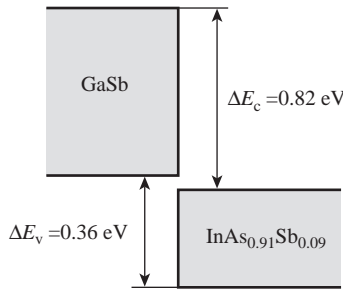


Figure 9.7 Schematic energy-band diagram for $\text{InAs}_{0.91}\text{Sb}_{0.09}/\text{GaSb}$ heterostructure obtained by Mebarki *et al.* [36]

9.1.4 III–V Semiconductor Heterostructure System: Lattice-matched Quaternary Alloy

(a) GaInPAs/InP

Although the straddling alignment is generally agreed upon, there is considerable disagreement regarding the band offsets of the $\text{Ga}_x\text{In}_{1-x}\text{P}_y\text{As}_{1-y}/\text{InP}$ heterostructure [27]. Let us assume a band-offset ratio of $\Delta E_c : \Delta E_v = 38 : 62$, which is derived from the $\text{Ga}_{0.47}\text{In}_{0.53}\text{As}/\text{InP}$ heterostructure. Using this ratio and E_0 in Table 6.28, we obtain the y -dependent ΔE_c and ΔE_v values for the $\text{Ga}_x\text{In}_{1-x}\text{P}_y\text{As}_{1-y}/\text{InP}$ and $\text{Ga}_x\text{In}_{1-x}\text{P}_y\text{As}_{1-y}/\text{Ga}_{0.47}\text{In}_{0.53}\text{As}$ heterostructures. The results can be approximated as (in eV)

$$\Delta E_c(y) = 0.23 - 0.23y \tag{9.4a}$$

$$\Delta E_v(y) = 0.37 - 0.37y \tag{9.4b}$$

for the $\text{Ga}_x\text{In}_{1-x}\text{P}_y\text{As}_{1-y}/\text{InP}$ heterostructure and

$$\Delta E_c(y) = 0.23y \quad (9.5a)$$

$$\Delta E_v(y) = 0.37y \quad (9.5b)$$

for the $\text{Ga}_x\text{In}_{1-x}\text{P}_y\text{As}_{1-y}/\text{Ga}_{0.47}\text{In}_{0.53}\text{As}$ heterostructure.

(b) AlGaAsSb/GaSb

The band offsets in a perfectly lattice-matched $\text{Al}_{0.47}\text{Ga}_{0.53}\text{As}_{0.04}\text{Sb}_{0.96}/\text{GaSb}$ heterostructure were determined to be $\Delta E_c = 0.35$ eV and $\Delta E_v = 0.24$ eV, respectively, furnishing a fractional ratio of $\Delta E_c : \Delta E_v = 59 : 41$ [38].

(c) AlGaAsSb/InP

Ostinelli *et al.* [39] carried out PL on an $\text{Al}_{0.168}\text{Ga}_{0.832}\text{AsSb}/\text{InP}$ heterostructure and obtained staggered type-II offsets of $\Delta E_c = 0.32$ eV and $\Delta E_v = 0.66$ eV with electrons (holes) localized in the InP ($\text{Al}_{0.168}\text{Ga}_{0.832}\text{AsSb}$) layer. These results give $\Delta E_c = 0.94\Delta E_g$ and $\Delta E_v = 1.94\Delta E_g$.

(d) AlGaAsSb/InAs

Nelson *et al.* [40] measured PL spectra of the $\text{Al}_{0.8}\text{Ga}_{0.2}\text{As}_{0.14}\text{Sb}_{0.86}/\text{InAs}$ heterostructure and obtained a staggered lineup with $\Delta E_c = 1.60$ eV and $\Delta E_v = 0.24$ eV with electrons (holes) localized in the InAs ($\text{Al}_{0.8}\text{Ga}_{0.2}\text{As}_{0.14}\text{Sb}_{0.86}$) layer. These results predicted the relationship $\Delta E_c = 1.18\Delta E_g$ and $\Delta E_v = 0.18\Delta E_g$.

(e) GaInAsSb/GaSb

The band lineup for $\text{Ga}_x\text{In}_{1-x}\text{As}_y\text{Sb}_{1-y}/\text{GaSb}$ heterostructure is believed to be type II in nature. Mikhailova and Titkov [41] reviewed the topic. Averaging the experimental data in this review gives $\Delta E_c = 1.62\Delta E_g$ and $\Delta E_v = 0.62\Delta E_g$. These relationships indicate that the transition composition from broken-gap to staggered lineup will be at $x \sim 0.24$. Afrailov *et al.* [42] observed a broken-gap character at $x = 0.11$, whereas Mebarki *et al.* [43] found the staggered band offsets to be $\Delta E_c = 0.33 \pm 0.05$ eV and $\Delta E_v = 0.12 \pm 0.05$ eV ($x = 0.77$) with electrons localized in the $\text{Ga}_x\text{In}_{1-x}\text{As}_y\text{Sb}_{1-y}$ layer.

(f) GaInAsSb/InP

The band-offset ratio of $\Delta E_c : \Delta E_v = 30 : 70$ in the $\text{Ga}_{0.64}\text{In}_{0.36}\text{As}_{0.84}\text{Sb}_{0.16}/\text{InP}$ heterostructure was obtained by Chang *et al.* [44] from optical absorption measurements.

(g) GaInAsSb/InAs

The band lineups in LPE-grown $\text{Ga}_x\text{In}_{1-x}\text{As}_y\text{Sb}_{1-y}/\text{InAs}$ heterostructure were investigated by Mikhailova *et al.* [45]. The broken-gap lineup was observed in the composition range $0.77 \leq x \leq 0.97$ and the staggered lineup in the range $0 < x < 0.7$.

(h) AlGaAsSb/GaInAsSb

The band offsets in the $\text{Al}_{0.22}\text{Ga}_{0.78}\text{As}_{0.02}\text{Sb}_{0.98}/\text{Ga}_{0.75}\text{In}_{0.25}\text{As}_{0.04}\text{Sb}_{0.96}$ MQW structure grown on GaSb(100) were determined from optical absorption and PL measurements [46]. The offset ratio was determined to be $\Delta E_c : \Delta E_v = 66 : 34$.

(i) AlInAsSb/GaInAsSb

Chang *et al.* [47] grew $\text{Al}_{0.66}\text{In}_{0.34}\text{As}_{0.85}\text{Sb}_{0.15}/\text{Ga}_{0.64}\text{In}_{0.36}\text{As}_{0.84}\text{Sb}_{0.16}$ MQW structures on InP (100) by MOCVD and carried out low-temperature PL measurements. The band-offset ratio estimated from this study was $\Delta E_c : \Delta E_v = 75 : 25$.

(j) AlGaInP/AlInP

The band alignment in $(\text{Al}_{0.7}\text{Ga}_{0.3})_{0.53}\text{In}_{0.47}\text{P}/\text{Al}_x\text{In}_{1-x}\text{P}$ heterostructures was investigated by Ishitani *et al.* [48] using PL spectroscopy. They found that the X-valley discontinuity ΔE_c^X decreases with increasing x ($0.47 \leq x \leq 0.61$). The band-offset ratio obtained was $\Delta E_c : \Delta E_v = 75 : 25$ for $x = 0.53$.

(k) AlGaInP/GaInP

The band-offset ratios in $(\text{Al}_x\text{Ga}_{1-x})_{0.53}\text{In}_{0.47}\text{P}/\text{Ga}_{0.52}\text{In}_{0.48}\text{P}$ with x in the direct band-gap region ($x < 0.65$, see Figure 6.49) varied from $\Delta E_c^\Gamma : \Delta E_v = 49 : 41$ to $70 : 30$ [49–53]. Averaging these data gives $\Delta E_c^\Gamma : \Delta E_v = 65 : 35$. The corresponding band offsets ΔE_c^Γ , ΔE_c^X and ΔE_v are plotted against x in Figure 9.8. The band offsets can now be written as (in eV)

$$\Delta E_c^\Gamma = 0.43x \quad (9.6a)$$

$$\Delta E_c^X = 0.36 - 0.16x \quad (9.6b)$$

$$\Delta E_v = 0.24x \quad (9.6c)$$

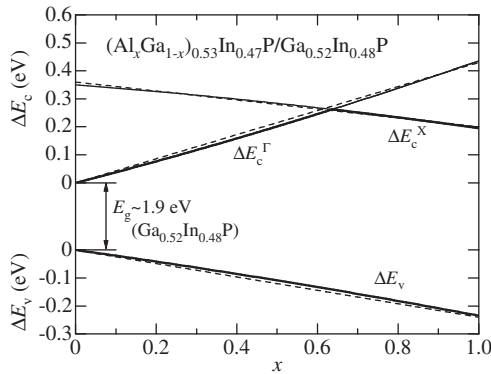


Figure 9.8 A full $(\text{Al}_x\text{Ga}_{1-x})_{0.53}\text{In}_{0.47}\text{P}/\text{Ga}_{0.52}\text{In}_{0.48}\text{P}$ heterostructure band diagram obtained by assuming a band-offset ratio of $\Delta E_c^\Gamma : \Delta E_v = 65 : 35$ and using E_0 and E_g^X in Table 6.28 (solid lines). The dashed lines represent the linear variations of ΔE_c and ΔE_v given by Equation (9.6)

The band offsets in $(\text{Al}_x\text{Ga}_{1-x})_{0.53}\text{In}_{0.47}\text{P}/\text{Ga}_{0.52}\text{In}_{0.48}\text{P}$ with x in the indirect band-gap region were studied by several authors [54, 55]. The effects of long-range ordering on the band alignment are discussed by Shao *et al.* [56].

(l) AlGaInAs/GaInAs

The band offsets in $(\text{Al}_x\text{Ga}_{1-x})_{0.48}\text{In}_{0.52}\text{As}/\text{Ga}_{0.47}\text{In}_{0.53}\text{As}$ were determined from $I - V$ [57] and PL and PLE measurements [58]. The offset ratios determined from these studies were $\Delta E_c : \Delta E_v = 72 : 28$ and $73 : 27$, respectively. Assuming $\Delta E_c : \Delta E_v = 73 : 27$ and using E_0 in Table 6.28, we can obtain the x -dependent ΔE_c and ΔE_v . The results are shown in Figure 9.9, and can be given by (in eV)

$$\Delta E_c(x) = 0.54x \tag{9.7a}$$

$$\Delta E_v(x) = 0.20x \tag{9.7b}$$

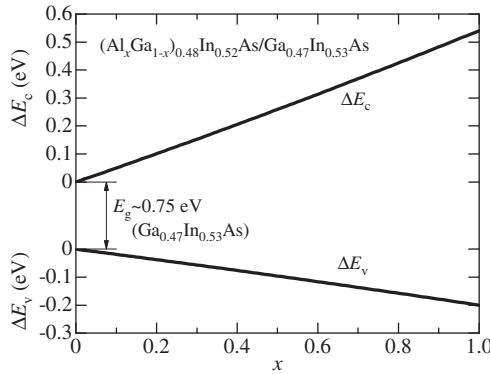


Figure 9.9 A full $(\text{Al}_x\text{Ga}_{1-x})_{0.48}\text{In}_{0.52}\text{As}/\text{Ga}_{0.47}\text{In}_{0.53}\text{As}$ heterostructure band diagram obtained by assuming a band-offset ratio of $\Delta E_c : \Delta E_v = 73 : 27$ and using E_0 in Table 6.28

9.1.5 III–V Semiconductor Heterostructure System: Lattice-mismatched Alloy System

(a) w-AlGaN/w-GaN

The straddling lineup is generally agreed upon, but there is considerable disagreement regarding the band offsets between $\text{Al}_x\text{Ga}_{1-x}\text{N}$ (AlN) and GaN reported by different authors [59–65]. Using the mean value of these data, we obtain $\Delta E_c : \Delta E_v = 65 : 35$. Using $E_0 = 6.2 \text{ eV}$ (AlN) and 3.420 eV (GaN) in Table 6.2, we obtain the band offsets for the $\text{Al}_x\text{Ga}_{1-x}\text{N}/\text{GaN}$ heterostructure as follows (in eV)

$$\Delta E_c(x) = 1.81x \tag{9.8a}$$

$$\Delta E_v(x) = 0.97x \tag{9.8b}$$

Dependence of the AlN/GaN band discontinuity on growth temperature was determined using XPS [66]. A large strain-induced asymmetry of the band offset was suggested from an *ab initio* electronic structure study [67].

(b) w-AlInN/w-InN

The VB offsets $\Delta E_v = 3.10 \pm 0.04$ eV [68] and 4.0 ± 0.2 eV [69] were determined in an AlN/InN heterointerface using photoelectron spectroscopy. These ΔE_v values and values of $E_0 = 6.2$ eV (AlN) and 0.70 eV (InN) in Table 6.2 provide the band-offset ratios $\Delta E_c : \Delta E_v = 44 : 56$ and $27 : 73$, respectively.

(c) w-GaInN/w-GaN

The band offsets in the $\text{Ga}_x\text{In}_{1-x}\text{N(InN)/GaN}$ heterostructure were determined using various techniques [70–74]. The mean offset ratio obtained from these studies was $\Delta E_c : \Delta E_v = 67 : 33$.

(d) GaInAs/GaAs

The band discontinuity in a strained-layer system depends not only on the heterostructure system involved but also on the amount of mismatch strain at the interface. The strain field can produce marked effects on the electronic properties through the DP interactions. The hydrostatic component of the strain causes a shift in the bulk energy levels of the strained layer, while the shear component causes splitting of certain degenerate VB levels, namely, the HH and LH levels. The exact energy levels of the heterostructure layer should, therefore, be determined including the strain modification of the layer.

In the case of biaxial strain parallel to [010] and [001], the strain components in $\text{Ga}_x\text{In}_{1-x}\text{As/GaAs(100)}$ heterojunctions are

$$e_{xx} = e_{yy} = -\delta, e_{zz} = \frac{2C_{12}}{C_{11}}\delta, e_{xy} = e_{yz} = e_{zx} \quad (9.9)$$

with

$$\delta = \frac{\Delta a}{a} \quad (9.10)$$

where δ is defined to be positive for compressive strain, C_{ij} is the elastic stiffness constant of $\text{Ga}_x\text{In}_{1-x}\text{As}$ and Δa is the lattice-constant difference between $\text{Ga}_x\text{In}_{1-x}\text{As}$ and GaAs. The corresponding change in the band-gap energy for $\text{Ga}_x\text{In}_{1-x}\text{As}$ layer can be written as

$$\Delta E_{c,v1} = \left(-2a_0^\Gamma \frac{C_{11}-C_{12}}{C_{11}} + b \frac{C_{11}+2C_{12}}{C_{11}} \right) \delta = -\delta_h + \frac{1}{2}\delta E_s \quad (9.11a)$$

$$\Delta E_{c,v2} = \left(-2a_0^\Gamma \frac{C_{11}-C_{12}}{C_{11}} - b \frac{C_{11}+2C_{12}}{C_{11}} \right) \delta = -\delta_h - \frac{1}{2}\delta E_s \quad (9.11b)$$

where v1 and v2 represent the $|3/2, \pm 3/2\rangle$ (HH-like) and $|3/2, \pm 1/2\rangle$ (LH-like) bands, respectively, a_0^Γ and b are the hydrostatic-pressure and shear DPs, respectively. In obtaining Equation (9.11), the SO split-off energy Δ_0 is assumed to be $\Delta_0 \gg \delta E_s$. Introducing the InAs ($x=0$)

values for a_0^Γ , b and C_{ij} ($\delta = 0.07$) into Equation (9.11), we obtain the hydrostatic-pressure and shear-strain shifts δ_h and δE_s in the strained InAs layer to be about -0.40 and -0.26 eV, respectively. Thus, the band-gap discontinuity between GaAs and fully strained InAs is

$$\Delta E_0 = E_0(\text{GaAs}) - [E_0(\text{InAs}) + \delta_h] \sim 1.43 - (0.36 + 0.40) = 0.67 \text{ eV} \quad (9.12)$$

Similarly, the discontinuity between GaAs and fully relaxed InAs is given by

$$\Delta E_0 = E_0(\text{GaAs}) - E_0(\text{InAs}) \sim 1.43 - 0.36 = 1.07 \text{ eV} \quad (9.13)$$

The InAs/GaAs heterostructure has about 7% lattice mismatch and the corresponding critical thickness is as low as two monolayers. Using XPS, Kowalczyk *et al.* [75] determined the band offsets in the InAs/GaAs(100) heterostructure to be $\Delta E_c = 0.90 \pm 0.07$ eV and $\Delta E_v = 0.17 \pm 0.07$ eV, respectively. The resulting offset ratio is $\Delta E_c : \Delta E_v = 16 : 84$. The sample used by Kowalczyk *et al.* [75] was an InAs/GaAs(100) single heterojunction with a 20 Å thick InAs layer, which is much thicker than the critical thickness for the generation of dislocation. Hence, the lattice strain is relaxed in their sample. In fact, the obtained band-gap discontinuity $\Delta E_0 = \Delta E_c + \Delta E_v = 1.07$ eV exactly agrees with that predicted from Equation (9.13).

If we assume an offset ratio of $\Delta E_c : \Delta E_v = 16 : 84$ for the fully relaxed $\text{Ga}_x\text{In}_{1-x}\text{As}/\text{GaAs}$ heterostructure, we can obtain the x -dependent offsets ΔE_c and ΔE_v (in eV)

$$\Delta E_c(x) = 0.17x \quad (9.14a)$$

$$\Delta E_v(x) = 0.90x \quad (9.14b)$$

The largest δ and ΔE_0 values can be expected at $x = 0$ for the strained $\text{Ga}_x\text{In}_{1-x}\text{As}/\text{GaAs}$ heterostructure. Since both δ and $\Delta E_0 \equiv E_0(\text{GaAs}) - E_0(\text{Ga}_x\text{In}_{1-x}\text{As})$ for the strained $\text{Ga}_x\text{In}_{1-x}\text{As}/\text{GaAs}$ heterostructure decrease almost linearly with increasing x , the hydrostatic component (δ_h) to ΔE_0 ratio may be roughly independent of x and is given by $\delta_h/\Delta E_0 \sim 0.4$ ($0.40/1.07$ at $x = 0$).

There are no experimental data on the band offsets in strained $\text{Ga}_x\text{In}_{1-x}\text{As}/\text{GaAs}$ heterostructures for lower x values, except for $x = 0$. Samples of larger x reported recently [27, 76–78] give a mean band-offset ratio of $\Delta E_c : \Delta E_v = 60 : 40$ ($0.6 < x \leq 0.98$). Using this ratio and the strained-InAs ($x = 0$) E_0 value, we can obtain an energy-band diagram for the strained $\text{Ga}_x\text{In}_{1-x}\text{As}/\text{GaAs}$ heterostructure. This result is shown in Figure 9.10. The band offsets ΔE_c ,

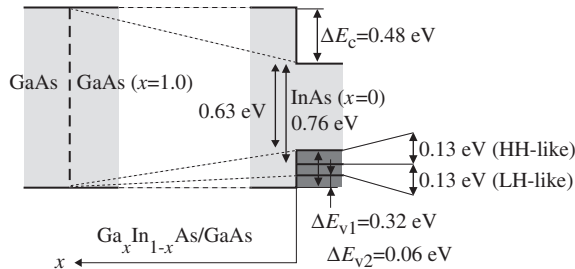


Figure 9.10 Schematic energy-band diagram for strained $\text{Ga}_x\text{In}_{1-x}\text{As}/\text{GaAs}$ heterostructure obtained by using a band-offset ratio of $\Delta E_c : \Delta E_v = 60 : 40$ and strained-InAs E_0 value of 0.76 eV

ΔE_{v1} (CB – HH) and ΔE_{v2} (CB – LH) versus x can be written as (in eV)

$$\Delta E_c(x) = 0.48x \tag{9.15a}$$

$$\Delta E_{v1}(x) = 0.32x \tag{9.15b}$$

$$\Delta E_{v2}(x) = 0.06x \tag{9.15c}$$

(e) Dilute-nitride-based heterostructure system

1. *GaN_xAs_{1-x}/GaAs*—Recent experimental studies suggest that the band lineup in the dilute-nitride GaN_xAs_{1-x}/GaAs heterostructure for N ≤ 4.5 at% is type I [79–83], although an earlier XPS study suggested a type-II lineup [84]. The schematic band diagram for this heterostructure system is shown in Figure 9.11. It is commonly accepted that N incorporation mainly affects the CB states and causes band-gap reduction (Section 6.3.5). Based on the BAC model, the N states produced in GaAs lead to a characteristic splitting of the Γ₆-CB state into two non-parabolic subbands E_- and E_+ (Figure 9.11(b), see also Figure 6.29(b)). The different lattice constants between *c*-GaN and GaAs can induce tensile strain parallel to [010] and [001] in pseudomorphic GaN_xAs_{1-x} layers on GaAs(100) (Figure 1.27). This strain argument predicts that the LH band should be type I, while the HH band is type II, as illustrated in Figure 9.11(c). The CB offsets $\Delta E_c = (0.7 - 0.95)\Delta E_g$ were reported [79–83].

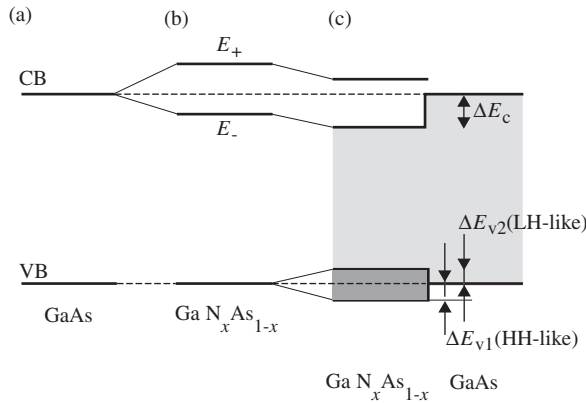


Figure 9.11 Schematic energy-band diagram for GaN_xAs_{1-x}/GaAs heterostructure. Strain argument depicted in (c) predicts the LH and HH bands to be type I and type II, respectively

2. *GaInNAs/GaAs*—The schematic energy-band diagram for the dilute-nitride Ga_xIn_{1-x}N_yAs_{1-y}/GaAs heterostructure is shown in Figure 9.12. As mentioned in Section 9.1.4, the band-offset ratios in fully relaxed and strained Ga_xIn_{1-x}As/GaAs heterostructures are assumed to be given by $\Delta E_c : \Delta E_v = 16 : 84$ and $60 : 40$, respectively. The band lineup in Figure 9.12(a) corresponds to the strained heterostructure. Strain-induced splitting of the HH and LH bands cannot be expected in the fully relaxed heterostructure system. Adding N to Ga_xIn_{1-x}As splits the CB minimum into E_- and E_+ and lowers the band-gap energy, with negligible interaction with the

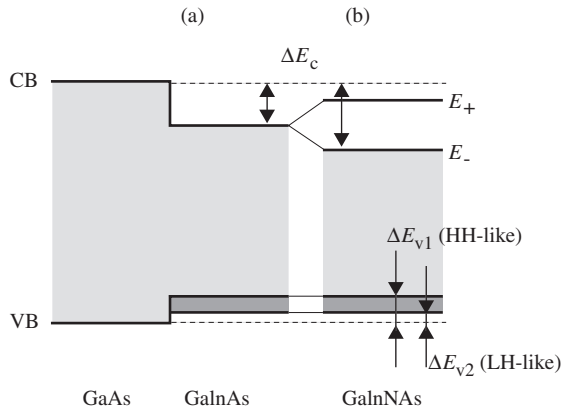


Figure 9.12 Schematic energy-band diagrams for strained heterostructure systems: (a) $\text{Ga}_x\text{In}_{1-x}\text{As}/\text{GaAs}$ and (b) dilute-nitride $\text{Ga}_x\text{In}_{1-x}\text{N}_y\text{As}_{1-y}/\text{GaAs}$

VB states (Figure 9.12(b)). We can, thus, expect an increase (decrease) in the ΔE_c (ΔE_v) portion. Indeed, the band discontinuities have been found to be $\sim 80\%$ in the CB and $\sim 20\%$ in the VB for $\text{Ga}_x\text{In}_{1-x}\text{N}_y\text{As}_{1-y}/\text{GaAs}$ heterostructures [85, 86].

3. *GaNAsSb/GaAs*—As seen in Figure 9.11(b), incorporating N into GaAs essentially lowers the CB minimum. This is complementary to the Sb effect, which mainly increases the VB maximum. In this respect, the $\text{GaN}_x\text{As}_y\text{Sb}_{1-x-y}/\text{GaAs}$ heterostructure is an interesting system where ΔE_c and ΔE_v can be independently tuned by adjusting N and Sb concentrations, respectively. The band discontinuities in this heterostructure system have been studied by several authors [87–90] and are found to change from type II to type I by incorporating N into $\text{GaAs}_x\text{Sb}_{1-x}$.

9.1.6 II–VI Semiconductor Heterostructure System

(a) (II, II)–O-based heterostructure system

The band alignment in the $\text{Mg}_{0.15}\text{Zn}_{0.85}\text{O}/\text{CdS}$ heterostructure was studied using X-ray and UV photoelectron spectroscopy and found to be a staggered type-II alignment with electrons localized in the $\text{Mg}_{0.15}\text{Zn}_{0.85}\text{O}$ layer ($\Delta E_c = 1.1$ eV and $\Delta E_v = 1.2$ eV) [91].

The XPS technique was used to obtain the band offsets in the $\text{Zn}_{0.95}\text{Cd}_{0.05}\text{O}/\text{ZnO}(0001)$ heterostructure [92]. The band offsets obtained were $\Delta E_c = 0.30$ eV and $\Delta E_v = 0.17$ eV, with electrons and holes localized in the $\text{Zn}_{0.95}\text{Cd}_{0.05}\text{O}$ layer (type I).

(b) (II, II)–S-based heterostructure system

The band offsets in free-standing *c*- $\text{Zn}_{0.7}\text{Cd}_{0.3}\text{S}/\text{c-ZnS}$ SL were determined from low-temperature PL to be $\Delta E_c = 0.461$ eV and $\Delta E_v = 0.088$ eV ($\Delta E_c : \Delta E_v = 84 : 16$) [93].

(c) (II, II)–Se-based heterostructure system

The band alignments in ZnSe-based heterostructures, such as $\text{Be}_x\text{Zn}_{1-x}\text{Se}/\text{ZnSe}$, $\text{Mg}_x\text{Zn}_{1-x}\text{Se}/\text{ZnSe}$ and $\text{Zn}_x\text{Cd}_{1-x}\text{Se}/\text{ZnSe}$, are type I. From magneto-transmission measurements on a series

of BeZnSe/ZnMnSe QWs, Kim *et al.* [94] estimated the VB offset in $\text{Be}_x\text{Zn}_{1-x}\text{Se}/\text{ZnSe}$ to be approximately 40% of the band-gap difference.

The VB offset in the $\text{Mg}_x\text{Zn}_{1-x}\text{Se}/\text{ZnSe}$ heterostructure was determined from optical and photoelectron spectra to be as much as 87% of the band-gap difference [95].

The band offsets in the $\text{Zn}_x\text{Cd}_{1-x}\text{Se}/\text{ZnSe}$ heterostructure were determined using various techniques, such as optical absorption [96], reflectance [97], electrical conductivity and inter-subband absorption [98], PLE [99] and CL and DLTS [100]. These data gave a band-offset ratio which varied from $\Delta E_c : \Delta E_v = 67 : 33$ to $87 : 13$. We obtained $\Delta E_c : \Delta E_v = 72 : 28$ as the average band-offset ratio. Guénaud *et al.* [99] reported that the HH excitons are type I, whereas the LH excitons are type II. The type-II excitons were considered to occur as a result of the compressive strain state and to have small VB offset ($\Delta E_c : \Delta E_v = 87 : 13$) in the $\text{Zn}_x\text{Cd}_{1-x}\text{Se}/\text{ZnSe}$ ($x = 0.82 - 0.88$) heterostructure. The band offsets in the $\text{Zn}_x\text{Cd}_{1-x}\text{Se}/\text{MgSe}$ heterostructure have also been studied [101].

(d) (II, II)–Te-based heterostructure system

It is generally accepted that the strained $\text{Zn}_x\text{Cd}_{1-x}\text{Te}/\text{CdTe}$ heterostructure is of mixed type, i.e. the electrons and heavy holes are confined in a CdTe layer, while the light holes are confined in a $\text{Zn}_x\text{Cd}_{1-x}\text{Te}$ layer [102–105]. This is the result of sufficient residual tensile strain existing in the $\text{Zn}_x\text{Cd}_{1-x}\text{Te}$ layer grown on $\text{Zn}_y\text{Cd}_{1-y}\text{Te}$ ($x > y$). Similarly, band alignments of type I and type II have been observed in $\text{Zn}_x\text{Cd}_{1-x}\text{Te}/\text{ZnTe}$ heterostructures below and above $x \sim 0.1$ respectively, grown on GaAs(100) [106]. The electrons and holes in type II can be confined in the $\text{Zn}_x\text{Cd}_{1-x}\text{Te}$ and ZnTe layers, respectively.

The VB offset between CdTe and HgTe has been the subject of a number of investigations. In early experiments, both a small offset of 40 meV and a roughly 10 times larger value were deduced (see von Truchseß *et al.* [107]). However, more recent experiments using various techniques provide consistent VB offsets somewhere around 0.4 eV [108–113]. The most recent study gives temperature-dependent offset data of $\Delta E_v = 0.57 \pm 0.06$ eV at 5 K and its temperature coefficient $d\Delta E_v/dT \sim -0.4$ meV/K [114]. Strong evidence has also been provided to suggest that the temperature dependence of the band offsets can be essentially neglected [112].

Figure 9.13 shows the schematic band diagram for the $\text{Cd}_x\text{Hg}_{1-x}\text{Te}/\text{CdTe}$ heterostructure. The HgTe/CdTe lineup corresponds to that reported by Becker *et al.* [114]. The results

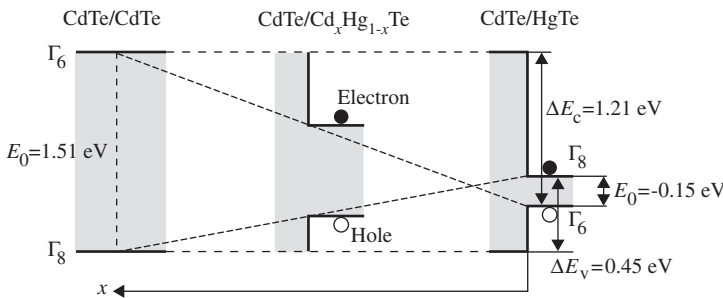


Figure 9.13 Schematic energy-band diagram for $\text{Cd}_x\text{Hg}_{1-x}\text{Te}/\text{CdTe}$ heterostructure. The HgTe/CdTe lineup corresponds to that reported by Becker *et al.* [114] at 300 K. The band offsets can be written as Equation (9.16)

suggest that the band offsets can be expressed as (in eV)

$$\Delta E_c(x) = 1.21 - 1.21x \quad (9.16a)$$

$$\Delta E_v(x) = 0.45 - 0.45x \quad (9.16b)$$

Thus, the $\text{Cd}_x\text{Hg}_{1-x}\text{Te}/\text{CdTe}$ heterostructure is type II ($x = 0$) and becomes type I for $x > 0.09$.

(e) Zn–(VI, VI)-based heterostructure system

Shahzad *et al.* [115] carried out PL and PLE measurements on $\text{ZnS}_x\text{Se}_{1-x}/\text{ZnSe}$ SLs ($x \leq 0.26$) and obtained a very small CB offset (≤ 10 meV) between ZnSe wells and $\text{ZnS}_x\text{Se}_{1-x}$ barriers with a type-I lineup. Subsequently, Lomascolo *et al.* [116] undertook PL measurements on a $\text{ZnS}_{0.18}\text{Se}_{0.82}/\text{ZnSe}$ SL at hydrostatic pressures up to 8 GPa and confirmed a transition from type I to type II near 4.5 GPa. The CB offset estimated in this study was $\Delta E_c \sim 6$ meV at zero pressure. We can thus conclude that the band-offset ratio for $\text{ZnS}_x\text{Se}_{1-x}/\text{ZnSe}$ heterostructure is roughly given by $\Delta E_c : \Delta E_v = 0 : 100$.

ZnSe/ZnTe is known to comprise a staggered type-II heterostructure. The same band alignment can be expected and has been confirmed in $\text{ZnSe}_x\text{Te}_{1-x}/\text{ZnSe}$ and $\text{ZnSe}_x\text{Te}_{1-x}/\text{ZnTe}$ heterostructures [117, 118].

(f) (II, II)–VI-based and II–(VI, VI)-based heterostructure systems

The band offsets in $\text{MgZnSe}/\text{ZnCdSe}$ and $\text{ZnCdSe}/\text{ZnSSe}$ heterostructures were determined experimentally by Pelucchi *et al.* [119] and Wu *et al.* [120], respectively.

(g) (II, II)–(VI, VI)-based heterostructure system

The band lineup for $\text{Mg}_x\text{Zn}_{1-x}\text{S}_y\text{Se}_{1-y}/\text{ZnSe}$ heterostructure is believed to be type I. The band-offset ratio was studied experimentally by several authors [121–126]. These studies provided offset ratios which varied largely from $\Delta E_c : \Delta E_v = 10 : 90$ [124] to $60 : 40$ [122]. We obtained $\Delta E_c : \Delta E_v = 36 : 64$ as the mean value.

The band offsets in $\text{Zn}_{0.7}\text{Cd}_{0.3}\text{S}_{0.06}\text{Se}_{0.94}/\text{ZnS}_{0.06}\text{Se}_{0.94}$ lattice-matched to GaAs have been characterized by DLTS [127] and the band-offset ratio obtained was $\Delta E_c : \Delta E_v = 75 : 25$.

(h) (II, II, II)–VI-based heterostructure system

The band alignment in $\text{Be}_x\text{Mg}_y\text{Zn}_{1-x-y}\text{Se}/\text{ZnSe}$ grown on GaAs(100) was investigated using PL and PLE [128] and the band-offset ratio was found to be $\Delta E_c : \Delta E_v = 60 : 40$.

The band offsets in $\text{Mg}_{0.50}\text{Zn}_{0.27}\text{Cd}_{0.23}\text{Se}/\text{Zn}_{0.53}\text{Cd}_{0.47}\text{Se}$ lattice-matched to InP were investigated using contactless ER [129]; the offset ratio was determined to be $\Delta E_c : \Delta E_v = 82 : 18$ ($\Delta E_c = 0.59$ eV).

9.2 SCHOTTKY BARRIER HEIGHT

9.2.1 General Considerations

A Schottky barrier is a metal/semiconductor junction which has rectifying characteristics. Rectifying properties depend both on the metal work function and type of conductivity of

the semiconductor. The choice of a metal for fabricating the Schottky barrier with a particular semiconductor is, thus, determined by its electronic work function ϕ_M . For an n -type semiconductor, ϕ_M should be large, while for a p -type semiconductor, it should be less than the electron affinity χ_e of the semiconductor. The barrier heights can then be written, respectively, as

$$n\text{-type} : \phi_n = \phi_M - \chi_e \tag{9.17a}$$

$$p\text{-type} : \phi_p = E_g - \phi_M + \chi_e \tag{9.17b}$$

where E_g is the band-gap energy of the semiconductor. The maximum value of the barrier height for an ideal Schottky–Mott contact is about equal to the band-gap energy of the semiconductor: $\phi_n + \phi_p = E_g$. The work functions ϕ_M of some important metals used as the Schottky contacts are summarized in Table 9.2 of Adachi [1].

9.2.2 Group-IV Semiconductor Alloy

(a) SiGe binary alloy

Extended studies on metal/ $\text{Si}_x\text{Ge}_{1-x}$ have shown the complexity of the mechanism of Schottky barrier formation [130]. The results are still puzzling. However, a common trend has been observed: the Schottky barrier height ϕ_p increases with increasing x . The experimental data for ϕ_n and ϕ_p obtained by Aubry-Fortuna *et al.* [130] is shown in Figure 9.14. These authors observed that for lower- ϕ_M metals (Zr and Ti), ϕ_n decreases with x , while ϕ_p increases. For a higher ϕ_M metal (Pt), ϕ_n greatly increased. In the intermediate- ϕ_M metal (W), ϕ_n exactly follows the increase of E_g in $\text{Si}_x\text{Ge}_{1-x}$ with x , while ϕ_p remains constant. Nevertheless, whatever the metal, the sum $\phi_n + \phi_p$ gives the E_g variation as a function of x (Equation (9.17)), and the Fermi level is located at the same position for both n - and p -type layers. Figure 9.14(c)

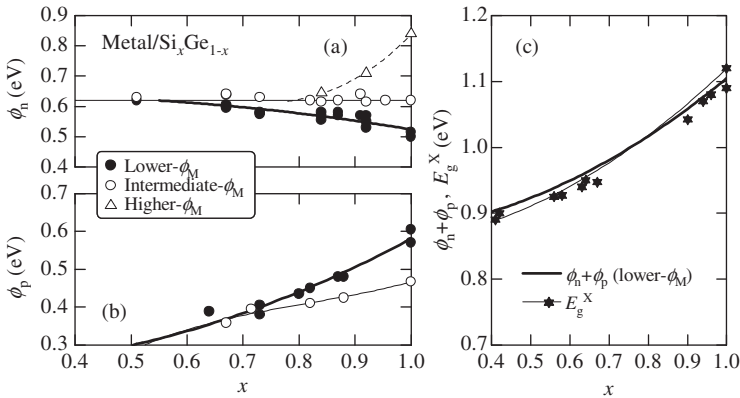


Figure 9.14 Schottky barrier heights (a) ϕ_n and (b) ϕ_p for metal/ $\text{Si}_x\text{Ge}_{1-x}$ contacts. The experimental data are taken from Aubry-Fortuna *et al.* [130]. The sum $\phi_n + \phi_p$ for the lower- ϕ_M metals, together with the band-gap energy E_g^X (Figure 6.8), are plotted against x in (c)

shows a comparison of the sum $\phi_n + \phi_p$ for the lower- ϕ_M metals plotted in Figures 9.14(a) and 9.14(b) with the variation in E_g^X with x in $\text{Si}_x\text{Ge}_{1-x}$ (Figure 6.8). As for metal/Si and metal/Ge contacts [1], the results in Figure 9.14(c) suggest that the Schottky barrier height for metal/ $\text{Si}_x\text{Ge}_{1-x}$ contact exhibits the Schottky–Mott contact nature very well.

(b) CSiGe ternary alloy

The Schottky barrier height on $\text{C}_x\text{Si}_y\text{Ge}_{1-x-y}$ has been studied by several authors [130]. Adding C to SiGe leads to an increase in the W or Ti/ p -type Schottky barrier height which is larger than that of the band-gap energy E_g , showing a change in the Fermi level position. Nevertheless, as in the case of $\text{Si}_x\text{Ge}_{1-x}$, a weaker dependence on ϕ_M compared to that of Si is observed. High values of the ideality factor with increasing C content have also been observed.

9.2.3 III–V Semiconductor Ternary Alloy

(a) (III, III)–N alloy

The Schottky rectifier properties of $n\text{-Al}_x\text{Ga}_{1-x}\text{N}$ have been studied using various metal contacts. The Schottky barrier height ϕ_n versus x obtained by depositing Au, Ni and Pd metals on $n\text{-Al}_x\text{Ga}_{1-x}\text{N}$ is shown in Figure 9.15. The experimental data are taken from various sources [131–135]. These plots suggest that it is difficult to establish an ideal Schottky contact and, thus, to obtain simple relationships such as that shown in Equation (9.17). This may be due to interface states caused by surface reactions of metal and semiconductor atoms and/or to any effects of crystalline imperfection. The $n\text{-Al}_x\text{Ga}_{1-x}\text{N}$ samples plotted in Figure 9.15 were epitaxially grown on sapphire [131, 132, 134, 135] or on 6H-SiC substrate [133].

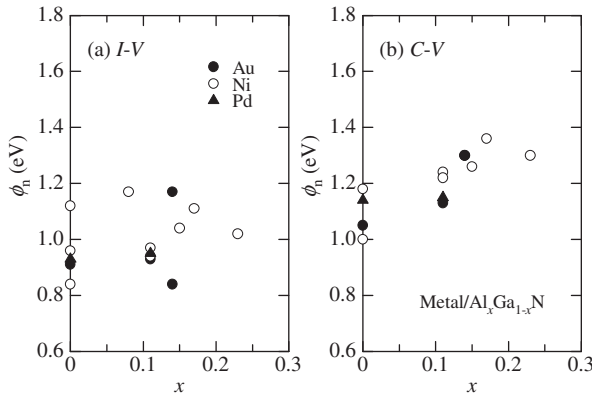


Figure 9.15 Schottky barrier height ϕ_n versus x for samples with Au, Ni and Pd metals deposited on $n\text{-Al}_x\text{Ga}_{1-x}\text{N}$: (a) $I - V$ and (b) $C - V$ measurements. The experimental data are taken from various sources (see text)

Zhang *et al.* [136] reported the x -dependent breakdown voltage in an $n\text{-Al}_x\text{Ga}_{1-x}\text{N}$ Schottky rectifier. The breakdown voltage increased from 2.3 kV for $x = 0$ (GaN) to 4.3 kV for $x = 0.25$. They also demonstrated that the use of p^+ guard rings is effective in preventing premature edge breakdown.

(b) (III, III)–P alloy

Figure 9.16 shows the experimental ϕ_n and ϕ_p values for Au/Ga_xIn_{1-x}P Schottky barriers obtained by several authors [137–139]. The GaP and InP values are taken from Adachi [1]. The barrier height ϕ_n in Figure 9.16(a) increases almost linearly with increasing x , while ϕ_p in Figure 9.16(b) shows no strong dependence on x . The sum of ϕ_n and ϕ_p , together with E_0 and E_g^X , are plotted against x in Figure 9.16(c). The Au/Ga_xIn_{1-x}P rectifiers show Schottky–Mott-like characteristics.

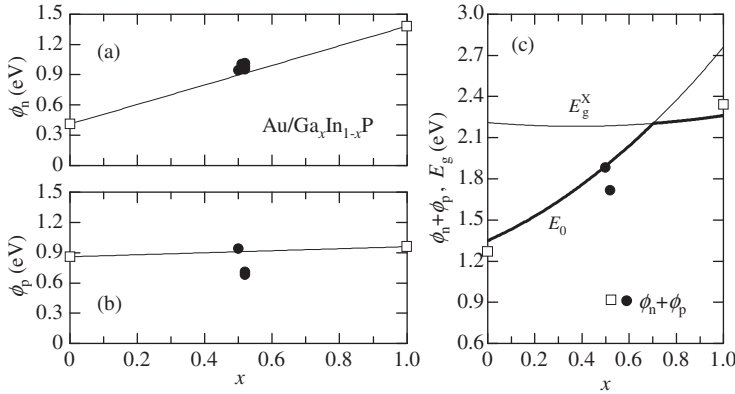


Figure 9.16 Schottky barrier heights (a) ϕ_n and (b) ϕ_p for Au/Ga_xIn_{1-x}P contacts. The experimental data are taken from various sources (see text). The open squares in (a) and (b) represent the endpoint binary data in Adachi [1]. The sum $\phi_n + \phi_p$, together with E_0 and E_g^X (Table 6.10), are plotted against x in (c)

The Schottky barrier heights for the common III–V and II–VI semiconductors allow a pattern in which the barrier height of p -type semiconductors (ϕ_p) can be determined solely by the anion of the semiconductor [140]. The corresponding barrier height of n -type semiconductors (ϕ_n) may be determined from the relationship of $\phi_n + \phi_p = E_g$. Hence, the difference in the barrier heights of the two n -type semiconductors with the same anion is equal to the difference in the band-gap energies between them. In Figure 9.16(b), we can see that the Au/Ga_xIn_{1-x}P system obeys this rule, namely, the ‘common anion’ rule.

The dependence of x on the Schottky barrier height ϕ_n for Ti/Pt/Au metals on Al_xIn_{1-x}P ($0 < x < 0.5$) has been studied using I – V and C – V measurements [141]. The results obtained suggest that ϕ_n increases almost linearly with x at a rate of ~ 14 meV/at%[Al]. This value is slightly smaller than that of E_0 , ~ 22 meV/at%[Al] (Table 6.9). Thus, the metal/Al_xIn_{1-x}P system may not obey the common anion rule (i.e. ϕ_p is dependent of x).

(c) (III, III)–As alloy

1. AlGaAs—The ϕ_n and ϕ_p values as a function of x for Al/Al_xGa_{1-x}As Schottky system have been plotted in Figure 9.17. The experimental data are taken from Adachi [26]. The solid lines in Figures 9.17(a) and 9.17(b) show the linear fits of these data (in eV)

$$\phi_n(x) = 0.77 + 0.84x \quad (0 \leq x \leq 0.425) \tag{9.18a}$$

$$\phi_n(x) = 1.22 - 0.22x \quad (0.45 < x \leq 1.0) \tag{9.18b}$$

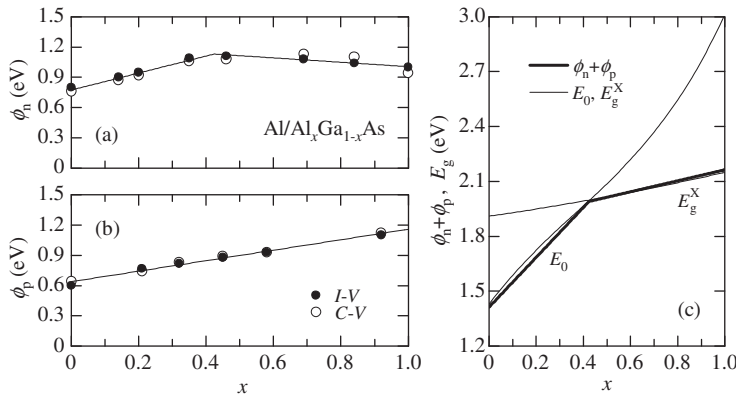


Figure 9.17 Schottky barrier heights (a) ϕ_n and (b) ϕ_p for Al/Al_xGa_{1-x}As contacts. The experimental data are taken from Adachi [26]. The solid lines in (a) and (b) show the linear least-squares fits of Equation (9.18). The sum $\phi_n + \phi_p$, together with E_0 and E_g^X (Table 6.11), are plotted against x in (c)

$$\phi_p(x) = 0.64 + 0.52x \tag{9.18c}$$

It can be easily seen from Equation 9.18(c) that the Al/Al_xGa_{1-x}As system does not obey the common anion rule. However, the sum of ϕ_n and ϕ_p plotted in Figure 9.17(c) is almost equal to the fundamental absorption edge E_0 (or E_g^X).

The x -dependent Schottky barrier heights ϕ_n and ϕ_p in Figure 9.17 resemble those of the CB and VB offsets ($\Delta E_c, \Delta E_v$) shown in Figure 9.5. Tersoff [142] pointed out that the band lineups at semiconductor heterojunctions are simply correlated with the difference in the Schottky barrier heights formed by using the same metal on the semiconductors of the heterojunction pair. In essence, this means that the physical mechanism responsible for determining the Fermi level in Schottky barrier formation also determines the band lineups in heterostructures.

2. *AllnAs*—Figure 9.18 shows the ϕ_n and ϕ_p values plotted as a function of x for Al/Al_xIn_{1-x}As Schottky system. The experimental data are taken from various sources [143–145].

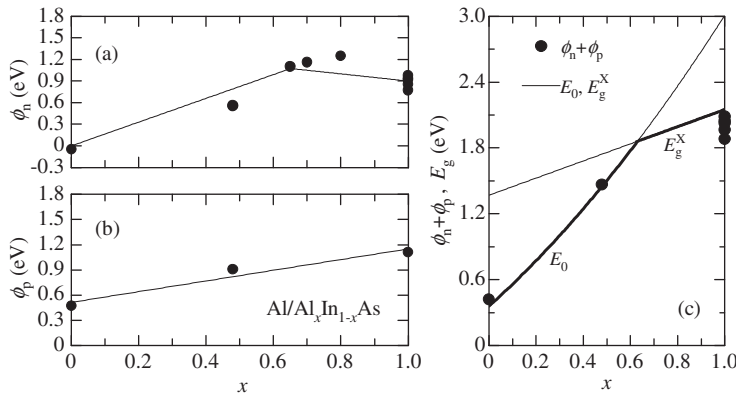


Figure 9.18 Schottky barrier heights (a) ϕ_n and (b) ϕ_p for Al/Al_xIn_{1-x}As contacts. The sum $\phi_n + \phi_p$, together with E_0 and E_g^X (see Table 6.13), are plotted against x in (c)

The AlAs and InAs data are obtained from Adachi [146]. No experimental data has been reported for the Al/p-InAs Schottky barrier height (ϕ_p). In Figure 9.18(b), therefore, we plot the experimental ϕ_p for Au/p-InAs contact [146]. It should be noted that any metal/n-InAs ($x = 1.0$) contact usually shows Ohmic behavior (i.e. $\phi_n \leq 0$ eV) [146]. The ϕ_p versus x plots in Figure 9.18(b) suggest that the Al/Al_xIn_{1-x}As system does not obey the common anion rule. However, the simple relationship $\phi_n + \phi_p \sim E_0(E_g^X)$ holds in Figure 9.18(c).

3. *GaInAs*—The Schottky barrier height ϕ_n for Au/Ga_xIn_{1-x}As contact has been determined using $I-V$ and $C-V$ measurements [147]. Figure 9.19 shows the results of these

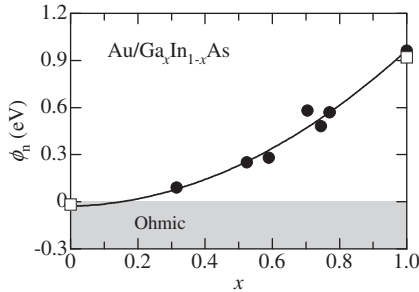


Figure 9.19 Schottky barrier height ϕ_n for Au/Ga_xIn_{1-x}As contact. The experimental data are taken from Adachi [1] (open squares) and Kajiyama *et al.* [147] (solid circles). The solid line shows the quadratic least-squares fit of Equation (9.19). The negative ϕ_n sign for $x \leq 0.15$ indicates the downward bending of the CB at the interface (Ohmic contact)

measurements. The solid line represents the quadratic least-squares fit of the experimental data (in eV)

$$\phi_n = -0.03 + 0.05x + 0.95x^2 \tag{9.19}$$

The Au/Ga_xIn_{1-x}As contact is predicted to be Ohmic for $x \leq 0.15$ ($\phi_n \leq 0$ eV). The negative ϕ_n sign stands for the downward bending of the CB at the interface.

A Schottky barrier height of $\phi_n \sim 0.2$ eV is predicted for metal/n-Ga_{0.47}In_{0.53}As lattice-matched to InP. The barrier height control is an important tool in fabricating various devices. Diode engineered for high barrier height systematically showed a higher thermal stability than low-barrier diodes. Many attempts have therefore been made to enhance the barrier height of n-Ga_xIn_{1-x}As by inserting various thin interlayers between the metal and n-Ga_xIn_{1-x}As layer. Such interlayers were counter-doped p^+ -Ga_xIn_{1-x}As, n-InP, p-InP, n-GaAs, n-Ga_xIn_{1-x}P at different thickness and dopant densities, etc. [148, 149]. An effective barrier height up to $\phi_n \sim 0.7$ eV has been achieved.

(d) (III, III)–Sb alloy

Figures 9.20(a) and 9.20(b) show the Shottky barrier height ϕ_n for Au/Al_xGa_{1-x}Sb and Au/Ga_xIn_{1-x}Sb contacts, respectively. The experimental data are taken from Chin *et al.* [150] and Keeler *et al.* [151], respectively. The solid line in Figure 9.20(a) shows the linear least-squares fit of the experimental data and provides $\phi_n \sim 1.02$ eV for Au/AlSb ($x = 1.0$) contact. The

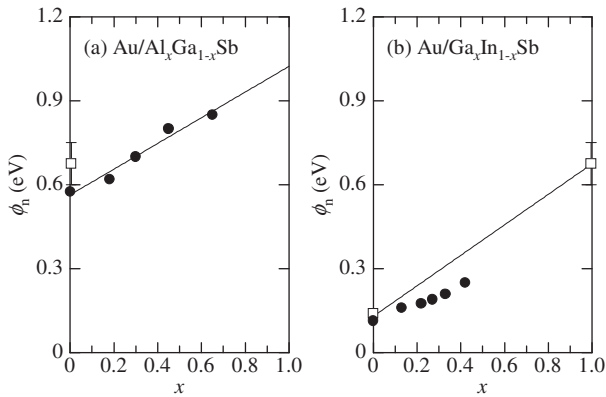


Figure 9.20 Schottky barrier height ϕ_n for (a) Au/Al_xGa_{1-x}Sb and (b) Au/Ga_xIn_{1-x}Sb contacts. The experimental data in (a) are taken from Chin *et al.* [150] and in (b) from Keeler *et al.* [151]. The open squares in (a) and (b) represent the endpoint binary data taken from Adachi [1]. The solid line in (a) shows the linear least-squares fit and estimates $\phi_n \sim 1.02$ eV for Au/AlSb contact

barrier height ϕ_p for Au/AlSb is ~ 0.56 eV [1]. The sum $\phi_n + \phi_p \sim 1.58$ eV for Au/AlSb contact is, thus, slightly smaller than the AlSb band-gap energy $E_g^X = 1.615$ eV (Table 6.1).

The Schottky barrier height for Au/Ga_xIn_{1-x}Sb can be expected to be $\phi_p \leq 0$ eV (i.e. Ohmic) [1]. Note, however, that Keeler *et al.* [151] obtained $0.017 \leq \phi_p \leq 0.022$ eV for Au contacts on *p*-Ga_xIn_{1-x}Sb ($0.62 \leq x \leq 0.905$) layers.

(e) Ga-(V, V) alloy

GaP_{0.35}Sb_{0.65} is an InP lattice-matched material. In order to overcome the low value of the Schottky barrier height on *n*-InP ($\phi_n \sim 0.4$ eV [1, 146]), Loualiche *et al.* [152] fabricated a Au/GaP_{0.35}Sb_{0.65} Schottky barrier on InP and obtained a value of $\phi_n \sim 0.6$ eV. This value is the highest ever reported on InP lattice-matched materials that do not contain aluminum.

The Schottky barrier height ϕ_n for Au/GaAs_xSb_{1-x} contact has been determined using *I-V* and *C-V* measurements [153]. Figure 9.21 shows these results, together with the *x* dependence

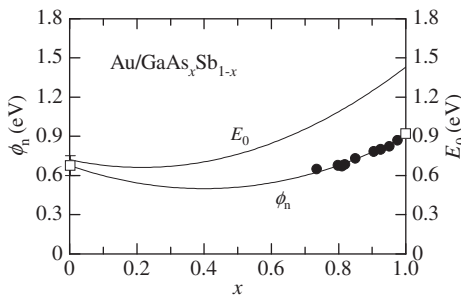


Figure 9.21 Schottky barrier height ϕ_n for Au/GaAs_xSb_{1-x} contact, together with E_0 for GaAs_xSb_{1-x} (Table 6.23). The experimental data are obtained from Zhao *et al.* [153]. The open squares represent the endpoint binary data taken from Adachi [1]

of E_0 (Table 6.23). The solid line represents the quadratic least-squares fit given by (in eV)

$$\phi_n(x) = 0.68 - 0.88x + 1.11x^2 \tag{9.20}$$

We can see that both E_0 and ϕ_n show a remarkable nonlinearity with respect to x .

9.2.4 III–V Semiconductor Quaternary Alloy

(a) (III, III)–(V, V) alloy

1. *GaInPAs*—We show in Figure 9.22 the Schottky barrier heights ϕ_n and ϕ_p as a function of y for Au metal on $\text{Ga}_x\text{In}_{1-x}\text{P}_y\text{As}_{1-y}/\text{GaAs}$. The sum of ϕ_n and ϕ_p , together with E_0 (Table 6.28), are also plotted against y . The experimental data are taken from Lee *et al.* [154] and Sugino and Kousaka [155]. The Au metal on $\text{Ga}_x\text{In}_{1-x}\text{P}_y\text{As}_{1-y}/\text{GaAs}$ exhibits the Schottky–Mott barrier characteristics satisfactorily (Equation (9.17)).

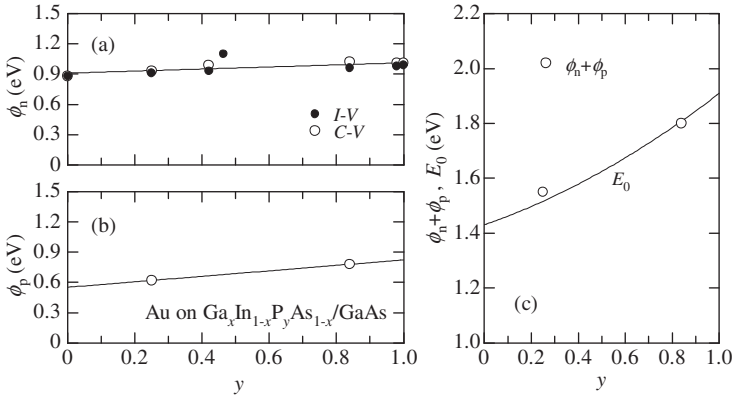


Figure 9.22 Schottky barrier heights (a) ϕ_n and (b) ϕ_p for Au on $\text{Ga}_x\text{In}_{1-x}\text{P}_y\text{As}_{1-y}/\text{GaAs}$. The sum $\phi_n + \phi_p$, together with E_0 (Table 6.28), are plotted against y in (c). The experimental data in (a)–(c) are taken from Lee *et al.* [154] and Sugino and Kousaka [155]

The Schottky barrier properties of Au metal on $\text{Ga}_x\text{In}_{1-x}\text{P}_y\text{As}_{1-y}/\text{InP}$ are shown in Figure 9.23. The ϕ_n data are taken from Morgan *et al.* [156] and Bhattacharya and Yeaman [157], while those for ϕ_p are from Escher *et al.* [158]. The solid lines represent the linear least-squares fits (in eV)

$$\phi_n(x) = 0.20 + 0.44y \tag{9.21a}$$

$$\phi_p(x) = 0.47 + 0.30y \tag{9.21b}$$

The heavy solid line in Figure 9.23(c) shows the sum of these values against y .

2. *AlGaAsSb* and *GaInAsSb*—The Schottky barrier heights for Au, Al and Sb metals on n - and p - $\text{Al}_{0.5}\text{Ga}_{0.5}\text{As}_{0.05}\text{Sb}_{0.95}/\text{GaSb}$ layers were studied by Polyakov *et al.* [159]. These authors

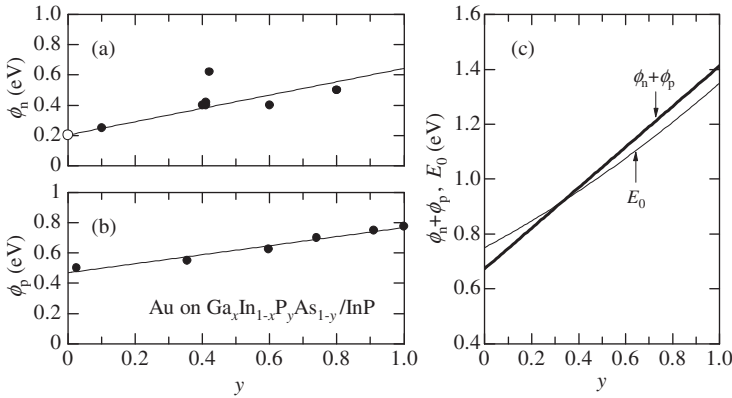


Figure 9.23 Schottky barrier heights (a) ϕ_n and (b) ϕ_p for Au on $\text{Ga}_x\text{In}_{1-x}\text{P}_y\text{As}_{1-y}/\text{InP}$. The experimental data in (a) are taken from Morgan *et al.* [156] and Bhattacharya and Yeaman [157] and in (b) from Escher *et al.* [158]. The open circle is taken from Figure 9.19. The solid lines in (a) and (b) show the linear least-squares fits of Equation (9.21). The sum of ϕ_n and ϕ_p , together with E_0 (Table 6.28), are plotted against y in (c)

found that the Schottky barriers are high for Au (1.3 eV) and Al (1.2 eV) on n -type material and very low on p -type materials. The behavior of Sb was unique with $\phi_{n,p}$ being 0.6–0.7 eV. The reason for the surface location of the Fermi-level pinning due to Au and Al metals may be related to a predominance of Ga-antisite-type native acceptors at the surface, which is not the case for Sb metal.

The Schottky barriers for Al, Au and Sb metals on n - $\text{Ga}_x\text{In}_{1-x}\text{As}_y\text{Sb}_{1-y}/\text{GaSb}$ ($x = 0.85$) were determined by Polyakov *et al.* [160]. All these Schottky barriers had heights of ~ 0.5 eV, with the surface Fermi level located at $E_v + 0.16$ eV.

(b) (III, III, III)–V alloy

1. AlGaInN —Figure 9.24 plots the ϕ_n versus x for $\text{Pd}/\text{Al}_x\text{Ga}_{0.98-x}\text{In}_{0.02}\text{N}$ contact obtained from $I-V$ and $C-V$ measurements [161]. The alloy samples were grown on (0001)-sapphire substrates by MOCVD. It was found that the larger difference in ϕ_n between $I-V$

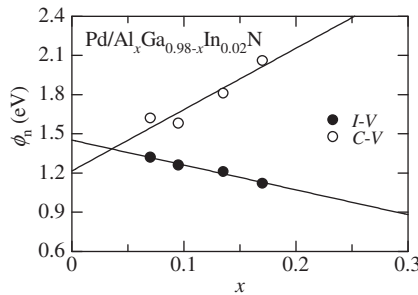


Figure 9.24 Schottky barrier height ϕ_n for $\text{Pd}/\text{Al}_x\text{Ga}_{0.98-x}\text{In}_{0.02}\text{N}$ contact obtained by Liu *et al.* [161]

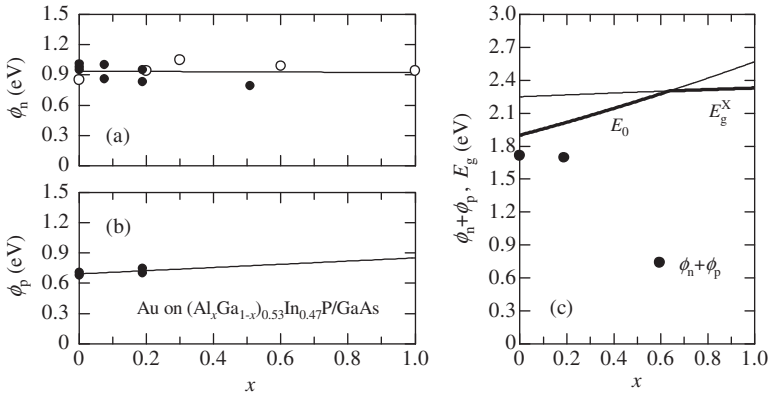


Figure 9.25 Schottky barrier heights (a) ϕ_n and (b) ϕ_p for Au on $(Al_xGa_{1-x})_{0.53}In_{0.47}P/GaAs$. The sum of ϕ_n and ϕ_p , together with E_0 and E_g^X (Table 6.28), are plotted against x in (c). The experimental data are taken from Nanda *et al.* [137] (solid circles) and Wang *et al.* [162] (open circles)

and $C - V$ measurements could not be quantitatively explained by the traditional electron transport mechanisms of the Schottky barrier rectifier, such as the tunneling effect, image-force effect or barrier inhomogeneity theory.

2. *AlGaInP*—The Schottky barrier heights ϕ_n and ϕ_p for Au metal on $(Al_xGa_{1-x})_{0.53}In_{0.47}P/GaAs$ are shown in Figure 9.25. The experimental data are taken from Nanda *et al.* [137] (solid circles) and Wang *et al.* [162] (open circles). The unique feature of this rectifying contact system is that both ϕ_n and ϕ_p show no strong dependence on alloy composition. If we accept the common anion rule, no strong x dependence of ϕ_p can be expected. In Figure 9.25(c), the sum of ϕ_n and ϕ_p obtained by Nanda *et al.* [137], together with E_0 and E_g^X (Table 6.28), are plotted against composition x . It is apparent that $\phi_n + \phi_p \neq E_0$ (or E_g^X) for this rectifying contact system.
3. *AlGaInAs*—The Schottky barrier height ϕ_n for Au metal on $(Al_xGa_{1-x})_{0.48}In_{0.52}As/InP$ has been obtained using $I - V$ and $C - V$ measurements [163]. These results are plotted in Figure 9.26. The ideality factors determined from the forward-bias $I - V$ characteristics were

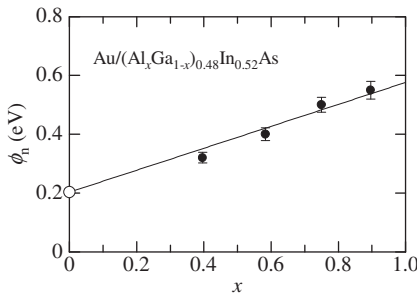


Figure 9.26 Schottky barrier height ϕ_n for Au on $(Al_xGa_{1-x})_{0.48}In_{0.52}As/InP$. The experimental data are taken from Schramm *et al.* [163]. The data represented by the open circle is taken from Figure 9.19. The solid line shows the linear least-squares fit of Equation (9.22)

in the range 1.08 – 1.2, indicating that the Schottky contacts were of high quality. The open circle represents the Au/Ga_{0.47}In_{0.53}As barrier height taken from Figure 9.19. The solid line shows the linear least-squares fit of these data (in eV)

$$\phi_n(x) = 0.20 + 0.37x \tag{9.22}$$

9.2.5 II–VI Semiconductor Alloy

(a) (II, II)–Te ternary alloy

The Schottky barrier height ϕ_p for In metal on Mg_xZn_{1-x}Te determined by C–V and photoelectron measurements [164] is plotted in Figure 9.27(a). The solid line shows the linear least-squares fit of these data (solid circles). This fit predicts a negative ϕ_p value of –0.36 eV (Ohmic contact) for $x=1.0$ (MgTe). The open circle also represents the In/*p*-ZnTe data in Adachi [165]. The dashed line corresponds to the common anion rule, $\phi_p = 1.06$ eV. Using this ϕ_p value and assuming ideal Schottky–Mott contact, we can estimate $\phi_n \sim 1.4$ and ~ 1.2 eV for In/*n*-MgTe and In/*n*-ZnTe contacts, respectively.

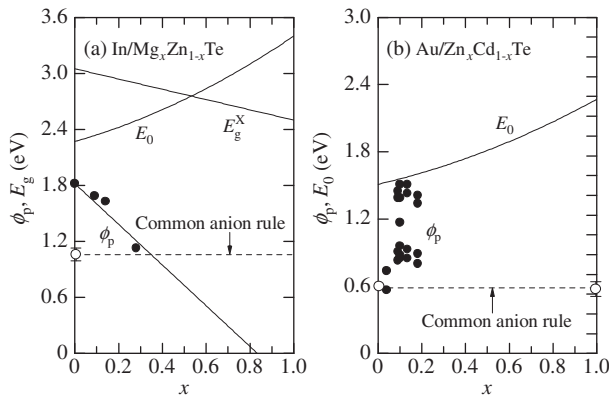


Figure 9.27 (a) Schottky barrier height ϕ_p for In/Mg_xZn_{1-x}Te contact, together with E_0 and E_g^X (Figure 6.58). The experimental data are taken from Akkad *et al.* [164]. The solid line shows the linear least-squares fit. The open circle represents the In/ZnTe data taken from Adachi [165]. The dashed line indicates the common anion rule ($\phi_p = 1.06$ eV). (b) Schottky barrier height ϕ_p for Au/Zn_xCd_{1-x}Te contact (see text), together with E_0 for Zn_xCd_{1-x}Te (Table 6.30). The open circles show the Au/ZnTe and Au/CdTe data [1, 165]. The dashed line indicates the common anion rule ($\phi_p = 0.6$ eV)

The Schottky barrier height ϕ_p for Au metal on Zn_xCd_{1-x}Te is plotted against x in Figure 9.27(b). The experimental ϕ_p data are taken from various sources [166–168]. These data scatter largely and fall within $\phi_p = 1.0 \pm 0.4$ eV ($0 < x < 0.2$). The open circles also show the Au/*p*-ZnTe and Au/*p*-CdTe data in Adachi [1, 165]. Using the common anion rule ($\phi_p = 0.6$ eV, dashed line) and assuming ideal Schottky–Mott contact, we obtain $\phi_n \sim 1.7$ and ~ 0.9 eV for Au/*n*-ZnTe and Au/*n*-CdTe contacts, respectively. The ϕ_n value reported for Au/*n*-CdTe in the literature is 0.59–1.0 eV [1, 165]. No ϕ_n value has been reported for any metal/*n*-ZnTe contact.

(b) Zn–(VI, VI) ternary alloy

ZnS_xSe_{1-x} can be grown lattice-matched to GaAs ($x = 0.06-0.07$). The Schottky contacts were formed on n -ZnS_{0.07}Se_{0.93} epilayers grown on n -GaAs by MBE for metals with different work functions, Yb, Al, Cr, Cu, Au and Pd [169]. The ϕ_n value for Au/ n -ZnS_{0.07}Se_{0.93} contact has been plotted in Figure 9.28. The open circles represent the Au/ n -ZnS and Au/ n -ZnSe data taken from Adachi [1, 165]. The solid line also shows the linearly interpolated result between the endpoint binary data (in eV)

$$\phi_n(x) = 1.45 + 0.65x \tag{9.23}$$

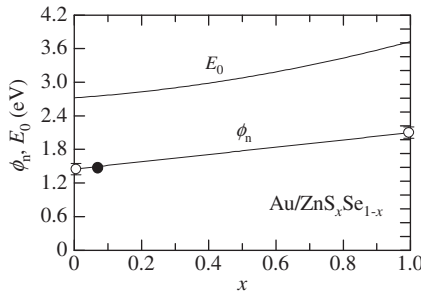


Figure 9.28 Schottky barrier height ϕ_n for Au/ZnS_xSe_{1-x} contact, together with E_0 for ZnS_xSe_{1-x} (Table 6.30). The experimental data ($x = 0.07$) is taken from Wang *et al.* [169]. The open circles show the Au/ZnS and Au/ZnSe data taken from Adachi [1, 165]. The solid line indicates the linearly interpolated result given by Equation (9.23)

REFERENCES

- [1] S. Adachi, *Properties of Group-IV, III–V and II–VI Semiconductors*, John Wiley & Sons, Ltd, Chichester, 2005.
- [2] K. Brunner, K. Eberl, and W. Winter, *Phys. Rev. Lett.* **76**, 303 (1996).
- [3] A. A. Demkov and O. F. Sankey, *Phys. Rev. B* **48**, 2207 (1993).
- [4] D. C. Houghton, G. C. Aers, N. L. Rowell, K. Brunner, W. Winter, K. Eberl, *Phys. Rev. Lett.* **78**, 2441 (1997).
- [5] R. L. Williams, G. C. Aers, N. L. Rowell, K. Brunner, W. Winter, and K. Eberl, *Appl. Phys. Lett.* **72**, 1320 (1998).
- [6] S. H. Ke, T. Uda, and K. Terakura, *Phys. Rev. B* **59**, 15013 (1999).
- [7] G. N. Northrop, J. F. Morar, D. J. Wolford, and J. A. Bradley, *J. Vac. Sci. Technol. B* **10**, 2018 (1992).
- [8] S. Fukatsu and Y. Shiraki, *Appl. Phys. Lett.* **63**, 2378 (1993).
- [9] M. Wachter, K. Thonke, and R. Sauer, *Thin Solid Films* **222**, 10 (1992).
- [10] T. Bajer, U. Mantz, K. Thonke, R. Sauer, F. Schäffler, H. -J. Herzog, *Phys. Rev. B* **50**, 15191 (1994).
- [11] M. L. W. Thewalt, D. A. Harrison, C. F. Reinhart, J. A. Wolk, and H. Lafontaine, *Phys. Rev. Lett.* **79**, 269 (1997).
- [12] H. H. Cheng, S. T. Yen, and R. J. Nicholas, *Phys. Rev. B* **62**, 4638 (2000).
- [13] B. L. Stein, E. T. Yu, E. T. Croke, A. T. Hunter, T. Laursen, A. E. Bair, J. W. Mayer, and C. C. Ahn, *Appl. Phys. Lett.* **70**, 3413 (1997).

- [14] B. L. Stein, E. T. Yu, E. T. Croke, A. T. Hunter, T. Laursen, J. W. Mayer, and C. C. Ahn, *J. Vac. Sci. Technol. B* **16**, 1639 (1998).
- [15] R. Hartmann, U. Gennser, H. Sigg, D. Grützmacher, and K. Ensslin, *Appl. Phys. Lett.* **73**, 1257 (1998).
- [16] J. Kolodzey, F. Chen, B. A. Orner, D. Guerin, and S. I. Shah, *Thin Solid Films* **302**, 201 (1997).
- [17] Y. Zhang, A. Mascarenhas, and L.-W. Wang, *Appl. Phys. Lett.* **80**, 3111, (2002), and references cited therein.
- [18] D. Patel, M. J. Hafich, G. Y. Robinson, and C. S. Menoni, *Phys. Rev. B* **48**, 18031 (1993).
- [19] M. D. Dawson, S. P. Najda, A. H. Kean, G. Duggan, D. J. Mowbray, O. P. Kowalski, M. S. Skolnick, and M. Hopkinson, *Phys. Rev. B* **50**, 11190 (1994).
- [20] I.-J. Kim, Y.-H. Cho, K.-S. Kim, B.-D. Choe, and H. Lim, *Appl. Phys. Lett.* **68**, 3488 (1996).
- [21] R. Dingle, W. Wiegmann, and C. H. Henry, *Phys. Rev. Lett.* **33**, 827 (1974).
- [22] R. Dingle, A. C. Gossard, and W. Wiegmann, *Phys. Rev. Lett.* **34**, 1327 (1975).
- [23] R. C. Miller, A. C. Gossard, D. A. Kleinman, and O. Munteanu, *Phys. Rev. B* **29**, 3740 (1984).
- [24] R. C. Miller, D. A. Kleinman, and A. C. Gossard, *Phys. Rev. B* **29**, 7085 (1984).
- [25] G. Duggan, H. I. Ralph, and K. J. Moore, *Phys. Rev. B* **32**, 8395 (1985).
- [26] S. Adachi, *GaAs and Related Materials: Bulk Semiconducting and Superlattice Properties*, World Scientific, Singapore, (1994).
- [27] S. Adachi, in *Properties of Lattice-matched and Strained Indium Gallium Arsenide*, EMIS Datareviews Series No. 8 (edited by P. Bhattacharya), INSPEC, London, 1993, p. 84.
- [28] J. Böhrer, A. Krost, T. Wolf, and D. Bimberg, *Phys. Rev. B* **47**, 6439 (1993).
- [29] E. Lugagne-Delpon, J. P. André, and P. Voisin, *Solid State Commun.* **86**, 1 (1993).
- [30] W. Seidel, O. Krebs, P. Voisin, J. C. Harmand, F. Aristone, and J. F. Palmier, *Phys. Rev. B* **55**, 2274 (1997).
- [31] J. P. Landesman, J. C. Garcia, J. Massies, P. Maurel, G. Jezequel, J. P. Hirtz, and P. Alnot, *Appl. Phys. Lett.* **60**, 1241 (1992).
- [32] J. M. López-Villegas P. Roura, J. Bosch, J. R. Morante, A. Georgakilas, and K. Zekentes, *J. Electrochem. Soc.* **140**, 1492 (1993).
- [33] J.-H. Huang and T. Y. Chang, *J. Appl. Phys.* **76**, 2893 (1994).
- [34] K. Tanaka, N. Kotera, and H. Nakamura, *J. Appl. Phys.* **85**, 4071 (1999).
- [35] A. K. Srivastava, J. L. Zyskind, R. M. Lum, B. V. Dutt, and J. K. Klingert, *Appl. Phys. Lett.* **49**, 41 (1986).
- [36] M. Mebarki, A. Kadri, and H. Mani, *Solid State Commun.* **72**, 795 (1989).
- [37] S. S. Kizhaev, S. S. Molchanov, N. V. Zotova, E. A. Grebenschikova, Y. P. Yakovlev, E. Hulicius, T. šimeček, K. Melichar, and J. Pangrác, *Tech. Phys. Lett.* **27**, 964 (2001).
- [38] H. A. Kaci, D. Boukredimi, and M. Mebarki, *Phys. Status Solidi A* **163**, 101 (1997).
- [39] O. Ostinelli, G. Almuneau, and W. Bächtold, *Semicond. Sci. Technol.* **21**, 681 (2006).
- [40] J. S. Nelson, S. R. Kurtz, L. R. Dawson, and J. A. Lott, *Appl. Phys. Lett.* **57**, 578 (1990).
- [41] M. P. Mikhailova and A. N. Titkov, *Semicond. Sci. Technol.* **9**, 1279 (1994).
- [42] M. A. Afrailov, A. N. Baranov, A. P. Dmitriev, M. P. Mikhailova, Y. P. Smorchkova, I. N. Timchenko, V. V. Sherstnev, Y. P. Yakovlev, and I. N. Yassievich, *Sov. Phys. Semicond.* **24**, 876 (1990).
- [43] M. Mebarki, D. Boukredimi, and S. Sadik, J. L. Lazzari, *J. Appl. Phys.* **73**, 2360 (1993).
- [44] J. R. Chang, Y. K. Su, and Y. T. Lu, *J. Appl. Phys.* **86**, 6908 (1999).
- [45] M. P. Mikhailova, K. D. Moiseev, T. I. Voronina, T. S. Lagunova, and Y. P. Yakovlev, *Semicond.* **41**, 161 (2007).
- [46] W. Z. Shen, S. C. Shen, W. G. Tang, Y. Chang, Y. Zhao, and A. Z. Li, *J. Phys.: Condens. Matter* **8**, 4751 (1996).
- [47] J. R. Chang, Y. K. Su, C. L. Lin, K. M. Wu, W. C. Huang, Y. T. Lu, D. H. Jaw, and W. L. Li, S. M. Chen, *Appl. Phys. Lett.* **75**, 238 (1999).
- [48] Y. Ishitani, E. Nomoto, T. Tanaka, and S. Minagawa, *J. Appl. Phys.* **81**, 1763 (1997).

- [49] C. T. H. F. Liedenbaum, A. Valster, A. L. G. J. Severens, G. W. 't Hooft, *Appl. Phys. Lett.* **57**, 2698 (1990).
- [50] O. P. Kowalski, J. W. Cockburn, D. M. Mowbray, M. S. Skolnick, R. Teissier, and M. Hopkinson, *Appl. Phys. Lett.* **66**, 619 (1995).
- [51] H. K. Yow, P. A. Houston, and M. Hopkinson, *Appl. Phys. Lett.* **66**, 2852 (1995).
- [52] A. D. Prins, J. L. Sly, A. T. Meney, D. J. Dunstan, O'reilly E. P. A. R. Adams, and A. Valster, *J. Phys. Chem. Solids* **56**, 423 (1995).
- [53] T. M. Ritter, B. A. Weinstein, R. E. Viturro, and D. P. Bour, *Phys. Status Solidi B* **211**, 869 (1999).
- [54] M. D. Dawson, G. Duggan, and D. J. Arent, *Phys. Rev. B* **51**, 17660 (1995).
- [55] D. Vignaud and F. Mollot, *J. Appl. Phys.* **93**, 384 (2003).
- [56] J. Shao, A. Dörnen, R. Winterhoff, and F. Scholz, *Phys. Rev. B* **66**, 035109 (2002).
- [57] Y. Sugiyama, T. Inata, T. Fujii, Y. Nakata, S. Muto, and S. Hiyamizu, *Jpn. J. Appl. Phys.* **25**, L648 (1986).
- [58] A. Sandhu, Y. Nakata, S. Sasa, K. Kodama, and S. Hiyamizu, *Jpn. J. Appl. Phys.* **26**, 1709 (1987).
- [59] G. Martin, S. Strite, A. Botchkarev, A. Agarwal, A. Rockett, H. Morkoc, W. R. L. Lambrecht, and B. Segall, *Appl. Phys. Lett.* **65**, 610 (1994).
- [60] J. Baur, K. Maier, M. Kunzer, U. Kaufmann, and J. Schneider, *Appl. Phys. Lett.* **65**, 2211 (1994).
- [61] J. R. Waldrop and R. W. Grant, *Appl. Phys. Lett.* **68**, 2879 (1996).
- [62] K. B. Nam, J. Li, K. H. Kim, J. Y. Lin, and H. X. Jiang, *Appl. Phys. Lett.* **78**, 3690 (2001).
- [63] D. R. Hang, C. H. Chen, Y. F. Chen, H. X. Jiang, and J. Y. Lin, *J. Appl. Phys.* **90**, 1887 (2001).
- [64] C. T. Foxon, S. V. Novikov, L. X. Zhao, and I. Harrison, *Appl. Phys. Lett.* **83**, 1166 (2003).
- [65] A. N. Westmeyer, S. Mahajan, K. K. Bajaj, J. Y. Lin, H. X. Jiang, D. D. Koleske, and R. T. Senger, *J. Appl. Phys.* **99**, 013705 (2006).
- [66] S. W. King, C. Ronning, R. F. Davis, M. C. Benjamin, and R. J. Nemanich, *J. Appl. Phys.* **84**, 2086 (1998).
- [67] F. Bernardini, and V. Fiorentini, *Phys. Rev. B* **57**, R9427 (1998).
- [68] C. -L. Wu, C. -H. Shen, and S. Gwo, *Appl. Phys. Lett.* **88**, 032105 (2006).
- [69] P. D. C. King, T. D. Veal, P. H. Hefferson, C. F. McConville, T. Wang, P. J. Parbrook, H. Lu, and W. J. Schaff, *Appl. Phys. Lett.* **90**, 132105 (2007).
- [70] C. Manz, M. Kunzer, H. Obloh, A. Ramakrishnan, and U. Kaufmann, *Appl. Phys. Lett.* **74**, 3993 (1999).
- [71] H. Zhang, E. J. Miller, E. T. Yu, C. Poblentz, and J. S. Speck, *Appl. Phys. Lett.* **84**, 4644 (2004).
- [72] C. -F. Shin, N. -C. Chen, P. -H. Chang, and K. -S. Liu, *Jpn. J. Appl. Phys.* **44**, 7892 (2005).
- [73] T. Ohashi, P. Holmström, A. Kikuchi, and K. Kishino, *Appl. Phys. Lett.* **89**, 041907 (2006).
- [74] Z. H. Mahmood, A. P. Shah, A. Kadir, M. R. Gokhale, S. Ghosh, A. Bhattacharya, and B. M. Arora, *Appl. Phys. Lett.* **91**, 152108 (2007).
- [75] S. P. Kowalczyk, W. J. Schaffer, E. A. Kraut, and R. W. Grant, *J. Vac. Sci. Technol.* **20**, 705 (1992).
- [76] V. D. Kulakovskii, T. G. Andersson, and L. V. Butov, *Semicond. Sci. Technol.* **8**, 477 (1993).
- [77] W. S. Chi, and Y. S. Huang, *Semicond. Sci. Technol.* **10**, 127 (1995).
- [78] L. Lu, J. Wang, Y. Wang, W. Ge, G. Yang, and Z. Wang, *J. Appl. Phys.* **83**, 2093 (1998).
- [79] Y. Zhang, A. Mascarenhas, H. P. Xin, and C. W. Tu, *Phys. Rev. B* **61**, 7479 (2000).
- [80] I. A. Buyanova, G. Pozina, P. N. Hai, W. M. Chen, H. P. Xin, and C. W. Tu, *Phys. Rev. B* **63**, 033303 (2000).
- [81] P. Krispin, S. G. Spruytte, J. S. Harris, and K. H. Ploog, *J. Appl. Phys.* **90**, 2405 (2001).
- [82] S. Tomic, E. P. O'Reilly, P. J. Klar, H. Grüning, W. Heimbrodt, W. M. Chen, and I. A. Buyanova, *Phys. Rev. B* **69**, 245305 (2004).
- [83] R. Kudrawiec, M. Motyka, M. Gladysiewicz, J. Misiewicz, J. A. Gupta, and G. C. Aers, *Solid State Commun.* **138**, 365 (2006).
- [84] T. Kitatani, M. Kondow, T. Kikawa, Y. Yazawa, M. Okai, and K. Uomi, *Jpn. J. Appl. Phys.* **38**, 5003 (1999).

- [85] M. Hetterich, M. D. Dawson, A. Y. Egorov, D. Bernklau, and H. Riechert, *Appl. Phys. Lett.* **76**, 1030 (2000).
- [86] G. Dumitras, and H. Riechert, *J. Appl. Phys.* **94**, 3955 (2003).
- [87] J. C. Harmand, A. Caliman, E. V. K. Rao, L. Largeau, J. Ramos, R. Teissier, L. Travers, G. Ungaro, B. Theys, and I. F. L. Dias, *Semicond. Sci. Technol.* **17**, 778 (2002).
- [88] F. Bousbih, S. B. Bouzid, R. Chtourou, F. F. Charfi, J. C. Harmand, and G. Ungaro, *Mater. Sci. Eng. C* **21**, 251 (2002).
- [89] S. A. Lourenco, I. F. L. Dias, L. C. P. Poc as, J. L. Duarte, J. B. B. de Oliveira, and J. C. Harmand, *J. Appl. Phys.* **93**, 4475 (2003).
- [90] R. Kudrawiec, K. Ryczko, J. Misiewicz, H. B. Yuen, S. R. Bank, M. A. Wistey, H. P. Bae, and J. S. Harris, Jr., *Appl. Phys. Lett.* **86**, 141908 (2005).
- [91] G. V. Rao, F. Säuberlich, and A. Klein, *Appl. Phys. Lett.* **87**, 032101 (2005).
- [92] J.-J. Chen, F. Ren, Y. Li, D. P. Norton, S. J., Pearton, A. Osinsky, J. W. Dong, P. P. Chow, and J. F. Weaver, *Appl. Phys. Lett.* **87**, 192106 (2005).
- [93] T. Yokogawa, T. Ishikawa, J. L. Merz, and T. Taguchi, *J. Appl. Phys.* **75**, 2189 (1994).
- [94] M. Kim, C. S. Kim, S. Lee, J. K. Furdyna, and M. Dobrowolska, *J. Cryst. Growth* **214/215**, 325 (2000).
- [95] M. Wört, E. Griehl, T. Reisinger, R. Flierl, B. Haserer, T. Semmler, T. Frey, W. Gebhardt, *Phys. Status Solidi B* **202**, 805 (1997).
- [96] P. M. Young, E. Runge, M. Ziegler, and H. Ehrenreich, *Phys. Rev. B* **49**, 7424 (1994).
- [97] F. Liaci, P. Bigenwald, O. Briot, B. Gil, N. Briot, T. Cloitre, and R. L. Aulombard, *Phys. Rev. B* **51**, 4699 (1995).
- [98] V. Pellegrini, A. Tredicucci, F. Beltram, L. Vanzetti, M. Lazzarino, and A. Franciosi, *J. Appl. Phys.* **79**, 929 (1996).
- [99] C. Guénaud, E. Deleporte, A. Filoramo, P. Lelong, C. Delalande, C. Morhain, E. Tournié, and J. P. Faurie, *J. Appl. Phys.* **87**, 1863 (2000).
- [100] V. I. Kozlovsky, Y. G. Sadofyev, and V. G. Litvinov, *Nanotechnol.* **11**, 241 (2000).
- [101] M. W. Wang, J. F. Swenberg, M. C. Phillips, E. T. Yu, J. O. McCaldin, R. W. Grant, and T. C. McGill, *Appl. Phys. Lett.* **64**, 3455 (1994).
- [102] H. Mariette, F. Dal'bo N. Magnea, G. Lentz, and H. Tuffigo, *Phys. Rev. B* **38**, 12443 (1988).
- [103] J. Allegre, J. Calatayud, B. Gil, H. Mathieu, H. Tuffigo, G. Lentz, N. Magnea, and H. Mariette, *Phys. Rev. B* **41**, 8195 (1990).
- [104] E. Deleporte, J. M. Berroir, C. Delalande, N. Magnea, H. Mariette, J. Allegre, and J. Calatayud, *Phys. Rev. B* **45**, 6305 (1992).
- [105] J. Calatayud, J. Allègre, H. Mathieu, N. Magnéa, and H. Mariette, *Phys. Rev. B* **47**, 9684 (1993).
- [106] V. I. Kozlovsky, Y. G. Sadofyev, and V. G. Litvinov, *J. Cryst. Growth* **214/215**, 983 (2000).
- [107] von Truchseß M. V. Latussek, F. Goschenhofer, C. R. Becker, G. Landwehr, E. Batke, R. Sizmann, and P. Helgesen, *Phys. Rev. B* **51**, 17618 (1995).
- [108] A. Qteish, and R. J. Needs, *J. Phys.: Condens. Matter* **3**, 617 (1991).
- [109] P. M. Young, and E. Ehrenreich, *Phys. Rev. B* **43**, 12057 (1991).
- [110] R. Sizmann, P. Helgesen, T. Colin, T. Skauli, and S. Lφvold, *Appl. Phys. Lett.* **64**, 881 (1994).
- [111] Z. Yang, Z. Yu, Y. Lansari, S. Hwang, J. W. Cook, Jr., and J. F. Schetzina, *Phys. Rev. B* **49**, 8096 (1994).
- [112] von Truchseß M. V. Latussek, C. R. Becker, and E. Batke, *J. Cryst. Growth* **159**, 1128 (1996).
- [113] D. Eich, K. Ortner, U. Groh, Z. H. Chen, C. R. Becker, G. Landwehr, R. Fink, and E. Umbach, *Phys. Status Solidi A* **173**, 261 (1999).
- [114] C. R. Becker, V. Latussek, Pfeuffer-Jeschke A. G. Landwehr, and L. W. Molenkamp, *Phys. Rev. B* **62**, 10353 (2000).
- [115] K. Shahzad, D. J. Olego, C. G. Van de Walle, *Phys. Rev. B* **38**, 1417 (1988).
- [116] M. Lomascolo, G. H. Li, K. Syassen, R. Cingolani, and I. Suemune, *Phys. Rev. B* **50**, 14635 (1994).
- [117] S. Li, and J. B. Khurgin, *Appl. Phys. Lett.* **60**, 1969 (1992).

- [118] S. Li, and J. B. Khurgin, *Appl. Phys. Lett.* **61**, 1694 (1992).
- [119] E. Pelucchi, S. Rubini, B. Bonanni, A. Franciosi, and M. Peressi, *Appl. Phys. Lett.* **78**, 1574 (2001).
- [120] Y. Wu, K. Ichino, Y. Kawakami, S. Fujita, and S. Fujita, *Jpn. J. Appl. Phys.* **31**, 1737 (1992).
- [121] K. Kondo, H. Okuyama, and A. Ishibashi, *Appl. Phys. Lett.* **64**, 3434 (1994).
- [122] J. Suda, Y. Kawakami, S. Fujita, and S. Fujita, *Jpn. J. Appl. Phys.* **33**, L986 (1994).
- [123] T. Miyajima, F. P. Logue, J. F. Donegan, J. Hegarty, H. Okuyama, A. Ishibashi, and Y. Mori, *Appl. Phys. Lett.* **66**, 180 (1995).
- [124] K. Shahzad, J. Petruzzello, J. M. Gaines, and C. Ponzoni, *Appl. Phys. Lett.* **67**, 659 (1995).
- [125] H. Hamadeh, M. Lünenbürger, H. Kalisch, and M. Heuken, *J. Cryst. Growth* **184/185**, 867 (1998).
- [126] H. P. Wagner, M. Kühnelt, H. Wenisch, and D. Hommel, *Phys. Rev. B* **63**, 235319 (2001).
- [127] P. F. Baude, M. A. Haase, G. M. Haugen, K. K. Law, T. J. Miller, K. Smekalin, J. Phillips, and P. Bhattacharya, *Appl. Phys. Lett.* **68**, 3591 (1996).
- [128] K. Godo, H. Makino, M. W. Cho, J. H. Chang, S. K. Hong, T. Yao, M. Y. Shen, and T. Goto, *J. Appl. Phys.* **91**, 5811 (2002).
- [129] M. Muñoz, H. Lu, X. Zhou, M. C. Tamargo, and F. H. Pollak, *Appl. Phys. Lett.* **83**, 1995 (2003).
- [130] Aubry-Fortuna V. M. Barthula, G. Trembiay, F. Meyer, P. Warren, and K. Lyutovitch, *J. Appl. Phys.* **89**, 5533, (2001), and references cited therein.
- [131] M. R. H. Khan, H. Nakayama, T. Detschprohm, K. Hiramatsu, and N. Sawaki, *Jpn. J. Appl. Phys.* **34**, 6375 (1995).
- [132] S. Arulkumaran, T. Egawa, G-Y. Zhao, H. Isikawa, T. Jimbo, and M. Umeno, *Jpn. J. Appl. Phys.* **39**, L351 (2000).
- [133] D. Qiao, L. S. Yu, S. S. Lau, J. M. Redwing, J. Y. Lin, and H. X. Jiang, *J. Appl. Phys.* **87**, 801 (2000).
- [134] E. D. Readinger, B. P. Luther, S. E. Mohney, and E. L. Piner, *J. Appl. Phys.* **89**, 7983 (2001).
- [135] Y. Liu, M. Z. Kausar, P. P. Ruden, Z. Hassan, Y. C. Lee, S. S. Ng, and F. K. Yam, *Appl. Phys. Lett.* **88**, 022109 (2006).
- [136] A. P. Zhang, G. Dang, F. Ren, J. Han, A. Y. Polyakov, N. B. Smimov, A. V. Govorkov, J. M. Redwing, X. A. Cao, and S. J. Pearton, *Appl. Phys. Lett.* **76**, 1767 (2000).
- [137] A. Nanda, M. J. Hafich, T. J. Vogt, L. M. Woods, G. A. Patrizi, and G. Y. Robinson, *Appl. Phys. Lett.* **61**, 81 (1992).
- [138] E. Y. Chang, Y.-L. Lai, K.-C. Lin, and C.-Y. Chang, *J. Appl. Phys.* **74**, 5622 (1993).
- [139] S. D. Kwon, H. K. Kwon, B. -D. Choe, H. Lim, and J. Y. Lee, *J. Appl. Phys.* **78**, 2482 (1995).
- [140] J. O. McCaldin, T. C. McGill, and C. A. Mead, *J. Vac. Sci. Technol.* **13**, 802 (1976).
- [141] Y. Zhu, Y. Ishimaru, N. Takahashi, and M. Shimizu, *J. Appl. Phys.* **80**, 1617 (1996).
- [142] J. Tersoff, *Phys. Rev. B* **32**, 6968 (1985).
- [143] L. P. Sadwick, C. W. Kim, K. L. Tan, and D. C. Streit, *IEEE Electron Dev Lett.* **12**, 626 (1991).
- [144] F. Gueissaz, M. Gailhanou, R. Houdré, and M. Ilegems, *Appl. Phys. Lett.* **60**, 1099 (1992).
- [145] J.-I. Chyi, J.-L. Shieh, R.-J. Lin, J.-W. Pan, and R.-M. Lin, *J. Appl. Phys.* **77**, 1813 (1995).
- [146] S. Adachi, *Handbook on Physical Properties of Semiconductors: Volume 2 III-V Compound Semiconductors*, Kluwer Academic, Boston, 2004.
- [147] K. Kajiyama, Y. Mizushima, and S. Sakata, *Appl. Phys. Lett.* **23**, 458 (1973).
- [148] P. Kordoš, M. Marso, R. Meyer, and H. Lüth, *J. Appl. Phys.* **72**, 2347 (1992).
- [149] C. Marinelli, L. Sorba, M. Lazzarino, D. Kumar, E. Pelucchi, B. H. Müller, D. Orani, S. Rubini, A. Franciosi, S. D. Franceschi, and F. Beltram, *J. Vac. Sci. Technol. B* **18**, 2119 (2000).
- [150] R. Chin, R. A. Milano, and H. D. Law, *Electron. Lett.* **16**, 627 (1980).
- [151] W. J. Keeler, A. P. Roth, and E. Fortin, *Can. J. Phys.* **58**, 63 (1980).
- [152] S. Loualiche, A. L. Corre, S. Salaun, J. Caulet, B. Lambert, M. Gauneau, D. Lecrosnier, and B. Deveaud, *Appl. Phys. Lett.* **59**, 423 (1991).
- [153] J. H. Zhao, P. F. Tang, and J. Jeong, *Solid-State Electron.* **35**, 21 (1992).
- [154] J.-K. Lee, Y.-H. Cho, B.-D. Choe, K. S. Kim, H. I. Jeon, H. Lim, and M. Razeghi, *Appl. Phys. Lett.* **71**, 912 (1997).

- [155] T. Sugino, and T. Kousaka, *Electron. Lett.* **34**, 595 (1998).
- [156] D. V. Morgan, J. Frey, and W. J. Devlin, *J. Electrochem. Soc.* **127**, 1202 (1980).
- [157] P. K. Bhattacharya, and M. D. Yeaman, *Solid-State Electron.* **24**, 297 (1981).
- [158] J. S. Escher, L. W. James, R. Sankaran, G. A. Antypas, R. L. Moon, and R. L. Bell, *J. Vac. Sci. Technol.* **13**, 874 (1976).
- [159] A. Y. Polyakov, M. Stam, A. G. Milnes, A. E. Bochkarev, and S. J. Pearton, *J. Appl. Phys.* **71**, 4411 (1992).
- [160] A. Y. Polyakov, A. G. Milnes, L. V. Druzhinina, and I. V. Tunitskaya, *Solid-State Electron.* **36**, 1371 (1993).
- [161] Y. Liu, H. Jiang, T. Egawa, B. Zhang, and H. Ishikawa, *J. Appl. Phys.* **99**, 123702 (2006).
- [162] Y. C. Wang, J. M. Kuo, F. Ren, J. R. Lothian, and W. E. Mayo, *Solid-State Electron.* **42**, 1045 (1998).
- [163] C. Schramm, H. G. Bach, H. Künzel, and J. P. Praseuth, *J. Electrochem. Soc.* **138**, 2808 (1991).
- [164] F. E. Akkad, A. Felimban, and F. Sallam, *J. Vac. Sci. Technol. A* **5**, 111 (1987).
- [165] S. Adachi, *Handbook on Physical Properties of Semiconductors: Volume 3 II–VI Compound Semiconductors*, Kluwer Academic, Boston, 2004.
- [166] Q. Li, W. Jie, L. Fu, and G. Zha, *Nucl. Instrum. Methods Phys. Res. A* **564**, 544 (2006).
- [167] G. Zha, W. Jie, D. Zeng, Y. Xu, W. Zhang, and F. Xu, *Surf. Sci.* **600**, 2629 (2006).
- [168] X. Cheng, S. Zhu, B. Zhao, Z. He, D. Gao, and J. Fang, *Appl. Surf. Sci.* **253**, 8404 (2007).
- [169] A. Z. Wang, W. A. Anderson, and M. A. Haase, *J. Appl. Phys.* **77**, 3513 (1995).

10 Optical Properties

10.1 INTRODUCTORY REMARKS

10.1.1 Optical Dispersion Relations

The complex dielectric function

$$\varepsilon(E) = \varepsilon_1(E) + i\varepsilon_2(E) \quad (10.1)$$

can be used to describe the optical properties of the medium at all photon energies $E = \hbar\omega$ [1,2]. The complex refractive index $n^*(E)$ can also be given by

$$n^*(E) = n(E) + ik(E) = \varepsilon(E)^{1/2} = [\varepsilon_1(E) + i\varepsilon_2(E)]^{1/2} \quad (10.2)$$

where $n(E)$ is the ordinary (real) refractive index and $k(E)$ is the extinction coefficient. From Equation (10.2), we obtain

$$\varepsilon_1(E) = n(E)^2 - k(E)^2 \quad (10.3a)$$

$$\varepsilon_2(E) = 2n(E)k(E) \quad (10.3b)$$

and

$$n(E) = \sqrt{\frac{(\varepsilon_1(E)^2 + \varepsilon_2(E)^2)^{1/2} + \varepsilon_1(E)}{2}} \quad (10.4)$$

$$k(E) = \sqrt{\frac{(\varepsilon_1(E)^2 + \varepsilon_2(E)^2)^{1/2} - \varepsilon_1(E)}{2}} \quad (10.5)$$

The absorption coefficient $\alpha(E)$ and normal-incidence reflectivity $R(E)$ can be given by

$$\alpha(E) = \frac{4\pi}{\lambda} k(E) \quad (10.6)$$

$$R(E) = \frac{(n(E)-1)^2 + k(E)^2}{(n(E)+1)^2 + k(E)^2} \quad (10.7)$$

where λ is the wavelength of light in vacuum.

10.1.2 Static and High-frequency Dielectric Constants

No detailed experimental data on the static and high-frequency dielectric constants, ϵ_s and ϵ_∞ , of semiconductor alloys have been reported. The simplest linear interpolation scheme for an $A_xB_{1-x}C$ alloy is

$$\epsilon(x) = x\epsilon_{AC} + (1-x)\epsilon_{BC} \tag{10.8}$$

Based on the Clausius–Mossotti relationship, we can also obtain

$$\frac{\epsilon(x)-1}{\epsilon(x)+2} = x \frac{\epsilon_{AC}-1}{\epsilon_{AC}+2} + (1-x) \frac{\epsilon_{BC}-1}{\epsilon_{BC}+2} \tag{10.9}$$

It has already been shown that Equations (10.8) and (10.9) give nearly the same results [2]. Readers will find the ϵ_s and ϵ_∞ values for some non-alloyed group-IV, III–V and II–VI semiconductors in Tables 10.2 and 10.3 of Adachi [1].

10.2 GROUP-IV SEMICONDUCTOR ALLOY

10.2.1 Binary Alloy

(a) CSi

The $n(E)$ dispersion in 3C-SiC, together with that for diamond and Si, in the region below the fundamental absorption edge is shown in Figure 10.1(a). The experimental data are taken

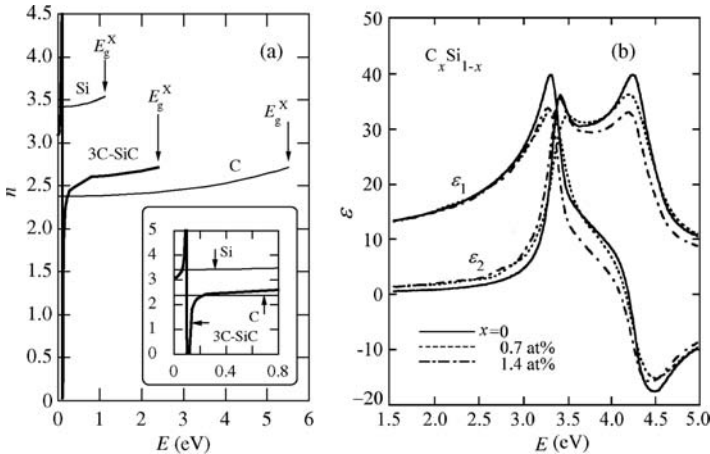


Figure 10.1 (a) $n(E)$ spectrum for 3C-SiC, together with those for diamond (C) and Si in the region below the fundamental absorption edge at 300 K. The experimental data are taken from Adachi [3]. (b) $\epsilon(E)$ spectra for C_xSi_{1-x} at 300 K. [Reprinted with permission from *Jpn. J. Appl. Phys.*, Optical characterization of $Si_{1-x}C_x/Si$ ($0 \leq x \leq 0.014$) semiconductor alloys by H. Lee *et al.*, **34**, L1340. Copyright (1995), Institute of Pure and Applied Physics]

from Adachi [3]. Principally, the diamond-type crystals show no reststrahlen structure. Since 3C-SiC has the zinc-blende structure, the reststrahlen peak can be clearly seen in Figure 10.1(a) at $E \sim 0.1$ eV.

The optical properties of C_xSi_{1-x} ($x \leq 0.014$) in the IR–UV region have been studied using SE [4,5]. We reproduce in Figure 10.1(b) the $\varepsilon(E)$ spectra obtained by Lee *et al.* [5]. We can see that increasing the C concentration decreases the E_1 (~ 3.4 eV) and E_2 CP strengths (~ 4.3 eV), as has also been observed by Kissinger *et al.* [4].

(b) CGe

The optical properties of C_xGe_{1-x} with low C concentrations have been studied in the reststrahlen [6] and interband transition regions [6–8]. The optical absorption in the fundamental absorption edge is shifted toward the higher-energy side with increasing x [6,7]. The SE $\varepsilon(E)$ spectra measured by Krishnamurthy *et al.* [8] showed that increasing the C concentration decreases the $E_1/(E_1 + \Delta_1)$ (~ 2.4 eV) and E_2 CP strengths (~ 4.2 eV), in a similar manner to that observed in C_xSi_{1-x} .

(c) SiGe

The optical properties of relaxed Si_xGe_{1-x} alloy have been studied by many authors [3]. The $\alpha(E)$ spectra in the reststrahlen region of Si_xGe_{1-x} are rather complex due to a number of single- and multiple-phonon bands. The absorption coefficient is weak for the whole composition range, with a peak value of ~ 30 cm^{-1} . Figure 10.2 shows, as an example, the reststrahlen absorption spectra for Si_xGe_{1-x} measured by Braunstein [9]. The samples used were selected

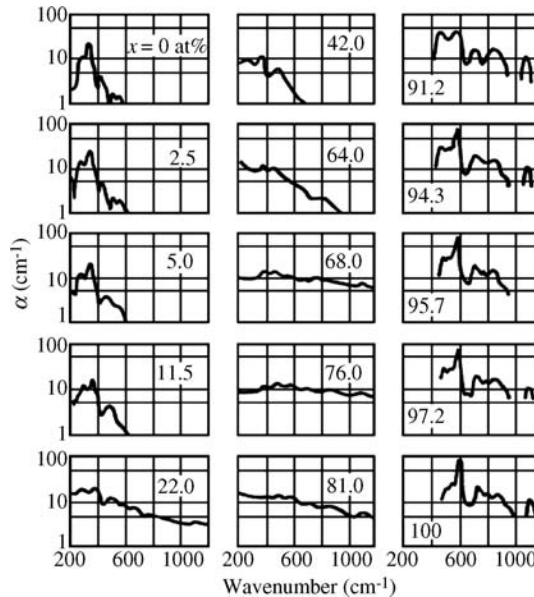


Figure 10.2 Far-IR absorption spectra for Si_xGe_{1-x} at 300 K. [Reprinted with permission from R. Braunstein, *Phys. Rev.* **130**, 879–887 (1963). Copyright (1963) American Physical Society]

for homogeneity of composition and low free-carrier concentration. Nevertheless, most of the spectra for $0.22 \leq x \leq 0.81$ showed strong background absorption due to free carriers. Bulk single crystals were used in the x from 0 to 0.2 and from 0.9 to 1.0; the intermediate compositions were coarse polycrystals. For several at% Si in Ge or vice versa, the general features of the spectra are similar to the lattice absorption spectra of the dominant constituent, except for slight changes in the positions and shapes of the bands. Aside from the Ge- and Si-like bands present in the alloy, new bands starting at 214 and 508 cm^{-1} are formed at the Ge and Si ends of the alloy, respectively. Both of these bands grow in intensity and shift slightly with position as the Ge and Si content are increased.

Braunstein [10] studied the free-hole absorption in $p\text{-Si}_x\text{Ge}_{1-x}$ of various compositions. He observed the intervalence-band absorption and determined some of the VB parameters of this alloy system.

The optical absorption in the fundamental absorption edge of $\text{Si}_x\text{Ge}_{1-x}$ has been measured by Braunstein *et al.* [11]. The optical constants in the IR–UV region of $\text{Si}_x\text{Ge}_{1-x}$ have also been determined by several authors. The $\varepsilon(E)$ and $n^*(E)$ spectra for $\text{Si}_x\text{Ge}_{1-x}$ are shown in Figure 10.3. The experimental data are taken from Adachi [3]. The temperature dependence of the optical constants for $\text{Si}_x\text{Ge}_{1-x}$ has also been investigated using SE [3].

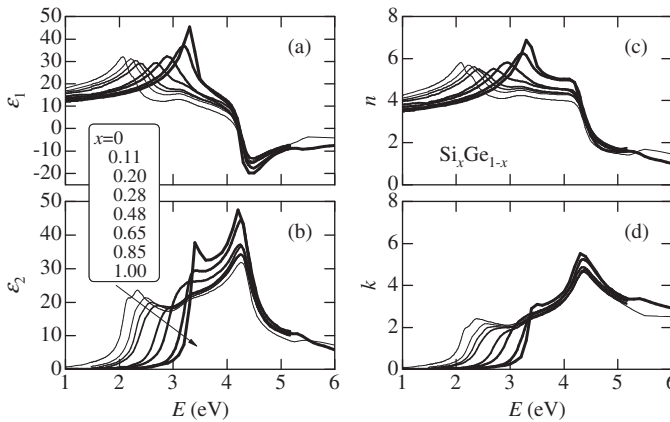


Figure 10.3 Optical constants in the IR–UV region of $\text{Si}_x\text{Ge}_{1-x}$ at 300 K. The experimental data are taken from Adachi [3]

The $\varepsilon(E)$ spectra for strained and relaxed $\text{Si}_x\text{Ge}_{1-x}$ alloys have been determined using SE [12] and it was found that the built-in strain caused a modification of the spectra in the E_1 CP region. Ordering in some group-IV semiconductor alloys has also been investigated and in comparison with disordered alloys no large changes in the optical response were found [13].

(d) GeSn

The optical properties of $\text{Ge}_x\text{Sn}_{1-x}$ ($x < 0.2$) have been studied using optical absorption [14–16] and SE [17]. The onsets of the direct/indirect optical transitions can be clearly observed in each $\alpha(E)$ spectrum. However, it is difficult to determine which of the onsets is due to the direct (E_0) or indirect transitions (E_g^L) (Figure 6.10(a)).

The experimental $\varepsilon(E)$ spectra for $\text{Ge}_x\text{Sn}_{1-x}$ [17] revealed that increasing Sn concentration decreases the $E_1/(E_1 + \Delta_1)$ ($\sim 2.2 \text{ eV}$) and E_2 CP strengths ($\sim 4.2 \text{ eV}$). For example, the ε_2

strength at the E_2 peak decreased from $\varepsilon_2(E_2) \sim 31$ ($x = 1.0$) to ~ 23 ($x = 0.82$). The CP energies were also found to show strong nonlinearity with respect to x (Figure 6.10(b)).

10.2.2 Ternary Alloy

The optical properties of $C_xSi_yGe_{1-x-y}$ have been studied by IR absorbance in the phonon absorption region [18], by optical absorption in the fundamental absorption edge [19] and by SE in the IR–UV region [20–22].

The IR absorption spectra [18] showed that the threefold-degenerate localized phonon mode of C defects in Si splits into a number of phonon modes. The $\alpha(E)$ spectrum in the fundamental absorption edge revealed a clear sub-gap absorption tail in an alloy of $C_{0.01}Si_{0.11}Ge_{0.88}$ with C primarily interstitial, not substitutional [19].

The SE $\varepsilon(E)$ spectra for $C_xSi_yGe_{1-x-y}$ [22] suggested that the CP strengths are reduced slightly and that the absorption at energies $E \leq 3$ eV is increased with increasing x . The essentially same results have also been obtained by other authors [20,21].

Aella *et al.* [23] carried out SE measurements on $Si_xGe_ySn_{1-x-y}$ ($x \leq 0.25$, $1 - x - y \leq 0.11$) and determined the composition dependence of E_2 from the spectral derivative analysis.

10.3 III–V SEMICONDUCTOR TERNARY ALLOY

10.3.1 (III, III)–N Alloy

(a) *c*-(III,III)–N alloy

The optical constants of *c*-AlN, *c*-GaN and *c*-Al_{*x*}Ga_{1-*x*}N have been determined using SE [24]. We reproduce these results in Figure 10.4. The samples used were grown on GaAs(100) or 3C-SiC(100) by MBE. The $n(E)$ data for *c*-GaN measured by Köhler *et al.* [25] are also shown

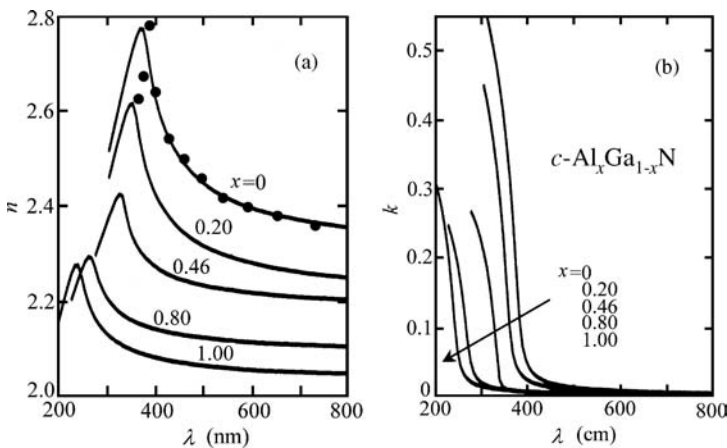


Figure 10.4 (a) $n(E)$ and (b) $k(E)$ spectra for *c*-Al_{*x*}Ga_{1-*x*}N at 300 K. [Reprinted with permission from *Jpn. J. Appl. Phys.*, Optical constants of Cubic GaN, AlN, and AlGa_{*N*} Alloys by T. Suzuki *et al.*, **39**, L497. Copyright (2000), Institute of Pure and Applied Physics]

by the solid circles. The refractive indices at $\lambda = 400$ nm in Figure 10.4 can be written as a function of x as

$$n(x) = 2.610 - 0.880x + 0.364x^2 \tag{10.10}$$

The n values in $c\text{-Al}_x\text{Ga}_{1-x}\text{N}$ with lower x contents are somewhat larger than those in $w\text{-Al}_x\text{Ga}_{1-x}\text{N}$, while those with higher x contents are almost equal to the $w\text{-Al}_x\text{Ga}_{1-x}\text{N}$ values.

IR reflectivity in $c\text{-Ga}_x\text{In}_{1-x}\text{N}$ samples ($0.769 \leq x \leq 1.000$) grown on 3C-SiC/Si(100) by MBE has been measured in the wavenumber range between 450 and 1200 cm^{-1} [26]. SE has also been used to determine the optical constants in the IR–UV region of $c\text{-Ga}_x\text{In}_{1-x}\text{N}$ ($x = 0.93\text{--}1.00$) grown on GaAs(100) by MBE [27]. A parametric dielectric-function model is used to analyze the experimental SE data.

(b) $w\text{-AlGaN}$

The $\varepsilon(E)$ spectra in the IR region of $w\text{-Al}_x\text{Ga}_{1-x}\text{N}$ have been measured by several authors [3,28,29]. These authors demonstrated the sensitivity afforded by IR measurements in determining the optical phonon frequencies.

The $n(E)$ dispersion in the transparent region of $w\text{-Al}_x\text{Ga}_{1-x}\text{N}$ has been measured by a number of authors [30–35]. Several authors obtained not only the ordinary-ray $n(E)$ dispersion ($n_o, c \perp E$) but also extraordinary-ray dispersion ($n_e, c \parallel E$) [31,34]. We show in Figure 10.5 the $n_o(E)$ and $n_e(E)$ dispersions in $w\text{-Al}_x\text{Ga}_{1-x}\text{N}$ ($0 \leq x \leq 1.0$) determined using a prism coupling waveguide technique [31]. The data clearly show the natural birefringence, i.e. $\Delta n = n_e - n_o \neq 0$; its sign is positive for all samples and all wavelengths investigated. The temperature dependence of the $n(E)$ dispersion has also been studied by several authors [30,35].

The absolute $\alpha(E)$ values have been determined for $w\text{-Al}_x\text{Ga}_{1-x}\text{N}$ grown on (0001)-sapphire substrates [36,37]. The $\alpha(E)$ spectra measured by Omnès *et al.* [36] showed a sharp transition for E close to the excitonic gaps ($0 \leq x \leq 0.35$); however, the saturated $\alpha(E)$ values above the excitonic peaks ($\alpha \sim 2 \times 10^4 \text{ cm}^{-1}$) were about an order of magnitude smaller than those reported by Angerer *et al.* [37] ($0 \leq x \leq 1.0$). High-quality $w\text{-GaN}$ gave a saturated α value of $\sim (1 - 2) \times 10^5 \text{ cm}^{-1}$ [3].

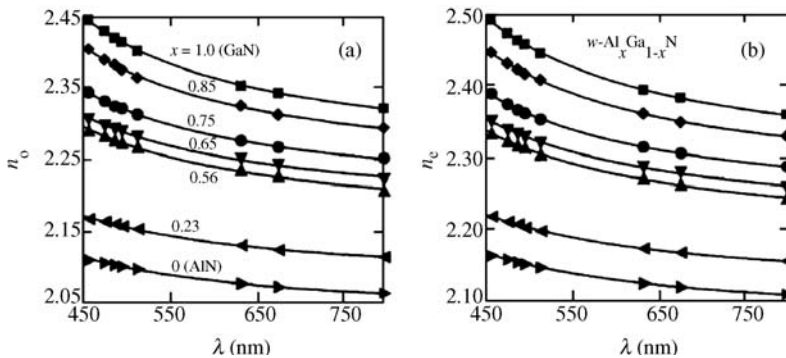


Figure 10.5 (a) Ordinary-ray (n_o) and (b) extraordinary-ray refractive indices (n_e) for $w\text{-Al}_x\text{Ga}_{1-x}\text{N}$ at 300 K. [Reprinted with permission from G. Webb-Wood, Ü. Özgür, H. O. Everitt, F. Yun, and H. Morkoç, *Phys. Status Solidi A* **188**, 793 (2001), Copyright (2001) Wiley–VCH]

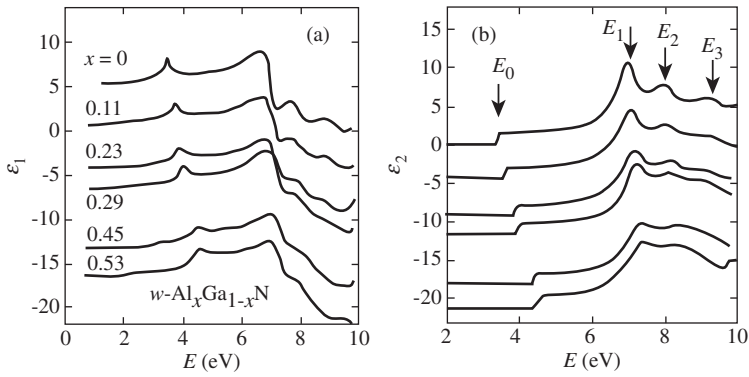


Figure 10.6 $\epsilon(E)$ spectra for $w\text{-Al}_x\text{Ga}_{1-x}\text{N}$ at 300 K. Successive spectra are vertically shifted by -4.4 , -9.2 , -11.6 , -18.0 and -21.2 , respectively. [Reprinted with permission from C. Buchheim *et al.*, *Phys. Status Solidi B* **242**, 2610 (2005), Copyright (2005) Wiley-VCH]

The SE $\epsilon(E)$ spectra for $w\text{-Al}_x\text{Ga}_{1-x}\text{N}$ have been measured by many authors (see e.g. [33,35,38–40]). Figure 10.6 shows the $\epsilon(E)$ spectra obtained by Buchheim *et al.* [40] for samples at $x = 0$ – 0.53 . The four CPs (E_0 – E_3) can be clearly seen in the lower x samples. As expected, these CPs undergo a continuous shift to higher energies with increasing x . However, the E_3 CP shows a different behavior: it decreases with increasing x to overlap with E_2 at high x contents. The origin of such an unusual shift is unclear at present. The $\epsilon(E)$ -related optical constants have been interpreted by a simplified interband-transition model, known as the MDF [2,41].

(c) $w\text{-AlInN}$

The optical photon behaviors in $w\text{-Al}_x\text{In}_{1-x}\text{N}$ with the limited composition of $0.12 \leq x \leq 0.21$ have been investigated using IR ellipsometry [42]. The $n(E)$ dispersion in polycrystalline $w\text{-Al}_x\text{In}_{1-x}\text{N}$ films has been determined by measuring reflectivity spectra [45]. The modeled $n(E)$ dispersion has also been reported by Laws *et al.* [43]. The optical absorption spectra $\alpha(E)$ have been measured to determine the fundamental absorption edge in $w\text{-Al}_x\text{In}_{1-x}\text{N}$ [44,45].

The SE $\epsilon(E)$ spectra for $w\text{-Al}_x\text{In}_{1-x}\text{N}$ have been measured by Goldhahn *et al.* [46]. These results are reproduced in Figure 10.7. The samples used were grown on (0001)-sapphire substrates. The data presented in Figure 10.7 correspond to those for the ordinary ray. The five CPs (E_0 – E_4) can be clearly seen in the $\epsilon(E)$ spectra. The unknown peak (A) has also been found in the lower-energy side of the E_1 peak.

(d) $w\text{-GaInN}$

The reflectivity spectra $R(E)$ in the reststrahlen region of $w\text{-Ga}_x\text{In}_{1-x}\text{N}$ have been measured by Osamura *et al.* [47]. The samples were polycrystallites grown by electron-beam plasma deposition. The refractive index and natural birefringence in $w\text{-Ga}_x\text{In}_{1-x}\text{N}$ ($0.934 \leq x \leq 0.964$) have been determined by a prism coupling method in conjunction with multilayer optical waveguide analysis [48] and found to show positive birefringence ($\Delta n = n_e - n_o > 0$). Laws *et al.* [43] obtained the modeled $n(E)$ dispersion curves with x from 0.75 to 0.95. The optical absorption spectra $\alpha(E)$ have also been determined by several authors [49–51].

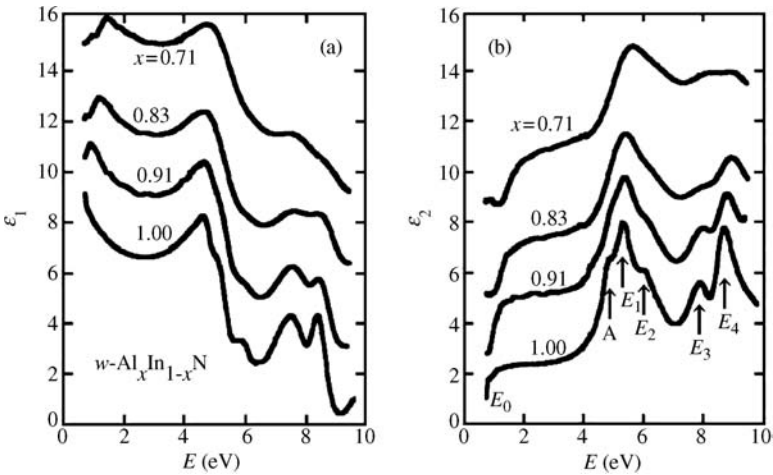


Figure 10.7 $\epsilon(E)$ spectra for $w\text{-Al}_x\text{In}_{1-x}\text{N}$ at 300 K. Successive spectra are vertically shifted by 2.7, 5.1 and 8.7, respectively. [Reprinted with permission from R. Goldhahn *et al.*, *Phys. Status Solidi A* **203**, 42 (2006), Copyright (2006) Wiley–VCH]

The $\epsilon(E)$ spectra in the visible–UV region of $w\text{-Ga}_x\text{In}_{1-x}\text{N}$ have been measured by SE [52,53] and electron energy-loss spectroscopy [54]. The SE $\epsilon(E)$ spectra exhibited a clear maximum at the fundamental absorption edge, which allowed the determination of the Ga content x [52]. The $\epsilon_1(E)$ data in the transparent region have also been analyzed using the Sellmeier-type dispersion model [53].

10.3.2 (III, III)–P Alloy

(a) AlGaP

$\text{Al}_x\text{Ga}_{1-x}\text{P}$ is one of the least studied III–V ternaries. The IR reflectivity has been measured [55]. The low-temperature $\alpha(E)$ spectra in the fundamental absorption edge of $\text{Al}_x\text{Ga}_{1-x}\text{P}$ ($0 \leq x \leq 1.0$) have also been determined [56]. The $n(E)$ values at several wavelengths for $\text{Al}_x\text{Ga}_{1-x}\text{P}$ ($0 \leq x \leq 0.3$) have been measured using a phase diffraction grating method [57].

The $\epsilon(E)$ spectra in the visible–UV region of $\text{Al}_x\text{Ga}_{1-x}\text{P}$ have been measured using SE [58,59]. The $\epsilon(E)$ spectra obtained by Choi *et al.* [59] have been reproduced in Figure 10.8. The samples were grown on GaP(100) by gas-source MBE. The interference oscillations can be seen in the transparent region of the alloys. The energy at which the oscillations disappear provides an estimate of E_0 . The CPs, such as E_0 , E_1 and E_2 , can be clearly identified in these spectra.

(b) AlInP

$\text{Al}_x\text{In}_{1-x}\text{P}$ with $x \sim 0.5$ can be epitaxially grown on GaAs substrate. The optical properties of $\text{Al}_x\text{In}_{1-x}\text{P}$ are not well known, except for $\text{Al}_{0.5}\text{In}_{0.5}\text{P}$. Data on the optical constants of $\text{Al}_{0.5}\text{In}_{0.5}\text{P}$ can be found as the endpoint material of the $\text{Al}_x\text{Ga}_y\text{In}_{1-x-y}\text{P}/\text{GaAs}$ quaternary.

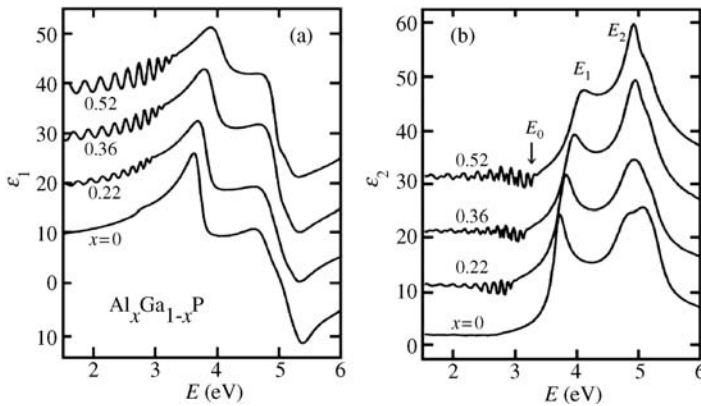


Figure 10.8 $\varepsilon(E)$ spectra for $\text{Al}_x\text{Ga}_{1-x}\text{P}$ at 300 K. Successive spectra are offset in multiples of 10 for clarity. [Reprinted with permission from S. G. Choi *et al.*, *J. Appl. Phys.* **87**, 1287–1290 (2000). Copyright (2000), American Institute of Physics]

(c) *GaInP*

The IR reflectivity in $\text{Ga}_x\text{In}_{1-x}\text{P}$ has been measured in the spectral ranges of 260–500 [60] and 220–500 cm^{-1} [61]. Brillouin scattering has been used to determine the complex refractive indices $n^*(E)$ in the region below the fundamental absorption edge of $\text{Ga}_{0.52}\text{In}_{0.48}\text{P}$ lattice-matched to GaAs [62]. The optical absorption and hydrostatic-pressure effect at the fundamental absorption edge of $\text{Ga}_x\text{In}_{1-x}\text{P}$ ($0.36 \leq x \leq 0.5$) have also been measured by Goñi *et al.* [63]. A crossover from direct to indirect fundamental gap is found to occur at $p = 5.0$ ($x = 0.36$) and 2.7 GPa ($x = 0.5$) at 300 K.

The optical properties of $\text{Ga}_x\text{In}_{1-x}\text{P}$ ($0.494 \leq x \leq 0.584$) grown on GaAs have been investigated using SE [64]. The optical functions of $\text{Ga}_{0.52}\text{In}_{0.48}\text{P}$ lattice-matched to GaAs have also been determined using SE [65,66]. The $\varepsilon(E)$ and $n^*(E)$ spectra for $\text{Ga}_{0.52}\text{In}_{0.48}\text{P}$ determined by SE as an endpoint material of the $\text{Al}_x\text{Ga}_y\text{In}_{1-x-y}\text{P}/\text{GaAs}$ quaternary [3] are shown in Figure 10.9. The effects of ordering on the optical properties of GaInP_2 alloy have

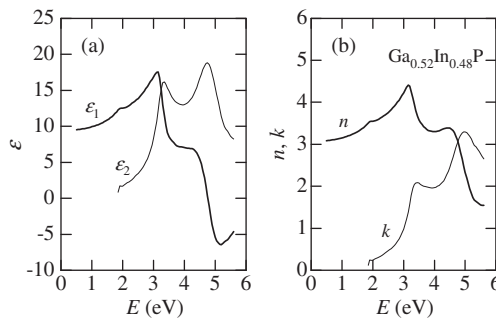


Figure 10.9 Optical constants in the IR–UV region of $\text{Ga}_{0.52}\text{In}_{0.48}\text{P}/\text{GaAs}$ at 300 K. The experimental data are taken from Adachi [3]

also been investigated using SE [67] and found to be relatively weak, yet significant near the fundamental absorption edge and for the higher-lying CPs.

10.3.3 (III, III)–As Alloy

(a) AlGaAs

The $\varepsilon(E)$ and $n^*(E)$ spectra in the reststrahlen region of $\text{Al}_x\text{Ga}_{1-x}\text{As}$ ($0 \leq x \leq 1.0$) [3] have been plotted in Figure 10.10. The experimental data are taken from Adachi [3]. The two phonon bands, GaAs-like and AlAs-like, are clear and distinct in Figure 10.10. No additional structure was found in the frequency range $50\text{--}700\text{ cm}^{-1}$ [3].

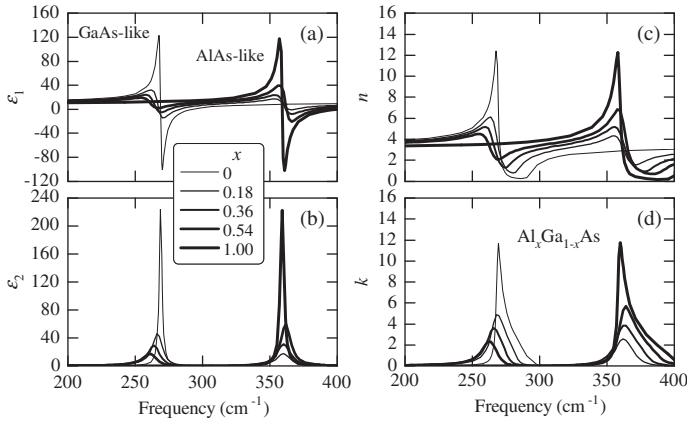


Figure 10.10 Optical constants in the reststrahlen region of $\text{Al}_x\text{Ga}_{1-x}\text{As}$ at 300 K. The experimental data are taken from Adachi [3]

The $n(E)$ dispersion in the transparent region of $\text{Al}_x\text{Ga}_{1-x}\text{As}$ is shown in Figure 10.11. These curves are obtained from a method for calculating $n(E)$ dispersion below E_0 [3,68]. The composition dependence of the strength parameters is expressed as continuous functions of x . This insures that the $n(E)$ dispersion in both optional composition x and photon energy E can be calculated, as demonstrated in Figure 10.11.

Aspnes *et al.* [69] reported the room-temperature optical constants in the near-IR–UV region of $\text{Al}_x\text{Ga}_{1-x}\text{As}$ of target compositions $x = 0\text{--}0.80$ in steps of 0.10 at energies between 1.5 and 6.0 eV determined by SE. The actual compositions were not different from the target compositions by more than 0.02. The accuracy of the pseudodielectric function at selected wavelengths in the technologically relevant composition range of $x = 0\text{--}0.5$ was less than 2% of its peak value. These results are plotted in Figure 10.12.

The optical properties in the far-IR–UV region of GaAs, AlAs and $\text{Al}_x\text{Ga}_{1-x}\text{As}$ published up until 1992 have been reviewed by Adachi [70]. There have been several publications since 1993. They concern $\alpha(E)$ in the fundamental absorption edge [71], $n(E)$ in the terahertz– E_0 (E_g) region [72–77] and SE $\varepsilon(E)$ in the near-IR–UV region [78,79].

(b) AlInAs

The absorption coefficients $\alpha(E)$ and refractive indices $n(E)$ of $\text{Al}_x\text{In}_{1-x}\text{As}$, including $\text{Al}_{0.48}\text{In}_{0.52}\text{As}/\text{InP}$, have been measured by several authors [80–84] (see $n(E)$ in Figure 10.31).

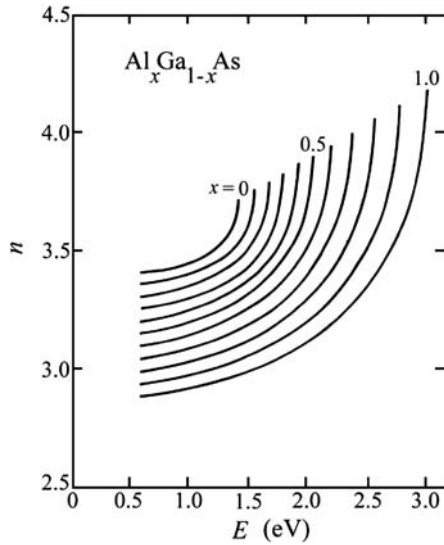


Figure 10.11 $n(E)$ spectra for $\text{Al}_x\text{Ga}_{1-x}\text{As}$ with increments in x of 0.1 at 300 K. [Reprinted with permission from S. Adachi, *J. Appl. Phys.* **58**, R1–R29 (1985). Copyright (1985), American Institute of Physics]

The optical properties in the interband transition region of $\text{Al}_x\text{In}_{1-x}\text{As}$ have been studied using SE by Rodríguez and Armelles [58] ($0 \leq x \leq 1.0$), Dinges *et al.* [85] ($x = 0.48$) and Kamlet and Terry [86] ($0.305 \leq x \leq 0.635$). Figure 10.13(a) shows the $\epsilon(E)$ spectra for $x = 0.48$ obtained by Kamlet and Terry [86]. The $n^*(E)$ spectra were calculated from these $\epsilon(E)$ spectra and are shown in the lower part of Figure 10.13(a). The E_1 and E_2 peaks can be clearly identified at $E \sim 3$ and ~ 4.6 eV, respectively.

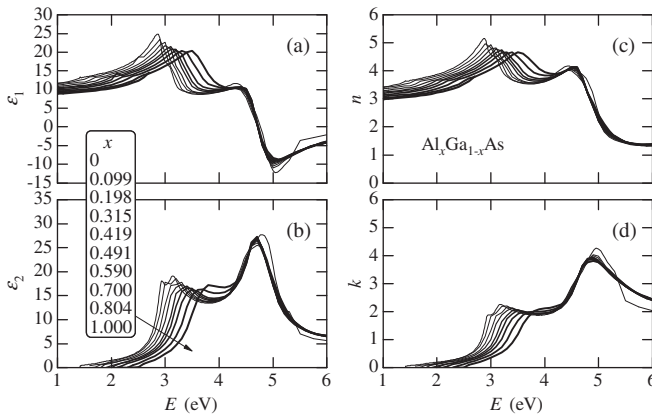


Figure 10.12 Optical constants in the near-IR–UV region of $\text{Al}_x\text{Ga}_{1-x}\text{As}$ at 300 K. The experimental data are taken from Adachi [3]

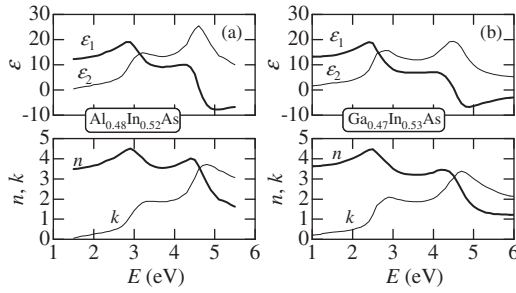


Figure 10.13 (a) Optical constants in the near-IR-UV region of $\text{Al}_{0.48}\text{In}_{0.52}\text{As}/\text{InP}$ at 300 K. The experimental data are taken from Kamlet and Terry [86]. (b) Optical constants in the near-IR-UV region of $\text{Ga}_{0.47}\text{In}_{0.53}\text{As}/\text{InP}$ at 300 K. The experimental data are taken from Adachi [3]

(c) GaInAs

There have been many reports on the optical properties of $\text{Ga}_x\text{In}_{1-x}\text{As}$. This is especially true for $\text{Ga}_{0.47}\text{In}_{0.53}\text{As}$ lattice-matched to InP [87]. More recently, some authors have carried out reflectivity measurements in the reststrahlen region of $\text{Ga}_x\text{In}_{1-x}\text{As}$ to characterize the behavior of the long-wavelength optical phonons in strained epilayers [88–90] and also to elucidate plasma reflection [91].

The $n(E)$ dispersion in $\text{Ga}_x\text{In}_{1-x}\text{As}$ ($0.53 \leq x \leq 1.00$) has been determined from reflectance measurements by Takagi [92]. Note that his extrapolated $x = 0.47$ value, $n \sim 3.43$ at $E = 1.2$ eV, is considerably smaller than that reported by Adachi [3] ($n \sim 3.6$, see Figure 10.31).

The optical properties in the visible-UV region of $\text{Ga}_x\text{In}_{1-x}\text{As}$ over the entire composition range ($0 \leq x \leq 1.0$) have been studied using SE [93,94]. Figure 10.14 shows these results [93]. The peaks in ϵ_2 at $\sim 2.5\text{--}3$ and ~ 4.5 eV correspond to the $E_1/(E_1 + \Delta_1)$ and E_2 CPs,

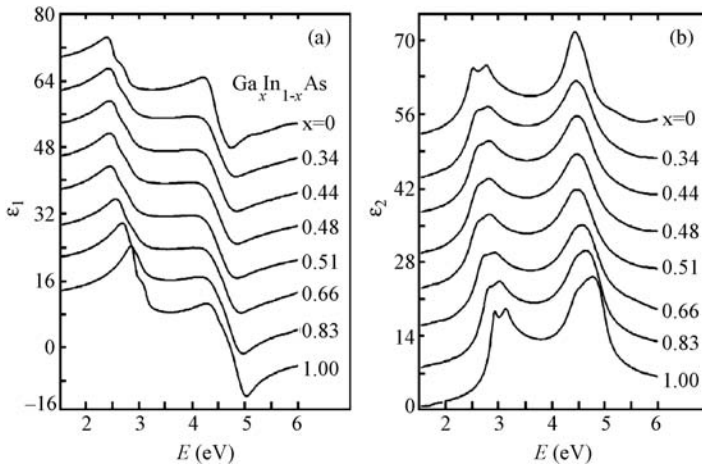


Figure 10.14 $\epsilon(E)$ spectra for $\text{Ga}_x\text{In}_{1-x}\text{As}$ at 300 K. Successive spectra are offset by 8 and 7 in (a) and (b), respectively. [Reprinted with permission from T. J. Kim *et al.*, *Phys. Rev. B* **68**, 115323 (2003). Copyright (2003) by the American Physical Society]

respectively. Several authors also used SE to obtain $\varepsilon(E)$ spectra for $\text{Ga}_{0.47}\text{In}_{0.53}\text{As}/\text{InP}$. The corresponding $\varepsilon(E)$ -related spectra are shown in Figure 10.13(b) [3]. A series of strained and relaxed $\text{Ga}_x\text{In}_{1-x}\text{As}$ layers on GaAs have also been examined using SE [95–98]. Additional information relating to the critical thickness for pseudomorphic growth of $\text{Ga}_x\text{In}_{1-x}\text{As}$ on GaAs has been derived [97].

10.3.4 (III, III)–Sb Alloy

(a) AlGaSb

The IR optical constants of $\text{Al}_x\text{Ga}_{1-x}\text{Sb}$ have been determined in the spectral range of $20\text{--}520\text{ cm}^{-1}$ [99–102]. The reststrahlen parameters obtained have been given in tabular form [99,101,102].

The $n(E)$ dispersion in the $0.5\text{--}1.3\text{ eV}$ region of $\text{Al}_x\text{Ga}_{1-x}\text{Sb}$ ($0 \leq x \leq 0.73$) has been determined from reflectivity measurements by Ance and Van Mau [103]. These results and those for AlSb and GaSb presented in Adachi [3] are shown in Figure 10.15. The optical absorption spectra $\alpha(E)$ for $\text{Al}_x\text{Ga}_{1-x}\text{Sb}$ ($x \leq 0.41$) have also been measured at 2 K and fitted by taking into account the excitonic effects [104].

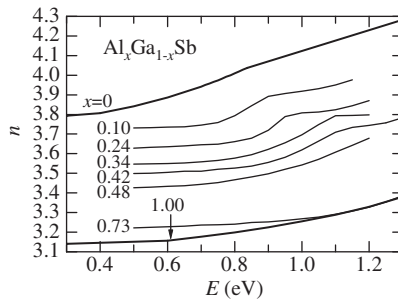


Figure 10.15 $n(E)$ spectra for $\text{Al}_x\text{Ga}_{1-x}\text{Sb}$ at 300 K. The experimental data are taken from Adachi [3]

SE has been used to characterize epitaxial $\text{Al}_x\text{Ga}_{1-x}\text{Sb}$ layers for different x compositions in the $1.4\text{--}6\text{ eV}$ region [102,105,106]. The CP parameters and their composition dependence are determined by performing a standard CP analysis. The $\varepsilon(E)$ spectra obtained by Choi *et al.* [106] are reproduced in Figure 10.16.

(b) GaInSb

The IR reflectivity spectra of $\text{Ga}_x\text{In}_{1-x}\text{Sb}$ have been measured in the range $135\text{--}285\text{ cm}^{-1}$ by Brodsky *et al.* [107] and $100\text{--}350\text{ cm}^{-1}$ by Feng *et al.* [108]. The reststrahlen parameters have been tabulated by Brodsky *et al.* [107]. The absorption spectra $\alpha(E)$ in the fundamental absorption edge of $\text{Ga}_x\text{In}_{1-x}\text{Sb}$ have also been measured at 300 K [109].

Imai and Adachi [110] have obtained the optical constants in the $1.5\text{--}5.4\text{ eV}$ region of $\text{Ga}_x\text{In}_{1-x}\text{Sb}$ using SE at 300 K. The samples were grown by a conventional Bridgman method. The $n^*(E)$ spectra obtained by Imai and Adachi [110] are shown in Figure 10.17. These authors also determined the x -dependent CP parameters from the MDF analysis.

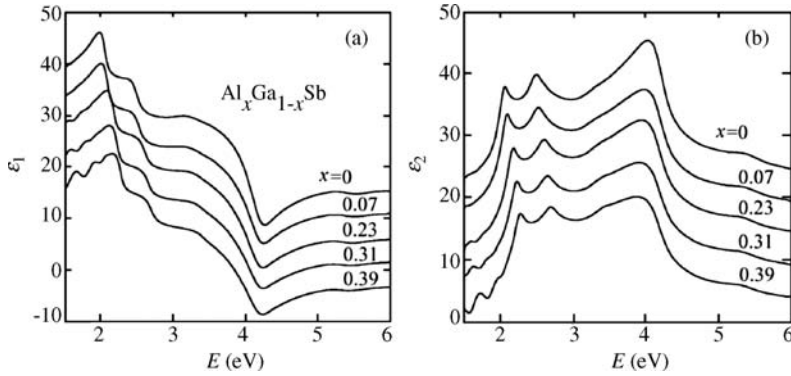


Figure 10.16 $\epsilon(E)$ spectra for $\text{Al}_x\text{Ga}_{1-x}\text{Sb}$ at 300 K. Successive spectra are offset upward from the $x = 0.39$ spectrum by multiples of 5 for clarity. [Reprinted with permission from S. G. Choi, C. J. Palmstrom, Y. D. Kim, S. L. Cooper, and D. E. Aspnes, *J. Appl. Phys.* **98**, 104108 (2005). Copyright (2005), American Institute of Physics]

10.3.5 Dilute-nitride III-(V, V) Alloy

(a) GaNP

The IR reflectivity spectra of dilute-nitride $\text{GaN}_x\text{P}_{1-x}$ have been measured in the spectral ranges of $300\text{--}600\text{ cm}^{-1}$ ($0.006 \leq x \leq 0.0285$) [111] and $50\text{--}4000\text{ cm}^{-1}$ ($0 \leq x \leq 0.15$) [112]. These spectra led to the determination of the GaN- and GaP-like phonon frequencies.

The nature of the fundamental absorption edge of $\text{GaN}_x\text{P}_{1-x}$ was elucidated using the $\alpha(E)$ spectra [113–115]. The experimental data obtained by Rudko *et al.* [113] suggest that the absorption edge of $\text{GaN}_x\text{P}_{1-x}$ with $x = 0.01\text{--}0.03$ exhibits a direct band-gap-like behavior. The $\alpha(E)$ spectra obtained by Buyanova *et al.* [114] have been explained by the BAC model (Section 6.3.5). On the other hand, the low-temperature absorption data obtained by

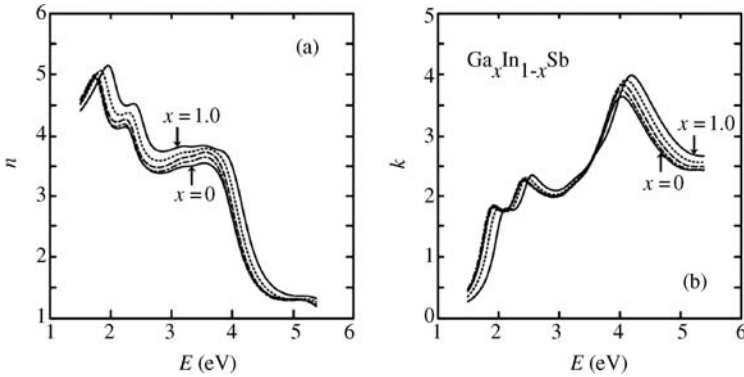


Figure 10.17 $n(E)$ and $k(E)$ spectra for $\text{Ga}_x\text{In}_{1-x}\text{Sb}$ with increments in x of 0.25 at 300 K. [Reprinted with permission from *Jpn. J. Appl. Phys.*, Optical constants of $\text{In}_{1-x}\text{Ga}_x\text{Sb}$ ternary alloys: Experiment and modeling by S. Imai and S. Adachi, **32**, 3860. Copyright (1993), Institute of Pure and Applied Physics]

Fluegel *et al.* [115] indicate that the host CB minimum near X does not plunge downward with increased N doping. These results challenge the validity of the BAC and polymorphous model for $\text{GaN}_x\text{P}_{1-x}$, but corroborate the conclusion that due to the dissimilarity between $\text{GaN}_x\text{P}_{1-x}$ and $\text{GaN}_x\text{As}_{1-x}$, seeking a universal model for the band-gap lowering that applies to both the isoelectronic doping systems is unrealistic.

SE has been used to investigate the electronic energy-band structure of $\text{GaN}_x\text{P}_{1-x}$ [114,116]. The $\varepsilon_2(E)$ spectra obtained by Leibiger *et al.* [116] are reproduced in Figure 10.18. The vertical dotted lines mark the CPs, E_0 , E_1 , E'_0 , E_2 and E'_1 , determined by MDF analysis.

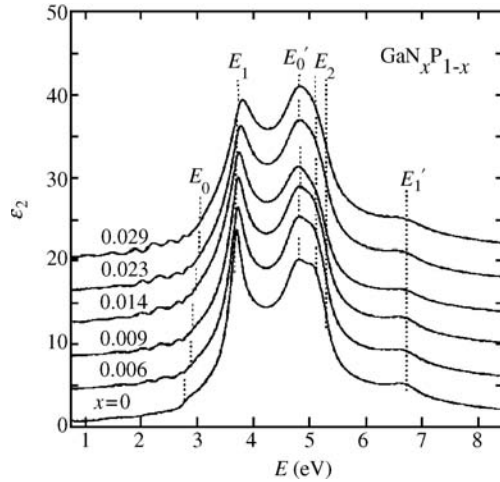


Figure 10.18 $\varepsilon_2(E)$ spectra for dilute-nitride $\text{GaN}_x\text{P}_{1-x}$ at 300 K. Successive spectra are offset in multiples of 4 for clarity [Reprinted with permission from G. Leibiger, V. Gottschalch, M. Schubert, G. Benndorf, and R. Schwabe, *Phys. Rev. B* **65**, 245207 (2002). Copyright (2002) by the American Physical Society]

(b) GaNAs

The absorption coefficient $\alpha(E)$ in the fundamental absorption edge of $\text{GaN}_x\text{As}_{1-x}$ has been measured by several authors (see e.g. [117–119]). The $\alpha(E)$ spectra recorded by Tisch *et al.* [119] ($0 \leq x \leq 0.05$) are shown in Figure 10.19. It can be seen that for all samples α^2 depends linearly on E up to $\sim 10^8 \text{ cm}^{-2}$. The slope of the linear part of α^2 decreases and the Urbach tail increases with increasing N fraction. The decrease in the fundamental absorption edge (E_-) with increasing x can be clearly seen (see also Figure 6.29(b)).

The optical properties of $\text{GaN}_x\text{As}_{1-x}$ have been studied using SE by many authors (see e.g. [120–122]). The $\varepsilon(E)$ spectra recorded by Leibiger *et al.* [122] are shown in Figure 10.20. The $\varepsilon(E)$ -related spectra, $\varepsilon(E)$ and $n^*(E)$, were found to agree very well with the MDF approach [120–122]. Note that the fundamental absorption edge (E_-) observed in Figure 10.20 follows the well-known redshift with increasing x .

(c) GaNSb

FTIR measurements on $\text{GaN}_x\text{Sb}_{1-x}$ have been undertaken by Jefferson *et al.* [123]. The divergence of transitions from the VB to E_- and E_+ has been observed with increasing N incorporation, consistent with the BAC model (Figure 6.29(c)).

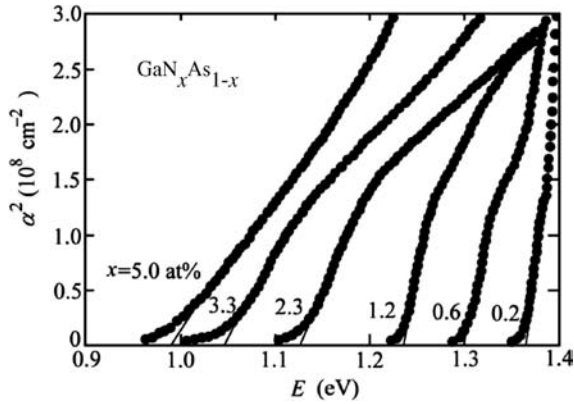


Figure 10.19 α^2 versus E plots for dilute-nitride $\text{GaN}_x\text{As}_{1-x}$ at 300 K. [Reprinted with permission from U. Tisch, E. Finkman, and J. Salzman, *Appl. Phys. Lett.* **81**, 463 (2002). Copyright (2002), American Institute of Physics]

(d) InNP

Optical absorption measurements were carried out to investigate the N incorporation effect into InP [124]. A band-gap reduction of ~ 0.15 eV was observed with N incorporation of ~ 0.9 at%.

(e) InNAs

IR reflectivity and Hall-effect measurements have been carried out to determine the x -dependent electron effective mass in $\text{InN}_x\text{As}_{1-x}$ [125] (Figure 7.11). The N-induced reduction of the fundamental absorption edge has also been confirmed in $\text{InN}_x\text{As}_{1-x}$ by plotting α^2 versus E [126] (Figure 6.31(b)).

10.3.6 Al-(V, V) Alloy

An AlPSb layer lattice-matched to InP was grown by gas-source MBE [127]. Using an ellipsometer, the refractive index of this alloy at $\lambda = 1.55 \mu\text{m}$ was determined to be 3.037.

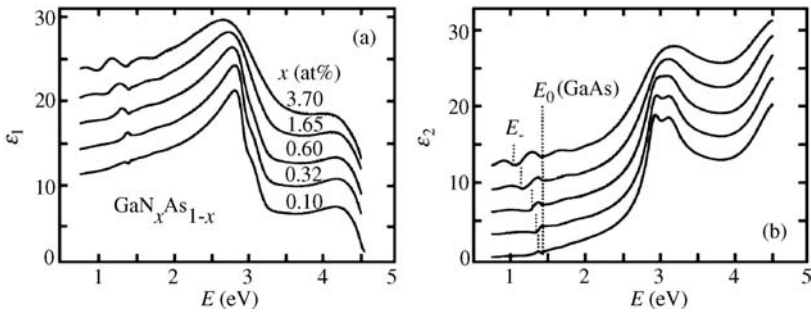


Figure 10.20 $\varepsilon(E)$ spectra for dilute-nitride $\text{GaN}_x\text{As}_{1-x}$ at 300 K. Successive spectra are offset upward from the $x = 0.10$ at% spectrum by multiples of 3 for clarity. [Reprinted with permission from G. Leibiger, V. Gottschalch, B. Rheinländer, J. Šik, and M. Schubert, *J. Appl. Phys.* **89**, 4927 (2001). Copyright (2001), American Institute of Physics]

Saadallah *et al.* [128] carried out photothermal deflection measurements on an MBE-grown $\text{AlAs}_{0.08}\text{Sb}_{0.92}/\text{GaSb}$ layer and determined the $n(E)$ and $\alpha(E)$ spectra, in addition to the thickness of the layer and its thermal conductivity. The Sellmeier parameters which were determined are: $A = 8.82$, $B = 0.79$ and $C = 0.589 \mu\text{m}$ (see Equation (10.71) in Adachi [1]). The fundamental absorption edge of $\text{AlAs}_{0.08}\text{Sb}_{0.92}$ was also estimated to be $\sim 1.55 \text{ eV}$ (Figure 6.32(b)).

10.3.7 Ga-(V, V) Alloy

(a) GaPAs

The $n(E)$ dispersion in $\text{GaP}_x\text{As}_{1-x}$ has been studied by several authors [129–131]. The $n(E)$ data obtained by Clark and Holonyak [129] and Casey [130] agree closely between 1.2 and 1.75 eV where comparison is possible. The experimental data at 87 and 300 K by Clark and Holonyak [129] were fitted to the first-order Sellmeier equation. This enables us to calculate the $n(E)$ dispersion in a given alloy of composition x and photon energy E . These results are shown in Figure 10.21. The calculated $n(E)$ values are taken from Adachi [3]. The resulting $n(E)$ dispersion is found to decrease with increasing x .

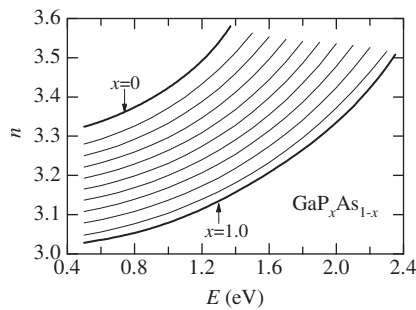


Figure 10.21 $n(E)$ dispersion in the transparent region of $\text{GaP}_x\text{As}_{1-x}$ with increments in x of 0.1 at 300 K. The n values are taken from Adachi [3]

Clark and Holonyak [129] investigated the optical absorption spectra in the IR and fundamental absorption edge regions of $\text{GaP}_x\text{As}_{1-x}$. They observed the free-carrier and interconduction-band absorption in GaAs-rich alloys and donor-related absorption in GaP-rich alloys. The Burstein–Moss shift of the fundamental absorption edge was also observed. The optical absorption in $\text{GaP}_x\text{As}_{1-x}$ ($0.29 \leq x \leq 0.43$) has also been examined by Nelson *et al.* [132] who observed distinct free-exciton peaks ($n = 1$ and 2) at 4.2 K and a peak ($n = 1$) at $T \geq 77 \text{ K}$. The direct-exciton binding energy G for $\text{GaP}_x\text{As}_{1-x}$ obtained by Nelson *et al.* [132] is plotted in Figure 10.22 as a function of x , together with the corresponding values for GaP and GaAs taken from Adachi [1]. The direct-exciton (E_0) and indirect-exciton binding energies (E_g^X) for GaP are 13 and 22 meV, respectively (see Table 10.4 in Adachi [1]). The G values for $\text{GaP}_x\text{As}_{1-x}$ in Figure 10.22 are considerably smaller than those obtained from the linear interpolation scheme.

Thomson *et al.* [133] measured the fundamental reflectivity spectra of $\text{GaP}_x\text{As}_{1-x}$ at 80 and 295 K. More recently, Kim *et al.* [134] reported the $\varepsilon(E)$ spectra of $\text{GaP}_x\text{As}_{1-x}$ layers grown

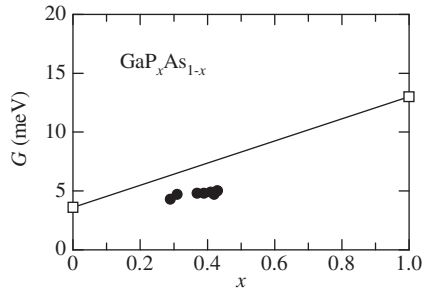


Figure 10.22 Direct-exciton binding energy G versus x for $\text{GaP}_x\text{As}_{1-x}$. The experimental data (solid circles) are taken from Nelson *et al.* [132]. The open squares show the endpoint binary data taken from Adachi [1]

by VPE on GaAs(100) ($x = 0.2$ and 0.4) and on GaP(100) ($x = 0.7$). The measured $\varepsilon(E)$ spectra revealed distinct structures at energies of the E_0 , E_1 , $E_1 + \Delta_1$, E_0' and E_2 CPs.

(b) GaPSb

$\text{GaP}_x\text{Sb}_{1-x}$ lattice-matched to InP was grown by gas-source MBE [127]. Using an ellipsometer, the refractive index of this alloy at $\lambda = 1.55 \mu\text{m}$ was determined to be 3.579. A highly reflective distributed Bragg reflector was demonstrated using $\text{AlP}_x\text{Sb}_{1-x}/\text{GaP}_x\text{Sb}_{1-x}$, which showed a stop-band width of 206 nm with maximum reflectivity exceeding 99% at $\lambda \sim 1.6 \mu\text{m}$.

(c) GaAsSb

The IR reflectivity spectra of $\text{GaAs}_x\text{Sb}_{1-x}$ have been measured in the $200\text{--}320 \text{ cm}^{-1}$ range by Lukovsky and Chen *et al.* [135]. A reflectance band was observed in the $x = 0.85$ composition, whereas at least two bands were evident in the $x = 0.20$ and 0.25 samples. In the latter two samples, the structure near 240 cm^{-1} was due to the phonon modes, whereas the structure at lower energies ($\sim 230 \text{ cm}^{-1}$) was due to free-carrier plasma effects.

Optical absorption measurements were undertaken on $\text{GaAs}_x\text{Sb}_{1-x}$ by several authors [136–138]. The measured data were used to determine E_0 [136] and its temperature dependence [137,138].

The fundamental reflectivity spectra were measured on evaporated $\text{GaAs}_x\text{Sb}_{1-x}$ films on glasses and on bulk samples [139]. SE and PR were used to determine the x dependence of some CPs, such as E_0 , E_1 and E_2 , in epitaxial $\text{GaAs}_x\text{Sb}_{1-x}/\text{GaAs}(100)$ layers ($0.44 \leq x \leq 1.00$) [140]. More recently, Serries *et al.* [141] used SE and Raman scattering to investigate pseudomorphically strained $\text{GaAs}_x\text{Sb}_{1-x}$ layers ($0.35 \leq x \leq 0.78$) grown on InP(100).

10.3.8 In-(V, V) Alloy

(a) InPAs

The reflectivity spectra in the reststrahlen region of $\text{InP}_x\text{As}_{1-x}$ have been measured by several authors [142,143]. These studies gave similar results; however, the InP- and InAs-like

oscillator strengths determined by Lockwood *et al.* [143] vary considerably from those reported by Kekelidze *et al.* [142]. The plasma reflection characteristics have also been studied by Charache *et al.* [91].

The alloy composition dependence of E_0 has been determined by plotting α^2 versus E [144]. The $\varepsilon(E)$ spectra have also been obtained for $\text{InP}_x\text{As}_{1-x}/\text{InP}(100)$ samples using SE [145]. The x dependence of the E_1 , $E_1 + \Delta_1$ and E_2 CPs have been determined by analyzing the second-derivative spectra of $\varepsilon(E)$. The $\varepsilon(E)$ spectra obtained by Choi *et al.* [145] have been reproduced in Figure 10.23.

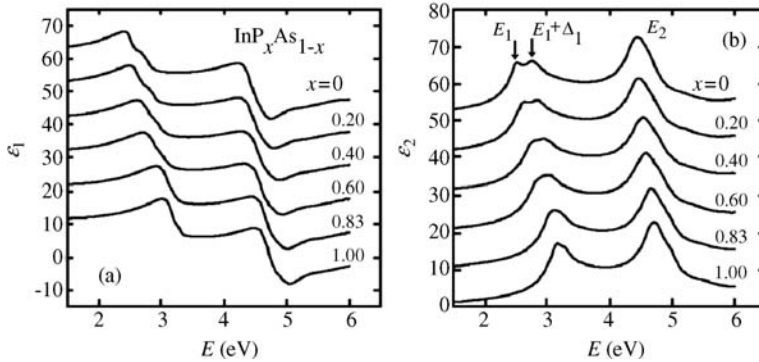


Figure 10.23 $\varepsilon(E)$ spectra for $\text{InP}_x\text{As}_{1-x}$ at 300 K. Successive spectra are offset in multiples of 10 for clarity [Reprinted with permission from S. G. Choi, C. J. Palmstrøm, Y. D. Kim, D. E. Aspnes, H. J. Kim, and Y.-C. Chang, *Appl. Phys. Lett.* **91**, 041917 (2007). Copyright (2007), American Institute of Physics]

(b) *InPSb*

The optical absorption spectra $\alpha(E)$ have been measured to determine the x dependence of E_0 for MOCVD- $\text{InP}_x\text{Sb}_{1-x}$ layers [146] (Figure 6.37(a)). The spectra show long band tails, which extend further into the gap as the Sb concentration is increased. The band tails are considered to be caused by compositional clustering.

(c) *InAsSb*

The optical reflectivity in the reststrahlen region of $\text{InAs}_x\text{Sb}_{1-x}$ has been studied in the $135\text{--}285\text{ cm}^{-1}$ range by Lucovsky *et al.* [135] and in the $50\text{--}300\text{ cm}^{-1}$ range by Rowell *et al.* [147]. Plasma-edge reflectance data obtained by Thomas and Woolley [148] suggested that ε_∞ for $\text{InAs}_x\text{Sb}_{1-x}$ can be given by the linear interpolation between the endpoint binary data within experimental accuracy.

Optical absorption and transmittance measurements have been carried out to characterize $\text{InAs}_x\text{Sb}_{1-x}$ layers grown on GaAs [149,150], GaSb [151] and InAs [152]. The data are mainly used to determine E_0 in these alloy layers. Note that all these substrates are transparent for light wavelengths at or below the $\text{InAs}_x\text{Sb}_{1-x}$ gap ($0 \leq x \leq 1.00$).

SE measurements have been undertaken for $\text{InAs}_x\text{Sb}_{1-x}$ layers grown on InAs(100) [153,154]. The alloy compositions investigated were $0.89 \leq x \leq 0.96$ [153] and $0 \leq x \leq 0.06$ [154].

10.4 III–V SEMICONDUCTOR QUATERNARY ALLOY

10.4.1 Dilute-nitride Quaternary Alloy

(a) GaInNP

The optical properties of $\text{Ga}_x\text{In}_{1-x}\text{N}_y\text{P}_{1-y}$ epilayers on GaP(100) have been investigated using SE [155]. The compositions of $\text{Ga}_x\text{In}_{1-x}\text{N}_y\text{P}_{1-y}$ layers were changed to satisfy the lattice-matching condition, i.e. $x \sim 1-y$, with $0 \leq y \leq 0.035$. The SE-derived spectra, $n(E)$, $k(E)$ and $\alpha(E)$, were presented in graphical form.

(b) GaInNAs

Far-IR SE has been used to investigate the reststrahlen properties of $\text{Ga}_x\text{In}_{1-x}\text{N}_y\text{As}_{1-y}$ ($x > 0.87, y < 0.03$) [156]. The plasma reflection spectra have also been measured to determine the CB dispersion relationships in $\text{Ga}_x\text{In}_{1-x}\text{N}_y\text{As}_{1-y}$ [157]. This study also reported the temperature- and pressure-dependent optical absorption at the fundamental absorption edge of free-standing $\text{Ga}_x\text{In}_{1-x}\text{N}_y\text{As}_{1-y}$ layers ($0.91 \leq x \leq 1.00, 0 \leq y \leq 0.025$) lattice-matched to GaAs.

The $n(E)$ dispersion in the transparent region of strained $\text{Ga}_x\text{In}_{1-x}\text{N}_y\text{As}_{1-y}$ layers has been measured by several authors [156,158]. The SE-derived $n(E)$ and $k(E)$ spectra were analyzed using the MDF approach [156]. The SE $\varepsilon(E)$ spectra in the interband transition region of $\text{Ga}_x\text{In}_{1-x}\text{N}_y\text{As}_{1-y}$ have also been reported by Skierbiszewski [157]. These results have been reproduced in Figure 10.24. It can be seen that the N incorporation has a large effect on the optical dispersion relationships in the $E_1/(E_1 + \Delta_1)$ transition region (~ 3 eV).

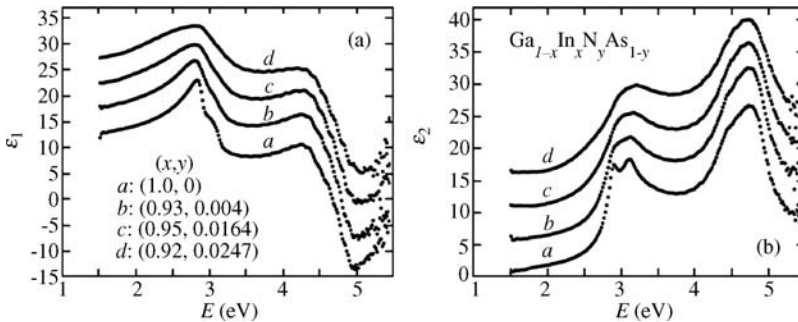


Figure 10.24 $\varepsilon(E)$ spectra for dilute-nitride $\text{Ga}_x\text{In}_{1-x}\text{N}_y\text{As}_{1-y}$ at 300 K. Successive spectra are offset in multiples of 5 for clarity [Reprinted with permission from C. Skierbiszewski, *Semicond. Sci. Technol.* **17**, 803 (2002), Copyright (2002) Institute of Physics]

10.4.2 (III, III)–(V, V) Alloy

(a) AlGaPAs

The IR reflectivity spectra in the $200\text{--}500\text{cm}^{-1}$ range of $\text{Al}_x\text{Ga}_{1-x}\text{P}_y\text{As}_{1-y}$ have been measured by Sen and Lucovsky [159]. The reststrahlen parameters obtained were reported in tabular form. The optical absorption spectra $\alpha(E)$ at the fundamental absorption edge of

$\text{Al}_x\text{Ga}_{1-x}\text{P}_y\text{As}_{1-y}$ have also been measured by Kuznetsov *et al.* [160]. The single-crystalline alloys used were grown on GaP by LPE with several pairs of composition (x, y) .

(b) *AlGaAsSb*

The IR reflectivity spectra in the range of $75\text{--}400\text{ cm}^{-1}$ for $\text{Al}_x\text{Ga}_{1-x}\text{As}_y\text{Sb}_{1-y}/\text{GaSb}$ have been measured by Mezerreg *et al.* [161]. The reststrahlen parameters obtained were presented in tabular form.

Alibert *et al.* [162] obtained the $n(E)$ dispersion in LPE-grown $\text{Al}_x\text{Ga}_{1-x}\text{As}_y\text{Sb}_{1-y}/\text{GaSb}$ layers. The $n(E)$ data were determined from accurate measurement of the p -polarized light reflection as a function of the incident angle. The data in the limit $E \rightarrow 0\text{ eV}$ (i.e. ϵ_∞ values) showed very strong nonlinearity with respect to x [162]. The $n(E)$ data for $\text{Al}_x\text{Ga}_{1-x}\text{As}_y\text{Sb}_{1-y}/\text{InP}$ ($x = 0.1$) have also been determined from reflectance measurements [163]. The $n(E)$ dispersion in $\text{Al}_x\text{Ga}_{1-x}\text{As}_y\text{Sb}_{1-y}/\text{InP}$ obtained from the MDF calculation [2] is shown in Figure 10.25. The solid circles represent the experimental data taken from Blum *et al.* [163].

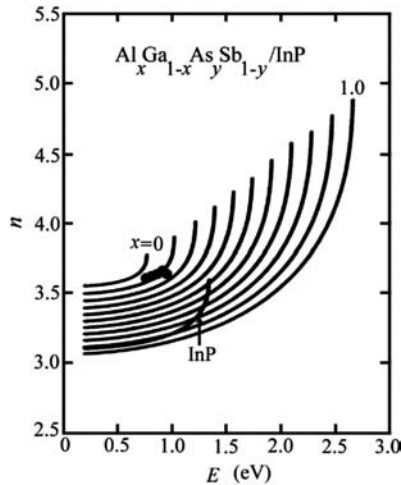


Figure 10.25 $n(E)$ dispersion in the transparent region of $\text{Al}_x\text{Ga}_{1-x}\text{As}_y\text{Sb}_{1-y}/\text{InP}$ with increments in x of 0.1 at 300 K, together with that for InP. The $n(E)$ curves are calculated from the simplified interband-transition model [2]. The experimental data by Blum *et al.* [163] are represented by the solid circles ($x = 0.1$)

The absorption coefficients for LPE-grown $\text{Al}_x\text{Ga}_{1-x}\text{As}_y\text{Sb}_{1-y}$ layers on GaAs with $(x, y) = (0, 0.9)$ and $(0.06, 0.9)$ have been determined at several temperatures between 20 and 300 K [164]. Note that this material system is not a lattice-matched system.

(c) *GaInPAs*

The IR reflectivity spectra of $\text{Ga}_x\text{In}_{1-x}\text{P}_y\text{As}_{1-y}/\text{InP}$ have been measured by several authors [3]. The optical constants in the reststrahlen region can be usually determined by using Kramers–Krönig transformation or from the fit to an oscillator model. However, no detailed reststrahlen parameters have been determined for $\text{Ga}_x\text{In}_{1-x}\text{P}_y\text{As}_{1-y}/\text{InP}$. This is because many IR studies were focused on multi-phonon behaviors (Section 4.2).

The $n(E)$ measurements in the transparent region were carried out using various techniques [3]. Accurate experimental data relating to the optional composition of $\text{Ga}_x\text{In}_{1-x}\text{P}_y\text{As}_{1-y}$ are, however, not yet available. Thus, some type of calculation is necessary. Different approaches have been used to calculate the $n(E)$ dispersion. Our calculated $n(E)$ curves for $\text{In}_x\text{Ga}_{1-x}\text{As}_y\text{P}_{1-y}/\text{InP}$ based on the simplified interband-transition model [2] are presented in Figure 10.26.

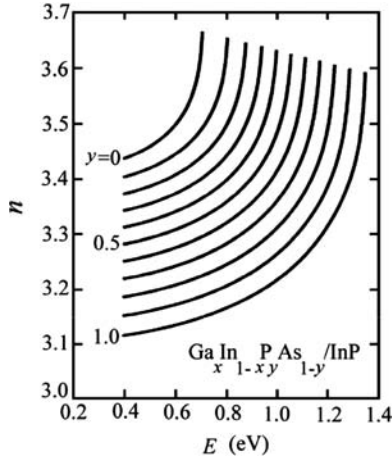


Figure 10.26 $n(E)$ dispersion in the transparent region of $\text{Ga}_x\text{In}_{1-x}\text{P}_y\text{As}_{1-y}/\text{InP}$ with increments in y of 0.1 at 300 K. The $n(E)$ curves are calculated from the simplified interband-transition model [2]

Near-band-edge absorption in $\text{Ga}_x\text{In}_{1-x}\text{P}_y\text{As}_{1-y}/\text{InP}$ has been studied by many investigators [3]. The spectra depicted the sharp decline of α , common to the direct-band-gap semiconductors. Since the experimental information seemed to be limited to narrow composition and wavelength ranges, Fiedler and Schlachetzki [165] calculated the absorption coefficients for $\text{Ga}_x\text{In}_{1-x}\text{P}_y\text{As}_{1-y}$ using the extrapolation scheme.

The optical constants in the interband transition region of $\text{Ga}_x\text{In}_{1-x}\text{P}_y\text{As}_{1-y}/\text{InP}$ have been studied using SE [3]. Kelso *et al.* [166] reported the room-temperature optical constants for $\text{Ga}_x\text{In}_{1-x}\text{P}_y\text{As}_{1-y}/\text{InP}$ of target compositions $y = 0-1.0$ in steps of 0.2 at energies $E = 1.5-6.0$ eV measured by SE. The samples were grown by LPE with carrier concentrations in the $10^{16}-10^{17}$ cm^{-3} range. The complex optical constants, $\varepsilon(E)$ and $n^*(E)$, obtained from this study [3,166] are shown in Figure 10.27.

The $n(E)$ data in the transparent region ($\lambda = 808, 850$ and 980 nm) of $\text{Ga}_x\text{In}_{1-x}\text{P}_y\text{As}_{1-y}/\text{GaAs}$ have been determined using variable-angle SE [167]. As expected, the n value decreased with increasing E_0 , i.e. increasing y (Figure 6.44(a)).

(d) *GaInAsSb*

The IR reflectivity spectra for $\text{Ga}_x\text{In}_{1-x}\text{As}_y\text{Sb}_{1-y}/\text{GaSb}$ epilayers have been measured by Mezerreg *et al.* [161] and Pickering [168]. The reststrahlen parameters obtained were presented in tabular form [161]. Studies on $\text{Ga}_x\text{In}_{1-x}\text{As}_y\text{Sb}_{1-y}/\text{InAs}$ have also been undertaken by Pickering [168].

Bi *et al.* [169] reported the IR absorption properties of MBE-grown $\text{Ga}_x\text{In}_{1-x}\text{As}_y\text{Sb}_{1-y}$ layers on GaAs and GaSb substrates. They also obtained $n(E)$ curves in the $600-3200$ cm^{-1} range

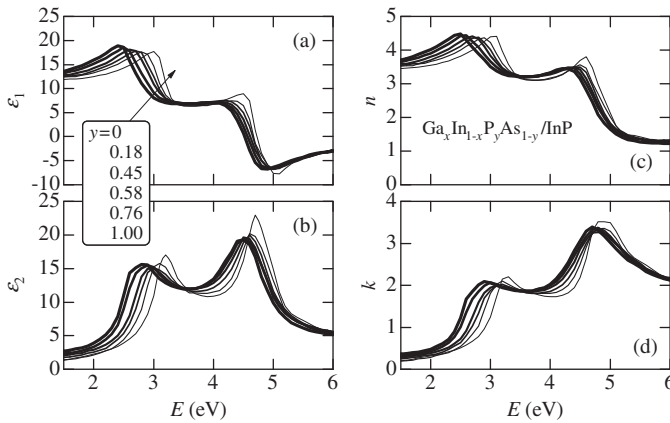


Figure 10.27 Optical constants in the near-IR-UV region of $\text{Ga}_x\text{In}_{1-x}\text{P}_y\text{As}_{1-y}/\text{InP}$ at 300 K. The experimental data are taken from Adachi [3]

with $(x, y) = (0.734, 0.109)$ and $(0.753, 0.093)$. These data agreed well with the theoretical prediction by Adachi [2,170]. From the far-field patterns in a $\text{Ga}_x\text{In}_{1-x}\text{As}_y\text{Sb}_{1-y}/\text{Al}_x\text{Ga}_{1-x}\text{As}_y\text{Sb}_{1-y}/\text{GaSb}$ double-heterostructure laser of lasing wavelength at $2.2\ \mu\text{m}$, Loural *et al.* [171] determined the active-layer n value to be 3.78. This value exactly agrees with the theoretical prediction based on the simplified interband-transition model [2,170]. Figure 10.28 shows the $n(E)$ curves with x increments of 0.1 for (a) $\text{Ga}_x\text{In}_{1-x}\text{As}_y\text{Sb}_{1-y}/\text{GaSb}$ and (b) $\text{Ga}_x\text{In}_{1-x}\text{As}_y\text{Sb}_{1-y}/\text{InAs}$ calculated from the simplified interband-transition model [2,170].

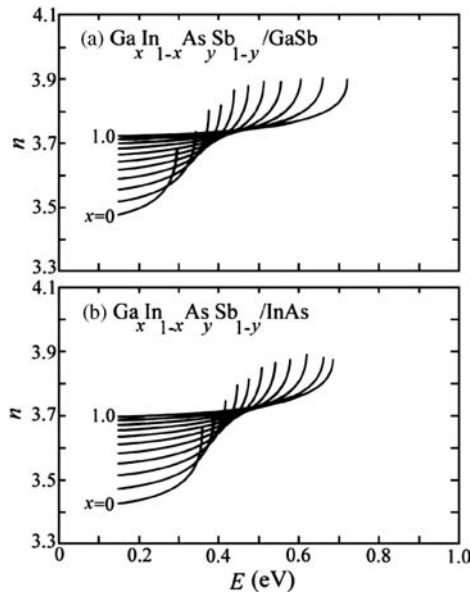


Figure 10.28 $n(E)$ dispersion in the transparent region of (a) $\text{Ga}_x\text{In}_{1-x}\text{As}_y\text{Sb}_{1-y}/\text{GaSb}$ and (b) $\text{Ga}_x\text{In}_{1-x}\text{As}_y\text{Sb}_{1-y}/\text{InAs}$ with increments in x of 0.1 at 300 K. The $n(E)$ curves are calculated from the simplified interband-transition model [2,170]

The high-energy endpoint on each curve in Figure 10.28 corresponds to the n value at the band edge E_0 . A noticeable feature found in this figure is that these alloy systems show a refractive-index anomaly, i.e. the smaller E_0 -gap material has a smaller refractive index. Note that almost all III–V and II–VI semiconductor alloys, such as $\text{Al}_x\text{Ga}_{1-x}\text{As}$ and $\text{Ga}_x\text{In}_{1-x}\text{P}_y\text{As}_{1-y}$, show no such anomalies in refractive-index (Figures 10.11 and 10.26).

10.4.3 (III, III, III)–V Alloy

(a) AlGaInP

The IR properties of $(\text{Al}_x\text{Ga}_{1-x})_{0.53}\text{In}_{0.47}\text{P}/\text{GaAs}$ have been studied by Hofmann *et al.* using far-IR SE [172]. They suggested that far-IR SE may be used to identify small degrees of long-range ordering in this quaternary.

By fitting the SE $n(E)$ data with the first-order Sellmeier equation, Adachi *et al.* [173] determined a set of the dispersion parameters A , B and C in the transparent region of the $(\text{Al}_x\text{Ga}_{1-x})_{0.53}\text{In}_{0.47}\text{P}$ quaternary that can be written as (C in μm)

$$A(x) = 5.38 + 2.16x \tag{10.11a}$$

$$B(x) = 4.01 - 3.01x \tag{10.11b}$$

$$C(x)^2 = 0.184 - 0.019x + 0.024x^2 \tag{10.11c}$$

As $\lambda \rightarrow \infty$ in the first-order Sellmeier equation, we obtain $n(\lambda \rightarrow \infty)^2 = \epsilon_\infty = A + B$.

Figure 10.29 shows the $n(E)$ dispersion with increments in x of 0.1 for $(\text{Al}_x\text{Ga}_{1-x})_{0.53}\text{In}_{0.47}\text{P}/\text{GaAs}$ calculated from the simplified interband-transition model [2]. The solid circles represent the experimental data for $x = 0, 0.42$ and 1.0 obtained by Tanaka *et al.* [174].

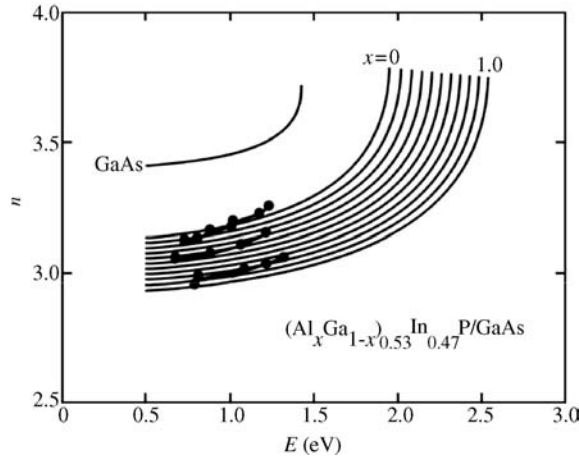


Figure 10.29 $n(E)$ dispersion in the transparent region of $(\text{Al}_x\text{Ga}_{1-x})_{0.53}\text{In}_{0.47}\text{P}/\text{GaAs}$ with increments in x of 0.1 at 300 K, together with that for GaAs. The $n(E)$ curves are calculated from the simplified interband-transition model [2]. The solid circles represent the experimental data for $x = 0, 0.42$ and 1.0 reported by Tanaka *et al.* [174]

The optical constants in the interband transition region of $(\text{Al}_x\text{Ga}_{1-x})_{0.53}\text{In}_{0.47}\text{P}/\text{GaAs}$ have been measured by SE [3]. Figure 10.30 shows the complex optical constants, $\epsilon(E)$ and $n^*(E)$, taken from

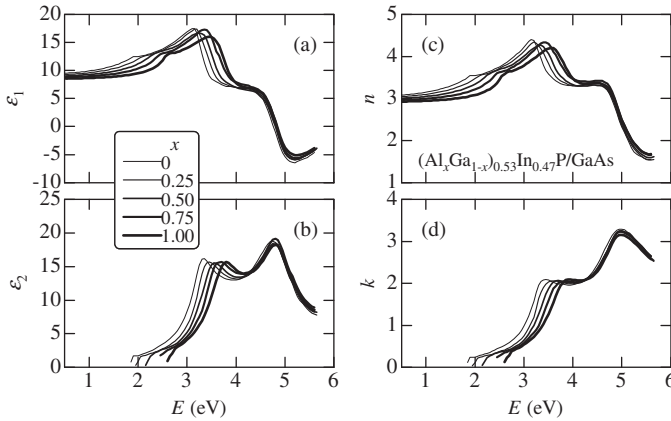


Figure 10.30 $\epsilon(E)$ -related spectra in the IR–UV region of $(\text{Al}_x\text{Ga}_{1-x})_{0.53}\text{In}_{0.47}\text{P}/\text{GaAs}$ at 300 K. The experimental data are taken from Adachi [3]

Adachi [3]. The two major features seen in Figure 10.30 are due to the E_1 and E_2 CPs at $\sim 3.2\text{--}3.7$ eV and ~ 4.8 eV, respectively. The E_1 structure moves toward higher energy with increasing x , while the E_2 structure does not perceptibly do so. The $E_1 + \Delta_1$ structure is not clearly discernible in $(\text{Al}_x\text{Ga}_{1-x})_{0.53}\text{In}_{0.47}\text{P}/\text{GaAs}$. These spectra were fitted by the MDF very well [175,176].

(b) AlGaInAs

The $n(E)$ dispersion in the transparent region and in the region a little above the E_0 edge of $(\text{Al}_x\text{Ga}_{1-x})_{0.48}\text{In}_{0.52}\text{As}$ has been measured by several authors [3]. Figure 10.31 shows the experimental $n(E)$ data for $(\text{Al}_x\text{Ga}_{1-x})_{0.48}\text{In}_{0.52}\text{As}/\text{InP}$. These data are taken from Adachi [3]. Mondry *et al.* [82] modeled the experimental $n(E)$ data with the first-order Sellmeier equation. The heavy solid lines in Figure 10.31 represent the endpoint ternary data that they obtained.

The fundamental absorption edge in $(\text{Al}_x\text{Ga}_{1-x})_{0.48}\text{In}_{0.52}\text{As}/\text{InP}$ has been measured by Masu *et al.* [177]. The spectra showed a sharp decline in $\alpha(E)$, common to direct-band-gap

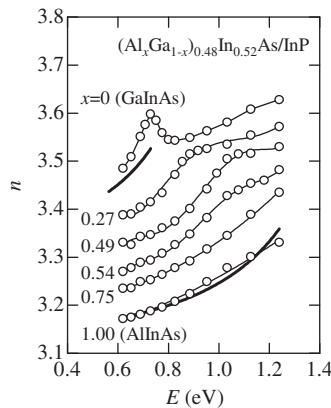


Figure 10.31 $n(E)$ dispersion in $(\text{Al}_x\text{Ga}_{1-x})_{0.48}\text{In}_{0.52}\text{As}/\text{InP}$ at 300 K. The experimental data are taken from Adachi [3]. The heavy solid lines represent the endpoint ternary data by Mondry *et al.* [82]

semiconductor materials. Using LPE Swarup *et al.* [178] also measured the absorption spectra of $\text{Al}_x\text{Ga}_y\text{In}_{1-x-y}\text{As}$ layers grown on the (111)As face of GaAs substrates.

The optical constants in the interband transition region of $(\text{Al}_x\text{Ga}_{1-x})_{0.48}\text{In}_{0.52}\text{As}/\text{InP}$ have been determined using SE [3]. The refractive indices in the wavelength range 1.0–1.9 μm of $(\text{Al}_x\text{Ga}_{1-x})_{0.48}\text{In}_{0.52}\text{As}/\text{InP}$ have also been determined by SE [179]. The $n(E)$ curves with increments in x of 0.1 for $(\text{Al}_x\text{Ga}_{1-x})_{0.48}\text{In}_{0.52}\text{As}/\text{InP}$ calculated from the simplified interband-transition model [2] are shown in Figure 10.32.

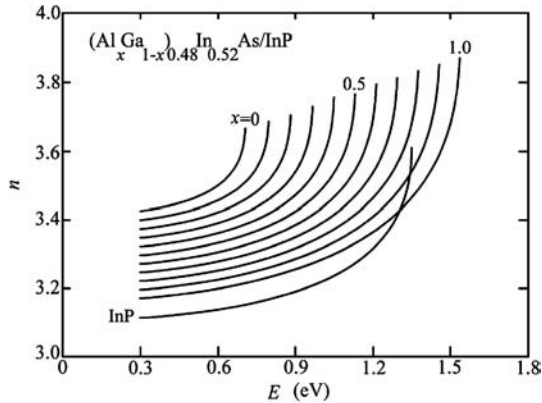


Figure 10.32 $n(E)$ dispersion in the transparent region of $(\text{Al}_x\text{Ga}_{1-x})_{0.48}\text{In}_{0.52}\text{As}/\text{InP}$ with increments in x of 0.1 at 300 K, together with that for InP. The $n(E)$ curves are calculated from the simplified interband-transition model [2,3]

10.4.4 III–(V, V, V) Alloy

A very limited number of reports are available for the optical properties of III–(V, V, V) quaternaries. The IR reflectivity spectra for $\text{InP}_x\text{As}_y\text{Sb}_{1-x-y}$ layers grown on (111)InAs have been measured by Belov *et al.* [180]. The optical transmission measurements on LPE-grown $\text{InP}_x\text{As}_y\text{Sb}_{1-x-y}/\text{InAs}$ have also been carried out by Esina *et al.* [181]. Adachi [3] calculated the $n(E)$ dispersion in $\text{AlP}_x\text{As}_y\text{Sb}_{1-x-y}$, $\text{GaP}_x\text{As}_y\text{Sb}_{1-x-y}$ and $\text{InP}_x\text{As}_y\text{Sb}_{1-x-y}$ lattice-matched to GaAs, InP or InAs with increments in x of 0.1 using the simplified interband-transition model.

10.5 II–VI SEMICONDUCTOR ALLOY

10.5.1 (II, II)–O Ternary Alloy

(a) BeZnO

Transmittance measurements on $\text{Be}_x\text{Zn}_{1-x}\text{O}$ /sapphire samples have been carried out [182,183]. The measured spectra are used to determine the composition dependence of E_0 (Figure 6.54(a)).

(b) MgZnO

The reststrahlen properties of $\text{Mg}_x\text{Zn}_{1-x}\text{O}$ have been investigated using far-IR reflectivity [184] and SE [185]. Variation in the optical phonon modes with x has been determined in the hexagonal and cubic regions [185].

The $n(E)$ dispersion in $w\text{-Mg}_x\text{Zn}_{1-x}\text{O}$ has been determined for x in the hexagonal [186,187] and cubic regions [188,189]. The n values obtained by Teng *et al.* [187] have been reproduced in Figure 10.33. The thermo-optical coefficient dn/dT for $c\text{-Mg}_x\text{Zn}_{1-x}\text{O}$ ($0.57 \leq x \leq 1.0$) has also been determined by Zhou *et al.* [190].

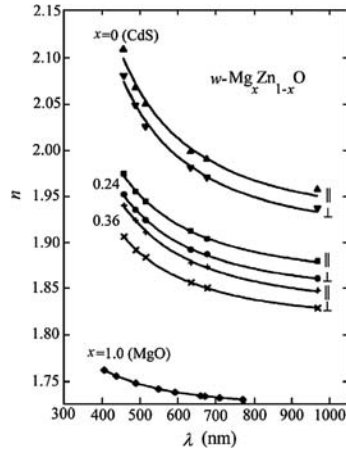


Figure 10.33 Ordinary-ray (n_o) and extraordinary-ray refractive-index spectra (n_e) for $w\text{-Mg}_x\text{Zn}_{1-x}\text{O}$ at 300 K, together with that for $c\text{-MgO}$. [Reprinted with permission from C. W. Teng *et al.*, *Appl. Phys. Lett.* **76**, 979 (2000). Copyright (2000), American Institute of Physics]

The absorption coefficient $\alpha(E)$ in the fundamental absorption edge of $w\text{-Mg}_x\text{Zn}_{1-x}\text{O}$ has been reported [187]. The pressure dependence of $\alpha(E)$ has also been reported [191].

The optical properties in the interband transition region of $\text{Mg}_x\text{Zn}_{1-x}\text{O}$ have been investigated using SE [186,192–194] and reflectivity [195]. The SE $\varepsilon(E)$ spectra for $w\text{-Mg}_x\text{Zn}_{1-x}\text{O}$ obtained by Kang *et al.* [192] have been reproduced in Figure 10.34. The $n = 1$ excitonic peak can clearly be seen in the $\varepsilon(E)$ spectra. This is especially true for samples with low x . The higher-lying CPs can also be identified at ~ 7 and ~ 9 eV for $x = 0\text{--}0.53$ [193].

(c) ZnCdO

The optical absorption spectra $\alpha(E)$ in the fundamental absorption edge of $\text{Cd}_x\text{Zn}_{1-x}\text{O}$ have been measured by several authors [196–199]. The data were used to determine the composition dependence of E_0 (Figure 6.54(c)).

10.5.2 (II, II)–S Ternary Alloy

(a) MgZnS

The optical absorption in $w\text{-Mg}_x\text{Zn}_{1-x}\text{S}$ has been measured for $0 \leq x \leq 0.25$ [200]. The samples were grown on (0001)-sapphire substrates by PLD. The absorption edge showed blueshift with increasing x (Figure 6.55(a)).

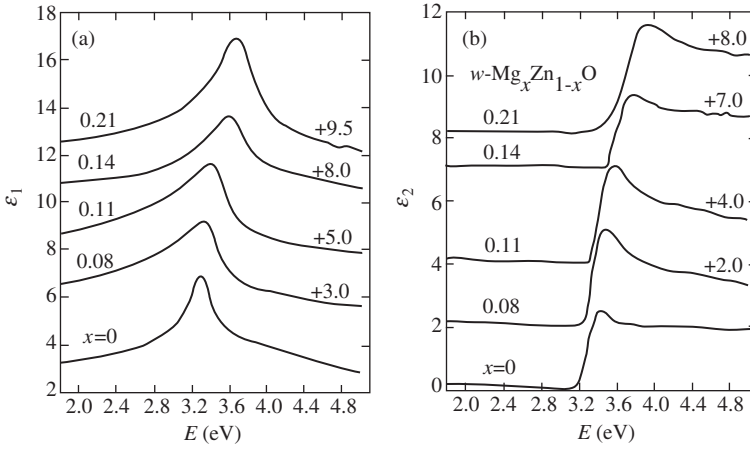


Figure 10.34 $\epsilon(E)$ spectra for $w\text{-Mg}_x\text{Zn}_{1-x}\text{O}$ at 300 K. [Reprinted with permission from *Solid State Commun.*, Spectroscopic ellipsometry study of $\text{Zn}_{1-x}\text{Mg}_x\text{O}$ thin films deposited on $\text{Al}_2\text{O}_3(0001)$ by J. H. Kang, Y. R. Park and K. J. Kim, **115**, 127–130. Copyright (2000), Elsevier]

(b) ZnCdS

Transmittance and reflectance measurements in the reststrahlen region of $w\text{-Zn}_x\text{Cd}_{1-x}\text{S}$ have been carried out by Lisitsa *et al.* [201]. The $n(E)$ dispersion in $c\text{-Zn}_x\text{Cd}_{1-x}\text{S}$ has also been studied by reflectivity measurements [202]. These results are reproduced in Figure 10.35.

Optical absorption $\alpha(E)$ in the fundamental absorption edge of $w\text{-Cd}_x\text{Zn}_{1-x}\text{S}$ has been measured at 77 and 150 K [203]. The samples were grown by a sublimation method. The pressure

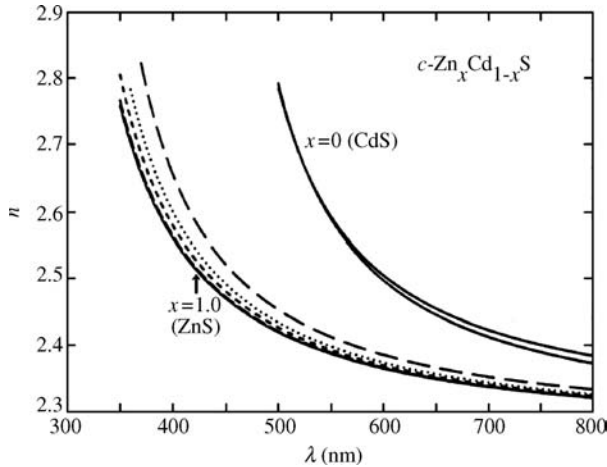


Figure 10.35 $n(E)$ dispersion in the transparent region of $c\text{-Zn}_x\text{Cd}_{1-x}\text{S}$ at 300 K. The dashed curves correspond to $x = 0.83, 0.91, 0.95$ and 0.983 from right to left. [From P. Chen *et al.*, *Semicond. Sci. Technol.* **13**, 1439 (1998), Copyright (1998) Institute of Physics]

dependence of the fundamental absorption edge has also been measured on chemical-transport-grown $w\text{-Cd}_x\text{Zn}_{1-x}\text{S}$ layers up to their respective phase transition [204].

10.5.3 (II, II)–Se Ternary Alloy

(a) *BeZnSe*

The $n(E)$ dispersion in $c\text{-Be}_x\text{Zn}_{1-x}\text{Se}$ layers grown on GaAs substrates by MBE has been measured using a prism coupler technique [205]. The data were fitted to the Sellmeier dispersion equation. These results are shown in Figure 10.36, together with the $n(E)$ dispersion in ZnSe ($x=0$) [3].

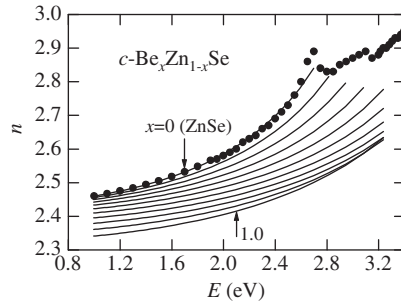


Figure 10.36 $n(E)$ dispersion in the transparent region of $c\text{-Be}_x\text{Zn}_{1-x}\text{Se}$ with increments in x of 0.1 at 300 K. The $n(E)$ curves are calculated from the first-order Sellmeier parameters reported by Peiris *et al.* [205]. The ZnSe data are taken from Adachi [3]

The optical properties of $c\text{-Be}_x\text{Zn}_{1-x}\text{Se}$ have been studied using SE in the spectral ranges 2.5–29 eV [206], 1.5–6.0 eV [207] and 1.25–5.0 eV [208]. The SE $\varepsilon_2(E)$ spectra for $c\text{-Be}_x\text{Zn}_{1-x}\text{Se}$ with $0 \leq x \leq 1.0$ and $E = 2.5\text{--}9$ eV [206] are reproduced in Figure 10.37. The very weak structures due to the Zn $3d$ transitions were identified in the spectral region above 10 eV.

(b) *BeCdSe*

SE was used to obtain the $\varepsilon(E)$ spectra in the range of 0.75–6.5 eV for $w\text{-Be}_x\text{Cd}_{1-x}\text{Se}$ with $x = 0.075$ [209,210]. The E_0 , E_1 and E_2 CPs were identified at ~ 2 , ~ 4 and ~ 6 eV, respectively. The alloys at $x \geq 0.1$ were also grown, but they exhibited chemical instability.

(c) *MgZnSe*

The $n(E)$ dispersion in $c\text{-Mg}_x\text{Zn}_{1-x}\text{Se}$ layers grown on GaAs(100) and silica glasses by MBE has been measured by Peiris *et al.* [211] and Derkowska *et al.* [212], respectively. Peiris *et al.* [211] reported the first-order Sellmeier constants as a function of x . The $n(E)$ dispersion calculated using these constants, together with the experimental $n(E)$ data for ZnSe ($x=0$) [3] are shown in Figure 10.38. The bold solid line is also obtained from the first-order Sellmeier parameters for ZnSe [213].

The absorption coefficients $\alpha(E)$ in the fundamental absorption edge of MBE-grown $c\text{-Mg}_x\text{Zn}_{1-x}\text{Se}/\text{GaAs}$ layers ($0 \leq x \leq 0.36$) have been measured at 2 K by Wörz *et al.* [214]. These results have been reproduced in Figure 10.39. The E_0 and $E_0 + \Delta_0$ excitons can be

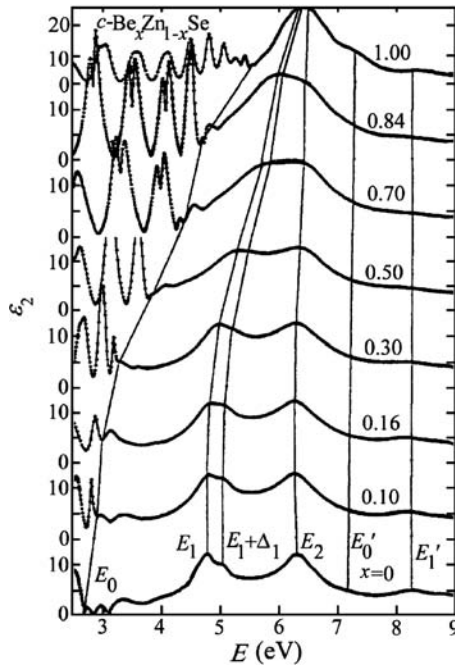


Figure 10.37 $\epsilon_2(E)$ spectra for $c\text{-Be}_x\text{Zn}_{1-x}\text{Se}$ at 300 K. [Reproduced with permission from K. Wilmers *et al.*, *J. Electron. Mater.* **28**, 670–677 (1999), Copyright (1999) Springer Science and Business Media]

clearly detected for x up to 0.28. The difference between the $n = 1$ ($1s$) and 2 ($2s$) excitons yields the Rydberg energy

$$Ry^* = \frac{4}{3}(E_{1s} - E_{2s}) \tag{10.12}$$

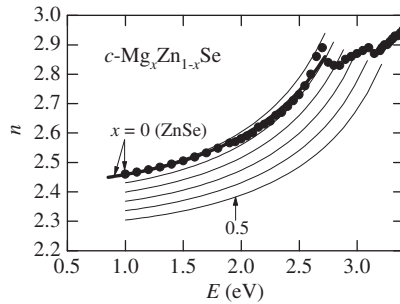


Figure 10.38 $n(E)$ dispersion in the transparent region of $c\text{-Mg}_x\text{Zn}_{1-x}\text{Se}$ with increments in x of 0.1 at 300 K. The $n(E)$ curves are calculated from the first-order Sellmeier parameters reported by Peiris *et al.* [211]. The bold solid line (ZnSe) is also calculated from the first-order Sellmeier parameters reported by Adachi [213]. The ZnSe data are taken from Adachi [3] (solid circles)

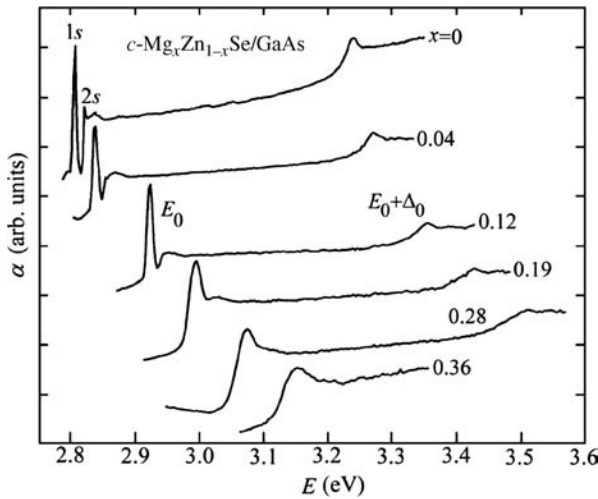


Figure 10.39 $\alpha(E)$ spectra in the fundamental absorption edge of MBE-grown $c\text{-Mg}_x\text{Zn}_{1-x}\text{Se/GaAs}$ layers ($0 \leq x \leq 0.36$) at 2 K. [Reprinted with permission from M. Wörz *et al.*, *Phys. Status Solidi B* **202**, 805 (1997), Copyright (1997) Wiley-VCH]

which in this case, is equal to the exciton binding energy G . The composition dependence obtained by Wörz *et al.* [214] can be written as $G = (20 \pm 0.2) + (37.5 \pm 7)x$ meV.

The optical properties in the interband transition region of $c\text{-Mg}_x\text{Zn}_{1-x}\text{Se}$ have been studied using SE [207,215]. The SE data analysis suggested that increasing x leads to a gradual increase in the $E_0/(E_0 + \Delta_0)$ and $E_1/(E_1 + \Delta_1)$ CP energies.

(d) *MgCdSe*

The optical properties of $w\text{-Mg}_x\text{Cd}_{1-x}\text{Se}$ ($0 \leq x \leq 0.46$) were investigated by optical absorption measurements at 300 K [216]. SE was also used to obtain the $\varepsilon(E)$ spectra for $w\text{-Mg}_x\text{Cd}_{1-x}\text{Se}$ in the range of 0.75–6.5 eV with $x = 0.15$ and 0.29 [210] and in the range of 1.25–4.5 eV with $x = 0$ –0.40 [217].

(e) *ZnCdSe*

The $n(E)$ dispersion in $c\text{-Zn}_x\text{Cd}_{1-x}\text{Se}$ has been measured by Peiris *et al.* [211,218]. These authors reported the first-order Sellmeier parameters as a function of x [211]. The $n(E)$ dispersion calculated using these parameters are shown in Figure 10.40, together with the experimental ZnSe data [3]. The bold solid line also represents the first-order Sellmeier parameters for ZnSe obtained by Adachi [213]. A temperature shift of $\Delta n/\Delta T = 1.0 \times 10^{-4} \text{ K}^{-1}$ ($T = 50$ –300 K) has also been reported by analyzing laser emission wavelengths from a $\text{Zn}_x\text{Cd}_{1-x}\text{Se}$ -based distributed feedback laser [219].

SE has been used to study the optical properties of $c\text{-Zn}_x\text{Cd}_{1-x}\text{Se}$ by several groups [220–223]. The samples used in these studies were epitaxial films grown by MBE on GaAs with $x = 0$ –1.0 [220], 0.75–1.0 [221] and 0.66–1.0 [222] and on InP with $x = 0.53$ [223].

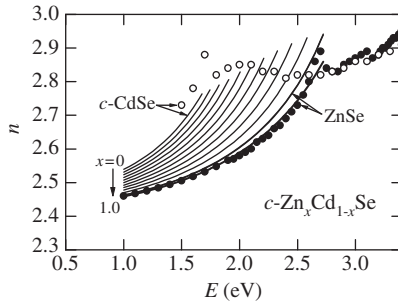


Figure 10.40 $n(E)$ dispersion in the transparent region of $c\text{-Zn}_x\text{Cd}_{1-x}\text{Se}$ with increments in x of 0.1 at 300 K. The $n(E)$ curves are calculated from the first-order Sellmeier parameters reported by Peiris *et al.* [211]. The bold solid line (ZnSe) is also calculated from the first-order Sellmeier parameters reported by Adachi [213]. The $c\text{-CdSe}$ ($x=0$) and ZnSe ($x=1.0$) data are taken from Adachi [3]

Suzuki and Adachi [224] used the MDF calculation to obtain a closed analytic formula for the optical constants of $c\text{-Zn}_x\text{Cd}_{1-x}\text{Se}$ as a function of x . Figure 10.41 shows the MDF-calculated $n(E)$ spectra in the region below and above the $E_0/(E_0 + \Delta_0)$ edge of $c\text{-Zn}_x\text{Cd}_{1-x}\text{Se}$ with increments in x of 0.2 [224]. The solid and open circles represent the experimental data taken from Adachi [3] (ZnSe) and Holden *et al.* [223] ($\text{Zn}_{0.53}\text{Cd}_{0.47}\text{Se}$), respectively.

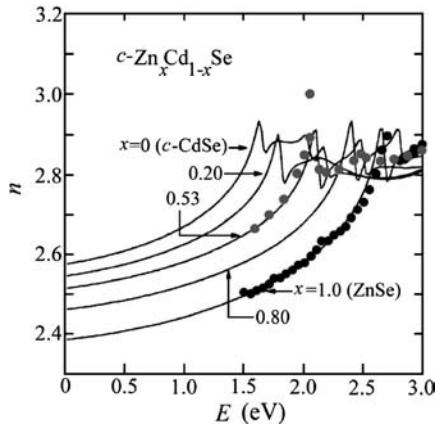


Figure 10.41 Theoretical $n(E)$ spectra in the region below and above the $E_0/(E_0 + \Delta_0)$ edge of $c\text{-Zn}_x\text{Cd}_{1-x}\text{Se}$ with increments in x of 0.2 at 300 K. The black and gray circles represent the experimental data for ZnSe and $\text{Zn}_{0.53}\text{Cd}_{0.47}\text{Se}$, respectively. [Reprinted with permission from K. Suzuki and S. Adachi, *J. Appl. Phys.* **83**, 1018 (1998). Copyright (1998), American Institute of Physics]

(f) CdHgSe

IR reflectivity spectra of $c\text{-Cd}_x\text{Hg}_{1-x}\text{Se}$ ($x=0\text{--}0.32$) have been reported by Kumazaki *et al.* [225]. They found that the measured reflectivity can be explained by the dynamic dielectric function constructed as the sum of the interband, intraband and phonon contributions.

The temperature and composition dependence of n in the transparent region of c - $\text{Cd}_x\text{Hg}_{1-x}\text{Se}$ has been determined by means of a fringe-spacing analysis [226]. The optical absorption properties near the fundamental absorption edge of c - and w - $\text{Cd}_x\text{Hg}_{1-x}\text{Se}$ have also been reported [226–229].

The fundamental reflectivity spectra for c - $\text{Cd}_x\text{Hg}_{1-x}\text{Se}$ have been measured [230]. The SE $\varepsilon(E)$ spectra for c - $\text{Cd}_x\text{Hg}_{1-x}\text{Se}$ ($x = 0$ – 0.3) have also been measured in the 1.7–5.6 eV region at 300 K [231].

10.5.4 (II, II)–Te Ternary Alloy

(a) *BeZnTe*

The optical properties in the interband transition region of $\text{Be}_x\text{Zn}_{1-x}\text{Te}$ have been investigated using reflectivity [232]. The x dependence of E_0 has been determined from this study. SE has also been used to measure $\varepsilon_2(E)$ in $\text{Be}_x\text{Zn}_{1-x}\text{Te}$ [233–235].

(b) *MgZnTe*

The $n(E)$ dispersion in c - $\text{Mg}_x\text{Zn}_{1-x}\text{Te}$ layers ($0 \leq x \leq 0.67$) grown on GaAs(100) by MBE has been determined from reflectivity measurements [236]. Figure 10.42 shows the $n(E)$ dispersion calculated using first-order Sellmeier parameters [236], together with the experimental ZnTe data [3]. The bold solid line (ZnTe) has also been calculated using first-order Sellmeier parameters [213].

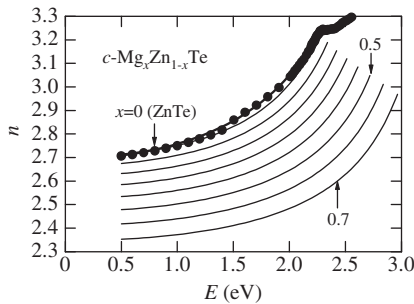


Figure 10.42 $n(E)$ dispersion in the transparent region of c - $\text{Mg}_x\text{Zn}_{1-x}\text{Te}$ with increments in x of 0.1 at 300 K. The $n(E)$ curves are calculated from the first-order Sellmeier parameters reported by Liu *et al.* [236]. The bold solid line (ZnTe) is also calculated from the first-order Sellmeier parameters reported by Adachi [213]. The experimental data are taken from Adachi [3] (solid circles)

The optical absorption coefficients $\alpha(E)$ in the fundamental absorption edge of bulk c - $\text{Mg}_x\text{Zn}_{1-x}\text{T}$ crystals ($0 \leq x \leq 0.48$) grown by the Bridgman method have been measured at 4.2 K [237]. These results have been reproduced in Figure 10.43. The $n = 1$ ($1s$) excitonic peak can be clearly seen at the E_0 edge of each sample.

SE measurements have been carried out on MBE-grown c - $\text{Zn}_x\text{Cd}_{1-x}\text{Se}/\text{GaAs}(100)$ layers ($0 \leq x \leq 0.52$) [238]. The composition dependence of the excitonic E_0 , $E_0 + \Delta_0$ and E_2 gaps has been determined in this study.

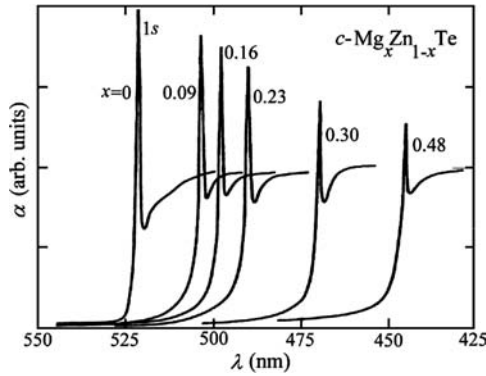


Figure 10.43 $\alpha(E)$ spectra in the fundamental absorption edge of $c\text{-Mg}_x\text{Zn}_{1-x}\text{Te}$ ($0 \leq x \leq 0.48$) at 4.2 K. [Reprinted with permission from S.-J. Chung *et al.*, *J. Phys. Chem. Solids* **60**, 799–805 (1999), Copyright (1999) Elsevier]

(c) *MgCdTe*

The IR reflectivity spectra for $c\text{-Mg}_x\text{Cd}_{1-x}\text{Te}$ with $x = 0\text{--}0.6$ have been measured in the range of $100\text{--}500\text{ cm}^{-1}$ at 300 K [239]. The $n(E)$ dispersion in $c\text{-Mg}_x\text{Cd}_{1-x}\text{Te}$ has also been measured at 4 K by André and Dang [240], at 77 and 300 K by Lugauer *et al.* [241] and at 300 K by Luttmann *et al.* [242]. Figure 10.44 shows the $n(E)$ spectra calculated from first-order Sellmeier parameters by Luttmann *et al.* [242], together with the experimental CdTe $n(E)$ data taken from Adachi [3].

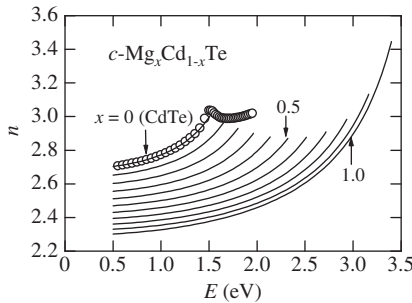


Figure 10.44 $n(E)$ dispersion in the transparent region of $c\text{-Mg}_x\text{Zn}_{1-x}\text{Te}$ with increments in x of 0.1 at 300 K. The $n(E)$ curves are calculated from the first-order Sellmeier parameters reported by Luttmann *et al.* [242]. The experimental CdTe data are taken from Adachi [3]

SE measurements have been performed to determine the $\epsilon(E)$ spectra for $c\text{-Mg}_x\text{Cd}_{1-x}\text{Te}$ [242–244]. The composition-dependent higher-order CPs, such as E_1 , $E_1 + \Delta_1$ and E_2 , have been determined from these $\epsilon(E)$ spectra.

(d) *ZnCdTe*

The IR reflectivity in the reststrahlen region of $\text{Zn}_x\text{Cd}_{1-x}\text{Te}$ has been measured by several authors [245–248]. The $n(E)$ dispersion in $\text{Zn}_x\text{Cd}_{1-x}\text{Te}$ has also been measured at room

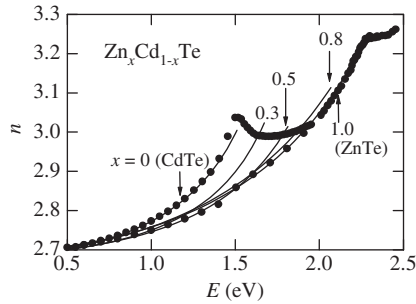


Figure 10.45 $n(E)$ dispersion in the transparent region of $\text{Zn}_x\text{Cd}_{1-x}\text{Te}$ at 300 K. The $n(E)$ curves are calculated from the first-order Sellmeier parameters [249]. The open circles represent the CdTe ($x = 0$) and ZnTe ($x = 1.0$) data taken from Adachi [3]

temperature in the 1.1–2.5 eV range by Adachi and Kimura [249]. The samples used by these authors were grown by the conventional Bridgman method. These results have been reproduced in Figure 10.45.

The optical absorption spectra in the near-IR and mid-IR regions of $\text{Zn}_x\text{Cd}_{1-x}\text{Te}$ have been measured at 300 K [250–252] and at 2 K [252]. The absorption coefficients $\alpha(E)$ are found to exhibit an exponential dependence on E according to the Urbach rule [251].

The room-temperature reflectivity spectra in the interband transition region of $\text{Zn}_x\text{Cd}_{1-x}\text{Te}$ have been measured by several authors [253–256]. The $R(E)$ spectra revealed the higher-lying CPs, E_0 , E_1 , $E_1 + \Delta_1$, etc. The optical properties in the interband transition region of $\text{Zn}_x\text{Cd}_{1-x}\text{Te}$ have also been investigated using SE [257–260]. The $n(E)$ and $k(E)$ spectra obtained by Adachi and Kimura have been reproduced in Figure 10.46 [257]. These spectra were parameterized to enable the calculation of the optical response in a $\text{Zn}_x\text{Cd}_{1-x}\text{Te}$ alloy having an arbitrary composition x and photon energy E .

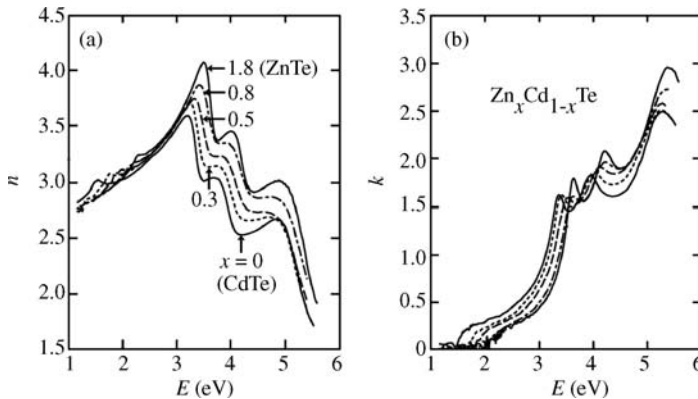


Figure 10.46 $n(E)$ and $k(E)$ spectra for $\text{Zn}_x\text{Cd}_{1-x}\text{Te}$ with $x = 0, 0.3, 0.5, 0.8$ and 1.0 at 300 K. [Reprinted with permission from *Jpn. J. Appl. Phys.*, Optical constants of $\text{Zn}_{1-x}\text{Cd}_x\text{Te}$ ternary alloys: Experiment and modeling by S. Adachi and T. Kimura, **32**, 3496. Copyright (1993), Institute of Pure and Applied Physics]

(e) *ZnHgTe*

The IR optical properties of $\text{Zn}_x\text{Hg}_{1-x}\text{Te}$ have been studied by a number of authors [261–264]. The absorption coefficients $\alpha(E)$ in the fundamental absorption edge of $\text{Zn}_x\text{Hg}_{1-x}\text{Te}$ have also been measured by several authors [264–266]. SE has been carried out on $\text{Zn}_x\text{Hg}_{1-x}\text{Te}$ in the range between 0.75 and 5.7 eV by Castaing *et al.* [267].

(f) *CdHgTe*

The optical properties in the reststrahlen region of $\text{Cd}_x\text{Hg}_{1-x}\text{Te}$ have been investigated by a number of groups [263,268–271]. The $\alpha(E)$ spectra in the IR region have also been measured by a number of authors [272–278]. An empirical formula for the intrinsic optical absorption coefficient in the Kane region is given by Chu *et al.* [279].

The $n(E)$ dispersion in $\text{Cd}_x\text{Hg}_{1-x}\text{Te}$ has been measured at different temperatures from 77 up to 350 K [273,275,280,281]. Figure 10.47 shows the results obtained by Kučera [280]. Liu *et al.* [281] also obtained $n(\lambda, T)$ from transmittance interference spacing

$$n(\lambda, T)^2 = A + \frac{B}{1 - (C/\lambda)^2} + D\lambda^2 \quad (10.13)$$

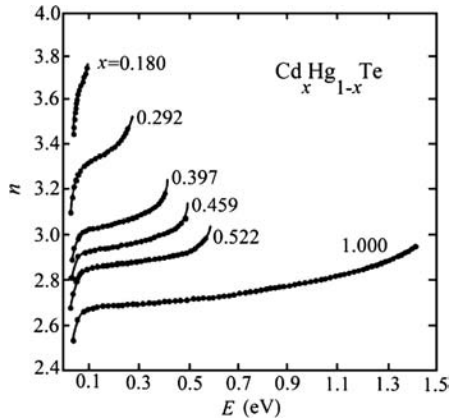


Figure 10.47 $n(E)$ dispersion in $\text{Cd}_x\text{Hg}_{1-x}\text{Te}$ with $x = 0.180$ – 1.000 at 300 K. [Reprinted with permission from Z. Kučera, *Phys. Status Solidi A* **100**, 659–665 (1987), Copyright (1987) Wiley–VCH]

where λ is the wavelength and A , B , C and D are fitting parameters which vary with composition x and temperature T . This formula can be used for $x = 0.200$ – 0.443 at $T = 4.2$ – 300 K. The formula can also be used with $x \leq 0.540$ at different temperatures and with $x = 0.54$ – 1.0 at room temperature.

The fundamental reflectivity spectra in the interband transition region of $\text{Cd}_x\text{Hg}_{1-x}\text{Te}$ have been measured at 315 K by Gałazka and Kisiel [282] and at 115–300 K by Rodzik and Kisiel [283]. The optical properties of $\text{Cd}_x\text{Hg}_{1-x}\text{Te}$ have also been studied using SE in the 1.8–5.5 eV spectral region by Viña *et al.* [284] and in the 1.5–6.0 eV region by Arwin and Aspnes [285]. The dependence of $\varepsilon(E)$ on T has been discussed by Kim and Sivananthan [286] and Johs *et al.* [287].

10.5.5 Zn-(VI, VI) Ternary Alloy

(a) ZnOS

A series of $w\text{-ZnO}_x\text{S}_{1-x}$ films with $0 \leq x \leq 1.0$ were deposited by rf reactive sputtering on different substrates [288] and the composition dependence of E_0 was then determined from optical transmission measurements (Figure 6.59(a)).

(b) ZnSSe

The IR reflectivity and absorption in $c\text{-ZnS}_x\text{Se}_{1-x}$ have been measured by several authors [289,290]. The $n(E)$ and $k(E)$ curves for $c\text{-ZnS}_x\text{Se}_{1-x}$ have also been determined from optical transmittance measurements [291]. Ozaki and Adachi [292] carried out MDF analysis to obtain a closed analytic formula for the optical constants of $c\text{-ZnS}_x\text{Se}_{1-x}$ as a function of x . Figure 10.48 shows the MDF-calculated $n(E)$ dispersion in the $E_0/(E_0 + \Delta_0)$ region of $c\text{-ZnS}_x\text{Se}_{1-x}$ with increments in x of 0.1 [292].

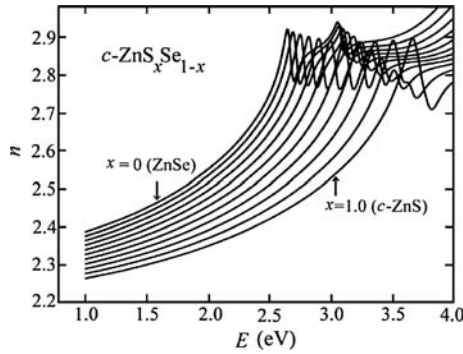


Figure 10.48 $n(E)$ dispersion in the transparent region of $c\text{-ZnS}_x\text{Se}_{1-x}$ with increments in x of 0.1 at 300 K. The $n(E)$ curves are obtained from the MDF calculation. [Reprinted with permission from S. Ozaki and S. Adachi, *J. Appl. Phys.* **75**, 7470 (1994). Copyright (1994), American Institute of Physics]

The low-temperature absorption coefficients $\alpha(E)$ in the E_0 region of MOCVD-grown $c\text{-ZnS}_x\text{Se}_{1-x}$ layers were measured by Gebhard and Schötz [293]. The hydrostatic-pressure dependent $\alpha(E)$ spectra were also reported by the same authors [294].

The room-temperature $R(E)$ spectra in the interband transition region of $c\text{-ZnS}_x\text{Se}_{1-x}$ were measured by Ebina *et al.* [295]. Several peaks related to the higher-lying CPs were determined as a function of x . The R values (≤ 0.3) are, however, considerably smaller than those obtained by Ozaki and Adachi [292], suggesting that the sample surfaces used by Ebina *et al.* were of poorer quality.

Jans *et al.* [221] carried out SE measurements on MBE-grown $c\text{-ZnS}_x\text{Se}_{1-x}/\text{GaAs}$ samples. They reported only the $\varepsilon(E)$ spectrum for $\text{ZnS}_{0.15}\text{Se}_{0.85}$. Ozaki and Adachi [292] presented the MDF-calculated $\varepsilon(E)$ spectra in the 1–6 eV region of $c\text{-ZnS}_x\text{Se}_{1-x}$ with increments in x of 0.2.

(c) ZnSTe

A strongly nonlinear pressure dependence of the band gaps and large downward shifts of the CB edges as a function of x in $c\text{-ZnS}_x\text{Te}_{1-x}$ has been found from optical transmittance

data [296] (Figure 6.59(c)). SE has also been used to determine the $\varepsilon(E)$ spectra in the 1.5–6.0 eV region of $c\text{-ZnS}_x\text{Te}_{1-x}$ films deposited by hot-wall epitaxy [297].

(d) *ZnSeTe*

The optical properties in the reststrahlen region of $\text{ZnSe}_x\text{Te}_{1-x}$ have been measured by several authors [298,299]. A series of $\text{ZnSe}_x\text{Te}_{1-x}$ films with $0 \leq x \leq 1.0$ were grown on GaAs(100) substrates by MBE to determine the x dependence of $n(E)$ [300]. Ozaki and Adachi [301] used the MDF method to obtain a closed analytic formula for the optical constants of $\text{ZnSe}_x\text{Te}_{1-x}$ as a function of x . Figure 10.49 shows the MDF-calculated $n(E)$ dispersion in the $E_0/(E_0 + \Delta_0)$ region of $\text{ZnSe}_x\text{Te}_{1-x}$ with increments in x of 0.1 [301].

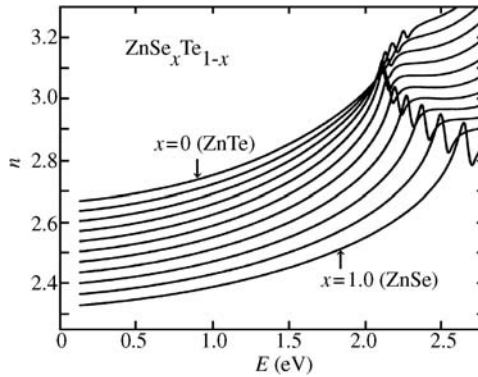


Figure 10.49 $n(E)$ dispersion in the transparent region of $\text{ZnSe}_x\text{Te}_{1-x}$ with increments in x of 0.1 at 300 K. The $n(E)$ curves are obtained from the MDF calculation. [Reprinted with permission from *Jpn. J. Appl. Phys.*, Optical constants of $\text{ZnSe}_x\text{Te}_{1-x}$ ternary alloys by S. Ozaki and S. Adachi, **32**, 2620–2625. Copyright (1993), Japanese Society of Applied Physics]

The hydrostatic-pressure dependent $\alpha(E)$ spectra were measured by Wu *et al.* [302]. The first- and second-order pressure coefficients of the fundamental absorption edge were determined as a function of x .

The fundamental reflectivity spectra in the interband transition region of $\text{ZnSe}_x\text{Te}_{1-x}$ were measured at 300 K by Ebina *et al.* [303]. The CP energies, such as $E_0, E_0 + \Delta_0, E_1, E_1 + \Delta_1$ and E_2 , were determined as a function of x . It should be noted however, that the R values (≤ 0.4) obtained were considerably smaller than those reported by Ozaki and Adachi [301], suggesting that Ebina *et al.* had used sample surfaces of inferior quality [303]. Ozaki and Adachi [301] also reported the MDF-calculated $\varepsilon(E)$ spectra in the 1–6 eV region of $\text{ZnSe}_x\text{Te}_{1-x}$ with increments in x of 0.1.

10.5.6 Cd–(VI, VI) Ternary Alloy

(a) *CdSSe*

The optical properties in the reststrahlen region of $w\text{-CdS}_x\text{Se}_{1-x}$ have been studied by several authors [304–307]. The $n(E)$ dispersion in the transparent region of $w\text{-CdS}_x\text{Se}_{1-x}$ has been measured with $0 \leq x \leq 1.0$ in the temperature range between 100 and 600 K by

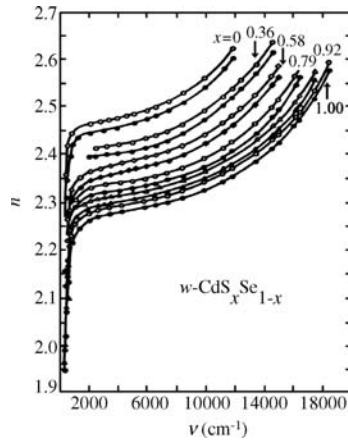


Figure 10.50 $n(E)$ dispersion in the transparent region of $w\text{-CdS}_x\text{Se}_{1-x}$ with $x = 0, 0.36, 0.58, 0.79, 0.92$ and 1.00 at 300 K . The solid and open symbols correspond to those for $E \perp c$ (n_o) and $E \parallel c$ (n_e), respectively. [Reprinted with permission from M. P. Lisitsa, L. F. Gudymenko, V. N. Malinko, and S. F. Terekhova, *Phys. Status Solidi* **31**, 389 (1969), Copyright (1969) Wiley-VCH]

Lisitsa *et al.* [308]. These authors presented the results in a variety of graphical and tabular forms. The $n(E)$ data at 300 K have been reproduced in Figure 10.50. The natural birefringence $n_e(E \parallel c) > n_o(E \perp c)$ is evident for all samples investigated. Femtosecond time-resolved refractive-index changes in $\text{CdS}_{0.75}\text{Se}_{0.25}$ and CdS have also been measured using a pump-probe deflection technique [309]. The $n(E)$ curves for polycrystalline $\text{CdS}_x\text{Se}_{1-x}$ films deposited on quartz substrates by pulsed-laser ablation technique have also been reported [310].

The $\alpha(E)$ spectra in the E_0 region of $w\text{-CdS}_x\text{Se}_{1-x}$ have been measured for polarizations $E \perp c$ and $E \parallel c$ [311]. The $\alpha(E)$ spectra for polycrystalline $\text{CdS}_x\text{Se}_{1-x}$ samples have also been reported [310].

The UV reflectivity of $w\text{-CdS}_x\text{Se}_{1-x}$ single crystals has been investigated at 90 K using linearly polarized light [312]. The x -dependent CPs, such as E_1, E_0', E_2 and E_1' , were determined and correlated with the electronic dipole transitions in the BZ.

(b) CdSTe

Long-wavelength IR spectroscopy has been used to study the lattice vibrations in $\text{CdS}_x\text{Te}_{1-x}$ [313]. The sphalerite-wurtzite phase transition is found to occur in the $x = 0.20\text{--}0.25$ range.

The optical constants, n and α , of flash-evaporated $\text{CdS}_x\text{Te}_{1-x}$ films with $0 \leq x \leq 1.0$ have been determined from reflectance and transmittance measurements [314]. As expected, the n value at $\lambda = 2\ \mu\text{m}$ decreased with increasing x . Thin films of polycrystalline $\text{CdS}_x\text{Te}_{1-x}$ ($0 \leq x \leq 1.0$) have also been prepared by vacuum evaporation. The complex refractive indices $n^* = n + ik$ for these films have been determined in the wavelength range of $250\text{--}3200\text{ nm}$ from reflectance and transmittance measurements [315].

SE has been used to determine the optical constants in the IR-UV spectral region of polycrystalline $\text{CdS}_x\text{Te}_{1-x}$ films ($0 \leq x \leq 1.0$) grown on borosilicate glasses by PLD [316]. A modified MDF is used to analyze the measured SE spectra.

(c) CdSeTe

The IR reflectivity for Bridgman-grown $\text{CdS}_x\text{Se}_{1-x}$ ($0 \leq x \leq 1.0$) was investigated by several authors [317,318]. The composition dependence of the phonon frequencies did not show any discontinuity when the crystal structure changed from zinc-blende to wurtzite. More recently, Feng *et al.* [319] undertook IR reflectivity studies on $\text{CdS}_x\text{Se}_{1-x}$ ($x \leq 0.36$). The samples used were grown by the Bridgman method and were single crystals with the zinc-blende structure. Optical constants, such as n and α , for $\text{CdS}_x\text{Se}_{1-x}$ in the limited composition ranges have also been reported [320–322].

10.5.7 (II, II)–(VI, VI) Quaternary Alloy**(a) MgZnSSe**

The $n(E)$ dispersion in $\text{Mg}_x\text{Zn}_{1-x}\text{S}_y\text{Se}_{1-y}/\text{GaAs}$ has been measured by several authors [323–325]. These data showed that the smaller E_0 -gap material has a larger n value, as in many tetrahedral semiconductor alloys. The optical absorption in the fundamental absorption edge of $\text{Mg}_x\text{Zn}_{1-x}\text{S}_y\text{Se}_{1-y}/\text{GaAs}$ has also been measured by Lunz *et al.* [325].

SE has been used to determine the temperature dependence of E_0 from 300 K to growth temperature in alloy compositions used in cladding layers and waveguides for blue–green light-emitting devices [326].

(b) MgZnSeTe

The refractive index n at $\lambda = 600$ nm for $\text{Mg}_x\text{Zn}_{1-x}\text{Se}_y\text{Te}_{1-y}/\text{InP}$ has been measured by Naniwae *et al.* [327]. The n value decreased almost linearly as the Mg content x increased in accordance with $n = 2.99 - 1.09x$. The pressure-dependent absorption coefficients $\alpha(E)$ for $\text{Mg}_x\text{Zn}_{1-x}\text{Se}_y\text{Te}_{1-y}$ have also been measured to investigate the band anticrossing effects [328], as popularly observed in dilute-nitride III–V alloys.

10.5.8 (II, II, II)–VI Quaternary Alloy**(a) BeMgZnSe**

The $n(E)$ dispersion in $\text{Be}_x\text{Mg}_y\text{Zn}_{1-x-y}\text{Se}/\text{GaP}$ has been measured at 300 K using SE [329]. The n value at $\lambda = 370$ nm decreased almost linearly as the alloy E_0 value increased in accordance with $n = 4.61 - 0.49E_0$. SE has also been used to determine the composition dependence of CPs in $\text{Be}_x\text{Mg}_y\text{Zn}_{1-x-y}\text{Se}/\text{GaAs}$ [330].

(b) BeZnCdSe

SE has been used to characterize bulk $\text{Be}_x\text{Zn}_y\text{Cd}_{1-x-y}\text{Se}$ grown by the Bridgman method [331]. The first-order Sellmeier equation is used to model the experimental $n(E)$ data in the transparent region of the bulk alloys.

(c) MgZnCdSe

The $n(E)$ dispersion in the transparent region of $\text{Mg}_x\text{Zn}_y\text{Cd}_{1-x-y}\text{Se}/\text{InP}$ has been measured by Morita *et al.* [332] and Guo *et al.* [333]. The experimental $n(E)$ data obtained by Guo *et al.* [333] have been reproduced in Figure 10.51. These data were obtained using a prism coupler

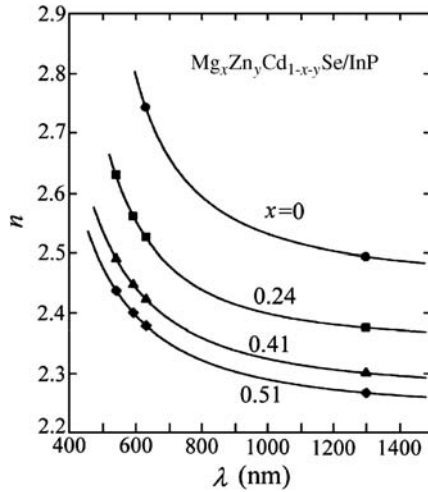


Figure 10.51 $n(E)$ dispersion in the transparent region of $\text{Mg}_x\text{Zn}_y\text{Cd}_{1-x-y}\text{Se/InP}$ at 300 K. [Reprinted with permission from S. P. Guo, O. Maksimov, M. C. Tamargo, F. C. Peiris, and J. K. Furdyna, *Appl. Phys. Lett.* **77**, 4107 (2000). Copyright (2000), American Institute of Physics]

technique. Peiris *et al.* [334] also reported the refractive-index step Δn between $\text{Mg}_x\text{Zn}_y\text{Cd}_{1-x-y}\text{Se}$ and $\text{Zn}_x\text{Cd}_{1-x}\text{Se}$ at $\lambda = 632.8$ nm.

REFERENCES

- [1] S. Adachi, *Properties of Group-IV, III-V and II-VI Semiconductors*, John Wiley & Sons, Ltd, Chichester, 2005.
- [2] S. Adachi, *Optical Properties of Crystalline and Amorphous Semiconductors: Materials and Fundamental Principles*, Kluwer Academic, Boston, 1999.
- [3] S. Adachi, *Optical Constants of Crystalline and Amorphous Semiconductors: Numerical Data and Graphical Information*, Kluwer Academic, Boston, 1999.
- [4] W. Kissinger, M. Weidner, H. J. Osten, and M. Eichler, *Appl. Phys. Lett.* **65**, 3356 (1994).
- [5] H. Lee, S. R. Kurtz, J. A. Floro, J. Strane, C. H. Seager, S. R. Lee, E. D. Jones, J. F. Nelson, T. Mayer, and S. T. Picraux, *Jpn. J. Appl. Phys.* **34**, L1340 (1995).
- [6] J. S. Schrader, J. L. Huguenin-Love, R. J. Soukup, N. J. Ianno, C. L. Exstrom, S. A. Darveau, R. N. Udey, and V. L. Dalal, *Sol. Ener. Mater. Sol. Cells* **90**, 2338 (2006).
- [7] K. Kolodzey, P. A. O'Neil, S. Zhang, B. A. Orner, K. Roe, K. M. Unruh, C. P. Swann, M. M. Waite, and S. I. Shah, *Appl. Phys. Lett.* **67**, 1865 (1995).
- [8] M. Krishnamurthy, K. -K. Yang, and W. H. Weber, *Appl. Phys. Lett.* **69**, 2572 (1996).
- [9] R. Braunstein, *Phys. Rev.* **130**, 879 (1963).
- [10] R. Braunstein, *Phys. Rev.* **130**, 869 (1963).
- [11] R. Braunstein, A. R. Moore, and F. Herman, *Phys. Rev.* **109**, 695 (195).
- [12] C. Pickering and R. T. Carline, *J. Appl. Phys.* **75**, 4642 (1994).
- [13] J. C. Tsang, V. P. Kesan, J. L. Freeouf, F. K. LeGoues, and S. S. Iyer, *Phys. Rev. B* **46**, 6907 (1992).
- [14] G. He and H. A. Atwater, *Phys. Rev. Lett.* **79**, 1937 (1997).
- [15] H. P. L. de Guevara, A. G. Rodríguez, H. Navarro-Contreras, and M. A. Vidal, *Appl. Phys. Lett.* **84**, 4532 (2004).

- [16] H. P. L. de Guevara, A. G. Rodríguez, H. Navarro-Contreras, and M. A. Vidal, *Appl. Phys. Lett.* **91**, 161909 (2007).
- [17] V. R. D'Costa, C. S. Cook, A. G. Birdwell, C. L. Littler, M. Canonico, S. Zollner, J. Kouvetakis, and J. Menéndez, *Phys. Rev. B* **73**, 125207 (2006).
- [18] L. V. Kulik, C. Guedj, M. W. Dashiell, J. Kolodzey, and A. Hairie, *Phys. Rev. B* **59**, 15753 (1999).
- [19] B. A. Orner, J. Olowolafe, K. Roe, J. Kolodzey, T. Laursen, J. W. Mayer, and J. Spear, *Appl. Phys. Lett.* **69**, 2557 (1996).
- [20] H. Lee, J. A. Floro, J. Strane, S. R. Lee, E. D. Jones, T. Mayer, and S. T. Picraux, *Mater. Res. Soc. Symp. Proc.* **379**, 211 (1995).
- [21] B.-K. Yang, M. Krishnamurthy, and W. H. Weber, *J. Appl. Phys.* **84**, 2011 (1998).
- [22] S. Zollner, J. Hildreth, R. Liu, P. Zaumseil, M. Weidner, and B. Tillack, *J. Appl. Phys.* **88**, 4102 (2000).
- [23] P. Aella, C. Cook, J. Tolle, S. Zollner, A. V. G. Chizmeshya, and J. Kouvetakis, *Appl. Phys. Lett.* **84**, 888 (2004).
- [24] T. Suzuki, H. Yaguchi, H. Okumura, Y. Ishida, and S. Yoshida, *Jpn. J. Appl. Phys.* **39**, L497 (2000).
- [25] U. Köhler, D. J. As, B. Schöttker, T. Frey, K. Lischka, J. Scheiner, S. Shokhovets, and R. Goldhahn, *J. Appl. Phys.* **85**, 404 (1999).
- [26] K. Torii, N. Usukura, A. Nakamura, T. Sota, S. F. Chichibu, T. Kitamura, and H. Okumura, *Appl. Phys. Lett.* **82**, 52 (2003).
- [27] R. Goldhahn, J. Scheiner, S. Shokhovets, T. Frey, U. Köhler, D. J. As, and K. Lischka, *Appl. Phys. Lett.* **76**, 291 (2000).
- [28] Z. G. Hu, M. Strassburg, N. Dietz, A. G. U. Perera, A. Asghar, and I. T. Ferguson, *Phys. Rev. B* **72**, 245326 (2005).
- [29] K. Kazan, P. Masri, and M. Sumiya, *J. Appl. Phys.* **100**, 013508 (2006).
- [30] U. Tisch, B. Meyler, O. Katz, E. Finkman, and J. Salzman, *J. Appl. Phys.* **89**, 2676 (2001).
- [31] G. Webb-Wood, Ü. Özgür, H. O. Everitt, F. Yun, and H. Morko, *Phys. Status Solidi A* **188**, 793 (2001).
- [32] R. Hui, S. Taherion, Y. Wan, J. Li, S. X. Jin, J. Y. Lin, and H. X. Jiang, *Appl. Phys. Lett.* **82**, 1326 (2003).
- [33] N. Antoine-Vincent, F. Natali, M. Mihailovic, A. Vasson, J. Leymarie, P. Disseix, D. Byrne, F. Semon, and J. Massies, *J. Appl. Phys.* **93**, 5222 (2003).
- [34] N. A. Sanford, L. H. Robins, A. V. Davydov, A. Shapiro, D. V. Tsvetkov, A. V. Dmitriev, S. Keller, U. K. Mishra, and S. P. DenBaars, *J. Appl. Phys.* **94**, 2980 (2003).
- [35] N. Antoine-Vincent, F. Natali, M. Mihailovic, P. Disseix, A. Vasson, J. Leymarie, D. Byrne, F. Semon, and J. Massies, *Phys. Status Solidi A* **195**, 543 (2003).
- [36] F. Omnès, N. Marengo, B. Beaumont, P. de Mierry, E. Monroy, F. Calle, and E. Muñoz, *J. Appl. Phys.* **86**, 5286 (1999).
- [37] H. Angerer, D. Brunner, F. Freudenberg, O. Ambacher, M. Stutzmann, R. Höpler, T. Metzger, E. Born, G. Dollinger, A. Bergmaier, S. Karsch, and H. -J. Körner, *Appl. Phys. Lett.* **71**, 1504 (1997).
- [38] M. Stutzmann, O. Ambacher, A. Cros, M. S. Brandt, H. Angerer, R. Dimitrov, N. Reinacher, T. Metzger, R. Höpler, D. Brunner, F. Freudenberg, R. Handschuh, and C. Deger, *Mater. Sci. Eng. B* **50**, 212 (1997).
- [39] T. Wethkamp, K. Wilmers, N. Esser, W. Richter, O. Ambacher, H. Angerer, G. Jungk, R. L. Johnson, and M. Cardona, *Thin Solid Films* **313–314**, 745 (1998).
- [40] C. Buchheim, R. Goldhahn, M. Rakel, C. Cobet, N. Esser, U. Rossow, D. Fuhrmann, and A. Hangleiter, *Phys. Status Solidi B* **242**, 2610 (2005).
- [41] T. Kawashima, H. Yoshikawa, S. Adachi, S. Fuke, and K. Ohtsuka, *J. Appl. Phys.* **82**, 3528 (1997).
- [42] A. Kasic, M. Schubert, J. Off, and F. Scholz, *Appl. Phys. Lett.* **78**, 1526 (2001).
- [43] G. M. Laws, E. C. Larkins, I. Harrison, C. Molloy, and D. Somerford, *J. Appl. Phys.* **89**, 1108 (2001).

- [44] Q. Guo, T. Tanaka, M. Nishio, and H. Ogawa, *Jpn. J. Appl. Phys.* **42**, L141 (2003).
- [45] W. Terashima, S. -B. Che, Y. Ishitani, and A. Yoshikawa, *Jpn. J. Appl. Phys.* **45**, L539 (2006).
- [46] R. Goldhahn, P. Schley, A. T. Winzer, G. Gobsch, V. Cimalla, O. Ambacher, M. Rakel, C. Cobet, N. Esser, H. Lu, and W. J. Schaff, *Phys. Status Solidi A* **203**, 42 (2006).
- [47] K. Osamura, S. Naka, and Y. Murakami, *J. Appl. Phys.* **46**, 3432 (1975).
- [48] N. A. Sanford, A. Munkholm, M. R. Kramers, A. Shapiro, I. Levin, A. V. Davydov, S. Sayan, L. S. Wielunski, and T. E. Madey, *Phys. Status Solidi C* **2**, 2783 (2005).
- [49] T. Nagatomo, T. Kuboyama, H. Minamino, and O. Omoto, *Jpn. J. Appl. Phys.* **28**, L1334 (1989).
- [50] C. A. Parker, J. C. Roerts, S. M. Bedair, M. J. Reed, S. X. Liu, N. A. El-Masry, and L. H. Robins, *Appl. Phys. Lett.* **75**, 2566 (1999).
- [51] W. Walukiewicz, J. W. Ager III, K. M. Yu, Z. Liliental-Weber, J. Wu, S. X. Li, R. E. Jones, and J. D. Denlinger, *J. Phys. D: Appl. Phys.* **39**, R83 (2006).
- [52] J. Wagner, A. Ramakrishnan, D. Behr, H. Obloh, M. Kunzer, and K. -H. Bachem, *Appl. Phys. Lett.* **73**, 1715 (1998).
- [53] M. H. Lee, K. J. Kim, and E. Oh, *Solid State Commun.* **114**, 325 (2000).
- [54] V. J. Keast, A. J. Scott, M. J. Kappers, C. T. Foxon, and C. J. Humphreys, *Phys. Rev. B* **66**, 125319 (2002).
- [55] G. Lucovsky, R. D. Burnham, and A. S. Alimonda, *Phys. Rev. B* **14**, 2503 (1976).
- [56] A. Onton, M. R. Lorenz, J. M. Woodall, and R. J. Chicotka, *J. Cryst. Growth* **27**, 166 (1974).
- [57] P. Dias, V. A. Mishurnyi, E. L. Portnoi, B. S. Ryvkin, and V. B. Smirnitkii, *Sov. Tech. Phys. Lett.* **3**, 290 (1977).
- [58] J. M. Rodríguez and G. Armelles, *J. Appl. Phys.* **69**, 965 (1991).
- [59] S. G. Choi, Y. D. Kim, S. D. Yoo, D. E. Aspnes, D. H. Woo, and S. H. Kim, *J. Appl. Phys.* **87**, 1287 (2000).
- [60] G. Lucovsky, M. H. Brodsky, M. F. Chen, R. J. Chicotka, and A. T. Ward, *Phys. Rev. B* **4**, 1945 (1971).
- [61] E. Jahne, W. Pilz, M. Giehler, and L. Hildisch, *Phys. Status Solidi B* **91**, 155 (1979).
- [62] A. Hassine, J. Sapriel, P. L. Berre, P. Legay, F. Alexandre, and G. Post, *J. Appl. Phys.* **77**, 6569 (1995).
- [63] A. R. Goñi, K. Syassen, K. Strössner, and M. Cardona, *Phys. Rev. B* **39**, 3178 (1989).
- [64] H. Lee, D. Biswas, M. V. Klein, H. Morkoç, D. E. Aspnes, B. D. Choe, J. Kim, and C. O. Griffiths, *J. Appl. Phys.* **75**, 5040 (1994).
- [65] M. Schubert, V. Gottschalch, C. M. Herzinger, H. Yao, P. G. Snyder, and J. A. Woollam, *J. Appl. Phys.* **77**, 3416 (1995).
- [66] R. Ferrini, G. Zuizzetti, M. Patrini, A. Parisini, L. Tarricone, and B. Valenti, *Eur. Phys. J. B* **27**, 449 (2002).
- [67] D. H. Levi, J. F. Geisz, and B. Johs, *Proc. SPIE* **5530**, 326 (2004).
- [68] S. Adachi, *J. Appl. Phys.* **58**, R1 (1985).
- [69] D. E. Aspnes, S. M. Kelso, R. A. Logan, and R. Bhat, *J. Appl. Phys.* **60**, 754 (1986).
- [70] S. Adachi, *GaAs and Related Materials: Bulk Semiconducting and Superlattice Properties*. World Scientific, Singapore, 1994.
- [71] R. P. Seisyan, V. A. Kosobukin, S. A. Vaganov, M. A. Markosov, T. S. Shamirzaev, K. S. Zhuravlev, A. K. Bakarov, and A. I. Toropov, *Phys. Status Solidi C* **2**, 900 (2005).
- [72] R. G. Kaufman, G. R. Hulse, D. J. Vezzetti, A. L. Moretti, K. A. Stair, G. P. Devane, and T. E. Bird, *J. Appl. Phys.* **75**, 8053 (1994).
- [73] J. -H. Shin, and Y. -H. Lee, *J. Appl. Phys.* **76**, 8048 (1994).
- [74] R. J. Deri and M. A. Emanuel, *J. Appl. Phys.* **77**, 4667 (1995).
- [75] Y. Kokubo and I. Ohta, *J. Appl. Phys.* **81**, 2042 (1997).
- [76] S. Gehrsitz, F. K. Reinhart, C. Gourdon, N. Herres, A. Vonlanthen, and H. Sigg, *J. Appl. Phys.* **87**, 7825 (2000).

- [77] Z. G. Hu, M. B. M. Rinzan, S. G. Matsik, A. G. U. Perera, G. Von Winckel, A. Stintz, and S. Krishna, *J. Appl. Phys.* **97**, 093529 (2005).
- [78] C. H. Kuo, S. Anand, H. Fathollahnejad, R. Ramamurti, R. Droopad, and G. N. Maracas, *J. Vac. Sci. Technol. B* **13**, 681 (1995).
- [79] S. -J. Cho, and P. G. Snyder, *J. Vac. Sci. Technol. B* **17**, 2045 (1999).
- [80] É. Matyas, *Sov. Phys. Semicond.* **13**, 1194 (1979).
- [81] P. Roura, M. López-de Miguel A. Cornet, and J. R. Morante, *J. Appl. Phys.* **81**, 6916 (1997).
- [82] M. J. Mondry, D. I. Babic, J. E. Bowers, and L. A. Coldren, *IEEE Photon. Technol. Lett.* **4**, 627 (1992).
- [83] H. Asai and H. Iwamura, *Inst. Phys. Conf. Ser.* **145**, 985 (1996).
- [84] J. -H. Baek, B. Lee, S. W. Choi, J. H. Lee, and E. -H. Lee, *Appl. Phys. Lett.* **68**, 2355 (1996).
- [85] H. W. Dinges, H. Burkhard, R. Lösch, H. Nickel, and W. Schlapp, *Appl. Surf. Sci.* **54**, 477 (1992).
- [86] L. I. Kamlet, F. L. Terry, Jr., *Thin Solid Films* **313–314**, 177 (1998).
- [87] S. Adachi, *Physical Properties of III–V Semiconductor Compounds: InP, InAs, GaAs, GaP, InGaAs, and InGaAsP*, John Wiley & Sons, Ltd, New York, 1992.
- [88] G. Yu, N. L. Rowell, D. J. Lockwood, and P. J. Poole, *Appl. Phys. Lett.* **81**, 2175 (2002); erratum, *ibid.* **82**, 1136 (2003).
- [89] G. Yu, N. L. Rowell, D. J. Lockwood, and P. J. Poole, *Appl. Phys. Lett.* **86**, 221904 (2005).
- [90] D. J. Lockwood, G. Yu, N. L. Rowell, and P. J. Poole, *J. Appl. Phys.* **101**, 113524 (2007).
- [91] G. W. Charache, D. M. DePoy, J. E. Reynolds, P. F. Baldasaro, K. E. Miyano, T. Holden, F. H. Pollak, P. R. Sharps, M. L. Timmons, C. B. Geller, W. Mannstadt, R. Asahi, A. J. Freeman, and W. Wolf, *J. Appl. Phys.* **86**, 452 (1999).
- [92] T. Takagi, *Jpn. J. Appl. Phys.* **17**, 1813 (1978).
- [93] T. J. Kim, T. H. Ghong, Y. D. Kim, D. E. Aspnes, T. Mori, T. Yao, and B. H. Koo, *Phys. Rev. B* **68**, 115323 (2003).
- [94] T. J. Kim, T. H. Ghong, and Y. D. Kim, *J. Kor. Phys. Soc.* **44**, 726 (2004).
- [95] R. T. Carline, C. Pickering, N. S. Garawal, D. Lancefield, L. K. Howard, and M. T. Emeny, *Proc. SPIE* **1678**, 285 (1992).
- [96] V. A. Yakovlen, *Mater. Res. Soc. Symp. Proc.* **340**, 373 (1994).
- [97] L. C. Andreani, D. D. Nova, S. D. Lernia, M. Geddo, G. Guizzetti, M. Patrini, C. Bocchi, A. Bosacchi, C. Ferrari, and S. Franchi, *J. Appl. Phys.* **78**, 6745 (1995).
- [98] M. Geddo, G. Guizzetti, M. Patrini, T. Ciabattoni, L. Seravalli, P. Frigeri, and S. Franchi, *Appl. Phys. Lett.* **87**, 263120 (2005).
- [99] G. Lucovsky, K. Y. Cheng, and G. L. Pearson, *Phys. Rev. B* **12**, 4135 (1975).
- [100] N. Kitamura and T. Wada, *Mater. Lett.* **19**, 105 (1994).
- [101] R. Ferrini, M. Galli, G. Guizzetti, M. Patrini, A. Bosacchi, S. Franchi, and R. Magnanini, *Phys. Rev. B* **56**, 7549 (1997).
- [102] R. Ferrini, M. Patrini, and S. Franchi, *J. Appl. Phys.* **84**, 4517 (1998).
- [103] C. Ance and A. N. Van Mau, *J. Phys. C: Solid State Phys.* **9**, 1565 (1976).
- [104] A. Bignazzi, E. Grilli, M. Guzzi, C. Bocchi, A. Bosacchi, S. Franchi, and R. Magnanini, *Phys. Rev. B* **57**, 2295 (1998).
- [105] S. Dileria, M. Geddo, G. Guizzetti, M. Patrini, A. Bosacchi, S. Franchi, and R. Magnanini, *Mat. Res. Soc. Symp. Proc.* **406**, 389 (1996).
- [106] S. G. Choi, C. J. Palmstrem, Y. D. Kim, S. L. Cooper, and D. E. Aspnes, *J. Appl. Phys.* **98**, 104108 (2005).
- [107] M. H. Brodsky, G. Lucovsky, M. F. Chen, and T. S. Plaskett, *Phys. Rev. B* **2**, 3303 (1970).
- [108] Z. C. Feng, S. Perkowitz, R. Rousina, and J. B. Webb, *Can. J. Phys.* **69**, 386 (1991).
- [109] R. Rousina, C. Halpin, and J. B. Webb, *J. Appl. Phys.* **68**, 2181 (1990).
- [110] S. Imai and S. Adachi, *Jpn. J. Appl. Phys.* **32**, 3860 (1993).
- [111] G. Leibiger, V. Gottschalch, A. Kasic, and M. Schubert, *Appl. Phys. Lett.* **79**, 3407 (2001).

- [112] J. B. Wang, Z. F. Li, W. Lu, D. J. Chen, B. Shen, and Y. D. Zheng, *J. Vac. Sci. Technol. A* **22**, 1956 (2004).
- [113] G. Y. Rudko, I. A. Buyanova, W. M. Chen, H. P. Xin, and C. W. Tu, *Appl. Phys. Lett.* **81**, 3984 (2002).
- [114] I. A. Buyanova, M. Izadifard, A. Kasic, H. Arwin, W. M. Chen, H. P. Xin, Y. G. Hong, and C. W. Tu, *Phys. Rev. B* **70**, 085209 (2004).
- [115] B. Fluegel, Y. Zhang, J. F. Geisz, and A. Mascarenhas, *Phys. Rev. B* **72**, 073203 (2005).
- [116] G. Leibiger, V. Gottschalch, M. Schubert, G. Benndorf, and R. Schwabe, *Phys. Rev. B* **65**, 245207 (2002).
- [117] K. Uesugi and I. Suemune, *Jpn. J. Appl. Phys.* **36**, L1572 (1997).
- [118] R. Chtourou, F. Bousbih, S. B. Bouzid, F. F. Charfi, J. C. Harmand, G. Ungaro, and L. Largeau, *Appl. Phys. Lett.* **80**, 2075 (2002).
- [119] U. Tisch, E. Finkman, and J. Salzman, *Appl. Phys. Lett.* **81**, 463 (2002).
- [120] W. K. Hung, M. Y. Chern, Y. F. Chen, Z. L. Yang, and Y. S. Huang, *Phys. Rev. B* **62**, 13028 (2000).
- [121] J. Šik, M. Schubert, G. Leibiger, V. Gottschalch, and G. Wagner, *J. Appl. Phys.* **89**, 294 (2001).
- [122] G. Leibiger, V. Gottschalch, B. Rheinländer, J. Šik, and M. Schubert, *J. Appl. Phys.* **89**, 4927 (2001).
- [123] P. H. Jefferson, T. D. Veal, L. F. J. Piper, B. R. Bennett, C. F. McConville, B. N. Murdin, L. Buckie, G. W. Smith, and T. Ashley, *Appl. Phys. Lett.* **89**, 111921 (2006).
- [124] W. G. Bi and C. W. Yu, *J. Appl. Phys.* **80**, 1934 (1996).
- [125] W. K. Hung, K. S. Cho, M. Y. Chern, Y. F. Chen, D. K. Shih, H. H. Lin, C. C. Lu, and T. R. Yang, *Appl. Phys. Lett.* **80**, 796 (2002).
- [126] D. -K. Shih, H. -H. Lin, L. -W. Sung, T. -Y. Chu, and T. -R. Yang, *Jpn. J. Appl. Phys.* **42**, 375 (2003).
- [127] H. Shimomura, T. Anan, and S. Sugou, *J. Cryst. Growth* **162**, 121 (1996).
- [128] F. Saadallah, N. Yacoubi, F. Genty, and C. Alibert, *J. Appl. Phys.* **94**, 5041 (2003).
- [129] G. D. Clark, Jr., N. Holonyak, Jr., *Phys. Rev. B* **156**, 913 (1967).
- [130] H. C. Casey, Jr., *J. Appl. Phys.* **45**, 2766 (1974).
- [131] A. N. Pikhin, A. D. Yas'kov, *Sov. Phys. Semicond.* **14**, 389 (1980).
- [132] R. J. Nelson, N. Holonyak, Jr., and W. O. Groves, *Phys. Rev. B* **13**, 5415 (1976).
- [133] A. G. Thompson, J. C. Woolley, and M. Rubenstein, *Can. J. Phys.* **44**, 2927 (1966).
- [134] K. J. Kim, M. H. Lee, J. H. Bahng, K. Shim, and B. D. Choe, *J. Appl. Phys.* **84**, 3696 (1998).
- [135] G. Lucovsky and M. F. Chen, *Solid State Commun.* **8**, 1397 (1970).
- [136] M. Yano, Y. Suzuki, T. Ishii, Y. Matsushita, and M. Kimata, *Jpn. J. Appl. Phys.* **17**, 2091 (1978).
- [137] K. G. Merkel, V. M. Bright, M. A. Marciniak, C. L. A. Cerny, and M. O. Manasreh, *Appl. Phys. Lett.* **65**, 2442 (1994).
- [138] R. Lukic-Zrnica, B. P. Gorman, R. J. Cottier, T. D. Golding, C. L. Littler, and A. G. Norman, *J. Appl. Phys.* **92**, 6939 (2002).
- [139] N. N. Sirota and E. E. Matyas, *Phys. Status Solidi A* **4**, K143 (1971).
- [140] R. Ferrini, M. Geddo, G. Guizzetti, M. Patrini, S. Franchi, C. Bocchi, F. Germini, A. Baraldi, and R. Magnanini, *J. Appl. Phys.* **86**, 4706 (1999).
- [141] D. Serries, M. Peter, N. Herres, K. Winkler, and J. Wagner, *J. Appl. Phys.* **87**, 8522 (2000).
- [142] N. P. Kekelidze, G. P. Kekelidze, and Z. D. Makharadze, *J. Phys. Chem. Solids* **34**, 2117 (1973).
- [143] D. J. Lockwood, N. L. Rowell, and G. Yu, *J. Appl. Phys.* **102**, 033512 (2007).
- [144] I. V. Bodnar, A. I. Lukomskii, and G. F. Smirnova, *Phys. Status Solidi A* **37**, K173 (1976).
- [145] S. G. Choi, C. J. Palmström, Y. D. Kim, D. E. Aspnes, H. J. Kim, and Y. -C. Chang, *Appl. Phys. Lett.* **91**, 041917 (2007).
- [146] E. H. Reihlen, M. J. Jou, Z. M. Fang, and G. B. Stringfellow, *J. Appl. Phys.* **68**, 4604 (1990).
- [147] N. L. Rowell, D. J. Lockwood, G. Yu, Y. Z. Gao, X. Y. Gong, M. Aoyama, and T. Yamaguchi, *J. Vac. Sci. Technol. A* **22**, 935 (2004).
- [148] M. B. Thomas and J. C. Woolley, *Can. J. Phys.* **49**, 2052 (1971).
- [149] W. Dobbelaere, J. D. Boeck, and G. Borghs, *Appl. Phys. Lett.* **55**, 1856 (1989).

- [150] V. K. Dixit, B. Bansal, V. Venkataraman, H. L. Bhat, K. S. Chandrasekharan, and B. M. Arora, *J. Appl. Phys.* **96**, 4989 (2004).
- [151] M. A. Marciniak, R. L. Hengehold, Y. K. Yeo, and G. W. Turner, *J. Appl. Phys.* **84**, 480 (1998).
- [152] G. B. Stringfellow and P. E. Greene, *J. Electrochem. Soc.* **118**, 805 (1971).
- [153] H. Y. Deng and N. Dai, *Phys. Rev. B* **73**, 113102 (2006).
- [154] Y. Z. Gao, X. Y. Gong, and T. Yamaguchi, *Jpn. J. Appl. Phys.* **45**, 5732 (2006).
- [155] T. Imanishi, A. Wakahara, S. M. Kim, H. Yonezu, and Y. Furukawa, *Phys. Status Solidi A* **202**, 854 (2005).
- [156] G. Leibiger, V. Gottschalch, and M. Schubert, *J. Appl. Phys.* **90**, 5951 (2001).
- [157] C. Skierbiszewski, *Semicond. Sci. Technol.* **17**, 803 (2002).
- [158] T. Kitatani, M. Kondow, K. Shinoda, Y. Yazawa, and M. Okai, *Jpn. J. Appl. Phys.* **37**, 753 (1998).
- [159] P. N. Sen and G. Lucovsky, *Phys. Rev. B* **12**, 2998 (1975).
- [160] V. V. Kuznetsov, V. N. Razbegaev, S. Él-Giziri, *Sov. Phys. Semicond.* **23**, 552 (1989).
- [161] A. Mezerreg, C. Llinares, J. L. Lazzari, and A. Montaner, *Thin Solid Films* **221**, 196 (1992).
- [162] C. Alibert, M. Skouri, A. Joullie, M. Benouna, and S. Sadiq, *J. Appl. Phys.* **69**, 3208 (1991).
- [163] O. Blum, I. J. Fritz, L. R. Dawson, and T. J. Drummond, *Electron. Lett.* **31**, 1247 (1995).
- [164] P. Swarup, R. K. Jain, S. N. Verma, S. Charan, h. and D. M. Tandle, *Phys. Status Solidi A* **65**, K183 (1981).
- [165] F. Fiedler and A. Schlachetzki, *Solid-State Electron.* **30**, 73 (1987).
- [166] S. M. Kelso, D. E. Aspnes, M. A. Pollack, and R. E. Nahory, *Phys. Rev. B* **26**, 6669 (1982).
- [167] S. G. Wallace, B. J. Robinson, P. Mascher, H. K. Haugen, D. A. Thompson, D. Dalacu, and L. Martinu, *Appl. Phys. Lett.* **76**, 2791 (2000).
- [168] C. Pickering, *J. Electron. Mater.* **15**, 51 (1986).
- [169] W. G. Bi, A. Z. Li, and S. S. Tan, *Mat. Res. Soc. Symp. Proc.* **216**, 213 (1991).
- [170] S. Adachi, *J. Appl. Phys.* **61**, 4869 (1987).
- [171] M. S. S. Lournal, M. B. Z. Morosini, J. L. Herrera-Pérez, A. A. G. Von Zuben, A. C. F. da Silveir, and N. B. Patel, *Electron. Lett.* **29**, 1240 (1993).
- [172] T. Hofmann, G. Leibiger, V. Gottschalch, I. Pietzonka, and M. Schubert, *Phys. Rev. B* **64**, 155206 (2001).
- [173] S. Adachi, H. Kato, A. Moki, and K. Ohtsuka, *J. Appl. Phys.* **75**, 478 (1994).
- [174] H. Tanaka, Y. Kawamura, and H. Asahi, *J. Appl. Phys.* **59**, 985 (1986).
- [175] S. Ozaki, S. Adachi, M. Sato, and K. Ohtsuka, *J. Appl. Phys.* **79**, 439 (1996).
- [176] M. Schubert, J. A. Woollam, G. Leibiger, B. Rheinländer, I. Pietzonka, T. Saß, and V. Gottschalch, *J. Appl. Phys.* **86**, 2025 (1999).
- [177] K. Masu, T. Mishima, S. Hiroi, M. Konagai, and K. Takahashi, *J. Appl. Phys.* **53**, 7558 (1982).
- [178] P. Swarup, R. K. Jain, S. N. Verma, S. Charan, and D. M. Tandle, *Phys. Status Solidi A* **72**, K189 (1982).
- [179] H. W. Dinges, H. Burkhard, R. Lösch, H. Nickel, and W. Schlapp, *Mater. Sci. Eng. B* **21**, 174 (1993).
- [180] A. G. Belov, G. M. Zinger, M. A. Il'in, Yu. N. Korchagin, E. P. Rashevskaya, and A. I. Ryskin, *Sov. Phys. Solid State* **22**, 839 (1980).
- [181] N. P. Esina, N. V. Zotova, B. A. Matveev, L. D. Neulmina, N. M. Stus', and G. N. Talalakin, *Sov. Phys. Semicond.* **15**, 1372 (1981).
- [182] Y. R. Ryu, T. S. Lee, J. A. Lubguban, A. B. Corman, H. W. White, J. H. Leem, M. S. Han, Y. S. Park, C. J. Youn, and W. J. Kim, *Appl. Phys. Lett.* **88**, 052103 (2006).
- [183] M. S. Han, J. H. Kim, T. S. Jeong, J. M. Park, C. J. Youn, J. H. Leem, and Y. R. Ryu, *J. Cryst. Growth* **303**, 506 (2007).
- [184] J. Chen and W. Z. Shen, *Appl. Phys. Lett.* **83**, 2154 (2003).
- [185] C. Bundesmann, A. Rahm, M. Lorenz, M. Grundmann, and M. Schubert, *J. Appl. Phys.* **99**, 113504 (2006).
- [186] R. Schmidt, B. Rheinländer, M. Shubert, D. Spemann, T. Butz, J. Lenzner, E. M. Kaidashev, M. Lorenz, A. Rahm, H. C. Semmelhack, and M. Grundmann, *Appl. Phys. Lett.* **82**, 2260 (2003).

- [187] C. W. Teng, J. F. Muth, Ü. Özgür, M. J. Bergmann, H. O. Everitt, A. K. Sharma, C. Jin, and J. Narayan, *Appl. Phys. Lett.* **76**, 979 (2000).
- [188] R. Schmidt-Grund, A. Carstens, B. Rheinländer, D. Spemann, H. Hochmut, G. Zimmermann, M. Lorenz, M. Grundmann, C. M. Herzinger, and M. Schubert, *J. Appl. Phys.* **99**, 123701 (2006).
- [189] P. Yu, H. Wu, N. Chen, T. Xu, Y. Lao, and J. Liang, *Opt. Mater.* **28**, 271 (2006).
- [190] H. P. Zhou, W. Z. Shen, N. B. Chen, and H. Z. Wu, *Appl. Phys. Lett.* **85**, 3723 (2004).
- [191] J. A. Sans and A. Segura, *High Pressure Res.* **24**, 119 (2004).
- [192] J. H. Kang, Y. R. Park, and K. J. Kim, *Solid State Commun.* **115**, 127 (2000).
- [193] R. Schmidt-Grund, M. Schubert, B. Rheinländer, D. Fritsch, H. Schmidt, E. M. Kaidashev, M. Lorenz, C. M. Herzinger, and M. Grundmann, *Thin Solid Films* **455–456**, 500 (2004).
- [194] T. D. Kang, H. Lee, W. -I. Park, and G. -C. Yi, *Thin Solid Films* **455–456**, 609 (2004).
- [195] H. Tampo, H. Shibata, K. Maejima, A. Yamada, K. Matsubara, P. Fons, S. Niki, T. Tainaka, C. Chiba, and H. Kanie, *Appl. Phys. Lett.* **91**, 261907 (2007).
- [196] T. Makino, Y. Segawa, M. Kawasaki, A. Ohtomo, R. Shiroki, K. Tamura, T. Yasuda, and H. Koinuma, *Appl. Phys. Lett.* **78**, 1237 (2001).
- [197] S. Y. Lee, Y. Li, J. -S. Lee, J. K. Lee, M. Nastasi, S. A. Crooker, Q. X. Jia, H. -S. Kang, and J. -S. Kang, *Appl. Phys. Lett.* **85**, 218 (2004).
- [198] J. Ishihara, A. Nakamura, S. Shigemori, T. Aoki, and J. Temmyo, *Appl. Surf. Sci.* **244**, 381 (2005).
- [199] X. J. Wang, I. A. Buyanova, W. M. Chen, M. Izadifard, S. Rawal, D. P. Norton, S. J. Pearton, A. Osinsky, J. W. Dong, and A. Dabiran, *Appl. Phys. Lett.* **89**, 151909 (2006).
- [200] H. C. Ong and J. Y. Dai, *Appl. Phys. Lett.* **81**, 1444 (2002).
- [201] M. P. Lisitsa, M. Y. Valakh, and N. K. Konovets, *Phys. Status Solidi* **34**, 269 (1969).
- [202] P. Chen, J. E. Nicholls, M. O'Neill, J. H. C. Hogg, B. Lunn, D. E. Ashenford, M. Fay, and A. G. Cullis, *Semicond. Sci. Technol.* **13**, 1439 (1998).
- [203] M. R. Muhamad, *Jpn. J. Appl. Phys.* **32**, 3385 (1993).
- [204] A. Béliveau and C. Carlone, *Phys. Rev. B* **41**, 9860 (1990).
- [205] F. C. Peiris, U. Bindley, J. K. Furdyna, H. Kim, A. K. Ramdas, and M. Grimsditch, *Appl. Phys. Lett.* **79**, 473 (2001).
- [206] K. Wilmers, T. Wethkamp, N. Esser, C. Cobet, W. Richter, V. Wagner, H. Lugauer, F. Fischer, T. Gerhard, M. Keim, and M. Cardona, *J. Electron. Mater.* **28**, 670 (1999).
- [207] H. Lee, I. -Y. Kim, J. Powell, D. E. Aspnes, S. Lee, F. Peiris, and J. K. Furdyna, *J. Appl. Phys.* **88**, 878 (2000).
- [208] A. Bukaluk, A. A. Wronkowska, A. Wronkowski, H. Arwin, F. Firszt, S. Łęgowski, H. Męczyńska, and J. Szatkowski, *Appl. Surf. Sci.* **175–176**, 531 (2001).
- [209] A. A. Wronkowska, A. Wronkowski, F. Firszt, S. Łęgowski, H. Męczyńska, A. Marasek, and W. Paszkowicz, *Phys. Status Solidi C* **1**, 641 (2004).
- [210] F. Firszt, A. A. Wronkowska, A. Wronkowski, S. Łęgowski, A. Marasek, H. Męczyńska, M. Pawlak, W. Paszkowicz, K. Strzałkowski, and A. J. Zakrzewski, *Cryst. Res. Technol.* **40**, 386 (2005).
- [211] F. C. Peiris, S. Lee, U. Bindley, and J. K. Furdyna, *J. Appl. Phys.* **86**, 918 (1999).
- [212] B. Derkowska, B. Sahraoui, X. N. Phu, G. Glowacki, and W. Bala, *Opt. Mater.* **15**, 199 (2000).
- [213] S. Adachi, *Handbook on Physical Properties of Semiconductors: Volume 3 II–VI Compound Semiconductors*, Kluwer Academic, Boston, 2004.
- [214] M. Wörz, E. Griehl, T. Reisinger, R. Flierl, B. Haserer, T. Semmler, T. Frey, and W. Gebhardt, *Phys. Status Solidi B* **202**, 805 (1997).
- [215] K. J. Kim, M. H. Lee, J. H. Bahng, C. Y. Kwak, and E. Oh, *Solid State Commun.* **105**, 17 (1998).
- [216] D. -H. Shin, C. -D. Kim, H. -H. Jang, S. -H. Choe, D. -T. Kim, C. -S. Yoon, and W. -T. Kim, *J. Cryst. Growth* **177**, 167 (1997).
- [217] A. A. Wronkowska, A. Wronkowski, H. Arwin, F. Firszt, S. Łęgowski, H. Męczyńska, and J. Szatkowski, *Vacuum* **63**, 233 (2001).
- [218] F. C. Peiris, S. Lee, U. Bindley, and J. K. Furdyna, *J. Appl. Phys.* **84**, 5194 (1998).

- [219] M. Illing, G. Bacher, A. Forchel, D. Hommel, B. Jobst, and G. Landwehr, *Appl. Phys. Lett.* **67**, 1 (1995).
- [220] Y. D. Kim, M. V. Klein, S. F. Ren, Y. C. Chang, H. Luo, N. Samarth, and J. K. Furdyna, *Phys. Rev. B* **49**, 7262 (1994).
- [221] J. C. Jans, J. Petruzzello, J. M. Gaines, and D. J. Olego, *Proc. SPIE* **1985**, 260 (1993).
- [222] J. Lee, F. Flack, N. Samarth, and R. W. Collins, *Appl. Opt.* **36**, 5372 (1997).
- [223] T. Holden, P. Ram, F. H. Pollak, and J. L. Freeouf, *Phys. Rev. B* **56**, 4037 (1997).
- [224] K. Suzuki and S. Adachi, *J. Appl. Phys.* **83**, 1018 (1998).
- [225] K. Kumazaki, N. Nishiguchi, and M. Cardona, *Solid State Commun.* **58**, 425 (1986).
- [226] C. J. Summers and J. G. Broerman, *Phys. Rev. B* **21**, 559 (1980).
- [227] P. S. Kireev and V. V. Volkov, *Sov. Phys. Semicond.* **7**, 949 (1974).
- [228] N. Himei and J. Muto, *J. Mater. Sci.: Mater. Electron.* **11**, 145 (2000).
- [229] V. B. Pujari, S. H. Mane, V. S. Karande, J. S. Dargad, and L. P. Deshmukh, *Mater. Chem. Phys.* **83**, 10 (2004).
- [230] I. N. Borisov, P. S. Kireev, V. V. Mikhailin, and V. M. Bezborodova, *Sov. Phys. Semicond.* **5**, 734 (1971).
- [231] K. Kumazaki, L. Viña, C. Umbach, and M. Cardona, *Phys. Status Solidi B* **156**, 371 (1989).
- [232] O. Maksimov and M. C. Tamargo, *Appl. Phys. Lett.* **79**, 782 (2001).
- [233] M. R. Buckley, F. C. Peiris, O. Maksimov, M. Muñoz, and M. C. Tamargo, *Appl. Phys. Lett.* **81**, 5156 (2002).
- [234] M. Muñoz, O. Maksimov, M. C. Tamargo, M. R. Buckley, and F. C. Peiris, *Phys. Status Solidi C* **1**, 706 (2004).
- [235] J. S. de Almeida, and R. Ahuja, *Appl. Phys. Lett.* **89**, 061913 (2006).
- [236] X. Liu, U. Bindley, Y. Sasaki, and J. K. Furdyna, *J. Appl. Phys.* **91**, 2859 (2002).
- [237] S. -J. Chung, Y. Kwon, C. -S. Yoon, B. -H. Kim, D. Cha, C. -D. Kim, W. -T. Kim, and C. U. Hong, *J. Phys. Chem. Solids* **60**, 799 (1999).
- [238] A. J. Franz, F. C. Peiris, X. Liu, U. Bindley, and J. K. Furdyna, *Phys. Status Solidi B* **241**, 507 (2004).
- [239] S. Nakamura, T. Fukumoto, A. Mitsuishi, and K. Itoh, *J. Phys. Soc. Jpn* **35**, 1437 (1973).
- [240] R. André and L. S. Dang, *J. Appl. Phys.* **82**, 5086 (1997).
- [241] H. -J. Lugauer, F. Fischer, T. Litz, A. Waag, D. Hommel, and G. Landwehr, *Semicond. Sci. Technol.* **9**, 1567 (1994).
- [242] M. Luttmann, F. Bertin, and A. Chabli, *J. Appl. Phys.* **78**, 3387 (1995).
- [243] S. G. Choi, Y. D. Kim, S. D. Yoo, D. E. Aspnes, I. Miotkowski, and A. K. Ramdas, *Appl. Phys. Lett.* **71**, 249 (1997).
- [244] Y. S. Ihn, T. J. Kim, T. H. Ghong, Y. D. Kim, D. E. Aspnes, and J. Kossut, *Thin Solid Films* **455–456**, 222 (2004).
- [245] H. Harada and S. Narita, *J. Phys. Soc. Jpn* **30**, 1628 (1971).
- [246] L. K. Vodop'yanov, E. A. Vinogradov, A. M. Blinov, and V. A. Rukavishnikov, *Sov. Phys. Solid State* **14**, 219 (1972).
- [247] S. Perkowitz, L. S. Kim, and Z. C. Feng, *Phys. Rev. B* **42**, 1455 (1990).
- [248] D. N. Talwar, Z. C. Feng, and P. Becla, *Phys. Rev. B* **48**, 17064 (1993).
- [249] S. Adachi and T. Kimura, *Jpn. J. Appl. Phys.* **32**, 3866 (1993).
- [250] A. Ebina, K. Saito, and T. Takahashi, *J. Appl. Phys.* **44**, 3659 (1973).
- [251] A. J. Syllaios, P. -K. Liao, B. J. Greene, H. F. Schaake, H. -Y. Liu, and G. Westphal, *J. Electron. Mater.* **26**, 567 (1997).
- [252] D. Ohlmann, M. Mazilu, R. Levy, and B. Hönerlage, *J. Appl. Phys.* **82**, 1355 (1997).
- [253] A. Kisiel, *Acta Phys. Polon. A* **38**, 691 (1970).
- [254] K. Saito, A. Ebina, and T. Takahashi, *Solid State Commun.* **11**, 841 (1972).
- [255] S. G. Kroitoru, O. G. Maksimova, and V. V. Sobolev, *Sov. Phys. Semicond.* **9**, 1191 (1976).
- [256] V. V. Sovolev, O. G. Maksimova, and S. G. Kroitoru, *Phys. Status Solidi B* **103**, 499 (1981).

- [257] S. Adachi and T. Kimura, *Jpn. J. Appl. Phys.* **32**, 3496 (1993).
- [258] O. Castaing, R. Granger, J. T. Benhlal, and R. Triboulet, *J. Phys.: Condens. Matter* **8**, 5757 (1996).
- [259] E. M. Larramendi, E. Purón, and O. de Melo, *Semicond. Sci. Technol.* **17**, 8 (2002).
- [260] P. D. Paulson, B. E. McCandless, and R. W. Birkmire, *J. Appl. Phys.* **95**, 3010 (2004).
- [261] G. L. Bastard, R. Granger, S. Rolland, Y. Marqueton, and R. Triboulet, *J. Phys. (France)* **50**, 3223 (1989).
- [262] M. P. Volz, F. R. Szofran, S. L. Lehoczky, and C. -H. Su, *Solid State Commun.* **75**, 943 (1990).
- [263] D. Bagot, R. Granger, and S. Rolland, *Phys. Status Solidi B* **183**, 395 (1994).
- [264] C. -H. Wu, D. -Y. Chu, C. -Y. Sun, and T. -R. Yang, *Jpn. J. Appl. Phys.* **34**, 4687 (1995).
- [265] B. Toulouse, R. Granger, S. Rolland, and R. Triboulet, *J. Phys. (France)* **48**, 247 (1987).
- [266] F. El-Akkad, and A. R. Farhan, *J. Phys. D: Appl. Phys.* **28**, 1958 (1995).
- [267] O. Castaing, J. T. Benhlal, R. Granger, and R. Triboulet, *J. Phys. I (France)* **6**, 907 (1996).
- [268] J. Baars and F. Sorger, *Solid State Commun.* **10**, 875 (1972).
- [269] D. N. Talwar and M. Vandevyver, *J. Appl. Phys.* **56**, 1601 (1984).
- [270] S. P. Kozyrev, V. N. Pyrkov, L. K. Vodop'yanov, *Sov. Phys. Solid State* **34**, 1984 (1992).
- [271] S. P. Kozyrev, L. K. Vodopyanov, and R. Triboulet, *Phys. Rev. B* **58**, 1374 (1998).
- [272] M. W. Scott, *J. Appl. Phys.* **40**, 4077 (1969).
- [273] E. Finkman and Y. Nemirovsky, *J. Appl. Phys.* **50**, 4356 (1979).
- [274] L. D. Saginov, V. P. Ponomarenko, V. A. Fedirko, and V. I. Stafeev, *Sov. Phys. Semicond.* **16**, 298 (1982).
- [275] E. Finkman and S. E. Schacham, *J. Appl. Phys.* **56**, 2896 (1984).
- [276] J. Chu, Z. Mi, and D. Tang, *J. Appl. Phys.* **71**, 3955 (1992).
- [277] B. Li, J. H. Chu, Y. Chang, Y. S. Gui, and D. Y. Tang, *Infrared Phys. Technol.* **37**, 525 (1996).
- [278] V. Nathan, *J. Appl. Phys.* **83**, 2812 (1998).
- [279] J. Chu, B. Li, and D. Tang, *J. Appl. Phys.* **75**, 1234 (1994).
- [280] Z. Kučera, *Phys. Status Solidi A* **100**, 659 (1987).
- [281] K. Liu, J. H. Chu, and D. Y. Tang, *J. Appl. Phys.* **75**, 4176 (1994).
- [282] R. R. Gałazka and A. Kisiel, *Phys. Status Solidi* **34**, 63 (1969).
- [283] A. Rodzik and A. Kisiel, *J. Phys. C: Solid State Phys.* **16**, 203 (1983).
- [284] L. Viña, C. Umbach, M. Cardona, and L. Vodopyanov, *Phys. Rev. B* **29**, 6752 (1984).
- [285] H. Arwin and D. E. Aspnes, *J. Vac. Sci. Technol. A* **2**, 1316 (1984).
- [286] C. C. Kim and S. Sivananthan, *J. Electron. Mater.* **26**, 561 (1997).
- [287] B. Johs, C. M. Herzinger, J. H. Dinan, A. Cornfeld, and J. D. Benson, *Thin Solid Films* **313–314**, 137 (1998).
- [288] B. K. Meyer, A. Polity, B. Farangis, Y. He, D. Hasselkamp, T. Krämer, and C. Wang, *Appl. Phys. Lett.* **85**, 4929 (2004).
- [289] O. Brafman, I. F. Chang, G. Lengyel, S. S. Mitra, E. Carnall, Jr., *Phys. Rev. Lett.* **19**, 1120 (1967).
- [290] D. Schmeltzer, R. Beserman, and D. Slamovits, *Phys. Rev. B* **22**, 4038 (1980).
- [291] M. Ambrico, D. Smaldone, C. Spezzacatena, V. Stagno, G. Perna, and V. Capozzi, *Semicond. Sci. Technol.* **13**, 1446 (1998).
- [292] S. Ozaki and S. Adachi, *J. Appl. Phys.* **75**, 7470 (1994).
- [293] W. Gebhard, G. Schötz, in *Properties of Wide Bandgap II–VI Semiconductors*, EMIS Datareviews Series No. 17 (edited by R. Bhargava), INSPEC (IEE), London, 1997, p. 113.
- [294] E. Griebel, G. F. Schötz, C. Birzer, W. Kerner, T. Reisinger, B. Hahn, and W. Gebhardt, *Acta Phys. Polon. A* **88**, 995 (1995).
- [295] A. Ebina, E. Fukunaga, and T. Takahashi, *Phys. Rev. B* **10**, 2495 (1974).
- [296] W. Walukiewicz, W. Shan, K. M. Yu, J. W. Ager III, E. E. Haller, I. Miotkowski, M. J. Seong, H. Alawadhi, and A. K. Ramdas, *Phys. Rev. Lett.* **85**, 1552 (2000).
- [297] C. Y. Bang, M. S. Lee, T. J. Kim, Y. D. Kim, D. E. Aspnes, Y. M. Yu, B. O, and Y. D. Choi, *J. Kor. Phys. Soc.* **39**, 462 (2001).
- [298] V. M. Burlakov, A. P. Litvinchuk, and V. N. Pyrkov, *Sov. Phys. Solid State* **27**, 131 (1985).

- [299] T. R. Yang and C. C. Lu, *Physica B* **284–288**, 1187 (2000).
- [300] F. C. Peiris, U. Bindley, and J. K. Furdyna, *J. Electron. Mater.* **30**, 677 (2001).
- [301] S. Ozaki and S. Adachi, *Jpn. J. Appl. Phys.* **32**, 2620 (1993).
- [302] J. Wu, W. Walukiewicz, K. M. Yu, W. Shan, J. W. Ager III, E. E. Haller, I. Miotkowski, A. K. Ramdas, and C. -H. Su, *Phys. Rev. B* **68**, 033206 (2003).
- [303] A. Ebina, M. Yamamoto, and T. Takahashi, *Phys. Rev. B* **6**, 3786 (1972).
- [304] J. F. Parrish, C. H. Perry, O. Brafman, I. F. Chang and S. S. Mitra, in *II–VI Semiconducting Compounds* (edited by D. G. Thomas), Benjamin, New York, 1967, p. 1164.
- [305] H. W. Verleur and A. S. Barker, Jr., *Phys. Rev.* **155**, 750 (1967).
- [306] R. Beserman and M. Balkanski, *Phys. Rev. B* **1**, 608 (1970).
- [307] R. Beserman, *Solid State Commun.* **23**, 323 (1977).
- [308] M. P. Lisitsa, L. F. Gudymenko, V. N. Malinko, and S. F. Terekhova, *Phys. Status Solidi* **31**, 389 (1969).
- [309] E. C. Fox, E. J. Canto-Said, and H. M. van Driel, *Appl. Phys. Lett.* **59**, 1878 (1991).
- [310] G. Perna, S. Pagliara, V. Capozzi, M. Ambrico, and T. Ligonzo, *Thin Solid Films* **349**, 220 (1999).
- [311] M. S. Brodin, M. V. Kurik, and S. P. Yurtsenyuk, *Sov. Phys. Solid State* **7**, 2516 (1966).
- [312] R. L. Hengehold and C. R. Fraime, *Phys. Rev.* **174**, 808 (1968).
- [313] Y. A. Mityagin, V. G. Plotnichenko, L. K. Vodop'yanov, and L. D. Budennaya, *Sov. Phys. Solid State* **19**, 1811 (1977).
- [314] K. Ohata, J. Saraie, and T. Tanaka, *Jpn. J. Appl. Phys.* **12**, 1641 (1973).
- [315] D. A. Wood, D. W. Lane, K. D. Rogers, and J. A. Coath, *J. Electron. Mater.* **28**, 1403 (1999).
- [316] K. Wei, F. H. Pollak, J. L. Freeouf, D. Shvydka, and A. D. Compaan, *J. Appl. Phys.* **85**, 7418 (1999).
- [317] E. A. Vinogradov, L. K. Vodop'yanov, and G. S. Oleinik, *Sov. Phys. Solid State* **15**, 322 (1973).
- [318] M. Górska and W. Nazarewicz, *Phys. Status Solidi B* **65**, 193 (1974).
- [319] Z. C. Feng, P. Becla, L. S. Kim, S. Perkowitz, Y. P. Feng, H. C. Poon, K. P. Williams, and G. D. Pitt, *J. Cryst. Growth* **138**, 239 (1994).
- [320] M. Neumann-Spallart, E. Galun, G. Hodes, C. Lévy-Clément, Y. Marfaing, E. Muranevich, and R. Tenne, *J. Appl. Phys.* **73**, 7753 (1993).
- [321] S. Cohen, R. Weil, and E. Muranevich, *J. Appl. Phys.* **76**, 593 (1994).
- [322] M. M. El-Nahass, A. A. M. Farag, and H. E. A. El-Sayed, *Appl. Phys. A* **77**, 819 (2003).
- [323] H. Okuyama, K. Nakano, T. Miyazima, and K. Akimoto, *Jpn. J. Appl. Phys.* **30**, L1620 (1991).
- [324] M. Ukita, H. Okuyama, M. Ozawa, A. Ishibashi, K. Akimoto, and Y. Mori, *Appl. Phys. Lett.* **63**, 2082 (1993).
- [325] U. Lunz, B. Jobst, S. Einfeldt, C. R. Becker, D. Hommel, and G. Landwehr, *J. Appl. Phys.* **77**, 5377 (1995).
- [326] U. Lunz, C. Schumacher, J. Nürnberger, K. Schüll, A. Gerhard, U. Schüssler, B. Jobst, W. Faschinger, and G. Landwehr, *Semicond. Sci. Technol.* **12**, 970 (1997).
- [327] K. Naniwae, H. Iwata, and K. Yashiki, *Appl. Phys. Lett.* **74**, 3984 (1999).
- [328] J. Wu, W. Walukiewicz, K. M. Yu, J. W. Ager III, W. Shan, E. E. Haller, I. Miotkowski, A. K. Ramdas, and S. Miotkowska, *Appl. Phys. Lett.* **80**, 34 (2002).
- [329] Y. Niiyama and M. Watanabe, *Semicond. Sci. Technol.* **20**, 1187 (2005).
- [330] V. Wagner, A. Fleszar, J. Geurts, G. Reuser, M. Keim, A. Waag, G. Landwehr, K. Wilmers, N. Esser, and W. Richter, *J. Cryst. Growth* **214/215**, 340 (2000).
- [331] A. A. Wronkowska, F. Firszt, H. Arwin, A. Wronkowski, M. Wakula, K. Strzalkowski, and W. Paszkowicz, *Phys. Status Solidi C* **3**, 1193 (2006).
- [332] T. Morita, H. Shinbo, H. Shinbo, T. Nagano, I. Nomura, A. Kikuchi, and K. Kishino, *J. Appl. Phys.* **81**, 7575 (1997).
- [333] S. P. Guo, O. Maksimov, M. C. Tamargo, F. C. Peiris, and J. K. Furdyna, *Appl. Phys. Lett.* **77**, 4107 (2000).
- [334] F. C. Peiris, J. K. Furdyna, S. P. Guo, and M. C. Tamargo, *J. Appl. Phys.* **89**, 3748 (2001).

11 Elasto-optic, Electro-optic and Nonlinear Optical Properties

11.1 ELASTO-OPTIC EFFECT

11.1.1 Group-IV Semiconductor Alloy

Data relating to elasto-optic behavior plays an important role not only in the design of elasto-optic devices, such as light modulators, deflectors and switches, but also in the analysis of lattice-mismatched semiconductor heterostructures. Photoelasticity is dependent on wavelength [1–4]. The photoelastic coefficient in 6H-SiC has been measured by Geidur [5]. Since the fundamental absorption edge of 6H-SiC is an indirect band gap, its contribution to the photoelasticity is negligibly small. Neither theoretical nor experimental studies relating to photoelasticity have been carried out on any group-IV semiconductor alloy.

11.1.2 III–V Semiconductor Alloy

A method for calculating the photoelastic coefficients in III–V semiconductors has been described by Adachi and Oe [6]. This model was applied to $\text{Al}_x\text{Ga}_{1-x}\text{As}$ and $\text{Ga}_x\text{In}_{1-x}\text{P}_y\text{As}_{1-y}/\text{InP}$. The photoelastic coefficient α_{pe} for $\text{Al}_x\text{Ga}_{1-x}\text{As}$ under $X||[100]$ stress has been reproduced in Figure 11.1. The black and gray circles correspond to the experimental data for GaAs ($x = 0$) and $\text{Al}_{0.5}\text{Ga}_{0.5}\text{As}$, respectively. The definition of α_{pe} can be found in Adachi [1].

More recently, Kikkarin *et al.* [7] have calculated the spectral dependence of the photoelastic constants, p_{11} , p_{12} and p_{44} , for $\text{Al}_x\text{Ga}_{1-x}\text{As}$ with x up to 0.3. They also discussed the acousto-optic interaction in $\text{Al}_x\text{Ga}_{1-x}\text{As}/\text{GaAs}$ waveguides.

11.1.3 II–VI Semiconductor Alloy

The photoelastic constants p_{ij} can be determined from the Brillouin scattering cross-sections [1]. Ziobrowski *et al.* [8] used Brillouin scattering on $\text{Be}_x\text{Zn}_{1-x}\text{Se}$ and obtained p_{ij} at $\lambda = 488 \text{ nm}$ ($0 \leq x \leq 0.25$). Adachi and Hamaguchi [9] carried out resonant Brillouin scattering measurements on $\text{Zn}_x\text{Cd}_{1-x}\text{Te}$ and obtained the spectral dependence of p_{44} for $x = 0.65$ and 0.80. The data suggest that the sign for p_{44} in $\text{Zn}_x\text{Cd}_{1-x}\text{Te}$ is negative in the region remote from the E_0 edge and becomes positive when the wavelength approaches the band edge, as in ZnTe and CdTe [4].

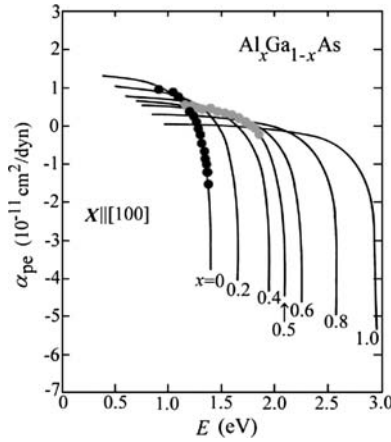


Figure 11.1 Photoelastic coefficient α_{pe} for $\text{Al}_x\text{Ga}_{1-x}\text{As}$ with increments in x of 0.2. The black and gray circles correspond to the experimental data for GaAs ($x = 0$) and $\text{Al}_{0.5}\text{Ga}_{0.5}\text{As}$, respectively. [Reprinted with permission from S. Adachi and K. Oe, *J. Appl. Phys.* **54**, 6620 (1983). Copyright (1983), American Institute of Physics]

11.2 LINEAR ELECTRO-OPTIC CONSTANT

11.2.1 Group-IV Semiconductor Alloy

Principally, the diamond lattice shows no linear electro-optic effect [1]. The linear electro-optic constant r_{41} for 3C-SiC has been reported to be $-2.7 \pm 0.5 \text{ pm/V}$ at $\lambda = 632.8 \text{ nm}$ [10]. There is an ordered alloy phase in $\text{Si}_x\text{Ge}_{1-x}$ (Section 1.3.2) and this phase will exhibit a linear electro-optic effect [11], but no data are available at present.

11.2.2 III–V Semiconductor Alloy

The linear electro-optic effect in $\text{Al}_x\text{Ga}_{1-x}\text{As}$ has been studied by Glick *et al.* [12]. They measured the electro-optic phase difference in an $\text{Al}_{0.17}\text{Ga}_{0.83}\text{As}$ waveguide and determined r_{41} at $\lambda = 1.1523 \mu\text{m}$, as shown in Table 11.1.

Bach *et al.* [13] have measured r_{41} for $\text{Ga}_x\text{In}_{1-x}\text{P}_y\text{As}_{1-y}/\text{InP}$ ($y = 0.20$ and 0.34). The values they obtained are summarized in Table 11.1. Figure 11.2 also shows the theoretical r_{41} dispersion obtained by Adachi and Oe [14], together with the data produced by Bach *et al.* ($y = 0.34$) [13]. It can be seen that the theoretical r_{41} curve shows strong dispersion near E_0 ($\lambda \sim 1.1 \mu\text{m}$). This curve was obtained from an electric-field-induced modulation of the electronic energy-band structure.

11.2.3 II–VI Semiconductor Alloy

The linear electro-optic constant r_{41} at $\lambda = 1.5 \mu\text{m}$ of Bridgman-grown $\text{Zn}_{0.1}\text{Cd}_{0.9}\text{Te}$ has been measured by Zappettini *et al.* [15] (see Table 11.1). The implementation of a $\text{Zn}_{0.1}\text{Cd}_{0.9}\text{Te}$ -based electro-optic switch which reaches -30 dB of extinction ratio and sub millisecond response time has also been presented by the same authors.

Table 11.1 Linear electro-optic constant r_{41} for some III–V and II–VI semiconductor alloys. S = clamped value

System	Alloy	x (y)	r_{41} (pm/V)	λ (μm)	Comments
III–V	$\text{Al}_x\text{Ga}_{1-x}\text{As}$	0	-1.80^a	10.6	S
		0.17	-1.43^b	1.1523	
	$\text{Ga}_x\text{In}_{1-x}\text{P}_y\text{As}_{1-y}/\text{InP}$	0.20 (y)	-1.34^c	1.32	
		0.34 (y)	-1.43^c	1.25	
		0.34 (y)	-1.44^c	1.32	
		1.00 (y)	-1.68^a	1.50	S
II–VI	$\text{Zn}_x\text{Cd}_{1-x}\text{Te}$	0	4.1^a	10.6	S (r_{41})
		0.1	4.3^d	1.5	S (r_{41})
		1.0	3.9^a	10.6	S (r_{41})

^aS. Adachi, *Properties of Group-IV, III–V and II–VI Semiconductors*. John Wiley & Sons, Ltd, Chichester, 2005

^bM. Glick *et al.*, *J. Appl. Phys.* **63**, 5877 (1988)

^cH. G. Bach *et al.*, *Appl. Phys. Lett.* **42**, 692 (1983)

^dA. Zappettini *et al.*, *J. Electron. Mater.* **30**, 743 (2001)

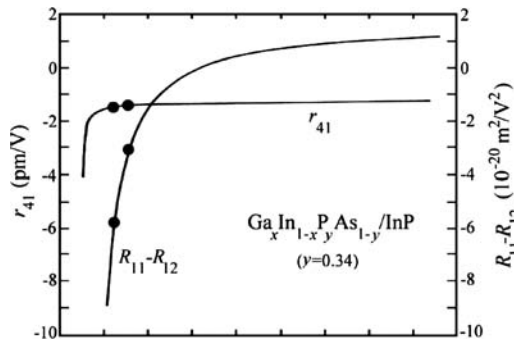


Figure 11.2 Theoretical r_{41} and $R_{11}-R_{12}$ curves along with the experimental data of Bach *et al.* [13] for $\text{Ga}_x\text{In}_{1-x}\text{P}_y\text{As}_{1-y}/\text{InP}$ with $y=0.34$. [Reprinted with permission from S. Adachi and K. Oe, *J. Appl. Phys.* **56**, 1499 (1984). Copyright (1984), American Institute of Physics]

The electro-optic constants r_{ij} of $w\text{-CdS}_x\text{Se}_{1-x}$ have been measured by several authors [16,17]. The results obtained by Baldassarre *et al.* [16] are $r_{13} = -1.5$ pm/V and $r_{33} = 2.4$ pm/V at $\lambda = 632.8$ nm for $x = 0.75$. More recently, Bini and Razzetti [17] reported the unclamped electro-optic constant

$$r_c^T = r_{13}^T - \left(\frac{n_o}{n_e}\right)^3 r_{33}^T \quad (11.1)$$

to be 5.81 ± 0.03 pm/V for $x = 0.5$, where n_o and n_e are, respectively, the ordinary and extraordinary refractive indices and r_{ij}^T is the unclamped electro-optic tensor component [14]. These authors also obtained $r_c^T = 6.45 \pm 0.03$ pm/V for $w\text{-CdS}$ and 7.23 ± 0.04 pm/V for

w-CdSe. A smaller alloy value than those of the endpoint binaries is considered to be due to the microscopic strains present in the alloy.

11.3 QUADRATIC ELECTRO-OPTIC CONSTANT

11.3.1 Group-IV Semiconductor Alloy

No detailed data are available for group-IV semiconductor alloys.

11.3.2 III–V Semiconductor Alloy

Bach *et al.* [13] have studied the quadratic electro-optic effect in $\text{Ga}_x\text{In}_{1-x}\text{P}_y\text{As}_{1-y}/\text{InP}$ double-heterostructure waveguides. They obtained the quadratic electro-optic constants $R_{11} - R_{12} = -0.8 \times 10^{-20} \text{ m}^2/\text{V}^2$ at $\lambda = 1.32 \mu\text{m}$ for $y = 0.20$ and $R_{11} - R_{12} = -5.8 \times 10^{-20} (-3.1 \times 10^{-20}) \text{ m}^2/\text{V}^2$ at $\lambda = 1.25 (1.32) \mu\text{m}$ for $y = 0.35$. These results ($y = 0.35$) are shown in Figure 11.2, together with the theoretical $R_{11} - R_{12}$ values calculated by Adachi and Oe [18]. It can be seen that the quadratic electro-optic constant $R_{11} - R_{12}$ shows very strong dispersion compared with the linear electro-optic constant (r_{41}).

11.3.3 II–VI Semiconductor Alloy

No detailed data are available for II–VI semiconductor alloys.

11.4 FRANZ–KELDYSH EFFECT

11.4.1 Group-IV Semiconductor Alloy

Although the Franz–Keldysh effect in the indirect absorption edge of SiC has been discussed [19], no detailed data are available for group-IV semiconductor alloys.

11.4.2 III–V Semiconductor Alloy

To our knowledge, there have been no publications relating to the direct measurement of the absorption edge shift in $\text{Al}_x\text{Ga}_{1-x}\text{As}$ under an applied electric field. The Franz–Keldysh effect in $\text{Ga}_x\text{In}_{1-x}\text{P}_y\text{As}_{1-y}/\text{InP}$ has been studied experimentally by several authors [13,20–22]. The change in the optical absorption coefficient $\Delta\alpha$ observed in $\text{InP}/\text{GaInPAs}/\text{InP}$ *p-i-n* double heterostructures [22] is found to be comparable with that obtained from the quantum-confined Stark effect ($\sim 10^{-3} \text{ cm}^{-1}$).

11.4.3 II–VI Semiconductor Alloy

Samuel *et al.* [23] measured the absorption coefficients near the fundamental absorption edge of $\text{Zn}_x\text{Cd}_{1-x}\text{Se}$ and $\text{CdS}_x\text{Se}_{1-x}$. They found that most of the results can be explained by the Dow–Redfield theory of the internal Franz–Keldysh effect. An enhancement of the two-photon

absorption coefficient has also been observed to occur in the space charge region of the $\text{Cd}_x\text{Hg}_{1-x}\text{Te}$ p - n junction, which can be attributed to the Franz–Keldysh effect induced by the built-in electric field [24].

11.5 NONLINEAR OPTICAL CONSTANT

11.5.1 Group-IV semiconductor alloy

The independent non-vanishing tensor elements of the nonlinear optical constants for semiconductors of certain symmetry classes are given in [1]. Principally, the diamond lattice does not show a second-order nonlinear optical effect [1]. No detailed data are available on the third-order nonlinear optical constants for group-IV semiconductor alloys.

11.5.2 III–V semiconductor alloy

The second-order nonlinear optical susceptibilities for $w\text{-Al}_x\text{Ga}_{1-x}\text{N}$ with $0 \leq x \leq 0.666$ have been measured by Sanford *et al.* [25]. These authors determined the nonlinear optical susceptibility constants d_{31} and d_{33} at $\lambda = 1.064 \mu\text{m}$ as a function of x under the assumption of $d_{31} = d_{15}$. These results are shown in Figure 11.3(a), together with the endpoint data taken from Adachi [1]. The nonlinear susceptibility constant d_{31} decreases almost linearly with increasing x , while d_{33} largely scatters.

The nonlinear optical susceptibility d_{14} at $\lambda = 1.064 \mu\text{m}$ in $\text{Al}_x\text{Ga}_{1-x}\text{As}$ has been measured using a reflected second harmonics method by Ohashi *et al.* [26]. They reported the magnitudes of d_{14} relative to GaAs over the whole alloy range $0 \leq x \leq 1.0$. These results are shown in Figure 11.3(b). The GaAs and AlAs d_{14} values in Adachi [3] are in the ranges 119–170 and 32 pm/V, respectively.

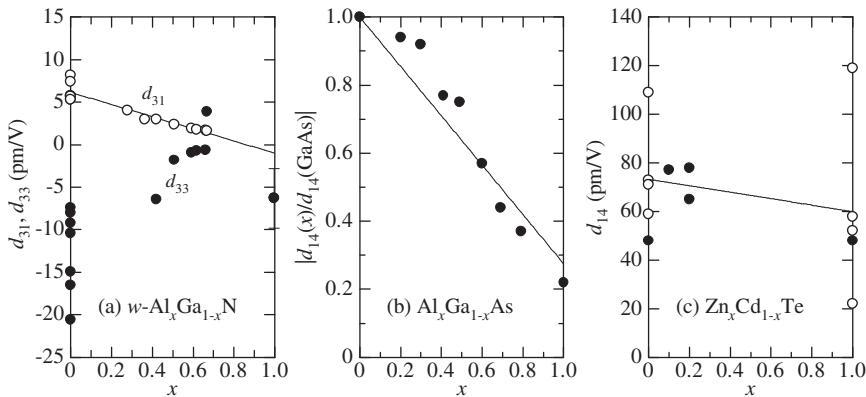


Figure 11.3 Second-order nonlinear optical susceptibility constants d_{ij} in (a) $w\text{-Al}_x\text{Ga}_{1-x}\text{N}$, (b) $\text{Al}_x\text{Ga}_{1-x}\text{As}$ and (c) $\text{Zn}_x\text{Cd}_{1-x}\text{Te}$. The experimental data in (a) are taken from Adachi [1] and Sanford *et al.* [25], in (b) from Ohashi *et al.* [26] and in (c) from Adachi [4] (open circles) and Zappettini *et al.* [31] (solid circles)

The third-order nonlinear susceptibility $|\chi^{(3)}|$ in $\text{Ga}_x\text{In}_{1-x}\text{P}_y\text{As}_{1-y}/\text{InP}$ ($\lambda_g \sim 1.5 \mu\text{m}$) has been determined using a forward degenerate four-wave mixing method [27]. The $|\chi^{(3)}|$ value obtained was $\sim 3.8 \times 10^{-3}$ esu.

The two-photon absorption coefficient β has been discussed both theoretically and experimentally for non-alloyed group-IV, III-V and II-VI semiconductors [1]. Krishnamurthy *et al.* [28] showed that theoretically, β can be increased or decreased by adding In or Al to the GaN compound. Experimentally, Villeneuve *et al.* [29] obtained the spectral dependence of β near half the band gap of $\text{Al}_{0.18}\text{Ga}_{0.82}\text{As}$. The β increased with decreasing wavelength λ ($\sim 0.05 \text{ cm}^2/\text{GW}$ at $\lambda = 1.65 \mu\text{m}$ and $\sim 1.2 \text{ cm}^2/\text{GW}$ at $\lambda \sim 1.49 \mu\text{m}$). The three-photon absorption coefficient α in $\text{Al}_{0.18}\text{Ga}_{0.82}\text{As}$ was also measured for photon energies between one-half and one-third the band gap by Kang *et al.* [30]. They found that α decreases with decreasing λ from $\alpha \sim 0.13 \text{ cm}^3/\text{GW}^2$ at $\lambda = 1.66 \mu\text{m}$ to $\alpha \sim 0.03 \text{ cm}^3/\text{GW}^2$ at $\lambda = 1.50 \mu\text{m}$.

11.5.3 II-VI semiconductor alloy

The second harmonic generation efficiency has been examined in the near-IR region ($\lambda = 1.5$ and $1.9 \mu\text{m}$) of $\text{Zn}_x\text{Cd}_{1-x}\text{Te}$ with $x = 0, 0.1, 0.2$ and 1.0 [31]. The d_{14} data for $\text{Zn}_x\text{Cd}_{1-x}\text{Te}$ [31], together with the endpoint data taken from Adachi [4], have been plotted in Figure 11.3(c). The solid line represents the linear least-squares fit given by $d_{14} = 73 - 13x \text{ pm/V}$.

The second-order nonlinear constant d_{14} of $\text{Cd}_x\text{Hg}_{1-x}\text{Te}$ with $x = 0.277$ has been determined to be $350 \pm 40 \text{ pm/V}$ [32]. The second harmonic generation has also been measured at $\lambda = 1.06 \mu\text{m}$ as a function of x for $w\text{-Zn}_x\text{Cd}_{1-x}\text{S}$ and $w\text{-CdS}_x\text{Se}_{1-x}$ [33].

The two-photon absorption phenomena have been studied in several II-VI semiconductor alloys [34,35]. The maximum value of the two-photon absorption coefficient β is observed for $x = 0.4$ in $c\text{-Mg}_x\text{Zn}_{1-x}\text{Se}$ ($0 \leq x \leq 0.4$) [34]. In $c\text{-Zn}_x\text{Cd}_{1-x}\text{Se}$ and $w\text{-Zn}_x\text{Cd}_{1-x}\text{Se}$ ($0 \leq x \leq 1.0$), the reduction in the band gap is accompanied by a smooth rise of β [35]. Tunability of the two-photon absorption coefficient has also been demonstrated by adjusting the electrical field in a $\text{Cd}_x\text{Hg}_{1-x}\text{Te}$ photodiode with a cutoff wavelength of $5.2 \mu\text{m}$ [24].

REFERENCES

- [1] S. Adachi, *Properties of Group-IV, III-V and II-VI Semiconductors*, John Wiley & Sons, Ltd, Chichester, 2005.
- [2] S. Adachi, *Handbook on Physical Properties of Semiconductors: Volume 1 Group IV Semiconductors*, Kluwer Academic, Boston, 2004.
- [3] S. Adachi, *Handbook on Physical Properties of Semiconductors: Volume 2 III-V Compound Semiconductors*, Kluwer Academic, Boston, 2004.
- [4] S. Adachi, *Handbook on Physical Properties of Semiconductors: Volume 3 II-VI Compound Semiconductors*, Kluwer Academic, Boston, 2004.
- [5] S. A. Geidur, *Opt. Spectrosc.* **49**, 105 (1980).
- [6] S. Adachi and K. Oe, *J. Appl. Phys.* **54**, 6620 (1983).
- [7] S. M. Kikkarin, D. V. Petrov, A. V. Tsarev, and I. B. Yakovkin, *Proc. SPIE* **1932**, 234 (1993).
- [8] P. Ziobrowski, M. Drozdowski, M. Szybowicz, F. Firszt, S. Łęgowski, and H. Męczyńska, *J. Appl. Phys.* **93**, 3805 (2003).
- [9] S. Adachi and C. Hamaguchi, *J. Phys. Soc. Jpn* **44**, 343 (1978).
- [10] X. Tang, K. G. Irvine, D. Zhang, and M. G. Spencer, *Appl. Phys. Lett.* **59**, 1938 (1991).
- [11] R. A. Soref, *J. Appl. Phys.* **72**, 626 (1992).

- [12] M. Glick, F.-K. Reinhart, and D. Martin, *J. Appl. Phys.* **63**, 5877 (1988).
- [13] H. G. Bach, J. Krauser, H. P. Nolting, R. A. Logan, and F. K. Reinhart, *Appl. Phys. Lett.* **42**, 692 (1983).
- [14] S. Adachi and K. Oe, *J. Appl. Phys.* **56**, 74 (1984).
- [15] A. Zappettini, L. Cerati, A. Milani, S. M. Pietralunga, P. Boffi, and M. Martinelli, *J. Electron. Mater.* **30**, 743 (2001).
- [16] L. Baldassarre, A. Cingolani, and M. Sibilano, *Opt. Commun.* **26**, 72 (1978).
- [17] S. Bini and C. Razzetti, *Phys. Status Solidi A* **148**, 603 (1995).
- [18] S. Adachi and K. Oe, *J. Appl. Phys.* **56**, 1499 (1984).
- [19] R. G. Verenchikova and A. O. Konstantinov, *Sov. Phys. Semicond.* **18**, 242 (1984).
- [20] R. H. Kingston, *Appl. Phys. Lett.* **34**, 744 (1979).
- [21] K. Okamoto, S. Matsuoka, Y. Nishiwaki, and K. Yoshida, *J. Appl. Phys.* **56**, 2595 (1984).
- [22] B. Knüpfner, P. Kiesel, A. Höfler, P. Riel, G. H. Döhler, and E. Veuhoff, *Appl. Phys. Lett.* **62**, 2072 (1993).
- [23] L. Samuel, Y. Brada, and R. Beserman, *Phys. Rev. B* **37**, 4671 (1988).
- [24] H. Y. Cui, Z. F. Li, Z. L. Liu, C. Wang, X. S. Chen, X. N. Hu, Z. H. Ye, and W. Lu, *Appl. Phys. Lett.* **92**, 021128 (2008).
- [25] N. A. Sanford, A. V. Davydov, D. V. Tsvetkov, A. V. Dmitriev, S. Keller, U. K. Mishra, S. P. DenBaars, S. S. Park, J. Y. Han, and R. J. Molnar, *J. Appl. Phys.* **97**, 053512 (2005).
- [26] M. Ohashi, T. Kondo, R. Ito, S. Fukatsu, Y. Shiraki, K. Kumata, and S. S. Kano, *J. Appl. Phys.* **74**, 596 (1993).
- [27] M. N. Islam, E. P. Ippen, E. G. Burkhardt, and T. J. Bridges, *J. Appl. Phys.* **59**, 2619 (1986).
- [28] S. Krishnamurthy, K. Nashold, and A. Sher, *Appl. Phys. Lett.* **77**, 355 (2000).
- [29] A. Villeneuve, C. C. Yang, G. I. Stegeman, C.-H. Lin, and H.-H. Lin, *Appl. Phys. Lett.* **62**, 2465 (1993).
- [30] J. U. Kang, A. Villeneuve, M. Sheik-Bahae, G. I. Stegeman, K. Al-hemyari, J. S. Aitchison, and C. N. Ironside, *Appl. Phys. Lett.* **65**, 147 (1994).
- [31] A. Zappettini, S. M. Pietralunga, A. Milani, D. Piccinin, M. Feré, and M. Martinelli, *J. Electron. Mater.* **30**, 738 (2001).
- [32] A. W. Wark, D. Pugh, L. E. A. Berlouis, and F. R. Cruickshank, *J. Appl. Phys.* **89**, 306 (2001).
- [33] R. A. Soref and H. W. Moos, *J. Appl. Phys.* **35**, 2152 (1964).
- [34] B. Derkowska, B. Sahraoui, X. N. Phu, G. Glowacki, and W. Bala, *Opt. Mater.* **15**, 199 (2000).
- [35] M. S. Brodin and D. B. Goer, *Sov. Phys. Semicond.* **5**, 219 (1971).

12 Carrier Transport Properties

12.1 INTRODUCTORY REMARKS

The electrical resistivity ρ , together with the thermal resistivity W , for $\text{Cu}_x\text{Au}_{1-x}$ is shown in Figure 12.1. The solid and open circles correspond to the ordered (CuAu and Cu_3Au) and disordered alloys, respectively. The experimental data are taken from various sources. The W data plots in Figure 12.1(b) are the same as those in Figure 2.24. The solid and dashed lines in Figure 12.1(a) are calculated from Equation (A.17) with $C_{\text{CuAu}} = 60 \mu\Omega \text{ cm}$ and with and without properly taking into account the effect of alloy ordering at $x = 0.5$ and 0.75 (CuAu and Cu_3Au), respectively. As mentioned in Section 2.5.1, the Wiedemann–Franz law states that the ratio of the thermal conductivity K ($=W^{-1}$) to the electrical conductivity σ ($=\rho^{-1}$) is proportional to the temperature. Thus, at any temperature σ (ρ) is proportional to K (W), as can be seen in Figure 12.1.

In semiconductor alloys, the potential fluctuations of electrons are a result of the compositional disorder. This effect produces a peculiar scattering mechanism, namely, alloy scattering. Alloy-scattering-limited mobility is represented as [1]

$$\mu_e^{\text{al}} = \frac{\sqrt{2\pi}}{3} \frac{e\hbar^4 N_{\text{al}}}{(kT)^{1/2} (m_e)^{5/2} x(1-x) (\Delta U_e)^2} \quad (12.1)$$

where m_e is the electron effective mass, N_{al} is the density of alloy sites, ΔU_e is the alloy scattering potential and x and $(1-x)$ are the mole fractions of the endpoint materials. The alloy scattering mechanism shown in Equation (12.1) leads to a decrease in the electron mobility μ_e at $x \neq 0$ or 1.0 .

Not only the electrons but also the holes are subject to potential fluctuations as a result of the compositional disorder. Alloy scattering may, therefore, be observable both in n - and p -type semiconductor alloys. However, because of its mass dependence (i.e. $m_{e,h}^{-5/2}$), the scattering strength may be weaker in p -type alloys than in n -types.

The electron and hole Hall mobilities (μ_e and μ_h) measured at room temperature for a number of non-alloyed group-IV, III–V and II–VI semiconductors are summarized in Table 12.1. These values, together with the bowing parameters c_e and c_h listed in Table 12.2, can be used for obtaining the mobilities of alloys of arbitrary composition. Electron and hole saturation drift velocities, minority carrier lifetimes and impact ionization coefficients for some non-alloyed group-IV, III–V and II–VI semiconductors can be found in Adachi [2].

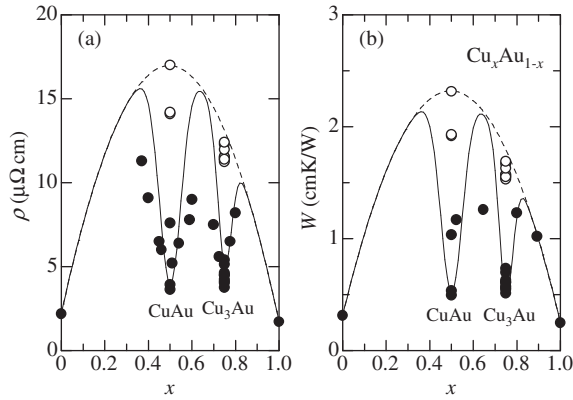


Figure 12.1 Electrical ρ and thermal resistivities W for $\text{Cu}_x\text{Au}_{1-x}$ at 300 K. The theoretical curves are obtained from Equation (A.17) (Equation (2.25)) with $C_{\text{CuAu}} = 60 \mu\Omega \text{ cm}$ (ρ) and 8.15 cm K/W (W) and with (solid lines) and without properly taking into account the alloy ordering effect at $x = 0.5$ and 0.75 (CuAu and Cu_3Au) (dashed lines), respectively

Table 12.1 Room-temperature electron and hole Hall mobilities μ_e and μ_h for some cubic and hexagonal semiconductors. d = diamond, zb = zinc-blende, h = hexagonal, w = wurtzite, rs = rocksalt

System	Material	μ_e (cm ² /V s)	μ_h (cm ² /V s)	System	Material	μ_e (cm ² /V s)	μ_h (cm ² /V s)
IV	Diamond (d)	2800	1500	II-VI	MgO (rs)		10
	Si (d)	1750 ^a	480		ZnO (w)	440	267
	Ge (d)	4330	2400		ZnS (zb)	275	72
	3C-SiC (zb)	980	~60		ZnS (w)	140	
	6H-SiC (h)	375	100		ZnSe (zb)	1500	355
III-V	BP (zb)	190	500	ZnTe (zb)	600	100	
	AlN (w)	125	14	CdO (rs)	216		
	AlP (zb)	80	450	CdS (zb)	85		
	AlAs (zb)	294	105	CdS (w)	390	48	
	AlSb (zb)	200	420	CdSe (w)	900	50	
	GaN (zb)	760	350	CdTe (zb)	1260 ^a	104	
	GaN (w)	1245	370	HgS (zb)	230		
	GaP (zb)	189	140	HgSe (zb)	22000		
	GaAs (zb)	9340	450	HgTe (zb)	32000	320	
	GaSb (zb)	12040	1000				
	InN (w)	3100	39				
	InP (zb)	6460	180				
	InAs (zb)	33000	450				
	InSb (zb)	77000	1100				

^aDrift (conductivity) mobility

Table 12.2 Bowing parameters c_e and c_h for the electron and hole mobilities μ_e and μ_h in some group-IV binaries, and III–V and II–VI ternaries

System	Alloy	c_e (cm ² /V s)	c_h (cm ² /V s)	System	Alloy	c_e (cm ² /V s)	c_h (cm ² /V s)	
IV	C _x Si _{1-x}	5200	3600	II–VI	Cd _x Hg _{1-x} Se	30000		
	Si _x Ge _{1-x}	11000	2200		Zn _x Cd _{1-x} Te			160
III–V	w-Al _x Ga _{1-x} N	900			c-ZnS _x Se _{1-x}	2800		
	Ga _x In _{1-x} P		40		ZnSe _x Te _{1-x}	3200		
	Al _x Ga _{1-x} As	18000	520					
	Al _x In _{1-x} As	35000						
	Ga _x In _{1-x} As	26000	600					
	Al _x Ga _{1-x} Sb		2500					
	Ga _x In _{1-x} Sb	42000	1000					
	GaP _x Sb _{1-x}	20000						
	GaAs _x Sb _{1-x}		2500					
	InP _x As _{1-x}	30000						
	InP _x Sb _{1-x}	110000						
InAs _x Sb _{1-x}	30000							

12.2 LOW-FIELD MOBILITY

12.2.1 Group-IV Semiconductor Alloy

(a) CSi binary alloy

The electron and hole mobilities μ_e and μ_h for Si ($x=0$), diamond ($x=1.0$) and 3C-SiC ($x=0.5$), respectively are shown in Figure 12.2(a). The solid lines represent the quadratic fits of Equation (A.17) with $c_{e,h}$ in Table 12.2. Note that 3C-SiC is an ordered form of C_xSi_{1-x}, or in other words, a compound. We can, thus, expect no alloy scattering in 3C-SiC. However, the 3C-SiC mobilities are smaller than the mean values of diamond and Si, especially for μ_h . The lower 3C-SiC values may be due to its poorer crystalline quality.

(b) SiGe binary alloy

Figure 12.2(b) shows the electron and hole mobilities μ_e and μ_h for Si_xGe_{1-x}. It is obvious that not only is alloy scattering, but also that the other scattering mechanisms and the effective masses modified through the change of the band structure influence the electron mobility in this alloy. The mass and temperature dependence of each scattering mechanism is summarized in Table 12.2 of Adachi [2], including alloy scattering ($\mu \propto m_{e,h}^{-5/2}$, $\mu \propto T^{-1/2}$). The most prominent example is the decrease in μ_e at $x \sim 0.15$, which corresponds to the transition from a Ge-like CB (L) to a Si-like CB (X or Δ) (Figure 6.8). The main effect on μ_e is, thus, associated with the increase in the electron conductivity mass in the Si-like CB for $x \geq 0.15$ (Figure 7.3). For Si_xGe_{1-x}, μ_h was not found to be strongly dependent on x .

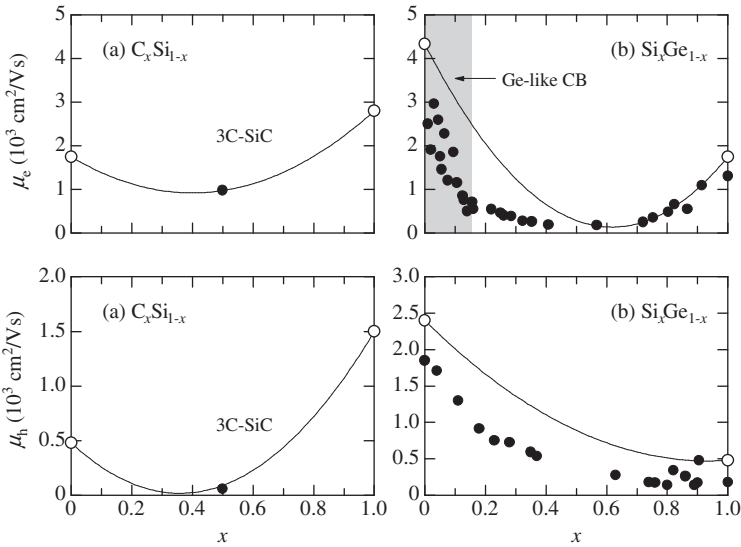


Figure 12.2 Electron and hole mobilities μ_e and μ_h for (a) C_xSi_{1-x} and (b) Si_xGe_{1-x} at 300 K. The solid lines show the calculated results using Equation (A.17) and the numeric parameters in Tables 12.1 and 12.2

12.2.2 III–V Semiconductor Ternary Alloy

(a) (III, III)–N alloy

The electron mobility μ_e for some (III, III)–V ternary alloys, $w-Al_xGa_{1-x}N$, $w-Al_xIn_{1-x}N$ and $w-Ga_xIn_{1-x}N$, plotted against x is shown in Figure 12.3. The μ_e values for $w-Al_xGa_{1-x}N$ can be expressed by Equation (A.5) with $c_e = 900 \text{ cm}^2/\text{V s}$ (Table 12.2). No large μ_e values have been obtained for $w-Al_xIn_{1-x}N$ and $w-Ga_xIn_{1-x}N$ ternaries. Very weak temperature dependence of

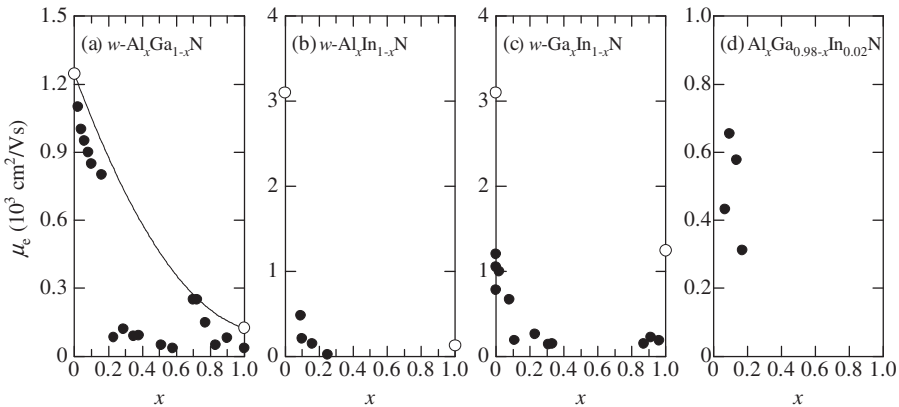


Figure 12.3 Electron mobility μ_e for (a) $w-Al_xGa_{1-x}N$, (b) $w-Al_xIn_{1-x}N$, (c) $w-Ga_xIn_{1-x}N$ and (d) $w-Al_xGa_{0.98-x}In_{0.02}N$ at 300 K. The solid line in (a) shows the result calculated using Equation (A.5) and the numeric parameters in Tables 12.1 and 12.2

the free-electron density in w - $\text{Ga}_x\text{In}_{1-x}\text{N}$ with In-rich compositions ($x \leq 0.08$) [3] suggests that the materials are metallic-like.

(b) (III, III)–P alloy

The electron and hole mobilities for $\text{Ga}_x\text{In}_{1-x}\text{P}$ are shown in Figure 12.4. Some data correspond to those for $\text{Ga}_x\text{In}_{1-x}\text{P}$ lattice-matched to GaAs. The lowest CB in InP ($x = 0$) is located at the Γ point, while that in GaP is at the X point. The large (small) μ_e value for InP (GaP) is principally due to the small (large) electron effective mass in the Γ (X) valley, as shown in Figure 12.4(a) by the open circles. There is a clear relationship between the electron effective mass m_e^c (or m_e^Γ) and electron mobility μ_e . We can estimate from Equations (12.19) and (12.21) in Adachi [2] the X- and Γ -valley electron mobilities to be ~ 220 (InP) and $\sim 990 \text{ cm}^2/\text{V s}$ (GaP), respectively. These values are plotted in Figure 12.4(a) by the open triangles.

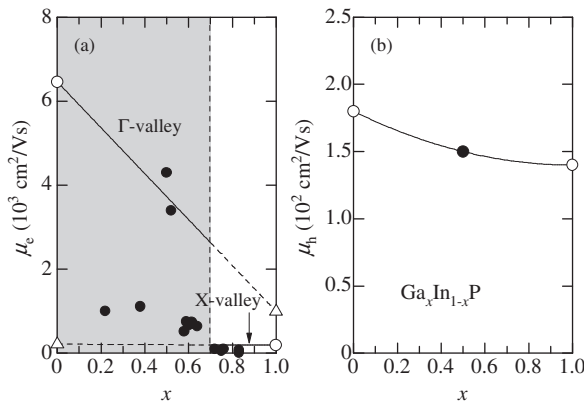


Figure 12.4 Electron and hole mobilities μ_e and μ_h for $\text{Ga}_x\text{In}_{1-x}\text{P}$ at 300 K. The solid line in (b) shows the result calculated using Equation (A.5) and the numeric parameters in Tables 12.1 and 12.2

(c) (III, III)–As alloy

The electron and hole mobilities for some (III, III)–As ternaries are plotted in Figure 12.5. The $\text{Al}_x\text{Ga}_{1-x}\text{As}$ and $\text{Al}_x\text{In}_{1-x}\text{As}$ ternaries show the Γ –X crossover at $x \sim 0.4$ and ~ 0.6 , respectively (Figures 6.20 and 6.22). These alloys may, thus, provide an abrupt change in μ_e at such crossover points due to the different effective masses at the Γ and X valleys. From Equations (12.19) and (12.21) in Adachi [2], we can estimate the X- and Γ -valley electron mobilities to be ~ 330 (GaAs) and $\sim 830 \text{ cm}^2/\text{V s}$ (AlAs), respectively. These values are also shown in Figure 12.5(a) by the open triangles. Similarly, we can estimate the X-valley electron mobility to be $\sim 270 \text{ cm}^2/\text{V s}$, as plotted in Figure 12.5(b) by the open triangle (InAs). The Γ -electron bowing parameters for μ_e and those for μ_h are listed in Table 12.2. The low-field transport properties of $\text{Al}_x\text{Ga}_{1-x}\text{As}$ have also been reviewed in more detail in Adachi [1].

(d) (III, III)–Sb alloy

The electron and hole mobilities for some (III, III)–Sb ternaries are plotted in Figure 12.6. Like (Al, III)–As in Figure 12.5, the $\text{Al}_x\text{Ga}_{1-x}\text{Sb}$ and $\text{Al}_x\text{In}_{1-x}\text{Sb}$ alloys show the Γ –X crossover at

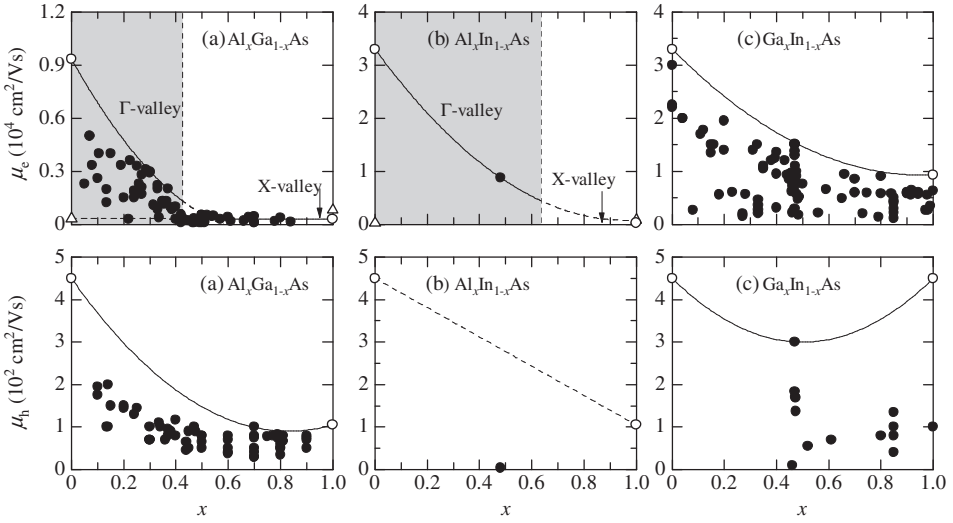


Figure 12.5 Electron and hole mobilities μ_e and μ_h for (a) $\text{Al}_x\text{Ga}_{1-x}\text{As}$, (b) $\text{Al}_x\text{In}_{1-x}\text{As}$ and (c) $\text{Ga}_x\text{In}_{1-x}\text{As}$ at 300 K. The solid lines show the calculated results using Equation (A.5) and the numeric parameters in Tables 12.1 and 12.2

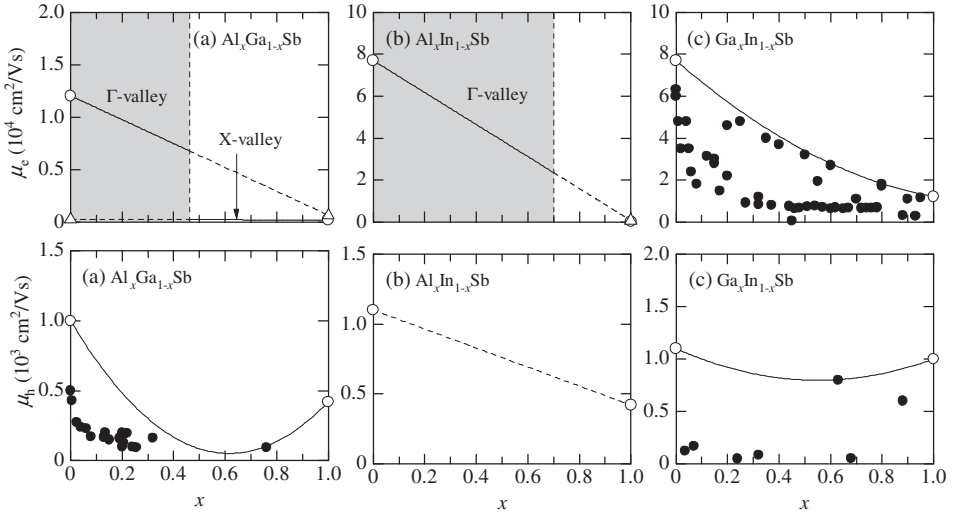


Figure 12.6 Electron and hole mobilities μ_e and μ_h for (a) $\text{Al}_x\text{Ga}_{1-x}\text{Sb}$, (b) $\text{Al}_x\text{In}_{1-x}\text{Sb}$ and (c) $\text{Ga}_x\text{In}_{1-x}\text{Sb}$ at 300 K. The solid lines show the calculated results using Equation (A.5) and the numeric parameters in Tables 12.1 and 12.2

$x \sim 0.5$ and ~ 0.7 , respectively (Figures 6.25 and 6.26). We can, thus, expect an abrupt change in μ_e at such crossover points, although no enough experimental data are available. The dependence of μ_e on x in $\text{Ga}_x\text{In}_{1-x}\text{Sb}$ can be successfully explained using $c_e = 42000 \text{ cm}^2/\text{Vs}$ (Table 12.2).

(e) *Dilute-nitride III–(V, V) alloy*

The electron mobility should be lower in dilute-nitride III–V alloys due to strong carrier scattering and enhanced electron effective masses [4,5]. The experimental mobility μ_e for dilute-nitride $\text{GaN}_x\text{As}_{1-x}$ and $\text{InN}_x\text{As}_{1-x}$ ternaries is shown in Figure 12.7. It can be seen that the addition of small concentrations of N to GaAs or InAs leads to a large reduction in μ_e . The reduction in μ_e determined experimentally seemed to be larger than that predicted theoretically [4,5].

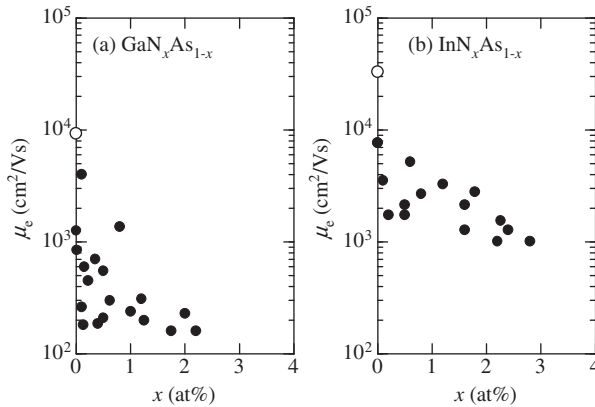


Figure 12.7 Electron mobility μ_e for (a) dilute-nitride $\text{GaN}_x\text{As}_{1-x}$ and (b) dilute-nitride $\text{InN}_x\text{As}_{1-x}$ at 300 K. The open circles show the endpoint binary data taken from Table 12.1

Since the VB of the III–V semiconductors is mainly characterized by the electron orbital of the group V anions [2], we can expect that N addition will not have a strong effect on the hole mobility. However, the experimental μ_h value dramatically decreased from $\sim 300 \text{ cm}^2/\text{V s}$ at $x = 0$ at% (GaAs) to $\sim 80 \text{ cm}^2/\text{V s}$ at $x = 1$ at% [6]. This drop in μ_h is likely correlated with the increase in crystalline defects introduced by nitrogen doping.

(f) *Ga–(V, V) alloy*

Figure 12.8 shows the electron and hole mobilities for some Ga–(V, V) ternary alloys. As in $\text{Al}_x\text{Ga}_{1-x}\text{As}$, the CB in $\text{GaP}_x\text{As}_{1-x}$ shows the $\Gamma - X$ crossover at $x = 0.48$ (Figures 6.33). $\text{GaP}_x\text{As}_{1-x}$, thus, shows an abrupt change in μ_e near $x = 0.48$. The open triangles in Figures 12.8 (a) and 12.8(b) plot the X- and Γ -valley electron mobilities for GaAs (GaSb) and GaP as estimated from Equations (12.19) and (12.21) in Adachi [2], respectively.

(g) *In–(V, V) alloy*

The experimental electron mobility for some In–(V, V) ternaries have been plotted in Figure 12.9. The solid lines represent the μ_e versus x curves calculated from Equation (A.5) with c_e taken from Table 12.2.

12.2.3 III–V Semiconductor Quaternary Alloy

(a) *Dilute-nitride alloy*

The free-electron concentration and mobility have been found to be significantly reduced by the incorporation of N into Si-doped dilute-nitride $\text{Ga}_x\text{In}_{1-x}\text{N}_y\text{P}_{1-y}$ [7] and $\text{Ga}_x\text{In}_{1-x}\text{N}_y\text{As}_{1-y}$ [8,9].

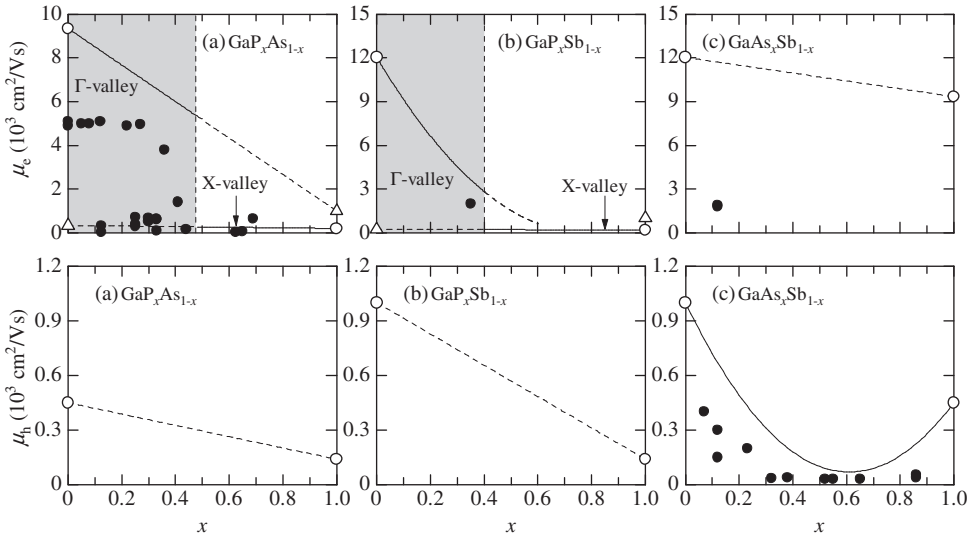


Figure 12.8 Electron and hole mobilities μ_e and μ_h for (a) $\text{GaP}_x\text{As}_{1-x}$, (b) $\text{GaP}_x\text{Sb}_{1-x}$ and (c) $\text{GaAs}_x\text{Sb}_{1-x}$ at 300 K. The solid lines show the calculated results using Equation (A.5) and the numeric parameters in Tables 12.1 and 12.2

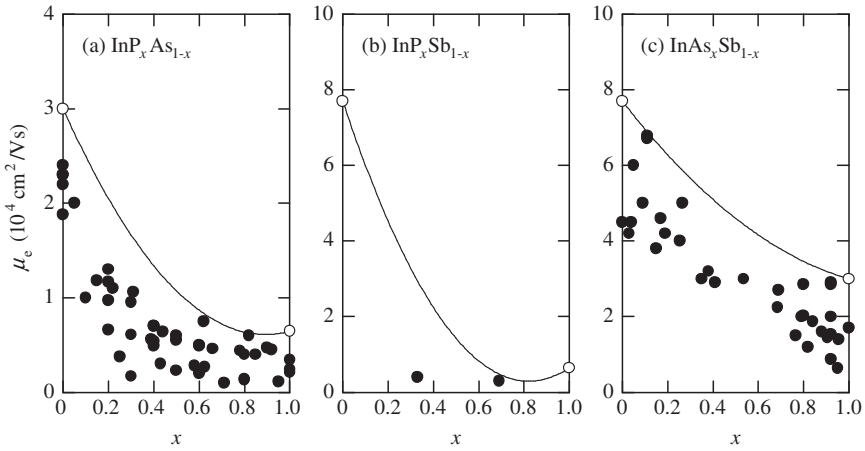


Figure 12.9 Electron mobility μ_e for (a) $\text{InP}_x\text{As}_{1-x}$, (b) $\text{InP}_x\text{Sb}_{1-x}$ and (c) $\text{InAs}_x\text{Sb}_{1-x}$ at 300 K. The solid lines show the results calculated using Equation (A.5) and the numeric parameters in Tables 12.1 and 12.2

No significant effect of N incorporation has, however, been observed on the hole transport properties of Be-doped $\text{Ga}_x\text{In}_{1-x}\text{N}_y\text{As}_{1-y}$ [9] and Zn-doped $\text{GaN}_x\text{As}_{1-x}\text{Sb}_{1-x-y}$ [10].

(b) (III, III)-(V, V) alloy

The variation in μ_e and μ_h with y for $\text{Ga}_x\text{In}_{1-x}\text{P}_y\text{As}_{1-y}/\text{InP}$ is shown in Figure 12.10. The solid lines represent the quadratic expressions given by (in $\text{cm}^2/\text{V s}$)

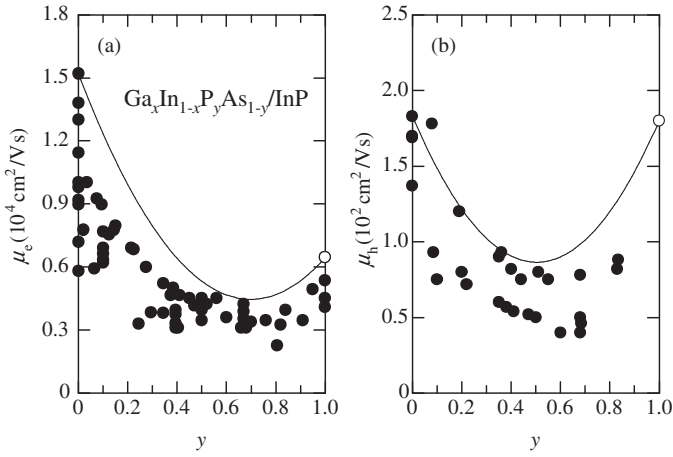


Figure 12.10 Electron and hole mobilities μ_e and μ_h for $\text{Ga}_x\text{In}_{1-x}\text{P}_y\text{As}_{1-y}/\text{InP}$ at 300 K. The solid lines show the results calculated using Equation (12.2)

$$\mu_e(y) = 15200 - 30740y + 22000y^2 \quad (12.2a)$$

$$\mu_h(y) = 183 - 383y + 380y^2 \quad (12.2b)$$

As can be seen in Figure 12.10, alloy scattering produces a mobility minimum at $y \sim 0.7$ and ~ 0.5 for μ_e and μ_h , respectively. The low-field transport properties of $\text{Ga}_x\text{In}_{1-x}\text{P}_y\text{As}_{1-y}/\text{InP}$ have also been reviewed in more detail in Adachi [11].

(c) (III, III, III)-Valley

The electron mobility μ_e versus x for $w\text{-Al}_x\text{Ga}_{0.98-x}\text{In}_{0.02}\text{N}$ [12] has been plotted in Figure 12.3(d). As in $w\text{-Al}_x\text{Ga}_{1-x}\text{N}$ (Figure 12.3(a)), μ_e for $w\text{-Al}_x\text{Ga}_{0.98-x}\text{In}_{0.02}\text{N}$ greatly decreases with increasing x .

The electron mobility μ_e as a function of x for $(\text{Al}_x\text{Ga}_{1-x})_{0.53}\text{In}_{0.47}\text{P}/\text{GaAs}$ and $(\text{Al}_x\text{Ga}_{1-x})_{0.48}\text{In}_{0.52}\text{As}/\text{InP}$ is plotted in Figures 12.11(a) and 12.11(b), respectively. The solid lines in Figures 12.11(a) and 12.11(b) show, respectively, the quadratic expressions given by (in $\text{cm}^2/\text{V s}$)

$$\mu_e(x) = 4300 - 6000x + 3000x^2 \quad (12.3a)$$

$$\mu_e(x) = 15200 - 38400x + 32000x^2 \quad (12.3b)$$

The experimental data in Figure 12.11(a) are taken from Sotoodeh *et al.* [13] (open circle) and Hofmann *et al.* [14] (solid circles). The CB in $(\text{Al}_x\text{Ga}_{1-x})_{0.53}\text{In}_{0.47}\text{P}/\text{GaAs}$ shows the $\Gamma - X$ crossover at $x \sim 0.64$ (Figure 6.49). Thus, the experimental μ_e data for $x > 0.64$ in Figure 12.11 (a) seem to be questionably large.

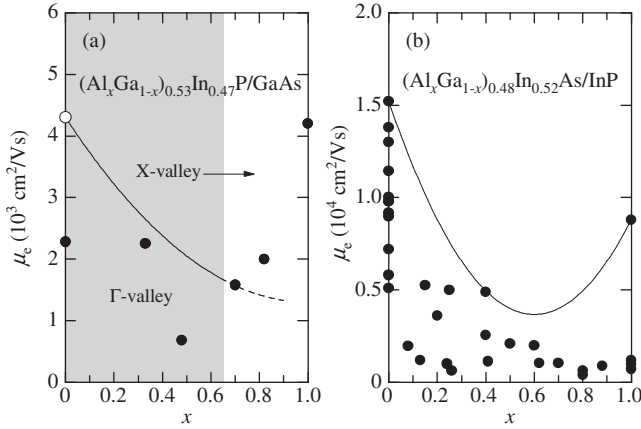


Figure 12.11 Electron mobility μ_e for (a) $(Al_xGa_{1-x})_{0.53}In_{0.47}P/GaAs$ and (b) $(Al_xGa_{1-x})_{0.48}In_{0.52}As/InP$ at 300 K. The solid lines show the calculated results using Equation (12.3)

12.2.4 II–VI Semiconductor Alloy

(a) (II, II)–O ternary alloy

The large band-gap alloy $Mg_xZn_{1-x}O$ is the subject of growing interest in connection with the development of UV optoelectronic devices based on ZnO. The low-field hole mobility μ_h is plotted against x for $Mg_xZn_{1-x}O$ in Figure 12.12(a). The $x = 0.2$ data provides the highest alloy μ_h value of $6.42\text{ cm}^2/V\text{ s}$ [15].

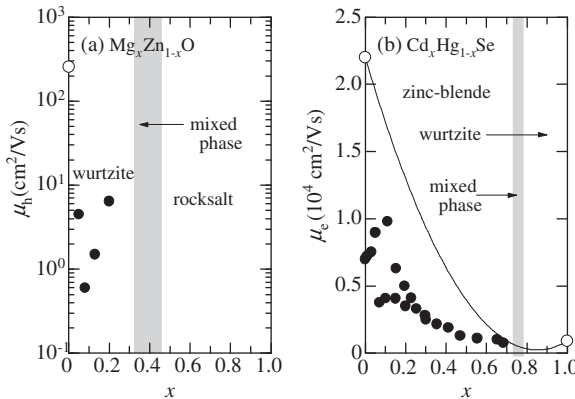


Figure 12.12 Electron mobility μ_e for (a) $Mg_xZn_{1-x}O$ and (b) $Cd_xHg_{1-x}Se$ at 300 K. The solid line in (b) shows the results calculated using Equation (A.5) and the numeric parameters in Tables 12.1 and 12.2

(b) (II, II)–Se ternary alloy

The electron Hall mobility for Bridgman-grown $Mg_xZn_{1-x}Se$ ($x \leq 0.07$) and $Mg_xCd_{1-x}Se$ ($x \leq 0.4$) has been measured at $T = 11\text{--}300\text{ K}$ [16]. The μ_e values for $Mg_xZn_{1-x}Se$

($\text{Mg}_x\text{Cd}_{1-x}\text{Se}$) with $x = 0.07$ (0.4) are ~ 225 (~ 100) and ~ 20 (~ 0.2) $\text{cm}^2/\text{V s}$ at 300 and 11 K, respectively. The very low μ_e values observed at low temperatures were considered to be due to the conduction at the impurity band.

The electron mobility μ_e for Bridgman-grown Fe-doped $\text{Zn}_x\text{Hg}_{1-x}\text{Se}$ with $x \leq 0.072$ has been measured in the temperature range 1.7–300 K [17]. The electron mobility for $\text{Cd}_x\text{Hg}_{1-x}\text{Se}$ has also been measured by several authors. The experimental data for $\text{Cd}_x\text{Hg}_{1-x}\text{Se}$ are shown in Figure 12.12(b). The solid line represents the dependence of μ_e on x using Equation (A.5) with the numeric parameters shown in Tables 12.1 and 12.2.

(c) (II, II)–Te ternary alloy

Figure 12.13 shows the electron Hall mobility μ_e for some (II, II)–Te ternaries. The hole Hall mobility μ_h for $\text{Zn}_x\text{Cd}_{1-x}\text{Te}$ is also plotted in the lower part of Figure 12.13. Because $\text{Zn}_x\text{Cd}_{1-x}\text{Te}$ is one of the most promising materials for use in room-temperature nuclear detectors, the carrier ‘drift’ mobilities were usually measured in conjunction with the value of the $\mu\tau$ (drift mobility–lifetime) product. Note that the solid triangles (μ_e) in Figure 12.13(b) correspond to the electron drift mobility, not the Hall mobility. The highest μ_e value for CdTe ($x = 0$) reported so far is $1260 \text{ cm}^2/\text{V s}$ [18], which is considerably smaller than that predicted from the dashed line in Figure 12.13(b) ($\sim 1600 \text{ cm}^2/\text{V s}$).

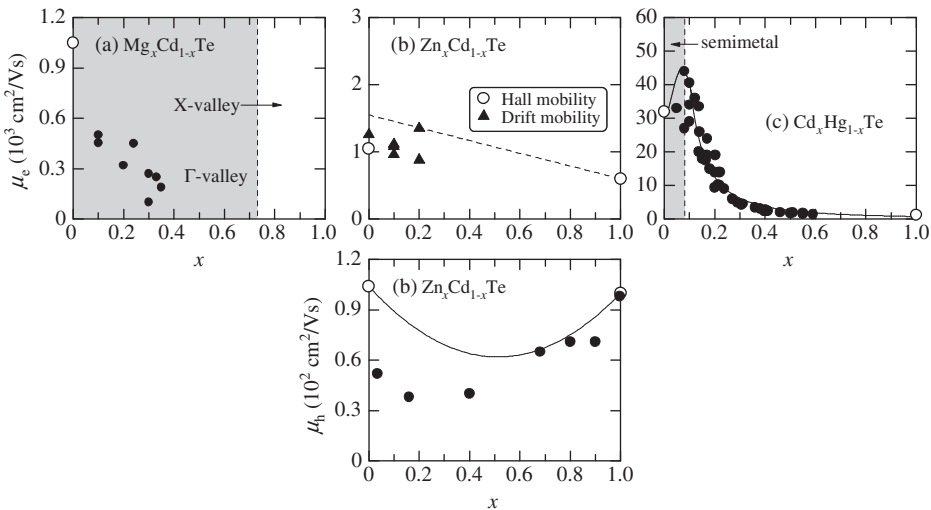


Figure 12.13 Electron and hole Hall mobilities μ_e and μ_h for (a) $\text{Mg}_x\text{Cd}_{1-x}\text{Te}$, (b) $\text{Zn}_x\text{Cd}_{1-x}\text{Te}$ and (c) $\text{Cd}_x\text{Hg}_{1-x}\text{Te}$ at 300 K. The electron drift mobilities are also shown by the solid triangles in (b). The solid line in (b) shows the result calculated using Equation (A.5) and the numeric parameters in Tables 12.1 and 12.2

As seen in Figure 12.13(c), the electron Hall mobility for $\text{Cd}_x\text{Hg}_{1-x}\text{Te}$ increases monotonically from $x = 0$ to a peak at the semiconductor–semimetal transition $x \sim 0.08$ with a peak mobility of $44000 \text{ cm}^2/\text{V s}$ and then drops monotonically with further increase in x . The low-field electron and hole transport properties of $\text{Cd}_x\text{Hg}_{1-x}\text{Te}$ have been reviewed in more detail in Miles [19].

(d) Zn-(V, V) ternary alloy

The electron Hall mobility for c -ZnS_xSe_{1-x} and ZnSe_xTe_{1-x} ternaries is shown in Figures 12.14(a) and 12.14(b), respectively. The limited data predict that these alloys have considerably large bowing parameters c_e , as listed in Table 12.2.

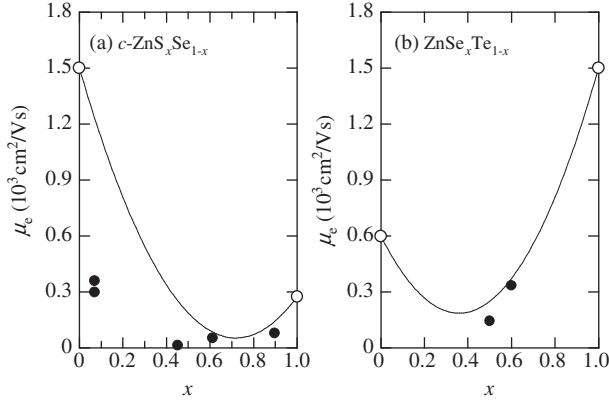


Figure 12.14 Electron mobility μ_e for (a) c -ZnS_xSe_{1-x} and (b) ZnSe_xTe_{1-x} at 300 K. The solid lines show the calculated results using Equation (A.5) and the numeric parameters in Tables 12.1 and 12.2

12.3 HIGH-FIELD TRANSPORT

12.3.1 Group-IV Semiconductor Alloy

No detailed studies concerning the high-field transport properties of group-IV semiconductor alloys have been reported.

12.3.2 III-V Semiconductor Ternary Alloy

(a) (III, III)-N alloy

The high-field transport phenomena in Al_xGa_{1-x}N and Ga_xIn_{1-x}N have been investigated using Monte Carlo simulation [20,21]. The electron drift velocity-field ($v_e - E$) characteristics obtained from these studies are summarized in Figure 12.15. The electron velocity at high fields tends to level off and is defined as the saturation velocity $v_{e,sat}$.

(b) (III, III)-P alloy

The high-field transport properties of Ga_{0.5}In_{0.5}P/GaAs have been studied by several authors. Sakamoto *et al.* [22] determined the $v_e - E$ curve for E up to 20 kV/cm at 300 K. Yee *et al.* [23] reported the temperature-dependent $v_{e,sat}$ up to 200°C by analyzing Ga_{0.5}In_{0.5}P/GaAs HBT characteristics. These results are shown in Figure 12.16. The electron drift velocity peaks at $E \sim 15 \text{ kV/cm}$ with a value of $v_p \sim 1.0 \times 10^7 \text{ cm/s}$.

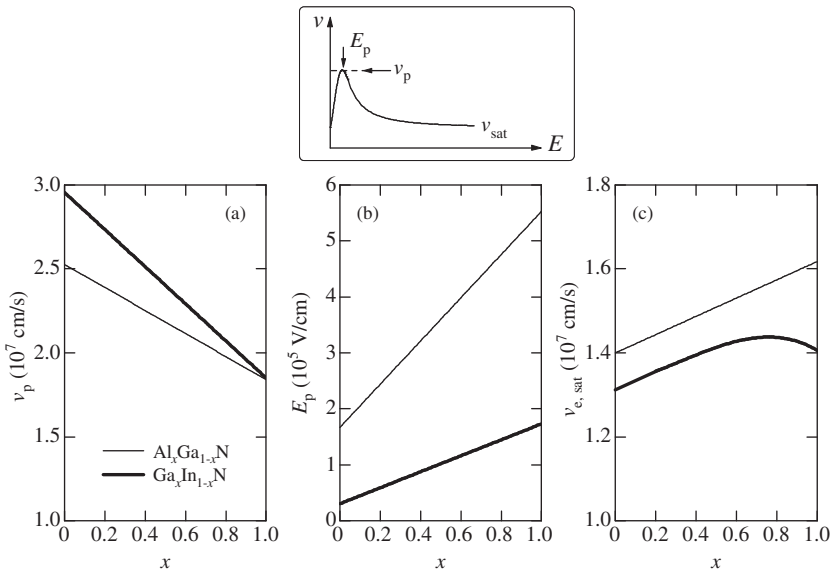


Figure 12.15 (a) Peak electron drift velocity v_p , (b) peak field E_p and (c) electron saturation velocity $v_{e,\text{sat}}$ for $\text{Al}_x\text{Ga}_{1-x}\text{N}$ and $\text{Ga}_x\text{In}_{1-x}\text{N}$ obtained using the Monte Carlo simulation at 300 K

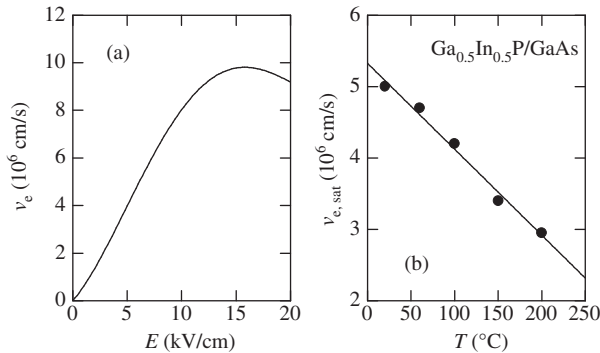


Figure 12.16 (a) Electron drift velocity versus field curve and (b) electron saturation velocity as a function of temperature for $\text{Ga}_{0.5}\text{In}_{0.5}\text{P}/\text{GaAs}$ at 300 K. The experimental data in (a) are taken from Sakamoto *et al.* [22] and in (b) from Yee *et al.* [23]

(c) (III, III)-As alloy

The v_e - E curves for $\text{Al}_x\text{Ga}_{1-x}\text{As}$ have been determined using a pump-probe technique and transferred-electron devices [24]. As can be seen in Figure 12.17(a), the electron drift velocity at any fixed field decreases with increasing x . The hole drift velocity versus field (v_h - E) curves for $\text{Al}_{0.45}\text{Ga}_{0.55}\text{As}$ have also been studied using an ensemble Monte Carlo technique [25]. These results, together with the experimental v_h - E curve for GaAs, are shown in the lower part of Figure 12.17(a).

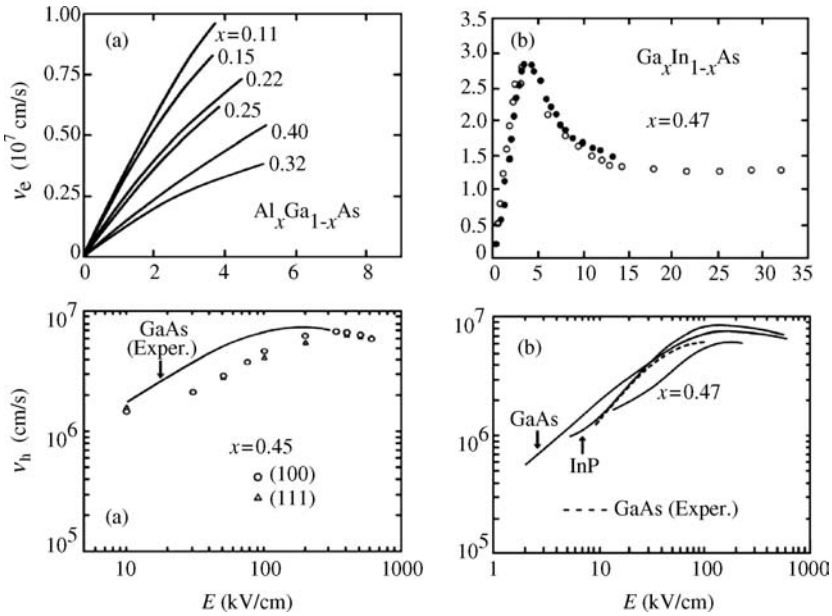


Figure 12.17 Electron and hole velocities versus field curves for (a) $\text{Al}_x\text{Ga}_{1-x}\text{As}$ and (b) $\text{Ga}_x\text{In}_{1-x}\text{As}$. The data plotted in (a) are taken from Bhattacharya *et al.* [24] ($v_e - E$) and Brennan and Hess [25] ($v_h - E$, Monte Carlo simulation) and in (b) from Balynas *et al.* [26] ($v_e - E$) and Adachi [11] ($v_h - E$)

Figure 12.17(b) plots the $v_{e,h} - E$ curves for $\text{Ga}_{0.47}\text{In}_{0.53}\text{As}/\text{InP}$ [11,26]. We also show in the lower part of Figure 12.17(b) the experimental and calculated $v_h - E$ curves for GaAs and InP, respectively. The hole velocity saturation in these materials occurs at fields of about 100 kV/cm, which are much higher than those for the electrons (<10 kV/cm). The peak hole velocities $v_p \sim 7 \times 10^6$ cm/s are also considerably lower than those for the electrons. The dependence of doping on the $v_e - E$ curve in $n\text{-Ga}_{0.47}\text{In}_{0.53}\text{As}/\text{InP}$ has also been studied by analyzing transferred-electron device characteristics [27]. The high-field transport properties of $\text{Al}_x\text{Ga}_{1-x}\text{As}$ and $\text{Ga}_x\text{In}_{1-x}\text{As}$ ternaries have been discussed in more detail in Adachi [1,11].

(d) Dilute-nitride III-(V, V) alloy

A strong negative differential velocity effect has been observed in dilute-nitride $\text{GaN}_x\text{As}_{1-x}$ [28]. This phenomenon occurs when electrons are accelerated by an electric field in the high nonparabolic CB of $\text{GaN}_x\text{As}_{1-x}$ and is fundamentally different from those observed in transferred-electron devices and Bloch oscillations in SL.

12.3.3 III-V Semiconductor Quaternary Alloy

The high-field transport properties of $\text{Ga}_x\text{In}_{1-x}\text{P}_y\text{As}_{1-y}/\text{InP}$ have been investigated both theoretically and experimentally [11]. A variety of theoretical calculations have given a fundamental understanding of the subject. The calculated peak drift velocity and field were

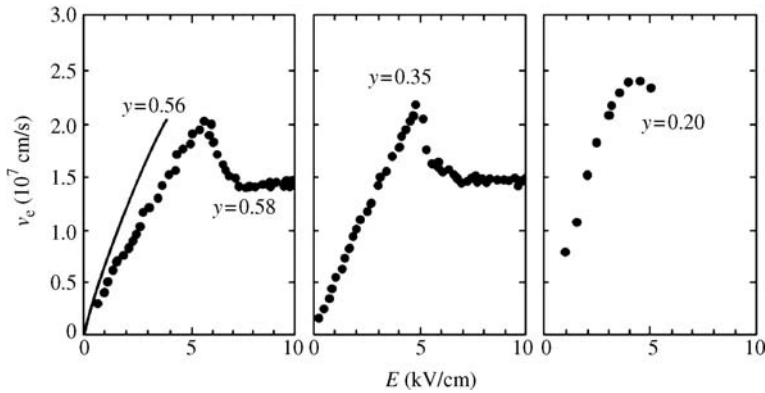


Figure 12.18 Electron velocity versus field curve for $\text{Ga}_x\text{In}_{1-x}\text{P}_y\text{As}_{1-y}/\text{InP}$ with $y = 0.20\text{--}0.58$ (see Adachi [11])

strongly dependent on the degree of alloy scattering. The example in Figure 12.18 shows the $v_e - E$ curves for $\text{Ga}_x\text{In}_{1-x}\text{P}_y\text{As}_{1-y}/\text{InP}$ with $y = 0.20, 0.35, 0.56$ and 0.58 [11]. There is a considerable difference between the $y = 0.56$ and 0.58 data. This may be a result of the difference in the low-field mobilities. It can be seen that the drift velocity v initially rises with increasing E at a rate characteristic of low-field Hall mobility μ_H , $v = \mu_H E / \gamma$, where γ is the Hall factor [2].

12.3.4 II–VI Semiconductor Alloy

No detailed studies on high-field transport phenomena in II–VI semiconductor alloys have been reported.

12.4 MINORITY-CARRIER TRANSPORT

12.4.1 Group-IV Semiconductor Alloy

(a) SiGe binary alloy

The minority-electron mobility for $\text{Si}_x\text{Ge}_{1-x}$ has been measured on $n\text{pn}$ $\text{Si}_x\text{Ge}_{1-x}/\text{Si}$ HBTs with pseudomorphic p -type $\text{Si}_x\text{Ge}_{1-x}$ base layers ($0.6 \leq x \leq 0.8$, $p \sim 8 \times 10^{19} \text{ cm}^{-3}$) [29]. These results have been plotted in Figure 12.19 together with those for Si ($p \sim 8 \times 10^{19} \text{ cm}^{-3}$). The majority-carrier mobilities for Si and Ge ($n \sim 8 \times 10^{19} \text{ cm}^{-3}$) are also plotted in Figure 12.19 by the open circles. The endpoint mobility data were taken from Adachi [30]. Rieh *et al.* [29] also measured the minority-electron mobility as a function of temperature and observed a sharp increase with decreasing temperature.

The minority-electron lifetime in $\text{Si}_x\text{Ge}_{1-x}$ has been measured by several authors (see Chakraborty *et al.* [31]). The data scatter widely from ~ 1.5 to $700 \mu\text{m}$. More recently, Ulyashin *et al.* [32] determined the minority-electron lifetime in Czochralski-grown $\text{Si}_x\text{Ge}_{1-x}$ ($x \geq 0.93$) and found a dramatic decrease with increasing Ge content.

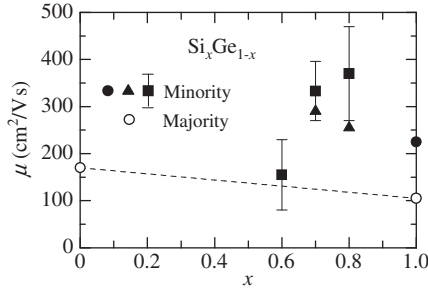


Figure 12.19 Minority-electron mobility μ for $\text{Si}_x\text{Ge}_{1-x}$ measured on npn $\text{Si}_x\text{Ge}_{1-x}/\text{Si}$ HBTs by Rieh *et al.* [29] ($p \sim 8 \times 10^{19} \text{ cm}^{-3}$). The solid triangles and squares are determined using a magnetotransport and a cut-off frequency technique, respectively. The solid and open circles show the minority-electron and majority-electron mobilities for Si and Ge ($n \sim 8 \times 10^{19} \text{ cm}^{-3}$) [30]

(b) CSiGe ternary alloy

The minority-electron lifetime in $\text{C}_x\text{Si}_y\text{Ge}_{1-x-y}$ has been measured by several authors [33–36]. These studies suggest that the lifetime τ decreases dramatically or weakly due to C incorporation, e.g. $\tau \sim 0.1\text{--}0.2 \mu\text{s}$ for a layer of $x = 1$ at% and $y = 0.88$ which is two orders of magnitude smaller than that obtained in SiGe layers [36]. In contrast, no clear degradation of lifetime was observed with the addition of 1–2 at% C ($\tau \sim 22\text{--}35 \text{ ns}$) [33].

12.4.2 III–V Semiconductor Ternary Alloy

(a) (III, III)–N alloy

The minority-hole diffusion length L in $w\text{-Ga}_x\text{In}_{1-x}\text{N}$ ($x = 0\text{--}0.79$) has been measured on undoped and Si-doped samples [37]. The values for undoped samples varied from 0.3 to 10.5 μm and exhibited no correlation with x . On the other hand, the diffusion lengths for doped samples increased with increasing x from 0.4 ($n \sim 7 \times 10^{18} \text{ cm}^{-3}$) to 15.9 μm ($n \sim 1 \times 10^{17} \text{ cm}^{-3}$). The corresponding lifetimes varied between 0.2 ns and 16 μs .

The minority-electron and minority-hole diffusion lengths in p - and n -type $w\text{-Ga}_x\text{In}_{1-x}\text{N}$ have been determined using an electron-beam-induced current technique [38]. These results are reproduced in Figure 12.20. The minority-electron diffusion length is little affected by x and decreased with increasing acceptor (Mg) doping concentration, while the minority-hole diffusion length is little affected by the donor (Si) doping concentration but increases slightly with increasing x .

(b) (III, III)–As alloy

Levine *et al.* [39,40] measured the electron velocity in a compositionally graded $p\text{-Al}_x\text{Ga}_{1-x}\text{As}$ layer using a pump-probe technique. The minority-electron velocity of $\sim 2.5 \times 10^7 \text{ cm/s}$ was obtained in a 0.42 μm -thick strongly graded (a quasi-electric field of 8.8 kV/cm) and highly doped ($p = 4 \times 10^{18} \text{ cm}^{-3}$) $\text{Al}_x\text{Ga}_{1-x}\text{As}$ layer from $x = 0.3$ to 0 [40]. This velocity is an order of magnitude higher than that for a quasi-electric field of 1.2 kV/cm ($\sim 2.3 \times 10^6 \text{ cm/s}$) [39].

Ahrenkiel [41] reviewed the minority-carrier lifetime and diffusion length in $\text{Al}_x\text{Ga}_{1-x}\text{As}$. The carrier lifetime in $\text{Al}_x\text{Ga}_{1-x}\text{As}$ is found to be controlled by a defect or nonradiative

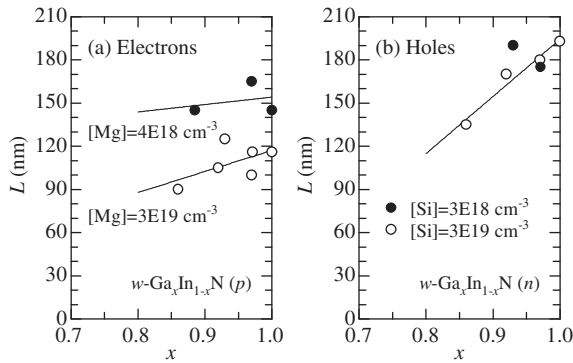


Figure 12.20 Minority-electron and minority-hole diffusion lengths in L (a) p -type and (b) n -type $w\text{-Ga}_x\text{In}_{1-x}\text{N}$ measured by Kumakura *et al.* [38]. The solid lines are drawn only as a guide for the eye

Shockley–Read–Hall recombination mechanism. It appears to be dependent on the epitaxial growth technique, as well as the Al composition. The data indicate that the lifetime may rapidly increase near the direct–indirect crossover composition $x \sim 0.4$. The bulk lifetime of $8.8 \mu\text{s}$ in $\text{Al}_{0.23}\text{Ga}_{0.77}\text{As}$ is still among the highest reported for this material [42].

The minority-electron and minority-hole drift velocities in p - and $n\text{-Ga}_{0.47}\text{In}_{0.53}\text{As}$ layers were measured by Degani *et al.* [43] and Hill *et al.* [44], respectively. A low-field drift mobility of $6000 \text{ cm}^2/\text{V s}$ for $p \sim 10^{17} \text{ cm}^{-3}$ and a high-field drift velocity of $2.6 \times 10^7 \text{ cm/s}$ at 7.5 kV/cm were observed [43]. The minority-hole drift velocity was also found to be relatively constant at $(4.8 \pm 0.2) \times 10^6 \text{ cm/s}$ for $E = 54\text{--}108 \text{ kV/cm}$, indicating that velocity saturation occurs at fields below 54 kV/cm [44]. Chand [45] reviewed the minority-carrier lifetime and diffusion length in strained and lattice-matched $\text{Ga}_x\text{In}_{1-x}\text{As}$ layers. More recently, Vignaud *et al.* [46] measured the minority-electron lifetime τ in $p\text{-Ga}_{0.47}\text{In}_{0.53}\text{As}$ and obtained the relationship $\tau = Cp^{-2}$ where $C = 1.2 \times 10^{28} \text{ s/cm}^6$ and p is measured in cm^{-3} .

(c) Ga–(V, V) alloy

Vignaud *et al.* [46] measured the minority-electron lifetime τ in $p\text{-Ga}_{0.51}\text{In}_{0.49}\text{Sb}$ and obtained the relationship of $\tau = Cp^{-2}$ where $C = 2.5 \times 10^{28} \text{ s/cm}^6$ and p is measured in cm^{-3} . This value is almost twice as large than that in $p\text{-Ga}_{0.47}\text{In}_{0.53}\text{As}$ (Section 12.4.2(b)).

12.4.3 III–V Semiconductor Quaternary Alloy

(a) (III, III)–(V, V) alloy

While poor lifetimes have limited the applicability of dilute-nitride materials in photovoltaic applications, Welser *et al.* [47] achieved minority-carrier characteristics that approach those of conventional GaAs/AlGaAs HBTs. They found that a combination of growth algorithm optimization and compositional grading is critical for improving minority-carrier properties in dilute-nitride $\text{Ga}_x\text{In}_{1-x}\text{N}_y\text{As}_{1-y}$. The minority-carrier lifetime was also found to be inversely proportional to not only nitrogen but also to carbon acceptor doping.

Information on minority-carrier lifetime and diffusion length is available for $\text{Ga}_x\text{In}_{1-x}\text{P}_y\text{As}_{1-y}$ quaternary [48–50]. The minority-carrier lifetime and diffusion length in $\text{Ga}_x\text{In}_{1-x}\text{As}_y\text{Sb}_{1-y}$ have

also been determined using various techniques, such as transient PR and time-resolved PL [51–54], or by fabricating light-emitting diodes, photodetectors, etc. [55,56].

(b) (III, III, III)–V alloy

A value of $170 \pm 10 \text{ cm}^2/\text{V s}$ for the minority-electron mobility in $p\text{-(Al}_x\text{Ga}_{1-x})_{0.53}\text{In}_{0.47}\text{P}/\text{GaAs}$ has been obtained using a time-of-flight method [57]. Time-resolved PL has also been used to determine the minority-carrier lifetime in $(\text{Al}_x\text{Ga}_{1-x})_{0.53}\text{In}_{0.47}\text{P}/\text{GaAs}$ as a function of temperature between 100 and 325 K [58]. A monotonic reduction in the lifetime is observed at all temperatures with increasing x . Different temperature dependence of the lifetime between high and low x fraction samples has also been observed [58].

12.4.4 II–VI Semiconductor Alloy

The minority-electron transport in $p\text{-Mg}_{0.1}\text{Zn}_{0.9}\text{O}$ has been studied under local electron-beam irradiation [59]. The irradiation resulted in an increase of up to 25% in minority-electron diffusion length from the initial value of $\sim 2.12 \mu\text{m}$.

The minority-electron diffusion length in $p\text{-Zn}_x\text{Cd}_{1-x}\text{Te}$ has been measured by several authors [60,61]. The results are: $2.2\text{--}3.8 \mu\text{m}$ for $x = 0.01\text{--}1.00$ ($p \sim 10^{14}\text{--}10^{15} \text{ cm}^{-3}$) [60]; $\sim 6\text{--}15 \mu\text{m}$ for $x = 0.1$ ($p \sim 4 \times 10^{13}\text{--}4 \times 10^{16} \text{ cm}^{-3}$) [61].

Photoconductive decay has been used to determine minority-hole lifetime in $n\text{-Zn}_x\text{Hg}_{1-x}\text{Te}$ and its dependence on surface passivation [62]. The measured value showed good agreement with the summation of the values for the Auger and Shockly–Read–Hall lifetimes.

The lifetimes and diffusion lengths for bulk and epitaxial, doped and undoped $\text{Cd}_x\text{Hg}_{1-x}\text{Te}$ samples have been reviewed by several authors [63]. The Shockly–Read–Hall recombination plays a dominant role in limiting the lifetime at low temperatures. There is a large range of diffusion lengths for any given composition and carrier concentration. The likely cause is a corresponding variation in the carrier lifetime.

12.5 IMPACT IONIZATION COEFFICIENT

12.5.1 Group-IV Semiconductor Alloy

Impact ionization by hot carriers in an electric field is characterized by the ionization coefficients α for electrons and β for holes, which give the number of secondary carriers created by an initial hot carrier per cm of travel in an electric field E .

In Si, α is greater than β at 330 kV/cm. In Ge, β is larger than α at the same electric field due to the small hole effective mass which allows the holes to gain energy more easily than in Si. The β/α ratio for $\text{Si}_x\text{Ge}_{1-x}$ at $E = 330 \text{ kV/cm}$ [64] is shown in Figure 12.21. It can be seen that the ratio decreases with increasing x , in agreement with the theoretical prediction [65].

12.5.2 III–V Semiconductor Ternary Alloy

(a) (III, III)–N alloy

Some authors have carried out experiments to determine the impact ionization coefficient in GaN [66] and $\text{Al}_{0.4}\text{Ga}_{0.6}\text{N}$ [67]. The ionization coefficient can be usually fitted by

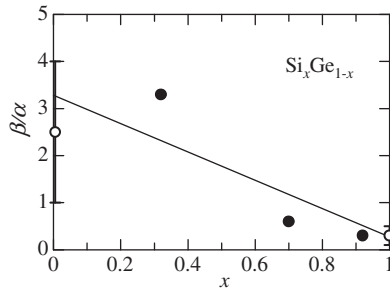


Figure 12.21 β/α ratio for $\text{Si}_x\text{Ge}_{1-x}$ at $E = 330 \text{ kV/cm}$. The experimental data are taken from Lee *et al.* [64]. The open circles represent the endpoint data [30]

$$\alpha(E) \text{ or } \beta(E) = A \exp\left(-\frac{B}{E}\right)^m \quad (12.4)$$

where $m = 1$ for the low electric field in the avalanche region and $m = 2$ for the higher electric field [2]. The A and B observed for $\text{Al}_{0.4}\text{Ga}_{0.6}\text{N}$ are $A = 6.0 \times 10^5 \text{ cm}^{-1}$ ($3.4 \times 10^6 \text{ cm}^{-1}$) and $B = 3.6 \times 10^6 \text{ V/cm}$ ($7.9 \times 10^6 \text{ V/cm}$) for α (β) with $m = 1$ [67].

(b) (III, III)–P alloy

The α (β) parameters in Equation (12.4) for $\text{Ga}_{0.52}\text{In}_{0.48}\text{P/GaAs}$ reported by Fu *et al.* [68] and Ghin *et al.* [69] are, respectively, $A = 3.85 \times 10^6 \text{ cm}^{-1}$ ($1.71 \times 10^6 \text{ cm}^{-1}$) and $B = 3.71 \times 10^6 \text{ V/cm}$ ($3.19 \times 10^6 \text{ V/cm}$) with $m = 1.0$ (1.0) and $A = 4.57 \times 10^5 \text{ cm}^{-1}$ ($4.73 \times 10^5 \text{ cm}^{-1}$) and $B = 1.413 \times 10^6 \text{ V/cm}$ ($1.425 \times 10^6 \text{ V/cm}$) with $m = 1.73$ (1.65). The experimental α and β values for $\text{Ga}_{0.52}\text{In}_{0.48}\text{P/GaAs}$ are significantly smaller than those for GaAs.

(c) (III, III)–As alloy

The impact ionization coefficients α and β for $\text{Al}_x\text{Ga}_{1-x}\text{As}$ have been studied by many authors [1,70–73]. These data suggest that $\alpha \geq \beta$ for $0 \leq x \leq 0.88$. A recent study reports that the ionization coefficients converge as x increases from 0.36 to 0.61 but become very different at higher x , resulting in a small β/α ratio for $x \geq 0.63$ [73].

The impact ionization phenomena in $\text{Al}_{0.48}\text{In}_{0.52}\text{As/InP}$ have been studied by several authors (see Goh *et al.* [74]). The parameterized ionization coefficients are: $A = 2.10 \times 10^6 \text{ cm}^{-1}$, $B = 1.62 \times 10^6 \text{ V/cm}$ and $m = 1.29$ (α); $A = 2.40 \times 10^6 \text{ cm}^{-1}$, $B = 1.86 \times 10^6 \text{ V/cm}$ and $m = 1.36$ (β) [74].

The anomalous temperature dependence of the electron impact ionization coefficient in $\text{Ga}_{0.47}\text{In}_{0.53}\text{As/InP}$ has been investigated both experimentally and theoretically. The positive temperature coefficient of α was proposed by Ritter *et al.* [75] to explain the reduction in the common-emitter breakdown voltage of $\text{Ga}_{0.47}\text{In}_{0.53}\text{As/InP}$ HBTs with increasing temperature. Malik *et al.* [76] also observed a reduction in the common-emitter breakdown voltage with increasing temperature and ascribed it to the effect of collector leakage. Neviani *et al.* [77] confirmed a positive temperature dependence of α at 125 kV/cm in $\text{Ga}_{0.47}\text{In}_{0.53}\text{As}$ and explained in terms of the band-gap reduction with temperature. Figure 12.22 shows the temperature-dependent $\text{Ga}_{0.47}\text{In}_{0.53}\text{As}$ data, along with those for GaAs [77].

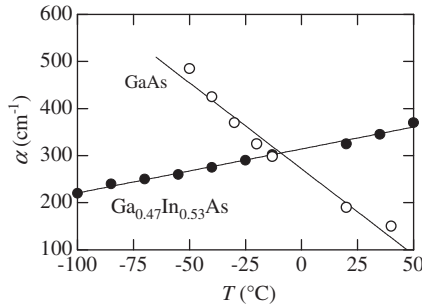


Figure 12.22 Electron impact ionization coefficient α versus temperature T for $\text{Ga}_{0.47}\text{In}_{0.53}\text{As}$ at a fixed field $E = 125 \text{ kV/cm}$ and for GaAs at $E = 225 \text{ kV/cm}$. [Reprinted with permission from A. Neviani, G. Meneghesso, E. Zanoni, M. Hafizi, and C. Canali, *IEEE Electron Dev. Lett.* **18**, 619–621 (1997); Copyright (1997) IEEE]

In contrast, Yee *et al.* [78] observed a negative temperature dependence of α in $\text{Ga}_{0.47}\text{In}_{0.53}\text{As}/\text{InP}$ *p-i-n* diodes at E over 200 kV/cm . Subsequently, Ng *et al.* [79] found a positive temperature dependence of α in $\text{Ga}_{0.47}\text{In}_{0.53}\text{As}$ *p-i-n* diodes at low electric fields, below $\sim 200 \text{ kV/cm}$, but a negative dependence at high fields. The hole ionization coefficient β showed little change with temperature.

Theoretically, the weak field dependence of α was predicted by Bude and Hess [80], who explained this anomalous behavior in terms of the DOS in the Γ - and satellite-valley CBs of $\text{Ga}_{0.47}\text{In}_{0.53}\text{As}$. Isler [81] argued that phonon-assisted impact ionization can be important in $\text{Ga}_{0.47}\text{In}_{0.53}\text{As}$ and leads to the positive temperature coefficient of α at low electric fields. The Monte-Carlo technique has also been used to analyze the electric field and temperature dependence of α in $\text{Ga}_{0.47}\text{In}_{0.53}\text{As}$ using a three-valley [82] and a four-valley model [83].

The experimental α and β for $\text{Ga}_{0.47}\text{In}_{0.53}\text{As}$ are found to have the relationship $\alpha > \beta$ [78,84]. The α and β coefficients for strained $\text{Ga}_{0.2}\text{In}_{0.8}\text{As}$ have also been measured by fabricating lateral *p-i-n* diodes [85]. The results indicate that both α and β are larger than those for GaAs and furthermore β is larger than α .

(d) (III, III)-Sb alloy

Hildebrand *et al.* [86] reported resonance enhancement of β in a low field region for $\text{Al}_x\text{Ga}_{1-x}\text{Sb}$ with $x = 0.065$ where E_0 is equal to Δ_0 (Figure 6.25). The β/α ratio exceeded 20. Zhingarev *et al.* [87] also measured α , β and their ratio for $\text{Al}_x\text{Ga}_{1-x}\text{Sb}$ ($x = 0-0.23$). Kuwatsuka *et al.* [88] observed no strong enhancement of β/α in $\text{Al}_x\text{Ga}_{1-x}\text{Sb}$ near $x = 0.06$. The β/α ratio obtained by Kuwatsuka *et al.* was ~ 5 at the low electric field of $1.6 \times 10^5 \text{ V/cm}$. More recently, Gouskov *et al.* [89] studied the impact ionization phenomena in $\text{Al}_x\text{Ga}_{1-x}\text{Sb}$ at $x = 0, 0.04$ and 0.08 and obtained a maximum β/α at $x = 0.04$.

Theoretically, Rmou *et al.* [90] showed that if the alloy disorder in $\text{Al}_x\text{Ga}_{1-x}\text{Sb}$ is neglected, β exhibits a continuous variation with Δ_0/E_0 ; if not, β is strongly increased and shows a maximum at $x = 0.02$.

(e) Dilute-nitride III-(V, V) alloy

A *p-i-n* avalanche photodiode using $\text{GaN}_x\text{As}_{1-x}/\text{GaAs}$ was demonstrated [91]. The β/α ratio obtained was 0.4.

(f) Ga-(V, V) alloy

The α and β values were determined for $\text{GaAs}_x\text{Sb}_{1-x}$ ($x = 0.875$ and 0.90) at 77 and 300 K [92]. The β/α ratios reported were ~ 0.3 at 300 K ($x = 0.875$), ~ 0.4 at 77 K and ~ 0.6 at 300 K ($x = 0.90$).

(g) In-(V, V) alloy

The impact ionization coefficients for $\text{InAs}_{0.12}\text{Sb}_{0.88}$ were investigated and it was found that β is about 5 times larger than α in the field $E = (4 - 6) \times 10^4$ V/cm [93].

12.5.3 III-V Semiconductor Quaternary Alloy**(a) (III, III)-(V, V) alloy**

The α and β values at high electric fields (> 180 kV/cm) for $\text{Ga}_x\text{In}_{1-x}\text{P}_y\text{As}_{1-y}/\text{InP}$ have been determined by Osaka *et al.* [94,95]. The β/α ratio versus y for $\text{Ga}_x\text{In}_{1-x}\text{P}_y\text{As}_{1-y}/\text{InP}$ [95] is reproduced in Figure 12.23. The ratio was found to increase with increasing y and to become unity, $\alpha = \beta$, at $y \sim 0.6$.

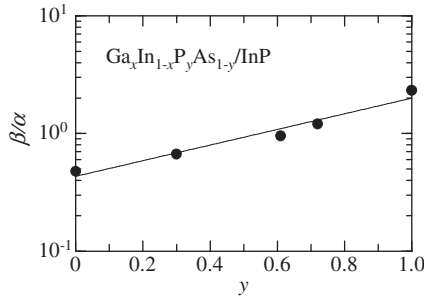


Figure 12.23 β/α ratio for $\text{Ga}_x\text{In}_{1-x}\text{P}_y\text{As}_{1-y}/\text{InP}$. The experimental data are taken from Osaka *et al.* [95]

As in $\text{Ga}_{0.47}\text{In}_{0.53}\text{As}$, anomalous low-field behavior of α was observed in $\text{Ga}_x\text{In}_{1-x}\text{P}_y\text{As}_{1-y}/\text{InP}$ [96]. No anomaly for β was observed in this quaternary [97].

The impact ionization phenomena in $\text{Ga}_{0.80}\text{In}_{0.20}\text{As}_{0.17}\text{Sb}_{0.83}/\text{GaSb}$ have been studied by fabricating mesa photodiodes [98]. The α and β values in Equation (12.4) have been determined to be $A = 2.41 \times 10^6 \text{ cm}^{-1}$ and $B = 4.45 \times 10^5 \text{ V/cm}$ with $m = 2.0$ (α) and $A = 1.98 \times 10^6 \text{ cm}^{-1}$ and $B = 3.69 \times 10^5 \text{ V/cm}$ with $m = 2.0$ (β), respectively. The resulting β/α ratio is $\sim 4-7$.

(b) (III, III, III)-V alloy

The parameterized α and β values in Equation (12.4) have been determined for $\text{Al}_{0.24}\text{Ga}_{0.24}\text{In}_{0.53}\text{As}/\text{InP}$ to be $A = 2.29 \times 10^7 \text{ cm}^{-1}$ and $B = 3.59 \times 10^6 \text{ V/cm}$ with $m = 1.0$ (α) and $A = 1.42 \times 10^7 \text{ cm}^{-1}$ and $B = 3.73 \times 10^6 \text{ V/cm}$ with $m = 1.0$ (β), respectively ($E = 400-500$ kV/cm) [99]. The relationship $\alpha > \beta$ can be predicted from these parameters. The impact ionization coefficients α and β for a strained $\text{Al}_{0.22}\text{Ga}_{0.63}\text{In}_{0.15}\text{As}$ layer grown on $\text{Al}_{0.3}\text{Ga}_{0.7}\text{As}/\text{GaAs}$ by MBE have also been determined by fabricating lateral *p-i-n* diodes [85].

12.5.4 II–VI Semiconductor Alloy

Although Brennan and Mansour [100] calculated the electron impact ionization coefficient for $\text{Cd}_x\text{Hg}_{1-x}\text{Te}$, no detailed experimental data are available for II–VI semiconductor alloys.

REFERENCES

- [1] S. Adachi, *GaAs and Related Materials: Bulk Semiconducting and Superlattice Properties*, World Scientific, Singapore, 1994.
- [2] S. Adachi, *Properties of Group-IV, III–V and II–VI Semiconductors*, John Wiley & Sons, Ltd, Chichester, 2005.
- [3] S. -K. Lin, K. -T. Wu, C. -P. Huang, C. -T. Liang, Y. H. Chang, Y. F. Chen, P. H. Chang, N. C. Chen, C. A. Chang, H. C. Peng, C. F. Shih, K. S. Liu, and T. Y. Lin, *J. Appl. Phys.* **97**, 046101 (2005).
- [4] M. P. Vaughan and B. K. Ridley, *Phys. Rev. B* **72**, 075211 (2005).
- [5] S. Fahy, A. Lindsay, H. Ouerdane, E. P. O'Reilly, *Phys. Rev. B* **74**, 035203 (2006).
- [6] A. J. Ptak, S. W. Johnston, S. Kurtz, D. J. Friedman, and W. K. Metzger, *J. Cryst. Growth* **251**, 392 (2003).
- [7] Y. G. Hong, A. Nishikawa, and C. W. Tu, *Appl. Phys. Lett.* **83**, 5446 (2003).
- [8] Y. -S. Kang, L. H. Robins, A. G. Birdwell, A. J. Shapiro, W. R. Thurber, M. D. Vaudin, M. M. E. Fahmi, D. Bryson, and S. N. Mohammad, *J. Appl. Phys.* **98**, 093714 (2005).
- [9] N. Miyashita, Y. Shimizu, and Y. Okada, *J. Appl. Phys.* **102**, 044904 (2007).
- [10] G. M. Peake, K. E. Waldrip, T. W. Hargett, N. A. Modine, and D. K. Serkland, *J. Cryst. Growth* **261**, 398 (2004).
- [11] S. Adachi, *Physical Properties of III–V Semiconductor Compounds: InP, InAs, GaAs, GaP, InGaAs, and InGaAsP*, John Wiley & Sons Ltd, New York, 1992.
- [12] Y. Liu, H. Jiang, T. Egawa, B. Zhang, and H. Ishikawa, *J. Appl. Phys.* **99**, 123702 (2006).
- [13] M. Sotoodeh, A. H. Khalid, and A. A. Rezazadeh, *J. Appl. Phys.* **87**, 2890 (2000).
- [14] T. Hofmann, G. Leibiger, V. Gottschalch, I. Pietzonka, and M. Schubert, *Phys. Rev. B* **64**, 155206 (2001).
- [15] Z. P. Wei, B. Yao, Z. Z. Zhang, Y. M. Lu, D. Z. Shen, B. H. Li, X. H. Wang, J. Y. Zhang, D. X. Zhao, X. W. Fan, and Z. K. Tang, *Appl. Phys. Lett.* **89**, 102104 (2006).
- [16] K. Perzyńska, F. Firszt, S. Łęgowski, H. Męczyńska, J. Szatkowski, M. Biernacka, A. Gajlewicz, S. Tarasenko, and P. Zaleski, *J. Cryst. Growth* **214/215** 904 (2000).
- [17] W. Dobrowolski, R. R. Gałazka, E. Grodzicka, J. Kossut, and B. Witkowska, *Phys. Rev. B* **48**, 17848 (1993).
- [18] J. C. Erickson, H. W. Yao, R. B. James, H. Hermon, and M. Greaves, *J. Electron. Mater.* **29**, 699 (2000).
- [19] R. W. Miles, in *Properties of Narrow Gap Cadmium-based Compounds*, EMIS Datareviews Series No. 10 (edited by P. Capper), INSPEC, London, 1994, p. 221.
- [20] A. F. M. Anwar, S. Wu, and R. T. Webster, *IEEE Trans. Electron Dev.* **48**, 567 (2001).
- [21] E. Bellotti, F. Bertazzi, and M. Goano, *J. Appl. Phys.* **101**, 123706 (2007).
- [22] R. Sakamoto, K. Nakata, and S. Nakajima, *Physica B* **272**, 250 (1999).
- [23] M. Yee, P. A. Houston, and J. P. R. David, *J. Appl. Phys.* **91**, 1601 (2002).
- [24] P. K. Bhattacharya, U. Das, and M. J. Ludowise, *Phys. Rev. B* **29**, 6623 (1984).
- [25] K. Brennan and K. Hess, *J. Appl. Phys.* **59**, 964 (1986).
- [26] V. Balynas, A. Krotkus, A. Stalnonis, A. T. Gorelionok, N. M. Shmidt, and J. A. Tellefsen, *Appl. Phys. A* **51**, 357 (1990).
- [27] D. Hahn and A. Schlachetzki, *J. Electron. Mater.* **21**, 1147 (1992).

- [28] A. Patanè, A. Ignatov, D. Fowler, O. Makarovskiy, L. Eaves, L. Geelhaar, and H. Riechert, *Phys. Rev. B* **72**, 033312 (2005).
- [29] J. -S. Rieh, P. K. Bhattacharya, and E. T. Croke, *IEEE Trans. Electron Dev.* **47**, 883 (2000).
- [30] S. Adachi, *Handbook on Physical Properties of Semiconductors: Volume 1 Group IV Semiconductors*, Kluwer Academic, Boston, 2004.
- [31] S. Chakraborty, M. K. Bera, S. Bhattacharya, P. K. Bose, and C. K. Maiti, *Thin Solid Films* **504**, 73 (2006).
- [32] A. G. Ulyashin, N. V. Abrosimov, A. Bentzen, A. Suphellen, E. Saunar, and B. G. Svensson, *Mater. Sci. Semicond. Process.* **9**, 772 (2006).
- [33] R. Shivaram, G. Niu, J. D. Cressler, and E. T. Croke, *Solid-State Electron.* **44**, 559 (2000).
- [34] S. K. Samanta, S. Maikap, S. Chatterjee, and C. K. Maiti, *Solid-State Electron.* **47**, 893 (2003).
- [35] M. S. Carroll and C. A. King, *J. Appl. Phys.* **93**, 1656 (2003).
- [36] I. Z. Mitrovic, O. Buii, S. Hall, J. Zhang, Y. Wang, P. L. F. Hemment, H. A. W. El Mubarek, and P. Ashburn, *Semicond. Sci. Technol.* **20**, 95 (2005).
- [37] A. Cremades, M. Albrecht, J. Krinke, R. Dimitrov, M. Stutzmann, and H. P. Strunk, *J. Appl. Phys.* **87**, 2357 (2000).
- [38] K. Kumakura, T. Makimoto, N. Kobayashi, T. Hashizume, T. Fukui, and H. Hasegawa, *J. Cryst. Growth* **298**, 787 (2007).
- [39] B. F. Levine, W. T. Tsang, C. G. Bethea, and F. Capasso, *Appl. Phys. Lett.* **41**, 470 (1982).
- [40] B. F. Levine, C. G. Bethea, W. T. Tsang, F. Capasso, K. K. Thornber, R. C. Fulton, and D. A. Kleinman, *Appl. Phys. Lett.* **42**, 769 (1983).
- [41] R. K. Ahrenkiel, in *Properties of Aluminium Gallium Arsenide*, EMIS Datareviews Series No. 7 (edited by S. Adachi), INSPEC, London, 1993, p. 221.
- [42] R. A. J. Thomeer, P. R. Hageman, and L. J. Giling, *Appl. Phys. Lett.* **64**, 1561 (1994).
- [43] J. Degani, R. F. Leheny, R. E. Nahory, and J. P. Heritage, *Appl. Phys. Lett.* **39**, 569 (1981).
- [44] P. Hill, J. Schlafer, W. Powazinik, E. Eichen, and R. Olshansky, *Appl. Phys. Lett.* **50**, 1260 (1987).
- [45] N. Chand, in *Properties of Lattice-matched and Strained Indium Gallium Arsenide*, EMIS Datareviews Series No. 8 (edited by P. Bhattacharya), INSPEC, London, 1993, p. 127.
- [46] D. Vignaud, D. A. Yarekha, J. F. Lampin, M. Zaknounge, S. Godey, and F. Mollot, *Appl. Phys. Lett.* **90**, 242104 (2007).
- [47] R. E. Welsler, R. S. Setzko, K. S. Stevens, E. M. Rehder, C. R. Lutz, D. S. Hill, and P. J. Zampardi, *J. Phys. Condens. Matter* **16**, S3373 (2004).
- [48] S. Sakai, M. Umeno, and Y. Amemiya, *Jpn. J. Appl. Phys.* **19**, 109 (1980).
- [49] M. M. Tashima, L. W. Cook, and G. E. Stillman, *J. Electron. Mater.* **11**, 831 (1982).
- [50] C. H. Henry, B. F. Levine, R. A. Logan, and C. G. Bethea, *IEEE J. Quantum. Electron.* **QE-19**, 905 (1983).
- [51] J. M. Borrego, S. Saroop, R. J. Gutmann, G. W. Charache, T. Donovan, P. F. Baldasaro, and C. A. Wang, *J. Appl. Phys.* **89**, 3753 (2001).
- [52] D. Donetsky, S. Anikeev, G. Belenky, S. Luryi, C. A. Wang, and G. Nichols, *Appl. Phys. Lett.* **81**, 4769 (2002).
- [53] S. Anikeev, D. Donetsky, G. Belenky, S. Luryi, C. A. Wang, J. M. Borrego, and G. Nichols, *Appl. Phys. Lett.* **83**, 3317 (2003).
- [54] C. A. Wang, D. A. Shiau, D. Donetsky, S. Anikeev, G. Belenky, and S. Luryi, *Appl. Phys. Lett.* **86**, 101910 (2005).
- [55] T. N. Danilova, B. E. Zhurtanov, A. N. Imenkov, and Y. P. Yakovlev, *Semicond.* **39**, 1235 (2005).
- [56] V. Bhagwat, Y. G. Xiao, I. Bhat, P. Dutta, T. F. Refaat, M. N. Abedin, and V. Kumar, *J. Electron. Mater.* **35**, 1613 (2006).
- [57] S. A. Wood, C. H. Molloy, P. M. Smowton, P. Blood, and C. C. Button, *IEEE J. Quantum Electron.* **36**, 742 (2000).
- [58] P. C. Mogenssen, G. Jones, N. Cain, P. Blood, D. J. Mowbray, S. W. Bland, D. Peggs, and R. P. Petrie, *Inst. Phys. Conf. Ser.* **162**, 161 (1999).

- [59] O. Lopatiuk, W. Burdett, L. Chernyak, K. P. Ip, Y. W. Heo, D. P. Norton, S. J. Pearton, B. Hertog, P. P. Chow, and A. Osinsky, *Appl. Phys. Lett.* **86**, 012105 (2005).
- [60] P. Lemasson, A. Forveille-Boutry, and R. Triboulet, *J. Appl. Phys.* **55**, 592 (1984).
- [61] J. Franc, P. Höschl, E. Belas, R. Grill, P. Hlídek, P. Moravec, and J. Bok, *Nucl. Instrum. Methods Phys. Res. A* **434**, 146 (1999).
- [62] K. N. Oh, K. H. Kim, J. K. Hong, Y. C. Chung, S. U. Kim, and M. J. Park, *J. Cryst. Growth* **184**, 1247 (1998).
- [63] P. Capper, Y. Nemirovsky, R. Fastow, C. L. Jones, in *Properties of Narrow Gap Cadmium-based Compounds*, EMIS Datareviews Series No. 10 (edited by P. Capper), INSPEC, London, 1994, pp. 227–241.
- [64] J. Lee, A. L. Gutierrez-Aitken, S. H. Li, and P. K. Bhattacharya, *IEEE Trans. Electron Dev.* **43**, 977 (1996).
- [65] K. Yeom, J. M. Hinckley, and J. Singh, *J. Appl. Phys.* **80**, 6773 (1996).
- [66] K. Kunihiro, K. Kasahara, Y. Takahashi, and Y. Ohno, *IEEE Electron Dev. Lett.* **20**, 608 (1999).
- [67] T. Tut, M. Gokkavas, B. Butun, S. Butun, E. Ulker, and E. Ozbay, *Appl. Phys. Lett.* **89**, 183524 (2006).
- [68] S. -L. Fu, T. P. Chin, M. C. Ho, C. W. Tu, and P. M. Asbeck, *Appl. Phys. Lett.* **66**, 3507 (1995).
- [69] R. Ghin, J. P. R. David, S. A. Plimmer, M. Hopkinson, G. J. Rees, D. C. Herbert, and D. R. Wight, *IEEE Trans. Electron Dev.* **45**, 2096 (1998).
- [70] C. K. Chia, J. P. R. David, G. J. Rees, S. A. Plimmer, R. Grey, and P. N. Robson, *J. Appl. Phys.* **84**, 4363 (1998).
- [71] S. A. Plimmer, J. P. R. David, R. Grey, and G. J. Rees, *IEEE Trans. Electron Dev.* **47**, 1089 (2000).
- [72] X. G. Zheng, P. Yuan, X. Sun, G. S. Kinsey, A. L. Holmes, B. G. Streetman, and J. C. Campbell, *IEEE J. Quantum Electron.* **36**, 1168 (2000).
- [73] B. K. Ng, J. P. R. David, G. J. Rees, R. C. Tozer, M. Hopkinson, and R. J. Airey, *IEEE Trans. Electron Dev.* **49**, 2349 (2002).
- [74] Y. L. Goh, A. R. J. Marshall, D. J. Massey, J. S. Ng, C. H. Tan, M. Hopkinson, J. P. R. David, S. K. Jones, C. C. Button, and S. M. Pinches, *IEEE J. Quantum Electron.* **43**, 503 (2007).
- [75] D. Ritter, R. A. Hamm, A. Feyngenson, and M. B. Panish, *Appl. Phys. Lett.* **60**, 3150 (1992).
- [76] R. J. Malik, N. Chand, J. Nagle, R. W. Ryan, K. Alavi, and A. Y. Cho, *IEEE Electron Dev. Lett.* **13**, 557 (1992).
- [77] A. Neviani, G. Meneghesso, E. Zanoni, M. Hafizi, and C. Canali, *IEEE Electron Dev. Lett.* **18**, 619 (1997).
- [78] M. Yee, J. P. R. David, P. A. Houston, C. H. Tan, and A. Krysa, *IEEE Trans. Electron Dev.* **50**, 2021 (2003).
- [79] W. K. Ng, C. H. Tan, J. P. R. David, P. A. Houston, M. Yee, and J. S. Ng, *Appl. Phys. Lett.* **83**, 2820 (2003).
- [80] J. Bude and K. Hess, *J. Appl. Phys.* **72**, 3554 (1992).
- [81] M. Isler, *Phys. Rev. B* **63**, 115209 (2001).
- [82] C. H. Tan, G. J. Rees, P. A. Houston, J. S. Ng, W. K. Ng, and J. P. R. David, *Appl. Phys. Lett.* **84**, 2322 (2004).
- [83] K. Y. Choo and D. S. Ong, *J. Appl. Phys.* **98**, 023714 (2005).
- [84] J. S. Ng, C. H. Tan, J. P. R. David, G. Hill, and G. J. Rees, *IEEE Trans. Electron Dev.* **50**, 901 (2003).
- [85] Y. C. Chen and P. K. Bhattacharya, *J. Appl. Phys.* **73**, 465 (1993).
- [86] O. Hildebrand, W. Kuebart, and M. H. Pilkuhn, *Appl. Phys. Lett.* **37**, 801 (1980).
- [87] M. Z. Zhingarev, V. I. Korol'kov, M. P. Mikhailova, and V. V. Sazonov, *Sov. Tech. Phys. Lett.* **7**, 637 (1981).
- [88] H. Kuwatsuka, T. Mikawa, S. Miura, N. Yasuoka, M. Ito, T. Tanahashi, and O. Wada, *J. Appl. Phys.* **70**, 2169 (1991).
- [89] L. Gousskov, B. Orsal, M. Pérotin, M. Karim, A. Sabir, P. Coudray, S. Kibeya, and H. Luquet, *Appl. Phys. Lett.* **60**, 3030 (1992).

- [90] A. Rmou, H. Luquet, L. Gousskov, M. Perotin, and P. Coudray, *Jpn. J. Appl. Phys.* **33**, 4657 (1994).
- [91] G. S. Kinsey, D. W. Gotthold, A. L. Holmes, Jr., B. G. Streetman, and J. C. Campbell, *Appl. Phys. Lett.* **76**, 2824 (2000).
- [92] V. M. Andreev, M. Z. Zhingarev, O. O. Ivent'eva, V. I. Korol'kov, and M. P. Mikhaïlova, *Sov. Phys. Semicond.* **15**, 701 (1981).
- [93] B. A. Matveev, M. P. Mikhaïlova, S. V. Slobodchikov, N. N. Smirnova, N. M. Stus', and G. N. Talalakin, *Sov. Phys. Semicond.* **13**, 294 (1979).
- [94] F. Osaka, T. Mikawa, and T. Kaneda, *Appl. Phys. Lett.* **46**, 1138 (1985).
- [95] F. Osaka, T. Mikawa, and T. Kaneda, *IEEE J. Quantum Electron.* **QE-21**, 1326 (1985).
- [96] N. Shamir and D. Ritter, *IEEE Trans. Electron Dev.* **47**, 488 (2000).
- [97] N. Shamir and D. Ritter, *IEEE Electron Dev. Lett.* **21**, 509 (2000).
- [98] I. A. Andreev, M. P. Mikhaïlova, S. V. Mel'nikov, Y. P. Smorchkova, and Y. P. Yakovlev, *Sov. Phys. Semicond.* **25**, 861 (1991).
- [99] M. Tsuji, K. Makita, I. Watanabe, and K. Taguchi, *Appl. Phys. Lett.* **65**, 3248 (1994).
- [100] K. F. Brennan and N. S. Mansour, *J. Appl. Phys.* **69**, 7844 (1991).

Index

Page numbers in *italic* refer to figures or tables. Alloys are listed according to elemental composition.

- Abeles's model 63–4
- AlAsSb
 - band-gap energies 174–5
 - optical properties 323
 - phonon frequencies 108
 - thermal conductivity 70
- AlGaAs
 - band offsets
 - GaAs interface 278–9
 - GaN interface 278
 - band-gap energies 157–60
 - deformation potential 263–4, 269–70, 271–2
 - effective masses 239–41
 - elastic properties 90, 96
 - electro-optic constant 358, 359
 - Franz–Keldysh effect 360
 - impact ionization coefficient 383
 - low-field mobility 369, 377–8
 - microhardness 93
 - minority-carrier transport 380–1
 - nonlinear optical constant 361–2
 - optical properties 316, 317
 - phonon frequencies 106–7, 113–15, 120
 - photoelastic constant 357, 358
 - piezoelectric constant 128–9
 - thermal conductivity 68, 69
 - thermal diffusivity 75–6
- AlGaAsSb
 - band offsets
 - GaInAsSb interface 282
 - InP/InAs/GaSb interfaces 281
 - band-gap energies 187–8, 196
 - optical properties 328
 - Schottky barrier 296–7
- AlGaN
 - and coherent epitaxy 37
 - phonon frequencies 108, 109
- AlGaInAs
 - band offsets, GaInAs interface 283
 - band-gap energies 194–5
 - effective masses 250, 251
 - impact ionization coefficient 385
 - optical properties 331–2
 - Schottky barrier 298–9
 - thermal conductivity 74
- AlGaN
 - crystal lattice parameters 25, 26
 - low-field mobility 373–4
 - Schottky barrier 297–8
 - thermal conductivity 68, 69, 70
- AlGaInP
 - band offsets
 - AlInP interface 282
 - GaInP interface 282–3
 - band-gap energies 187, 191, 193–4, 196
 - effective masses 250
 - elastic properties 81, 86
 - low-field mobility 373–4
 - minority-carrier transport 382
 - optical properties 330–1
 - Schottky barrier 298
 - thermal conductivity 74
- AlGaN
 - band offsets, GaN interface 283–4
 - band-gap energies 149–51
 - and critical thickness 38
 - deformation potential 261–2, 263
 - impact ionization coefficient 382
 - low-field mobility 368, 376, 377
 - minority-carrier transport 380
 - nonlinear optical constant 361
 - optical properties 311–12
 - phonon frequencies 105–6
 - piezoelectric constant 125
 - Schottky barrier 291

- AlGaNaS
 band-gap energies 184–5
 optical properties 326–7
- AlGaP
 band-gap energies 153, 154
 effective masses 238–9
 optical properties 314
- AlGaPAs
 band-gap energies 186–7
 optical properties 326–7
- AlGaSb
 band-gap energies 163–5
 effective masses 242–3
 impact ionization coefficient 384
 lattice parameters 26, 27
 low-field mobility 369–70
 Schottky barrier 294–5
- AlInAs
 band offsets
 GaInAS interface 280
 InP interface 279
 band-gap energies 160–1
 deformation potential 264
 effective masses 240, 241
 elastic properties 89, 90
 optical properties 316–17, 318
 Schottky barrier 293–4
- AlInAsSb
 band offsets, GaInAsSb interface 282
 band-gap energies 187, 188–9, 196
- AlInN
 band offsets, GaN interface 284
 band-gap energies 150, 152
 low-field mobility 368–9
 optical properties 313, 314
- AlInP
 band offsets
 AlGaInP interface 282
 GaInP interface 277–8
 band-gap energies 153–5
 deformation potential 262–3
 effective masses 238–9, 240
 optical properties 314–15
- AlInSb
 band-gap energies 165–6
 effective masses 242–3
 low-field mobility 369–70
 optical properties 319, 320
- alloy scattering 365
- alloys defined and described 1
- AIPAs
 band-gap energies 174–5
 effective masses 245
- AIPaSb
 band-gap energies 174–5
 effective masses 245
 optical properties 322
- Au/GaInP rectifiers 292
- band offsets *see* heterojunction band offsets
- band-gap energies
 background and theory
 bowing parameter 136
 interpolation of parameters 4–7
 ordered/disordered alloy 136–9
 quasi-cubic band model 133–6, 135
- group IV alloys
 binary 139–45
 ternary 145–7, 149
- III–V ternary alloys
 Al–(V, V) 174–5
 Ga–(V, V) 175–9
 In–(V, V) 179–84
 dilute-nitride III–(V, V) 166–74
 (III, III)–As 157–63
 (III, III)–N 149–53
 (III, III)–P 153–7
 (III, III)–Sb 163–6
 summary 183–4
- III–V quaternary alloys
 dilute-nitride 184–93
 (III, III, III)–V 193–5
 III–(V, V, V) 195
 summary 196–7
- II–VI ternary alloys
 Cd–(VI, VI) 210–12
 Zn–(VI, VI) 208–10
 (II, II)–O 197–8
 (II, II)–S 198–201
 (II, II)–Se 201–4
 (II, II)–Te 204–8
 summary 214–16
- II–VI quaternary alloys
 (II, II, II)–VI 213–14
 (II, II)–(VI, VI) 212–13
 summary 214–16
- BeCdSe
 band-gap energies 199, 201, 202
 optical properties 335
- BeCdTe, band-gap energies 199, 201, 202
- BeMgCdSe, band-gap energies 213–14

- BeMgZnSe
 band offsets, ZnSe interface 289
 band-gap energies 213, 214
 optical properties 346
 BeS/BeSe/BeTe, elastic properties 90–1, 93–4
 BeZnCdSe, optical properties 346
 BeZnO
 band-gap energies 197, 198, 199, 215
 optical properties 332
 BeZnSe
 band offsets, ZnSe interface 287–8
 band-gap energies 199, 201–2
 elastic properties 84–5, 86, 94
 optical properties 335, 336
 phonon frequencies 111, 118
 photoelastic constant 357
 BeZnTe
 band-energies 199, 201–2, 215
 band-gap energies 199, 204–5
 optical properties 339
 phonon frequencies 111
 bilayer model 34–5
 binary mixed valence compounds 2–4
 bond distances 21
 bowing parameters 5, 6, 7, 136
 dilute-nitride III–V alloys 167
 electron and hole mobilities 367
 III–V ternaries 184
 II–VI ternaries 215
 Brillouin scattering 357

 carrier transport properties 365–7
 high-field mobility 376–9
 impact ionization coefficient 382–6
 low-field mobility 367–76
 minority-carrier transport 379–82
 CdHgS, band-gap energies 199, 200–1
 CdHgSe
 band-gap energies 199, 201, 203–4, 215
 low-field mobility 374
 optical properties 338–9
 CdHgTe
 band offsets, CdTe interface 288–9
 band-gap energies 199, 208, 215
 Debye temperature 58–9
 effective masses 252, 254
 Frank–Keldysh effect 361
 impact ionization coefficient 386
 low-field mobility 375
 minority-carrier transport 382
 nonlinear optical constant 362
 optical properties 342
 phonon frequencies 109, 111
 specific heat 56
 thermal conductivity 74–5
 thermal expansion coefficient 63
 CdSeTe
 band-gap energies 211–12
 optical properties 346
 phase diagram 50
 CdSSe
 band-gap energies 210–11
 effective masses 253
 electro-optic constant 359–60
 Franz–Keldysh effect 360–1
 optical properties 344–5
 CdSTe
 band-gap energies 211
 lattice parameters 31
 optical properties 345
 phase diagram 49–50
 CGe
 band-gap energies 140–1, 147, 149
 optical properties 309
 chalcopyrite structures 14
 cleavage plane 41
 coherent epitaxy
 bilayer model 32–3
 critical thickness 37–9
 elastic strain and lattice deformation 33–7
 lattice-mismatch of dilute-nitrides 167–8
 compliance constants 81, 82–3
 composite structures *see* coherent epitaxy
 compound semiconductors 1, 10
 conduction band structure 133, 134
 critical thickness 37–9
 crystal density
 calculation 22
 data 18, 19
 crystal structure 2
 lattice constant/parameters 15–31
 random alloy 11
 spontaneous ordering 11–15
 CSi
 band offsets
 Si interface 276–7
 SiGe interface 277
 band-gap energies 139–40, 147–9
 Debye temperature 57–8
 effective masses 234–7
 elastic properties 89
 electro-optic constant 358

- CSi (*Continued*)
 Fröhlich coupling constant 130
 lattice mismatch in epilayers 35–6
 low-field mobility 367
 microhardness 92
 optical properties 308–9
 piezoelectric constant 125, 127
 thermal conductivity 66, 67
 thermal diffusivity 75–6
- CSiGe
 band offsets, Si interface 276–7
 band-gap energies 145–7
 minority-carrier transport 380
 optical properties 311
 Schottky barrier 291
- CuAu
 elastic properties 82
 electrical resistivity 365, 366
 lattice constant 15–16
 thermal resistivity 65–6, 365, 366
- CuAu-I structure 12, 14, 15, 66
- CuPt-B structure 12, 14, 15
 energy-band diagram 136, 137
- Debye temperature 52–3, 56–7
 group IV alloy 57–8
 III–V alloy 58
 II–VI alloy 58–9
- deformation potential (intervalley)
 group IV alloy 270–1
 III–V alloy 271–2
- deformation potential (intravalley)
 group IV alloy 259–61
 high-symmetry points 267–9
 III–V ternary alloy 261–6
 high-symmetry points 269–70
 III–V quaternary alloy 266
 II–VI quaternary alloy 266–7
- deformation potential (phonon) 121–3
- density-of-state effective mass 229, 232
- diamond structure 21
- dielectric constants 308
- dispersion 307
- drift velocities 365
- effective masses
 background and theory
 compositional dependence 254
 electron effective mass 229–30, 231
 hole effective mass 230–2, 233, 234, 235, 236
 interpolation scheme 232–4
 temperature and pressure
 dependence 254–6
 group IV binary alloys 234–8
 III–V ternary alloys
 Al–(V, V) 245, 246
 Ga–(V, V) 245–6
 In–(V, V) 246–7
 dilute-nitride III–(V, V) 243–5
 (III, III)–As 239–42
 (III, III)–N 238, 239
 (III, III)–P 238–9
 (III, III)–Sb 242–3
 III–V quaternary alloys
 dilute-nitride 248
 (III, III, III)–V 250–1
 (III, III)–(V, V) 248–50
 II–VI ternary alloys
 (II, II)–VI 251–3
 II–(VI, VI) 253
 II–VI quaternary alloys
 (II, II)–(VI, VI) 253–4
 elastic constants 81, 82–3
 group IV alloy 81
 III–V alloy 81, 83–4
 II–VI 84–6
 pressure effect 88
 and sound velocity 96–7
 temperature effect 86–8
 third-order constant 39
see also Young's modulus
 elastic strain 33–7
 elasto-optic effect 357–8
 electrical resistivity 365, 366
 electro-optic constants
 linear 358–60
 quadratic 360–1
 electron mobility *See* low-field mobility;
 minority-carrier transport
 elemental semiconductors 1, 2
 energy-band structure *see* band-gap energies;
 effective masses
 epitaxy *see* coherent epitaxy
 Franz–Keldysh effect 360–1
 Fröhlich coupling constant 129–31
 GaAsIn, phase diagram 46, 47
 GaAsInP
 specific heat 55
 thermal conductivity and diffusivity 75–6

- GaAsSb
 band-gap energies 178–9
 effective masses 246
 impact ionization coefficient 385
 optical properties 324
 phonon frequencies 100, 108
 Schottky barrier 295–6
 thermal conductivity 73
- GaInAs
 band offsets
 AlGaInAs interface 283
 AlInAs interface 280
 GaAs interface 284–6
 GaN interface 284
 InP interface 279–80
 band-gap energies 161, 163
 deformation potential 265
 effective masses 240, 241–2, 256
 elastic properties 89, 90
 impact ionization coefficient 383–4
 low-field mobility 377–8
 near neighbour distances 28
 optical properties 318–19
 phase diagram 46, 47
 piezoelectric constant 128
 Schottky barrier 294
 thermal conductivity 68, 69, 70
- GaInAsSb
 band offsets
 AlGaAsSb interface 282
 AlInAsSb interface 282
 GaSb/InP/InAs interfaces 281
 band-gap energies 196
 effective masses 249–50
 optical properties 328–30
 Schottky barrier 296–7
 thermal conductivity 70, 71, 72
- GaN
 band offsets, GaN interface 284
 band-gap energies 150, 151, 152–3
 and critical thickness 38
 deformation potential 262, 263
 low-field mobility 368, 376, 377
 near neighbour distances 28, 29
 optical properties 313–14
 phase diagram 47–8
 phonon frequencies 105–6
 piezoelectric constant 126–8
 thermal conductivity 68, 69, 70
- GaNAs
 band offsets, GaAs interface 286–7
 band-gap energies 166–7, 168, 185
 effective masses 248, 254, 256
 optical properties 326
- GaInNP
 band-gap energies 185
 optical properties 326
- GaInP
 band offsets
 AlGaInP interface 282–3
 AlInP interface 277–8
 GaAs interface 277
 band-gap energies 137–9, 155–7
 deformation potential 263
 effective masses 239, 240
 elastic properties 89, 90
 Franz–Keldysh effect 360
 impact ionization coefficient 383
 low-field mobility 369
 nonlinear optical constant 362
 optical properties 315–16
 phonon frequencies 100, 108, 115
 photoelastic constant 357
 Schottky barrier 292
 thermal conductivity 73
- GaInPAs
 band offsets, InP interface 280–1
 band-gap energies 187, 189–91, 196–7
 and coherent epitaxy 34–5, 38
 deformation potential 266, 267
 effective masses 248–9, 256
 elastic properties 81, 86, 87, 88, 96
 Fröhlich coupling constant 131
 impact ionization coefficient 385
 low-field mobility 372–3, 378–9
 microhardness 92–3, 94
 minority-carrier transport 381–2
 near neighbour distances 28, 29
 phonon frequencies 108
 piezoelectric constant 128–9
 Schottky barrier 296
 thermal conductivity 70, 71, 72
- GaInPSb, minority-carrier transport 381–2
- GaInSb
 band-gap energies 166, 167, 168
 effective masses 242–3
 elastic properties 81, 83, 85
 microhardness 93
 minority-carrier transport 381
 optical properties 319, 320
 phase diagram 46, 47
 phase transition 40–1

- GaInSb (*Continued*)
 phonon frequencies 107, 108
 Schottky barrier 294–5
 thermal conductivity 68, 69, 70
- GaNAs
 band offsets, GaAs interface 286
 band-gap energies 166–7, 168, 171–2
 and coherent epitaxy 36
 deformation potential 265–6
 effective masses 243–4
 impact ionization coefficient 384
 low-field mobility 371, 378
 mode Grüneisen parameter 121
 optical properties 321, 322
- GaNAsSb, band offsets, GaAs interface 287
- GaN_P
 effective masses 243
 optical properties 320–1
- GaN_P, band-gap energies 170–1
- GaN_PAs, band-gap energies 185–6
- GaN_Sb
 band-gap energies 172
 optical properties 321
- GaPAs
 band-gap energies 175–6
 deformation potentials 263–4, 266, 269–70
 effective masses 245, 246
 low-field mobility 371, 372
 optical properties 323–4
 phonon frequencies 108, 115, 116, 122–3
- GaP_Sb
 band-gap energies 176–7
 optical properties 324
 Schottky barrier 295
- GaSbAs, low-field mobility 371, 372
- GeSn
 band-gap energies 144–5, 147, 148
 optical properties 309–10
- Grimm–Sommerfeld rule 2–4
- Grüneisen parameter 119–21
 phonon deformation potential 121–3
- Hall mobilities 366, 367
- heterojunction band offsets 275
 group IV systems 275–7
 III–V lattice matched system
 ternary alloy 277–80
 quaternary alloy 280–3
 III–V lattice mis-matched system 283–7
 II–V systems 287–9
- HgSeTe, phase diagram 51
- high-field transport
 group IV 376
 III–V ternary alloys
 dilute-nitride III–(V, V) 378
 (III, III)–As 377–8
 (III, III)–N 376
 (III, III)–P 376–7
 III–V quaternary alloys 378–9
 II–IV alloys 379
- high-frequency dielectric constant 308
- hole effective mass 230–2, 233, 234, 235, 236
- hole mobilities 366, 367
- impact ionization coefficient
 group IV alloys 382
 III–V ternary alloys
 dilute-nitride III–(V, V) 384–5
 Ga–(V, V) 385
 In–(V, V) 385
 (III, III)–As 383–4
 (III, III)–N 382–3
 (III, III)–P 383
 (III, III)–Sb 384
 III–V quaternary alloys
 (III, III, III)–V 385
 (III, III)–(V, V) 385
 II–VI 386
- InAsSb
 band offsets, GaSb interface 280
 band-gap energies 181–3
 effective masses 247
 impact ionization coefficient 385
 low-field mobility 371, 372
 optical properties 325
- InGaAs, Fröhlich coupling 129
- InNAs
 band-gap energies 173
 effective masses 244–5
 low-field mobility 371
- InNP
 band-gap energies 173
 optical properties 322
- InNSb
 band-gap energies 174
 effective masses 245
- InPAs
 band-gap energies 179, 180
 Debye temperature 58
 effective masses 246–7, 255, 256

- low-field mobility 371, 372
- optical properties 324–5
- specific heat 54, 55
- thermal conductivity 70, 71
- InPAsSb
 - band-gap energies 195, 196
 - effective masses 250–1
- InPSb
 - band-gap energies 179–81
 - low-field mobility 371, 372
 - optical properties 325
- interpolation schemes
 - band-gap 4–7
 - effective masses 232–4
- intravalley/intervalley deformation potential
 - see* deformation potential
- ionicity 9, 10
- isotopic abundance 9
- lattice constants/parameters
 - Cu–Au alloy 15–16
 - group IV semiconductor 19–22
 - III–V semiconductor 22–9
 - II–VI semiconductor 29–31
 - non-alloyed semiconductors 16–19
- lattice strain/deformation/mismatch
 - see* coherent epitaxy
- lattice-matching data 22, 23, 24, 30
- linear electro-optic constant 358–60
- long-wavelength phonon *see* phonon
- low-field mobility 366, 367
 - group IV binary alloys 367–8
 - III–V ternary alloys
 - dilute-nitride III–(V, V) 370
 - Ga–(V, V) 371
 - In–(V, V) 371
 - (III–III)–As 369
 - (III–III)–N 368–9
 - (III–III)–P 369
 - (III–III)–Sb 369–70
 - III–V quaternary alloys
 - dilute-nitride 371–2
 - (III, III, III)–V 373–4
 - (III, III)–(V, V) 372–3
 - II–VI ternary alloys
 - Zn–(V, V) 375
 - (II, II)–O 374
 - (II, II)–Se 374–5
 - (II, II)–Te 375
- Luttinger's parameters 231, 233, 234
- Matthews–Blakeslee theory 38
- melting points 51, 52–3
 - see also* phase diagrams
- MgCdSe
 - band-gap energies 199, 201, 202–3, 215
 - low-field mobility 374–5
 - optical properties 337
- MgCdTe
 - band-gap energies 199, 206, 215
 - optical properties 340
- MgZnCdSe
 - band offsets, ZnCdSe interface 289
 - band-gap energies 214
 - optical properties 346–7
- MgZnO
 - band offsets, CdS interface 287
 - band-gap energies 197–8, 199, 215
 - and coherent epitaxy 37
 - deformation potential 267
 - effective masses 251–2
 - low-field mobility 374
 - minority-carrier transport 382
 - optical properties 332–3
 - phase diagram 48–9
- MgZnS
 - band-gap energies 198–9, 205
 - optical properties 333–4
- MgZnSe
 - band offsets
 - ZnCdSe interface 289
 - ZnSe interface 287–8
 - band-gap energies 199, 201, 202, 215
 - low-field mobility 374–5
 - nonlinear optical constant 362
 - optical properties 335–7
 - thermal expansion coefficient 63
- MgZnSeTe
 - optical properties 346
 - phonon frequencies 112
- MgZnSSe
 - band offsets, ZnSe interface 289
 - band-gap energies 212–13
 - effective masses 253–4
 - optical properties 346
 - phonon frequencies 111–12
- MgZnSTe, band-gap energies 212, 213
- MgZnTe
 - band-gap energies 199, 205–6, 215
 - optical properties 339–40
 - Schottky barrier 299

- microhardness
 group IV alloy 92
 III-V alloy 92-3
 II-VI alloy 93-6
- minority-carrier transport
 group IV alloys
 binary 379-80
 ternary 380
 III-V ternary alloys
 (III, III)-Ga 381
 (III, III)-N 380
 III-V quaternary alloys
 (III, III, III)-V 382
 (III, III)-(V, V) 381-2
 II-IV alloys 382
- mode Grüneisen *see* Grüneisen parameter
- molecular weight
 calculating 9-10
 non-alloyed semiconductor data 18, 19
- multilayer structures *see* coherent epitaxy
- nonlinear optical constant 361-2
- optical properties
 dielectric constants 308
 dispersion relations 307
 group IV alloys
 binary 308-11
 ternary 311
 III-V ternary alloys
 Al-(V, V) 322-3
 Ga-(V, V) 323-4
 In-(V, V) 324-6
 dilute-nitride III-(V, V) 320-2
 (III, III)-As 316-20
 (III, III)-N 311-14
 (III, III)-P 314-16
 III-V quaternary alloys
 dilute-nitride 326
 (III, III, III)-V 330-2
 (III, III)-(V, V) 326-30
 III-(V, V, V) 332
 II-VI ternary alloys
 Cd-(VI, VI) 344-6
 Zn-(VI, VI) 343-4
 (II, II)-O 332-3
 (II, II)-S 333-5
 (II, II)-Se 335-9
 (II, II)-Te 339-42
 II-VI quaternary alloys
 (II, II, II)-VI 346-7
 (II, II)-(VI, VI) 346
see also elasto-optic; electro-optic
- ordering *see* spontaneous ordering
- periodic table 2
- phase diagrams
 group IV alloys 45
 III-V alloys 45-8
 II-VI alloys 48-51
- phase transition, structural 39-41
- Phillips ionicity 9, 10
- phonon frequencies/modes 99-100, 101, 102, 104-5, 110
 group IV alloy 100-4, 112-13
 III-V alloy 104-9, 113-15
 II-VI alloy 109-12, 115-19
 mode Grüneisen parameter 119-21
 phonon deformation potential 121-3
 temperature and pressure dependence 112-19
- photoelastic coefficient 357-8
- piezoelectric semiconductors 97, 126
 stress and strain constants 125-9
- pseudomorphic epitaxy 37-9
- quadratic electro-optic constant 360-1
- reflectivity 307
- refractive index 307
- resistivity
 electrical 365, 366
 thermal 64, 65, 67, 68, 365, 366
- Schottky barrier 289-90
 group IV alloys 290-1
 III-V ternary alloys
 Ga-(V, V) 295-6
 (III, III)-As 292-4
 (III, III)-N 291
 (III, III)-P 292
 (III, III)-Sb 294-5
 III-V quaternary alloys
 (III, III, III)-V 297-9
 (III, III)-(V, V) 296-7
 II-VI ternary alloys
 Zn-(VI, VI) 300
 (II, II)-Te 299
- semiconductor types 1
- SiC 1, 2
 Franz-Keldysh effect 360
 phonon frequencies 100, 102

- SiGe
 band offsets, Si interface 276
 band-gap energies 148
 relaxed alloy 141–3
 strained alloy 143–4
 and critical thickness 38, 39
 crystal lattice parameters 19–22
 deformation potential 259–61, 269
 effective masses 237–8
 elastic properties 81, 84, 85
 electro-optic constant 358
 Fröhlich coupling constant 130
 impact ionization coefficient 382, 383
 low-field mobility 367–8
 minority-carrier transport 379–80
 optical properties 309–10
 ordered structures 12, 13–14
 phase diagram 45, 46
 phonon frequencies 100–4, 113, 121–2
 Schottky barrier 290–1
 specific heat 53–4
 thermal conductivity 66, 68
 SiGeSn, band gap energies 147
 SiSn, band gap energies 148–9
 sound velocity 96–7
 specific heat
 group IV alloys 51, 52–3, 53–4
 III–V alloys 54–5
 II–VI alloys 55
 spontaneous ordering
 energy-band gaps 136–9
 group IV alloy 11, 12
 III–V alloy 12, 14–15
 II–VI alloy 12, 15
 structural phase transition 39–41
 surface energy 41

 tetrahedral rule 3–4
 thermal conductivity 52–3, 63–6, 67
 group IV alloy 66–8
 III–V alloy 68–74
 II–VI alloy 74–5
 thermal diffusivity 75–6
 thermal expansion coefficient 52–3
 group IV alloys 59–61
 III–V alloys 61–3
 II–VI alloys 63
 thermal resistivity 64, 65, 67, 68,
 365, 366
 thin films *see* critical thickness
 transport *see* carrier transport

 valence band structure 133, 134
 valence binary compounds 3–4
 valence electrons 2–3
 Varshni parameters 159–60, 163
 Vegard law 20, 25–6, 28, 36, 37, 57, 141

 Wiedemann–Franz law 65, 365
 wurtxite structure 21

 Young’s modulus
 group IV alloy 89
 III–V alloy 89–90
 II–VI alloy 90–2

 zinc blende structure 21
 energy band diagram 136, 137
 ZnCdO
 band-gap energies 198, 199, 215
 optical properties 333
 ZnCdS
 band offsets, ZnS interface 287
 band-gap energies 199, 200, 215
 deformation potential 267
 nonlinear optical constant 362
 optical properties 334–5
 phase transition 40, 41
 phonon frequencies 109, 111
 ZnCdSe
 band offsets
 MgSSe interface 289
 MgZnCdSe interface 289
 MgZnSe interface 289
 ZnSe interface 287–8
 band-gap energies 199, 201, 203, 215
 elastic properties 91–2
 Franz–Keldysh effect 360–1
 nonlinear optical constant 362
 optical properties 337–8
 phase transition 40, 41
 phonon frequencies 109–11, 115–16, 118
 ZnCdSSe, band offsets, ZnSSe interface 289
 ZnCdTe
 band offsets
 CdTe interface 288
 ZnTe interface 288
 deformation potential 266–7
 elastic properties 85, 87, 88
 electro-optic constant 358–60
 lattice parameters 29, 30, 31
 phase diagram 49
 low-field mobility 375

ZnCdTe (*Continued*)

- nonlinear optical constant 361, 362
- optical properties 340–1
- phonon frequencies 109–11
- photoelastic constant 357
- Schottky barrier 299
- structural phase transition 39, 40

ZnHgS, band-gap energies 199, 200, 215

ZnHgTe

- band-gap energies 199, 207–8
- effective masses 252–3
- microhardness 94–5
- minority-carrier transport 382
- optical properties 342
- phonon frequencies 109
- thermal conductivity 74
- thermal expansion coefficient 63

ZnOS

- band-gap energies 208–9
- optical properties 343

ZnOSe

- band-gap energies 209
- deformation potential 267

ZnSeTe

- band-gap energies 209, 210
- elastic properties 91–2, 94
- low-field mobility 376
- optical properties 344
- phonon frequencies 118

ZnSSe

- band offsets, ZnSe/ZnCdSe interfaces 289
- band-gap energies 209–10
- deformation potential 267
- low-field mobility 376
- optical properties 343
- Schottky barrier 300
- thermal expansion coefficient 63

ZnSTe

- band-gap energies 209, 210
- deformation potential 267
- optical properties 343–4